DOE-BES Principal Investigators' Meeting

Physical Behavior of Materials

March 19-21, 2019

Gaithersburg Marriott Washingtonian Center

Gaithersburg, MD

Program and Abstracts

Chairs : Chia-Ling Chien, *Johns Hopkins Univ.* Shanhui Fan, *Stanford Univ.*

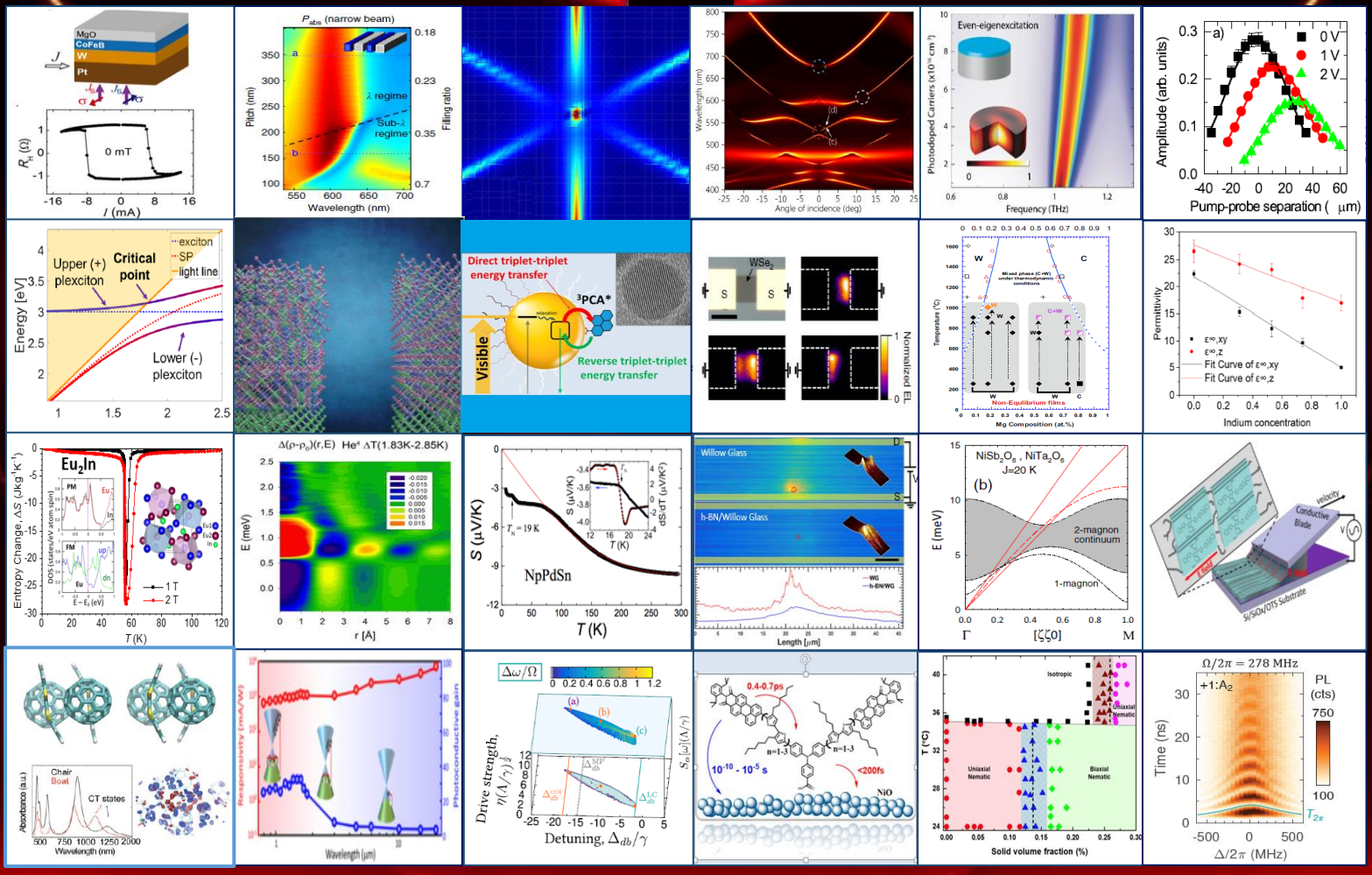

U.S. Department of Energy

Office of Science – Basic Energy Sciences

Division of Materials Sciences and Engineering

Cover Images:

1	2	3	4	5	6
7	8	9	10	11	12
13	14	15	16	17	18
19	20	21	22	23	24

1- Zero field switching of perpendicular ferromagnetic layers. C-L Chien
2- Effectiveness of anti-Hermitian coupling in a semiconductor nanobeam array with two beam widths. Maps of the spectral absorption of the narrow nanobeams versus array pitch. S. Fan
3- Complex vector of non-Abelian Berry connection in k_x, k_y plane. M. Stockman
4- The bound state in the continuum formation in the hybrid plasmonic-photonic system. A. Boltessaeva
5- Absorption (colormap) as a function of fluence and frequency for even eigenmodes of the metasurface. W. Padilla
6- Spin drag measurements for the determination of the spin-orbit. V. Sih
7- Molecular Emission near Metal Interfaces: The Polaritonic Regime . V. Menon
8- Growth of amorphous and epitaxial $ZnSiP_2$–Si alloys on Si. A. Tamboli
9- Strategy for generating deterministic TADPL processes at CdSe–PCA interfaces. M. Zamkov
10- Optical and EL image of a WSe_2 device, showing that emission is only observed near the grounded source contacts. A. Javey
11- A diagram for the phases of $Mg_xZn_{1-x}O$ alloy system. M. McCluskey
12- High frequency permittivity as a function of indium concentration in $(Bi_{1-x}In_x)_2Se_3$ films. S. Law
13- Giant magnetocaloric effect associated with magnetoelastic transformation in Eu2In. V. Pecharsky
14- Real-Space Dynamic Atom-Atom Correlation in Liquid Helium. T. Egami
15- The temperature dependence of Seebeck of NpPdSn. K. Gofryk
16- Heat Spreading by Hexagonal Boron Nitride, Li Shi
17- Approximate phonon and spin excitation spectra of the compounds, for momentum along the magnetic chains ($\zeta = qa/\pi$). J. Neumeier
18- Application of electric field effect to align solution-sheared polymer semiconductor molecules. Z. Bao
19- Chair- and boat structures of the DBTTF-C60 complex (top right and left). Calculated absorption spectra of DBTTF-C60 complexes. Charge-density isosurface plots of the CT states (HOMO to LUMO) as shown in the absorption spectra for the chair (blue) and boat (red) complexes (bottom right). S. Ren
20- Carrier Multiplication in Au-patched Graphene Nanoribbons, M. Jarrahi
21- Frequency Combs in a Lumped-Element Josephson-Junction Circuit. H. Tureci
22- Electron Transfer Kinetics of Dye-Sensitized NiO, Y. Wu
23- Phase diagram of the hybrid molecular-colloidal NLC exhibiting uniaxial nematic, isotropic, biaxial nematic, and colloidal uniaxial phases. I. Smalyukh
24- Time resolved photoluminescence, proportional to A_2 population, as a function of detuning Δ, showing oscillations between $|b) = |+1)$ and $|A2)$ ($\theta = 0$). D. Awschalom.

This document was produced under contract number DE-SC0014664 between the U.S. Department of Energy and Oak Ridge Associated Universities.

The research grants and contracts described in this document are supported by the U.S. DOE Office of Science, Office of Basic Energy Sciences, Materials Sciences and Engineering Division.

FOREWORD

This booklet is a collection of extended abstracts of the projects presented at the 2019 "Physical Behavior of Materials" Principle Investigators' meeting, and is sponsored by the Division of Materials Sciences and Engineering (DMS&E) of the Department of Energy, Office of Basic Energy Sciences (BES). The meeting is held on March 19–21, 2019, at the Gaithersburg Marriot Washingtonian Center, Gaithersburg, Maryland.

The Principle Investigators' meeting is organized to bring together all the principle investigators supported by the Physical Behavior of Materials program to facilitate exchange of ideas, promote collaborations and dissemination of the latest scientific knowledge and discoveries among participants. For BES and the participating investigators, it also serves the purpose of providing an overview and assessment of the whole program. The meeting also helps identify new research topical areas and future directions. This meetings brings together leading experts in topical areas of research supported by our program and is designed to stimulate and inspire new ideas.

The Physical Behavior of Materials program supports transformative, ground-breaking research activities in materials science and condensed matter physics. The primary mission of the program is to support fundamental science and use-inspired basic research that promise to advance our knowledge of material's physical behavior under external stimuli. The primary scientific interests of the program include electronic, electromagnetic, magnetic and thermal properties of materials, including novel light-matter interactions and quantum information sciences that are relevant to the Basic Energy Sciences mission. The program has a rich portfolio in many exciting, high-risk high-reward projects in both experimental and theoretical areas.

The 2019 Principle Investigators' meeting is chaired by Prof. Chia-Ling Chien of Johns Hopkins University and Prof. Shanhui Fan of Stanford University. The meeting brings together over 85 scientists and is organized to include 23 oral presentations in 10 oral sessions and 57 poster presentations in two sessions. The oral presentations are grouped in topics of similar research areas.

We gratefully acknowledge the contributions of all the attendees, and thank all investigators for sharing their exciting ideas and latest findings. We also gratefully acknowledge the outstanding support of Linda Severs from the Oak Ridge Institute for Science and Education, and Teresa Crockett of the DMS&E, and the staff of the Gaithersburg Marriot Washingtonian Center.

Refik Kortan, Ph.D.
Program Manager,
Division of Materials Sciences and Engineering
Office of Basic Energy Sciences
Department of Energy
March 2019

Table of Contents

Physical Behavior Principal Investigators Meeting
March 19–21, 2019
Gaithersburg Marriott Washingtonian, Gaithersburg, MD

Meeting Chairs:
Chia-Ling Chien (Johns Hopkins Univ.) and Shanhui Fan (Stanford Univ.)

Monday, March 18, 2019	
	*** Dinner (On your own) ***
Tuesday, March 19, 2019	
7:30 – 8:30 am	Registration & *** Breakfast***
8:30 – 8:40 am	**Welcome, *Meeting Chairs***
8:40 – 9:10 am	**"Division and Program Updates"** Linda Horton, *Director, Division of Materials Sciences and Engineering* Refik Kortan, *Program Manager, Physical Behavior of Materials*
Session I	***Chair: Chia-Ling Chien (Johns Hopkins Univ.)***
9:10 – 9:40 am	Mark Stockman *(Georgia State University)* *"Ultrafast Topological Phenomena in Two-Dimensional Materials, Topological Insulators, and Weyl Semimetals"*
9:40 – 10:10 am	Alexandra Boltasseva *(Purdue University)* *"Exploring Enhanced Light-Matter Interactions: From Near-Field Strong Coupling to Ultra-fast Single Photon Emission"*
10:10 – 10:30 am	*** Break ***
Session II	***Chair: Shanhui Fan (Stanford Univ.)***
10:30 – 11:00 am	Willie Padilla *(Duke University)* *"Metamaterials as a Platform for the Development of Novel Materials for Energy Applications"*
11:00 – 11:30 am	Steven Anlage (*University of Maryland*) *"Physical Behavior of Quantum Metamaterials"*

11:30 – 12:00 pm	Vanessa Sih *(University of Michigan)* *"Electron Spin Polarization in Large Electric Fields"*
12:00 – 1:30 pm	**Working Lunch (*poster introductions: session I*)**
Session III	***Chair: Harry Atwater (Caltech)***
1:30 – 2:00 pm	Stephen Forrest *(University of Michigan)* *"Organic Exciton-Polaritons in the Ultrastrong Coupling Regime"*
2:00 – 2:30 pm	Vinod Menon *(City College of New York)* *"Control of Molecular Excitations and Energy Transfer via Strong Light-Matter Coupling"*
Session IV	***Chairs: Chia-Ling Chien (JHU), Shanhui Fan (Stanford U.)***
2:30 – 5:30 pm	**Poster Session I**
5:30 – 6:30 pm	*** Dinner *(Scientific Highlights of the Day: Discussion and Input from Attendees)****
Session V	***Chair: Anton Malko (UT Dallas)***
6:30 – 7:00 pm	Adele Tamboli *(NREL)* *"Harnessing Order Parameter in Ternary II-IV-V_2 Semiconductors"*
7:00 – 7:30 pm	Mikhail Zamkov *(Bowling Green State University)* *"Semiconductor Excitonic Nanoshells for Energy Conversion Applications"*
Session VI	***Chairs: Chia-Ling Chien (JHU), Shanhui Fan (Stanford U.)***
7:30 – 9:30 pm	Continuation of Poster Session I

Wednesday, March 20, 2019

7:30 – 8:30 am	***Breakfast***
Session VII	***Chair: Chris Van de Walle (UCSB)***
8:30 – 9:00 am	Ali Javey *(LBNL)* *"Making Semiconductor Monolayers Perfectly Bright"*
9:00 – 9:30 am	Matthew McCluskey *(Washington State University)* *"Defects in Oxide Semiconductors and Ternary Alloys"*
9:30 - 10:00 am	Stephanie Law *(University of Delaware)* *"Unique Optical Excitations in Topological Insulators"*
10:00 – 10:30 am	*** *Break* ***
Session VIII	***Chair: Yet-Ming Chiang (MIT)***
10:30 – 11:00 am	Vitalij Pecharsky *(Ames Laboratory)* *"Extraordinary Responsive Magnetic Rare Earth Materials"*
11:00 – 11:30 am	Takeshi Egami *(ORNL)* *"Structure and Dynamics of Liquid and Glass in Real Space and Time"*
11:30 – 12:00 pm	Krzysztof Gofryk *(INL)* *"Exotic Magneto-Elastic Phenomena in Actinide Materials in High Magnetic Fields"*
12:00 – 1:30 pm	**Working Lunch (*poster introductions: session II*)**
Session IX	***Chair: Gang Chen (MIT)***
1:30 – 2:00 pm	Li Shi *(University of Texas at Austin)* *"Electronic Thermal Transport in h-BN/Graphene/h-BN Heterostructure"*
2:00 – 2:30 pm	John Neumeier *(Montana State University)* *"Quasi-One-Dimensional Transition-Metal Oxides and Sulfides — Growth of Single Crystals and Their Physical Properties"*
Session X	***Chairs: Chia-Ling Chien (JHU), Shanhui Fan (Stanford U.)***
2:30 – 5:30 pm	**Poster Session II**

5:30 – 6:30 pm	*** Dinner *(Scientific Highlights of the Day: Discussion and Input from Attendees)****

Session XI	***Chair: Ivan Smalyukh (University of Colorado)***
6:30 – 7:00 pm	Zhenan Bao (*Stanford University)* *"Tuning Organic Semiconductor Packing and Morphology through Non-equilibrium Solution Processing"*
7:00 – 7:30 pm	Shenqiang Ren *(University at Buffalo)* *"Organic Multiferroics: Strongly Correlated Molecular Solids"*

Session XII	***Chairs: Chia-Ling Chien (JHU), Shanhui Fan (Stanford U.)***
7:30 – 9:30 pm	Continuation of Poster Session II

Thursday, March 21, 2019

7:30 – 8:30 am	***Breakfast***

Session XIII	***Chair: Irfan Siddiqi (LBNL)***
8:30 – 9:00 am	Mona Jarrahi (*UCLA*) *"Room-Temperature Terahertz Detection with Quantum-Level Sensitivity through Plasmonic Photomixing"*
9:00 – 9:30 am	Hakan Tureci *(Princeton University)* "*Quantum Electrodynamic Modeling of Superconducting Circuits Far From Equilibrium*"
9:30 – 10:00 am	*** *Break* ***

Session XIV	***Chair: David Waldeck (University of Pittsburgh)***
10:00 – 10:30 am	Yiying Wu *(Ohio State University)* *"Interface Design and Machine Learning for Dye-Sensitized Solar Fuels and Halide Perovskites"*
10:30 - 11:00 am	Edward Flagg *(West Virginia University)* *"Spin-Selective Modification of Quantum Dot Energy Levels via the AC Stark Effect"*
11:00 – 11:30 am	Closing Remarks by Meeting Chairs and PM

Session I

DOE Award # DE-SC0007043

Georgia State University Research Foundation

Quantum Nanoplasmonics Theory

Mark I. Stockman, PI, Vadym Apalkov, co-PI

Date of Report: February 26, 2019

Research period covered by the Report is one year: 2018. Publications are of 2017-2018.

Overall during this period, the grant provided a major support acknowledged in publications of Refs. [1-8]. The following publications received a supplementary support from the grant for this period: Refs. [9].

1 Program Scope

This is a program of fundamental theoretical studies. The main focus is on ultrafast and strong field quantum phenomena in nanostructured and nanofilm solids induced by ultrashort and intense laser pulses.

2 Recent Progress

The following major subprojects comprise the results of this program to be presented:

2.1. Femtosecond Valley Polarization and Topological Resonances in Transition Metal Dichalcogenides [7]

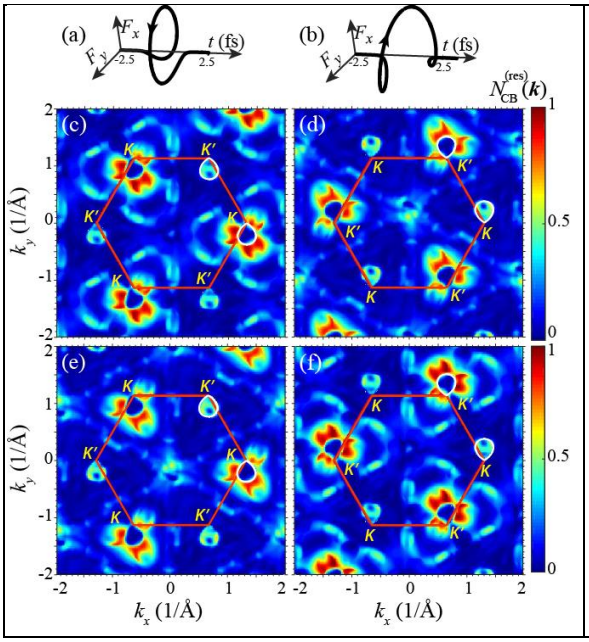

Fig. 1. Residual CB population $N_{CB}^{(res)}(\mathbf{k})$ for monolayer MoS_2 in the extended zone picture. The red solid line shows the first Brillouin zone boundary with K, K'-points indicated. The amplitude of the optical field is $F_0 = 0.25$ V/Å. (a) Waveform $\mathbf{F}(t)$ for right-handed circularly-polarized pulse. (b) The same as panel (a) but for left-handed circularly-polarized pulse [T-reversed to that in panel (a)]. (c) Residual population of spin-up electrons, $N_{CB\uparrow}^{(res)}(\mathbf{k})$, for right-handed pulse. (d) The same as (c), $N_{CB\uparrow}^{(res)}(\mathbf{k})$, but for left-handed pulse. (e) Residual population of spin-down electrons, $N_{CB\downarrow}^{(res)}(\mathbf{k})$, for right-handed pulse. (f) The same as (e), $N_{CB\downarrow}^{(res)}(\mathbf{k})$, but for left-handed pulse.

In this work, we theoretically introduce the fundamentally fastest induction of a significant population and valley polarization in a monolayer of a transition metal dichalcogenide (i.e., MoS_2 and WSe_2). This may be extended to other two-dimensional materials with the same hexagonal symmetry. This valley polarization can be written and read out by a pulse consisting of *just a single*

optical oscillation with a duration of a few femtoseconds and an amplitude of ~0.25 V/Å. Under these conditions, we predict an effect of *topological resonance*, which is due to the Bloch motion of electrons in the reciprocal space where the dynamic phase of the interband polarization is matched by the topological Berry phase. The electron population textures are formed in the reciprocal space due to the non-Abelian Berry curvature. The predicted phenomena can be applied for information storage and processing in PHz-band optoelectronics.

The field of a single-oscillation right-hand circular-polarized pulse is displayed Fig. 1(a) and the T -reversed, left-hand pulse in Fig. 1(b). The residual CB population for MoS_2 induced by such a pulse with an amplitude of $F_0 = 0.25 \text{VÅ}^{-1}$ is displayed in Figs. Fig. 1(c), (d) for spin-up ($s_z = 1/2$ or $\uparrow$) and Fig. 1(e), (f) for spin-down ($s_z = -1/2$ or $\downarrow$). Valley polarization is high: the right-handed pulse populates predominantly the K valleys, while the left-handed pulse excites mostly the K' valleys. Protected by the T -symmetry, the $K_\uparrow$-valley population for a given handedness pulse is inversed ($\mathbf{k} \leftrightarrow -\mathbf{k}$) to the $K'_\downarrow$-valley population for the opposite handedness; the same is true for $K_\downarrow$ and $K'_\uparrow$. Correspondingly, panel (c) is center-reflected to panel (f), and panel (d) to panel (e). The valley polarization is large, η_V ‰$40\% - 60\%$ for $F_0 = 0.1 - 0.25$ VÅ^{-1}. There is also an appreciable, though smaller, spin polarization due to SOC.

The selective valley population by a single optical oscillation and the texturing of the reciprocal space seen in Fig. 1 is fundamentally new effect that we called "*Topological Resonance*". It signature property is that in all cases when a given valley is favored by the angular momentum selection rules, its population predominantly occurs *outside* of a closed curve (called separatrix [10]). This is the case for K -valleys in Fig. 1 (c), (e) and for the K' -valleys in Fig. 1 (d), (f). In the opposite case, when the angular momentum selection rule suppresses a valley's population, then the momentum states inside the separatrix are predominantly but weakly populated as is the case for the K' -valleys in Fig. 1 (c), (e) and the K -valleys in Fig. 1 (d), (f). Formation of such textures is a fundamental effect, which is non-local in $\mathbf{k}$ and directly related to global topology of the Bloch bands. It is inherent in the strong-field excitation where an electron moves in the reciprocal space exploring the non-Abelian Berry connection, $A(\mathbf{k})$, along its Bloch trajectory.

A distinction of this work is that the significant CB population and valley polarization (along with a smaller spin polarization) can be written by a *single-oscillation* strong chiral pulse. The read-out can also be done by a single-oscillation chiral pulse: optical absorption of the read-out pulse of the same chirality will be reduced due to the Pauli blocking, while the opposite-chirality pulse absorption will not be attenuated because it interacts with the other, unpopulated valley. This one-optical-cycle recording and read-out make a basis of a fundamentally fastest optical memory.

The topological resonances can be present and pronounced not only in TMDC's but also in other materials with direct bandgap at the Brillouin zone boundary, e.g., hexagonal boron nitride et al. The topological resonances can also be present in materials where the direct bandgap is not at one of the T -invariant points such as the Γ -point or the M -points. The presence of the bandgap is essential because it causes a gradual accumulation of the non-Abelian Berry phase along the Bloch $\mathbf{k}$ -space electron trajectory, which is necessary to compensate the gradually accumulating dynamic phase.

The predicted induction of the valley polarization promises a wide range of important valleytronics applications, in particular, to PHz-band information processing and storage. The predicted topological resonance is a new concept, which will stimulate novel developments in topological strong-field optics of solids. In particular, the chiral, non-uniform electron distributions in the reciprocal space will cause chiral currents in the real space, which we will consider in the future.

2.2. Fundamentally Fastest Optical Processes at the Surface of a Topological insulator [8]

We have predicted that a single oscillation of a strong optical pulse can significantly populate the surface conduction band of a three-dimensional topological insulator (TI), Bi_2Se_3. Both linearly- and circularly-polarized pulses generate chiral textures of interference fringes of population in the surface Brillouin zones. These fringes constitute a self-referenced electron hologram carrying information on the topology of the surface Bloch bands, in particular, on the effect of the warping term of the low-energy Hamiltonian. These electron-interference phenomena are in a sharp contrast to graphene where there are no chiral textures for a linearly-polarized pulse and no interference fringes for circularly-polarized pulse. These predicted reciprocal space electron-population textures can be measured experimentally by time resolved angle resolved photoelectron spectroscopy (TR-ARPES) to gain direct access to non-Abelian Berry curvature at topological insulator surfaces.

Topological insulators (TI's) represent a modern class of crystalline materials where the bulk is semiconducting and the surfaces are semi-metallic. The Γ-point of the surface-state band is a Dirac point where the electron dispersion is gapless and linear as characteristic of Dirac fermions. In a good approximation, there is locking of spin and linear momentum caused by a strong spin-orbit interaction. This provides protection against back scattering and Anderson localization. The absence of the bandgap and, consequently, the linear electron dispersion at the Γ-point, are protected by time-reversal (T) symmetry. The Bloch bands near the Dirac point are chiral and carry the Berry phase of $\pm\pi$.

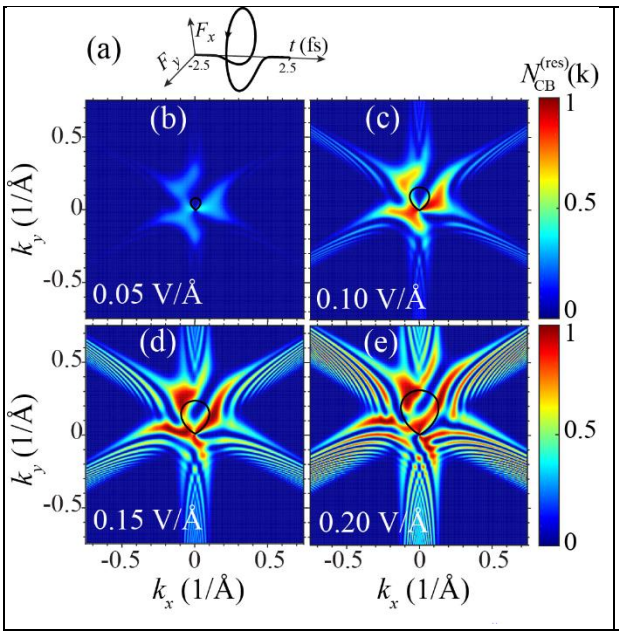

Fig. 2. Residual CB population as a function of crystal momentum. Excitation pulse is right-handed circularly polarized; its waveform is shown in panel (a). The amplitude of the pulse is (b) $F_0 = 0.05$ V/Å, (c) $F_0 = 0.10$ V/Å, (d) $F_0 = 0.15$ V/Å, and (e) $F_0 = 0.20$ V/Å. The solid closed black lines display the separatrices (see the text) for` the corresponding pulses.

For a single-oscillation right-hand circularly polarized pulse, residual CB population distributions in the reciprocal space are shown in Fig. 2 for several field amplitudes F_0. Here the residual CB population is also large for F_0 ‰0.1V/Å implying that the electron dynamics is highly irreversible. The CB population distribution shows a chiral pattern, which is correlated with the handedness of the pulse.

A solid closed black curve seen in Fig. 2 (b)-(e) is the separatrix [10]. This is defined as a set of initial points $\mathbf{q}$ for which electron trajectories pass precisely through the Dirac (Γ) point. Its parametric equation is $\mathbf{q}(t) = -\mathbf{k}(0,t)$, where $t \in (-\infty, \infty)$ is a parameter, and $\mathbf{k}(\mathbf{q},t)$ is a Bloch trajectory originating at a point $\mathbf{q}$. Thus, the separatrix is an electron trajectory starting at $\mathbf{k} = 0$ (i.e., at the Γ-point) and reflected in the xz-plane (P_{xz} - reflection). For initial crystal momentum $\mathbf{q}$ inside of the separatrix, the electron trajectory, $\mathbf{k}(\mathbf{q},t)$, encircles the Γ-point, otherwise it does not.

In a sharp contrast to graphene, in present model of TI, there are regions along the radial lines emanating from the Γ-point, where the non-Abelian Berry connection (dipole matrix element) is increased and possesses a non-trivial phase. These regions overlap in the vicinity of the Γ-point close to the separatrix. Consequently, the corresponding amplitudes of the VB$\rightarrow$CB transitions interfere causing the chiral pattern of interference fringes seen in Fig. 2. The separatrix itself is surrounded by regions of high CB population but not seen as a continuous arc in contrast to the case of graphene – cf. Ref. [10].

The electron interference patterns predicted in this work are self-referenced electron holograms that carry rich information about topological properties (the non-Abelian Berry phase) of the TI reciprocal space and the Bloch band dispersion (dynamic phase). Such self-referenced holograms can be measured using time-resolved angle-resolved photoelectron spectroscopy (TR-ARPES). In principle, it may be possible to restore the topology of the Bloch bands from these holograms. The asymmetric nature of the resulting carrier distribution will cause electric currents at the surfaces. We will consider these effects in the future.

3 Future Plans

We intend to further investigate behavior of solids in strong fields. The emphasis will be made on the fundamental problems related to the reduction of $\mathcal{P}$- and $\mathcal{T}$-symmetries of the solids by ultrafast strong fields. We will investigate such a novel problem as a strong field ultrafast imprinting of its symmetry on a two-dimensional solid causing a long-time chirality and currents, both electrical, spin-, and valley-currents. A number of such expected effects are related to the valley selectivity of such solids with respect to chiral (circular-polarized) exciting radiation. We also intend to study the anomalous Hall effect that appears in response to a pair of ultrashort pulsed: circularly and linearly polarized.

Another class of effects to be investigated is behavior of solids in combined strong stationary and optical fields. An example may be a sharp metal tip under a large positive bias subjected to a strong field of plasmon polaritons. Similar systems are studied and are of high interest for atomic probe tomography and microscopy (APT-M). Finally, based on recent published results and our own work on the spaser biomedical applications [11], we will aim at an explanation and theory of extraordinary sensitivity of a generating spaser to its environment, which allows one to use spasers for ultrasensitive environmental and biomedical probes.

4 Publications Resulting from the Grant in 2017-2018

1. V. E. Babicheva, S. Gamage, M. I. Stockman, and Y. Abate, *Near-Field Edge Fringes at Sharp Material Boundaries*, Opt. Expr. **25**, 23935-23944 (2017).
2. D.-B. Li, X.-J. Sun, Y.-P. Jia, M. I. Stockman, H. P. Paudel, H. Song, H. Jiang, and Z.-M. Li, *Direct Observation of Localized Surface Plasmon Field Enhancement by Kelvin Probe Force Microscopy*, Light Sci Appl. **6**, e17038-1-7 (2017).
3. S. A. O. Motlagh, J.-S. Wu, V. Apalkov, and M. I. Stockman, *Ultrafast Control of Electron Dynamics in 3d Topological Insulator*, Journal of Physics: Conference Series **906**, 012012 (2017).
4. S. A. Oliaei Motlagh, V. Apalkov, and M. I. Stockman, *Interaction of Crystalline Topological Insulator with an Ultrashort Laser Pulse*, Phys. Rev. B **95**, 085438-1-8 (2017).
5. J. Schötz, B. Förg, M. Förster, W. A. Okell, M. I. Stockman, F. Krausz, P. Hommelhoff, and M. F. Kling, *Reconstruction of Nanoscale near Fields by Attosecond Streaking*, IEEE J. Sel. Top. Quant. Elec. **23**, 1-11 (2017).
6. M. S. Wismer, M. I. Stockman, and V. S. Yakovlev, *Ultrafast Optical Faraday Effect in Transparent Solids*, Phys. Rev. B **96**, 224301-1-7 (2017).
7. S. A. Oliaei Motlagh, J.-S. Wu, V. Apalkov, and M. I. Stockman, *Femtosecond Valley Polarization and Topological Resonances in Transition Metal Dichalcogenides*, Phys. Rev. B **98**, 081406(R)-1-6 (2018).
8. S. A. Oliaei Motlagh, J.-S. Wu, V. Apalkov, and M. I. Stockman, *Fundamentally Fastest Optical Processes at the Surface of a Topological Insulator*, Phys. Rev. B **98**, 125410-1-11 (2018).
9. F. Nematollahi, V. Apalkov, and M. I. Stockman, *Phosphorene in Ultrafast Laser Field*, Phys. Rev. B **97**, 035407-1-6 (2018).
10. H. K. Kelardeh, V. Apalkov, and M. I. Stockman, *Attosecond Strong-Field Interferometry in Graphene: Chirality, Singularity, and {Berry} Phase*, Phys. Rev. B **93**, 155434-1-7 (2016).
11. E. I. Galanzha, R. Weingold, D. A. Nedosekin, M. Sarimollaoglu, J. Nolan, W. Harrington, A. S. Kuchyanov, R. G. Parkhomenko, F. Watanabe, Z. Nima, A. S. Biris, A. I. Plekhanov, M. I. Stockman, and V. P. Zharov, *Spaser as a Biological Probe*, Nat. Commun. **8**, 15528-1-7 (2017).

Exploring Enhanced Light-Matter Interactions: From Near-Field Strong Coupling to Ultra-Fast Single Photon Emission

Alexandra Boltasseva, Vladimir M. Shalaev, and Zubin Jacob
School of Electrical & Computer Engineering and Birck Nanotechnology Center, Purdue University, West Lafayette, Indiana 47907, United States

Program Scope

This project aims at exploring unusual light-matter interaction regimes by utilizing advanced nanophotonic designs and novel photonic materials with unconventional optical properties that enable exploration of new optical phenomena. The scope of the project spans three parts. The first is to utilize so-called epsilon-near-zero media (in other words, materials with extremely low index of refraction) to study fundamental optical phenomena. The second is to utilize plasmonic nanoantennas to realize high-speed room-temperature on-demand single photon sources. Our third goal is to investigate novel resonant phenomenon known as bound states in the continuum that can achieve theoretically infinite quality factors in open structures.

Epsilon-near-zero (ENZ) media are an emerging class of nanophotonic materials that engender electromagnetic fields with small phase variation due to their close-to-zero permittivity (and hence, extremely low index of refraction), leading to extraordinary light-matter interaction regime and new optical effects. We use naturally occurring, homogeneous ENZ media namely transparent conducting oxides (TCOs) such as aluminum doped zinc oxide (AZO), with low losses near the ENZ crossover, to study fundamental optical phenomena such as strong-coupling, near-field suppression, degenerate optical nonlinear enhancement, and optical time-reversal.

A room-temperature, high-speed, on-demand single-photon source is highly desirable for the realization of emerging quantum networks that hold a promise for unconditionally secure communication and distributed quantum computing. In many ways, practical success for quantum photonics hinges on the availability of suitable single-photon sources. Plasmonic nanoantennas are attractive alternatives to photonic cavities for speeding up spontaneous quantum emission at room temperature because rather than relying on a high-quality factor, these nanoantennas act by deep subwavelength confinement of the optical modes. This approach results in a much faster quantum device operation. In addition, spontaneous decay rates in quantum emitters coupled to such broadband and ultrafast plasmonic cavities can be sped up sufficiently to beat decoherence rates in matter at room temperature.

Bound states in the continuum (BICs) are eigenstates of the wave equation that coexist with the radiation continuum; however, they stay fully localized with theoretically infinite lifetimes and quality factors[1]. Such exceptional states have been repeatedly realized in dielectric systems without material loss to avoid the collapse of the BIC states due to losses[2]. Our design

overcomes this obstacle by operating in the strong coupling regime between photonic modes in a dielectric slab waveguide and plasmonic modes in a metallic grating. The strong coupling significantly alters the band diagram of the hybrid system giving rise to a plethora of rich physics such as slow light.

Recent Progress

For the first part of our project, we are building upon our work on the resonance pinning of gold antennae near ENZ[3]. We have demonstrated dispersive, less than unity index plasmon modes with gold antennas on an AZO substrate with a near-infrared ENZ point. We demonstrated that the resonance of dimer antennas has a reduced red-ship with diminishing gap sizes because of suppressed near-field interactions, as shown in Fig. 1(a). We developed a robust and accurate semi-analytic FP model to calculate electromagnetic near fields, dispersion, and resonances of single nanorod antennas on arbitrary substrates[4].

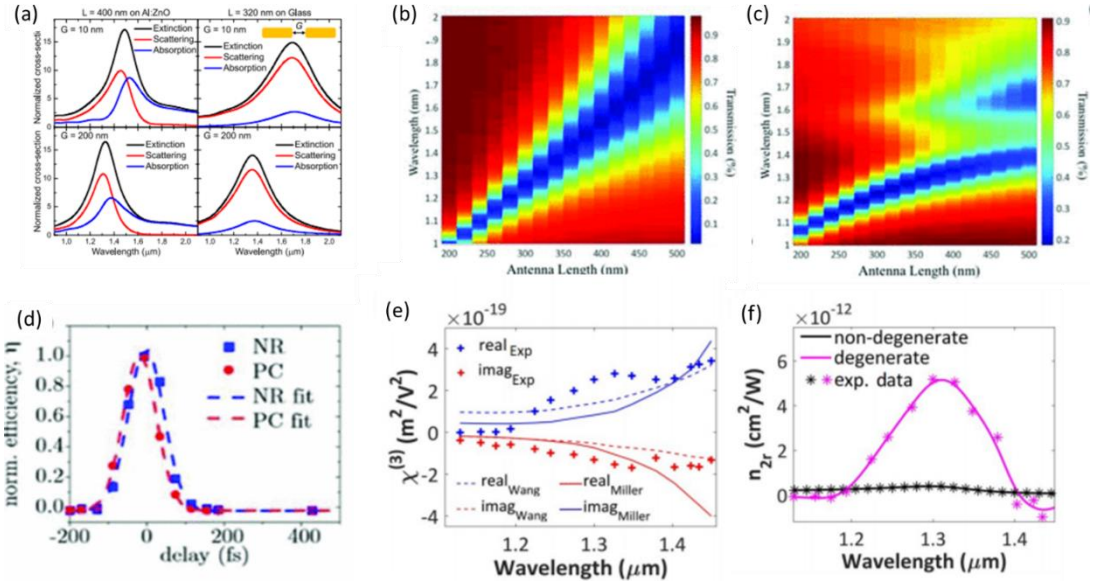

Figure 1 (a) Calculated scattering, extinction, and absorption cross sections of dimer antennas on both Al:ZnO (left column) and glass (right column) substrates. (b) Calculated transmission spectrum of gold antennas of varying length and incident wavelength for a simple glass substrate and c) for antennas on 23 nm AZO film on glass (d) Normalized PC and NR signals as a function of the temporal delay between the pump and probe beams. (e) Real and imaginary part of the measured nonlinear susceptibility $\chi^{(3)}$ (f) Comparison between the nonlinear Kerr coefficient n_{2r} for the degenerate case ($\lambda_{pump} = \lambda_{probe}$) and for the non-degenerate case ($\lambda_{pump} = 787$ nm) as a function of λ_{pump}.

We have observed strong-coupling signatures in plasmonic antennas fabricated on an ultrathin film of AZO[5]. Gold nanorod antenna have an approximately linear dispersion when excited with light polarized along the longitudinal axis (Fig 1(b)). However, the same antennae fabricated on a 23-nm layer of AZO show two distinct resonances which are split at the ENZ frequency of 1400 nm (Fig 1 (c)). We attribute this splitting to a strong coupling between the resonance of the antenna and the underlying ENZ film. Using thick Al-doped zinc oxide films we provided evidence of an extremely efficient time reversed surface. We observed phase-conjugate and negative refracted

waves in four-wave mixing experiments, shown in Fig 1(d). We observed both singles at efficiencies >200% for wavelengths near the ENZ point. We attribute this enhancement to the growth of the effective wavelength inside the AZO film $X_{eff} = \lambda_0/\eta$ which guarantees the subwavelength phase-matching condition and the nonlinear enhancement of nonlinear processes[6]. Finally, we report the increase of third-order nonlinear susceptibility $\chi^{(3)}$ and nonlinear Kerr-coefficient (Fig 1(e), (f)). A 6-fold enhancement in the third-order nonlinear susceptibility and over one order of magnitude increase in the nonlinear Kerr coefficient[7] is observed.

Following the second direction of our research, we recently realized efficient plasmon-enhanced devices based on the outlined principles include ultrabright room-temperature single-photon sources[8] and a high-efficiency hybrid plasmonic bullseye antenna[9]. In the first part, we employed nanoantennas made entirely from crystalline silver, a plasmonic material with record-low optical losses in the visible range. By embedding photostable single nitrogen-vacancy (NV) centers in nanodiamonds into these nanoantennas, we achieved room-temperature emissions topping at 30 million detected photons per second. Combining a similar design with controlled nanoantenna fabrication, we recently achieved the shortest fluorescence lifetime in NV centers to date and demonstrated that the NV spin coherence time is of the same order in the coupled and uncoupled configurations. In the second part, we have proposed and realized a design that combines low antenna loss, directional emission, and substantial decay rate enhancement, leading to a theoretical collection efficiency of 85% for a 0.9 NA objective and acceleration of the emission rate by a factor of 18, at the design wavelength of 670 nm.

In the final section of the project, we designed a hybrid system that comprises a dielectric slab waveguide coupled to a plasmonic grating. Strong coupling between the plasmonic and the photonic modes is realized with Rabi splitting of 150 meV[10]. At the BIC points, the radiation into free space is inhibited, and therefore the quality factors of the hybrid plasmonic-photonic modes around BICs are only metal loss limited. We can observe three types of BICs supported by the hybrid system: photonic symmetry-protected BIC, plasmonic symmetry-protected BIC, and Friedrich-Wintgen BICs. The symmetry-protected BICs appear at the normal incidence due to the incompatibility with the radiation modes. The Friedrich-Wintgen BICs appear at the vicinity of the avoided-crossing of the strongly-coupled modes due to destructive interference of the resonances at the correct phase-matching conditions. Due to the ability to control the interference between the modes, we can engineer the optical bandgap in the hybrid system as well as observe spectral bands of slow light. We observe three slow light bands that are centered at 550 nm, 577 nm, and 595 nm, with angular bandwidths of 8°, 5°, and 5°, respectively.

Future Plans

For the first part of our project, we will extend our studies further to design arrays of independently operating antennas with spectral responses invariant with antenna shape and dimensions. We plan on carrying out four-wave-mixing experiments utilizing strong-coupling to

enhance nonlinear responses. It is possible to use high nonlinearities of thick AZO films to manipulate optical pulse spectra for applications in ultrafast beam steering and wavefront shaping.

Regarding quantum single-photon sources, we believe that plasmonic cavities have the potential to transform the way quantum photonic systems operate. Immediate research opportunities lie in the construction of a room-temperature on-demand source of indistinguishable photons operating at THz rates[11]. Producing single indistinguishable photons at such high rates and at room temperature would strongly expedite long-distance quantum communication with portable chip-scale devices. Another important advancement offered by the plasmonic speed-up would be to perform a single-shot readout of the electron spin in single diamond color centers, which are regarded as viable candidates for implementing both quantum memories for photons and quantum registers for spin-based quantum logic.

For the third direction of our project concerning bound states in the radiation continuum, we plan on utilizing the immense field localization near the BIC points to enhance third order nonlinearities[12]. This, along with the capability to engineer the spectral response and the bandgap can be of vital importance in enhancing nonlinear light-matter interactions. Our plans include fabrication and experimental linear characterization of the hybrid plasmonic-photonic structure. Next steps will include nonlinear characterization of the device coupled to nonlinear organic dyes.

References

1. Marinica, D. C., Borisov, A. G., & Shabanov, S. V. Bound states in the continuum in photonics. *Physical review letters*, **100**, 183902 (2008).
2. Hsu, C. W., Zhen, B., Stone, A. D., Joannopoulos, J. D., & Soljačić, M. Bound states in the continuum. *Nature Reviews Materials*, **1**, 16048 (2016).
3. Kim, J. *et al.* Role of epsilon-near-zero substrates in the optical response of plasmonic antennas. *Optica* **3,** 339 (2016).
4. DeVault, C. T. *et al.* Suppression of near-field coupling in plasmonic antennas on epsilon-near-zero substrates. *Optica* **5,** 1557 (2018).
5. DeVault, C. *et al.* Low-Index Materials for Enhanced Optical Nonlinearities. in *2018 12th International Congress on Artificial Materials for Novel Wave Phenomena (Metamaterials)* 474–476 (IEEE, 2018). doi:10.1109/MetaMaterials.2018.8534086
6. Vezzoli, S. *et al.* Optical Time Reversal from Time-Dependent Epsilon-Near-Zero Media. *Phys. Rev. Lett.* **120,** 043902 (2018).
7. Carnemolla, E. G. *et al.* Degenerate optical nonlinear enhancement in epsilon-near-zero transparent conducting oxides. *Opt. Mater. Express* **8,** 3392 (2018).
8. Bogdanov, S. I. *et al.* Ultrabright Room-Temperature Sub-Nanosecond Emission from Single Nitrogen-Vacancy Centers Coupled to Nanopatch Antennas. *Nano Letters* **18**, 4837 (2018).
9. Andersen, S. K. *et al.* Hybrid plasmonic bullseye antennas for efficient photon collection. *Acs Photonics*, **5**, 692 (2018).
10. Azzam, S.I., Shalaev, V.M., Boltasseva, A. and Kildishev, A.V. Formation of bound states in the continuum in hybrid plasmonic-photonic systems. *Physical review letters*, **121,** 253901 (2018).

11. Wein, S., Lauk, N., Ghobadi, R. & Simon, C. Feasibility of efficient room-temperature solid-state sources of indistinguishable single photons using ultrasmall mode volume cavities. *Physical Review B* **97**, (2018).
12. Kodigala, A., Lepetit, T., Gu, Q., Bahari, B., Fainman, Y., & Kanté, B. Lasing action from photonic bound states in continuum. *Nature*, **541**, 196 (2017).

Publications

1. DeVault, C. T. *et al.* Suppression of near-field coupling in plasmonic antennas on epsilon-near-zero substrates. *Optica* **5,** 1557 (2018).
2. DeVault, C. *et al.* Low-Index Materials for Enhanced Optical Nonlinearities. in *2018 12th International Congress on Artificial Materials for Novel Wave Phenomena (Metamaterials)* 474 (IEEE, 2018). doi:10.1109/MetaMaterials.2018.8534086
3. Vezzoli, S. *et al.* Optical Time Reversal from Time-Dependent Epsilon-Near-Zero Media. *Phys. Rev. Lett.* **120,** 043902 (2018).
4. Carnemolla, E. G. *et al.* Degenerate optical nonlinear enhancement in epsilon-near-zero transparent conducting oxides. *Opt. Mater. Express* **8,** 3392 (2018).
6. Bogdanov, S. I. *et al.* Ultrabright Room-Temperature Sub-Nanosecond Emission from Single Nitrogen-Vacancy Centers Coupled to Nanopatch Antennas. *Nano Letters* **18**, 4837 (2018).
7. Andersen, S. K. *et al.* Hybrid plasmonic bullseye antennas for efficient photon collection. *Acs Photonics*, **5**, 692 (2018).
8. Bogdanov, S. *et al.* Ultrabright Room-Temperature Emission from Single Plasmon-Enhanced Nitrogen-Vacancy Centers in Diamond. in *Conference on Lasers and Electro-Optics* FTu4E.6 (OSA, 2018). doi:10.1364/CLEO_QELS.2018.FTu4E.6
9. Bogdanov, S. *et al.* Deterministic integration of single nitrogen-vacancy centers into nanopatch antennas. arXiv:1902.05996
10. Azzam, S.I., Shalaev, V.M., Boltasseva, A. and Kildishev, A.V. Formation of bound states in the continuum in hybrid plasmonic-photonic systems. *Physical review letters*, **121,** 253901 (2018).

Session II

Metamaterials as a Platform for the Development of Novel Materials for Energy Applications

Willie J. Padilla, Duke University

Program Scope

The program is focused on exploration of the fundamental properties of metamaterials (MMs) / metasurfaces and their potential for control of energy at the sub-wavelength scale in support of the mission of the Department of Energy and the office of Basic Energy Sciences. Electromagnetic metamaterials provide a platform for the discovery and design of new materials with novel structures, functions, and properties. The program will advance the knowledge base of these materials through fundamental investigations of the experimental and theoretical properties of metamaterials for the discovery, prediction and design of new materials with novel structures, functions, and properties. The proposed research activities emphasize a complete basic research program including the conceptual / computational design, fabrication / synthesis of the materials, and the characterization and analysis of their electromagnetic properties.

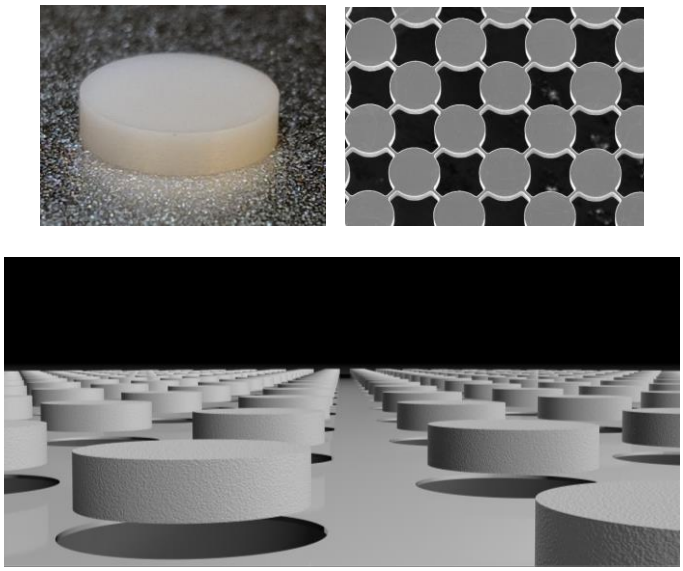

Figure 1. Top left shows an all-dielectric silicon terahertz metamaterial absorber fabricated on a polymer substrate. Top right shows a different all-dielectric terahertz metamaterial absorber. Bottom shows isometric cutaway view of a

Recent Progress

We have recently investigate the physics underlying absorption in all-dielectric metasurfaces. The material system explored consisted of a metasurface composed of silicon cylindrical particles arranged in a square array on a lossless substrate. Our approached utilized both temporal coupled mode theory (CMT) [1] and waveguide theory [2], as well as S-parameter and eigenvalue simulations. The main finding from CMT is that the absorption process in all-dielectric metasurfaces achieves critical coupling between the radiative loss (γ) and material loss (δ). Waveguide theory indicated that hybrid electric (EH_{111}) and hybrid magnetic (HE_{111}) modes can be excited within the particles, and their existence is determined entirely by the

geometry of the cylindrical resonators. Solving for the wave equation in cylindrical coordinates and using appropriate boundary conditions for the cylinder allowed us to obtain analytic formulas specifying the specific dependence of the modes on geometry. For the EH_{111} mode we use a perfect magnetic wall for the side-wall boundary and non-perfect magnetic wall for the top and bottom, [3] which yield,

$$J_1(k_r r) = 0 \tag{1}$$

$$\tan\left(\frac{k_z}{h}\right) = \frac{k_{z0}}{k_z} \tag{2}$$

where r and h are the radius and height of the cylinder, respectively, and the cylindrical axis is along the z-direction and k_z and k_r are the components of the k-vector along the z and r directions, respectively, within the cylindrical particle, and k_{z0} is the k-vector in the z-direction in free-space. The k-vectors satisfy the relationships $k_z^2 = k_0^2\varepsilon_{1r} - k_r^2$ and $k_{z0}^2 = k_0^2 - k_{r0}^2$, where $k_0 = \omega/c$ is the wavenumber in free-space, and ε_{1r} is the real part of the relative permittivity of the cylinder, related to the index of refraction by $n = \sqrt{\varepsilon_{1r}}$. The HE_{111} mode is described by,

$$\left[\frac{J_1{\prime}(u)}{uJ_1(u)} + \frac{K_1{\prime}(v)}{vK_1(v)}\right]\left[\varepsilon_{1r}\frac{J_1{\prime}(u)}{uJ_1(u)} + \frac{K_1{\prime}(v)}{vK_1(v)}\right] = \frac{k_z^2}{k_0^2}\left(\frac{1}{u^2} + \frac{1}{v^2}\right)^2 \tag{3}$$

$$k_z h = \pi \tag{4}$$

where $u = k_r r$ and $v = k_{r0} r$, where k_0 and k_{r0} are the incident and radial components of the wavevector in free-space, and $J_1(u)$ is the first order Bessel function of the first kind, and $K_1(v)$ is the first order modified Bessel function of the second kind, and prime denotes derivative with respect to the arguments.

The first non-trivial solution to Eq. (1) gives the radius and the height is determined by Eq. (2) for the EH_{111} mode, while radius and height for the HE_{111} mode are found from Eqs. (3) and (4). The frequencies of the two modes are degenerate when the ratio of radius to height is – from using Eqs. (1) and (4) – we find,

$$\frac{r}{h} = 1.22\frac{n}{\sqrt{n^2-1}} \tag{5}$$

We thus find that – for large refractive index – the hybrid electric and magnetic modes can be made to overlap in frequency when the ratio of the radius to height is equal to 1.22.

The radiative loss, however, is determined by the total geometry of the system, i.e. the radius, height, and periodicity. The perfect absorptive state is achieved by increasing the material loss of the cylindrical resonators, by adding dopants, until we reach critical coupling, i.e. $\gamma = \delta$. Eigenvalue simulations determined the radiative and material loss rates for each hybrid mode, and found that – as expected – they are all approximately equal, with a value of $24.5 \times 10^9\ 1/s$.

Further, eigenvalue simulations found resonant frequencies of 1.0440 THz and 1.0512 THz for the EH_{111} and HE_{111} modes, respectively, indicating that they are approximately degenerate. We also engaged in S-parameter simulations, where the all-dielectric metasurface was excited from two ports spaced equidistantly on either side of the resonator along the cylindrical axis direction. Radiation from the two ports could be driven in phase, where the electric fields at the center mirror plane of the resonator are parallel, which drives the EH_{111} even mode. The radiation can also be made to be anti-parallel at the mirror plane, which drives the HE_{111} odd mode. From exciting each mode separately, we found that each hybrid mode accounted for 50% of the total absorption, and that the two modes are uncoupled.

In related work we designed two different types of resonators – one with degenerate hybrid modes, and another where the resonance frequencies of the hybrids modes where shifted with respect to each other. We use CMT and a scattering matrix formalism to investigate the differences between these two absorbers. We found that in the degenerate case, that the theory predicted a null scattering matrix – what we term a zero rank absorber (ZRA) – shown in the top left of Fig. 1. The other case we found that the scattering matrix is not null, and we term this a coherent perfect absorber (CPA). [4] Thus in order for the CPA to absorb incident light, the fields must possess a particular symmetry, whereas the ZRA can absorb all incident light regardless of its coherent – or lack of – state.

In other work we studied a so-called bound-state-in-the-continuum (BIC), which results in the occurrence of infinitely high quality factor resonances with energies lying above the light line, which may be realized in photonic systems consisting of dielectric metasurfaces. We fabricated a low-loss silicon free standing metasurface (top right of Fig. 1) which supports various high Q-factor BIC modes. Our investigation focused on one particular mode which realizes a minimum in reflection closely followed by a minimum in transmission in frequency. At normal incident, the BIC mode may not be coupled to, as it is symmetry protected. However, by using off-normal light, we can break the symmetry of the system and couple to the high Q BIC. We engaged in s-parameter and eigenvalue simulations which found that the metasurface supports a surface leaky mode, which gets band-folded at the Brillouin zone and returns to the zone center at frequency of the BIC resonance. The leaky mode cannot be driven at normal incidence, and thus oblique incident light is needed to drive the mode and thus the BIC. The low loss metasurface was fabricated by deep reactive ion etching in silicon – see top right of Fig. 1. The BIC mode can be observed in transmission and through photodoping, we demonstrate dynamical control over the bound-states-in-the-continuum resonance quality factor – changing by over two orders of magnitude.

Future Plans

We will continue to develop the theory of all-dielectric metasurface absorbers and emitters. This will include their connection to Mie scattering and the Kerker conditions for zero back scattering (ZBS) and zero forward scattering (ZFS). We are currently investigating using

perturbation theory to explore multiple unit cell dielectric metasurfaces, due to the fact that – unlike metal-based metasurfaces – all-dielectric metasurfaces exhibit strong neighbor coupling. This coupling leads to the occurrence of many modes in a given spectral range for multiple unit cell structures, and is not simply additive spectral features as with metal-based metamaterials.

Another area of exploration is that of higher quality factor bound-states-in-the-continuum. The Q-factor of the BIC resonance supported by metasurfaces scales as $Q \sim N^2$, where N is the number of metasurface unit cells in the array. We are thus exploring – what we are calling – Born-von Karman BICs. These are resonators which lie upon the circumference of a large circle, such that modes that are excited in them, may propagate around multiple times. Thus the array is equivalent to an array of infinite size and we expect that this configuration should reach extremely high Q-factors. We also plan to explore the dependence of the high Q modes on whether there are an odd or even number of resonators in the array. We expect that the symmetry of the mode should be different for even an odd resonator numbers and will explore this dependence in detail. Further, for BICs that have N limited quality factors, this will allows one to achieve higher Q's. We will also explore the time dependence of the leaky surface wave that is responsible for the BIC, such as the velocity of this wave and its dependence on the number of resonators on the circumference, i.e. even or odd number.

Another area of future work involves achieving multiple different types of unit cell all-dielectric metasurfaces. As mentioned, there is significant interaction between the unit cells of all-dielectric resonators. Thus the net electromagnetic response of a multi-unit cell system is not additive in the spectrum. We are thus exploring randomizing placement of the different types of unit cells, rather than – for example – using a bipartite checker board type pattern. Although this configuration does not mitigate the nearest neighbor interactions, it eliminates the band folding and overlap due to having multiple length scales in a bipartite lattice. The goal is to achieve broad control of the emitted energy from surfaces by using multiple unit cell all-dielectric emitters that is rationally designable.

References

1. Haus, Hermann A. Waves and Fields in Optoelectronics. Englewood Cliffs, NJ :Prentice-Hall, 1984.

2. E. Snitzer and H. Osterberg, *Observed dielectric waveguide modes in the visible spectrum*, Journal of the Optical Society of America, 51 499 (1961).

3. P. Guillon and Yves Garault, *Accurate Resonant Frequencies of Dielectric Resonators*, IEEE Transactions on Microwave Theory and Techniques, MTT-25, 916 (1977).

4. Y. Chong, Li Ge, Hui Cao, A. Stone, *Coherent Perfect Absorbers: Time-Reversed Lasers*, Physical Review Letters. 105 053901 (2010).

Publications

1. Jonathan Y. Suen, Kebin Fan, and W.J. Padilla, *A Zero-Rank, Maximum Nullity Perfect Electromagnetic Wave Absorber*, Advanced Optical Materials 1801632 (2019).
2. Kebin Fan, Ilya V. Shadrivov, and W.J. Padilla, *Dynamic bound states in the continuum*, Optica **6**, 169 (2019).
3. Christian Nadell, Kebin Fan, and Willie Padilla, *Resonance-domain diffractive lens for the terahertz region*, Optics Letter **43**, 2384 (2018).
4. Andrew Cardin, Kebin Fan, and W.J. Padilla, *Role of loss in all-dielectric metasurfaces*, Optics Express **26**, 17669 (2018).
5. Kebin Fan, Jingdi Zhang, Xinyu Liu, Gu-Feng Zhang, Richard D. Averitt and W.J. Padilla, *Phototunable Dielectric Huygens' Metasurfaces*, Advanced Materials **30**, 1800278 (2018).
6. Willie J. Padilla and Richard D. Averitt, *Properties of dynamical electromagnetic metamaterials*, Journal of Optics **19**, 084003 (2017).
7. Xianshun Ming, Xinyu Liu, Liqun Sun, and Willie J. Padilla, *Degenerate critical coupling in all-dielectric metasurface absorbers*, Optics Express **25**, 24658 (2017).
8. Kebin Fan, Jonathan Y. Suen, Xinyu Liu, and Willie J. Padilla, *All-dielectric metasurface absorbers for uncooled terahertz imaging*, Optica **4**, 601 (2017).

Physical Behavior of Quantum Metamaterials

Steven M. Anlage, CNAM, Physics Department, University of Maryland

Program Scope

The goal is to create artificial quantum matter through engineered structures that mimic natural atoms and create new electronic and electromagnetic behavior not observed in nature. Our objective is to explore new quantum states of matter through creation of engineered quantum meta-atoms and their arrangement into structures that create qualitatively new types of quantum coherent behavior, especially in terms of their interaction with electromagnetic fields. The technical approach involves assembly of superconducting quantum devices that are nominally identical and strongly interacting with each other, and with a bath of microwave photons, and measuring their emergent behavior through electromagnetic response. The results will give fundamental insights into the nature of condensed matter and specific outcomes include investigation of proposed but un-realized states of matter, emergent quantum phenomena, and controlled super-radiant behavior. The work builds on metamaterials consisting of classical radio frequency Superconducting Quantum Interference Devices (rf SQUIDs), which have proven to be a rich nonlinear medium for creating new collective properties of artificial matter.

Recent Progress

The grant commenced on 07/01/2018 and 2 graduate students were recruited to begin work. Two efforts were started - one building on our strengths in classical metamaterials and the other to transform the effort into a purely quantum regime. The first project is to explore collective properties of metamaterials made up of rf SQUIDs. Experiments were conducted to image the collective response of the metamaterial as a function of external rf and dc driving flux. A remarkable transition from incoherent and disordered behavior at low rf flux amplitude to a strongly coherent and nearly uniform response at higher rf power can be attributed to activation of the Josephson nonlinearity in the SQUIDs. A set of realistic fully-nonlinear simulations on an HPC cluster reveals this transition arises from dramatic rearrangement of collective modes of the system.

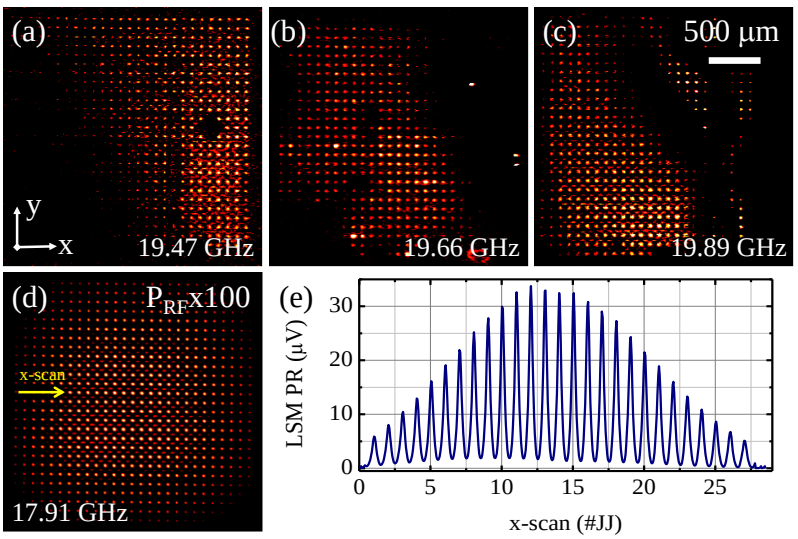

Laser scanning microscope images of a 27×27 rf SQUID metamaterial at 4.2 K at the rf flux bias frequencies shown. Images (a)-(c) taken at low rf flux amplitude show a disordered response influenced by defects, while image (d) taken at 10 times higher rf flux amplitude shows that the fundamental eigenmode of the array has taken over the response. The line cut (e) reveals the expected shape of individual rf SQUID meta-atom excitation in a perfectly coherent finite-size metamaterial.

The second project aims to transition the classical work into the quantum regime by replacing the rf SQUIDs with superconducting qubits having two dominant quantum states and coupling them together through collective electromagnetic modes. The initial setting for the experiment is the Quantum Transmission Line (QTL) metamaterial. The objective is to create a discrete transmission line medium made up of "meta-atoms" that are each endowed with a discrete energy level spectrum. The meta-atoms are coupled to each other either inductively or capacitively (or both) in such a way as to allow tunneling of photons from the discrete energy levels of one meta-atom to the next. A set of candidate rf flux qubits have been designed and are currently being prepared by e-beam lithography inside superconducting co-planar waveguide resonant device structures. The students have been trained in cryogenic rf measurements in a dilution refrigerator as well as full-wave and finite-difference time domain simulations of the microwave structures.

Future Plans

Our rf SQUID metamaterial work has created a small theoretical community dedicated to making predictions for new collective phenomena to observe in this unique nonlinear medium [1]-[7]. Predicted phenomena include Chimera states, which are spatially separated regions of coherent and incoherent response, and they can form spontaneously in an otherwise homogeneous nonlinear media like our SQUID metamaterials. Other possibilities include chaos, breathers (long-lived nonlinear excitations), and novel collective modes that require a strongly nonlinear medium for their existence. A new round of samples have been designed and are now in fabrication. When ready, these samples will be measured at UMD and also by collaborators in Germany.

The Quantum Transmission Line structures will be coming online in 2019 as the students perfect the junction and device fabrication processes. The immediate goal is to build QTLs with single qubits for basic characterization of vacuum Rabi splitting, Rabi oscillations, coherence time and de-phasing mechanisms. They will perform quantum tomography of the meta-atoms to demonstrate coherent quantum control and utilize collective know-how at UMD to optimize the coherence time of the individual meta-atoms. At the same time multiple-qubit QTLs will be fabricated on the same wafer and tested in the BlueFors dilution refrigerator, which can handle up to six samples on each cooldown.

References

[1] N. Lazarides, G. Neofotistos, and G. P. Tsironis, "Chimeras in SQUID metamaterials," Phys Rev B **91** (5), 054303 (2015).

[2] J. Hizanidis, N. Lazarides, G. Neofotistos, and G.P. Tsironis, "Chimera states and synchronization in magnetically driven SQUID metamaterials," The European Physical Journal Special Topics **225** (6), 1231-1243 (2016).

[3] J. Hizanidis, N. Lazarides, and G. P. Tsironis, "Robust chimera states in SQUID metamaterials with local interactions," Phys Rev E **94** (3), 032219 (2016).

[4] Amitava Banerjee and Debopriya Sikder, "Transient chaos generates small chimeras," Phys Rev E **98** (3), 032220 (2018).

[5] N. Lazarides and G. P. Tsironis, "Multistable dissipative breathers and collective states in SQUID Lieb metamaterials," Phys Rev E **98** (1), 012207 (2018).
[6] J. Hizanidis, N. Lazarides, and G. P. Tsironis, "Chimera states in networks of locally and non-locally coupled SQUIDs," arXiv:1902.02158 (2019).
[7] N. Lazarides, J. Hizanidis, and G. P. Tsironis, " Controlled Generation of Chimera States in SQUID Metasurfaces using DC Flux Gradients," arXiv:1902.01711 (2019).

Publications

Alexander P. Zhuravel, Seokjin Bae, Alexander V. Lukashenko, Alexander S. Averkin, Alexey V. Ustinov and Steven M. Anlage, "**Imaging collective behavior in an rf-SQUID metamaterial tuned by DC and RF magnetic fields**," Appl. Phys. Lett. **114**, 082601 (2019).

Seokjin Bae, Yuewen Tan, Alexander P Zhuravel, Lingchao Zhang, Shengwei Zeng, Yong Liu, Thomas A. Lograsso, Ruslan Prozorov, Ariando, T. Venkatesan, Steven M. Anlage, "**Dielectric Resonator Method For Determining Gap Symmetry Of Superconductors Through Anisotropic Nonlinear Meissner Effect**," arXiv:1901.08762.

Electron Spin Polarization in Large Electric Fields

Vanessa Sih, University of Michigan, Ann Arbor

Program Scope

This research program investigates the response of electron spin polarization in semiconductors to large accelerating electric fields. The goals of this research are to understand the mechanism that enables the electrical generation of a bulk spin polarization in non-magnetic materials, the role of spin-orbit effects and spin scattering in a strongly driven regime, and to determine whether a high-electric field regime that preserves or even amplifies spin polarization that has been theoretically predicted can be realized experimentally. The expectation is that this research will improve our understanding of the fundamental processes that cause the electrical generation of spin polarization and contribute to spin dephasing. This knowledge will contribute to the development of robust spin-based devices for information processing, storage, and communication.

Recent Progress

Current-induced spin polarization, a bulk electron spin polarization produced by an accelerating electric field, was first reported by two research groups in 2004 [1,2]. However, the mechanism for this effect and how it depends on material properties was unclear. Therefore, we conducted measurements of spin-orbit splittings and electrical spin generation efficiency on a series of samples with different strain, indium alloy concentration, mobility, and carrier density, in order to identify trends [P1] and compared our results with a model developed by Roberto Raimondi and his collaborators [3], which incorporated contributions from both the intrinsic spin-orbit coupling and extrinsic effects arising from impurity scattering. We did not fit out results to the model; instead, we used experimentally-determined parameters, including the magnitude of the Rashba and Dresselhaus-like spin splittings, the relative strength of the D'yakonov-Perel and Elliot-Yafet spin dephasing mechanisms, carrier concentration and

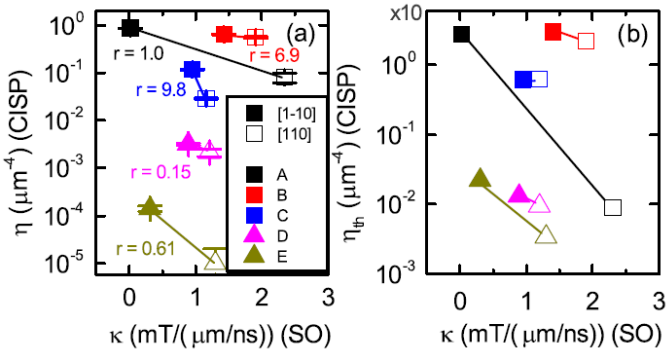

Figure 1: (a) The measured electrical spin generation efficiency plotted against the measured spin-orbit splitting for five samples. Squares indicate samples with higher indium concentrations (2.4-2.6%) and triangles indicate samples with 2.0% indium concentration. $r = \alpha/\beta$ is the ratio of spin splittings with linear Rashba and Dresselhaus symmetry and characterizes the anisotropy of the spin-orbit field. (b) Calculations based on the model using the experimentally-determined material parameters for the five samples. Adapted from Ref. [P1].

mobility, as inputs to calculate the theoretical spin generation rate. The model reproduces our earlier experimental finding that applying the electric field along the crystal axis that has the smaller spin-orbit splitting (due to a cancellation of the Rashba and Dresselhaus fields) produces a larger electrical spin generation [4] and exhibits good qualitative agreement with the observed dependences on carrier concentration and mobility [P1].

Performing measurements with high accelerating electric fields can introduce undesired effects, such as sample heating, that could mask the phenomena that we are interested in observing. For example, electrical spin generation has been observed to have a linear response with voltage at low electric fields, but this changes when larger electric fields are applied. In order to extend measurements to higher electric fields, we investigated the use of modified periodic waveforms to reduce sample heating effects on lock-in measurements of current-induced spin polarization. As shown in Fig. 2, sample heating causes the electrical spin generation rate to deviate from linear behavior when the off/on ratio is low (0 and 1), but the linear behavior can be recovered when the off/on ratio is increased, corresponding to a lower duty cycle [P2].

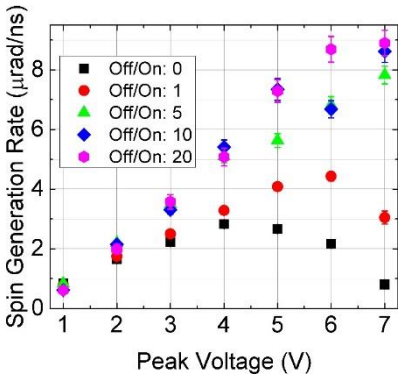

Figure 2: Spin generation rate as a function of applied voltage for off/on ratios 0, 1, 5, 10, and 20. This data has been multiplied by a correction factor to account for the modified waveforms, with error bars derived from the fit. Adapted from Ref. [P2].

We have also designed and fabricated lateral devices for measuring the charge Gunn effect and performed electrical characterization of these devices to establish the threshold voltage for the Gunn effect and how this is affected by illumination. We have adapted our measurement set-up so that we can now simultaneously measure the electron spin dynamics using time-resolved Kerr rotation and monitor changes in charge density through time-resolved reflectivity.

Future Plans

Now that we have a method to mitigate sample heating effects, we can proceed with realizing measurements at higher electric fields where new phenomena have been theoretically proposed to occur, including a change in carrier momentum distribution that would modify the dominant spin relaxation mechanism [4], the spin Gunn effect [5], and a nonlinear Edelstein effect [6]. The spin Gunn effect is particularly intriguing as it was predicted to result in large electron spin polarization in gallium arsenide and indium phosphide at room temperature, and the mechanism does not require spin-orbit interactions or applied magnetic field. However, this prediction was based on assumptions on the shape of the charge Gunn domain, which can be calculated but has not been directly measured. Using time-resolved reflectivity measurements, we plan to directly measure the charge Gunn profile and use optical pump-probe techniques to synchronize the Gunn effect with the optical probe so that we can observe the predicted spin amplification.

References

[1] Y. K. Kato, R. C. Myers, A. C. Gossard, and D. D. Awschalom, "Current-Induced Spin Polarization in Strained Semiconductors," Phys. Rev. Lett. **93**, 176601 (2004).

[2] A. Yu. Silov, P. A. Blajnov, J. H. Wolter, R. Hey, K. H. Ploog, and N. S. Averkiev, "Current-induced spin polarization at a single heterojunction," Appl. Phys. Lett. **85**, 5929-5931 (2004).

[3] C. Gorini, A. Maleki Sheikhabadi, K. Shen, I. V. Tokatly, G. Vignale, and R. Raimondi, "Theory of current-induced spin polarization in an electron gas," Phys. Rev. B **95**, 205424 (2017).

[4] B. M. Norman, C. J. Trowbridge, D. D. Awschalom, and V. Sih, "Current-Induced Spin Polarization in Anisotropic Spin-Orbit Fields," Phys. Rev. Lett. **112**, 056601 (2014).

[4] L. E. Golub and E. L. Ivchenko, "Spin Dynamics in Semiconductors in the Streaming Regime," arXiv:1404.6755v1 (2014).

[5] Y. Qi, Z.-G. Yu, and M. E. Flatté, "Spin Gunn Effect," Phys. Rev. Lett. **96**, 026602 (2006).

[6] G. Vignale and I. V. Tokatly, "Theory of the nonlinear Rashba-Edelstein effect: The clean electron gas limit," Phys. Rev. B **93**, 035310 (2016).

Publications supported by BES

[P1] "Current-induced spin polarization in InGaAs and GaAs epilayers with varying doping densities," M. Luengo-Kovac, S. Huang, D. Del Gaudio, J. Occena, R. S. Goldman, R. Raimondi, and V. Sih, Physical Review B **96**, 195206 (2017)

[P2] "Effect of modified periodic waveforms on current-induced spin polarization measurements," J. R. Iafrate, S. Huang, D. Del Gaudio, R. S. Goldman, and V. Sih, AIP Advances **8**, 065113 (2018)

Session III

Organic exciton-polaritons in the ultrastrong coupling regime

Stephen Forrest, Shaocong Hou, Yue Qu
Departments of Electrical Engineering and Computer Science, and Physics
University of Michigan
Ann Arbor, MI

Mandeep Khatoniar and Vinod Menon
Department of Physics
City College of New York,
NY, NY

Abstract

Excitons play a central role in photogeneration in organic detectors and solar cells. The efficiency of the exciton dissociation process is directly related to molecular structure of the donor and acceptor molecules and the film morphology. In our work, we have focused on understanding the microscopic nature of these interactions in both fullerene and nonfullerene based junctions, and have developed means to control charge transfer and energy transport. In particular, we have focused on long range transport of exciton-polaritons in open-ended structures that support ultrastrong coupling via excitation of Bloch Surface Waves (BSWs). We demonstrate a transition from weak, to strong, to ultrastrong coupling of Frenkel molecular excitons and Bloch surface wave photons at room temperature using this one-sided, all-dielectric optical structure. The all-dielectric structure comprises an organic semiconductor thin film of tetraphenyldibenzoperiflanthene (DBP) on the surface of a distributed Bragg reflector. We investigated the evolution of multiple vibronic polariton branches and their dominant absorption peaks as a function of coupling and in-plane momentum. Measurements are interpreted using both the transfer matrix method and a coupled-oscillator model. The dependence of Rabi splitting on the number of excitons and electrical field amplitude is also modeled showing a transition to ultrastrong coupling at film thicknesses $\geq$50 nm. This low-loss photonic structure enables phenomena such as long range polariton transport and high efficiency energy transfer in organic thin films. In particular, early results indicate polariton diffusion lengths in excess of 100 μm, suggesting that these cavities are ideal for long range energy transport in photovoltaic applications.

Furthermore have developed quantum mechanical models coupled with molecular dynamics simulations to understand the role that morphology plays on the energy of the charge transfer state – i.e. the intermediate between exciton and free polaron – and ultimately its ability to generate free charge at a low expense of energy. We find that quantum confinement of the exciton by crystalline domains in dilute donor-acceptor blends can result in substantial energy shifts in the state, thereby impacting its binding energy. Ultimately, this understanding of exciton and charge transfer state energetics has led to very high efficiency (>15%) organic solar cells, with prospects of reaching 20% in the not distant future. The models, experiments and implications of these findings will be discussed in my presentation.

Control of molecular excitations and energy transfer via strong light-matter coupling

Vinod Menon, Bin Liu, Rahul Deshmukh, Sitakanta Sathpathy
Dept. of Physics, City College & Graduate Center of CUNY

Anurag Panda, Stephen R. Forrest
Departments of Electrical Engineering and Computer Science, and Physics
University of Michigan

Matthew Sfeir
Advanced Science Research Center & Graduate Center of CUNY (Current affiliation)
Brookhaven National Labs (Prior affiliation)

Program Scope: Strong light-matter coupling in solid state systems results in the formation of half-light half-matter quasiparticles called "*exciton-polaritons*" that provide the best of both worlds – the photon component lends the small mass, coherence and ability to engineer the potential energy landscape, while the matter component provides the necessary nonlinearity and interactions which can be controlled on demand. Most demonstrations of strong coupling in solid state systems have been carried out with the goal of realizing low-threshold lasing and condensation. Here we take a departure from this goal and explore the possibility of engineering material properties such as luminescence, energy transfer and excited state dynamics in organic molecular systems through strong light-matter coupling.

Recent Progress: In this program review we will specifically discuss our recent efforts on (i) modification of singlet fission dynamics in an archetype organic material embedded in a cavity (ii) control of excited state proton transfer in a microcavity and (iii) modification of luminescence due to strong coupling of vibronic transitions to surface plasmons. Finally, we will briefly address the implications of strong coupling on energy transfer in a donor-acceptor system and possibilities to enhance the energy transfer rate and distance limitations.

Future Plans: During the next phase of the program we will focus on (i) manipulating energy transfer via strong coupling in a donor-acceptor system (ii) enhancing the propagation of exciton polaritons in disordered molecular solids and (iii) control of singlet fission dynamics.

Other collaborators: Joel Yuen-Zhou & Matthew Du – University of California San Diego,
Girish Agarwal – Texas A&M University,
George John, Ed Hohenstein and Divya K. Parappuram – City College of CUNY

Publications (September 2017 – present):

1. Polariton Chemistry: thinking (inside) the photon box," J. Yuen-Zhou and V. M. Menon *PNAS* (in press)
2. "Long range resonant energy transfer using optical topological transitions in metamaterials," R. Deshmukh, S-A. Biehs, E. Khwaja, G.S. Agarwal, and V. M. Menon *ACS Photonics* **5**, 2737 (2018)
3. "Theory of polariton long range excitation energy transfer," M. Du, L. A. Martinez, R. F. Ribeiro, Z. Hu, V. M. Menon, J.Yuen-Zhou *Chem. Science* **9**, 6659 (2018).

Session V

Harnessing Order Parameter in Ternary II-IV-V_2 Semiconductors

Adele C. Tamboli, National Renewable Energy Lab

Program Scope

In this program, we are developing a systematic understanding and control of cation order parameter and its impact on properties in II-IV-V_2 semiconductors. II-IV-V_2 materials are a class of compounds with structure and properties similar to III-Vs, but with a doubled conventional unit cell size due to the substitution of group II and IV elements for group III cations, as shown in Fig. 1.[P1] Building off a foundation of work on III-V ordering, we are exploring a set of materials with similar optoelectronic performance to III-Vs but wider tunability through chemical complexity. We study phosphides and nitrides, two structure types available in II-IV-V_2 materials. These materials can be readily integrated with III-Vs and silicon, enabling optoelectronic applications spanning the visible spectrum. The underlying scientific questions this work addresses are: How does cation disorder affect properties such as band structure and density of states? How do optical transition probabilities evolve with disorder? What is the impact on carrier localization? Can site disorder be controlled independently of crystalline "quality" (e.g. density of other defects)? Ultimately, we hope to understand how a wide variety of physical properties are determined by site occupancy.

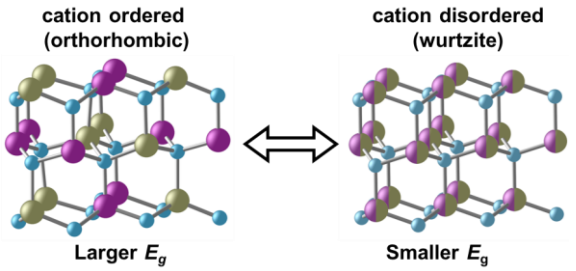

Fig. 1. Theoretical predictions and some experimental evidence have suggested that the band gap of II-IV-V_2 materials may be tunable by as much as 1 eV by tuning cation disorder. This would enable an alternative route to property tuning compared to traditional alloying approaches.

Recent Progress

Our recent work has focused primarily on understanding cation site disorder in ternary nitride semiconductors using both theory and experiment.

$ZnSnN_2$: Impact of cation disorder on properties

$ZnSnN_2$ has been studied extensively for photovoltaic applications,[P1,P4,R1–3] but fundamental questions remain regarding its order parameter and the impact of structure on properties. Like most II-IV-V_2 materials, the band gap of $ZnSnN_2$ is expected to depend on order parameter, with decreasing band gap as order parameter decreases. However, the difficulty of characterizing order parameter in $ZnSnN_2$ has meant that understanding its impact has been elusive. In particular, it has been predicted that property variation is largely driven by local, rather than long-range, ordering,[P4] which is more difficult to measure. To address this challenge, we have performed calculations of disorder in $ZnSnN_2$ using a motif Hamiltonian to describe *local* order separately from long-range order, e.g., whether each N atom is locally coordinated by 2 Zn and 2 Sn atoms (as in the ideal, ordered case), or whether deviations from these ideal motifs exist. Monte Carlo simulations were used to model the density of "disordered" motifs (e.g., a N atom

coordinated by 3 Zn's and 1 Sn, called a "31 motif") as a function of temperature. The resulting structures with varying local order were used as the basis for property calculations, including band edge positions, optical absorption coefficient, and carrier localization. We found up to about 20% off-stoichiometric motifs can reasonably exist under our deposition conditions, but higher levels of disorder are unlikely. Within these constraints, the band gap is expected to be tunable from 1.0 – 1.4 eV, which matches the range observed experimentally. This amount of disorder is expected to have minimal impact on transport properties. These results are described in more detail in *Lany et. al. (2017)*[P2]

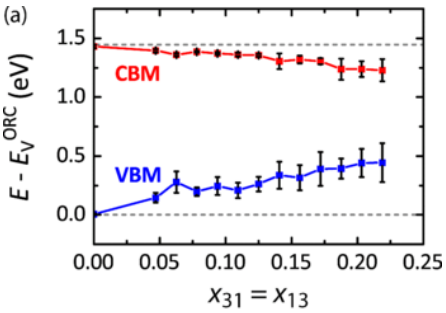

Fig. 2. Band edge positions as a function of the density of off-stoichiometric motifs (local disorder) in $ZnSnN_2$.

The observed properties of $ZnSnN_2$ also depend strongly on the presence of impurities; 10-30% oxygen contamination has been observed experimentally.[R1,P4] A reasonable prediction would be that increasing disorder and contamination would lead to degradation of properties, e.g. carrier localization and defect states within the band gap. However, we have found that the interplay of oxygen with disorder leads to an interesting phenomenon: *pristine* optoelectronic properties at certain compositions despite long-range disorder. This phenomenon emerges because neutral defect complexes can arise with perfect short-range order even in the presence of long-range disorder. Calculations predict that these structures have low mixing enthalpy and are thus likely to form (Fig. 3); the increased entropy from long-range disorder stabilizes these structures while the locally ordered motifs enable low energy configurations. The result is line-compound-like behavior in a system with long-range *disorder*, similar in some ways to entropy-stabilized alloys. However, the resulting electronic properties are free of charge localization, comparable to perfectly crystalline materials. This new way of combining long-range disorder with local order requires both multiple cations and multiple anions to satisfy both entropic and enthalpic contributions. More details will be provided in *Pan et al. (2019).*[P7] Experimental work to validate this theory is currently underway.

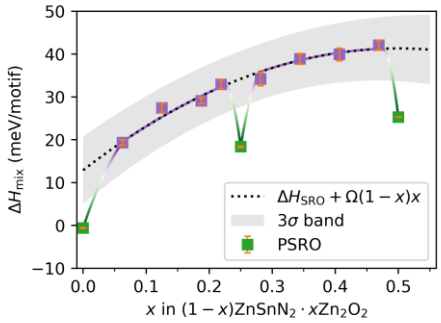

Fig. 3. At certain "magic" compositions, the $ZnSnN_2$-ZnO alloy system behaves as a line compound despite long-range disorder.

$ZnGeN_2$: Visible light emission from cation-disordered material

$ZnGeN_2$ is similar to GaN, with a predicted band gap of about 3.6 eV in its more stable, ordered structure. However, as with other II-IV-V_2 materials, tuning the cation order parameter is expected to reduce the band gap. No calculations have yet predicted the band gap of disordered $ZnGeN_2$, but we have begun to investigate this material experimentally by combinatorial sputtering, using similar techniques to our early investigations into $ZnSnN_2$.[R1] In contrast to

$ZnSnN_2$, $ZnGeN_2$ undergoes a long-range structural distortion between ordered and disordered forms, meaning that the purely local framework used to understand disorder in $ZnSnN_2$ cannot fully explain the behavior of $ZnGeN_2$. If the band gap shift is similar to that of other II-IV-V_2 compounds, the band gap of disordered $ZnGeN_2$ would be expected to be ~ 2.6 eV.

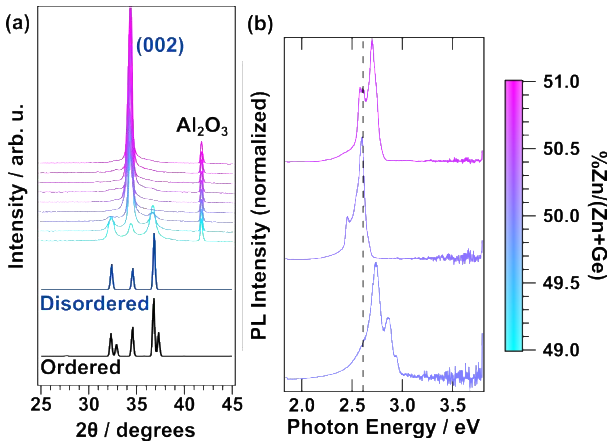

Fig. 4. Cation-disordered $ZnGeN_2$ epitaxially aligns with a sapphire substrate under Zn-rich growth conditions (a), and exhibits room temperature PL emission at 2.6 eV (b).

We have synthesized epitaxial yet cation-disordered $ZnGeN_2$ films on sapphire substrates via high temperature combinatorial sputtering. The ability to grow films that are epitaxially aligned while maintaining cation disorder resolves a key question of whether it is possible for materials to be selectively synthesized with disorder on the cation sublattice without significant densities of extended defects. We find that growing under Zn-rich conditions enables epitaxial orientation of these films, suggesting that Zn is acting as a surfactant mediating epitaxy. These disordered $ZnGeN_2$ films exhibit room temperature PL emission at 2.6 eV, as well as an optical absorption onset at the same energy – matching our expectations for the band gap of disordered $ZnGeN_2$.[P5]

Future Plans

New directions: Zn_2SbN_3 and $MgSnN_2$

While fundamental questions remain about ordering in $ZnSnN_2$ and $ZnGeN_2$, these two compounds are known materials that have been previously reported. Despite compelling properties, Mg-based II-IV-V_2 semiconductors have received little study by comparison, primarily due to the difficulty of growing Mg-containing materials. Synthesis of $MgSnN_2$ has not yet been reported in the literature, but it is predicted to be stable[R4] with an ordered band gap of ~2.5 eV,[R5] a rare occurrence for group IV and III-V semiconductors even with alloying. If disorder decreases the band gap, as expected, this single material could span the visible spectrum with its band gap. We have recently synthesized phase pure, wurtzite (cation-disordered) $MgSnN_2$ via combinatorial sputtering. Properties of this material and future directions will be discussed.

Even more exotic, metastable ternary nitrides, such as Zn_2SbN_3, have recently been predicted through the Center for Next Generation of Materials Design (CNGMD). The discovery of a disordered cation sublattice in Zn_2SbN_3, as well as room temperature PL emission slightly below the predicted, ordered band gap of 1.7 eV, have motivated us to investigate this material further.[P6] We will discuss how disorder plays out in a metastable compound as well as optoelectronic characterization of this material.

References

R1. Fioretti, A. N. *et al.* Combinatorial insights into doping control and transport properties of zinc tin nitride. *J. Mater. Chem. C* **3**, 11017–11028 (2015).

R2. Fioretti, A. N. *et al.* Effects of Hydrogen on Acceptor Activation in Ternary Nitride Semiconductors. *Advanced Electronic Materials* **3**, 1600544 (2017).

R3. Quayle, P. C. *et al.* Charge-neutral disorder and polytypes in heterovalent wurtzite-based ternary semiconductors: The importance of the octet rule. *Phys. Rev. B* **91**, 205207 (2015).

R4. Sun, W. *et al.* A Map of the Inorganic Ternary Metal Nitrides. *arXiv:1809.09202 [cond-mat]* (2018).

R5. *NREL Materials Database*. http://materials.nrel.gov, (2019).

Publications (Last 2 Years)

P1. Aaron D. Martinez, Angela N. Fioretti, Eric S. Toberer and **Adele C. Tamboli**, *Synthesis, Structure, and Optoelectronic Properties of II-IV-V_2 Materials.* J. Mater. Chem. A, 5, 11418 (2017) [Invited review, *Emerging Investigators* themed issue; back cover]. DOI: 10.1039/C7TA00406K

P2. Stephan Lany, Angela N. Fioretti, Paweł P. Zawadzki, Laura T. Schelhas, Eric S. Toberer, Andriy Zakutayev, and **Adele C. Tamboli**, *Monte Carlo simulations of disorder in $ZnSnN_2$ and the effects on the electronic structure.* Phys. Rev. Mater. **1**, 035401 (2017). DOI: 10.1103/PhysRevMaterials.1.035401

P3. Aaron D. Martinez, Elisa M. Miller, Andrew G. Norman, Rekha R. Schnepf, Noemi Leick, Craig Perkins, Paul Stradins, Eric S. Toberer, and **Adele C. Tamboli**. *Growth of amorphous and epitaxial $ZnSiP_2$-Si alloys on Si.* J. Mater. Chem. C. **6,** 2696 (2018). [Front Cover] DOI: 10.1039/c7tc05545e

P4. Angela N. Fioretti, Jie Pan, Brenden Ortiz, Celeste L. Melamed, Patricia D. Dippo, Laura T. Schelhas, John D. Perkins, Darius Kuciauskas, Stephan Lany, Andriy Zakutayev, Eric S. Toberer, and **Adele C. Tamboli**. *Exciton Photoluminescence and Benign Defect Complex Formation in Zinc Tin Nitride*. Materials Horizons **5,** 823 (2018). [Back Cover] DOI: 10.1039/C8MH00415C

P5. Celeste L. Melamed, Brooks Tellekamp, John S. Mangum, Patricia Dippo, Eric S. Toberer, and Adele C. Tamboli, *Blue-Green Emission from Epitaxial Yet Cation-Disordered $ZnGeN_{2-x}O_x$.* Submitted.

P6. Elisabetta Arca, John D. Perkins, Stephan Lany, Allison Mis, Bor-Rong Chen, Patricia Dippo, Jonathan L. Partridge, Wenhao Sun, Aaron Holder, Adele C. Tamboli, Michael F. Toney, Laura T. Schelhas, Gerbrand Ceder, William Tumas, Glenn Teeter, and Andriy Zakutayev, *Zn_2SbN_3: Growth and Characterization of a Metastable Photoactive Semiconductor*. Submitted.

P7. Jie Pan, Jacob Cordell, Garritt J. Tucker, Andriy Zakutayev, Adele C. Tamboli, and Stephan Lany, *Discovery of a line-compound-like solid-solution phase in $(ZnSnN_2)_{1-x}(ZnO)_{2x}$.* In preparation.

Semiconductor excitonic nanoshells for energy conversion applications

Mikhail Zamkov

The Center for Photochemical Sciences, Department of Physics, Bowling Green State University, Bowling Green, Ohio 43403. zamkovm@bgsu.edu

Program Scope

The project focuses on developing a novel class of semiconductor nanoparticles featuring size-*independent* tuning of quantum confinement characteristics. The proposed innovation is expected to lift the particle size limitations endured by colloidal nanocrystals and zero-dimensional (0D) quantum dots by allowing larger-size semiconductor nanostructures to show tunable optoelectronic properties. The general strategy for enabling the quantum confinement regime in bulk-size semiconductors relies on creating an energy gradient within a nanoparticle, which promotes the surface-localization of photoinduced charges through the use of a "nanoshell" morphology (Fig. 1a). As a result, the 2D quantum confinement is achieved in the surface layer of a semiconductor colloid, for which all three dimensions exceed its corresponding exciton Bohr radius.

The successful development of nanoshell quantum dots will allow improving many aspects of nanocrystal-based applications. Among the expected benefits, assemblies of nanoshells are expected to exhibit a lower density of grain boundaries than 0D nanocrystal solids, which is critical for enhancing the photoconductivity characteristics of solution-processed solar cells, photelectrodes, field effect transistors, and electroluminescent materials. Owing to a relatively large particle volume, nanoshell quantum dots will also display an enhanced biexciton quantum yield, which is the key aspect for achieving the population inversion in quantum dot lasers. Another important benefit of the nanoshell morphology lies in the ability to concentrate the absorbed radiation *via* the transfer of the photoinduced energy from the bulk domain to the peripheral quantum-confined layer. This process enhances the energy density within the excitonic domain, which is important for applications in multi-electron catalysis (e.g. hydrogen production, water splitting) and solar concentrators.

Recent Progress

Our research efforts in the first two years of the DOE project were focused on: (*i*) - the chemical synthesis of semiconductor colloids exhibiting the quantum confinement in the surface layer (nanoshell quantum dots); (*ii*) – the investigation of charge and energy transfer processes in nanoshell solids and assemblies of semiconductor nanoparticles with molecular acceptors; (*iii*) – ultrafast spectroscopy of biexciton dynamics in nanoshell quantum dots.

The first demostration of the prototype nanoshell architecture was accomplished by using a CdS/CdSe semiconductor combination.[1] The emerging generation of quantum dot optoelectronic devices offers an appealing prospect of a size-tunable band gap. The confinement-enabled control over electronic properties, however, requires nanoparticles to be sufficiently small, which leads to a large area of inter-particle boundaries in a film. Such interfaces lead to a high density of surface traps, which ultimately increase the electrical resistance of a solid. To address this issue, we developed an inverse energy-gradient core/shell architecture supporting the quantum confinement in 20-30 nm nanoparticles (Fig. 1b-e), which is far larger than their respective exciton Bohr radii (~ 5 nm). The assembly of such nanostructures exhibited a relatively low surface-to-volume ratio, which was manifested through the enhanced conductance (7-fold) in solution-processed films. The band gap emission of fabricated nanoshells has revealed a characteristic size-dependent behavior tunable *via* the shell thickness with associated quantum yields in the 4.4 – 16.0 % range.

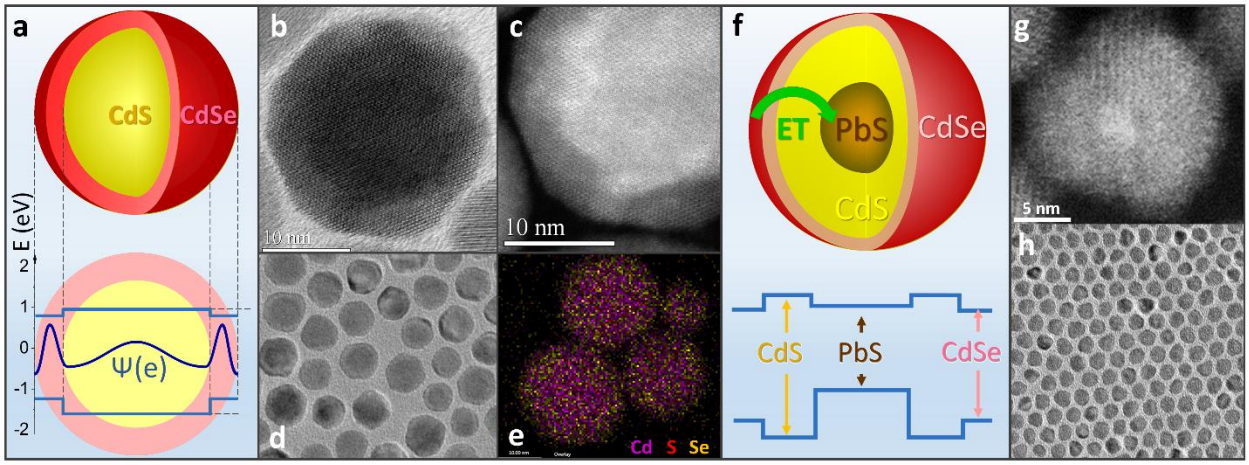

Figure 1. (a). Schematic illustration of the CdS/CdSe nanoshell geometry. The potential energy minima of the CdSe conduction and valence bands promote the shell-localization of both photoinduced charges. (b-e). High-resolution TEM and HAADF-STEM images of CdS/CdSe nanoshell quantum dots. (f). Schematic representation of excited state energy levels in fabricated core/barrier/shell NCs. (g). Dark field STEM image of a PbS/CdS/CdSe nanocrystal indicating the presence of the PbS and CdSe domains through a color contrast. (h). Low-resolution TEM image of PbS/CdS/CdSe NCs.

Following the synthesis of CdS/CdSe nanoshell quantum dots,[1] we have developed several other advanced nanoshell geometries, including dual-emitting PbS/CdS/CdSe nanoparticles comprising zero- and two-dimensional excitons in the same nano-object[2] and dual-barrier nanoshell quantum dots, CdS/CdSe/CdS, featuring long-lived biexciton populations.

Dual-emitting PbS/CdS/CdSe core/barrier/shell colloids exhibit a rather unique carrier confinement regime, characterized by the mixture of zero- and two-dimensional excitons in the PbS core and CdSe surface domains of the composite nano-object. An interstitial barrier separating the two confinement regions allows regulating the rate of energy and charge transfer between the two excitation types enabling a dual emission from the core and the shell semiconductors. As an example of potential applications, fabricated colloids were demonstrated as dual-color probes for

sensing the redox environment, where both the energetics and the timing of photoinduced charge transfer to an add-on analyte could be inferred from the ratiometric measurements.

Multiple exciton (MX) generation is beneficial to many applications of semiconductors, including photoinduced energy conversion, stimulated emission, and carrier multiplication. The utility of MX processes is generally enhanced in small-size semiconductor nanocrystals exhibiting the quantum confinement of photoinduced charges. Unfortunately, a reduced particle volume accelerates the non-radiative Auger decay of multiple excitations, greatly diminishing the MX feasibility in nanocrystal-based photovoltaic, laser, and photoelectrochemical devices. Recently, we have demonstrated that such Auger recombination of biexcitons could be suppressed through the use of a quantum-well (QW) nanoshell architecture. The reported nanoscale geometry effectively reduces Coulomb interactions between photoinduced charges underlying Auger decay. This leads to increased biexciton lifetimes, as was demonstrated through methods of ultrafast spectroscopy. In particular, we observed that the biexciton lifetime of CdSe-based QW nanoshells (CdS/CdSe/CdS) was increased more than thirty times relative to zero-dimensional CdSe NCs. The slower biexciton decay in QW nanoshells was attributed to a large confinement volume, which compared favorably to other existing MX architectures.

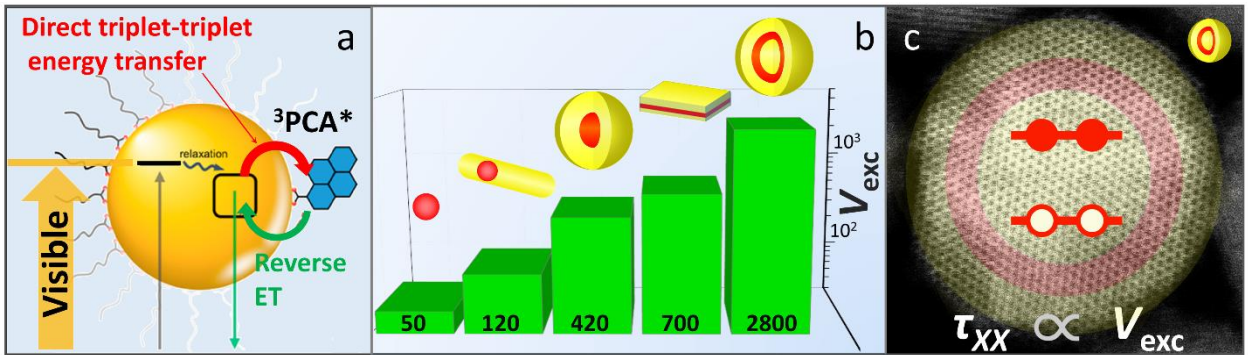

Figure 2. (a). The strategy for storing the photoinduced energy of semiconductor NCs *via* the triplet energy transfer to a conjugated acceptor. The thermally-controlled reverse transfer of triplet excitons from an acceptor enables a slow-rate singlet emission from NCs with millisecond lifetimes. (b). An estimated quantum-confinement volume corresponding to several reported MX geometries. From left to right: spherical CdSe quantum dots, CdSe/CdS dot-in-a-rod, CdSe/CdS core/shell, CdSe/CdS nanosheets, QW nanoshells, reported here. (c) A characteristic TEM image of a CdS/CdSe/CdS QW nanoshell.

The PI has authored the News & Views paper in Nature Energy focusing on the role on multiple excitons for solar energy generation. A particular aspect explored by this work was related to using an electrochemical cell as a strategy for harvesting multiple excitons from PbS nanocrystals. The new geometry benefits from forward device illumination, which is critical for collecting high-energy photons that usually get filtered by an oxide layer of the standard photovoltaic cell.

Our recent work on the energy transfer dynamics in nanocrystal-dye assemblies has demonstrates the possibility of storing the nanocrystal photoinduced energy form of long-lived triplet excitons induced in the surrounding molecules acceptors (Fig. 2a). In particular, we show

that the repopulation of the initial semiconductor nanocrystal excited state from the molecular triplet "reservoir" provides the opportunity to convert nanocrystal triplet excitons to "harvestable" singlet states. This work was done in collaboration with Dr. Castellano (NC State), where our groups have explored the possibility of the triplet energy transfer between nanocrystals (CdSe shell) and organic molecules. This work was recently published in Nature Chemistry.

Future Plans

The general direction for the future development of our research program will focus on expanding the nanoshell synthesis to other semiconductor combinations and exploring electrical characteristics of nanocrystal films processed from nanoshell colloids. Ultimately, the realization of quantum confinement characteristics in bulk-size semiconductors could contribute to the development of next-generation materials, where tunable optoelectronic properties are complemented with a superior charge transport of a solid state. We will also continue our work on optical spectroscopy of charge and energy transfer processes in fabricated nanoshells and their solids.

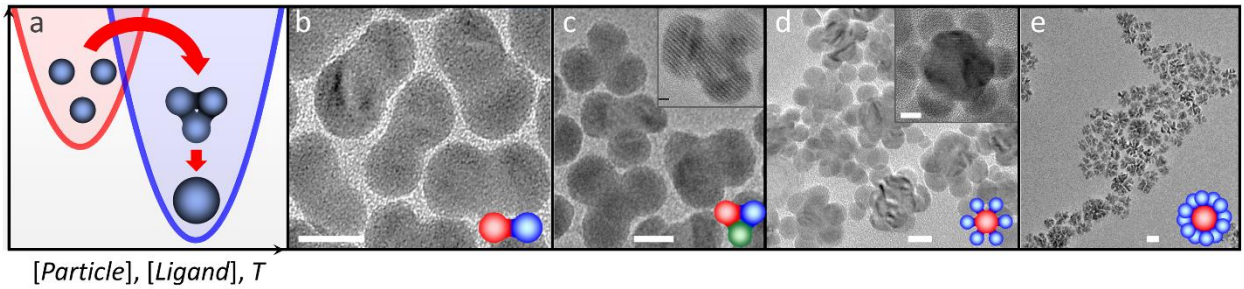

Figure 3. (a). The nucleation-barrier model for the fusion of dissimilar inorganic colloids. The reaction coordinate depends on the concentration of isolated nanoparticles and ion-solubilizing ligands. Nanocrystal clusters of n different-diameter colloids. (b). n ≈ 2. (c). n ≈ 3. (d). n = 7-10. (e). n > 10. The scale bar is 10 nm.

A special effort will be made towards expanding the library of nanoshell semiconductor combinations. In this regard, traditional synthetic routes will be reformed to allow for an arbitrary combination of core/shell materials. An important milestone in this line of research has been recently achieved by our group. We have developed the *nano-glue* growth method that allows assembling prefabricated particles into a composite structure (Fig. 3). Incidentally, the basic features of this method were "learned" from a detailed analysis of the CdS/CdSe nanoshell growth.[1] We have since evolved this approach into a general strategy for assembling dissimilar materials and nanoshells by means of a partial crystallographic fusion at hybrid interfaces.

References

1) Razgoniaeva, N.; Moroz, P.; Yang, M.; Budkina, D. S.; Eckard, H.; Augspurger, M.; Khon, D.; Tarnovsky, A. N.; Zamkov, M. *J. Am. Chem. Soc.*, **2017**, *139*, 7815-7822.

2) Razgoniaeva, N.; Yang, M.; Colegrove, C.; Kholmicheva, N.; Moroz, P.; Eckard, H.; Vore, A.; Zamkov, M. *Chem. Mater.*, **2017**, *29*, 7852-7858.

Publications from DOE-sponsored research (last 2 years)

1) Razgoniaeva, N.; Moroz, P.; Yang, M.; Budkina, D. S.; Eckard, H.; Augspurger, M.; Khon, D.; Tarnovsky, A. N.; Zamkov, M. "One-dimensional carrier confinement in "giant" CdS/CdSe excitonic nanoshells." *J. Am. Chem. Soc.*, **2017**, *139*, 7815-7822. https://doi.org/10.1021/jacs.7b02054

2) Razgoniaeva, N.; Yang, M.; Colegrove, C.; Kholmicheva, N.; Moroz, P.; Eckard, H.; Vore, A.; Zamkov, M. "Double-Well Colloidal Nanocrystals Featuring Two-Color Photoluminescence." *Chem. Mater.*, **2017**, 29, 7852-7858. https://doi.org/10.1021/acs.chemmater.7b02585

3) Zamkov, M. "Solar Hydrogen Generation: Exceeding 100% Efficiency." *Nat. Energy*, **2017**, 2, 17072. https://doi.org/10.1038/nenergy.2017.72

4) Razgoniaeva, N.; Rogers, S.; Moroz, P.; Cassidy, J.; Zamkov, M. "Improving the Spectral Resolution in Fluorescence Microscopy through Shaped-Excitation Imaging." *Methods Appl. Fluoresc.*, **2018**, 6, 045006 https://doi.org/10.1088/2050-6120/aad81c

5) Mongin, C.; Moroz, P.; Zamkov, M.; Castellano, F. N. "Thermally Activated Delayed Photoluminescence from Pyrenyl-Functionalized CdSe Quantum Dots" *Nat. Chem.*, **2018**, 10, 225-230. https://doi.org/10.1038/nchem.2906

6) Kholmicheva, N.; Royo Romero, L.; Cassidy, J.; Zamkov, M. "Prospects and Applications of Plasmon-Exciton Interactions in the Near-Field Regime" *Nanophotonics*, **2018**, *(Accepted)*, https://doi.org/10.1515/nanoph-2018-0143

7) Moroz, P.; Royo Romero, L.; Zamkov, M. "Colloidal Semiconductor Nanocrystals in Energy Transfer Reactions." Feature article. *Chem. Com.*, **2019**. (*Accepted*) https://doi.org/10.1039/C9CC00162J

8) Kholmicheva, N.; Budkina, D.; Porotnikov, D.; Boddy, A.; Bergman, I.; Khon, D.; Tarnovsky, A.; Zamkov, M. " The Suppression of the Auger Decay in CdS/CdSe Nanoshells" *Under revision* in *ACS Photonics*, **2019.**

9) Moroz, P.; Royo Romero, L.; Zamkov, M. "Delayed Photoluminescence in Metal-Conjugated Fluorophores." **2019** (*Submitted*).

Session VII

Electronic Materials Program

Joel W. Ager,[1,2] Daryl C. Chrzan,[1,2] Oscar D. Dubon,[1,2] Wladek Walukiewicz,[1,2] Junqiao Wu,[1,2] and Ali Javey[1,3]
[1]Materials Sciences Division, Lawrence Berkeley National Laboratory, Berkeley, CA
[2]Materials Science and Engineering, University of California, Berkeley, CA
[3]Electrical Engineering and Computer Science, University of California, Berkeley, CA

Program Scope

LBNL's Electronic Material Program (EMAT) discovers and creates semiconductors of novel composition and morphology for energy applications by *removing chemical and physical constraints* that limit materials performance and growth. Emphasis is placed on growth of single-crystalline semiconductors that are not epitaxially coupled with the underlying substrates, thus expanding the utility of semiconductors for new applications while enabling study of new material properties. In the case of monolayer semiconductors, elimination of the difference between the surface and the bulk allows us to control defects (including fixing/creating them) via surface treatments. In parallel, we utilize a toolbox of physical and chemical approaches to implement extreme control of band structures in both low dimensional and 3D materials using surface/interface effects. Finally, by exploiting new insights into the process of templated liquid-phase nucleation and growth, we synthesize high-quality single-crystal semiconductors on amorphous substrates.

Recent Progress

Discovery that strain can be induced during the growth of 2D materials.

The application of strain to semiconductors allows for controlled modification of their band structure. This principle is employed for the manufacturing of devices ranging from high-performance transistors to solid-state lasers. Traditionally, strain is typically achieved via growth on lattice-mismatched substrates. For 2D semiconductors, this is not feasible as they typically do not interact epitaxially with the substrate. Here, we demonstrate controlled strain engineering of 2D semiconductors during synthesis by utilizing the thermal coefficient of expansion mismatch between the substrate and semiconductor. Using WSe_2 as a model system, we demonstrate stable built-in strains ranging from 1% tensile to 0.2% compressive on substrates with different thermal coefficient of expansion. Consequently, we observe a dramatic modulation of the band structure, manifested by a strain-driven

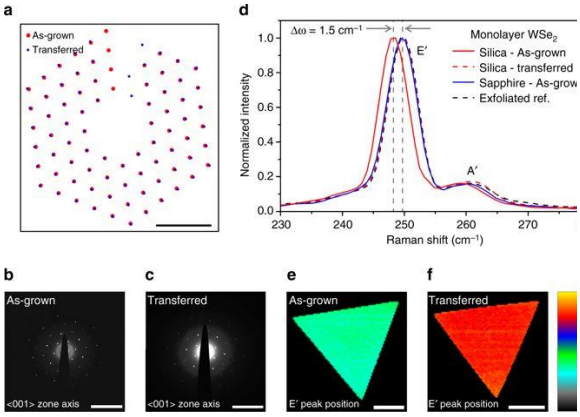

Figure 1. Transmission electron microscopy images and Raman spectroscopy of monolayer WSe_2. **a** Overlay of diffraction spots for as-grown and transferred monolayer WSe_2, showing a $1.39 \pm 0.28\%$ strain in samples grown directly on the TEM membrane. *Scale bar* is 10 nm^{-1}. **b** Electron diffraction patterns of a tensile strained WSe_2 monolayer grown directly on an 8 nm SiO_2 TEM membrane and **c** a WSe_2 monolayer transferred to the same thickness membrane. *Scale bar* is 10 nm^{-1}. **d** Raman spectra of WSe_2 monolayers grown on various substrates. **e**, **f** Raman mapping of E' peak position for a (**e**) tensile strained WSe_2 monolayer as-grown on fused silica and a (**f**) WSe_2 monolayer transferred to release strain; data are plotted using the same false color scheme. *Scale bar* is 20 μm, data range is 250.5 to 247.0 cm^{-1} From Ahn *et al.*, *Nature Comm.*, 2017.[1]

indirect-to-direct bandgap transition and brightening of the dark exciton in bilayer and monolayer WSe_2, respectively. The growth method developed here should enable flexibility in design of more sophisticated devices based on 2D materials.[1]

Extreme Epitaxial Strains in TMDCs

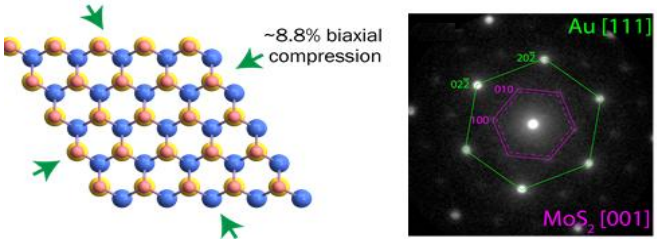

Fig. 2. Predicted epitaxial strain of monolayer MoS_2 induced by growth of Au (111), left. Right, observation of ca. 9% biaxial compressive strain in monolayer MoS_2 by 4D STEM: green, Au [111], dashed purple, unstrained MoS_2 [001] standard; purple, compressively strained MoS_2.

In prior EMAT work, we had shown theoretically and experimentally that Au will grow epitaxially on MoS_2.[2,3] Though this growth mode had been observed in the mid 1960's,[4] its origins were not fully understood. Notably, our detailed analysis of the epitaxial relationship using density functional theory revealed that TMDC substrates would be compliant, and that this compliance would enable epitaxial growth for systems with very large strain mismatch. Very recently, using facilities at the Molecular Foundry, we have discovered that Au does indeed grow epitaxially on MoS_2, and that mismatch strains of the order of 10% can be obtained. We also observed that there are a wide variety of epitaxial growth modes accessible to the system, and that this variety of modes leads to the potential for unusual strain states to be induced within the TMDC film (including shear stresses).

Electronic properties of MoS_2 revealed at high pressure

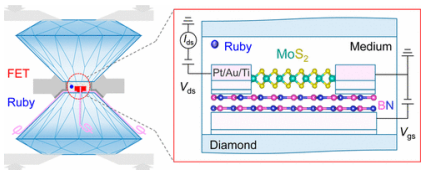

Fig. 3. FET nanodevice in a DAC. In this schematic, the layered MoS_2 and *h*-BN were used as the channel semiconductor and dielectric material, respectively. Each of the electrodes is composed of two parts, a patterned and deposited thin metal line (Au/Ti) inside the DAC chamber connected to a strip of Pt foil outside the chamber. From Chen *et al.*, Nano Letters, 2017.[5]

Hydrostatic pressure applied using diamond anvil cells (DAC) has been widely explored to modulate physical properties of materials by tuning their lattice degree of freedom. Independently, electrical field is able to tune the electronic degree of freedom of functional materials via, for example, the field-effect transistor (FET) configuration. Combining these two orthogonal approaches allows discovery of new physical properties and phases going beyond the known phase space. Such experiments are, however, technically challenging and have not been demonstrated. We reported a feasible strategy to prepare and measure FETs in a DAC by lithographically patterning the nanodevices onto the diamond culet. Multiple-terminal FETs were fabricated in the DAC using few-layer MoS_2 and BN as the channel semiconductor and dielectric layer, respectively. It is found that the mobility, conductance, carrier concentration, and contact conductance of MoS_2 can all be significantly enhanced with pressure. We expect that the approach could enable unprecedented ways to explore new phases and properties of materials under coupled mechano-electrostatic modulation.[5]

Large-area and bright pulsed electroluminescence in monolayer semiconductors.

Transition-metal dichalcogenide monolayers have naturally terminated surfaces and can exhibit a near-unity photoluminescence quantum yield in the presence of suitable defect passivation. To date, steady-state monolayer light-emitting devices suffer from Schottky contacts or require

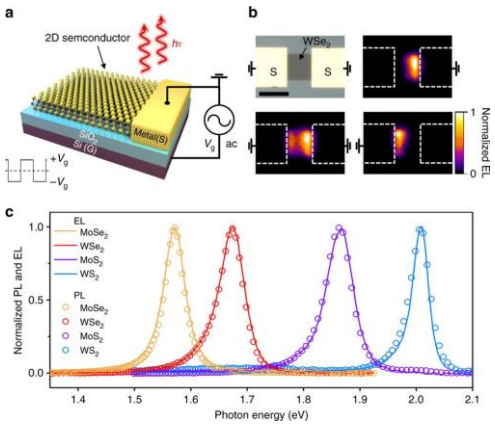

Fig. 4. Transient EL in TMDCs. **a** Schematic of the t-EL device. An AC voltage is applied between the gate and source electrodes and emission occurs near the source contact edge. **b** Optical and EL image of a WSe_2 device, showing that emission is only observed near the grounded source contacts. Scale bar is 10 μm. **c** EL and PL spectra measured for $MoSe_2$, WSe_2, MoS_2, and WS_2 monolayer devices. From Lien *et al.*, *Nature Commun.*[6]

complex heterostructures. We demonstrated a transient-mode electroluminescent device based on transition-metal dichalcogenide monolayers (MoS_2, WS_2, $MoSe_2$, and WSe_2) that overcomes these problems. Electroluminescence from this dopant-free two-terminal device is obtained by applying an AC voltage between the gate and the semiconductor. Notably, the electroluminescence intensity is weakly dependent on the Schottky barrier height or polarity of the contact. We fabricate a monolayer seven-segment display and achieve the first transparent and bright millimeter-scale light-emitting monolayer semiconductor device.[6]

Synthetic WSe_2 monolayers with high photoluminescence quantum yield.

In recent years, there have been tremendous advancements in the growth of monolayer transition metal dichalcogenides (TMDCs) by chemical vapor deposition (CVD). However, obtaining high photoluminescence quantum yield (PL QY), which is the key figure of merit for optoelectronics, is still challenging in the grown monolayers. Specifically, the as-grown monolayers often exhibit lower PL QY than their mechanically exfoliated counterparts. Recent EMAT work has synthesized synthetic tungsten diselenide (WSe_2) monolayers with PL QY exceeding that of exfoliated crystals by over an order of magnitude.[7] PL QY of ~60% is obtained in monolayer films grown by CVD, which is the highest reported value to date for WSe_2 prepared by any technique. The high optoelectronic quality is enabled by the combination of optimizing growth conditions via tuning the halide promoter ratio, and introducing a simple substrate decoupling method via solvent evaporation (SEMD process), which also mechanically relaxes the grown films. The achievement of scalable WSe_2 with high PL QY could potentially enable the emergence of technologically relevant devices at the atomically thin limit.

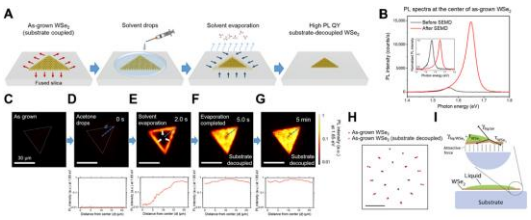

Fig 5. (**A**) Schematic SEMD process. An as-grown WSe_2 monolayer is immersed in a droplet of solvent. During the solvent evaporation, the substrate decoupling process of the WSe_2 monolayer is accomplished with the enhanced PL QY. (**B**) PL spectra measured at the center of an as-grown WSe_2 monolayer with an excitation power of 15 W cm^{-2} before and after the SEMD process; inset shows normalized spectra. (**C** to **G**) In situ PL imaging of the SEMD process in a WSe_2 monolayer. Scale bars, 30 μm (for all PL images). (**H**) Overlay of diffraction spots for as-grown and substrate-decoupled samples; 1.54 ± 0.05% tensile strain in the as-grown sample is released after the SEMD process. Scale bar, 5 nm^{-1}. Original diffraction patterns of the samples are shown in fig. S5. (**I**) Schematic describing the factors influencing the SEMD process of the WSe_2 monolayer. . Adapted from Kim *et al.*, *Science Advances*, 2019.[7]

Future Plans

Our recent discovery that certain monolayer TMDs can be made to be optically "perfect," with their luminescence dynamics appearing to be controlled only by intrinsic processes, allows us to use these

materials as a starting point for incisive studies of intrinsic and extrinsic defects.[8,9] It may be possible to also manipulate the Fermi level to suppress non-radiative recombination, as suggested by the data in Fig. 4. This could potential lead to bright and controllable optical emission from the full range of band gaps available in the TMDCs.

In our current work, we have demonstrated strain engineering of TMDCs using two mechanisms: (1) thermal mismatch strain that can be tuned using droplet evaporation and (2) epitaxial strain induced by deposition of a thin metallic film. Intriguingly, we have uncovered evidence of strain states (e.g. shear and rotations of layers with respect to one another) that have no precedent in traditional epitaxial growth. In the next three years, we will exploit our growing theoretical and experimental understanding of possible epitaxial relationships between TMDCs and metals to produce single monolayers with variable strain states. For example, by depositing a periodic array of Au dots, we should be able to create a periodic strain within a single monolayer of a TMDC. The implication is that the band gap will, itself, be periodic. Further, by tuning the Fermi level through gating, we should be able to create long wavelength 2D charge density waves that are likely to display nonlinear current vs. voltage characteristics. In another set of experiments, we will develop approaches to locally "weld" a TMDC film strained due to thermal mismatch to the substrate. We will then use the evaporating droplet method to release the remaining strains. This will give us the ability to essentially "write" a wide array of strain states into a single TMDC monolayer, and thereby tune opto-electronic properties.

Finally, it is clear that a broad range of semiconductor technologies would be impacted by the ability to inexpensively grow one material upon any other. Therefore, we are continuing our efforts to grow high quality, semiconductor films of any desired thickness upon any substrate that could have important implication for practical applications. Notably, in a number of cases we have discovered that it is possible to have non-epitaxial growth with crystallite sizes much larger than the film thickness,[10,11] and that this effect can be modulated in confined spaces.[12] In the next 3 years, we will push the limits of these approaches to lower substrate temperatures and to other material systems.

References

(1) Ahn, G. H.; Amani, M.; Rasool, H.; Lien, D.-H.; Mastandrea, J. P.; Ager III, J. W.; Dubey, M.; Chrzan, D. C.; Minor, A. M.; Javey, A. Strain-Engineered Growth of Two-Dimensional Materials. *Nat. Commun.* **2017**, *8*, 608.

(2) Kiriya, D.; Zhou, Y.; Nelson, C.; Hettick, M.; Madhvapathy, S. R.; Chen, K.; Zhao, P.; Tosun, M.; Minor, A. M.; Chrzan, D. C.; Javey, A. Oriented Growth of Gold Nanowires on MoS 2. *Adv. Funct. Mater.* **2015**, *25*, 6257–6264.

(3) Zhou, Y.; Kiriya, D.; Haller, E. E.; Ager, J. W.; Javey, A.; Chrzan, D. C. Compliant Substrate Epitaxy: Au on MoS_2. *Phys. Rev. B* **2016**, *93*, 054106.

(4) Jacobs, M. H.; Stowell, M. J. Moiré Patterns and Coherent Double-Positioning Boundaries in {111} Epitaxial Gold Films. *Philos. Mag.* **1965**, *11*, 591–603.

(5) Chen, Y.; Ke, F.; Ci, P.; Ko, C.; Park, T.; Saremi, S.; Liu, H.; Lee, Y.; Suh, J.; Martin, L. W.; Ager, J. W.; Chen, B.; Wu, J. Pressurizing Field-Effect Transistors of Few-Layer MoS 2 in a Diamond Anvil Cell. *Nano Lett.* **2017**, *17*, 194–199.

(6) Lien, D.-H.; Amani, M.; Desai, S. B.; Ahn, G. H.; Han, K.; He, J.-H.; Ager, J. W.; Wu, M. C.; Javey, A. Large-Area and Bright Pulsed Electroluminescence in Monolayer Semiconductors. *Nat. Commun.* **2018**, *9*, 1229.

(7) Kim, H.; Ahn, G. H.; Cho, J.; Amani, M.; Mastandrea, J. P.; Groschner, C. K.; Lien, D.; Zhao, Y.; Ager, J. W.; Scott, M. C.; Chrzan, D. C.; Javey, A. Synthetic WSe 2 Monolayers with High Photoluminescence Quantum Yield. *Sci. Adv.* **2019**, *5*, eaau4728.

(8) Amani, M.; Taheri, P.; Addou, R.; Ahn, G. H.; Kiriya, D.; Lien, D.-H.; Ager, J. W.; Wallace, R. M.; Javey, A. Recombination Kinetics and Effects of Superacid Treatment in Sulfur- and Selenium-Based Transition Metal Dichalcogenides. *Nano Lett.* **2016**, *16*, 2786–2791.

(9) Amani, M.; Lien, D.-H.; Kiriya, D.; Xiao, J.; Azcatl, A.; Noh, J.; Madhvapathy, S. R.; Addou, R.; KC, S.; Dubey, M.; Cho, K.; Wallace, R. M.; Lee, S.-C.; He, J.-H.; Ager, J. W.; Zhang, X.; Yablonovitch, E.; Javey, A. Near-Unity Photoluminescence Quantum Yield in MoS_2. *Science* **2015**, *350*, 1065–1068.

(10) Kapadia, R.; Yu, Z.; Wang, H.-H. H.; Zheng, M.; Battaglia, C.; Hettick, M.; Kiriya, D.; Takei, K.; Lobaccaro, P.; Beeman, J. W.; Ager, J. W.; Maboudian, R.; Chrzan, D. C.; Javey, A. A Direct Thin-Film Path towards Low-Cost Large-Area III-V Photovoltaics. *Sci. Rep.* **2013**, *3*, 2275.

(11) Kapadia, R.; Yu, Z.; Hettick, M.; Xu, J.; Zheng, M. S.; Chen, C. Y.; Balan, A. D.; Chrzan, D. C.; Javey, A. Deterministic Nucleation of InP on Metal Foils with the Thin-Film Vapor-Liquid-Solid Growth Mode. *Chem. Mater.* **2014**, *26*, 1340–1344.

(12) Mastandrea, J. P.; Ager, J. W.; Chrzan, D. C. Nucleation of Melting and Solidification in Confined High Aspect Ratio Thin Films. *J. Appl. Phys.* **2017**, *122*, 105304.

Publications primarily supported by DOE Physical Behavior of Materials 2017-2019

1. Kim, H.; Lien, D.-H.; Amani, M.; Ager, J. W.; Javey, A. Highly Stable Near-Unity Photoluminescence Yield in Monolayer MoS_2 by Fluoropolymer Encapsulation and Superacid Treatment. *ACS Nano* **2017**, *11*, 5179–5185.
2. Morales-Masis, M.; De Wolf, S.; Woods-Robinson, R.; Ager, J. W.; Ballif, C. Transparent Electrodes for Efficient Optoelectronics. *Adv. Electron. Mater.* **2017**, *3*, 1600529.
3. Liu, H.; Choe, H. S.; Chen, Y.; Suh, J.; Ko, C.; Tongay, S.; Wu, J. Variable Range Hopping Electric and Thermoelectric Transport in Anisotropic Black Phosphorus. *Appl. Phys. Lett.* **2017**, *111*, 102101.
4. Mastandrea, J. P.; Ager, J. W.; Chrzan, D. C. Nucleation of Melting and Solidification in Confined High Aspect Ratio Thin Films. *J. Appl. Phys.* **2017**, *122*, 105304.
5. Chen, Y.; Ke, F.; Ci, P.; Ko, C.; Park, T.; Saremi, S.; Liu, H.; Lee, Y.; Suh, J.; Martin, L. W.; Ager, J. W.; Chen, B.; Wu, J. Pressurizing Field-Effect Transistors of Few-Layer MoS_2 in a Diamond Anvil Cell. *Nano Lett.* **2017**, *17*, 194–199.
6. Zhao, P.; Amani, M.; Lien, D.-H.; Ahn, G. H.; Kiriya, D.; Mastandrea, J. P.; Ager, J. W.; Yablonovitch, E.; Chrzan, D. C.; Javey, A. Measuring the Edge Recombination Velocity of Monolayer Semiconductors. *Nano Lett.* **2017**, *17*, 5356–5360.
7. Ci, P.; Chen, Y.; Kang, J.; Suzuki, R.; Choe, H. S.; Suh, J.; Ko, C.; Park, T.; Shen, K.; Iwasa, Y.; Tongay, S.; Ager, J. W.; Wang, L.-W.; Wu, J. Quantifying van Der Waals Interactions in Layered Transition Metal Dichalcogenides from Pressure-Enhanced Valence Band Splitting. *Nano Lett.* **2017**, *17*, 4982–4988.
8. Ahn, G. H.; Amani, M.; Rasool, H.; Lien, D.-H.; Mastandrea, J. P.; Ager III, J. W.; Dubey, M.; Chrzan, D. C.; Minor, A. M.; Javey, A. Strain-Engineered Growth of Two-Dimensional Materials. *Nat. Commun.* **2017**, *8*, 608.
9. Heyman, J. N.; Schwartzberg, A. M.; Yu, K. M.; Luce, A. V.; Dubon, O. D.; Kuang, Y. J.; Tu, C. W.; Walukiewicz, W. Carrier Lifetimes in III-V-N Intermediate-Band Semiconductor. *Phys. Rev. Appl.* **2017**, *7*, 014016.
10. Fonseca, J. J.; Horton, M. K.; Tom, K.; Yao, J.; Walukiewicz, W.; Dubon, O. D. Structure–Property Relationship of Low-Dimensional Layered $GaSe_xTe_{1-x}$ Alloys. *Chem. Mater.* **2018**, *30*, 4226–4232.
11. Lien, D.-H.; Amani, M.; Desai, S. B.; Ahn, G. H.; Han, K.; He, J.-H.; Ager, J. W.; Wu, M. C.; Javey, A. Large-Area and Bright Pulsed Electroluminescence in Monolayer Semiconductors. *Nat. Commun.* **2018**, *9*, 1229.
12. Suh, J.; Tan, T. L.; Zhao, W.; Park, J.; Lin, D.-Y.; Park, T.-E.; Kim, J.; Jin, C.; Saigal, N.; Ghosh, S.; Wong, Z. M.; Chen, Y.; Wang, F.; Walukiewicz, W.; Eda, G.; Wu, J. Reconfiguring Crystal and Electronic Structures of MoS_2 by Substitutional Doping. *Nat. Commun.* **2018**, *9*, 199.
13. Xu, X.; Shukla, S.; Liu, Y.; Yue, B.; Bullock, J.; Su, L.; Li, Y.; Javey, A.; Fang, X.; Ager, J. W. Solution-Processed Transparent Self-Powered p-CuS-ZnS/n-ZnO UV Photodiode. *Phys. status solidi - Rapid Res. Lett.* **2018**, *12*, 1700381.

14. Kim, H.; Ahn, G. H.; Cho, J.; Amani, M.; Mastandrea, J. P.; Groschner, C. K.; Lien, D.; Zhao, Y.; Ager, J. W.; Scott, M. C.; Chrzan, D. C.; Javey, A. Synthetic WSe_2 Monolayers with High Photoluminescence Quantum Yield. *Sci. Adv.* **2019**, *5*, eaau4728.

15. Bullock, J.; Wan, Y.; Hettick, M.; Zhaoran, X.; Phang, S. P.; Yan, D.; Wang, H.; Ji, W.; Samundsett, C.; Hameiri, Z.; Macdonald, D.; Cuevas, A.; Javey, A. Dopant-Free Partial Rear Contacts Enabling 23% Silicon Solar Cells. *Adv. Energy Mater.* **2019**, 1803367.

Defects in oxide semiconductors and ternary alloys

Matthew D. McCluskey, Washington State University (WSU), Pullman, WA

Leah Bergman, University of Idaho (UI), Moscow, ID

Program Scope

This project investigates dopants and defects in oxide semiconductors. This class of materials has a range of potential energy applications, including light emission, photovoltaics, hydrogen production, and fuel cells. In general, oxide semiconductors are *n*-type or insulating as grown. Reliable *p*-type doping, necessary for high-performance devices, has proved to be an elusive goal [1].

To elucidate the physical properties of semiconductor alloys, we are performing systematic studies on ZnS_xO_{1-x}. Alloying enables one to tune the band gap of the semiconductor system and realize a wide range of applications. Our group surmounted materials challenges such as phase segregation and succeeded in growing high-quality thin films. The properties of $Mg_xZn_{1-x}O$ and Ga_2O_3, which have deep-UV band gaps, were also investigated. These studies provide insight into fundamental optical phenomena in oxide semiconductors, which could be important for future solar cell and light emission technologies.

To achieve the project goals, we have pursued a coordinated program of synthesis and optical characterization at WSU and UI (only 8 miles apart). Our fruitful bi-state collaboration takes advantage of resources at both institutions and provides students with excellent research opportunities.

Recent Progress

$\underline{Mg_xZn_{1-x}O}$ alloys up to $x = 0.80$ were grown via a sputtering technique at a low, non-equilibrium temperature of 250°C. X-ray diffraction (XRD) and optical transmission measurements showed these films had a single-phase wurtzite structure with a band-gap range 3.3–4.42 eV. The extent of their thermal stability was studied via controlled post-growth annealing. Low-Mg samples ($x < 0.4$) are highly stable, retaining the wurtzite crystal structure up to 900°C. The situation is different for high-Mg samples ($x > 0.5$). For that composition range, the alloys phase-separated at elevated temperatures. XRD and optical transmission analysis showed that the material separated into wurtzite Zn-rich domains (band gap ~ 3.5 eV) and cubic Mg-rich domains (band gap ~ 6 eV).

Figure 1 summarizes our findings regarding the thermal stability of thin films with respect to thermodynamically stable ceramics studied previously [2]. The stability dynamics of

metastable alloys is a key issue since the formation of phase-segregated clusters may occur in many oxide-based alloys due to their limited solubility. Such multiphase phases can significantly impact optical as well as transport properties of a semiconductor alloy operating in the extreme temperature range.

The oxide-chalcogenide alloy zinc oxysulfide ($ZnS_{1-x}O_x$) is a promising material for optoelectronic applications. The predicted large band-gap bowing may enable engineering of the band gap from the UV to the blue/green region of the electromagnetic spectrum, despite the band gaps of both endmembers being in the UV. $ZnS_{1-x}O_x$ is composed of relatively inexpensive, earth-abundant elements.

In the present work, $ZnS_{1-x}O_x$ thin films grown by sputtering were studied via resonant Raman spectroscopy. Films with low oxygen content exhibit ZnS longitudinal optical (LO) modes and additional modes attributed to O local vibrational modes (LVMs). The frequencies of these modes were explained by a simple mass-defect model. As the O content increases, pairs and larger clusters form, causing the O mode to transition from an LVM to a delocalized phonon. The composition dependence of the modes shows agreement with the modified random element isodisplacement (MREI) model.

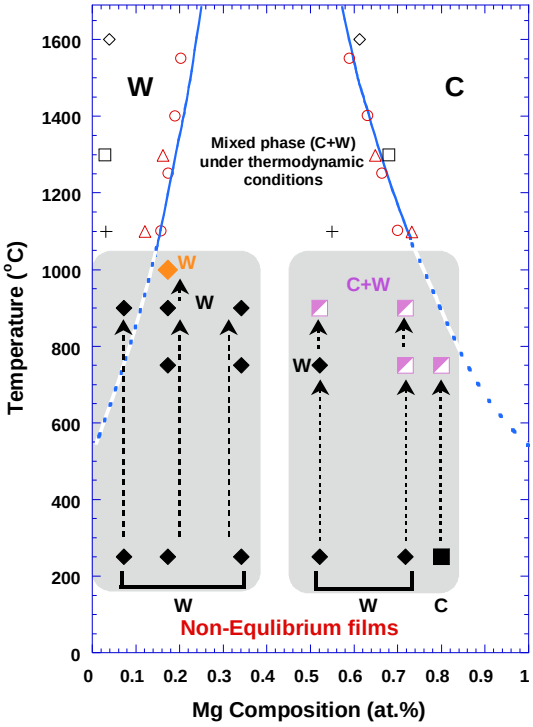

Fig. 1. Wurtzite (W) and cubic (C) phases of $Mg_xZn_{1-x}O$. Data above 1000° are for ceramics grown under thermodynamic equilibrium [2]. Solid and semisolid points are our sputtered samples (grown at 250°C, non-equilibrium). Arrows show the effect of annealing, where C+W is a mixed phase.

Figure 2 presents resonant Raman spectra of zincblende $ZnS_{1-x}O_x$ thin films for various compositions. The O-related mode is observed to shift toward higher energy with increased O content of the films. The ZnS LO mode shifts to lower frequencies and decreases in intensity. The higher-order ZnS LO and O-mode + *n*LO combination modes are suppressed with increasing O content due to alloy broadening.

Figure 3 shows the phonon mode behavior obtained from the MREI model for zincblende $ZnS_{1-x}O_x$. The model reproduces the observed slight decrease in the ZnS LO mode and the shift in the O-related mode. In addition to uncovering interesting physics, this work provides a nondestructive method for calibrating O concentration.

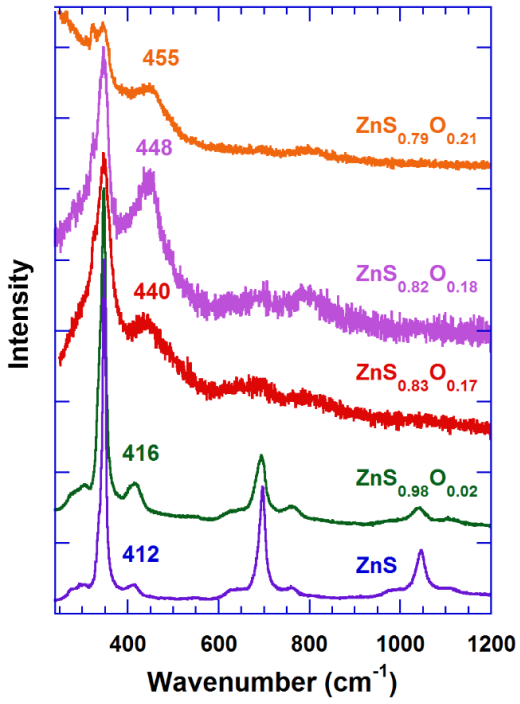

Fig. 2. Resonant Raman spectra for $ZnS_{1-x}O_x$ films at various compositions. The O-related mode (412) shifts toward higher energies with x. (The sample labeled "ZnS" has an estimated O concentration of $x \sim 0.01$.)

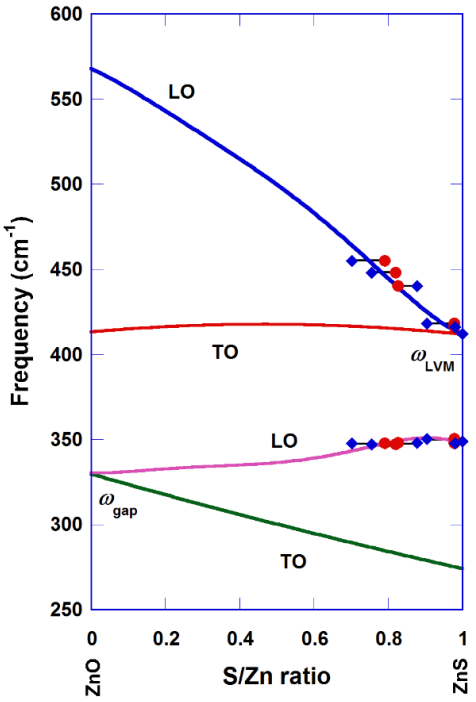

Fig. 3. Phonon frequencies of zincblende $ZnS_{1-x}O_x$ fit by the MREI model (solid lines). Diamonds and circles indicate composition as measured by two different methods.

Optical transmission spectroscopy was employed to determine the band gap of cubic (zincblende) $ZnS_{1-x}O_x$ from $x = 0$ to 0.3. To evaluate the optical band gap, data were fit to a model that included interference effects. As shown in Fig. 4, the band gap drops steeply for dilute oxygen concentrations, followed by a more gradual decrease for $x > 0.05$. This nonlinear behavior is attributed to a transition from isolated oxygen impurities to pairs and larger clusters. The extrapolated band gap reaches a minimum of ~2.9 eV at $x = 0.6$.

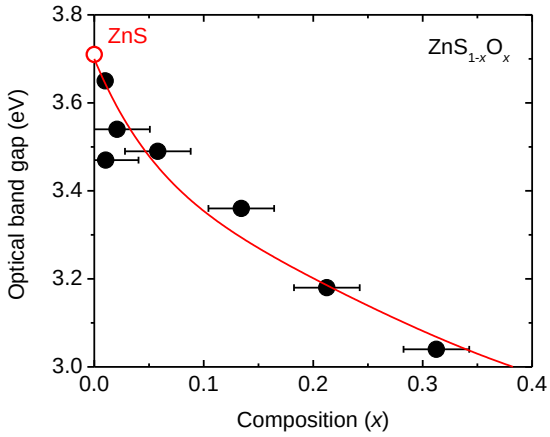

Fig. 4. Band gap versus composition for zincblende $ZnS_{1-x}O_x$ thin films. A fit to the data is shown by the solid line.

Single-crystal undoped and Mg-doped β-Ga_2O_3 were investigated. Mg-doped Ga_2O_3 samples exhibit a strong IR absorption peak at 5148 cm^{-1} [Fig. 5(a)]. Based on its similarity to absorption peaks from Ir^{4+} in other oxides, we attribute it to Ir impurities introduced by the iridium crucible during growth. The peak is due to an internal transition from the ground state to an excited *d*-orbital. A hydrogen anneal at 860°C was performed on the Mg-doped sample. A new hydrogen-related peak occurs in the IR spectrum at 3492 cm^{-1} (Fig. 6), attributed to the O–H bond-stretching mode of a MgH complex. Hydrogen passivation of magnesium acceptors renders them neutral, so they are no longer compensated by iridium donors. This greatly weakens the Ir^{4+} peak [Fig 5(b)].

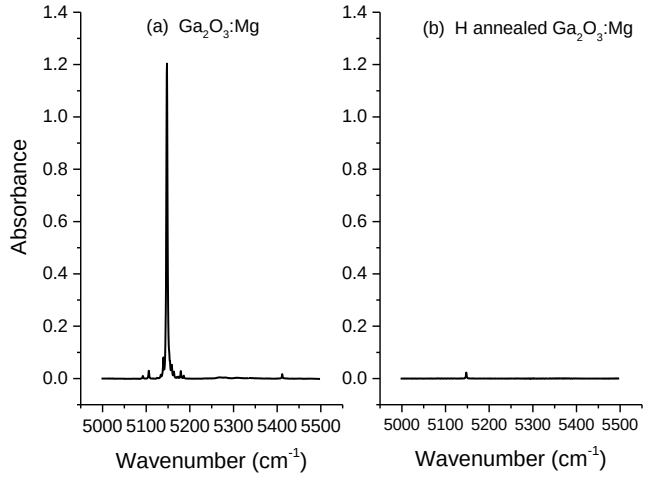

Fig. 5. IR absorption spectrum of Ir^{4+} in Mg-doped Ga_2O_3 before and after a hydrogen anneal.

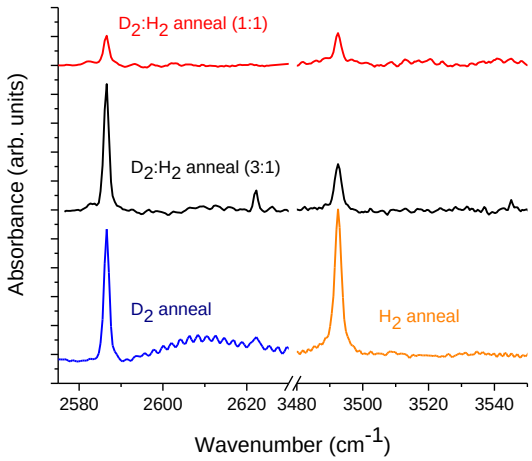

Fig. 6. IR absorption spectra of Ga_2O_3:Mg annealed in H_2 and/or D_2.

Future Plans

Defect properties of β-Ga_2O_3 will be investigated. Unintentional impurities and deliberately introduced dopants will be characterized by IR, UV/visible, and photoluminescence (PL) spectroscopy. Spatially resolved PL measurements will provide maps of optical properties with μm-to-mm length scales. Building on our work on semiconductor alloys, we will investigate the Ga_2O_3-Al_2O_3 system.

References

1. M.D. McCluskey, C.D. Corolewski, J. Lv, M.C. Tarun, S.T. Teklemichael, E.D. Walter, M.G. Norton, K.W. Harrison, and S. Ha, *J. Appl. Phys.* **117**, 112802 (2015).
2. D. Thapa, J. Huso, J. Lapp, N. Rajabi, J.L. Morrison, M.D. McCluskey, and L. Bergman, *J. Mater. Sci.:Mater. Electron.* **29**, 16782-16790 (2018) and references therein.

Publications

J. Huso, L. Bergman, and M.D. McCluskey, "Band gap of $ZnS_{1-x}O_x$ from optical transmission spectroscopy," *J. Appl. Phys.* (in press).

M.D. McCluskey, "Vibrational spectroscopy," in *Characterisation and Control of Defects in Semiconductors*, ed. F. Tuomisto (IET, United Kingdom, 2019), accepted.

J. Huso, J.R. Ritter, L. Bergman, and M.D. McCluskey, "High order oxygen local vibrational modes in $ZnS_{1-x}O_x$," *Phys. Stat. Solidi B* (accepted).

M.D. McCluskey, "Defects in ZnO," in *Defects in Advanced Electronic Materials and Novel Low Dimensional Structures*, ed. I. Buyanova, W. Chen, and J. Stehr (Elsevier, 2018), 1-25. ISBN 978-0081020531.

J.R. Ritter, J. Huso, P.T. Dickens, J.B. Varley, K.G. Lynn, and M.D. McCluskey, "Compensation and hydrogen passivation of magnesium acceptors in β-Ga_2O_3," *Appl. Phys. Lett.* **113**, 052101:1-5 (2018).

D. Thapa, J. Huso, J. Lapp, N. Rajabi, J. Morrison, M.D. McCluskey, and L. Bergman, "Thermal stability of ultra-wide-bandgap MgZnO alloys with wurtzite structure," *Journal of Materials Science: Materials in Electronics* **29**, 16782-16790 (2018).

N.S. Parmar, J.-W. Choi, L.A. Boatner, M.D. McCluskey, and K.G. Lynn, "Formation of high concentrations of isolated Zn vacancies and evidence for their acceptor levels in ZnO," *Journal of Alloys and Compounds* **729**, 1031-1037 (2017).

J. Huso, J.R. Ritter, D. Thapa, K.M. Yu, L. Bergman, and M.D. McCluskey, "Oxygen vibrational modes in $ZnS_{1-x}O_x$ alloys," *J. Appl. Phys.* **123**, 161537:1-5 (2017).

D. Thapa, J. Huso, K. Miklos, P.M. Wojcik, D.N. McIlroy, J.L. Morrison, C. Corolewski, M.D. McCluskey, T.J. Williams, M.G. Norton, and L. Bergman, "UV-luminescent MgZnO semiconductor alloys: Nanostructure and optical properties," *J. Mater. Sci.:Mater. Electron.* **28**, 2511–2520 (2017).

Unique optical excitations in topological insulators

PI: Stephanie Law

Department of Materials Science and Engineering, University of Delaware, Newark DE 19716

Program Scope

Topological insulators (TIs) exhibit a bulk bandgap crossed by surface states with linear dispersion and spin-momentum locking. Among other interesting properties, these surface states house exotic plasmonic excitations that are predicted to be two-dimensional, massless, and spin-polarized. The goal of this program is to explore the properties of Dirac plasmons in topological insulators (TIs), understand how these plasmons couple both to each other and to other excitations in the system, and discover how this coupling in both single-layer and multi-layer systems modifies the photonic band structure of the TI system. The first phase of the research focuses on exotic plasmonic excitations in single TI layers. Because the TI films are thinner than the wavelength of the incident light, plasmons will simultaneously be excited on the top and bottom surfaces of the films. We will also explore a recent theoretical prediction that TI nanoparticles will form a new hybrid plasmonic mode called a surface topological plasmon by strongly coupling to the TI α-phonon.

The second phase leverages our ability to grow periodic layered structures comprising TIs and trivial band insulators (BIs) by molecular beam epitaxy (MBE). Plasmons will be excited at each TI/BI interface and interact with each other through their evanescent electric fields. As we add more layers, more plasmonic modes become available. Similarly, strong interactions between plasmons arranged in a periodic superlattice are likely to lead to new optical states, which evolve into a photonic band structure. Once this is understood, we can move on to other questions including understanding the dispersion surface of a multilayered TI hyperbolic metamaterial, which is the natural endpoint of a multilayered system. The ultimate goal is to have a complete understanding of and control over Dirac plasmons in TIs.

Recent Progress

TI plasmons

TI films grown by molecular beam epitaxy with the Fermi energy in the conduction band can have three possible contributions to the electron density: massive bulk electrons, massless 2D Dirac electrons, and massive 2D electrons from a surface accumulation layer. We are interested in the properties of the coupled plasmons arising from the massless 2D Dirac electrons on the top and bottom surfaces of a TI thin film. Fortunately, the dispersion relationships for massive and massless plasmons are quite different. In particular, the plasmon frequency depends on both the wavevector and the film thickness in different ways for these three types of plasmons. To understand the dispersion of coupled Dirac plasmons in TI films, we grew Bi_2Se_3 films of three

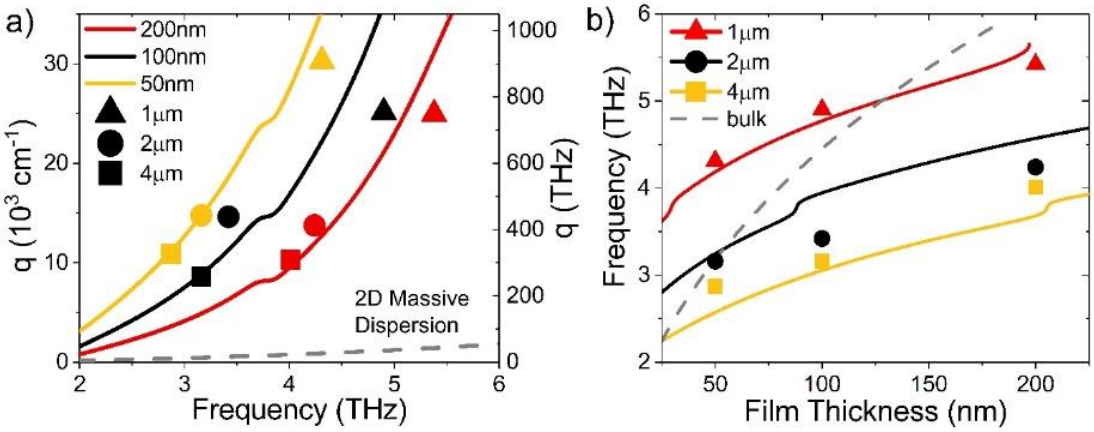

Figure 1 Experimental plasmon frequencies (solid symbols) and theoretical dispersion curves (solid lines) for coupled 2D Dirac plasmons. Dashed lines show massive plasmon dispersion. Figure from [1]

thicknesses (50nm, 100nm, and 200nm) and etched them into stripes of three different widths (1μm, 2μm, and 4μm) for a total of nine samples. Etching the films into stripes is necessary to match the wavevector of light in free space to that of the localized plasmon in the TI. We measured extinction spectra for all nine films and fitted the data using a Fano model. We extracted the plasmon frequency as a function of both wavevector and film thickness and plotted the experimental data against the theoretical curves, as shown in Figure 1 [1]. We found an exceptionally good match considering there are no fitting parameters in the theoretical curves. We are therefore confident that we have excited coupled Dirac plasmons in TI thin films. In addition to mapping the dispersion relationship, we also discovered that these materials show extraordinary optical properties. Our best samples showed mode indices of over 200, indicating that they can confine light to 1/200th of its free space wavelength. Normally, as the confinement of light increases, so does the scattering rate. However, we found that the plasmon lifetime (as determined by the full width half maximum of the resonance) was of order hundreds of femtoseconds. We attribute this long lifetime to the spin-momentum locking of the Dirac electrons, resulting in fewer scattering pathways for the electrons. These materials could find use as THz waveguides.

TI growth

To date, most TI films have shown substantial bulk doping. The high density of massive bulk carriers swamps the signal from the massless surface electrons in transport measurements. In addition, the presence of massive carriers is an additional scattering pathway for the Dirac carriers even in optical measurements. In order for TI films to reach their full potential, we need films in which the Fermi energy is within the bulk bandgap. It was previously thought that the high density of electron dopants came from selenium vacancies in the films. However, we found that TI films grown with a selenium cracker source showed a constant sheet density regardless of film thickness, indicating that point defects in the bulk of the film were not the dominant cause of electron doping [2]. After growing a series of Bi2(Se1-xTex)3 films and finding an increase in

doping as the tellurium content increased, we determined that the first few layers of the Bi2Se3 film were defective, and defects in these layers were doping the entire film [3]. This was unexpected, since Bi2Se3 is a van der Waals (vdW) material so the film-substrate interaction should be weak. Nevertheless, we found that inserting a trivially-insulating lattice-matched (Bi0.5In0.5)2Se3 buffer layer between the Bi2Se3 film and the sapphire substrate significantly reduced the density of trivial carriers while also increasing the electron mobility [4].

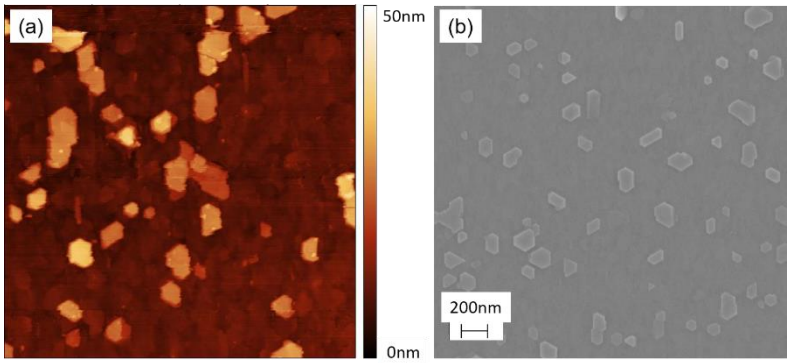

Figure 2 2μm x 2μm atomic force microscope image (a) and scanning electron microscope image (b) of self-assembled Bi_2Se_3 nanowires.

Subsequent work found that this same strategy could be used for Bi2Se3 films grown on GaAs(001), leading to films with low electron density grown on a technologically-relevant substrate. However, in the course of growing (Bi0.5In0.5)2Se3 (BIS) on GaAs(001), found that the phase space for this material pair is more complex than for Bi2Se3 on sapphire. By changing the selenium overpressure, we are able to obtain a variety of self-assembled nanostructures. For low selenium overpressures and low growth rates, the BIS buffer grows in the (221) orientation; Bi2Se3 films grown on this buffer layer also show this non-standard orientation. Previously, the (221) orientation could only be achieved by substrate pre-patterning. We are able to grow this orientation merely by controlling the anion and cation fluxes. The (221) orientation is interesting since, in this orientation, the van der Waals gaps are accessible from the surface for applications in ion intercalation.

For high selenium overpressures and low growth rates, we are able to obtain self-assembled catalyst-free nanowires, as shown in Figure 2. These nanowires form for pure Bi2Se3 and for (Bi1-xInx)2Se3 for x up to 0.5. Higher indium concentrations show continuous films with the expected morphology. Although this data is still being analyzed, we attribute the nanowire morphology to the long diffusion length of bismuth adatoms on GaAs(001). A combination of long adatom diffusion lengths, slow growth rates, high selenium fluxes, and reactive selenium molecules from our selenium cracker source are needed to form nanowires. These conditions are identical to the conditions necessary to form catalyst-free GaN nanowires and we believe the growth mechanism is the same. In future, we hope to be able to control the size and density of nanowires by changing the growth parameters. These nanowires are the ideal platform for us to study the unique surface topological plasmons that are predicted to arise in quantum-confined topological insulator nanostructures [5].

Future Plans

In the coming years, we plan to move from single-layer Bi2Se3 films to multi-layer stacks. In single-layer films, the plasmons on the top and bottom surface couple into an acoustic and optical mode. As discussed above, we have already probed this optical mode and found good agreement with theory. We can now move on to coupling in multi-layer systems. Initial optical measurements of multi-layer films indicate at least two plasmon modes. We plan to measure the dispersion of these modes to understand how plasmons are coupling across the interfaces. Once this is understood, we will vary the layer parameters to gain even more insight into the physics of these complex materials.

We are in the process of measuring the optical properties of our first generation of self-assembled nanowires to see if we observe any optical modes corresponding to the surface topological plasmon. We will continue to refine our efforts to grow quantum-confined topological insulator nanostructures and measure their optical properties. In addition, we will return to the experiment we originally intended to do with Bi2Se3 grown on BIS on GaAs: back gating to tune the plasmon frequency *in situ*. For this experiment, a doped GaAs substrate can be used as a back gate and the BIS buffer as the gate dielectric. Tunability of the plasmon resonance is necessary for device applications, but being able to gate the back surface of the TI separately from the front surface will also give insight into how the plasmons couple across the bulk of the TI.

Until now, all of our experiments on TI plasmons have been done on localized modes in etched nanostructures. We have recently created devices to excite propagating surface plasmon polaritons (SPPs) in TIs. Predictions indicate that propagating SPPs in TIs should be spin-polarized due to the inherent spin texture of the surface electrons. If a propagating SPP could be launched and the spin wave detected, we could measure the degree of spin polarization in the SPP and understand the propagation length and scattering mechanisms. Our initial data on launching a propagating SPP is promising.

References

1. T. P. Ginley and S. Law, "Coupled Dirac Plasmons in Topological Insulators," Adv. Opt. Mater. **6**, 1800113 (2018).
2. T. Ginley and S. Law, "Growth of Bi2Se3 topological insulator films using a selenium cracker source," J. Vac. Sci. Technol. B **34**, 02L105 (2016).
3. Y. Wang, T. P. Ginley, C. Zhang, and S. Law, "Transport properties of Bi2(Se1−xTex)3 thin films grown by molecular beam epitaxy," J. Vac. Sci. Technol. B **35**, 02B106 (2017).
4. Y. Wang, T. P. Ginley, and S. Law, "Growth of high-quality Bi2Se3 topological insulators using (Bi1-xInx)2Se3 buffer layers," J. Vac. Sci. Technol. B **36**, 02D101 (2018).
5. G. Siroki, D. K. K. Lee, P. D. Haynes, and V. Giannini, "Single-electron induced surface plasmons on a topological nanoparticle," Nat. Commun. **7**, 12375 (2016).

Publications

1. T. Ginley, Y. Wang, Z. Wang, and S. Law, "Dirac plasmons and beyond: the past, present, and future of plasmonics in 3D topological insulators," MRS Commun. **8**, 782–794 (2018).
2. Y. Wang, T. P. Ginley, and S. Law, "Growth of high-quality Bi2Se3 topological insulators using (Bi1-xInx)2Se3 buffer layers," J. Vac. Sci. Technol. B **36**, 02D101 (2018).
3. T. P. Ginley and S. Law, "Coupled Dirac Plasmons in Topological Insulators," Adv. Opt. Mater. **6**, 1800113 (2018).

Session VIII

Extraordinary Responsive Magnetic Rare Earth Materials

Vitalij K. Pecharsky, Thomas A. Lograsso, Yaroslav Mudryk, and Durga Paudyal
Ames Laboratory of US DOE, Iowa State University, Ames, Iowa, 50011-3020

Program Scope

Rare earth elements play a critical role in many technological applications, including permanent magnets, sensors, actuators, and solid state cooling, among other. Knowledge of the mechanisms of phase transformations driven by a minor stimulus, followed by a major perturbation of properties is of interest for understanding nonlinear relationships in the free energy, and is crucial for guiding the discovery of advanced energy materials. It is the latter that is the focus of this research, building upon the state-of-the-art synthesis, processing and characterization, integrated with theory, modeling and computations gauged against reliable experimental data.

Our main hypothesis is that by taking advantage of the distinctive electronic structures of the rare earths, combined with the expertise in synthesis, characterization, and modeling of compounds with varying complexity, we will be able to unravel the intricate relationships between localized and itinerant magnetism, bonding, and structure to predict and control metastability, sensitivity to a range of influences, and therefore, physical behaviors of materials. Using a group of diverse lanthanide-based model systems, which represent a range of discontinuous responses, this FWP seeks answers to the following fundamental questions: a) why do magnetostructural transitions (MSTs) occur in some compounds but not in the others, and why are the former scarce, while the latter are common? b) how do we account for the intimately coupled lattice and electronic (spin and orbital) phenomena, spin and valence fluctuations, loss and gain of inversion symmetry, and crystalline and magnetic anisotropies in our interpretation of the phase stability and properties? c) how do we create and manipulate non-equilibrium magnetic and structural states in metallic materials? d) How do we model and consistently predict the response of a crystal lattice to both strong, e.g., temperature and pressure, and weak, e.g., magnetic field external stimuli? e) how can we use the 4*f* electrons, where spin-orbit coupling is naturally strong, to modulate electronic structure of intermetallics and generate new types of quantum materials or/and quantum sensors?

Recent Progress

We have refined synthesis, characterization, and computational tools and employed them to (a) understand the electronic structure mechanism(s) by which the magnetism of rare earth sublattices, where the indirect 4*f*-5*d*-4*f* exchange interactions are dominant, can be affected by the introduction of non-magnetic elements, (b) quantify chemistry-structure-magnetic property relationships in model rare-earth intermetallic systems, (c) build a foundation towards predicting most favorable adjustments of the chemical and physical parameters critical in controlling the responsive behavior of magnetic materials, and (d) unravel the role 4*f*-electron anisotropy plays in influencing magnetostructural phase transformations. A few major achievements are highlighted below:

p-Electron Triggered Magnetoelastic Transition in Eu_2In: Magnetoelastic isosymmetric first-order magnetic transitions (FOMTs) that show practically no hysteresis are highly sought but uncommon: only a handful of material families, almost exclusively transition metal-based, are known to exhibit them. They were virtually unknown among lanthanide-rich intermetallics, yet,

we discovered an FOMT in Eu_2In that occurs at T_C = 55 K [1]. This transition is remarkable because it is associated with a large latent heat and an exceptionally high magnetocaloric effect in low magnetic fields, but with tiny lattice discontinuities and negligible hysteresis, all highly desired properties, *e.g.*, for magnetic cooling. An active role of the Eu-5*d* and In-4*p* states and a unique electronic structure borne by In to Eu charge transfer, altogether result in an unusual exchange mechanism that sets the transition in motion (Fig. 1). Understanding of the interplay between Eu-5*d* and In-4*p* electronic states opens the door toward developing new classes of magnetic functional materials.

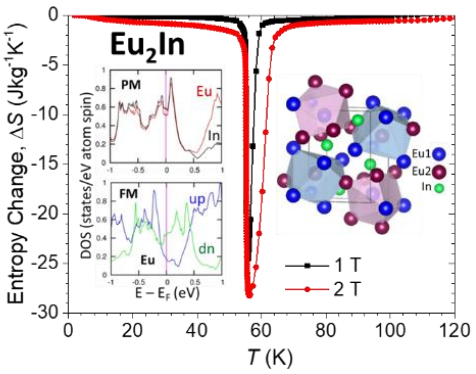

Fig. 1. Giant magnetocaloric effect associated with unique magnetoelastic transformation in Eu_2In compound. Strong Eu 5*d* and In 4*p* orbital overlap fills 5*d* band of divalent Eu, which spin polarizes in the ferromagnetic (FM) state enabling indirect 4*f*-4*f* interaction.

Role of 4*f*-electrons in crystallographic and magnetic complexity of mixed-lanthanide intermetallics: $HoCo_2$ exhibits a sequence of coupled magnetic and structural transformations [2], while other binary RCo_2 Laves phase alloys formed by heavy lanthanides show single transitions. Our recent study of $Er_{1-x}Dy_xCo_2$ [3] demonstrates that at x = 0.25 the system mimics the behavior of binary $HoCo_2$ by undergoing orthorhombic distortion that is not observed in either Er or Dy parent binaries, in addition to a first-order cubic to tetragonal transformation. Using both experiments and DFT we show how anisotropic 4*f* charge densities of different lanthanides effectively interact and collectively determine the magnetism and crystallography of mixed rare-earth compounds.

Enhancing magnetism with scandium: Adding scandium to Gd_5Ge_4 – a compound that responds vigorously to magnetic field, pressure and temperature – unexpectedly enhances ferromagnetism and improves reversibility of its distinctively first-order magnetostructural phase transformation. What makes the discovery unique is that gadolinium is the most ferromagnetic ground state element with the largest spin-only magnetic moment of 7 μ_B among all found in nature. Scandium, on the other hand, is practically non-magnetic. Not only the emergent ferromagnetism is improbable, but the $(Gd_{1-x}Sc_x)_5Ge_4$ system displays an unusual sequence of structural transformations (Fig. 2). None of the phenomena were expected from the conventional wisdom because Gd_5Ge_4 and Sc_5Ge_4 adopt the same crystal structure and are in low-magnetization state with no ferromagnetic ordering down to nearly absolute zero temperature. However, first-principles calculations predict robust ferromagnetism that emerges due to strong overlap of 3*d* electronic states of Sc with 5*d* states of Gd. The discovery has a broad impact on how scandium is viewed in magnetism, and it creates a new tool for controlling and manipulating chemistry and physics of energy-relevant rare-earth compounds.

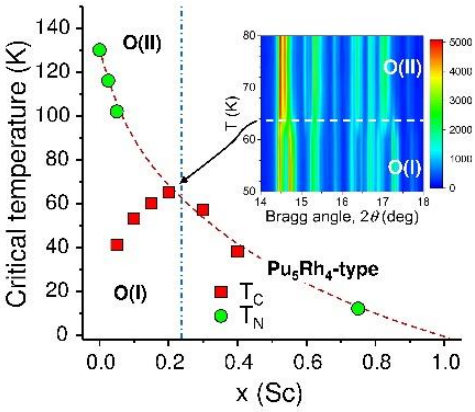

Fig. 2. Magnetic and structural phase diagram of the $(Gd_{1-x}Sc_x)_5Ge_4$ system. The inset shows discontinuous shifts of Bragg peaks for x = 0.2.

Future Plans

We will focus on (1) precise control of magnetic and/or structural transformations at the electronic scale, (2) underlying electronic structure mechanisms

that lead to strong magnetic responsiveness and MSTs in lanthanide-based compounds, (3) correlations between magnetic anisotropy and magnetostructural transformations, (4) exotic physical behaviors and their linkage with the band structure in rare earth compounds that lack crystallographic inversion symmetry, and (5) predictive approach to the discovery of new model systems using the refined computational tools.

We are in a strong position to take advantage of advanced synthesis (both polycrystals and single crystals), characterization, and theoretical and computational modeling tools. Our theoretical and computational results are always verified and refined against reliable experimental data obtained while examining a broad range of structure-property relationships at different length scales and as functions of multiple stimuli. The expected outcome is the development of a clear picture revealing relationships among chemical composition; crystal, magnetic, and microscopic structures; and physical properties of rare earth materials that are poised for breakthroughs in materials science, chemistry and physics of intermetallic phases. New materials with potentially functional physics are expected to emerge from various rare-earth intermetallic systems, and the science of responsive materials will, therefore, be elevated to a new high, where validated computations become refined enough for prediction-based engineering of energy-relevant materials. Following are a few specific examples of work in progress.

4*f* electrons and symmetry-enabled phenomena: Relatively uncommon, intermetallics without inversion symmetry recently became the goldmine for materials science. Loss (gain) of the center of inversion, at least doubles (halves), but may also result in an order of magnitude increase (reduction) of the number of structural degrees of freedom. Through magnetoelastic coupling, this creates instabilities that are likely to lead to unique magnetic responsiveness. Introduction of 4*f* electrons with systematic variations of spin-orbit coupling into the mix is poised to become a new area for high-impact research. Of special interest are modulations of band structures and topologies with 4*f* electrons made possible by transitions involving non-centrosymmetric structures that can be reversibly actuated by external perturbations, in addition to irreversible symmetry states achieved via chemical replacements. For example, R_7Pd_3 (R = La-Nd, Sm, Gd) crystallize in the non-centrosymmetric Th_7Fe_3 structure type (space group $P6_3mc$) [4]. Our comprehensive investigation of a strong anhysteretic FOMT in Nd_7Pd_3 using temperature-dependent x-ray and neutron powder diffraction, physical property measurements, and DFT calculations indicates that an extremely sharp magnetostructural transition in this compound is, in fact, magnetic symmetry-driven transformation between two non-centrosymmetric phases (Fig. 3). This discovery calls for a more inquisitive examination of the physical behaviors of other lanthanide-rich compounds containing precious metals (i.e. Rh, Ir, Pd, Pt), which crystallize in the Th_7Fe_3 structure at room temperature aiming to discover symmetry-related magnetic, transport, and structural phenomena.

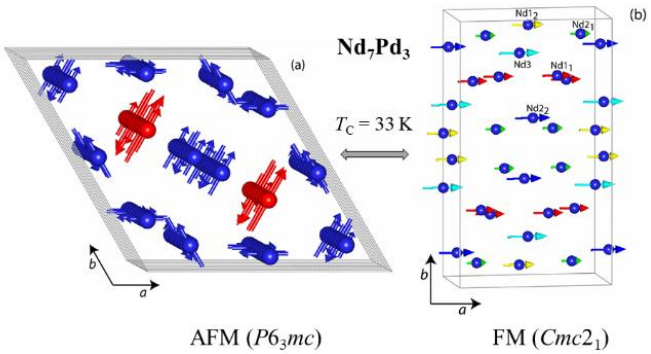

Fig. 3. Symmetry-driven magnetostructural transition between the antiferromagnetic (a) phase of Nd_7Pd_3 and the ferromagnetic (b) phase of Nd_7Pd_3 in $Cmc2_1$. Nd moments on 6c (2b) atoms of space group $P6_3mc$ are shown in blue (red).

Truly discontinuous magnetoelastic transitions: Our recent research uncovered an extraordinarily sharp, strongly first-order phase change in

Eu_2In (see above, [1]). As of now, the transition appears to be unique to Eu_2In, while the Gd_2In and Eu_2Sn analogues order antiferromagnetically via continuous, second-order phase transitions. In order to obtain basic understanding of electronic and structural features that are driving the FOMT transition in Eu_2In and may be critical for its realization in other lanthanide intermetallics a comprehensive study of this material is underway using both theory and experiment. In addition to experimental tools common for this FWP, a number of advanced characterization experiments will be performed both on proposal and collaborative bases: Mössbauer spectroscopy of Eu_2In and Eu_2Sn compounds at McGill University (with D. Ryan, Montreal, Canada) and neutron scattering at ILL (with C. Ritter, Grenoble, France). We plan to perform density functional theory coupled Heisenberg, disorder local moment [5], and spin fluctuation model calculations to further understand electronic structure behind the unique first order phase transformation in Eu_2In.

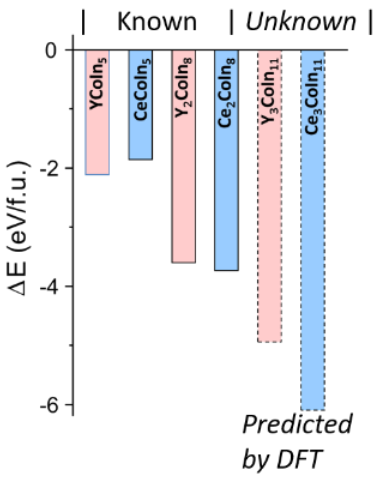

Fig. 4. DFT calculated stability of $R_mCo_nIn_{3m+2n}$ intermetallic compounds.

Harnessing predictive power of refined computational tools: Poorly informed screening of the immense number of conceivable chemistries and structures to discover new phenomena is both inefficient and risks missing novel phases and behaviors. To avoid it, we are aiming at the targeted assembly of novel compounds from geometrically compatible fragments of known structures. Formation energies, ranked against the parents and known combinations in existing compounds, will be evaluated using density functional theory, and used to guide subsequent experimental studies targeting the lowest-energy regions of the computed convex hull(s) to reveal novel thermodynamically stable compounds (Fig. 4). Rare earths and their intermetallics are uniquely suited for this effort because examples where a compound $R_xM_yX_z$ is structurally related to two or more phases within the same family but with different R, M, X, or *x*, *y*, *z* or all of the above, are abundant. This research is a first step toward a bigger goal of enabling theory-driven synthesis science leading to assembly of novel intermetallic structures from simpler building blocks.

References

[1] F. Guillou, A. K. Pathak, D. Paudyal, Y. Mudryk, F. Wilhelm, A. Rogalev, and V. K. Pecharsky, Nat. Comm., **9**, 2925 (2018).

[2] Y. Mudryk, D. Paudyal, A. K. Pathak, V. K. Pecharsky, and K. A. Gschneidner Jr., J. Mater. Chem. C **4**, 4521 (2016).

[3] A. K. Pathak, D. Paudyal, Y. Mudryk, and V. K. Pecharsky, Phys. Rev. B, **96**, 064412 (2017).

[4] J.M. Moreau and E. Parthé, J. Less-Common Met. **32**, 91 (1973).

[5] L. Petit, D. Paudyal, Y. Mudryk, K. A. Gschneidner, Jr., V. K. Pecharsky, M. Lueders, Z. Szotek, R. Banerjee, and J. B Staunton, Phys. Rev. Lett. **115**, 207201 (2015).

Publications

1. X. M. Chen, Y. Mudryk, A. K. Pathak, W. Feng, and V. K. Pecharsky, "Magnetic and Magnetocaloric Properties of Spin-Glass Material $DyNi_{0.67}Si_{1.34}$," *Journal of Magnetism and Magnetic Materials*, **436**, 91-96 (2017). 10.1016/j.jmmm.2017.04.033
2. T. A. Hackett, D. J. Baldwin, and D. Paudyal, "Electronic, Magnetic, and Magnetocrystalline Anisotropy Properties of Light Lanthanides," *Journal of Magnetism and Magnetic Materials*, **441**, 76-84 (2017). 10.1016/j.jmmm.2017.05.019
3. J. Liu, Y. Mudryk, D.H. Ryan, and V.K. Pecharsky, "On the Edge of Periodicity: Unconventional Magnetism of $Gd_{117}Co_{56.4}Sn_{114.3}$," *Journal of Alloys and Compounds*," **726**, 758-764 (2017). 10.1016/j.jallcom.2017.08.009
4. C. Celania, V. Smetana, A. Provino, V. Pecharsky, P. Manfrinetti, and A.-V. Mudring, "R_3Au_9Pn (R = Y, Gd–Tm; Pn = Sb, Bi): A Link between $Cu_{10}Sn_3$ and $Gd_{14}Ag_{51}$," *Inorganic Chemistry*, **56**, 7247-7256 (2017). 10.1021/acs.inorgchem.7b00898
5. Y. Mudryk, D. Paudyal, J. Liu, and V. K. Pecharsky, "Enhancing Magnetic Functionality with Scandium: Breaking Stereotypes in the Design of Rare Earth Materials," *Chemistry of Materials*, **29**, 3962-3970 (2017). 10.1021/acs.chemmater.7b00314
6. A. K. Pathak, D. Paudyal, Y. Mudryk and V. K. Pecharsky, "Role of 4f Electrons in Crystallographic and Magnetic Complexity," *Physical Review B*, **96**, 064412 (2017). 10.1103/PhysRevB.96.064412
7. N. K. Singh, S. Gupta, V. K. Pecharsky, and V. P. Balema, "Solvent-Free Mechanochemical Synthesis and Magnetic Properties of Rare Earth Based Metal-Organic Frameworks," *Journal of Alloys and Compounds*, **696**, 118-122 (2017). 10.1016/j.jallcom.2016.11.220
8. F. Guillou, A. K. Pathak, T. A. Hackett, D. Paudyal, Y. Mudryk, and V. K. Pecharsky, "Crystal, Magnetic, Calorimetric and Electronic Structure Investigation of $GdScGe_{1-x}Sb_x$ Compounds," *Journal of Physics-Condensed Matter*, **29**, 485802 (2017). 10.1088/1361-648X/aa93aa
9. E.M. Levin, C. Cooling, S.L. Bud'ko, W.E. Straszheim, and T.A. Lograsso, "Crystal Structure, Magnetization, ^{125}Te NMR, and Seebeck Coefficient of $Ge_{49}Te_{50}R_1$ (R = La, Pr, Gd, Dy, and Yb)" *Materials Chemistry and Physics*, **192**, 58-66 (2017). 10.1016/j.matchemphys.2017.01.038
10. K. Rudolph, A. K. Pathak, Y. Mudryk, and V. K. Pecharsky, "Magnetostructural Phase Transitions and Magnetocaloric Effect in $(Gd_{5-x}Sc_x)Si_{1.8}Ge_{2.2}$," *Acta Materialia*, **145**, 369-376 (2018). 10.1016/j.actamat.2017.12.024
11. V. Smetana, Y. Mudryk, V. K. Pecharsky, and A. V. Mudring, "Controlling Magnetism Via Transition Metal Exchange in the Series of Intermetallics $Eu(T1, T2)_5In$ (T = Cu, Ag, Au)," *Journal of Materials Chemistry C*, **6**, 1353-1362 (2018). 10.1039/c7tc04964a *The artcile was featured on the cover page of Journal of Materials Chemistry C*
12. S.G. Hunagund, S.M. Harstad, A.A. El-Gendy, S. Gupta, V.K. Pecharsky, and R.L. Hadimani, "Investigating Phase Transition Temperatures of Size-separated Gadolinium Silicide Magnetic Nanoparticles," *AIP Advances*, **8**, 056428 (2018). 10.1063/1.5007686

13. A. A. El-Gendy, S. Harstad, V. Vijayaraghavan, S. Gupta, V. K. Pecharsky, J. Zweit, and R. L. Hadimani, "Ferromagnetic Gd_5Si_4 Nanoparticles as T2 Contrast Agents for Magnetic Resonance Imaging," *IEEE Magnetics Letters*, **8**, 1507504 (2017). 10.1109/LMAG.2017.2728503

14. U. F. Kaneko, P. F. Gomes, A. F. García-Flores, J.-Q. Yan, T. A. Lograsso, G. E. Barberis, D. Vaknin, and E. Granado, "Nematic Fluctuations and Phase Transitions in LaFeAsO: A Raman Scattering Study," *Physical Review B*, **96**, 014506 (2017). 10.1103/PhysRevB.96.014506

15. Q. S. Lin, K. Aguirre, S. M. Saunders, T. A. Hackett, Y. Liu, V. Taufour, D. Paudyal, S. Budko, P. C. Canfield and G. J. Miller "Polar Intermetallics $Pr_5Co_2Ge_3$ and $Pr_7Co_2Ge_4$ with Planar Hydrocarbon-like Metal Clusters," *Chemistry - a European Journal*, **23**, 10516-10521 (2017). 10.1002/chem.201702798

16. L. Luo, L. Men, Z. Liu, Y. Mudryk, X. Zhao, Y. Yao, J.M. Park, R. Shinar, J. Shinar, K.-M. Ho, I.E. Perakis, J. Vela, and J. Wang, "Ultrafast Tetrahertz Snapshots of Exitonic Rydberg States and Electronic Coherence in an Organometal Halide Perovskite," *Nature Communications*, **8**, 15565 (2017). 10.1038/ncomms15565

17. C. Pappas, L. J. Bannenberg, E. Lelievre-Berna, F. Qian, C. D. Dewhurst, R. M. Dalgliesh, D. L. Schlagel, T. A. Lograsso, and P. Falus, "Magnetic Fluctuations, Precursor Phenomena, and Phase Transition in MnSi under a Magnetic Field," *Physical Review Letters*, **119**, 047203 (2017). 10.1103/PhysRevLett.119.047203

18. L. J. Bannenberg, F. Qian, R. M. Dalgliesh, N. Martin, G. Chaboussant, M. Schmidt, D. L. Schlagel, T. A. Lograsso, H. Wilhelm, and C. Pappas, "Reorientations, Relaxations, Metastabilities, and Multidomains of Skyrmion Lattices," *Physical Review B*, **96**, 184416 (2017). 10.1103/PhysRevB.96.184416

19. M. C. Martínez-Velarte, B. Kretz, M. Moro-Lagares, M. H. Aguirre, T. M. Riedemann, T. A. Lograsso, L. Morellon, M. R. Ibarra, A. Garcia-Lekue, and D. Serrate, "Chemical Disorder in Topological Insulators: A Route to Magnetism Tolerant Topological Surface States," *Nano Letters*, **17**, 4047−4054 (2017). 10.1021/acs.nanolett.7b00311

20. S. A. Pierson, O. Nacham, K. D. Clark, H. Nan, Y. Mudryk, and J. L. Anderson, "Synthesis and Characterization of Low Viscosity Hexafluoroacetylacetonate-Based Hydrophobic Magnetic Ionic Liquids," *New Journal of Chemistry*, **41**, 5498-5505 (2017). 10.1039/c7nj00206h

21. M.A. Tanatar, Y. Liu, J. Jarozynski, J.S. Brooks, T.A. Lograsso, and R. Prozorov, "Doping Evolution of the Anisotropic Critical Fields in the Iron-based Superconductor $(Ba_{1-x}K_x)Fe_2As_2$," *Physical Review B*, **96**, 184511 (2017). 10.1103/PhysRevB.96.184511

22. M. Li, V. Smetana, M. Wilk-Kozubek, Y. Mudryk, T. Alammar, V. K. Pecharsky, and A. V. Mudring, "Open-Framework Manganese(II) and Cobalt(II) Borophosphates with Helical Chains: Structures, Magnetic, and Luminescent Properties," *Inorganic Chemistry*, **56**, 11104-11112 (2017). 10.1021/acs.inorgchem.7b01423

23. Y. Liu, L. Zhou, K.W. Sun, W.E. Straszheim, M.A. Tanatar, R. Prozorov, and T.A. Lograsso, "Doping Evolution of the Second Magnetization Peak and Magnetic Relaxation in $(Ba_{1-x}K_x)Fe_2As_2$," *Physical Review B*, **97**, 054511 (2018). 10.1103/PhysRevB.97.054511

24. L. Petit, Z. Szotek, J. Jackson, M. Luders, D. Paudyal, Y. Mudryk, V. Pecharsky, K. A. Gschneidner, and J. B. Staunton, "Magnetic Properties of Gd Intermetallics," *Journal of Magnetism and Magnetic Materials*, **448**, 9-12 (2018). 10.1016/j.jmmm.2017.04.005

25. Y. Liu, Q. Lin, A. K. Pathak, D. Paudyal, and T. A. Lograsso, "Growth of $PrCo_2$ single crystals with a Boron Nitride crucible", *Journal of Crystal Growth,* **507**, 209-212 (2019). 10.1016/j.jcrysgro.2018.10.057

26. J. Liu, Y. Mudryk, D. H. Ryan, V. K. Pecharsky, "On the edge of periodicity: Unconventional magnetism of $Gd_{117}Co_{56.4}Sn_{114.3}$", *Journal of Alloys and Compounds,* **726**, 758-764 (2018). 10.1016/j.jallcom.2017.08.009

27. F. Guillou, A. K. Pathak, D. Paudyal, Y. Mudryk, F. Wilhelm, A. Rogalev, and V. K. Pecharsky, "Non-hysteretic first-order phase transition with large latent heat and giant low-field magnetocaloric effect", *Nature Communications*, **9**, 2925 (2018). 10.1038/s41467-018-05268-4

28. A. K. Pathak, C. M. Bonilla, D. Paudyal, Y. Mudryk, V. K. Pecharsky, "Anomalous specific heat and magnetic properties of $Tm_xDy_{1-x}Al_2$ ($0 \leq x \leq 1$)", *Journal of Alloys and Compounds*, **774**, 321-330 (2019). 10.1016/j.jallcom.2018.09.365

29. J. Liu, Y. Mudryk, V. Smetana, A.-V. Mudring, V. K. Pecharsky, "Anomalous effects of Sc substitution and processing on magnetism and structure of $(Gd_{1-x}Sc_x)_5Ge_4$", *Journal of Magnetism and Magnetic Materials*, **474**, 482-492 (2019). 10.1016/j.jmmm.2018.11.004

30. C. L. Wang, J. Liu, Y. Mudryk, Y. J. Zhu, B. Fu, Y. Long, V. K. Pecharsky, "Magnetic and magnetocaloric properties of $DyCo_2C_x$ alloys", *Journal of Alloys and Compounds*, **777**, 152-156 (2019). 10.1016/j.jallcom.2018.10.169

31. T. Alammar, I. Z. Hlova, S. Gupta, V. Balema, V. K. Pecharsky, and A.-V. Mudring, "Luminescence properties of mechanochemically synthesized lanthanide containing MIL-78 MOFs", *Dalton Transactions,* **47**, 7594-7601 (2018). 10.1039/C7DT04771A

32. C. Ritter, A. Provino, F. Fauth, S.K. Dhar, V.K. Pecharsky, and P. Manfrinetti, "From Tb_3Ni_2 to Tb_3CoNi: The Interplay Between Chemistry, Structure, and Magnetism," Physical Review Materials **3**, 024406 (2019). 10.1103/PhysRevMaterials.3.024406

33. P.J. Bora, S.M. Hastrad, S. Gupta, C.K. Pecharsky, K.J. Vinoy, P.C. Ramamurthy, and R.L. Hadimani, "Gadolinium Silicide (Gd_5Si_4) Nanoparticles for Tunable Broad band Microwawve Absorption," *Materials Research Express*, **6**, 055053 (2019). 10.1088/2053-1591/aafd55

34. M. K. Kashyap, T. A. Hackett, A. Provino, A. K. Pathak, V. K. Pecharsky, and P. Manfrinetti, "Formation, Stability and Magnetism of New $Gd_3TAl_3Ge_2$ Quaternary Compounds (T = Mn, Cu)," *Solid State Phenomena*, **289**, 93-101 (2019). 10.4028/www.scientific.net/SSP.289.93

Atomic Dynamics in Metallic and Other Liquids and Glasses

T. Egami, ***University of Tennessee and Oak Ridge National Laboratory,***
Y. Shinohara and J. R. Morris, ***Oak Ridge National Laboratory,***
W. Dmowski, ***University of Tennessee***

Program Scope

The science of liquids and glasses is much less developed than that of crystalline materials, even though liquids and glasses are as important as crystalline materials in energy-related applications. The main origin of this slow progress is the non-periodicity of their structures, which eluded the application of modern condensed-matter theories, many of which presume lattice periodicity. The overarching goal of this program is to establish a fundamental understanding of atomistic mechanisms which control the structural and dynamic properties of liquids and glasses through combination of tightly coupled experiment, simulation and theory. To achieve this overarching goal this project will focus on the following three specific aims: (1) advance the science of bulk metallic glasses to improve mechanical ductility and promote their possible application in spintronics, (2) develop better understanding of a basic unanswered question on the nature of liquid and glass and the origin of the glass transition, and (3) extend the study of local dynamics to various functional liquids relevant to the DOE mission. Owing to recent advances in experimental tools and computational power, we now have an excellent prospect of achieving substantial progress. In particular, we will examine the mechanism of rapid increase in viscosity of liquid upon cooling, using a new approach with inelastic neutron and x-ray scattering. The outcome of this proposed work will guide us to the development of glasses and liquids with superior properties, and ultimately contribute to the DOE mission through the development of the general physics of liquids and glasses.

Recent Progress

1. Curie-Weiss Law of Liquid Structure and Origin of Glass Transition

When a liquid is cooled without crystallization, *i.e.*, cooled into the supercooled state, eventually a liquid becomes a glass. How and why this occurs has been a long-standing mystery [1]. Our structural study of supercooled liquids through the glass transition could lead to the resolution of this mystery [2]. We used high energy X-ray scattering and electro-static levitation in combination with molecular dynamics (MD) simulation and showed that the height of the first peak of the structure function, $S(Q)$, of metallic alloy liquids follows the Curie-Weiss law with a *negative* Curie temperature. Fig. 1 shows $1/[S(Q_1)-1]$, where Q_1 is the first peak position. The negative value of the Curie temperature is evidence of strong structural frustration of glassy order,

which prevents the order from becoming long-range. The Curie-Weiss behavior of $S(Q)$ is characterized by its approach to an ideal liquid (or glass) state. We simulated the structure of the ideal glass by the reverse Monte-Carlo (RMC) method. This state is a new state of matter, with spherically symmetric long-range correlation without lattice periodicity (Fig. 2), and may have unusual properties, such as high stability and high strength.

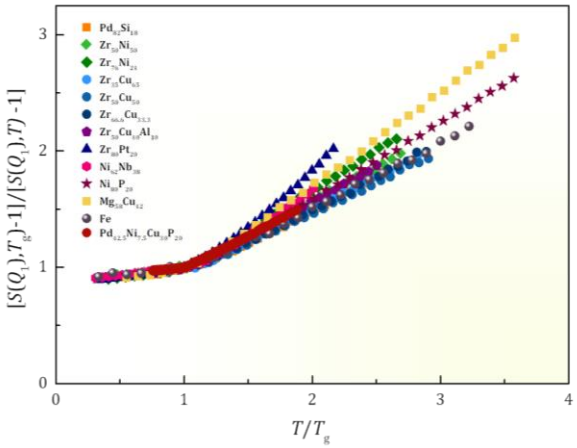

Fig. 1 $1/[S(Q_1) - 1]$ for various liquid metal alloys by MD simulation and x-ray diffraction (Pd-Ni-Cu-P) normalized to the values at T_g [2].

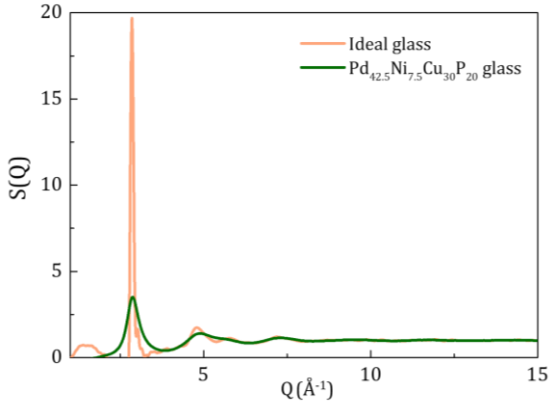

Fig. 2 $S(Q)$ of PdNiCuP glass and that of the ideal glass [2].

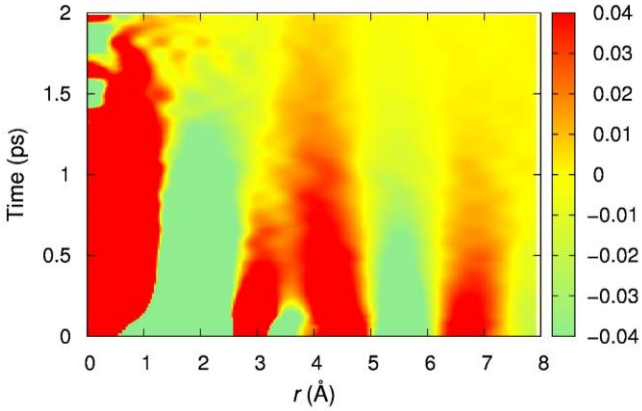

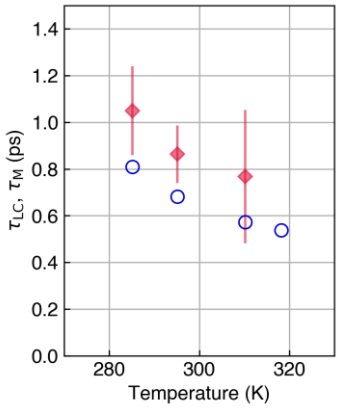

Fig. 3 (Left) The Van Hove function of water at T = 285K [P3], (Right) the Maxwell relaxation time, τ_M, compared to τ_{LC}, the time to lose one neighbor, as a function of time elucidating the origin of viscosity [P20].

2. Origin of Viscosity in Liquid

Even though viscosity is one of the fundamental properties of liquid, its microscopic origin is not fully understood. We determined the spatial and temporal correlation of molecular motions of water near room temperatures and its temperature variation on pico-second in time-scale and sub-nm in spatial scale through high-resolution inelastic x-ray scattering (IXS) measurement [P3]. The results, expressed in terms of the time-dependent pair-distribution function (PDF) called the

Van Hove function, show that the time-scale of the decay of the molecular correlation, τ_{LC}, is nearly equal to the Maxwell relaxation time, τ_M (= η/G_∞, η is viscosity G_∞ is instantaneous shear modulus) (Fig. 3 [P3, P20]). The Van Hove function, $G(r, t)$, is obtained by the double-Fourier-transformation of the dynamic structure factor, $S(Q, E)$, determined by inelastic scattering, to real-space and time. This conclusion validates our earlier finding that $\tau_M = \tau_{LC}$, and the topological changes in atomic or molecular connectivity are the origin of viscosity in liquid [3].

3. De Gennes Narrowing

The de Gennes narrowing phenomenon is frequently observed by neutron or x-ray scattering measurements of the dynamics of complex systems, such as liquids, proteins, colloids, and polymers. The characteristic slowing down of dynamics in the vicinity of the maximum of the total scattering intensity is commonly attributed to enhanced cooperativity. We arrived at an alternative view on its origin through the examination of the time-dependent pair correlation function, the Van Hove correlation function, for a model liquid in two, three, and four dimensions. We find that the relaxation time increases monotonically with distance and the dependence on distance varies with dimension. We propose that de Gennes narrowing in most of the time is a mere consequence of this geometrical effect, is not evidence of collective motion. Similarly the α-relaxation time, often used in describing the liquid dynamics, is not the real structural relaxation time. The correct analysis of dynamics requires the knowledge of the full Van Hove function [P15].

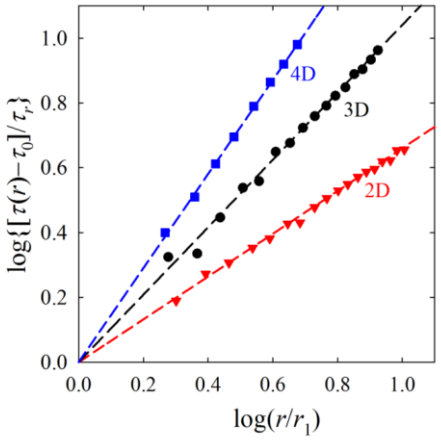

Fig. 4 Dependence of the relaxation time of the Van Hove function on distance, r, for 2, 3 and 4 dimensions in the log-scale [P15].

Future Plans

1. Viscosity of Salty Water and Electrolytes

70% of the earth is covered by salt water, and our body is mostly made of salt water. Yet how salt ions change the viscosity of water is not well-understood, particularly because many salts increase viscosity whereas some reduce it. We collected the IXS spectra for aqueous solution of various salts and determined the changes in the Van Hove function caused by the addition of salts. All of them appear to slow down the dynamics, which may challenge the conventional picture based on the structure modification by salts.

Various liquid electrolytes are used for semiconductor gating [4] and energy storage [5]. Molecular mobility of these liquids is a major issue in developing liquid electrolytes. We apply our Van Hove function technique to address this question. The energy resolution of the current

IXS method does not allow investigation of dynamics slower than 1 ps, so we will use the inelastic neutron scattering (INS) method with higher energy resolution. We are also developing the x-ray photon correlation spectroscopy method with the free-electron x-ray laser and the split-beam technique to address time-scale beyond 100 ps.

2. Ideal Glass

We will analyze the local structure of the ideal glass obtained by the RMC simulation for the $S(Q)$ of liquid extrapolated to the Curie temperature, and determine its properties by simulation. This could lead to the experimental realization of the ideal glass. We also will develop the theory of the atomic-level stresses to explain the Curie-Weiss law of the liquid structure discussed above.

3. Ductility of Metallic Glasses

Metallic glasses are mechanically strong, but many of them are brittle, preventing wide use as structural materials. We found that the ductility is related to the local anelastic response (local atomic rearrangement) which can be observed by x-ray diffraction under stress in terms of the deviation in the anisotropic PDF from that expected for the affine deformation. By simulating the anelastic response by the DFT calculation we will identify the electronic origin of anelasticity, such as the extent of the local orbital anisotropy, local covalency and charge transfer.

4. Spintronics and Metallic Glass

Spintronics, in which not only memory but also logic function is carried out by spin currents, is attractive because of speed and small energy consumption. The major drawback, however, is the read-out has to be still electronic, and the process of converting the spin signal to charge signal is not efficient. In collaboration with M. Chen at Johns Hopkins University we found that Au-Si metallic glass shows strong inverse spin Hall effect (ISHE) which is a measure of the strength of spin-charge coupling, whereas the effect is dramatically decreased when it is crystallized. We explained this result in terms of the unique nature of metallic glass that the structural symmetry is locally broken. However, the details of the microscopic mechanism of ISHE are still unclear. We propose a combined experimental and theoretical research to understand the ISHE in metallic glasses and to develop better BMG for spintronics.

References

1. P. W. Anderson, *Science* **267**, 1615 (1995).
2. C. W. Ryu, W. Dmowski, K. F. Kelton, G. W. Lee, E. S. Park, J. R. Morris and T. Egami, unpublished.
3. T. Iwashita, D. M. Nicholson and T. Egami, *Phys. Rev. Lett.*, **110,** 205504 (2013).
4. J. T. Ye, S. Inoue, K. Kobayashi, Y. Kasahara, H. T. Yuan, H. Shimotani and Y. Iwasa, *Nature Mater*. **22,** 125 (2010).
5. Y. Gogotsi, *Nature Nanotechnology* **13,** 625 (2018).

Publications supported by the DOE-BES ['17, '18]

P1. W. Dmowski, S. O. Diallo, K. Lokshin, G. Ehlers, G. Ferré, J. Boronat and T. Egami, "Observation of dynamic atom-atom correlation in liquid Helium in real space", *Nature Communications,* **8,** 15294 (2017).

P2. Yue Fan, T. Iwashita, and T. Egami, "Energy landscape-driven nonequilibrium evolution of inherent structure in disordered material", *Nature Communications,* **8,** 15417 (2017).

P3. T. Iwashita, B. Wu, W.-R. Chen, S. Tsutsui, A.Q. R. Baron and T. Egami, "Seeing real-space dynamics of liquid water through inelastic X-ray scattering", *Science Advances,* **3,** e1603079 (2017).

P4. J. S. Langer, "Thermal effects in dislocation theory II. Shear banding," *Phys. Rev. E* 95, 013004 (2017).

P5. J. S. Langer, "Yielding transitions and grain-size effects in dislocation theory," *Phys. Rev. E* 95, 033004 (2017).

P6. T. Egami, "Alex and the origin of high-temperature superconductivity", in *High-T_C Copper Oxide Superconductors and Related Novel Materials*, ed. A. Bussmann-Holder et al. Springer Series in Materials Science **255** (Springer Verlag, 2017) Chapter 4, pp. 35-46.

P7. W. Dmowski, S. Gierlotka, Y. Yokoyama, B. Palosz, and T. Egami, "Pressure-induced liquid-to-liquid transition in Zr-based superdooled melts and pressure quenched glasses", *Scientific Reports,* **7,** 6564 (2017).

P8. K. C. Le, T. M. Tran, and J. S. Langer, "Thermodynamic dislocation theory of high-temperature deformation in aluminum and steel", *Phys. Rev. E* **96,** 013004 (2017).

P9. J. S. Langer, "Thermodynamic theory of dislocation-enabled plasticity", *Phys. Rev. E* 96, 053005 (2017).

P10. T. Liu, Y. F. Gao and H. Bei. "Probing elastically or plastically induced structural heterogeneities in bulk metallic glasses by nanoindentation pop-in tests ", *AIP advances* **7,** 085216 (2017).

P11. S. Perticaroli, B. Mostofian, G. Ehlers, J. C. Neuefeind, S. O. Diallo, C. B. Stanley, L. Daemen, J. Katsaras, T. Egami, X. Cheng and J. D. Nickels, "Structural relaxation, viscosity, and network connectivity in a hydrogen bonding liquid", *Phys. Chem. Chem. Phys.*, **19,** 25859 (2017).

P12. R. J. Olsen, A. K. Gillespie, C. I. Contescu, J. W. Taylor, P. Pfeifer, and J. R. Morris, "A phase transition of H_2 in subnanometer pores observed at 75 Kelvin," *ACS Nano* 11, 11617 (2017).

P13. T. L. Meyer, R. Jacobs, D. Lee, L. Jiang, J. W. Freeland, C. Sohn, T. Egami, D. Morgan and Ho Nyung Lee, "Strain control of oxygen kinetics in Ruddlesden-Popper oxides", *Nature Communications,* **9,** 92 (2017).

P14. S. Zhao, T. Egami, G. M. Stocks, Y. Zhang, "Effect of *d* electrons on defect properties in NiCoCr and NiCoFeCr concentrated solid solution alloys", *Phys. Rev. Mater.* **2,** 013602 (2018).

P15. B. Wu, T. Iwashita and T. Egami, "Atomic dynamics in simple liquid: De Gennes narrowing revisited", *Phys. Rev. Lett.,* **120,** 135502 (2018).

P16. T. Nagase, A. Takeuchi, K. Amiya and T. Egami, "Solid state amorphization of metastable $Al_{0.5}$TiZrPdCuNi high entropy alloy investigated by high voltage electron microscopy", *Materials Chemistry and Physics,* **210,** SI 291 (2018).

P17. Y. Tong, W. Dmowski, H. Bei, Y. Yokoyama and T. Egami, "Mechanical rejuvenation in bulk metallic glass induced by thermo-mechanical creep", *Acta Mater.,* **148,** 384 (2018).

P18. A. Pramanick, W. Dmowski, T. Egami, A. Setiadi Budisuharto, F. Weyland, N. Novak, A. D. Christianson, J. M. Borreguero, D. L. Abernathy, MRV Jørgensen, "Stabilization of polar nano regions in Pb-free ferroelectrics", *Phys. Rev. Lett.* **120,** 207603 (2018).

P19. E. Novak, N. Jalarvo, S. Gupta, K. Hong, S. Förster, T. Egami, and M. Ohl, "Dynamics in the plastic crystalline phases of cyclohexanol and cyclooctanol studied by quasielastic neutron scattering", *J. Phys. Chem. B,* **122,** 6296 (2018).

P20. Y. Shinohara, W. Dmowski, T. Iwashita, B. Wu, D. Ishikawa, A. Q. R. Baron and T. Egami, "Viscosity and real space molecular motion of water: Observation with inelastic X-ray scattering", *Phys. Rev. E,* **98,** 022604 (2018).

P21. J. Ketkaew, W. Chen, H. Wang, A. Datye, M. Fan, G. Pereira, U. D. Schwarz, Z. Liu, R. Yamada, W. Dmowski, M. D. Shattuck, C. S. O'Hern, T. Egami, E. Bouchbinder and J. Schroers, "Mechanical glass transition revealed by the fracture toughness of metallic glasses", *Nature Commun.,* **9,** 3271 (2018).

P22. J. S. Langer, "Thermodynamic analysis of the Livermore molecular-dynamics simulations of dislocation-mediated plasticity", *Phys. Rev. E,* **98,** 023006 (2018).

P23. T. Egami, "Real-space description of dynamics of liquids," *Quantum Beam Science,* **2,** 22 (2018).

P24. J. Bellissard and T. Egami, "Simple theory of viscosity in liquids", *Phys. Rev. E,* **98,** 063005 (2018).

Actinide Materials under Extreme Conditions

Krzysztof Gofryk, Idaho National Laboratory

Current Program Scope

In order to better understand the thermal properties of actinide materials, one needs to understand its magneto-elastic properties, especially in the strong coupling regime between magnetism and lattice vibrations. Our recent research has revealed that single crystals of UO_2, subjected to strong magnetic fields along 3-fold axes in the magnetic state, exhibit the abrupt appearance of positive linear magnetostriction leading to a trigonal distortion. Upon reversal of the field the linear term also reverses sign, a hallmark of piezomagnetism [1,2]. This is the first time an 5*f*-elecron spin system shows this kind of behavior. Due to the novelty of the observed phenomena several important issues need to be addressed, which are related to the origin of the piezomagnetic ground state in UO_2. In particular; (*i*) the role of oxygen in Jahn-Teller interactions and its symmetry; (*ii*) magnetic properties of UO_2 in high magnetic field state; and (*iii*) microscopic origin of the competing crystallographic phases and its role in piezomagnetic properties in this material. In order to answer these questions, we have designed and performed series of experiments (some of them for the first time ever) involving National High Magnetic Fields Laboratories at Los Alamos (pulse fields) and Tallahassee (DC fields), and Advanced Photon Source at ANL (pulse fields).

Recent Progress

To disturb uranium-oxygen environment in the UO_2 cubic cell and associated Jahn-Teller interactions we have prepared single crystals of UO_{2+x} (x = 0, 0.033, 0.04, and 0.11) and performed high-field magnetostriction measurements in pulse magnetic fields up to 65 T. We have found that the change in the oxygen environment interrupts the local symmetry of the Jahn-Teller distortion and strength of its interactions. The small change in the oxygen stoichiometry leads to drastic change in the magneto-electric properties (due to change in the magnetic point group) and consequently to disappearance of the piezomagnetism in UO_2 (see Figure 1a, paper in preparation). We have also performed high-field torque measurements on oriented UO_2 crystals. These measurements, performed in DC magnetic fields up to 35 T and under rotation, will help us to understand the interplay of the complex non-collinear 3***k*** antiferromagnetic structure with the lattice. We observed that the magnetic torque shows characteristic anomalies at the same fields where the magnetic switching occurs in the magnetostriction (see Figure 2b). In addition, the application of the magnetic field that is lower than the critical field leads to the torque version of the "magneto-elastic butterfly" [1]. When the sample is rotated in the magnetic field (rotation towards <110> crystallographic axis) a switching effect is also observed, being consistent with the theoretical model we have developed for piezomagnetism in UO_2 [1] (paper in preparation). Our previous results showed that the magnetostriction of UO_2 (in the magnetic state) is composed of

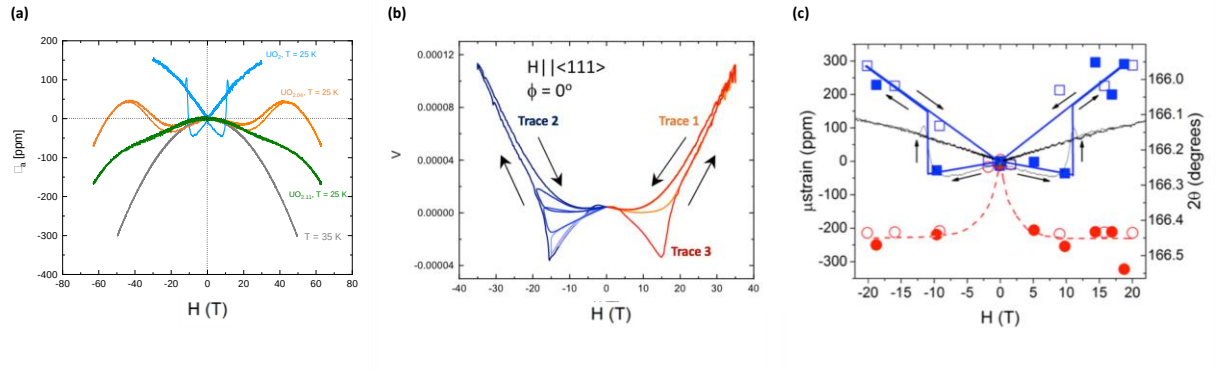

Figure 1. *(a) Isothermal axial strain ε_a vs. H of UO_{2+x} crystals parallel to <111> measured in pulsed magnetic fields up to 65 T and at T = 25 and 35 K. As seen the piezomagnetic behavior is only observed for the stochiometric UO_2; (b) Magnetic torque of UO_2 crystal (magnetic field applied along <111> axis). We see in trace 1 (orange) a very small torque signal to H ≈ 20 T on the field upsweep. During the field down-sweep the torque follows a monotonic quadratic decrease to zero as expected for a linear magnetization. Trace 2 (dark blue) was measured in a subsequent negative magnetic field pulse, and torque was observed to turn negative, displaying a minimum and a relatively rapid switch to positive values at approximately −16 T. Again, a quadratic decrease to zero torque with no remanence is observed during the field down-sweep. When the field direction is changed once again, trace 3 (red) is obtained, displaying a minimum at 16 T and a switch to positive values, with a monotonic quadratic decrease to zero as H is swept back to zero. A partial domain reorientation effect, magnetoelastic butterfly, is obtained when magnetic fields applied are lower than critical field (see Ref. [1] in more detail); (c) A plot of the relative strain calculated from the peak positions in the reversed field state of UO_2 crystal (magnetic field applied along <111> crystallographic direction). The peak corresponding to the dominant strain behavior, as determined by the bulk magnetostriction, is the blue squares, the and the secondary peak corresponding to negative strain is the red circles. Open symbols are used for rising fields and closed for falling fields. The blue solid line and red dashed line are guides to the eye for each, respectively. The solid line is the reversed field state magnetostriction taken in positive and negative field at 25 K;*

two contributions (stretching and expansion). The origin of this behavior is unclear although the positive magnetostriction seems to be related to piezomagnetic behavior and the characteristic change of sign when magnetic field changes direction. It is important, however, to understand its nature due to fact that this behavior is directly related to microscopic origin of piezomagnetic ground state in this material. In order to understand this phenomenon, we have initiated high resolution synchrotron x-ray diffraction measurements on UO_2 single crystals in pulse magnetic fields (up to 30 T) at Advanced Photon Source, ANL. The experiments have been performed in a back-reflection geometry and under alternating magnetic fields, in temperatures below and above the Neel temperature (T_N = 30 K). We have discovered that the 888 Bragg peak of UO_2 crystal (a cube diagonal) splits in the magnetic field when the sample is cooled down below the magnetic ordering temperature. When the direction of the magnetic field is reversed the peaks show some characteristics of piezomagnetic switching (see Figure 1c). The splitting of the 888 peak in the magnetic fields is highly unexpected and has never been observed before for cubic materials (paper in preparation). It is worth noting that this kind of measurement has never been done before and will establish a new direction of research for similar future measurements at APS.

Future Plans

The future plans include:

- Magnetostriction measurements of UO_2 crystals in ultra-high pulse magnetic fields (up to 200 T).
- Quantum oscillations measurements (the Shubnikov–de Haas effect) of HoSb, USb, and US single crystals in pulse magnetic fields up to 65 T.
- Magnetic torque measurements of US, USb, USb_2, and UN single crystals

References

[1] M. Jaime, M. Salamon, A. Saul, V. Zapf, N. Harrison, T. Durakiewicz, J.C. Lashley, D.A. Andersson, C. Stanek, J.L. Smith, and K. Gofryk, *Piezomagnetism and magnetoelastic memory in uranium dioxide*, Nature Communications 8, 99 (2017).

[2] M. Jaime, E.D. Bauer, and K. Gofryk, IEEE eXpress - in press

Publications

Journals:

1. M. Jaime, M. Salamon, A. Saul, V. Zapf, N. Harrison, T. Durakiewicz, J.C. Lashley, D.A. Andersson, C. Stanek, J.L. Smith, and K. Gofryk, Nature Communications 8, 99 (2017).

2. K. Shrestha, D. Antonio, M. Jaime, N. Harrison, D. S. Mast, D. Safarik, T. Durakiewicz, J-C. Griveau, and K. Gofryk, Scientific Reports 7, 6642 (2017).

3. K. Shrestha, M. Chou, D. Graf, H. D. Yang, B. Lorenz, and C. W. Chu, Physical Review B 95, 195113 (2017)

4. K. Shrestha, D. Graf, V. Marinova, B. Lorenz, C. W. Chu, Physical Review B 95, 075102 (2017).

5. K. Shrestha, V. Marinova, D. Graf, B. Lorenz, and C. W. Chu, Journal of Applied Physics 122, 125901 (2017).

6. H. Nhalil, D. Han, M-H Du, S. Chen, D. Antonio, K. Gofryk, and B. Saparov, J. Alloys and Compounds 746, 405 (2018)

7. D. Antonio, K. Shrestha, J, Harp, C. Adkins, Y. Zhang, J. Carmack, and K. Gofryk, J. Nuclear Materials 508, 154 (2018).

8. K. Shrestha, D. Antonio, J-C. Griveau, K. Prokes, P. Gaczynski, E. Colineau, R. Caciuffo, and K. Gofryk, Physical Review Materials 2, 074401 (2018).

9. H. Nhalil, R. Baral, B. O. Khamala, A. Cosio, S. R. Singamaneni, M. Fitta, D. Antonio, K. Gofryk, R. R. Zope, T. Baruah, B. Saparov, and H. S. Nair, Physical Review B – submitted.

10. K. Gofryk, J.-C. Griveau, E. Colineau, K. A. McEwen, W. J. Nellis, and J. L. Smith, ANS Transactions - in press

11. Bhawana Mali, Harikrishnan S. Nair, Hariharan Nhalil, Krzysztof Gofryk, T. W. Heitmann, and Suja Elizabeth, J. Appl. Physics – submitted.

12. M. Jaime, E.D. Bauer, and K. Gofryk, IEEE eXpress - in press

Talks:

1. K. Gofryk, The 47èmes Journées des Actinides, Poland, Karpacz, March 2017 [INVITED TALK, SESSION CHAIR]

2. K. Gofryk, award lecture during the Stig Sunner Award Ceremony at the 72nd Calorimetry Conference (CalCon 2017), Colorado Springs, USA, August 2017 [AWARD RECEIPIENT, SESSION CHAIR, SYMPHOSIUM CHAIR].

3. K. Gofryk, The International Conference on Thermoelectrics, ICT 2017, Pasadena, USA, July 2017

4. K. Gofryk, The 33rd International Thermal Conductivity Conference (ITCC) and the 21st International Thermal Expansion Symposium (ITES), Logan, USA, May 2017

5. K. Gofryk, American Physical Society Meeting, APS 2018, Los Angeles, USA, March 2018.

6. K. Gofryk, The 12th International Conference on Research in High Magnetic Fields (RHMF 2018), Santa Fe, USA June 2018 [INVITED TALK].

7. K. Gofryk, 12th Prague Colloquium on *f*-Electron Systems, Prague, Czech Republic, July 2018. [INVITED TALK, SESSION CHAIR]

8. K. Gofryk, The International Workshop on Dual Nature of *f*-electrons (IWDN2018), Wroclaw, Poland, July 2018 [INVITED TALK].

9. K. Gofryk, The Plutonium Futures–The Science 2018, San Diego, September 2018 [INVITED TALK, SESSION CHAIR].

10. K. Gofryk, NuMat 2018: The Nuclear Materials Conference, Seattle, October 2018

11. K. Gofryk, AVS 2018, Long Beach, October 2018 [SESSION CHAIR].
12. K. Gofryk, Uranium Science, Bristol, UK, January 2019 [INVITED TALK].

Session IX

Energy Carrier Transport in Functionalized Two-Dimensional Layered Chalcogenides

Principal Investigator: Li Shi, University of Texas at Austin

Collaborator: Steve Cronin, University of Southern California

Program Scope

The goal of this collaborative project is to study two-dimensional (2D) layered chalcogenides and tune and improve the electrical, optical, thermal and thermoelectric properties of this class of functional materials. Building on the progress made in our study of phonon and electron transport in pristine 2D layered heterostructures, we investigate both in-plane and cross-plane thermal and thermoelectric transport properties of surface functionalized chalcogenides, and develop tools and techniques for studying thermal and thermoelectric transport in 2D materials over smaller length scales and larger spectral ranges than was previously possible.

Recent Progress

In addition to in-plane and cross-plane thermoelectric transport measurements of 2D chalcogenides in collaboration with the Cronin group, over the previous two years we have investigated the heat spreading property of hexagonal boron nitride (h-BN) and pursued a new method to address the challenge in the measurement of the electronic thermal conductivity of 2D materials, as summarized below.

Large Reduction of Hot Spot Temperature in Graphene Electronic Devices with Heat-Spreading Hexagonal Boron Nitride

Due to its atomic flatness, high-energy surface optical phonons, chemical inertness, and absence of dangling bonds, h-BN has recently been identified as a superior dielectric support for graphene and other 2D electronic materials. When h-BN was used as a support for graphene as compared to SiO_2, the electron mobility of the graphene layer was seen to increase by nearly an order of magnitude due to the reduction of electron-hole puddles and inhomogeneity in the charge carrier concentration. Besides enhancing the electron mobility of graphene, h-BN possesses a room-temperature in-plane thermal conductivity as high as 390 W m^{-1} K^{-1}, which is more than two orders of magnitude larger than most common dielectrics including SiO_2. However, the cross-plane thermal conductivity of *h*-BN is only about 2 W m^{-1} K^{-1}. Therefore, the thermal benefit of an h-BN support for 2D electronic devices has remained elusive.

Here, we report sub-100 nm spatial resolution, quantitative Scanning Thermal Microscopy (SThM) measurements of the effect of an *h*-BN heat spreader for lowering the hot spot temperature of 2D electronic devices. The representative 2D devices used in this study are graphene channels fabricated on a silicon substrate and on a flexible Corning® Willow® Glass (WG) substrate. Similar to silicon electronic devices where the local power density can be much higher than the average value for an entire chip, which is about 100 W cm^{-2}, the local power density at the individual micron scale graphene device is as high as 16,000 W cm^{-2} during the experiments. The measurement and analysis results show that for equivalent power densities, an h-BN heat-spreading layer can yield a large reduction of the local hot spot temperature for the devices fabricated on both the silicon substrate and WG substrate. At the same power density, an 80 nm thick h-BN layer on the silicon substrate can yield a factor of 2.2 reduction of the hot spot temperature, whereas a 35 nm thick h-BN layer on the WG substrate is sufficient to obtain a factor of 4.1 reduction (Fig. 1). The larger effect of the h-BN heat spreader on WG than on SiO_2/Si is attributed to a smaller effective heat transfer coefficient per unit area for three-dimensional heat

conduction into the thick, low-thermal conductivity WG substrate than for one-dimensional heat conduction through the thin oxide layer on silicon. Consequently, the h-BN lateral heat-spreading length is much larger on WG than on SiO_2/Si, resulting in a larger degree of temperature reduction.

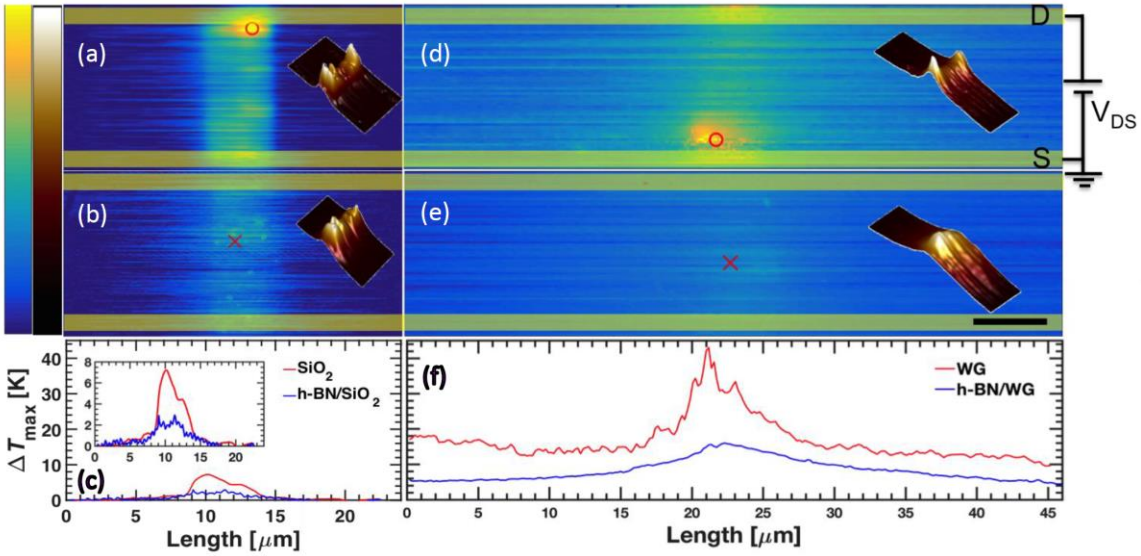

Figure 1. Thermal images of graphene supported on SiO_2/Si (a), h-BN/SiO_2/Si (b), WG (d), and h-BN/WG (e) substrates. The insets in the thermal images are three-dimensional temperature contours of the graphene channels. Each graphene channel was subjected to 2000 W cm^{-2} of Joule heating except for (d), where the power density is 1600 W cm^{-2}. The open circles "o" and "x" mark the locations of the hottest temperature in each image. The horizontal scan lines through each hot spot are shown in figures (c) and (f). An expanded view of the main figure in figure (c) is shown in the inset for clarity. The scale bar is 5 μm. The blue to yellow color bars range from 0 to 7 K for figures (a) and (b), and from 0 to 45 K for figures (d) and (e). The black to white color bars for the 3D insets range from 0 to 3 K, 0 to 7 K, 5 to 20 K, and 10 to 45 K for (a), (b), (d) and (e), respectively.

Electronic Thermal Transport in h-BN/Graphene/h-BN Heterostructures

When electron-electron interaction is strong compared to the electron kinetic energy, correlated electron phenomena such as superconductivity and superfluidity can emerge and be explored for revolutionary energy and quantum information technologies. An illustrative example is the recent observation of superconductivity and Mott insulator states in twisted bi-layer graphene at magic angles (*1*, *2*), where the electron kinetic energy is suppressed by the formation of flat energy bands in the moiré band structures (*3*). Knowledge of the electron-electron interaction strength is necessary in these efforts of manipulating the correlated electron phenomena. In bulk metals, electronic thermal transport measurements have provided more insight into electron-electron interaction than charge transport measurements alone (*4*–*6*), because momentum-conserving normal electron-electron collision relaxes the heat current but not the charge current in bulk metals. In single-layer graphene (SLG), in comparison, normal electron-electron scattering relaxes both the heat current and a small fraction of the charge current (*7*). Although the electronic thermal conductivity (κ_e) of graphene can be used to probe electron-electron interaction in graphene, existing attempts for κ_e measurements of graphene are fundamentally limited to very

low temperatures (*8*, *9*), where the electron-electron interaction effect on electronic thermal transport diminishes (*4*–*7*). Despite its importance and over a decade of experimental research on graphene, κ_e is one of the few transport properties that have yet to be measured for graphene at a temperature range relevant to both its unusual Dirac fermion behaviors and intended applications. Meanwhile, existing theoretical studies have investigated electronic thermal transport in graphene with the presence of either just electron-electron interaction (*7*, *10*) or mainly electron-phonon interaction (*11*, *12*), instead of with both interactions considered on an equal footing.

Here we report highly sensitive differential measurements of electronic thermal transport in monolayer graphene encased in hexagon boron nitride (h-BN) over a wide temperature range that extends above room temperature (Figs. 2-4). Our measurement results clearly show that electron-electron interaction suppress the κ_e in the extrinsic regime of electrostatically doped graphene below the Wiedemann-Franz law and Sommerfeld limit for free electron gas when the temperature is increased near the room temperature. Meanwhile, the additional entropy carried by electrons and holes in intrinsic graphene produces a κ_e peak that is well above the Sommerfeld limit at sufficiently high temperatures. The obtained quantitative insight into fundamental electron-electron interaction and electron-phonon interaction in graphene is valuable for the design of artificial 2D architectures such as rotationally controlled van der Waals heterostructures to engineer superconductivity and other coherence states.

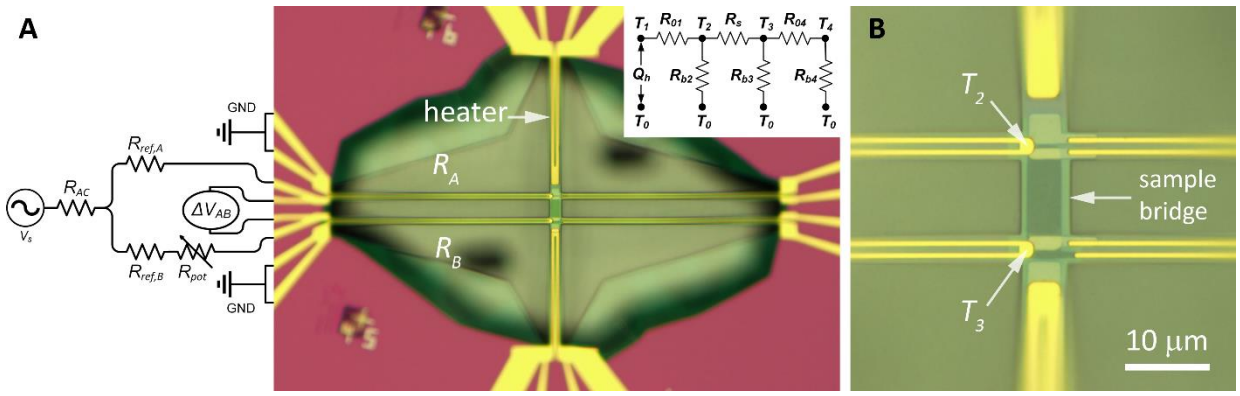

Figure 2. Optical micrograph of the measurement device (A) and the central sample region (B) The device consists of Cr/Au resistance-thermometer (RT) lines and leads supported by suspended SiO_2 beams of 460 nm thickness. The top inset shows the corresponding thermal circuit model of the device when RT_1 is used as the heater with heat dissipation rate of Q_h by passing a direct current. R_{bi} and R_s are the thermal resistance of the RT_i beam and the sample bridge, respectively, where the subscript i is 1, 2, 3, or 4. T_i is the midpoint temperature of the metal line RT_i and T_0 is the ambient temperature. During thermal measurement, RT_1 or RT_4 is heated and the corresponding change in resistance of all RTs are measured and used to obtain $\Delta T_i \equiv T_i - T_0$, R_{bi} and R_s. Also shown is the schematic of the Wheatstone bridge used for differential measurement of the variation of electrical resistance of RT_2 (R_A) and RT_3 (R_B) by measuring ΔV_{AB} using a lock-in amplifier. For differential measurements, lock-in source (V_s) is in series with $R_{AC} = 1\text{M}\Omega$, and $R_{ref,A}$ and $R_{ref,B}$ are reference resistors in series with R_A and R_B, respectively. R_{pot} is a potentiometer used to adjust the balance point of the Wheatstone bridge. The sample bridge consists of a h-BN-encased, monolayer graphene sample atop a SiO_2 beam covered by a thin layer of Pt. The gate voltage V_{gate} is applied to the Pt layer to modulate the charge carrier density of graphene. To measure modulation of the electronic thermal conductivity of graphene ($\delta\kappa_e$), RT_1

is used as the heater with the heat dissipation rate of Q_h to induce the temperature difference $(\Delta T_2 - \Delta T_3)$ along the sample bridge. Modulation of V_{gate} modifies the charge carrier density of graphene and consequently its electronic thermal conductivity κ_e by $\delta\kappa_e$, causing the modulation of T_i by δT_i. The resultant modulation of ΔV_{AB} (δV_{AB}) is measured and used to determine $(\delta T_2 - \delta T_3)$, $\delta\kappa_e$ and κ_e.

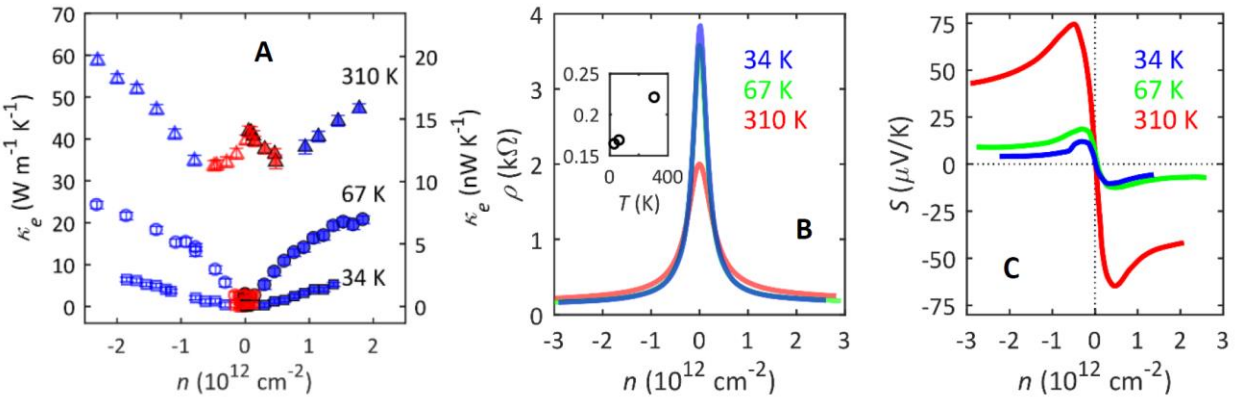

Figure 3. Measured electronic thermal conductivity (A), electrical resistivity (B), and Seebeck coefficient (C) of h-BN/graphene/h-BN heterostructure as a function of $n = n_e - n_h$, where n_e and n_h are the electron concentration and hole concentration. The inset in panel B shows graphene resistivity as a function of temperature for n = -2.9 x 10^{12} cm^{-2}.

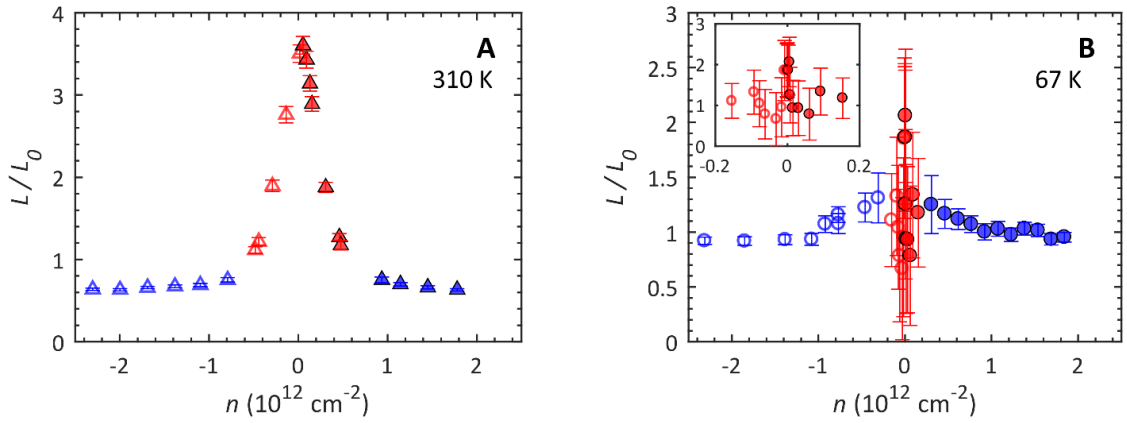

Figure 4. Lorenz number, $L \equiv \frac{\kappa_e}{\sigma T}$, normalized by the Sommerfeld limit for free electron gas, $L_0 = \frac{\pi^2}{3}\left(\frac{k_B}{e}\right)^2$, as a function of charge carrier density n at 310 K (A) and 67 K (B). Here, σ is the electrical conductivity, T is the temperature, k_B is the Boltzmann constant, e is the proton charge.

Future Plans

We plan to employ the highly sensitive differential measurement method to investigate in-plane collective energy transport of excitons in 2D materials, and to collaborate with the Cronin group to measure the cross-plane transport properties of excitons in 2D materials.

References

1. Y. Cao *et al.*, Unconventional superconductivity in magic-angle graphene superlattices. *Nature*. **556**, 43 (2018).
2. Y. Cao *et al.*, Correlated insulator behaviour at half-filling in magic-angle graphene superlattices. *Nature*. **556**, 80 (2018).
3. R. Bistritzer, A. H. MacDonald, Moiré bands in twisted double-layer graphene. *Proc Natl Acad Sci USA*. **108**, 12233 (2011).
4. W. E. Lawrence, J. W. Wilkins, Electron-Electron Scattering in the Transport Coefficients of Simple Metals. *Physical Review B*. **7**, 2317–2332 (1973).
5. M. J. Laubitz, Electron-Electron Scattering in the High-Temperature Thermal Resistivity of the Noble Metals. *Physical Review B*. **2**, 2252–2254 (1970).
6. A. H. MacDonald, M. J. Laubitz, Comment on "Low-temperature resistivity and thermoelectric ratio of copper and gold." *Physical Review B*. **21**, 2638–2640 (1980).
7. A. Principi, G. Vignale, Violation of the Wiedemann-Franz Law in Hydrodynamic Electron Liquids. *Physical Review Letters*. **115** (2015), doi:10.1103/PhysRevLett.115.056603.
8. S. Yiğen, A. R. Champagne, Wiedemann–Franz Relation and Thermal-Transistor Effect in Suspended Graphene. *Nano Lett.* **14**, 289–293 (2014).
9. J. Crossno *et al.*, Observation of the Dirac fluid and the breakdown of the Wiedemann-Franz law in graphene. *Science*. **351**, 6277 (2016).
10. M. S. Foster, I. L. Aleiner, Slow imbalance relaxation and thermoelectric transport in graphene. *Physical Review B*. **79** (2009), doi:10.1103/PhysRevB.79.085415.
11. E. Muñoz, Phonon-limited transport coefficients in extrinsic graphene. *Journal of Physics: Condensed Matter*. **24**, 195302 (2012).
12. T. Y. Kim, C.-H. Park, N. Marzari, The Electronic Thermal Conductivity of Graphene. *Nano Letters*. **16**, 2439–2443 (2016).

Publications Resulting from Work Supported by the DOE over the Previous Two Years

1. N. Poudel, S.J. Liang, D. Choi, B. Hou, L. Shen, H. Shi, L.K. Ang, L. Shi and S. Cronin, Cross-plane Thermoelectric and Thermionic Transport across Au/h-BN/Graphene Heterostructures. Sci Rep, 7, 14148 (2017).
2. D. Choi, N. Poudel, S. Park, D. Akinwande, S.B. Cronin, K. Watanabe, T. Taniguchi, Z. Yao and L. Shi, Large Reduction of Hot Spot Temperature in Graphene Electronic Devices with Heat-Spreading Hexagonal Boron Nitride. ACS Applied Materials & Interfaces, 10, 11101-11107 (2018).
3. J. Chen, J. Kim, N. Poudel, B. Hou, L. Shen, H. Shi, L. Shi and S. Cronin, Enhanced Thermoelectric Efficiency in Topological Insulator Bi_2Te_3 Nanoplates via Atomic Layer Deposition-based Surface Passivation. Applied Physics Letters, 113, 083904 (2018).
4. J. Chen, D.M. Hamann, D. Choi, N. Poudel, L. Shen, L. Shi, D.C. Johnson and S. Cronin, Enhanced Cross-Plane Thermoelectric Transport of Rotationally Disordered $SnSe_2$ via Se-Vapor Annealing. Nano letters, 18, 6876-6881 (2018).

Quasi-One-Dimensional Transition-Metal Oxides and Sulfides – Growth of Single Crystals and their Physical Properties

John J. Neumeier, Physics Department, Montana State University, Bozeman, MT 59717

Program Scope

Fermions that are constrained to low dimensions can exhibit boson-like properties, also known as Luttinger-liquid behavior. Single crystal growth of materials with the potential to exhibit such behavior, and the study of their properties, is the focus of this program. Bulk materials with crystallographic structures possessing low-dimensional structural elements, such as two-dimensional planes or one-dimensional chains, are grown in single crystal form. The materials are studied using a variety of experimental probes.

Recent Progress

Antimony and Tantalum Oxides: Single crystals of MSb$_2$O$_6$ and MTa$_2$O$_6$ where M is a 3d transition metal element have been grown. These compounds contain one-dimensional (1D) M-O-O-M chains (see Fig. 1). Along the c crystallographic direction, the chains in neighboring layers are rotated 90˚ with respect to one another. This leads to weak antiferromagnetic coupling along c. This coupling can be disrupted with modest magnetic field that is applied perpendicular to c, leading to two antiferromagnetic transitions. One for those chains parallel to the field, and one for those chains perpendicular to the field. This is shown in Fig. 2 for FeTa$_2$O$_6$ [1]. This effect is also exhibited by CoSb$_2$O$_6$, NiSb$_2$O$_6$, CoTa$_2$O$_6$, and NiTa$_2$O$_6$ [1,2]. Our work establishes that these compounds are quasi-1D in nature, which opens the door to further investigations. Of further interest is that the behavior shown in Fig. 2 leads to an anisotropic magnetocaloric effect; cooling or warming can be realized by rotating the sample in constant magnetic field.

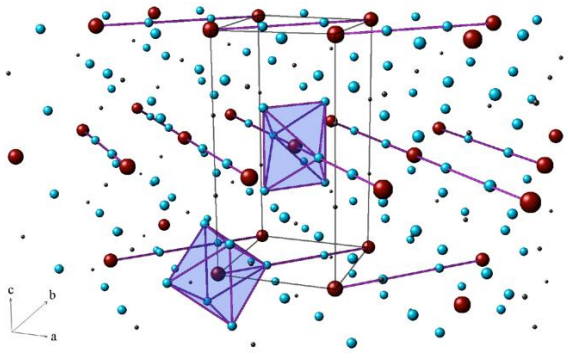

Fig. 1. Tetragonal P4$_2$/mnm structure typical for MSb$_2$O$_6$ and MTa$_2$O$_6$ compounds. Note the M-O-O-M chains in the unit cell (M in red, O in blue). The chain direction rotates by 90˚ between successive layers.

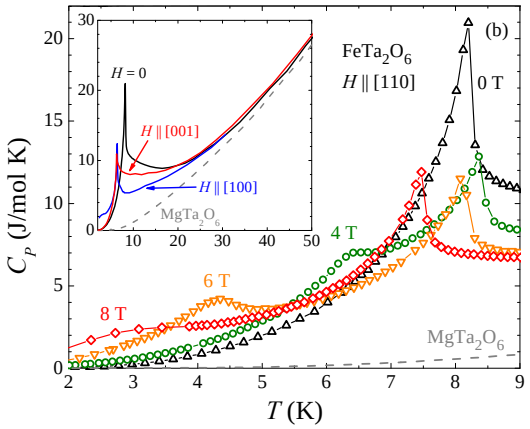

Fig. 2. Molar heat capacity of FeTa$_2$O$_6$ for various magnetic field orientations. With H parallel to [110] two antiferromagnetic transitions emerge. If H is parallel to the M-O-O-M chains, the transition is depressed most strongly.

Collaboration on MSb$_2$O$_6$ and MTa$_2$O$_6$ compounds with Dr. Joshua Cohn at the University of Miami has recently reported thermal conductivity κ measurements [3], where κ was found to be strongly suppressed in the Ta-containing compounds. This is associated with a resonant scattering strength that is an order of magnitude larger in the Ta compounds than in the Sb compounds. Collaboration with Dr. Eduardo Granado and graduate student Damaris Maimone in Brazil using Raman spectroscopy assigned all observed Raman-active modes with the help of *ab initio* lattice dynamics calculations [4]. This work revealed the temperature dependence of the modes, and specific phonons that are affected by the tetragonal-monoclinic phase transition at 400 K. Further work revealed a previously unexplored interaction between phonons and orbital excitations in CuSb$_2$O$_6$ [5]. Dr. Zahra Yamani at Chalk River Laboratories is investigating one of our large single crystals of NiTa$_2$O$_6$ using the DUALSPEC C5 polarized-beam triple-axis spectrometer in order to study the magnetic excitations. Ni possesses spin S = 1, which is known to lead to an exotic ground state in 1D, the Haldane gap. The experiments have confirmed the presence of a gap; further analysis is in progress.

Transition-Metal Sulfides: The transition-metal sulfide family contains numerous low-dimensional materials. In 2017 we began studying the chemistry of these materials to learn about the possibility to grow single crystals. We have synthesized polycrystalline BaNbS$_3$, which contains 1D Nb-Nb chains. Our work [6] revealed superconductivity below 0.89 K, determined the superconducting energy gap at E_g = 0.245 meV, and suggests that BaNbS$_3$ is a BCS superconductor. In our investigation, we measured the electrical resistivity, specific heat, Hall effect, and critical magnetic field. At present, there are no indications that the 1D crystal structure leads to unusual physical properties. We also investigated polycrystalline BaNb$_2$S$_5$, revealing a transition to superconductivity at T_c = 0.85 K and behavior consistent with BCS theory [7]. Undergraduate Alisa Drenner carried out a similar investigation of SrTa$_2$S$_5$ for her senior Capstone project [8]. Although superconductivity had previously been reported in this compound (T_c = 2.27 K), Alisa measured the electrical resistivity, specific heat, magnetic susceptibility, upper critical magnetic field, and determined the superconducting energy gap, culminating in the best characterization of this compound to date. In addition, Alisa has completed a similar study of BaTa$_2$S$_5$, which is in preparation for publication.

As a component of our investigations of transition-metal-sulfide chemistry, single-crystal growths have been conducted. We attempted to grow BaNbS$_3$ and BaNb$_2$S$_5$ using vapor transport with either TeCl$_4$ or iodine. Neither of these compounds grew. Instead, single crystals of Ba$_2$Nb$_3$S$_8$I were obtained; this compound has never before been reported. Undergraduate Mitch Baker conducted the growths for his senior Capstone project together with a summer visitor Dr. Michael Smith. The crystals grow as flakes a few mm in length with thicknesses of about 5-10 μm. Our collaborator Dr. Qisheng Lin at Ames Laboratory determined the crystal structure using single-crystal x-ray diffraction. The structure, trigonal with space group *P31c* (see Fig. 3), is built of 2D NbS$_2$ layers that are formed from NbS$_6$ trigonal prisms. These layers are separated by

salt-like BaS layers that incorporate iodine ions. The electrical resistivity (see Fig. 4) is metallic with superconductivity below T_c = 0.8 K. Further measurements of this compound are ongoing.

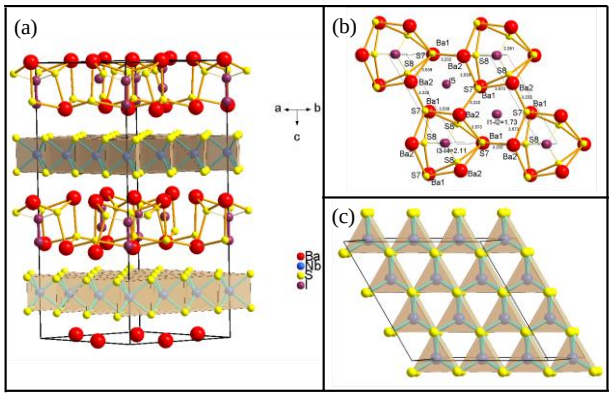

Fig. 3. (a) Trigonal P31c crystal structure of $Ba_2Nb_3S_8I$ as determined from single-crystal x-ray diffraction. Note the (b) complex BaS layers and (c) 2D NbS_2 layers.

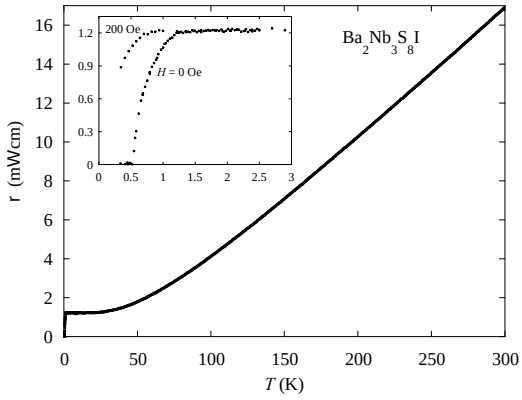

Fig. 4. Electrical resistivity ρ versus T for $Ba_2Nb_3S_8I$. Inset show the region near the superconducting transition along with data at 200 Oe, revealing a suppression of superconductivity.

Postdoc Shermane Benjamin has grown single crystals of nominal composition $BiNbS_3$. This compound has not previously been reported in single crystal form. The crystals grow as thin platelets with areas approaching 1 cm^2 and thicknesses of 50-100 μm; they are grown with the vapor transport medium $TeCl_4$ at 680 ˚C. The electrical resistivity is metallic; no superconductivity occurs above 0.35 K. Attempts to determine the crystal structure using x-ray diffraction have not yet proven successful due to the mosaic spread of the single crystals. Additional measurements on their physical properties are in progress.

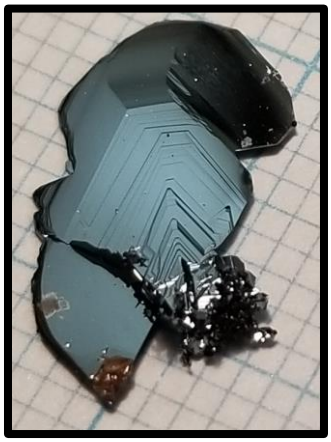

Fig. 5. $BiNbS_3$ single crystal on millimeter paper. It was grown using vapor transport with $TeCl_4$ as a transport medium at 680 ˚C.

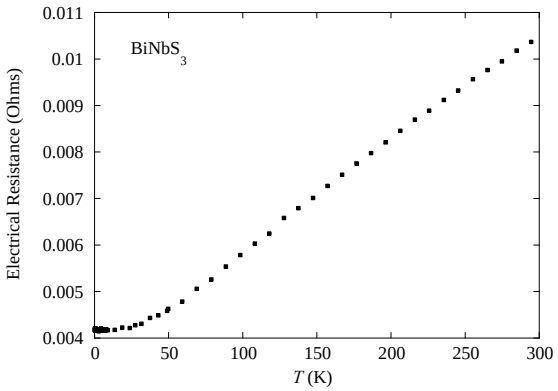

Fig. 6. Electrical resistance versus temperature for $BiNbS_3$ single crystal illustrating metallic behavior.

Future Plans

At present, the bulk of our laboratory work is focused on the transition-metal sulfides. We continue to study their chemistry and grow single crystals. Investigation of their physical properties will be a major focus for the remaining period of the program. Thermal expansion and thermal conductivity measurements on $BiNbS_3$ are underway. We are beginning electrical transport measurements in magnetic field of $BiNbS_3$ and $Ba_2Nb_3S_8I$, in order to investigate the coupling between the two-dimensional layers. Specific heat and magnetic susceptibility measurements are also planned. We carried out some measurements of the electrical resistivity of $BaNbS_3$ and $BiNbS_3$ under hydrostatic pressure up to18 kbar, and will extend these measurements to other compounds that we have synthesized. High pressure measurements are a promising way to investigate the role of hybridization between the transition metal and sulfur ions, since pressure is expected to enhance the electron exchange between the ions. The initial experiments look promising.

References

[1] A. B. Christian, A. T. Schye, K. O. White, and J. J. Neumeier, J. Phys. Condens. Matter 30 (2018) 195803.

[2] Aaron B. Christian, Ph. D. Dissertation, Montana State University, Bozeman, MT (2017); A. B. Christian, C. D. Hunt, and J. J. Neumeier, Phys. Rev. B 96 (2017) 024433; A. B. Christian, S H Masunaga, A. T. Schye, A. Rebello, J. J. Neumeier, and Y.-K. Yu, Phys. Rev. B 90 (2014) 224423.

[3] N. Prasai, A. B. Christian, J. J. Neumeier, and J. L. Cohn, Phys. Rev. B 98 (2018) 134449.

[4] D. T. Maimone, A. B. Christian, J. J. Neumeier, and E. Granado, Phys. Rev. B 97 (2018) 104304.

[5] D. T. Maimone, A. B. Christian, J. J. Neumeier, and E. Granado, Phys. Rev. B 97 (2018) 174415.

[6] J. J. Neumeier and M. G. Smith, Physica C 542 (2017) 1-5.

[7] M. G. Smith and J. J. Neumeier, Physica C 549 (2018) 88-92.

[8] Alisa K. Drenner, S. M. Benjamin, M. G. Smith, and J. J. Neumeier, Physica C 556 (2019) 19-23.

Publications

Magnetic and thermal properties of low-dimensional single-crystalline transition-metal antimonates and tantalates, Aaron B. Christian, Ph. D. Dissertation, Montana State University, Bozeman, MT (2017).

Local and long-range order and the influence of applied magnetic field on single-crystalline $NiSb_2O_6$, A. B. Christian, C. D. Hunt, and J. J. Neumeier, Phys. Rev. B 96 (2017) 024433.

Superconductivity in quasi-one dimensional $BaNbS_3$, J. J. Neumeier and M. G. Smith, Physica C 542 (2017) 1-5.

Lattice dynamics of ASb_2O_6 (A = Cu, Co) with trirutile structure, D. T. Maimone, A. B. Christian, J. J. Neumeier, and E. Granado, Phys. Rev. B 97 (2018) 104304.

Coupling of phonons with orbital dynamics and magnetism in $CuSb_2O_6$, D. T. Maimone, A. B. Christian, J. J. Neumeier, and E. Granado, Phys. Rev. B 97 (2018) 174415.

Observation of superconductivity in $BaNb_2S_5$, M. G. Smith and J. J. Neumeier, Physica C 549 (2018) 88-92.

Magnetic, thermal, and optical properties of single-crystalline $CoTa_2O_6$ and $FeTa_2O_6$ and their anisotropic magnetocaloric effect, A. B. Christian, A. T. Schye, K. O. White, and J. J. Neumeier, J. Phys. Condens. Matter 30 (2018) 195803.

Resonant scattering of phonons in the quasi-one-dimensional spin-chain compounds AB_2O_6 (A=Ni,Co; B=Sb,Ta), N. Prasai, A. B. Christian, J. J. Neumeier, and J. L. Cohn, Phys. Rev. B 98 (2018) 134449.

Physical properties and superconductivity of $SrTa_2S_5$, Alisa K. Drenner, S. M. Benjamin, M. G. Smith, and J. J. Neumeier, Physica C 556 (2019) 19-23.

Session XI

Tuning Organic Semiconductor Packing and Morphology through Non-equilibrium Solution Processing

Zhenan Bao, Stanford University

Program Scope

Electronic devices based on organic molecules provide remarkable opportunities for applications in organic field effect transistors (OFETs), electronic paper, RFID, photovoltaics (OPV), and sensors. Previously, little work has been devoted to the understanding of how the morphology and molecular packing are affected by the solution processing conditions. Our research group has developed the *solution shearing (SS) method* as a versatile method to prepare high performance OTFTs, especially from highly crystalline small molecule OSCs. We discovered for the first time that it was possible to reduce the π–π stacking distance between organic semiconductor molecules using the SS method [1]. We observed *an order of magnitude increase in charge carrier mobility* by simply changing the processing conditions. We subsequently were able to perform further investigations to understand the mechanism for trapping the metastable strained packing structures, by real time X-ray diffraction experiments or by engineering the fluid field during the OSC crystallization [2-3]. More importantly, SS provides us many 'knobs' to tune during processing to allow us to trap metastable non-equilibrium molecular assembly and morphology that are not easily accessible by typical film formation methods, such as spin coating. Understanding the effects of various solution processing conditions on molecular packing and morphology is essential for unprecedented charge transport and future large-scale production of organic electronics. Our long-term goal is to develop a systematic understanding of various important parameters that impact organic electronic material crystallization and morphology. Based on the obtained various structures achieved by non-equilibrium processing, we hope to correlate the charge transport with morphology. Non-equilibrium processing provides unprecedented access of a range of diverse morphologies that are not easily accessible by other methods. This will allow us to gain new fundamental understanding that may facilitate the development of novel organic materials that are currently unrealized or unexpected.

In our previous work, we have already made a number of significant strides toward understanding the crystallization and packing tuning of small molecule organic semiconductors. However, morphological control of polymer semiconductor is much less understood and developed. The understanding of an "ideal" polymer semiconductor morphology for charge transport has been evolving over time as we gain better experimental and theoretical understanding. It was long hypothesized that increasing crystallinity would be an effective means for enhancing charge transport due to the tendency of charge carriers to delocalize in the ordered regions of polymer thin films. However, with the discovery of new materials that exhibited relatively low crystallinity while still achieving excellent charge transport, there has been a re-evaluation of the charge transport mechanism in polymer OSC thin films [4]. Experimental work on the effects of molecular weight on charge transport suggested that a thin film morphology that promotes efficient intrachain charge transport is necessary for high charge transport efficiency. Finally, both theoretical and experimental work suggest that the "ideal" morphology is an efficient intrachain charge transport through long, rigid polymer chains combined with efficient interchain charge transport across small, densely dispersed ordered regions [5]. This model also suggests that aligned polymer chains and domains will potentially reduce the number of "hops" needed and result in more efficient charge transport.

In this work, we investigate several approaches to tune molecular packing, alignment and morphology of polymer semiconductors. All of the materials were fully characterized using DOE supported synchrotron X-ray scattering facilities in the Stanford Synchrotron Radiation Lightsource (SSRL) to determine the packing structures and morphology prepared under different SS conditions. Moreover, our established set-up for in-situ grazing-incidence X-ray diffraction (GIXD) and small angle X-ray scattering (SAXS) during SS provided important information about the evolution of morphology. Finally, the charge transport of the resulting films were measured to investigate the effects of alternation of morphology and molecular packing on charge transport.

Recent Progress

Understanding of microstructure evolution using meniscus-guided coating (MGC): We investigated the microstructural evolution of thin-films of a diketopyrrolopyrrole-terthiophene donor-acceptor polymer semiconductor using both *in-situ* and *ex-situ* X-ray diffraction methods. Our results suggest that there exist three separate deposition regimes—namely the shear-dominate, disorder-dominate, and Landau-Levich regimes—revealed by observing both polymer alignment via dry film thickness and optical dichroism, a property sensitive to the flow and shear fields. Our results indicate that more rapid solvent evaporation at higher coating speeds causes increased disorder, which can cause the nucleation of misaligned crystallites, affect the dichroic ratio, and may frustrate the alignment of polymer molecules in the amorphous regions of the film. Because the polymer studied and the deposition technique used are representative models, these results are likely general for aggregating, semicrystalline donor-acceptor polymers deposited with MGC.

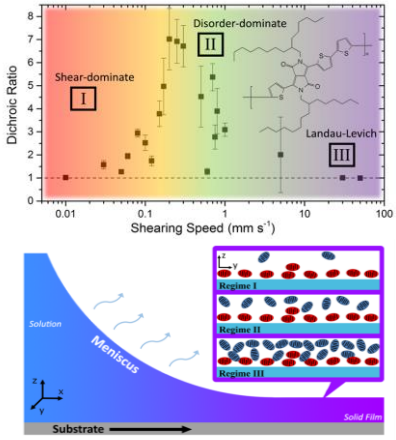

Figure 1. (**Top**) Deposition regimes demarcated by the trend in optical dichroic ratios as a function of coating speed using PDPP3T, the polymer studied. (**Bottom**) A schematic of meniscus-guided coating (MGC) highlighting, in the out-of-plane direction, the relative influence of polymer nucleation either at the air-liquid interface or at the substrate surface and their corresponding regime (**inset**). Red ovals indicate relatively ordered crystallites nucleated at the solid-liquid interface, while the blue ovals represent disordered ones nucleated

Controlling polymer chain alignment through processing is a means of tuning the charge transport of solution-based conjugated polymers: In this work, an external electric field (E-field) was applied to the coating blade (E-blade) to align polymer chain during solution-shearing, a meniscus-guided coating technique. A theoretical model based on dielectrophoresis quantitatively describes and predicts the alignment process and is used to guide the selection of the optimal conditions of the applied E-field. Using these conditions, more than two-fold increase in chain alignment was observed for E-bladed thin films of a diketopyrrolopyrrole (DPP) semiconducting polymer without affecting other morphological aspects such as film thickness, film coverage or fiber-like aggregation. Organic field effect transistors based on the E-bladed DPP polymer were fabricated at ambient conditions and over areas of a few cm^2. They displayed a 3-fold improvement in their mobilities and a strong enhancement in charge transport anisotropy compared to films prepared without E-field. These results suggest that a synergistic alignment effect from both the solution-shearing process and the applied E-field, and introduce a novel and general approach to control the morphology and the electrical properties of solution-coated conjugated polymer thin films.

Investigated alignment of polymer semiconductor nanostructures during solution coating using patterned blade: We designed a coating blade with micro-trenches to effectively generate an intensive unidirectional flow field to align and elongate polymer chains in the solution beneath the blade. To prevent chain relaxation from the extended conformation and aligned orientation during film drying, we hypothesize that, during the drying process, conjugated polymer nanofibril structures formed from conjugated polymer/elastomer phase separation may confine the conjugated polymer chains with an extended chain conformation. This may be possible as the relaxation of these larger aligned nanofibers in the elastomer matrix compared to that of a single polymer chains should be much slower kinetically at time scales relevant to drying. Additionally, the nanoconfinement introduced during this shear coating deposition may achieve improved stretchability. Indeed, we found that under optimized solution-shearing conditions, semiconducting polymer films with aligned nanoconfined morphology could be fabricated through the conjugated-polymer/elastomer phase-separation–induced elasticity (termed CONPHINE) methodology, which achieves morphological ordering at multiple length scales in a single coating step. Moreover, the enhanced chain dynamics and the suppressed crystallization from the nanoconfinement effect serve to largely improve the stretchability of the conjugated polymers.

Future Plans

We will perform studies to further understand how the solution-phase aggregate (if aggregating) or free polymer coil (if not), which are likely differ in size and shape if the solvent quality is changed and may affect or be affected differently by the velocity and shear fields induced during MGC. To better understand the morphology evolution during coating, we have set up an *in situ* characterization tools combined with solution shearing and roll-to-roll coating. We will perform experiments to observe when alignment of polymer semiconductors takes place during solution coating. This will be impacted by using patterned blades. Our current results also made us realize that we still lack the knowledge about solution-state polymer entanglement, solution-state pre-aggregation, polymer response to shear stress and their relaxation dynamics. All the above parameters are also dependent on polymer structure (conformation) rigidity and molecular weight. Therefore, additional future work will involve developing a deeper knowledge and understanding of solution-state structure and its evolution in order to better understand controlling alignment and morphology of polymer semiconductors.

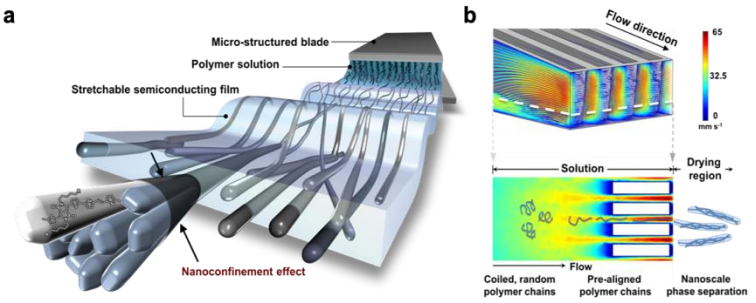

Figure 2. Achieving multiple length scale ordering of conjugated polymers in stretchable semiconductors through a combination of patterned-blade solution shearing method and the nanoconfinement effect. a) 3D schematic representing the alignment of polymer semiconductor nanofibers through solution-shearing method using a microtrench-patterned blade. b) Calculated 3D and 2D velocity fields (stream-line representation) of the solution between the coating blade and the substrate.

References

[1] G. Giri, E. Verploegen, S. C. B. Mannsfeld, S. Atahan-Evrenk, D. H. Kim, S. Y. Lee, H. a

Becerril, A. Aspuru-Guzik, M. F. Toney, and Z. Bao, “Tuning charge transport in solution-sheared organic semiconductors using lattice strain.,” *Nature*, 480, 504–8, 2011.
[2] G. Giri, R. Li, D.-M. Smilgies, E. Q. Li, Y. Diao, K. M. Lenn, M. Chiu, D. W. Lin, R. Allen, J. Reinspach, S. C. B. Mannsfeld, S. T. Thoroddsen, P. Clancy, Z. Bao, and A. Amassian, “One-dimensional self-confinement promotes polymorph selection in large-area organic semiconductor thin films.,” *Nat. Commun.*, 5, 3573, 2014.
[3] Y. Diao, B. C.-K. Tee, G. Giri, J. Xu, D. H. Kim, H. a Becerril, R. M. Stoltenberg, T. H. Lee, G. Xue, S. C. B. Mannsfeld, and Z. Bao, “Solution coating of large-area organic semiconductor thin films with aligned single-crystalline domains.,” *Nat. Mater.*,12, 665–71, 2013.
[4] D. Vankateshvaran, M. Nikolka, A. Sadhanala, V. Lemaur, M. Zelazny, M. Kep, M. Hurhangee, A. J. Kronemeijer, V. Pecunia, I. Nasrallah, I. Romano, K. Broch, I. McCulloch, D. Emin, Y. Olivier, J. Cornil, D. Veljonne, H. Sirringhaus, "Approaching disorder-free transport in high-mobility conjugated polymers," *Nature*, 515, 384-388, 2014.
[5] S. A. Mollinger, A. Salleo, A. J. Spakowitz, "Anomalous Charge Transport in Conjugated Polymers Reveals Underlying Mechanisms of Trapping and Percolation," *ACS. Cent. Sci.*, 2, 910-915, 2016.

Publications

1. Xu, J.; Ehrlich, A.; Zhu, C; Shaw L.; Wang, G.-J. N.; Katsumata T.; Wang, S.; Wu, H. -C.; Gu, X.; Lopez, F. M.; Bao, Z., Multi-scale ordering in highly stretchable polymer semiconducting films. **Nature Materials,** in press.
2. Xu, J., Wang, S.; Wang, G. J. N.; Zhu, C. X.; Luo, S. C.; Jin, L. H.; Gu, X. D.; Chen, S. C.; Feig, V. R.; To, J. W. F.; Rondeau-Gagne, S.; Park, J.; Schroeder, B. C.; Lu, C.; Oh, J. Y.; Wang, Y. M.; Kim, Y. H.; Yan, H.; Sinclair, R.; Zhou, D. S.; Xue, G.; Murmann, B.; Linder, C.; Cai, W.; Tok, J. B. H.; Chung, J. W.; Bao, Z., Highly stretchable polymer semiconductor films through the nanoconfinement effect. **Science** 2017, 355(6320): 59-64.
3. (Invited) S. Wang, J.Y. Oh, J. Xu, H. Tran, Z. Bao, "Skin-Inspired Electronics: An Emerging Paradigm ", **Acc. Chem. Res.** , 51, 5, 1033-1045, 2018.
4. X. Gu, Y. Zhou, K. Gu, T. Kurosawa, Y. Guo, Y. Li, H. Lin, B. C. Schroeder, H. Yan, F. Molina-Lopez, C. J. Tassone, C. Wang, S. C. B. Mannsfeld, H. Yan, D. Zhao, M. F. Toney, Z. Bao, Roll-to-Roll Printed Large-Area All-Polymer Solar Cells with 5% Efficiency Based on a Low Crystallinity Conjugated Polymer Blend, **Adv. Energy Mater**., 7, 1602742, 2017.
5. L. Shaw , H. Yan, X. Gu, P. Hayoz, R. T. Weitz, D. Kaelblein, M. F. Toney, and Z. Bao, "Microstructural Evolution of the Thin Films of a Donor–Acceptor Semiconducting Polymer Deposited by Meniscus-Guided Coating ", **Macromolecules** , 51, 11, 4325-4340, 2018.
6. (Invited) X. Gu, L. Shaw, K. Gu, M. F. Toney Z. Bao, "The Meniscus-guided Deposition of Semiconducting Polymers", **Nature Comm.** , 9, 534, 2018.
7. L. Shaw, The Deposition of Semiconducting Polymer Thin Films from Meniscus-guided Coating, Doctoral Dissertation, 2018.
8. F. Molina-Lopez, H. Yan, X. Gu, Y. Kim, M. F. Toney, Z. Bao, Electric field tuning molecular packing and electrical properties of solution-shearing coated organic semiconducting thin films, **Advanced Functional Materials**, 27, 1605503, 2017.
9. F. Molina-Lopez, H.-C. Wu, G.-J. N. Wang, H. Yan, L. Shaw, J. Xu, M. F. Toney, Z. Bao, "Enhancing Molecular Alignment and Charge Transport of Solution-Sheared Semiconducting Polymer Films by the Electrical-Blade Effect ", **Adv. Electron. Mater.**, 4, 1800110, 2018.

Organic Multiferroics

Shenqiang Ren (University at Buffalo, The State University of New York)

Program Scope

The research objective of this project is to explore the multiferroic properties of organic single crystal materials, comprised of two chemically and electronically distinct donor and acceptor molecules, which combine two or more ferroic properties in the same crystal lattice in a manner that is difficult or impossible to achieve in continuous inorganic crystalline solids. A new family of organic charge-transfer multiferroics emerges as a fascinating platform for the discovery of potential high Tc organic superconductors, photoactuators, and magnetoelectrics, due to its spin-dimerization, radical conductivity, exciton-lattice coupling, and weak hyperfine interaction and low spin-orbit coupling. The direct observations of room temperature spin and dipole ordering, as well as metallicity, in organic multiferroics are accomplished in organic charge-transfer solids.

Recent Progress

We seek fundamental understanding of the ferroic control in organic charge-transfer solids to explore room temperature multiferroicity and metallicity. By tuning external magnetic field, light, electric field and thermal field on organic multiferroics, some **key findings** are observed as follow:

Metallicity of organic hydrocarbon multiferroics for potential high Tc organic superconductors. (***Advanced Materials***, adma.201807178, 2019)[1]

The pioneering seminal work by Little has inspired the continuous search for high-temperature organic superconductors since 1964. Immense interest in aromatic molecular crystals is mainly drawn from their strong electronic correlation, and in the recent years, several new superconducting materials have been discovered in alkali-metal-intercalated aromatic molecular crystals. To exploit this potential, an understanding of electron pairing in aromatic molecule is indispensable, including the alkali-metal intercalation effect on the percolation networks of low-dimensional aromatic molecular crystals, and technologically important thin films with a broad range of stability to address small shielding fraction volume. Here we study the metallicity of potassium-doped p-terphenyl ($K_xC_{18}H_{14}$) hydrocarbon solids. With potassium doping, the solids were found to exhibit a metallic conductivity at room temperature, and then become insulating at lower temperatures. A thin film of this material is prepared, which shows a photoinduced conductivity and a bipolaron-mediated metal-to-insulator transition, indicating a promising candidate for high T_c molecular superconductor.

We carry out the solid state sintering reactions of $K_xC_{18}H_{14}$ in a sealed glass tube under high vacuum to study the potassium doping effect on metallicity in $K_xC_{18}H_{14}$. The reaction conditions are extracted from the synchrotron X-ray diffraction performed on $K_xC_{18}H_{14}$ ($K_xC_{18}H_{14}$: x= 2.5, 2.75, and 3.25). Inset of Figure 1a shows a two monolayer thick $K_{2.75}C_{18}H_{14}$ where the molecular chains are grown along [110] directions. Individual p-terphenyl molecules are resolved as three lobe structures and have the length of ~1.3 nm as expected. Moreover, the intercalated K atoms appear as protrusions at the end π-rings of p-terphenyl molecules. The STM images show long molecular chains growing on top of the p-terphenyl molecular layer (Figure 1a). We attribute the potassium doping induced metallic conductivity of $K_{2.75}C_{18}H_{14}$ to the intercalation of potassium into p-terphenyl, allowing the formation of the $K_{2.75}C_{18}H_{14}$ charge-transfer complex; a schematic diagram for potassium intercalation into p-terphenyl is shown in Figure 1c. The addition of electrons from potassium to the antibonding molecular orbitals of the p-terphenyl framework is expected to enhance the metallic conductivity through the formation of a percolating network for

electron transport. The dependence of MIT on doping ration provides macroscale evidence for the intercalation effect on metallicity (Figure 1d). The resistance of $K_xC_{18}H_{14}$ increases slowly when cooling the samples and then freezes into a charge-ordered insulating state with two orders of magnitude increase in resistivity at low temperature. Increasing the potassium ratio of the $K_xC_{18}H_{14}$ causes the transition temperature to decrease, suggesting the MIT is sensitive to the intercalation level. We therefore apply temperature dependence of Raman spectra to investigate the charge-sensitive C-C molecular bond vibration (Inset of Figure 6d). As $K_{2.75}C_{18}H_{14}$ changes from a metallic state to an insulator, the vibrating frequency of intra-ring C-C stretching shifts to a lower frequency region (Inset of Figure 1d). We construct a high-vacuum in-situ setup to monitor the potassium intercalation effect on the conductivity of $K_{2.75}C_{18}H_{14}$ under annealing (as shown in the inset of Figure 1e). Figure 1e shows the time-dependent resistivity of $K_{2.75}C_{18}H_{14}$ while the annealing temperature is maintained at 493 K, where $R_{t=0}$ is the sample resistivity at the moment when the sample temperature reaches 493 K. The resistivity of $K_{2.75}C_{18}H_{14}$ decreases continuously by two orders of magnitude over a short period of 1,200 s, with similar qualitative behavior observed in all in-situ conductivity experiments. We attribute this sharp enhancement in the electrical conductivity to the intercalation of potassium into p-terphenyl layers with the formation of a highly reduced state of p-terphenyl and percolation networks. Thermal analysis provides a probe to study the intercalation effect on the crystalline structure of $K_{2.75}C_{18}H_{14}$. Inset of Figure 1e represents thermogravimetric analysis (TGA) of pristine p-terphenyl and $K_{2.75}C_{18}H_{14}$ for the temperature range of 323-650 K. It is shown that pristine p-terphenyl remains stable up to a temperature of 440 K, while $K_{2.75}C_{18}H_{14}$ maintains stability to a higher temperature of 453 K. The decomposition of $K_{2.75}C_{18}H_{14}$ ends at a temperature of 583 K leading to a weight loss of 58%, which is very close to the weight percent (68%) of p-terphenyl in the $K_{2.75}C_{18}H_{14}$. After potassium intercalation, the enhancement in the thermal stability of p-terphenyl suggests the formation of the charge transfer salts, with the charge carrier of polarons and bipolarons.

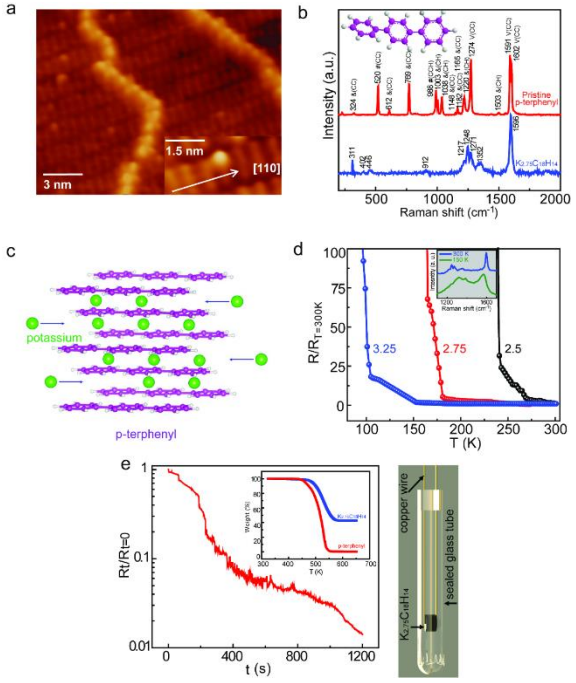

Figure 1. Structural and electrical characterization of potassium intercalated p-terphenyl. a) STM images of long potassium chains growth on top of the p-terphenyl molecular layer. Inset shows a two monolayer thick potassium doped p-terphenyl thin film where the molecular chains are running along [110] surface directions. b) Raman spectra of $K_{2.75}C_{18}H_{14}$ and pristine p-terphenyl samples. Inset shows the schematic diagram for structure of p-terphenyl molecular. V, stretching; &, bending (in-plane deformation); #, rocking (out-of-plane deformation). c) Schematic diagram for potassium intercalation into p-terphenyl. d) Temperature dependence of normalized resistivity and electrical conductivity of $K_xC_{18}H_{14}$ (x=2.5, 2.75 and 3.25, the reference temperature is 300 K). Inset shows the temperature dependence of Raman spectra for $K_{2.75}C_{18}H_{14}$. e) Time dependence of normalized resistivity (the reference resistivity is $R_{t=0}$). Inset shows the thermogravimetric analysis of pristine p-terphenyl and $K_{2.75}C_{18}H_{14}$, under nitrogen atmosphere, for the temperature range of 323-650 K. Right side of the figure shows the schematic diagram of high-vacuum annealing setup to monitor the in-situ electrical conductivity of $K_{2.75}C_{18}H_{14}$ sample.

Giant photostriction of organic charge-transfer multiferroics. (***PNAS***, 2018 115 (15))[2]

Photostrictive compounds are promising device materials because of their fundamental photophysical properties and light-induced strain applications. Although molecular charge transfer crystals exhibiting light-matter interactions have been successfully deployed in optoelectronics, an air-stable molecular material that couples photons and electrons, achieving photostriction through the coupling of light and mechanical degrees of freedom has not yet been discovered. Herein, we report a substantial light-induced dilation in a molecular material at room temperature, which is accompanied by simultaneous photocurrent generation. This finding opens new avenues for coupling optical, electronic, and mechanical functionalities for possible use in remote wireless photoswitchable devices. The DBTTF-C_{60} complex exhibits structural transformations upon application of external stimuli. Our experiments demonstrate light-induced volume changes at room temperature, which are suggested to occur by structuraltransformations. When the light (69.28 mW/cm^2) illuminates the DBTTF-C_{60}nanosheet, a height change (ΔH/H) is observed and the profile closely follows the shift in photocurrent density (Fig.2*A*). This photostrictive effect is directly related to the charge carrier generation from the light excitation, which serves as the electronic origin of the photostriction in DBTTF-C_{60}nanosheets. In addition, the photostrictive response is found to be nearly following the external light intensity (Fig.2*B*), which provides further evidence for the correlation between the photostriction and photogenerated carriers. As the light intensity increases to 69.28 mW/cm^2, the DBTTF-C_{60} nanosheets with an average thickness of 20 nm show a sizeable photostrictive effect with ΔH/H of ~5.7%, which is much larger than that of most inorganic photostrictive materials. When light illuminates nanosheets, charge transfer from DBTTF to C_{60} induces flattening of the DBTTF molecule, independent of whether it is in the boat or chair conformation; the cationic DBTTF$^+$ excited state is flat (Fig. 2*D*). This conformational change upon excitation would increase the size of the unit cell, and is suggested to contribute significantly to the substantial height change observed here. To verify this conclusion, we performed DFT calculations of the DBTTF-C_{60} system to determine the optimal lattice constants with DBTTF in the chair, boat, and flat cationic excited state, as shown in (Fig.2*D* and *2E)*. In all cases, the chair conformation is lowest in energy, and the excited state conformation is highest in energy. The most

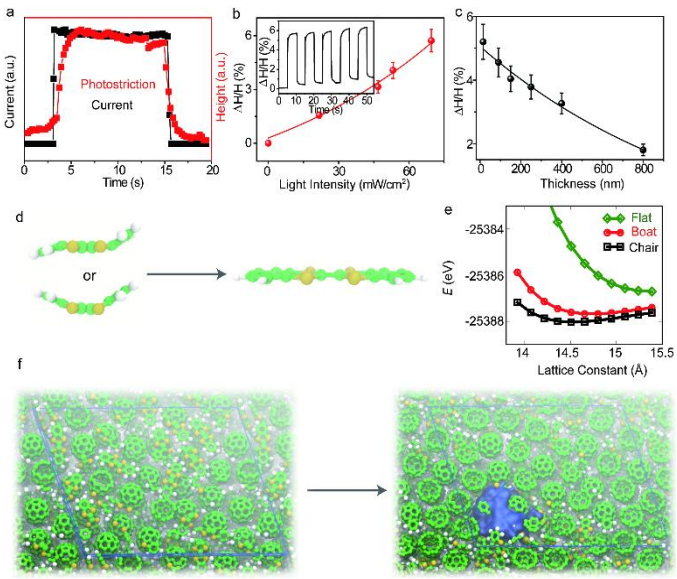

Figure 2. Photostriction phenomenon in the DBTTF-C_{60} nanosheets.(*A*) Height change of DBTTF-C_{60} nanosheets with light excitation 69.28 mW/cm^2, which closely follows the change in photocurrent density. (*B*) Photostrictive height change with increasing light intensity. Inset: Height change with the light ON and OFF. (*C*) The maximum height change of DBTTF-C_{60} nanosheets with decreasing thickness at the light excitation of 69.28mW/cm^2. (*D)* Schematic illustrating the flattening of the chair and boat conformation under light irradiation. (*E*) Total energy as a function of lattice constant in the *z*-direction for a DBTTF-C_{60} unit cell with DBTTF in the chair, boat, and flat (excited state) conformations. (*F*) Snapshots of the simulated bulk systems without (left) and with (right) an excess electron (blue). The pressure increases by roughly 2kbar with the electron present. Blue lines indicate the periodically replicated simulation cell. Carbon, sulfur, and hydrogen atoms are colored green, yellow, and white.

significant change in the unit cell size occurs along the z-direction, with a 6.5 % and 5.0 % increase upon electronically exciting the chair and boat conformation, respectively, to the flat excited state, in good agreement with ΔH/H for ultrathin films.

Future Plans

1) The synchrotron and neutron studies for the structural and spin study on organic multiferroics.
2) The strongly correlated behaviors and ferroic coupling properties of organic radical multiferroics.
3) The potential superconducting behaviors and their mechanism of organic charge-transfer multiferroics under the static and dynamic high pressure.
4) The magnetoelectric coupling of organic multiferroic thin films, consisting of molecular quantum magnets and ferroelectrics.

References

1. Y. Hu, G. Zhong, Y. Guan, N. Lee, Y. Zhang, Y. Li, T. Mitchell, J. N. Armstrong, J. Benedict, S. W. Hla, and S. Ren, Alkali-Metal-Intercalated Percolation Network Regulates Self-Assembled Electronic Aromatic Molecules, ***Advanced Materials***, adma.201807178, 2019

2. Z.Zhang, R. C. Remsing, H. Chakraborty, W. Gao, G. Yuan, M. L Klein, S. Ren, Light-induced dilation in nano-sheets of charge transfer complexes, ***Proceedings of the National Academy of Sciences,*** (2018), doi.org/10.1073/pnas.1800234115.

Publications

This is the first year of the project, six peer-reviewed research articles are listed below:

1. Y. Hu, G. Zhong, Y. Guan, N. Lee, Y. Zhang, Y. Li, T. Mitchell, J. N. Armstrong, J. Benedict, S. W. Hla, and S. Ren, Alkali-Metal-Intercalated Percolation Network Regulates Self-Assembled Electronic Aromatic Molecules, **Advanced Materials**, adma.201807178 (2019).

2. Ying-Shi Guan, Guohua Zhong, Yong Hu, Anthony F. Cannella, Changning Li, Namhoon Lee, Quanxi Jia, David C. Lacy*, and Shenqiang Ren* Magnetoelectric radical hydrocarbons, ***Advanced Materials***, doi.org/10.1002/adma.201806263, (2018).

3. Zhuolei Zhang, Huashan Li, Richards Miller, Hans Malissa, Shirin Jamali, Christoph Boehme, Jeffrey Grossman*, and Shenqiang Ren*, Freestanding organic charge-transfer conformal electronics, ***Nano Letters,*** (2018), DOI: 10.1021/acs.nanolett.8b01342.

4. Zhuolei Zhang, Richard C. Remsing, Himanshu Chakraborty, Wenxiu Gao, Guoliang Yuan, Michael L Klein*, Shenqiang Ren*, Light-induced dilation in nano-sheets of charge transfer complexes, ***Proceedings of the National Academy of Sciences,*** (2018), doi.org/10.1073/pnas.1800234115.

5. Ying-Shi Guan, Zhuolei Zhang, Yichao Tang, Jie Yin, Shenqiang Ren*, Kirigami Inspired Nanoconfined Polymer Conducting Nanosheets with 2,000% Stretchability, ***Advanced Materials*** (2018), doi.org/10.1002/adma.201706390.

6. Wenxiu Gao, Raymond Brennan, Yong Hu, Manfred Wuttig, Guoliang Yuan,* Eckhard Quandt,* and Shenqiang Ren,* Energy Transduction Ferroic Materials, ***Materials Today***, DOI: 10.1016/j.mattod. 2018.01.032 (2018).

7. Wenxiu Gao, Zhuolei Zhang, Peng-Fei Li, Yuan-Yuan Tang, Ren-Gen Xiong, Guoliang Yuan*, and Shenqiang Ren*, Chiral molecular ferroelectrics with polarized optical effect and electroresistive switching, ***ACS Nano***, DOI: 10.1021/acsnano.7b07090 (2018).

Session XI

Room-Temperature Terahertz Detection with Quantum-Level Sensitivity through Plasmonic Photomixing

Mona Jarrahi, University of California Los Angeles

Program Scope

The ability to excite surface plasmon waves has enabled many unique opportunities for routing and manipulating electromagnetic waves. It has enabled strong light concentration in the near-field, paving the way for higher resolution imaging and spectroscopy, deep electromagnetic focusing and beam shaping, higher efficiency photovoltaics, photodetectors, modulators, and radiation sources. On the basis of the unique properties of surface plasmon waves, we conduct fundamental studies on metallic multi-spectral plasmonic nanostructures for probing intensity, polarization, and spectral properties of electromagnetic waves from radio frequency (RF) to terahertz (THz) frequencies. The multi-spectral plasmonic nanostructures maximize the intensity and spatial overlap of an optical pump beam with the incident electromagnetic wave to be probed in a photo-absorbing semiconductor substrate. We conduct extensive studies on various polarization-dependent two-dimensional and three-dimensional multi-spectral plasmonic nanostructures fabricated on different photo-absorbing semiconductor substrates to explore their potentials for electromagnetic wave probing and determine fundamental physical limitations of bandwidth and sensitivity of the proposed electromagnetic wave probing technique. We study tradeoff between electromagnetic wave probing bandwidth and sensitivity and its relation with various geometric and material specifications of the analyzed multi-spectral plasmonic nanostructures. These studies offer a deep understanding of behavior of plasmonic nanostructures in response to external electromagnetic waves in a multi-spectral electromagnetic wave platform. They offer a new perspective on utilizing the unique capabilities of multi-spectral plasmonic nanostructures for probing the intensity, polarization, and spectral properties of electromagnetic waves from RF to THz frequencies. They also enable fundamental physical studies on ultrafast carrier dynamics at nanoscale and discoveries on the interaction of electrons, holes, excitons, photons and semiconductor lattice.

Recent Progress

During the first two years of this research program, we have explored the use of various two-dimensional and three-dimensional plasmonic light concentrators to enhance interaction of electromagnetic waves with photo-absorbing semiconductors at the nanoscale to exhibit unprecedented functionalities. Specifically, we have demonstrated (I) room-temperature terahertz detection with quantum-level sensitivity through plasmonic photomixing and (II) carrier multiplication in Au-patched graphene nano-stripes.

(I) Room-Temperature Terahertz Detection with Quantum-Level Sensitivity through Plasmonic Photomixing: Near-quantum-limited terahertz detection has so far only been possible through the use of cryogenically cooled superconducting mixers as frequency downconverters. We have introduced a terahertz detection scheme that uses plasmonic photomixing for frequency downconversion to offer quantum-level sensitivities at room temperature for the first time. Frequency downconversion is achieved by mixing terahertz radiation and a heterodyning optical beam with a terahertz beat frequency in a plasmonics-enhanced semiconductor active region (Fig.

1). We demonstrate detection sensitivities down to 3 times the quantum-limit at room temperature. With a versatile design capable of broadband spectrometry over a 0.1-5 THz bandwidth, this plasmonic photomixer has broad applicability to quantum optics.

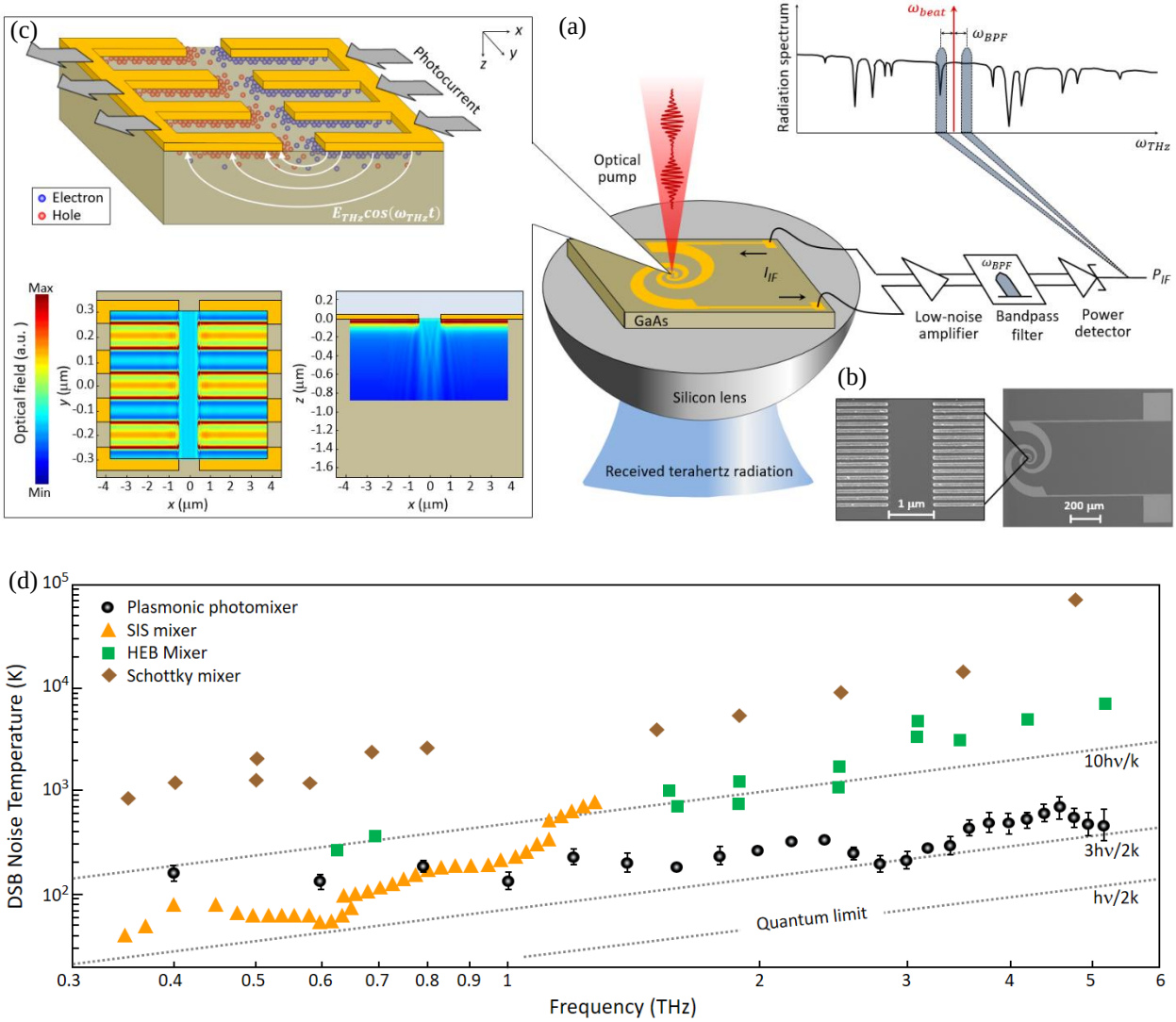

Fig. 1. Principles of terahertz detection through plasmonic photomixing. (a) When the plasmonic photomixer is pumped by a heterodyning optical beam with a terahertz beat frequency (ω_{beat}), the received terahertz radiation is downconverted to a photocurrent at $|\omega_{beat} - \omega_{THz}|$, which can be easily detected by RF electronics. (b) Scanning electron microscopy image of a fabricated plasmonic photomixer. (c) To achieve high THz-to-RF conversion efficiencies, two nanoscale Ti/Au gratings with a 50 nm thickness, 200 nm pitch, 100 nm spacing, and 300 nm thick Si_3N_4 anti-reflection coating are used as the photomixer contacts to enhance the optical pump intensity at the contact-semiconductor interface through the excitation of surface plasmon waves. These plasmonic contact electrode gratings provide a high optical power transmission (~ 85%) and a strong plasmonic enhancement when excited by a y-polarized optical pump beam at an ~784 nm wavelength, as illustrated in the top view (*xy*-plane) and cross-sectional view (*xz*-plane) color plots of the optical field in the GaAs substrate. (d) DSB noise temperature values of the plasmonic photomixer compared with previously demonstrated Schottky mixers, HEB mixers, and SIS mixers used in conventional spectrometers.

(II) Carrier Multiplication in Au-Patched Graphene Nano-Stripes: Graphene is a very attractive optoelectronic material with a broadband photoresponse. However, its responsivity is limited by low optical absorption and short carrier lifetime. We have demonstrated that the use of Au-patched graphene nano-stripes can modify the graphene Fermi energy level to enable a Coulomb induced intraband scattering around the Fermi level that enhances graphene photoresponse through carrier multiplication (Fig. 2).

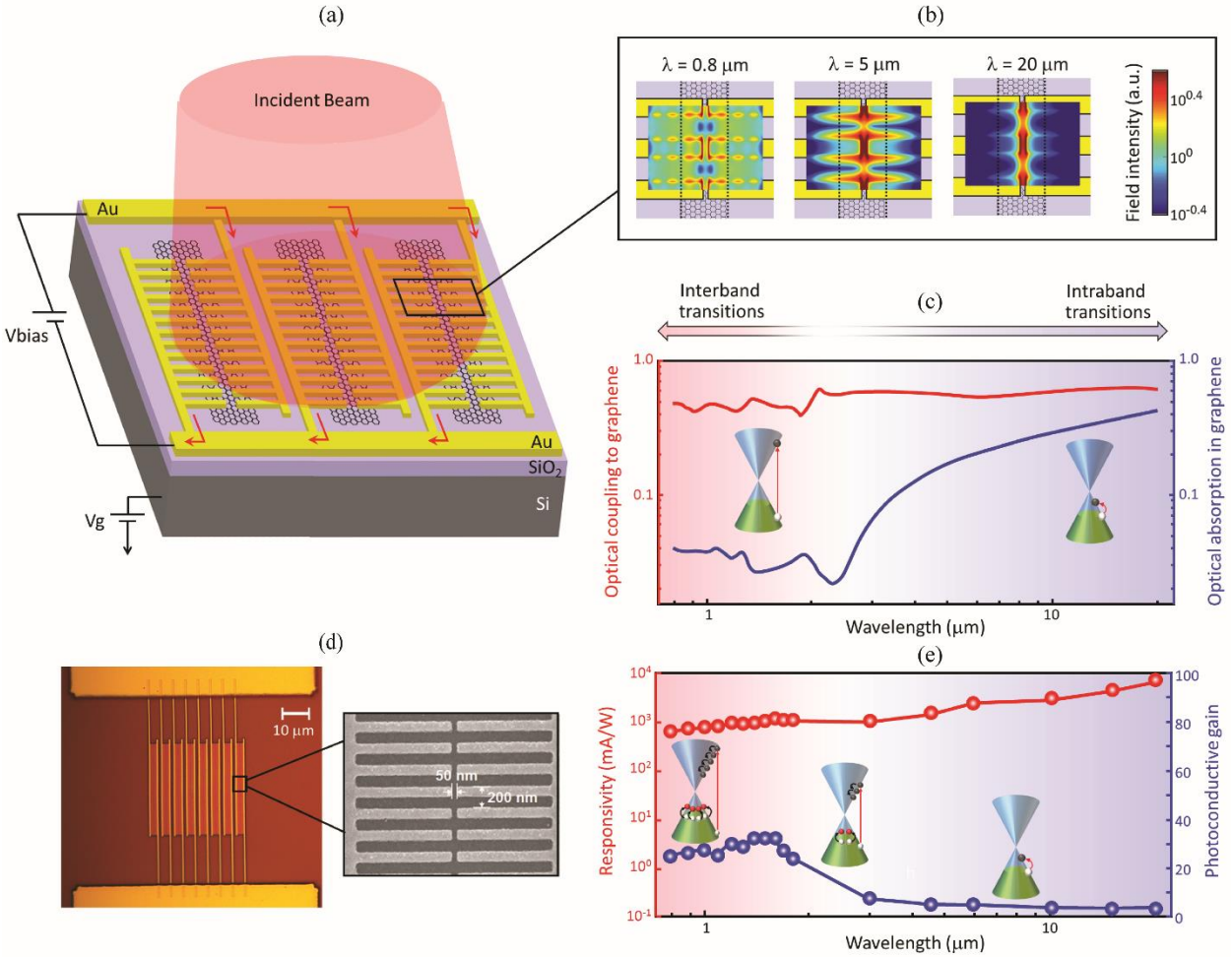

Fig. 2. High-responsivity and broadband photodetection through gold-patched graphene nano-stripes. (a) Schematic of a photodetector based on gold-patched graphene nano-stripes. It is fabricated on a high-resistivity Si substrate coated with a 130 nm thick SiO2 layer. The gate voltage applied to the Si substrate, Vg, controls the Fermi energy level of the graphene nano-stripes. The gold patches have a width of 100 nm, a periodicity of 200 nm, a height of 50 nm, a length of 1 μm, and a tip-to-tip gap size of 50 nm. (b) Color plot of the transmitted optical field, polarized normal to the graphene nano-stripes, through the gold patches at 0.8 μm, 5 μm, and 20 μm, indicating highly efficient and broadband optical coupling to the graphene nano-stripes. (c) Numerical estimates of the optical coupling (red curve) and optical absorption (blue curve) in the graphene nano-stripes as a function of the wavelength. (d) Optical microscope and SEM images of a fabricated photodetector based on the gold-patched graphene nano-stripes. (e) The measured responsivity (red data) and photoconductive gain (blue data) of the fabricated photodetector at an optical power of 2.5 μW, indicating a strong carrier multiplication in the near infrared regime. The carrier multiplication factor decreases at longer wavelength because of the lower photon energies and at high optical powers due to the increase in the carrier recombination rate.

Future Plans

For the next steps of this research program, we plan to investigate the impact of the geometry of the plasmonic metallic nanostructures and doping on band-bending in graphene nanostructures and their subsequent impact on the photovoltaic and photothermoelectric response of graphene nanostructures. We also plan to study thermal characteristics of plasmonic nanostructures integrated with photo-absorbing semiconductors at high optical pump powers and investigate the fundamental physical limitations of optical-to-terahertz conversion efficiency and terahertz detection sensitivity. To suppress the negative impacts of joule heating on the quantum efficiency of plasmonic photoconductors, we plan to utilize naturally-formed built-in electric fields in close proximity to the plasmonic metallic nanostructures for drifting the photo-generated carriers. Toward this goal, we plan to investigate various band-bending processes in photo-absorbing semiconductor heterostructures with specifically selected bandgap energy and doping levels.

Publications (Jan 2017- Jan 2019)

1. N. Wang, S. Cakmakyapan, Y.-J. Lin, H. Javadi, M. Jarrahi, "Room Temperature Terahertz Spectrometer with Quantum-Level Sensitivity," arXiv:1806.05256, 2018 (in review)
2. S. Cakmakyapan, P. K. Lu, A. Navabi, M. Jarrahi, "Gold-Patched Graphene Nano-Stripes for High-Responsivity and Ultrafast Photodetection from Visible to Infrared Regimes," Light: Science & Applications, 7, 20, 2018
3. E. C. Snively, N. T. Yardimci, B. T. Jacobson, M. Jarrahi, A. Murokh, P. Musumeci, "Non-invasive low charge electron beam time-of-arrival diagnostic using a plasmonics-enhanced photoconductive antenna," Applied Physics Letters, 113, 193501, 2018
4. N. T. Yardimci, M. Jarrahi, "Nanostructure-Enhanced Photoconductive Terahertz Emission and Detection," Small, 14, 1802437, 2018
5. N. T. Yardimci, D. Turan, S. Cakmakyapan, M. Jarrahi, "High-Responsivity and Broadband Photoconductive Terahertz Detector Based on a Plasmonic Nanocavity," Applied Physics Letters, 113, 251102, 2018
6. X. Li, N. T. Yardimci, M. Jarrahi, "A Polarization-Insensitive Plasmonic Photoconductive Terahertz Emitter," AIP Advances, 7, 115113, 2017
7. D. Turan, S. C. C. Garcia, E. Castro-Camus, M. Jarrahi, "Impact of the Metal Adhesion Layer on the Radiation Power of Plasmonic Photoconductive Terahertz Sources," Journal of Infrared, Millimeter and Terahertz Waves, 38, 1448, 2017
8. N. T. Yardimci, S. Cakmakyapan, S. Hemmati, M. Jarrahi, "A High-Power Broadband Terahertz Source Enabled by Three-Dimensional Light Confinement in a Plasmonic Nanocavity," Scientific Reports, 7, 4166, 2017
9. N. T. Yardimci, M. Jarrahi, "High Sensitivity Terahertz Detection through Plasmonic Nano-Antenna Arrays," Scientific Reports, 7, 42667, 2017

Non-equilibrium dynamics of interacting light-matter systems

PI: Hakan E. Tureci, Department of Electrical Engineering, Princeton University

Program Scope

This project aims to study the fundamental physics and technological applications of (i) superconducting circuits that contain one or multiple qubits coupled to a common electromagnetic environment and driven out of equilibrium by oscillatory sources, and (ii) the dynamics and control of exciton-polariton systems. The project will pursue the development of advanced quantum microwave engineering techniques that can efficiently deal with large, possibly complex 2D and 3D superconducting oscillators coupled to multiple Josephson-junction based artificial atoms. This includes in particular the accurate calculation of spectral densities seen by single qubits as well as interaction kernels in multi-qubit systems. We will also develop computational techniques to deal with the dynamics and control of exciton-polariton condensates in multi-cavity systems that are pumped spatially inhomogeneously.

Recent Progress

Here we review some of the highlights from publications [1-12] resulting from this grant.

Quantum Electrodynamic modeling of Superconducting Circuits: Any quantum-confined electronic system coupled to the electromagnetic continuum is subject to radiative decay and renormalization of its energy levels. When coupled to a cavity, these quantities can be strongly modified with respect to their values in vacuum (Purcell effect). Generally, this modification can be accurately captured by including only the closest resonant mode of the cavity. However in the circuit quantum electrodynamics architecture, it is found that the radiative decay rates are strongly influenced by far off-resonant modes. A multimode calculation accounting for the infinite set of cavity modes leads to divergences unless a cutoff is imposed. It has so far not been identified what the source of divergence is. We show in Ref. [4] that unless gauge invariance is respected, any attempt at the calculation of circuit QED quantities is bound to diverge. We then present a theoretical approach to the calculation of a finite spontaneous emission rate and the Lamb shift that is free of cutoff.

Simulating noise-assisted transport in a superconducting circuit-based device: The work in Ref. [8] is a collaboration with the experimental group of Andreas Wallraff (ETH Zurich) to study quantum transport phenomena typical to light-harvesting complexes in a synthetic platform (superconducting circuits). Our contribution to this work was the theoretical and computational study of the non-Markovian dynamics of three superconducting qubits (representing a model of a pigment protein complex consisting of three coupled chlorophyll molecules) that takes place

under the action of structured noise. We were able to explain the experimental results successfully, elucidating in a controlled setting the (apparently positive) role of noise in quantum transport.

Exploring the Quantum-to-Classical Cross-over of a Frequency Comb generated in a Josephson junction Circuit: In Ref. [9] we investigate the dynamics of a microwave-driven Josephson junction capacitively coupled to a linear resonator. In the regime of driving where the Josephson junction can be approximated as a Kerr oscillator, this minimal nonlinear system has been previously shown to exhibit a bistability in phase and amplitude. In the present study, we characterize the full phase diagram and show that besides a parameter regime exhibiting bistability, there is also a regime of self-oscillations characterized by a frequency comb in its spectrum. We address the fate of this comb-like spectrum under transition from a classical regime to a regime of strong quantum fluctuations, as the nonlinearity increases to become the dominant scale with respect to dissipation. We find that the nonlinearity responsible for the emergence of the frequency combs also leads to its dephasing, resulting in the broadening and ultimate disappearance of sharp spectral peaks. Our study explores the fundamental question of the impact of quantum fluctuations on quantum systems which do not possess a stable fixed point in the classical limit.

An active superconducting fabric for non-reciprocal quantum transport of excitations: As superconductor quantum technologies are moving towards large-scale integrated circuits, a robust and flexible approach to routing photons at the quantum level becomes a critical problem. Active circuits, which contain parametrically driven elements selectively embedded in the circuit, offer a viable solution. In Ref. [10], we present a general strategy for routing nonreciprocally quantum signals between two sites of a given lattice of oscillators, implementable with existing superconducting circuit components. Our approach makes use of a dual lattice of overdamped oscillators linking the nodes of the main lattice. Solutions for spatially selective driving of the lattice elements can be found, which optimally balance coherent and dissipative hopping of microwave photons to nonreciprocally route signals between two given nodes. In certain lattices these optimal solutions are obtained at the exceptional point of the dynamical matrix of the network. We also demonstrate that signal and noise transmission characteristics can be separately optimized.

Future Plans

In the next period, we plan to focus on the systematic derivation of reduced quantum models for microwave-driven quantum circuits from our first principles Heisenberg-Langevin approach [1,4]. One of the goals of this ongoing work is to elucidate the infidelities in current superconducting qubit readout schemes, and further, to devise methods to increase the readout fidelity.

Publications

1. **Non-Markovian dynamics of a superconducting qubit in an open multimode resonator,** M. Malekakhlagh, A. Petrescu, Hakan E. Tureci, Phys. Rev. A **94**, 063848 (2016).

2. **Non-Hermitian coupled-mode theory for incoherently pumped exciton-polariton condensates**, S. Khan, Hakan E. Tureci, Phys. Rev. A **94**, 053856 (2016).

3. **Spatial correlations in driven-dissipative photonic lattices,** M. Biondi, S. Lienhard, J. Blatter, H. Tureci, S. Schmidt, New. J. Phys. **19**, 125016 (2017).

4. **Cutoff-free Circuit Quantum Electrodynamics,** Moein Malekakhlagh, Alexandru Petrescu, Hakan E. Tureci, Phys. Rev. Lett. **119**, 073601 (2017).

5. **Non-equilibrium gas-liquid transition in the driven-dissipative photonic lattice,** M. Biondi, G. Blatter, H. E. Türeci, S. Schmidt, Phys. Rev. A **96**, 043809 (2017).

6. **Competing role of interactions in synchronization of exciton-polariton condensates,** Saeed Khan, Hakan E. Türeci, New J. Phys. **19**, 105008 (2017).

7. **Stable switching among high-order modes in polariton condensates,** Yongbao Sun, Yoseob Yoon, Saeed Khan, Li Ge, Mark Steger, Loren N. Pfeiffer, Ken West, Hakan E. Türeci, David W. Snoke, Keith A. Nelson, Phys. Rev. B **97**, 045303 (2018).

8. **Studying light-harvesting models with superconducting circuits,** Anton Potočnik, Arno Bargerbos, Florian A. Y. N. Schröder, Saeed A. Khan, Michele C. Collodo, Simone Gasparinetti, Yves Salathé, Celestino Creatore, Christopher Eichler, Hakan E. Türeci, Alex W. Chin, Andreas Wallraff, Nature Communications **9**, 904 (2018).

9. **Frequency Combs in a Lumped-Element Josephson-Junction Circuit,** Saeed Khan, Hakan E. Türeci, Phys. Rev. Lett. **120**, 153601 (2018).

10. **Non-reciprocal Signal Routing in an Active Quantum Network,** Anja Metelmann, Hakan E. Türeci, Phys. Rev. A **97**, 043833 (2018).

11. **Fluxon-based Quantum Simulation in Circuit QED,** Alexandru Petrescu, Hakan E. Türeci, Alexey V. Ustinov, Ioan M. Pop, Phys. Rev. B **98**, 174505 (2018).

Session XIV

Interfacial Design for Aqueous Photoelectrochemical Cells and Solar Flow Batteries

Yiying Wu, Department of Chemistry and Biochemistry, Ohio State University

Program Scope

Solid-electrolyte interfaces play crucial roles in controlling interfacial charge transfer and electrode stability, and represent one of the "transformative opportunities" as described in "Challenges at the Frontiers of Matter and Energy: Transformative Opportunities for Discovery Science", a DOE report from the Basic Energy Sciences Advisory Committee in 2015. The central theme of this project is to design amphiphilic push-pull dyes that form bilayer protection on semiconductor surfaces in aqueous solutions: an inner hydrophobic layer that prevents water from penetration and an outer layer that maintains the wetting of the electrode surface. The push-pull design also promotes efficient vectorial electron transfer at the electrode/electrolyte interfaces. These interfacial dye molecules will be used to sensitized p-type semiconductors such as NiO for p-type dye-sensitized photoelectrochemical cells (DSPEC). At the same time, we are also developing our niche in lead halide perovskite solar cells and optoelectronics. Our expertise in p-type semiconductors and the design of interfacial molecules is useful in both DSPEC and halide perovskites. We have also identified machine learning as a promising approach in addressing the complex challenges associated with halide perovskites.

Recent Progress

1: Machine-Leaning for Understanding Compatibility of Halide Perovskites with Small Molecules

Inorganic-organic halide perovskites have attracted great attention in photovoltaics and light emitting diode devices. However, various works have reported instability of perovskites under heat, moisture, oxygen, and ultra-violet light. Among the strategies that have been utilized to stabilize the material and passivate surface states, post treatment with organic small molecules or polymers is one facile but effective approach. For example, benzylamine have been used to modify the surface of perovskites to increase the moisture stability,[1] and pyridine as a Lewis base to passivate perovskites has significantly reduced the nonradiative electron-hole recombinations.[2] However, we have observed many other amines could directly destroy the methylammonium lead iodide ($MAPbI_3$) perovskite films. Therefore, *identifying the rules that can predict the compatibility between the perovskite film and a molecule based on its molecular structure is of fundamental and practical interest for future development of the post-treatment materials.* In this work, we applied machine-learning technique to study the trend of reactivity of different types of amines, which are used for the post-treatment of halide perovskite films. Fifty randomly selected amines are classified based on their compatibility with $MAPbI_3$. Machine learning models are constructed from the

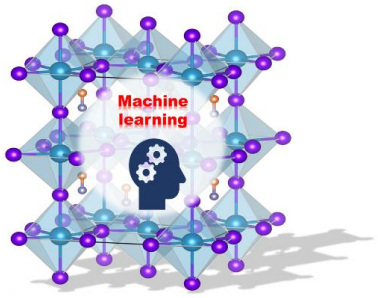

Figure 1: Machine learning for compatibility between perovskites with small molecules.

classification of these amines and their molecular descriptor features. The model has also been verified by accurately predicting compatibility of never-seen molecules and also provides chemical insights into molecular descriptors.

2: Membrane-Inspired Dye-Sensitized Photocathode for Solar Fuels: Electron Transfer, pH-Decoupled Energetics and Surface Excimer

Dye-sensitized photoelectrochemical cells (DSPECs) represent an attractive platform for solar fuel production.[3,4] My group has been working on dye-sensitized *photocathodes* for water reduction.[5,6] An achievement *highlighted by C&EN* [7] was a membrane-mimicking dye that protects NiO photocathodes to provide excellent stability in extremely acidic (pH = 0) conditions. The acidic stability also allows for the use of a cubane molybdenum-sulfide cluster as the hydrogen evolution reaction (HER) catalyst. Recently, we have carried out more detailed studies on this system to understand the interfacial molecular assembly, electron transfer kinetics and interfacial energerics.[8]

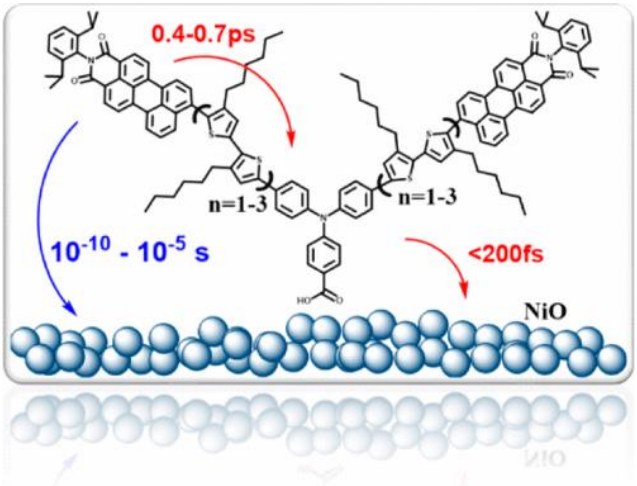

Figure 2. The molecular structure of BH4 and the schematic showing the energetics of the DSPEC.

(1) Interfacial electron transfer: As shown in Figure 2, these dyes—denoted as BH dyes—consist of a triphenylamine (TPA) donor and two perylenemonoimide (PMI) acceptors linked with oligothiophene. We have systematically studied the photophysical properties of these BH series molecules with various lengths of oligothiophene in solution via Density Functional Theory (DFT) calculations and time-resolved spectroscopic techniques. When dissolved in DMF, the molecules undergo ultrafast intramolecular charge transfer within 1 ps upon photoexciation. The charge-separated state then recombines within tens of picoseconds. The electron transfer kinetics of dye-sensitized mesoporous NiO photocathodes exhibit both fast and slow charge recombination processes (70 ps and 4.5 μs, respectively, for BH4). We assign the fast process as the geminate recombination, and the slow process from the excimer-facilitated intermolecular charge separation (see *Surface excimer* below). The effect of various lengths of π-linkers is modeled with a spatial attenuation factor of 0.20 $Å^{-1}$, with a longer spatial separation of charge recombination centers giving rise to a slower recombination rate between the reduced dye species and the NiO surface.

(2) pH-decoupled energetics: We have measured the pH dependence of the flat-band potential of NiO after dye-sensitization to prove the proposed protection mechanism resulting from the assembly of the BH dyes. A common phenomenon on most metal oxides is that the surface potential exhibits a Nernstian dependence on pH in aqueous solution, shifting by 59 mV per pH unit. This is due to the change in surface charge resulting from the extent of surface protonation. However, when NiO is sensitized by our proposed amphiphilic dyes, the inner hydrophobic layer should shut off surface protonation. Therefore, *a hypothesis is that the flat band potential of NiO should exhibit independence from pH.* Mott-Schottky measurements were used to determine the NiO flat band potential (E_{FB}) as a function of pH for bare NiO and BH4-sensitized NiO films. The BH4 sensitized NiO film revealed no change in the E_{FB} as a function of pH with a constant NiO E_{FB} of 0.22 ± 0.01 V vs NHE across a pH range of 2–5, thus indicating that the BH4 dye creates a dense hydrophobic assembly to repel the aqueous phase. Such an interfacial phenomenon is also observed at an atomic level in our MD simulations. By contrast, the bare NiO and the P1-sensitized NiO films show an expected Nernstian shift in the NiO E_{FB} as a function of pH with a slope of 60.4 mV/pH and 61.3 mV/pH, respectively. This work shows that properly designed interfacial molecules would allow the use of pH to tune the energy alignment between a semiconductor/liquid junction.

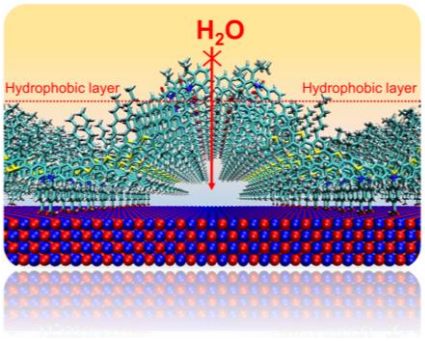

Figure 3: MD simulation showing the dense hydrophobic layer from the assembly of BH4 dyes that prevents the penetration of water.

(3) Surface excimer: When dye molecules are assembled on the surface of semiconductors, dye-dye interaction also plays an important role in the charge-transfer process upon photoexcitation.[9] We have observed the excimer formation on the BH4-sensitized metal oxide surface due to the π-π interaction between the PMI units of neighboring BH4 molecules through the analysis of UV-Vis absorption, photoluminescence and transient near-infrared absorption spectroscopies. It confirms the signature features associated with excimer formation of the covalent molecular PMI dimer as reported by Wasielewski et. al.[10] In addition, a long-lived (4.3 μs) signal, which is assigned to the mixture of oxidized and reduced BH4 molecules, has been observed on the BH4-sensitized Al_2O_3 film due to the proposed intermolecular charger transfer between the aggregated

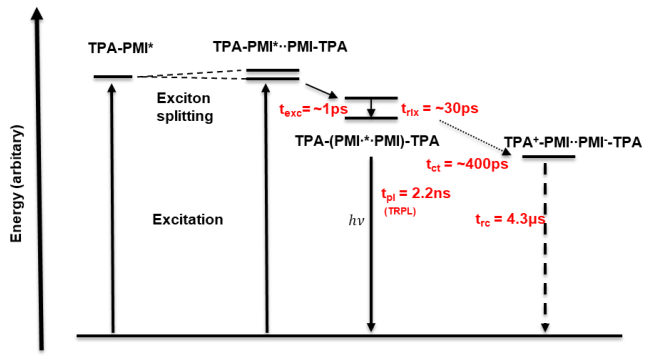

Figure 4. Schematic energy diagram of excimer formation and intermolecular charger transfer on BH4-sensitized Al_2O_3 film.

dye molecules (Figure 4). It sheds light on the mechanism for our observed slow recombination in the dye-sensitized NiO, and thus provides insight on how to slow down the recombination rate.

Future Plans

The instability of perovskites as a result of exposure to heat, moisture, oxygen, and ultra-violet light is the hurdle that limits their applications. *Our future plan is to apply machine learning to identify small molecules and polymers for the passivation and self-healing of perovskite films, and to understand the structure-activity relationship between the effectiveness of a molecule and its molecular features.* Quantitative and predictive models will be developed with the ultimate goal of predicting 'champion' molecules to achieve the long-term stability of perovskites with self-healing capability. Utilizing our newly installed near-ambient-pressure XPS, we will investigate the surface evolution of perovskite films under *in operando* conditions. The influence of these molecules on charge carrier transport will also be measured through electrochemical impedance spectroscopy and transient absorption spectroscopy.

References

1. Wang, F. *et al.* Phenylalkylamine Passivation of Organolead Halide Perovskites Enabling High-Efficiency and Air-Stable Photovoltaic Cells. *Adv. Mater.* **28,** 9986–9992 (2016).
2. Noel, N. K. *et al.* Enhanced photoluminescence and solar cell performance via Lewis base passivation of organic-inorganic lead halide perovskites. *ACS Nano* **8,** 9815–9821 (2014).
3. Ashford, D. L. *et al.* Molecular Chromophore-Catalyst Assemblies for Solar Fuel Applications. *Chem. Rev.* **115,** 13006–13049 (2015).
4. Yu, Z., Li, F. & Sun, L. C. Recent advances in dye-sensitized photoelectrochemical cells for solar hydrogen production based on molecular components. *Energy Environ. Sci.* **8,** 760–775 (2015).
5. Ji, Z., He, M., Huang, Z., Ozkan, U. & Wu, Y. Photostable p-type dye-sensitized photoelectrochemical cells for water reduction. *J. Am. Chem. Soc.* **135,** 11696–11699 (2013).
6. Click, K. A., Beauchamp, D. R., Huang, Z., Chen, W. & Wu, Y. Membrane-Inspired Acidically Stable Dye-Sensitized Photocathode for Solar Fuel Production. *J. Am. Chem. Soc.* **138,** 1174–1179 (2016).
7. Jacoby, M. Bilayer Dye Aids Solar Water-Splitting. *C&EN* **94, issue,** 28 (2016).
8. Yu, Y. *et al.* Electron Transfer Kinetics of a Series of Bilayer Triphenylamine-Oligothiophene-Perylenemonoimide Sensitizers for Dye-Sensitized NiO. *J. Phys. Chem. C* **121,** 20720–20728 (2017).
9. Zhang, L. & Cole, J. Dye Aggregation in Dye-Sensitized Solar Cells. *J. Mater. Chem. A* **5,** 19541–19559 (2017).
10. Lindquist, R. J. *et al.* Energy flow dynamics within cofacial and slip-stacked perylene-3,4-dicarboximide dimer models of π-aggregates. *J. Am. Chem. Soc.* **136,** 14912–14923 (2014).

Publications

1. Yu, Yongze; Tan, Xuanheng; Ning, Shougui; Wu, Yiying. Machine-Learning for Understanding Compatibility of Organic-Inorganic Hybrid Perovskite with Post-Treating Amines. ***ACS Energy Lett.***, 2019, 4, pp 397–404**.** (**DOI**: 10.1021/acsenergylett.8b02451)
2. Yongze Yu, Kevin A. Click, Shane M. Polen, Mingfu He, Christopher M. Hadad, and Yiying Wu, "Electron Transfer Kinetics of a Series of Bilayer Triphenylamine-Oligothiophene-Perylenemonoimide Sensitizers for Dye-Sensitized NiO." J. Phys. Chem. C 121.38 (2017): 20720-20728. (DOI: 10.1021/acs.jpcc.7b07859)
3. Draskovic, T. I., & Wu, Y. (2017). Electrocatalytic Properties of Cuprous Delafossite Oxides for the Alkaline Oxygen Reduction Reaction. *ChemCatChem*, *9*(20), 3837–3842. https://doi.org/10.1002/cctc.201700712.
4. Click, K. A., Schockman, B. M., Dilenschneider, J. T., McCulloch, W. D., Garrett, B. R., Yu, Y., … Wu, Y. (2017). Bilayer Dye Protected Aqueous Photocathodes for Tandem Dye-Sensitized Solar Cells. *The Journal of Physical Chemistry C*. https://doi.org/10.1021/acs.jpcc.7b01911

Manuscripts under review or submitted soon:

5. Yongze Yu, and Yiying Wu, "Excimer Formation and Long-Lived Charge Separation in Self-Assembled Membrane-Mimicking Dyes on Metal Oxides", submitted soon.
6. Yongze Yu; Kevin Click; Szu-Chia Chien; Jiaonan Sun; Allison Curtze; Li-Chiang Lin; Yiying Wu, "Decoupling pH-Dependence of Flat-Band Potential in Aqueous Dye-Sensitized Electrodes", submiited to *J. Phys. Chem. C* (under review).
7. Jiaonan Sun, Yongze Yu, Allison E. Curtze, Xichen Liang and Yiying Wu, "Dye-Sensitized Photocathodes for Oxygen Reduction: Efficient H_2O_2 Production and Aprotic Redox Reactions", submitted soon.

Combined Coherent Manipulation and Single-Shot Measurement of an Electron Spin in a Quantum Dot

PI: Edward B. Flagg
West Virginia University, Department of Physics and Astronomy
Morgantown, WV 26506

Program Scope

We are pursuing a scheme to measure the spin-state of a single electron trapped in an optically active quantum dot via a cycling transition induced by the AC Stark effect. The spin degree of freedom of an electron in a quantum dot (QD) is a candidate system to act as a quantum bit. The necessary capabilities of a single quantum bit are initialization, manipulation, and measurement of its quantum state. Optical spin initialization and manipulation are allowed by a transverse magnetic field (the Voigt configuration) that modifies the polarization selection rules of the transitions [1]. The lack of a cycling transition in the Voigt configuration, however, makes a single-shot measurement of the spin-state very difficult. Spin-state measurement can be accomplished in a longitudinal magnetic field (the Faraday configuration) [2], but the optical selection rules preclude spin manipulation. Therefore, there is a critical need for a method to perform a single-shot measurement of the electron spin-state while maintaining the initialization and manipulation capabilities of the Voigt configuration. Achievement of this measurement is an important problem because without the ability to perform all three operations, optically active QDs will not be viable quantum bits.

The central hypothesis driving the proposal is that the AC Stark effect is capable of modifying the optical transitions to allow a spin-preserving cycling transition, which can be used for a single-shot measurement. We performed preliminary simulations of the proposed experimental situations indicating that the single-shot measurement scheme can be successfully accomplished [3]. Recently, we have experimentally measured record large spin-selective AC Stark shifts sufficient to satisfy the requirements of the single-shot spin measurement scheme [see Publications section, Wilkinson].

We propose to test our central hypothesis and thereby achieve the overall objective of this project by addressing the following specific objectives:

Objective #1: Characterize the cycling transitions induced by the AC Stark effect on a QD in a Voigt configuration magnetic field. Our working hypothesis is that an AC Stark shift much larger than the Zeeman splitting in a Voigt configuration will result in a "pseudo-Faraday" configuration with spin-preserving cycling transitions.

Objective #2: Demonstrate single-shot measurement of the electron spin-state using spin-preserving cycling transitions. Our working hypothesis is that the cycling transitions will be sufficiently spin-preserving so as to be suitable for a high-fidelity measurement of the spin-state faster it is disturbed by the measurement back-action.

Objective #3: Demonstrate spin initialization and manipulation in the Voigt configuration, with single-shot spin measurement under AC Stark shift. Our working

hypothesis is that the system can be reconfigured more rapidly than the electron spin lifetime and that the reconfiguration does not additionally disturb the spin-state.

Recent Progress

We experimentally demonstrated spin-selective AC Stark shifts applied to a charged QD in zero magnetic field, and we have submitted a paper to *Applied Physics Letters* that is currently under review [see Publications section, Wilkinson]. The transition frequency of one spin manifold shifts by about 20 GHz, which is much larger than the 1 GHz linewidth, while the other transition is not shifted by the AC Stark effect. The polarization, power, and detuning of the laser causing the AC Stark effect determine the shifts of the transitions. Linear polarization shifts both transitions equally, while circular polarization shifts only one of them. Red-detuning of the laser causes a blue-shift of the transition, while blue-detuning causes a red-shift. In addition to the AC Stark shift, we observe another energy shift caused by dynamic polarization of the nuclear spins of the atoms comprising the QD. The direction of the nuclear polarization is determined by the polarization of the AC Stark laser.

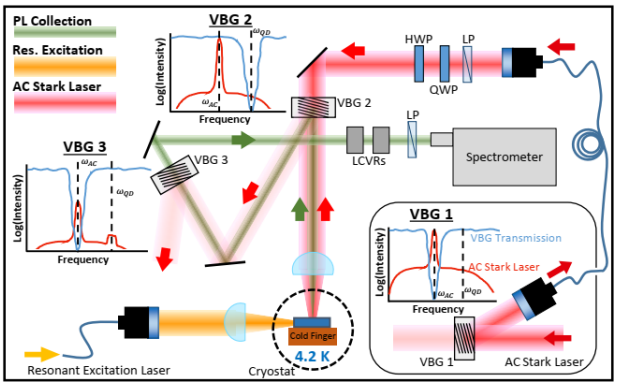

FIG. 1. Schematic of the optical setup. Inset plots show the filtering and attenuation of the AC Stark laser spectrum by the volume Bragg gratings (VBGs). Different optical paths are shown with different colors and propagation directions are indicated by colored arrows.

The AC Stark laser that switches between Voigt and pseudo-Faraday configurations must be circularly polarized, which requires that it be applied normal to the sample surface and have a fully controllable polarization. In addition, the strong scattering of the AC Stark laser must be filtered from the QD fluorescence. Figure 1 shows the experimental design used for these experiments. We have developed a new technique for filtering the scattered laser from the fluorescence by using volume Bragg gratings (VBGs). A resonant laser is coupled into the waveguide mode of the microcavity through the cleaved edge of the sample. This allows discrimination between the waveguide mode that contains the excitation laser, and the Fabry-Perot mode that contains the QD fluorescence [4]. This method has an advantage over schemes that use polarization to discriminate between fluorescence and laser scattering [5, 6] because it provides full polarization freedom to the measurement. The resonant laser is used to coherently excite the QD and cause fluorescence. Scanning the frequency of that laser over the resonances and recording the fluorescence intensity with the spectrometer allows measurement of the excitation spectrum of the QD and reveals the direction and magnitude of any resonance shifts.

Figure 2 shows a reference spectrum with no AC Stark laser, and two spectra showing AC Stark shifts with linear and circular polarization. The reference and linear spectra contain two degenerate transitions, while the circular polarization causes a splitting via a spin-selective AC

Stark effect. The laser is red detuned by $\Delta/2\pi$ = -1000 GHz and has a power density of 77.3 kW/cm^2 (total power 2.38 mW). That causes a blue shift of the affected transition(s). The circular polarization shifts only one transition to higher energy by a large amount while the other transition remains near the reference frequency as shown in Fig. 2(c). The lower-energy transition is actually red-shifted slightly due to interactions with the partially polarized nuclear spin ensemble of the atoms comprising the QD. This is called the Overhauser shift and is caused by electron spin pumping due to the AC Stark laser.

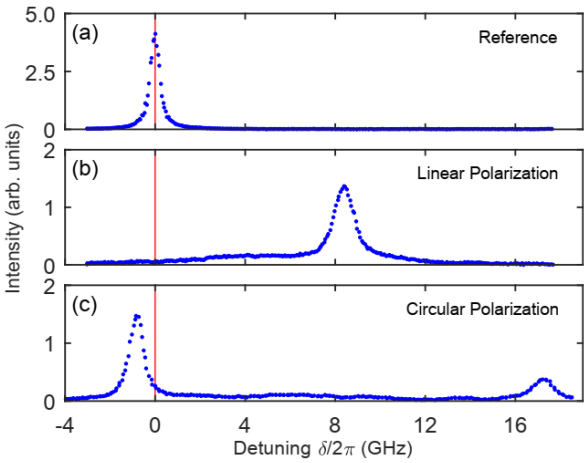

FIG. 2. Excitation spectra as functions of the resonant laser detuning, δ. (a) Reference spectrum with no AC Stark laser. (b) Spectrum with linearly polarized AC Stark laser. (c) Spectrum with circularly polarized AC Stark laser.

We can change the degree to which each transition shifts by changing the polarization of the AC Stark laser. Figure 3 shows the center frequencies of the peaks as a function of the polarization of the AC Stark laser. For each AC Stark laser polarization, two excitation spectra were recorded, one with σ− detection and one with σ+ detection. The detection polarization in turn determines which transition energy was measured. For linear laser polarization the transitions are nearly degenerate and blue-shifted from the reference frequency, as expected. As the laser becomes elliptically polarized, the transitions split because the AC Stark effect influences them differently (recall that $\Omega_\pm = \mathbf{d}_\pm \cdot \mathbf{E}$), which also causes electron spin pumping. The polarization of the electron spin causes dynamic nuclear polarization, and the Overhauser shift occurs. This is most obvious for circular polarization where the splitting is largest. In this case the lower-frequency transition is red-shifted by the Overhauser effect to below the reference frequency. The occurrence of the maximum splitting under circular polarization implies that the transition dipoles are highly circularly polarized. We have confirmed this with a calculation for the degree of circular polarization for the σ− (σ+) transition of 0.963 (0.955).

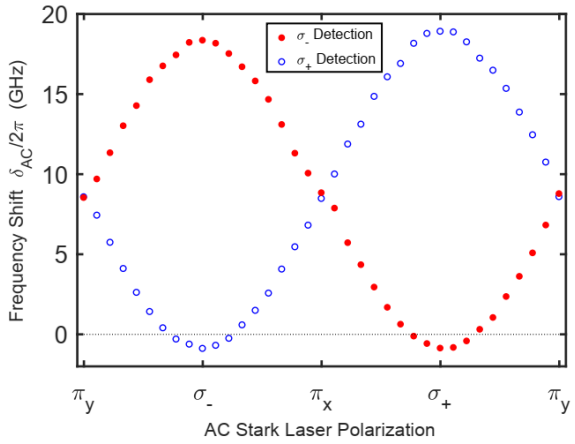

FIG. 3. Frequency shifts of excitation spectra peaks as a function of AC Stark laser polarization using orthogonal circular detection polarizations.

Future Plans

The next step in this project is to measure the energy level modifications caused by an AC Stark laser in a Voigt field. To change the polarization selection rules to produce cycling transitions, the AC Stark shift must be greater than the Zeeman splitting caused by the Voigt magnetic field. The

similarity between the pseudo-Faraday configuration and a true Faraday configuration can be determined by the circularity of the emission polarization. We will record high-resolution polarization-dependent spectra of the QD emission in the pseudo-Faraday configuration and extract the polarization of each transition as a function of the AC Stark laser intensity. We expect the emission polarizations to be rectilinear in the pure Voigt configuration, changing to elliptical in a transition regime as the AC Stark laser intensity is increased, and finally becoming mostly circular as the AC Stark shift becomes much larger than the Voigt configuration splitting.

References

1. Berezovsky, J., Mikkelsen, M. H., Stoltz, N. G., Coldren, L. A., and Awschalom, D. D. "**Picosecond Coherent Optical Manipulation of a Single Electron Spin in a Quantum Dot**" *Science* 320, no. 5874 (2008): 349–352. doi:10.1126/science.1154798
2. Delteil, A., Gao, W., Fallahi, P., Miguel-Sanchez, J., and Imamoğlu, A. "**Observation of Quantum Jumps of a Single Quantum Dot Spin Using Submicrosecond Single-Shot Optical Readout**" *Physical Review Letters* 112, no. 11 (2014): 116802. doi:10.1103/PhysRevLett.112.116802
3. Flagg, E. B. and Solomon, G. S. "**Optical Spin Readout Method in a Quantum Dot Using the AC Stark Effect**" *Physical Review B* 92, no. 24 (2015): 245309. doi:10.1103/PhysRevB.92.245309
4. Chen, D., Lander, G. R., and Flagg, E. B. "**Resonance Fluorescence of an InGaAs Quantum Dot in a Planar Cavity Using Orthogonal Excitation and Detection**" *JoVE (Journal of Visualized Experiments)* no. 128 (2017): e56435–e56435. doi:10.3791/56435
5. Vamivakas, N. A., Zhao, Y., Lu, C.-Y., and Atatüre, M. "**Spin-Resolved Quantum-Dot Resonance Fluorescence**" *Nature Physics* 5, no. 3 (2009): 198–202. doi:10.1038/nphys1182
6. Kuhlmann, A. V., Houel, J., Brunner, D., Ludwig, A., Reuter, D., Wieck, A. D., and Warburton, R. J. "**A Dark-Field Microscope for Background-Free Detection of Resonance Fluorescence from Single Semiconductor Quantum Dots Operating in a Set-and-Forget Mode**" *Review of Scientific Instruments* 84, no. 7 (2013): 073905. doi:10.1063/1.4813879

Publications

1. Wilkinson, T. A., Cottrill, D. J., Cramlet, J. M., Maurer, C. E., Flood, C. J., Bracker, A. S., Yakes, M., Gammon, D., Flagg, E. B., "**Spin-selective AC Stark shifts in a charged quantum dot**" arXiv:1812.02151 [quant-ph]

Poster Sessions

Physical Behavior of Materials Principal Investigators' Meeting

POSTER SESSION I

Tuesday, March 19, 2019

1) **Nanophotonics-Enhanced Solar Cells**
   Shanhui Fan, Stanford University

2) **Plasmonic Photovoltaics**
   Harry Atwater, California Institute of Technology

3) **Metamaterials**
   Costas Soukoulis, Ames Laboratory

4) **Quantum Metamaterials**
   David Awschalom, Argonne National Laboratory

5) **Generation and Remote Distribution of Quantum Entanglement in Solids**
   David Awschalom, Argonne National Laboratory

6) **Light-Matter Quantum Control: Coherence and Dynamics**
   Jiang Wang, Ames Laboratory

7) **Light-Matter Interaction Phenomena using Subwavelength Engineering of Material Properties**
   Igal Brener, Sandia National Laboratories, Albuquerque

8) **Excitons in Low-Dimensional Perovskites**
   William Tisdale, Massachusetts Institute of Technology

9) **A Nonlinear Approach to Weyl Transport**
   Kenneth Burch, Boston College

10) **EPSCOR Hot Carrier Dynamics in Low-Dimensional Systems**
    Ian Sellers, University of Oklahoma

11) **Exploring the Impact of the Local Environment on Charge Transfer States at Molecular Donor-Acceptor Heterojunctions**
    Barry Rand, Princeton University

12) **Exploring the Impact of the Local Environment on Charge Transfer States at Molecular Donor-Acceptor Heterojunctions**
    Noel Giebink, Pennsylvania State University

13) **Rational Design of Hybrid Nanocrystal/Silicone Architectures: From Fundamentals of Energy Transfer to Applications of Energy Sustainability**
Anton Malko, University of Texas, Dallas

14) **Physical Chemistry of Inorganic Nanostructures**
Paul Alivisatos, Lawrence Berkeley National Laboratory

15) **Atom-Defect Hybrid Quantum Systems**
Ania Jayich, University of California, Santa Barbara

16) **Nanostructured Colloidal Self-Assembly and Controlled Alignment of Anisotropic Nanoparticles**
Ivan I. Smalyukh, University of Colorado, Boulder

17) **High-Coherence Multilayer Superconducting Structures for Large Scale Qubit Integration and Photonic Transduction**
Irfan Siddiqi, Lawrence Berkeley National Laboratory

18) **Interfaces in Electronic and Structural Materials**
Yuri Mishin, George Mason University

19) **Bridging Atomistic and Continuum Scales in Phase-Field Modeling of Stressed Polycrystalline Materials with Solid/Liquid Interfacial Defects**
Archana Kamal, University of Massachusetts, Lowell

20) **Probing Coherent States of Light and Matter in Two-Dimensional Semiconductors**
Nathaniel Stern, Northwestern University

21) **Nanocrystal-Based Dyads for Solar to Electric Energy Conversion**
David Waldeck, University of Pittsburgh

22) **Uncovering and Surmounting Loss Mechanisms in Nitride Light Emitters**
Chris Van de Walle, University of California, Santa Barbara

23) **Coupling Electrons, Phonons, and Photons: Efficient Multiphysics Simulation of Nonequilibrium Quantum Transport in Electrically and Optically Excited Semiconductor Nanostructures**
Irena Knezevic, University of Wisconsin, Madison

24) **Microscopic Understanding of Thin Film Growth and Substrate Engineering of Organic Charge Transfer Complexes**
Pengpeng Zhang, Michigan State University

25) **Hybrid Quantum Systems: Spins, Photons and Superconducting Qubits**
Hongxing Tang, Yale University

26) Characterization of Functional Nanomachines
Michael Crommie, Lawrence Berkeley National Laboratory

27) Tunable Excitons and Pseudospins in Transition Metal Dichalcogenide Homobilayers
Elaine Li, University of Texas

28) Electronic Materials Programs
Daryl C. Chrzan, Lawrence Berkeley National Laboratory

29) Electronic Materials Programs
Joel Ager, Lawrence Berkeley National Laboratory

30) Rational Design of Hybrid Nanocrystal/Silicone Architectures: From Fundamentals of Energy Transfer to Applications of Energy Sustainability
Leah Bergman, University of Idaho

Physical Behavior of Materials Principal Investigators' Meeting

POSTER SESSION II

Wednesday, March 20, 2019

1) **Materials, Physics, and Nanostructures for Next Generation Spintronics**
   Chia-Ling Chien, Johns Hopkins University

2) **Phase Transitions in Mesoscopic Systems**
   Raymond Orbach, University of Texas

3) **Study of Materials and Interface Properties for High-Efficiency Spin Injection**
   Jing Shi, University of California, Riverside

4) **Magnon Current Transmission through Insulators**
   Sara Majetich, Carnegie Mellon University

5) **Optical, Electrical and Magnetic Studies of Hybrid Organic-Inorganic Perovskite Semiconductors**
   Valy Vardeny, University of Utah

6) **Spin Transport in Group IV Materials and 2D Membranes**
   Hanan Dery, University of Rochester

7) **Magnetization Dynamics and Cooperative Phenomena in Charge and Spin Frustrated Correlated Electron Materials**
   Hariharan Srikanth, University of South Florida

8) **Coherent Control of Spin-States in Organic Electronics**
   Christoph Boehme, University of Utah

9) **Super Beyond Halogens & Beyond Clusters**
   Puru Jena, Virginia Commonwealth University

10) **Effect of Mechanical Strain and Quantum Electronic Stress on Physical Behavior of Bulk Materials and on Growth Property of Solid Nanomembranes**
    Feng Liu, University of Utah

11) **EARLY CAREER: Probing Coherence in Nanoscale Energy Transport with High Spatial-Temporal Resolution**
    Bolin Liao, University of California, Santa Barbara

12) **Measurement of Near-Field Thermal Radiation Between Flat Surfaces with a Nanogap**
    Zhoumin Zhang, Georgia Tech Research Corp.

13) **Amorphous Structures and Polymorphic Transitions in Metallic Glasses**
Evan Ma, Johns Hopkins University

14) **Extreme Thermoelectric Behavior in Low-Dimensional Oxide Conductors**
Joshua Cohn, University of Miami

15) **Heat Conduction in Nanowire Structures**
Gang Chen, Massachusetts Institute of Technology

16) **Structure-Optical-Thermal Relationships of Carbon Nanotubes**
Stephen Cronin, University of Southern California

17) **Novel Materials for Renewable Energy**
Hongjie Dai, Stanford University

18) **Tuning Anisotropic Bonding via Chemistry and Pressure in Layered Pnictides and Chalcogenides**
Olivier Delaire, Duke University

19) **Probing Local, Hybrid Perovskite Photophysics through Spatially- and Temporally-Resolved Absorption/Emission Microscopy**
Masaru Kuno, University of Notre Dame

20) **Spin Functionality through Complex Oxide Heteroepitaxy**
Yuri Suzuki, Stanford University

21) **Understanding Compound Phase Transitions in New Heusler Alloy Colossal Magnetocaloric Materials**
Shane Stadler, Louisiana State University

22) **Thermodynamic and Kinetic Studies of High Temperature Proton Conductors (HTPC) Using Thin Films and Porous Bodies**
Anil Virkar, University of Utah

23) **Bridging Atomistic and Continuum Scales in Phase-Field Modeling of Solid-Liquid Interface Dynamics and Coalescence**
Alain Karma, Northeastern University

24) **Properties, Electrochemical Activity, and Stability of Solid Oxide Cell Materials under Extreme Conditions**
Scott Barnett, Northwestern University

25) **Electrochemically-Driven Phase Transitions in Battery Storage Compounds**
Yet-Ming Chiang, Massachusetts Institute of Technology

26) **EARLY CAREER: Understanding and Enhancing Rashba Splitting in Doped 2D Organic-Inorganic Halide Perovskites: Towards Efficient Spintronics and IR Photodetectors**
Luisa Whittaker-Brooks, University of Utah

27) **Digital Synthesis: A Pathway to Create and Control Novel States of Condensed Matter**
Anand Bhattacharya, Argonne National Laboratory

Poster Abstracts

Physical Chemistry of Inorganic Halide Perovskite Nanostructures

A. Paul Alivisatos, Department of Chemistry, UC Berkeley; Materials Sciences Division, Lawrence Berkeley National Laboratory

Peidong Yang, Department of Chemistry, UC Berkeley; Materials Sciences Division, Lawrence Berkeley National Laboratory

Stephen R. Leone, Department of Chemistry, UC Berkeley; Materials Sciences Division, Lawrence Berkeley National Laboratory

Eran Rabani, Department of Chemistry, UC Berkeley; Materials Sciences Division, Lawrence Berkeley National Laboratory

David T. Limmer, Department of Chemistry, UC Berkeley; Materials Sciences Division, Lawrence Berkeley National Laboratory

Program Scope

Recently, there has been a renaissance in the semiconducting halide perovskite family, as these materials have now demonstrated promise for a variety of optoelectronic and photonic applications. Particularly, the all-inorganic halide perovskites have seen increased attention, owing to their enhanced stability toward moisture, oxygen, and heat relative to the hybrid organic-inorganic perovskites (e.g. methylammonium lead iodide). The controlled synthesis, detailed structural analysis, optical, and electronic properties are of great fundamental interest. This program currently focuses on the synthesis and theory of inorganic halide perovskites and the characterization of their physical properties to 1) advance synthetic methodology of 0D, 1D, and 2D nanostructures, 2) establish and advance technology and instrumentation to study fundamental nanomaterial properties as well as the physical, chemical, and electronic interactions between them, and 3) apply the extracted knowledge to both develop integrated devices from these nanoscale building blocks and to feed this knowledge back into the virtuous cycle of design, synthesis, measurement and application.

Recent Progress

1. Targeted synthetic discovery of novel ionic halide nanostructures: Semiconducting nanostructures are a fundamental building block for nanoscience, and the continued development and control over the composition, size, and shape of these nanostructures is a central aim of this task. In this program's recent work on the physical chemistry of semiconductor nanostructures, new synthetic reactions were developed for the synthesis of all-inorganic halide perovskite nanomaterials that possess enhanced chemical and physical stability when compared against hybrid organic-inorganic perovskites. Control has been demonstrated over the resulting dimensionality, phase, and composition, thereby enabling the realization of high-quality materials with unique photophysical, electrical, and thermal properties. These new strategies have been employed to synthesize zero-dimensional (0D) halide nanocrystals (1), one-dimensional (1D)

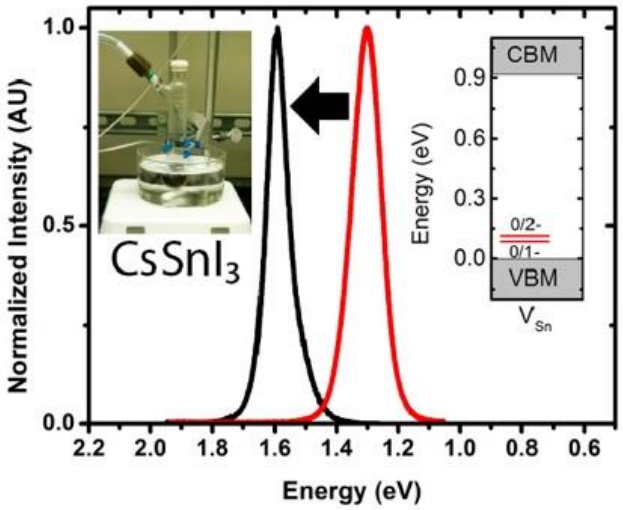

Figure 1. Lead-free, two-dimensional, strongly quantum confined cesium tin iodide nanoplates.

colloidal nanowires (2-4), Ruddlesden-Popper layered perovskite materials (5), and lead-free perovskite 0D nanocrystals and two-dimensional (2D) nanoplates (6,7).

Well known in oxide perovskites, the Ruddlesden-Popper (RP) layered structure is related to many interesting properties such as superconductivity and ferroelectricity. The direct observation of unusual atomic structure in two-dimensional $CsPbBr_3$ nanosheets was suggested to arise from the RP phase based on model simulations. Structural details of the plausible RP domains and domain boundaries between the RP and conventional perovskite phases have been revealed on the atomic level using aberration-corrected scanning transmission electron microscopy. These findings open the door to future inorganic halide RP phase synthesis and theoretical modeling.

Investigations into the underlying photophysics of cesium lead halide perovskite materials can also be combined with novel syntheses to design lead-free nanostructures with desirable optical properties. As such, 0D double perovskite nanocrystals with $Cs_2AgBiBr_6$, $Cs_2AgBiCl_6$, $Cs_2AgSbCl_6$, and $Cs_2AgInCl_6$ compositions and strongly confined 2D cesium tin iodide nanoplates (Figure 1) were synthesized and characterized for the first time (6,7). These novel syntheses will aid in the development of highly luminescent, lead-free ionic halide semiconductors.

2. <u>Molecular-level understanding of photoluminescence efficiency in perovskite nanocrystals</u>: With a high degree of synthetic control established for cesium lead halide perovskite nanomaterials, this program developed several complementary routes with which to access materials with exceptionally high luminescence efficiencies. As-synthesized colloidal samples typically exhibit high but non-unity photoluminescence quantum yield (PLQY) values, indicating that additional passivation and/or chemical modification is needed. Softer Lewis bases were demonstrated to effectively substitute into point defects in the form of surface halide vacancies, thereby passivating under-coordinated lead atoms just below the surface and healing the

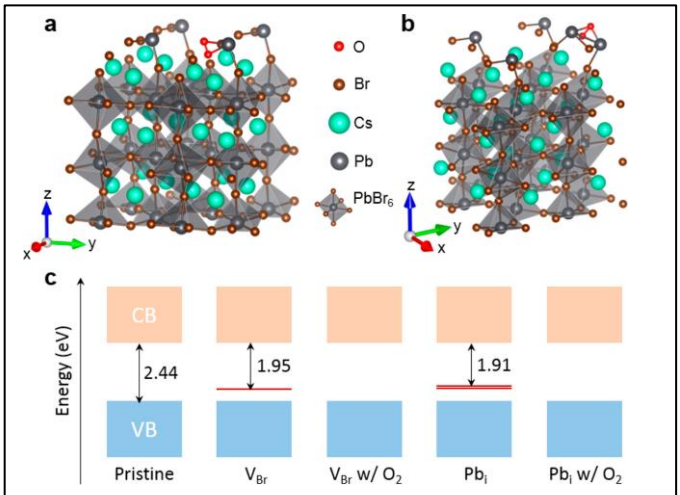

Figure 2. A collaborative experimental and theoretical study found that oxygen gas can bind under-coordinated surface lead atoms, significantly improving luminescence efficiency.

defective organic-inorganic interface (8). Alternatively, post-synthetic treatment with thiocyanate salts promotes a layer-by-layer chemical etching of the defective surface, thereby revealing the pristine layer below (9). Both passivation and etching allow the preparation of essentially trap-free nanocrystals with PLQY values that are within measurement error of unity. In a non-colloidal regime, nanowires prepared by chemical vapor transport display extremely low PLQY values of <0.02%, indicating a high concentration of deep trap states. A collaborative experimental and theoretical effort found that molecular oxygen can significantly increase PLQY to ~13%, with ab initio calculations (Figure 2) reinforcing that surface lead atoms are the predominant source of charge trapping (10). Together, these results provide a clear picture of the importance of controlling the coordination environment of lead atoms, thereby providing a rational framework for improving photonic and optoelectronic devices based on halide perovskite materials.

3. Understanding and exploiting the highly dynamic perovskite lattice: The predominantly ionic bonding character of lead halide perovskites results in highly dynamic crystal lattices, inherently allowing rapid ion exchange at solid-vapor and solid-liquid interfaces. Knowledge of anion exchange reactions was leveraged together with nanofabrication techniques to demonstrate spatially resolved multi-color emission in a single nanowire (Figure 3), and also combined with multiscale theoretical modeling to investigate halide anion interdiffusion in $CsPbCl_3$–$CsPbBr_3$ single crystalline nanowire heterojunctions (11,12). Molecular simulations determined low energetic barriers for halide vacancy formation as well as vacancy hopping, highlighting the role of the fluxional ionic lattice in facilitating anion exchange and diffusion.

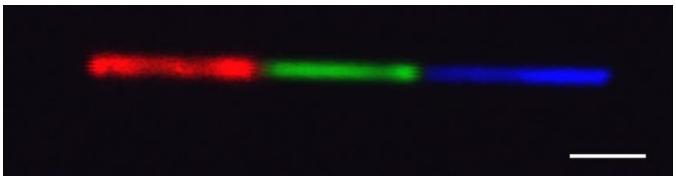

Figure 3. Confocal photoluminescence mapping of a three-color single nanowire heterojunction. Scale bar represents 3 μm.

In addition to facile ion exchange chemistry, rich structural phase transitions in halide perovskites can serve as post-synthetic handles for the fabrication of new heterostructures. A thermochromic solar cell for smart photovoltaic window applications was demonstrated by leveraging a thermally-driven, moisture-mediated reversible transition between a transparent non-perovskite phase (82% visible transparency) with low power output and a deeply colored perovskite phase (35% visible transparency) with high power output (13). Additionally, p-n junction formation was demonstrated in a single-crystalline halide perovskite $CsSnI_3$ nanowire by utilizing a localized, thermally driven phase transition from a double-chain yellow phase to an orthorhombic black phase (14). The formation energies of cation and anion vacancies in these two phases differ significantly, which leads to n- and p-type electrical characteristics for the double-chain and orthorhombic phases, respectively. Both the formation and directional propagation of the interface were directly observed with cathodoluminescence microscopy; in the future, this will give rise to powerful fundamental insights into solid-state phase transition dynamics, which can be connected to the resulting optical and electronic properties of the nanoscale interfaces.

Future Plans

In the future, we plan to pursue new colloidal and solid-state chemical syntheses that can target increasingly complex and advanced inorganic ionic halide semiconducting nanostructures. Highly luminescent, lead-free ionic building blocks are of particular interest, as is the development of a machine learning-assisted synthetic protocol. Nanoscale microscopy tools that were developed in the previous studies open the door to powerful insights into the fundamental nature of solid-state phase transitions, which can then be further leveraged for the synthesis of complex nanomaterials with desirable photophysical properties. This knowledge can also serve as a platform for adaptive photonics, where fluorophores respond to external stimuli.

Synthetic efforts in this area will continue to be guided by spectroscopic and computational findings from within the program. For example, transient extreme ultraviolet (XUV) spectroscopy measurements of lead halide perovskite nanocrystals are underway, as is the development of a semi-empirical pseudopotential for the same material systems.

References

1. Z Liu, Y Bekenstein, X Ye, SC Nguyen, J Swabeck, D Zhang, S-T Lee, **P Yang**, W Ma, **AP Alivisatos**. *J. Am. Chem. Soc.* 2017, 139, 5309-5312.
2. D Zhang, Y Yu, Y Bekenstein, AB Wong, **AP Alivisatos**, **P Yang**. *J. Am. Chem. Soc.* 2016, 138, 13155-13158.
3. M Lai, Q Kong, CG Bischak, Y Yu, L Dou, SW Eaton, NS Ginsberg, **P Yang**. *Nano Res.* 2017, 10, 1107-1114.
4. T Lei, M Lai, Q Kong, D Lu, W Lee, L Dou, V Wu, Y Yu, **P Yang**. *Nano Lett.* 2018, 18, 3538-3542.
5. Y Yu, D Zhang, **P Yang**. *Nano Lett.* 2017, 17, 5489-5494.
6. Y Bekenstein, JC Dahl, J Huang, WT Osowiecki, JK Swabeck, EM Chan, **P Yang, AP Alivisatos**. *Nano Lett*. 2018, 18, 3502-3508.
7. AB Wong, Y Bekenstein, J Kang, CS Kley, D Kim, NA Gibson, D Zhang, Y Yu, **SR Leone**, LW Wang, **AP Alivisatos, P Yang**. *Nano Lett.* 2018, 18, 2060-2066.
8. DP Nenon, K Pressler, J Kang, BA Koscher, JH Olshansky, WT Osowiecki, MA Koc, LW Wang, **AP Alivisatos**. *J. Am. Chem. Soc.* 2018, 140, 17660-17772.
9. BA Koscher, JK Swabeck, ND Bronstein, **AP Alivisatos**. *J. Am. Chem. Soc.* 2017, 139, 6566-6569.
10. D Lu, Y Zhang, M Lai, A Lee, C Xie, J Lin, T Lei, Z Lin, CS Kley, J Huang, **E Rabani**, **P Yang**. *Nano Lett.* 2018 18, 6967-6973.
11. L Dou, M Lai, CS Kley, Y Yang, CG Bischak, D Zhang, SW Eaton, NS Ginsberg, **P Yang**. *Proc. Natl. Acad. Sci.* 2017, 114, 7216-7221.
12. M Lai, A Obliger, D Lu, CS Kley, CG Bischak, Q Kong, T Lei, L Dou, NS Ginsberg, **DT Limmer**, **P Yang**. *Proc. Nat. Acad. Sci.* 2018, 115 (47), 11929-11934.
13. J Lin, M Lai, L Dou, CS Kley, H Chen, F Peng, J Sun, D Lu, SA Hawks, C Xie, F Cui, **AP Alivisatos, DT Limmer, P Yang**. Nat Mater. 2018, 17, 261-267.
14. Q Kong, W Lee, M Lai, CG Bischak, G Gao, AB Wong, T Lei, Y Yu, LW Wang, NS Ginsberg, **P Yang**. *Proc. Nat. Acad. Sci.* 2018, 115, 8889-8894.

Publications

A. Publications primarily funded and intellectually led by this FWP

1. D Zhang, Y Yu, Y Bekenstein, AB Wong, **AP Alivisatos** and **P Yang**. "Ultrathin Colloidal Cesium Lead Halide Perovskite Nanowires," *J. Am. Chem. Soc.* 138 (40), pp 13155–13158 (2016).
2. N Kornienko, KK Sakimoto, DM Herlihy, SC Nguyen, **AP Alivisatos**, CB Harris, A Schwartzberg, and **P Yang**. "Spectroscopic elucidation of energy transfer in hybrid inorganic-biological organisms for solar-to-chemical production," *Proc. Natl. Acad. Sci. U.S.A.* 113 (42), pp 11750–11755 (2016).
3. M Lai, Q Kong, CG Bischak, Y Yu, L Dou, SW Eaton, NS Ginsberg, and **P Yang**. "Structural, optical, and electrical properties of phase-controlled cesium lead iodide nanowires," *Nano Res.* 10 (4), pp 1107-1114 (2017).
4. L Dou, M Lai, CS Kley, Y Yang, CG Bischak, D Zhang, SW Eaton, NS Ginsberg, and **P Yang**. "Spatially Resolved Multi-Color $CsPbX_3$ Nanowire Heterojunctions via Anion Exchange," *Proc. Natl. Acad. Sci. U.S.A.* 114 (28), pp 7216-7221 (2017).
5. SN Raja, Y Bekenstein, MA Koc, S Fischer, D Zhang, L Lin, RO Ritchie, **P Yang**, and **AP Alivisatos**. "Polymer Encapsulation of Perovskite Nanocrystals: Enhanced Water and Light Stability and Polarization," *ACS Appl. Mater. Interfaces* 8 (51), pp 35523–35533 (2016).
6. Y Yu, D Zhang, C Kisielowski, L Dou, N Kornienko, Y Bekenstein, AB Wong, **AP Alivisatos**, and **P Yang**. "Atomic Resolution Imaging of Halide Perovskites," *Nano Lett.* 16 (12), pp 7530–7535 (2016).
7. YJ Bae, NA Gibson, TX Ding, **AP Alivisatos**, and **SR Leone**. "Understanding the Bias Introduced in Quantum Dot Blinking Using Change Point Analysis," *J. Phys. Chem. C* 120 (51), pp 29484–29490 (2016).
8. AD Balan, H Eshet, JH Olshansky, YV Lee, **E Rabani**, and **AP Alivisatos**. "Effect of Thermal Fluctuations on the Radiative Rate in Core/Shell Quantum Dots," *Nano Lett.* 17 (3), pp 1629–1636 (2017).
9. Z Liu, Y Bekenstein, X Ye, SC Nguyen, J Swabeck, D Zhang, S-T Lee, **P Yang**, W Ma, and **AP Alivisatos**. "Ligand Mediated Transformation of Cesium Lead Bromide Perovskite Nanocrystals to Lead Depleted Cs_4PbBr_6 Nanocrystals," *J. Am. Chem. Soc.* 139 (15), pp 5309–5312 (2017).
10. BA Koscher, JK Swabeck, ND Bronstein, and **AP Alivisatos**. "Essentially Trap-Free $CsPbBr_3$ Colloidal Nanocrystals by Postsynthetic Thiocyanate Surface Treatment," *J. Am. Chem. Soc.* 139 (19), pp 6566–6569 (2017).
11. LM Carneiro, SK Cushing, C Liu, Y Su, **P Yang**, **AP Alivisatos**, and **SR Leone**. "Excitation-wavelength-dependent small polaron trapping of photoexcited carriers in α-Fe_2O_3," *Nat. Mater.* 16, pp 819–825 (2017).
12. JH Olshansky, AD Balan, TX Ding, X Fu, YV Lee, and **AP Alivisatos**. "Temperature-Dependent Hole Transfer from Photoexcited Quantum Dots to Molecular Species: Evidence for Trap-Mediated Transfer," *ACS Nano* 11 (8), pp 8346–8355 (2017).

13. W. Lee, H Li, AB Wong, D Zhang, M Lai, Y Yu, Q Kong, E Lin, JJ Urban, JC Grossman, and **P Yang**. "Ultralow thermal conductivity in all-inorganic halide perovskites," *Proc. Natl. Acad. Sci. U.S.A.* 114 (33), pp 8693-8697 (2017).

14. Y Yu, D Zhang, and **P Yang**. "Ruddlesden-Popper Phase in Two-dimensional Inorganic Halide Perovskites: A Plausible Model and the Supporting Observations," *Nano Lett.* 17(9) 5489 (2017)

15. J Lin, M Lai, L Dou, CS Kley, H Chen, F Peng, J Sun, D Lu, SA Hawks, C Xie, F Cui, **AP Alivisatos, Limmer DT, P Yang**. Thermochromic halide perovskite solar cells. Nat Mater. 2018 Mar;17(3):261-267. DOI: 10.1038/s41563-017-0006-0.

16. JC Ondry, MR Hauwiller, **AP Alivisatos**. Dynamics and Removal Pathway of Edge Dislocations in Imperfectly Attached PbTe Nanocrystal Pairs: Toward Design Rules for Oriented Attachment. ACS Nano. 2018 Feb 26. DOI: 10.1021/acsnano.8b00638.

17. AB Wong, Y Bekenstein, J Kang, CS Kley, D Kim, NA Gibson, D Zhang, Y Yu, **SR Leone**, LW Wang, **AP Alivisatos, P Yang**. Strongly quantum confined colloidal cesium tin iodide perovskite nanoplates: lessons for reducing defect density and improving stability. *Nano Lett.* 2018 Mar. DOI: 10.1021/acs.nanolett.8b00077.

18. Y Bekenstein, JC Dahl, J Huang, WT Osowiecki, JK Swabeck, EM Chan, **P Yang, AP Alivisatos**. The Making and Breaking of Lead-Free Double Perovskite Nanocrystals of Cesium Silver-Bismuth Halide Compositions. *Nano Lett*. 2018 Jun 13;18(6):3502-3508. DOI: 10.1021/acs.nanolett.8b00560.

19. Q Kong, W Lee, M Lai, CG Bischak, G Gao, AB Wong, T Lei, Y Yu, LW Wang, NS Ginsberg and **P Yang**. Phase transition induced p-n junction in single halide perovskite nanowire. *Proceedings of National Academy of Sciences***,** Aug 2018, 201806515; DOI 10.1073/pnas.1806515115

20. NA Gibson, BA Koscher, **AP Alivisatos** and **SR Leone**. Excitation Intensity Dependence of Photoluminescence Blinking in $CsPbBr_3$ Perovskite Nanocrystals. The *Journal of Physical Chemistry C* 2018 122 (22), 12106-12113. DOI: 10.1021/acs.jpcc.8b03206.

21. IJ Porter, SK Cushing, LM Carneiro, AL, JC Ondry, JC Dahl, HT Chang, **AP Alivisatos** and **SR Leone**. Photoexcited Small Polaron Formation in Goethite (α-FeOOH) Nanorods Probed by Transient Extreme Ultraviolet Spectroscopy. *The Journal of Physical Chemistry Letters* 2018 9 (14), 4120-4124. DOI: 10.1021/acs.jpclett.8b01525

22. T Lei, M Lai, Q Kong, D Lu, W Lee, L Dou, V Wu, Y Yu, and **P Yang**. Electrical and Optical Tunability in All-Inorganic Halide Perovskite Alloy Nanowires. *Nano Lett.* 2018 18, 3538-3542. DOI: 10.1021/acs.nanolett.8b00603

23. SK Cushing, M Zurch, PM Kraus, LM Carneiro, A Lee, HT Chang, CJ Kaplan, and **SR Leone**. Hot phonon and carrier relaxation in Si(100) determined by transient extreme ultraviolet spectroscopy. *Struct. Dyn.* 2018 5, 054302. DOI: 10.1063/1.5038015

24. D Lu, Y Zhang, M Lai, A Lee, C Xie, J Lin, T Lei, Z Lin, CS Kley, J Huang, **E Rabani**, and **P Yang**. Giant Light-Emission Enhancement in Lead Halide Perovskites by Surface Oxygen Passivation. *Nano Lett.* 2018 18, 6967-6973.

25. M Lai, A Obliger, D Lu, CS Kley, CG Bischak, Q Kong, T Lei, L Dou, NS Ginsberg, **DT Limmer**, and **P Yang**. Intrinsic anion diffusivity in lead halide perovskites is facilitated by a soft lattice. *Proc. Nat. Acad. Sci.* 2018, 115 (47), 11929-11934.
26. L Kidon, H Wang, M Thoss, and **E Rabani**. On the memory kernel and the reduced system propagator. *J. Chem. Phys.* 2018 149, 104105. DOI: 10.1063/1.5047446
27. DP Nenon, K Pressler, J Kang, BA Koscher, JH Olshansky, WT Osowiecki, MA Koc, LW Wang, and **AP Alivisatos**. Design Principles for Trap-Free $CsPbX_3$ Nanocrystals: Enumerating and Eliminating Surface Halide Vacancies with Softer Lewis Bases. *J. Am. Chem. Soc.* 2018 140 (50), 17660-17772.
28. SK Cushing, A Lee, IJ Porter, LM Carneiro, HT Chang, M Zuerch, and **SR Leone**. Differentiating Photoexcited Carrier and Phonon Dynamics in the Δ, L, and Γ Valleys of Si(100) with Transient Extreme Ultraviolet Spectroscopy. *J. Phys. Chem. C* 2019, DOI: 10.1021/acs.jpcc.8b10887

B. Collaborative publications

1. I Hadar, JP Philbin, YE Panfil, S Neishdtadt, I Liberman, H Eshet, S Lazar, **E Rabani** and U Banin. "Semiconductor Seeded Nanorods with Graded Composition Exhibiting High Quantum-Yield, High Polarization, and Minimal Blinking," *Nano Lett.* 17, pp 2524-2531 (2017).
2. E Arnon, **E Rabani**, D Neuhauser, and R Baer. "Equilibrium Configurations of Large Nanostructures Using Embedded-Fragment Stochastic Density Functional Theory," *J. Chem. Phys.* 146, 224111 (2017).
3. M Park, N Kornienko, SE Reyes-Lillo, M Lai, JB Neaton, **P Yang**, and RA Mathies. "Critical Role of Methylammonium Librational Motion in Methylammonium Lead Iodide ($CH_3NH_3PbI_3$) Perovskite Photochemistry," *Nano Lett.* 17 (7), 4151−4157 (2017).
4. DM Monahan, L Guo, J Lin, L Dou, **P Yang** and GR Fleming. "Room-Temperature Coherent Optical Phonon in 2D Electronic Spectra of $CH_3NH_3PbI_3$ Perovskite as a Possible Cooling Bottleneck," *J. Phys. Chem. Lett.* 8 (14), 3211−3215 (2017).
5. A.-Y. Lu, H. Zhu, J. Xiao, C.-P. Chuu, Y. Han, M.-H. Chiu, C.-C. Cheng, C.-W. Yang, K.-H. Wei, Y. Yang, Y. Wang, D. Sokaras, D. Nordlund, P. Yang, D. A. Muller, M.-Y. Chou, X. Zhang, L.-J. Li, "Janus monolayers of transition metal dichalcogenides." Nature Nanotechnology 12, 744–749 (2017).
6. P Kraus, M Zurch, SK Susching, DM Neumark and **SR Leone**. The ultrafast X-ray spectroscopic revolution in chemical dynamics. Nature Reviews Chemistry 2, 82-94 (2018. DOI:10.1038/s41570-018-0008-8.
7. CZ Ning, L Dou and **P Yang.** Bandgap engineering in semiconductor alloy nanomaterials with widely tunable bandgaps and compositions. *Nature Reviews Materials*, 2, 1–15 (2017). DOI: 10.1038/natrevmats.2017.70
8. DL McCaffrey, SC Nguyen, SJ Cox, H Weller, **AP Alivisatos**, PL Geissler and RJ Saykally. Mechanism of ion adsorption to aqueous interfaces: Graphene/water vs. air/water. *Proc Natl Acad Sci* U S A. 2017 Dec 19;114(51):13369-13373. DOI:10.1073/pnas.1702760114.
9. Aubrey ML, Wiers BM, Andrews SC, Sakurai T, Reyes-Lillo SE, Hamed SM, Yu CJ, Darago LE, Mason JA, Baeg JO, Grandjean F, Long GJ, Seki S, Neaton JB, **Yang P** and

Long JR. Electron delocalization and charge mobility as a function of reduction in a metal-organic framework. *Nat Mater*. 2018 Jul;17(7):625-632. DOI: 10.1038/s41563-018-0098-1

10. M Park, AJ Neukirch, SE Reyes-Lillo, M Lai, SR Ellis, D Dietze, JB Neaton, **P Yang**, S Tretiak, RA Mathies. Excited-state vibrational dynamics toward the polaron in methylammonium lead iodide perovskite. *Nat Commun*. 2018 Jun 28;9(1):2525. DOI: 10.1038/s41467-018-04946-7.

11. CG Bischak, AB Wong, E Lin, DT Limmer, **P Yang** and NS Ginsberg. Tunable Polaron Distortions Control the Extent of Halide Demixing in Lead Halide Perovskites. *J Phys Chem Lett*. 2018 Jul 19;9(14):3998-4005. DOI: 10.1021/acs.jpclett.8b01512.

Plasmon and Photon Excitations in Two-Dimensional and Layered Materials

Harry A. Atwater, California Institute of Technology, Pasadena, CA 91125

Program Scope

Study of light-matter interactions in layered and two-dimensional materials represents a method to both achieve extreme optical confinement, approaching the atomic scale, and also a tool for observing and exploring new materials phenomena. Layered narrow bandgap and zero bandgap materials such as black phosphorus, graphene and layered chalcogenides support unusual and intriguing quantum-confined electronic states in thin layers and topological surface electronic states. Our research project seeks to understand the nature of localized and propagating plasmons and phonon polaritons in black phosphorus, graphene and surface states of topological insulators as well quantum confinement effects on electronic structure, transport and light emission in these materials.

Recent Progress

Quantum-confined states and tunable dichroism in black phosphorus

The incorporation of electrically tunable materials into photonic structures enables dynamic, electrical control of light propagation at the nanoscale. Few-layer black phosphorus is a promising material in this context due to its in-plane anisotropic, quantum well band structure, with a direct band gap that can be tuned from 0.3 to 2 eV with a number of layers and subbands that manifest as additional optical transitions across a wide range of energies. We performed an experimental investigation of three different, anisotropic electro-optic mechanisms that allow electrical control of the complex refractive index in few-layer black phosphorus from the mid-infrared to the visible: Pauli-blocking of

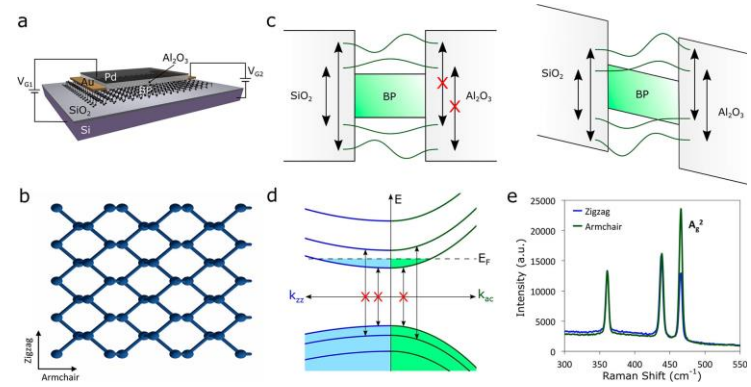

Figure 1. Anisotropic electro-optical effects in few-layer BP. (a) Schematic figure of infrared tunability devices. Few-layer BP is mechanically exfoliated on SiO_2/Si and then capped Al_2O_3. A semitransparent top contact of Pd is used to apply a field (V_{G1}) while the device floats and Ni/ Au contacts are used to gate (V_{G2}) the contacted heterostructure. (b) Crystal structure of BP with armchair (AC) and zigzag (ZZ) axes. (c) Illustration of: the quantum-confined Stark effect and symmetry-breaking modification of quantum well selection rules. The quantum-confined Stark effect causes a red-shifting of the intersubband transition energies. Modification of selection rules breaks the symmetry and orthogonality of the quantum well wave functions, allowing forbidden transitions to occur (e.g., from v_1 to c_2,). (d) Illustration of anisotropic Pauli-blocking (Burstein–Moss effect) in BP. Intersubband transitions are blocked due to the filling of the conduction band. Along the ZZ axis, all optical transitions are disallowed regardless of carrier concentration. (e) Raman spectra with excitation laser polarized along AC and ZZ axes. The intensity ratio between the A_g^2 peak and the A_g^1 peak is used to identify crystal axes.

intersubband optical transitions (the Burstein−Moss effect); the quantum-confined Stark effect; and the modification of quantum well selection rules by a symmetry-breaking, applied electric field. These effects generate near-unity tuning of the BP oscillator strength for some material thicknesses and photon energies, along a single in-plane crystal axis, transforming absorption from highly anisotropic to nearly isotropic. Lastly, the anisotropy of these electro-optical phenomena results in dynamic control of linear dichroism and birefringence, a promising concept for active control of the complex polarization state of light, or propagation direction of surface waves.

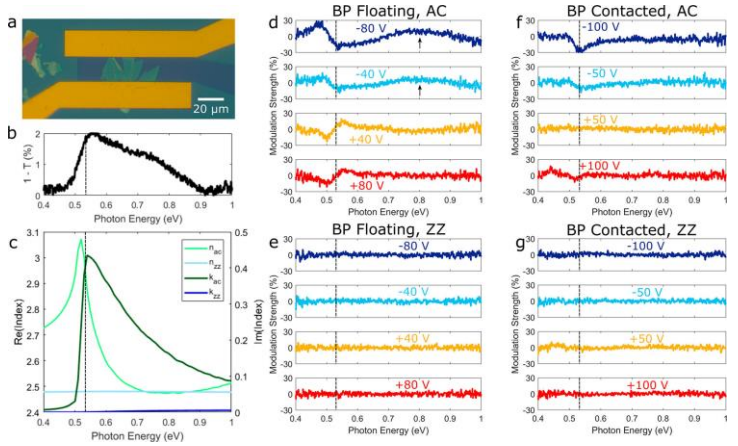

Figure 2. Electrically tunable linear dichroism: quantum-confined Stark and Burstein−Moss effects and forbidden transitions. (a) Optical image of a fabricated sample with two Au contact pads for direct electrical contact to the BP and a semitransparent Pd top contact between them, separated from the BP by a thin layer of Al_2O_3. (b) Zero-bias infrared extinction of 3.5 nm flake, polarized along the armchair (AC) axis. (c) Calculated index of refraction for 3.5 nm thick BP with a Fermi energy at the midgap. (d) Tunability of BP oscillator strength with a field applied to the floating device, for light polarized along the AC axis. (e) Corresponding tunability for light polarized along the zigzag (ZZ) axis. (f) Tunability of BP oscillator strength with gating of the contacted device, for light polarized along the AC axis. (g) Corresponding tunability for light polarized along the ZZ axis.

In order to probe and distinguish the electro-optical tuning mechanisms evident in few-layer BP, we use a combination of gating schemes wherein the BP either floats electrically in an applied field or is contacted, as shown in Figure 1a. We note that the samples are exfoliated on an oxide surface and encapsulated in Al_2O_3; therefore, while strain effects are known to influence the band gap of 2D materials,[1-3] including few-layer BP, these are identical for all measurements. Polarization-dependent optical measurements are taken aligned to the crystal axes, in order to probe the structural anisotropy shown in Figure 1b. This enables us to isolate the contribution of charge-carrier density effects, i.e., a Burstein−Moss shift, and external field effects, i.e., the quantum-confined Stark effect and control of forbidden transitions in the infrared, to the tunability of linear dichroism, qualitatively illustrated in Figure 1c,d.[4-7] In the anisotropic Burstein−Moss (BM) shift, the optical band gap of the material is changed as a result of band- filling and the consequent Pauli-blocking of intersubband transitions. As the carrier concentration of the sample is changed, the Fermi level moves into (out of) the conduction or valence band, resulting in a decrease (increase) of absorptivity due to the disallowing (allowing) of optical transitions. Because intersubband optical transitions are only allowed along the armchair axis of BP, this tunability occurs only for light polarized along this axis. In the quantum-confined Stark Effect, the presence of a strong electric field results in the leaking of electron and hole wave functions into the band gap as Airy functions, red-shifting the intersubband transitions energies.

To illustrate the mechanisms of tunable dichroism of BP in the mid-infrared, we measure tunability of transmittance using Fourier-transform infrared (FTIR) microscopy as a function of externally (V_{G1}) or directly applied bias (V_{G2}), presented for a 3.5 nm thick flake, as determined from atomic force microscopy, in Figure 2. Figure 2b presents the raw extinction of the flake along the armchair axis at zero bias, obtained by normalizing the armchair axis 271 extinction to that of the optically inactive zigzag axis. A band edge of approximately 0.53 eV is measured, consistent with a thickness of 3.5 nm. A broad, weak shoulder feature is observed at approximately 0.75 eV. The corresponding calculated optical constants for the flake are presented in Figure 2c for comparison. A Kubo formula approach is used for this calculation.

Electronically-tunable perfect absorption in graphene

Graphene has been the subject of intensive research as a promising candidate for tunable amplitude and phase modulation of THz and mid-infrared light. Despite these exciting predictions and attractive features of tunable graphene nanostructures, a major obstacle for realizing perfect absorption in graphene has been the low carrier mobility in processed graphene samples[8] as compared with the high carrier mobilities achievable in pristine or passivated and unpatterned graphene sheets,(25, 26) which have been assumed in theoretical works predicting unity absorption. The low graphene carrier mobility gives rise to a high nonradiative damping rate, which tends to under-couple the resonant modes of graphene nanoresonator arrays.(32) Since large-area high-performance functional graphene structures cannot rely on the high carrier mobility of exfoliated graphene flakes, achieving this performance level with graphene synthesized by chemical vapor deposition—with its attendant lower carrier mobility—is important.

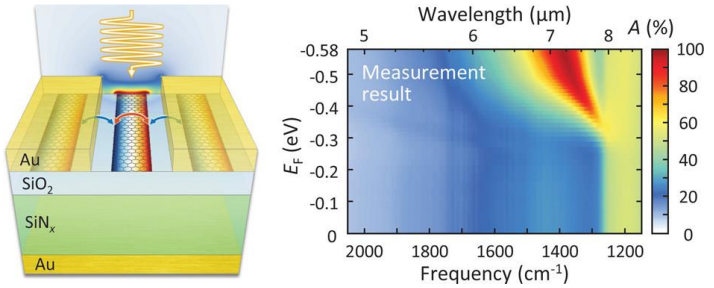

Figure 3. At left a schematic of the graphene nanoribbon structures coupled to noble metal plasmonic resonators; surface plasmons excited on the Au surface are funneled into the slit where the electromagnetic energy is strongly coupled to a single graphene ribbon, whose permittivity is tunable under gate control of the Fermi level, enable tunable perfect absorption, as illustrated at right in the infrared absorption spectra as a function of graphene Fermi level. The peak absorption at 1350 cm^{-1} reaches 97%.

We have experimentally demonstrated electronically tunable perfect absorption in graphene through graphene plasmonic nanostructures that exhibit dramatically higher resonant absorption, made possible by tailored nanophotonic designs that leverage the atomic thinness of graphene and the extreme confinement of graphene plasmons. First, we utilize lower-permittivity substrates, which allow better wavevector matching between free-space photons and graphene plasmons, to improve radiative coupling to graphene plasmonic ribbons (GPRs). Second, we combine the GPRs with noble metal plasmonic metallic antennas as sub-wavelength-scale intermediaries ($\sim\lambda_0/10$, λ_0: free-space wavelength) to further enhance radiative coupling to deep sub-wavelength-scale GPRs ($<\lambda_0/70$). Unlike other perfect absorbers solely relying on noble metal

plasmonic effects, our structures create perfect absorption in the graphene itself by utilizing graphene plasmonic resonances, providing an approach for tunable strong light–matter interactions. Notably, tunable perfect absorption is achieved with graphene nanoresonators covering less than 10% of the surface area, whereas an unpatterned graphene sheet covering 100% of the surface area exhibits low single-pass absorption (~2.3%).

Future Plans

The decay dynamics of excited carriers in graphene have attracted wide attention, as the gapless Dirac electronic band structure opens up relaxation channels that are not allowed in conventional materials. We are investigating mid-infrared emission in graphene originating from a previously unobserved decay channel: hot plasmons generated from optically excited carriers. In early work, we find a plasmon spectral flux that exceeds the blackbody emission flux by several orders of magnitude, and the observed Fermi-level dependence apparently rules out a Planckian light emission mechanism. Calculations for our experimental conditions indicate that a state of carrier inversion and plasmon gain may exist on the sub-100fs time scale, and that stimulated plasmon emission dominates spontaneous plasmon emission on this timescale, while the population inversion is lost at longer times, where spontaneous plasmon emission dominates stimulated emission. These observations have motivated an effort to explore mid-infrared stimulated and spontaneous emission processes.

References

1. Rodin, A. S.; Carvalho, A.; Castro Neto, A. H. Strain-Induced Gap Modification in Black Phosphorus. Phys. Rev. Lett. 2014, 112, 176801.
2. Wang, X.; Tian, H.; Xie, W.; Shu, Y.; Mi, W.-T.; Ali Mohammad, M.; Xie, Q.-Y.; Yang, Y.; Xu, J.-B.; Ren, T.-L. Observation of a Giant Two-Dimensional Band-Piezoelectric Effect on Biaxial-Strained Graphene. NPG Asia Mater. 2015, 7, No. e154.
3. Xu, K.; Wang, K.; Zhao, W.; Bao, W.; Liu, E.; Ren, Y.; Wang, M.; Fu, Y.; Zeng, J.; Li, Z.; et al. The Positive Piezoconductive Effect in Graphene. Nat. Commun. 2015, 6, 8119.
4. (35) Whitney, W. S.; Sherrott, M. C.; Jariwala, D.; Lin, W.-H.; Bechtel, H. A.; Rossman, G. R.; Atwater, H. A. Field Effect Optoelectronic Modulation of Quantum-Confined Carriers in Black Phosphorus. Nano Lett. 2017, 17, 78−84.
5. (36) Low, T.; Rodin, A. S.; Carvalho, A.; Jiang, Y.; Wang, H.; Xia, F.; Castro Neto, A. H. Tunable Optical Properties of Multilayer Black Phosphorus Thin Films. Phys. Rev. B: Condens. Matter Mater. Phys. 2014, 90, No. 075434.
6. (37) Lin, C.; Grassi, R.; Low, T.; Helmy, A. S. Multilayer Black Phosphorus as a Versatile Mid-Infrared Electro-Optic Material. Nano Lett. 2016, 16, 1683−1689.
7. (38) Deng, B.; Tran, V.; Xie, Y.; Jiang, H.; Li, C.; Guo, Q.; Wang, X.; Tian, H.; Koester, S. J.; Wang, H.; et al. Efficient Electrical Control of Thin-Film Black Phosphorus Bandgap. Nat. Commun. 2017, 8, 14474.
8. Pirkle, A.; Chan, J.; Venugopal, A.; Hinojos, D.; Magnuson, C. W.; McDonnell, S.; Colombo, L.; Vogel, E. M.; Ruoff, R. S.; Wallace, R. M. Appl. Phys. Lett. 2011, 99, 122108.

Publications

1. **"***Mimicking surface polaritons for unpolarized light with high-permittivity materials***",** G.T. Papadakis, A.R. Davoyan, P. Yeh and H.A. Atwater**, Physical Review Materials 3,** Art. Number: 015202 (2019).
2. *"Anisotropic Quantum Well Electro-Optics in Few-Layer Black Phosphorus"*, M.C. Sherrott, W.S. Whitney, D. Jariwala, S. Biswas, C.M. Went, J. Wong, G. R. Rossman and H.A. Atwater, **Nano Letters, 1,** pp. 269-276 (2019).
3. *"Electronically Tunable Perfect Absorption in Graphene"*, S. Kim, M.S. Jang, V.W. Brar, K.W. Mauser, L. Kim, and H.A. Atwater, **Nano Letters, 2**, pp. 971-979 (2018)
4. *"Optical magnetism in planar metamaterial heterostructures"*, G.T. Papadakis, D. Fleischman, A.R. Davoyan, P. Yeh and H.A. Atwater, **Nature Communications, 9**, Art. Number 296 (2018).
5. *"Dynamically controlled Purcell enhancement of visible spontaneous emission in a gated plasmonic heterostructure",* Y.J. Lu, R. Sokhoyan, W. Cheng, G.K. Shirmanesh, A.R. Davoyan, R.A. Pala, K. Thyagarajan, and H.A. Atwater**, Nature Communications, 8**, Art. Number 1631 (2017).
6. *"Millivolt Modulation of Plasmonic Metasurface Optical Response via Ionic Conductance",* K. Thyagarajan, R. Sokhoyan, L. Zornberg, and H.A. Atwater, Advanced Materials, 29, Art. Number 1701044 (2017).
7. *"Resonant thermoelectric nanophotonics",* K.W. Mauser, S. Kim, S. Mitrovic, D. Fleischman, R.A. Pala, K.C. Schwab and H.A. Atwater, **Nature Nanotechnology, 12**, p. 770 (2017).
8. *"Atomic-Scale Structural and Chemical Characterization of Hexagonal Boron Nitride Layers Synthesized at the Wafer-Scale with Monolayer Thickness Control",* W.H. Lin, V.W. Brar, D. Jariwala, M.C. Sherrott, W.S. Tseng, C-I Wu, N.C. Yeh, and H.A. Atwater, Chemistry of Materials, 29, pp. 4700-4707 (2017).
9. *"Experimental Demonstration of > 230 degrees Phase Modulation in Gate-Tunable Graphene-Gold Reconfigurable Mid-Infrared Metasurfaces",* M.C. Sherrott, P.W.C. Hon, K.T. Fountaine, J.C. Garcia, S.M. Ponti, V.W. Brar, L.A. Sweatlock and H.A. Atwater, Nano Letters, 17, pp. 3027-3034 (2017).
10. *"Field Effect Optoelectronic Modulation of Quantum-Confined Carriers in Black Phosphorus",* W.S. Whitney, M.C. Sherrott, D. Jariwala, W.H. Lin, H.A. Bechtel, G.R. Rossman, and H.A. Atwater, Nano Letters, 1, pp. 78-84 (2017).
11. *"Gate-Variable Mid-Infrared Optical Transitions in a (Bi1-xSbx)(2)Te-3 Topological Insulator",* W.S. Whitney, V.W. Brar, Y.B. Ou, Y.M. Shao, A.R. Davoyan, D.N. Basov, K. He, Q.K. Xue, and H.A. Atwater, Nano Letters, 17, pp. 255-260 (2017).

Quantum metamaterials

Principal Investigator:

David Awschalom – Argonne National Lab

Co-Principal Investigators:

Joseph Heremans – Argonne National Lab

Andrew Cleland – Argonne National Lab

David Schuster – University of Chicago

Brian Stephenson – Argonne National Lab

Daniel Lopez – Argonne National Lab

Program Scope

The quantum metamaterials effort at Argonne National Lab has been active at extending the established toolbox of techniques while building up new material growth capabilities related to quantum systems. Herein we highlight some of this recent progress regarding hybrid quantum systems, including studying mechanically driven spins in silicon carbide (SiC) with surface acoustic waves [1] as well as magnon-mediated quantum control of NV centers in diamond on ferromagnetic yttrium-iron-garnet [2]. Additionally, through close collaborations with other groups at MSD and Argonne, we continue to develop strain-sensitive X-ray imaging techniques that allow us to understand both the spin-phonon interactions [1,3] and the local crystalline strain surrounding these quantum defects[4,5]. These experiments build on and advance our understanding of defect lattice environments. This insight is key for improving the creation efficiency and coherence times of quantum systems, both essential parameters for the advancement of the field as a whole.

To complement this, ongoing synthesis efforts are discussed. These include homo-epitaxial microwave assisted CVD diamond growth alongside highly crystallized sputtered AlN thin films. Diamond growth is performed in the context of developing delta-doped and co-localized electronic-nuclear spin systems. Whereas AlN film growth and nanofabrication is targeted at the study of various quantum and crystalline defects in SiC via acoustic driving to create hybrid quantum system. These growth capabilities are complemented by an array of characterization tools which serve to guide iterative growth optimizations. Among these we note XRD based studies using both table-top tools and the synchrotron beam lines for the study crystalline properties, SEM/TEM observations of growth dynamics and morphology, and XPS chemical

investigations of the material interfaces. Such understanding is key in surpassing current limitation of quantum systems such as NbTiN/NbN superconducting devices which are extremely sensitive to things such as surface/interface oxidation and shifts of stoichiometry.

Finally, we will present some new advances in localizing defects and nuclear spins along with developing a quantum sensing platform based on a patterned polymer-brush-array technique. All of the presented results allow us to better tailor the material growth and defect characteristics to the needs of specific quantum applications.

Recent Progress

We have recently installed our diamond CVD tool in our lab (see Figure 1) and have hired a post-doctoral scholar (Nazar Delegan) who started in early November to lead the diamond growth effort. To date, we have grown more than 5 samples of diamond with our new tool, including high quality single-crystal diamond epilayer films. Additionally, each iterative deposition has been guided by an ever growing material characterization toolbox.

Figure 1 | Seki SDS6300 diamond microwave-assisted plasma-enhanced chemical vapor deposition (PE-CVD) tool at ANL.

We have improved the quality of our AlN sputtered films on SiC through use of a heated etch to improve the crystallinity. This is shown as a significant narrowing, by more than a factor of two, in the rocking curve width (see Figure 2) of the AlN (004) XRD peak. This is expected to directly translate into an improvement of the piezoelectric properties of the film and by extension in the spin-strain coupling with the SiC. In sum, these improvements to the piezoelectric film should benefit our hybrid quantum system effort looking at mechanically driven spins in SiC using surface acoustic waves [1].

Also, we have recently completed several manuscripts exploring the spin-phonon interactions [1] using x-ray imaging techniques to map out the local acoustic standing waves in SiC [3]. These efforts highlight the strength of combining multiple techniques to understand the spatial interaction between spins and phonons. Furthermore, intimate collaborations with the Galli group at the University of Chicago allowed us to foster a better understanding of the shear strain component as it pertains to the mechanical control of spins [1].

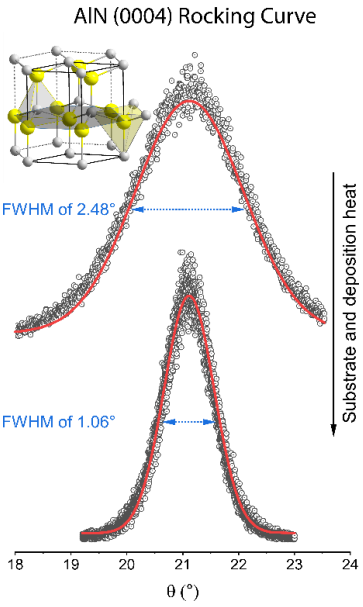

Figure 2 | Rocking curve of AlN film on 4H-SiC. We observe a significant improvement to the film quality due to heated etch and growth.

Finally, we have made several steps toward understanding the defect creation process in our commonly used host material systems. Using Bragg Coherent Diffraction Imaging, we were able to detail the annealing driven vacancy diffusion dynamics in both diamond [4] and SiC [5] nanoparticles. We have also begun using a localized nano-implantation technique to study the defect creation dynamics in an effort to improve creation efficiency and minimize unnecessary damage caused by the implantation process. This work is being done in collaboration using a modified focused ion beam at Sandia National Lab. The intent is to use their technical capabilities to nano-implant pristine SiC with silicon as a way to localize divacancy defects down to < 100 nm spots. We are in the process of studying the local strain imparted by the implantation process via nanoscale x-ray imaging (see Figure 3).

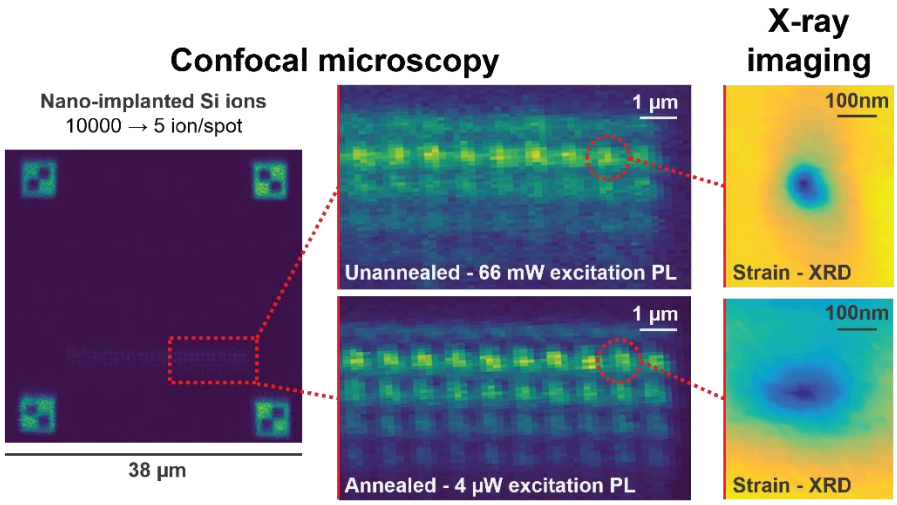

Figure 3 | Nanoimplanted silicon ions into 4H-SiC. A broad spatial photoluminescence scan of the nanoimplanted spots (left). A zoom-in photoluminescence of the high dosed implanted areas of an unannealed (center-top) and annealed (center-bottom) sample. Note the annealed sample requires less excitation power suggesting a significantly higher divacancy defect density. The strain sensitive x-ray imagined of individual implanted spots shows a distinct broadening of the local strain structure post anneal (right).

Future Plans

A few of our future plans related to synthesis, defect creation, and spin-phonon hybrid quantum systems are as follows -

We look to continue our growth of CVD diamond, including nitrogen delta-doping and small spin ensembles. Additionally, we intend to explore the use of isotopically purified precursors for the growth of diamond super-lattice structures and optically distinguishable 3D localized NV^- defect ensembles. The former presents interesting possibilities in light of phononic structures and photon-spin interaction, whereas the latter allows for controlled electron-nuclear spin systems. The traditionally employed (100) growth of diamond will be complimented with the ability to grow (111) oriented diamond for the purpose of obtaining highly oriented NV^- defects. This would allow an additional axis of control for various NV^- defect driven quantum sensing applications. Finally, the incorporation of other defect systems using similar delta-doping techniques, such as rare-earth and transition-metal, are being considered for their interesting properties in the context of quantum communication.

Incorporating our ever improving AlN film growth capabilities with nano-fabrication capabilities at the CNM/UChicago, we intend to fabricate quantum hybrid system devices and high Q mechanical resonators. This will include growing patterned AlN films on SiC membranes for improved photonic confinement. Such structures will serve to optimize the spin-strain interaction in mechanically driven hybrid systems.

We will continue our collaborative work with various groups at the APS. Using X-ray microscopy techniques to better understand the role of matrix crystal strain and defects in the vicinity of our quantum defects. This work is serving as a baseline in the development of new x-ray imaging techniques intended to allow us to perform phase-control mapping of acoustically generated strain waves in SiC. This approach would allow for a better understanding of the spin-phonon hybrid quantum systems we are exploring.

References

1. S. J. Whiteley, *et al.*, "Spin-phonon interactions in silicon carbide addressed by Gaussian acoustics," Nature Physics, advance online publication, (2019).
2. P. Andrich, *et al.*, "Long-range spin wave mediated control of defect qubits in nanodiamonds," *npj Quantum Information*, **3**, 28, (2017).
3. S. J. Whiteley, *et al.*, "Imaging dynamically-driven strain at the nanometer-scale using stroboscopic Scanning X-ray Diffraction Microscopy," *arXiv, 1808.04920*.
4. S. O. Hruszkewycz, *et al.*, "In situ study of annealing-induced strain relaxation in diamond nanoparticles using Bragg coherent diffraction imaging," *APL Materials*, **5**, 026105, (2017).
5. S. O. Hruszkewycz, *et al*. "Strain annealing of SiC nanoparticles revealed through Bragg coherent diffraction imaging for quantum," *Phys. Rev. Materials*, **2**, 086001, (2018).

Publications - 2-year list of publications SUPPORTED BY BES

1. S. J. Whiteley, G. Wolfowicz, C. P. Anderson, A. Bourassa, H. Ma, M. Ye, G. Koolstra, K. J. Satzinger, M. V. Holt, F. J. Heremans, A. N. Cleland, D. I. Schuster, G. Galli, D. D. Awschalom. P. Andrich, "Spin-phonon interactions in silicon carbide addressed by Gaussian acoustics," *Nature Physics*, advance online publication, (2019).
2. A. Shearrow, G. Koolstra, S. J. Whiteley, N. Earnest, P. S. Barry, F. J. Heremans, D. D. Awschalom, E. Shirokoff, D. I. Schuster. "Atomic layer deposition of titanium nitride for quantum circuits," *Appl. Phys. Lett.*, 113, 212601, (2018).
3. K. J. Satzinger, Y. P. Zhong, H. S. Chang, G. A. Peairs, A. Bienfait, M. H. Chou, A. Y. Cleland, C. R. Conner, E. Dumur, J. Grebel, I. Gutierrez, B. H. November, R. G. Povey, S. J. Whiteley, D. D. Awschalom, D. I. Schuster, A. N. Cleland. "Quantum control of surface acoustic wave phonons," *Nature*, 563, 661-665, (2018).
4. S. O. Hruszkewycz, S. Maddali, C. P. Anderson, W. Cha, K. C. Miao, M. J. Highland, A. Ulvestad, D. D. Awschalom, F. J. Heremans. "Strain annealing of SiC nanoparticles revealed through Bragg coherent diffraction imaging for quantum," *Phys. Rev. Materials*, **2**, 086001, (2018).
5. G. Wolfowicz, S. J. Whiteley, D.D. Awschalom. "Electrometry by optical charge conversion of deep defects in 4H-SiC," Proc. Natl. Acad. Sci., 201806998, 2018
6. P. Andrich, J. Li, X. Liu, F. J. Heremans, P. F. Nealey, D. D. Awschalom. "Microscale resolution thermal mapping using a flexible platform of patterned quantum sensors," *Nano Lett.*, (2018).
7. G. Wolfowicz, C. P. Anderson, A. L. Yeats, S. J. Whiteley, J. Niklas, O. G. Poluektov, F. Joseph Heremans, and D. D. Awschalom. "Optical charge state control of spin defects in 4H-SiC," *Nature Communications*, 8, 1876 (2017).
8. B. B. Zhou, P. C. Jerger, V. O. Shkolnikov, F. J. Heremans, G. Burkard, and D. D. Awschalom. "Holonomic quantum control by coherent optical excitation in diamond," *Phys. Rev. Lett.*, 119 (14) 140503 (2017).
9. A. L. Yeats et al., "Local optical control of ferromagnetism and chemical potential in a topological insulator" *PNAS* 114 (39) 10379-10383 (2017).
10. P. Andrich, C. F. de las Casas, X. Liu, H. L. Bretscher, J. R. Berman, F. J. Heremans, P. F. Nealey, and D. D. Awschalom, "Long-range spin wave mediated control of defect qubits in nanodiamonds," *npj Quantum Information*, 3, 28, (2017).
11. D. Christle, et al., "Isolated Spin Qubits in SiC with a High-Fidelity Infrared Spin-to-Photon Interface" *PRX* 7 021046 (2017)
12. B. B. Zhou, A. Baksic, H. Ribeiro, C. G. Yale, F. J. Heremans, P. C. Jerger, A. Auer, G. Burkard, A. A. Clerk, and D. D. Awschalom, "Accelerated quantum control using superadiabatic driving in a solid-state lambda system", *Nature Physics*, 13, 330–334, (2017).

Generation and Remote Distribution of Quantum Entanglement in Solids

Principal Investigator:

David Awschalom – Argonne National Lab

Co-Principal Investigators:

Andrew Cleland – Argonne National Lab
Aashish Clerk – University of Chicago
Giulia Galli – Argonne National Lab
Joseph Heremans – Argonne National Lab
Alex High – University of Chicago
Axel Hoffman – Argonne National Lab
Joseph Lykken – Fermi National Accelerator Lab
Xuedan Ma – Argonne National Lab
Xufeng Zhang – Argonne National Lab
Tian Zhong – University of Chicago

Program Scope

The 'Generation and Remote Distribution of Quantum Entanglement in Solids' effort at Argonne National Lab and Fermi National Accelerator Laboratory aims to realize large-scale entanglement networks. This requires development of novel experimental and theoretical strategies for the establishment of a real-world quantum network from the ground up. We will present our efforts in using a 30-mile-long fiber-optic link between Argonne and FermiLab to investigate new methods for generating and controlling quantum entanglement using solid-state quantum systems. In particular, we will discuss the first steps toward characterizing the optical quantum channel and the necessary timing protocols needed to stabilize the fiber channel at each end. This includes specific details of the technical elements, including improving collection efficiency and frequency down conversion, necessary to improve the entanglement rate along with long-lived solid-state nuclear spin memories to protect the quantum information while the entanglement swap is performed remotely. These efforts will not only provide a real-world testbed for quantum science, but also open new technological possibilities for long-distance entanglement networks.

Recent Progress

We have assembled a team of theorists and experimentalists to interrogate these questions by developing new platforms for generating and controlling remote entanglement in solids. Since the start of the program we have worked on several aspects of the quantum fiber testbed including:

- Installation of the fiber-link connectors in the labs at Argonne, including two neighboring satellite labs with the ability to easily fiber patch additional systems. We have also redesigned the lab facilities for the installation of the fiber-compatible dilution refrigerator and other cryogenic components.
- Hiring a scientist (Alan Dibos) who started early February 2019 and will be working specifically on the installation of the lasers for testing the optical network, the dilution refrigerator and cryogenic infrastructure, and nanofabrication of the high collection efficiency devices.
- Identification of the necessary equipment needed for the initial thrust to characterize the fiber network's optical transmission, timing, and stabilization. We are in the process of ordering the necessary components.
- Design of a versatile solid-state testbed at the Argonne node that allows for different quantum platforms to be swapped in and out, with the vision of a plug-and-play testbed for long-distance quantum entanglement.
- Identification of the preferred defect systems to begin using on the quantum testbed. We have started to grow and create defects for several candidate solid-state systems, including Yttria as a host material for rare-earth ions.

Future Plans

With the long-distance optical fiber in place we will begin construction on the quantum testbed to enable scientific explorations based on long-distance distributed entanglement while realizing "real-world" operating conditions for new quantum technologies.

Specific plans in the immediate future will include:

- Installation of a BlueFors dilution refrigerator system capable of going to 100 mK with a fiber-optic option to couple to the quantum fiber network.
- Working with cryostat companies to create the versatile platform needed for solid-state systems including a node capable of both free-space collection and integrated fiber-optic collection at cold temperatures.
- Characterization of the transmission, timing, and instability of the fiber network with the lasers and fast timing electronics currently on order. This will help define the protocols needed to mitigate the timing instability of a real-world system.
- Co-localize defect electron spins and nuclear spin in SiC as a way to position high quality defects in carefully controlled nuclear spin environments for nuclear register applications.

We are developing techniques to localized spin defects and nearby nuclear spins, leveraging the well-developed materials synthesis and characterization tools at Argonne.

- Begin nanofabrication of nanophotonic structures for collection efficiency enhancement including integrated tapered fibers and metalens structures on SiC and oxide substrates.
- Begin building an experiment to frequency down-convert visible and near-IR photons into the telecom band for highly efficiency fiber transmission using the proposed periodically poled lithium niobate non-linear crystal scheme.

Publications

No publications at this moment – first year of program

Properties, Electrochemical Activity, and Stability of Solid Oxide Cell Materials Under Extreme Conditions

Scott A Barnett, Northwestern University

Program Scope

This project focuses on reversible solid oxide cells (ReSOCs), a technology that can store electricity with high efficiency, reasonable cost, and high storage capacity, and can also be used for renewable (CO2-neutral) fuel production. A key question is how to make ReSOC electrode materials that provide the requisite performance and efficiency, while at the same time keeping degradation rates very low. Although this is a practical engineering consideration, it motivates fundamental scientific questions about the properties and durability of electrode materials under extreme conditions. Thus, this project aims to develop a comprehensive understanding and mechanistic modeling of ReSOC electrode characteristics and degradation mechanisms. Various effects that contribute to degradation during cell operation will be studied, including particle coarsening, surface segregation, and the extremely high effective oxygen pressures that are present during electrolysis operation. The resulting in-depth understanding of electrode performance and degradation will provide a basis for developing improved materials, and for choosing cell operating conditions that yield desired efficiency and long-term durability.

Recent Progress

Novel Oxygen Electrode

$(La,Sr)(Co,Fe)O_3$ (LSCF) has become the oxygen electrode material of choice in both R&D and industrial development of solid oxide fuel cells and electrolysis cells. In the past project period, we have developed a new oxygen electrode - $Sr(Ti_{0.3}Fe_{0.7-x}Co_x)O_{3-\delta}$ (STFC) - that has the potential to replace LSCF based on both improved performance and stability. Figure 1 compares the evolution of electrode resistance R_p during life tests carried out at 700 °C for LSCF and STFC with up to 15% Co. (a) and (b) show that increasing the amount of Co substituted in STFC substantially decreases the resistance, to values much lower than for LSCF. After an initial break-in period during which R_p decreased, R_p remained stable both with (b) and without (a) DC current. On the other hand, LSCF performance degraded over time in both cases (c and d). It was found that the polarization resistance values were ~ 3x lower than LSCF

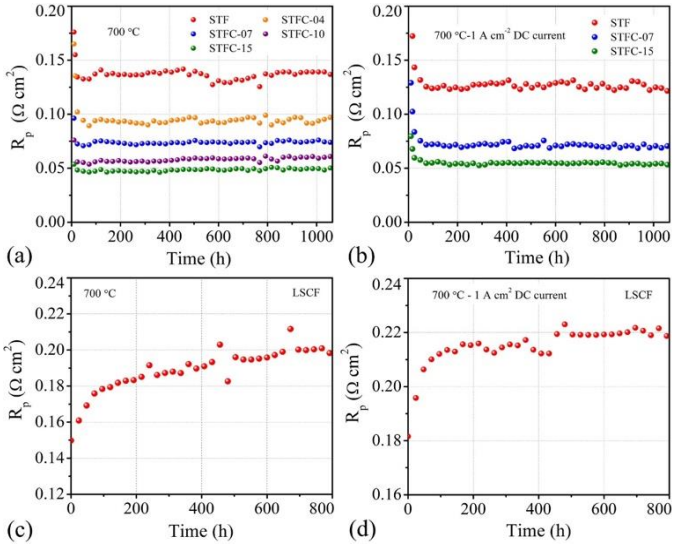

Figure 1. Evolution of cell polarization resistance (R_p) at 700 °C for the symmetric cells with STF-based and LSCF electrodes; (a) and (c) without current; (b) and (d) with 1 A cm^{-2} DC current. STF indicates $Sr(Ti_{0.3}Fe_{0.7-x}Co_x)O_{3-\delta}$ with x=0, whereas STFC-07 indicates x=0.07, for example.

over a wide range of conditions, with values low enough for operation down to ~ 600 °C. Studies of fundamental properties showed improved oxygen transport kinetics, including > 100x higher oxygen surface exchange and oxygen diffusion coefficients, along with ~ 10x higher oxygen vacancy concentration. Finally, STFC is composed of inexpensive earth-abundant materials, with no rare-earth elements and only a small amount of Co.

Fuel Electrodes with Self-Assembled Nanoparticles

In previous DOE-supported work, we reported on a new fuel electrode composition, $Sr(Ti,Fe,Ni)O_3$ (STFN), where the spontaneous formation (exsolution) of Ni-Fe alloy nanoparticles results in remarkably good electrochemical performance by promoting H_2 dissociative adsorption. More recently, we compared stoichiometric $Sr(Ti_{0.3}Fe_{0.63}Ni_{0.07})O_{3-\delta}$ (STFN0) and 5% Sr-deficient $Sr_{0.95}(Ti_{0.3}Fe_{0.63}Ni_{0.07})O_{3-\delta}$ (STFN5) compositions. Figure 2 shows that the cell performance with STFN0 is inferior to that of STFN5. It has been reported that A-site deficiency promotes nanoparticle exsolution, and this could potentially explain the improved performance. Surprisingly, however, this is not the case for STFN, as Figure 2 shows that the Sr-deficient and stoichiometric oxide surfaces showing no difference in the exsolved Ni-Fe nanoparticle size and density. There was only a small nanoparticle composition difference. Thus, the much worse performance of the stoichiometric composition is not due to the nanoparticles. Rather, it appears that this results because the exsolution leaves the perovskite highly B-site deficient; this yields a high density of defects that deleteriously impact oxide transport properties and thereby electrode performance. This provides new insight into design of exsolution anodes, with the A-site deficiency, the dopant cation amount, and the width of the perovskite single-phase region playing key roles.

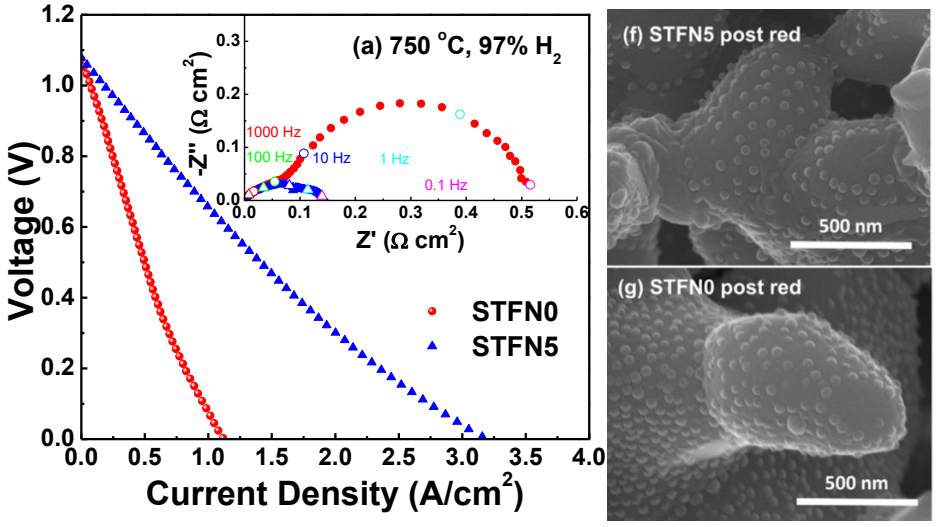

Figure 2. (Left) Comparison of *j-V* curves and EIS data from cells with STFN0 and STFN5 anodes, measured at 750 °C with anode H_2 partial pressure of 97% H_2. (Right) SEM pictures of for STFN5 and STFN0 oxide anode surfaces with nanoparticles after cell test under the same conditions.

A thermodynamic calculation was derived[1] that correctly predicts the Fe-Ni alloy nanoparticle composition x_{Fe}. The calculated equilibrium is between the alloy, oxide, and a fuel gas composition with effective oxygen partial pressure p_{O2}^{fuel}:

$$\left(\frac{p_{O2}^{\mathrm{STF-Fe}}}{p_{O2}^{fuel}}\right)^{3/4} = a_{Fe} \approx x_{Fe}\, exp\left[\frac{\Omega(1-x_{Fe})^2}{RT}\right] \qquad (1)$$

Where p_{O2}^{STF-Fe} is the partial pressure where pure Fe is at equilibrium with STF, which we measured using thermogravimetry, and a_{Fe} is the Fe activity. The latter term in eq. 1 gives an approximate expression for x_{Fe} based on a regular solution approximation for the Fe-Ni alloy with alloy interaction parameter Ω. Eq. 1 predicts that Fe is reduced from STF in the presence of Ni under conditions where STF alone is stable. Physically, this occurs because the entropy of mixing and a negative value of Ω make it thermodynamically favorable to form the Fe-Ni alloy. These suggests that it may be possible to tune nanoparticle composition to improve electrode performance using the fuel composition.

Cell Degradation Under Extreme Conditions

Figure 3 presents representative FIB-SEM 2D images from an as-reduced solid oxide electrolysis cell (a) and the same cell after a life test carried out for 1000 h at 800 ºC and 0.8 A/cm^2 (b). In the images, the electrode is shown along with a portion of the YSZ electrolyte on the left. The as-reduced electrode consists of well dispersed YSZ (darker grey), Ni (lighter grey), and pore (black) phases with ~ 0.5 μm feature sizes, very similar to prior reports for Ni-YSZ anodes in anode-supported SOFCs.[2,3] For the life tested cell, the structure at a distance > 5 μm from the electrolyte appears similar to that of the as-reduced electrode, but the region nearer the electrolyte is significantly changed. A nano-scale particle structure has formed at electrode/electrolyte interface, along with extended voids aligned along the interface. The nanoparticles are also present within the electrode, apparently filling areas that were initially pores. The altered interfacial layer and voids, which develops in cells tested at current density > 0.4 A/cm^2, eventually lead to cell failure. Analysis suggests that the nanoparticle formation results from the reduction of ZrO_2 in the electrolyte and formation of Ni-Zr alloy at the interface, due to an extremely low effective oxygen partial pressure that develops during cell operation with current. These results provide important insight into how to design and operate cells to avoid degradation and failure.

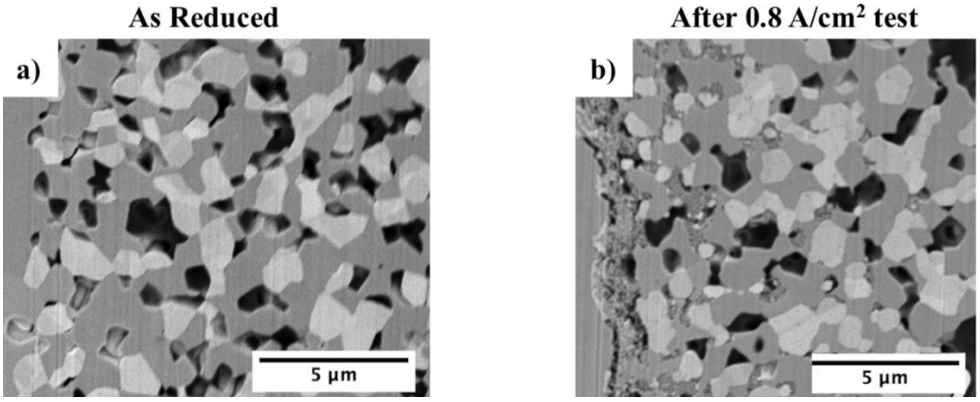

Figure 3. Representative 2D cross sections taken near the YSZ / Ni-YSZ interface (electrolyte is at left) in solid oxide electrolysis cells before life testing (a) and after life testing (b) for 1000 h at 800 ºC and 0.8 A/cm^2 (b). YSZ appears as a darker grey compared to the lighter grey Ni, while pores appear mostly black.

Future Plans

Studies of STFC oxygen electrodes will continue, including studies of their physical properties and transport kinetics, and their performance and stability under extreme cell operating conditions. The dynamics of exsolution processes from materials based on STFN will be further explored, including the possibility of re-dissolving the nanoparticles into the oxide under oxidizing condition, and the role of perovskite stoichiometry. Our work on the use of atomic layer deposition to alter surface chemistry and regenerate electrodes will be expanded to include different species and also fuel electrodes. A main emphasis will be on *in situ* measurements done under cell operating conditions that produce extreme oxygen partial pressures.

References

1 Zhu, T., Troiani, H. E., Mogni, L. V., Han, M. & Barnett, S. A. Ni-Substituted Sr(Ti,Fe)O 3 SOFC Anodes: Achieving High Performance via Metal Alloy Nanoparticle Exsolution. *Joule*, doi:10.1016/j.joule.2018.02.006 (2018).

2 Cronin, J. S., Wilson, J. R. & Barnett, S. A. Impact of pore microstructure evolution on polarization resistance of Ni-Yttria-stabilized zirconia fuel cell anodes. *J Power Sources* **196**, 2640-2643, doi:10.1016/j.jpowsour.2010.10.084 (2011).

3 Kennouche, D., Chen-Wiegart, Y. C. K., Cronin, J. S., Wang, J. & Barnett, S. A. Three-Dimensional Microstructural Evolution of Ni-Yttria-Stabilized Zirconia Solid Oxide Fuel Cell Anodes At Elevated Temperatures. *J Electrochem Soc* **160**, F1293-F1304, doi:10.1149/2.084311jes (2013).

Publications

1. T. Zhu, H.E. Troiani, L.V. Mogni, M. Han and S.A. Barnett, "Ni-Substituted Sr(Ti,Fe)O 3 SOFC Anodes: Achieving High Performance via Metal Alloy Nanoparticle Exsolution," *Joule* 10.1016/j.joule.2018.02.006 (2018) *Full DoE support.*
2. S.-L. Zhang, H. Wang, M.Y. Lu, A.-P. Zhang, L.V. Mogni, Q. Liu, C.-X. Li, C.-J. Li and S.A. Barnett, "Cobalt-substituted SrTi0.3Fe0.7O3−δ: a stable high-performance oxygen electrode

material for intermediate-temperature solid oxide electrochemical cells," *Energy & Environmental Science* 10.1039/c8ee00449h (2018) *Main support by DoE.*

3. Q. Liu, H. Wang, D. Kennouche, C. Riscoe, D. Butts and S.A. Barnett, "Effect of Reversing-Current Operation on the Structure and Electrochemical Performance Evolution of Ni-YSZ Fuel Electrodes," *Journal of The Electrochemical Society* 165 (2018) F870-F875 *Partial support by DoE.*
4. R. Glaser, T. Zhu, H.E. Troiani, A. Caneiro, L.V. Mogni and S. Barnett, "Enhanced electrochemical response of Sr(Ti0.3Fe0.7Ru0.07)O3-δ anodes by exsolved Ru-Fe nanoparticles," *Journal of Materials Chemistry A* 6 (2018) 5193 – 5201 *Full DoE support.*
5. Tenglong Zhu, HoracioTroiani, Liliana V Mogni, Mariano Santaya, Mingfan Han, and Scott A Barnett, "Ni-substituted $Sr(Ti,Fe)O_3$ Solid Oxide Fuel Cell Anodes: Effect of A-site Deficiency," submitted *Main support by DoE*
6. Travis A. Schmauss, Justin G. Railsback, Matthew Y. Lu, Kevin Y. Zhao, Scott A. Barnett, "Performance Enhancement in SSC-GDC Porous Cathodes with ZrO_2 Atomic Layer Deposition for Low-Temperature Solid Oxide Fuel Cells," submitted *Main support by DoE*

Digital Synthesis: A Pathway to Create and Control Novel States of Condensed Matter

Anand Bhattacharya, Dillon D. Fong
Materials Science Division, Argonne National Laboratory

Program Scope: Digital Synthesis is a strategy to create materials in an atomic layer-by-layer fashion to tailor new properties. With this approach, we are able to control local dipole electrostatic fields *within* a unit cell, create cation-ordered analogs of known materials and control charge transfer and band lineup in heterostructures between different materials. Thus, our program seeks to create new materials out of known ingredients to yield novel properties, and to manipulate these with external fields and currents. We synthesize our materials using precision synthesis techniques, and characterize them with tools that probe structure and the electronic and magnetic degrees of freedom. Ideally, atomically abrupt interfaces would ensure that we have model systems where the properties we find represent a true reconstruction of the electronic and magnetic degrees of freedom within the material. However, in reality interfaces always have defects – for example cation interdiffusion, or oxygen vacancies – and it is important that we characterize these so we can understand their role and can devise strategies to mitigate or exploit them. We bring a range of tools to bear to address these issues, including X-ray scattering with synchrotron sources, scanning transmission electron microscopy, electronic and thermal transport, magnetic characterizations and neutron scattering.

Recent Progress: Our program has advanced fundamental understanding in the areas of oxide thin film synthesis and defect interactions at surfaces and heterointerfaces. We describe highlights in these areas.

In situ synchrotron X-ray studies of growth: Molecular beam epitaxy (MBE) is a synthesis technique that permits the control of materials growth one atomic plane at a time [1]. Achieving this level of precision requires an *in situ* means of monitoring the growth process, which is normally accomplished with reflection high energy electron diffraction (RHEED) [2]. A more powerful means of monitoring synthesis is with the use of synchrotron X-rays, which not only allows monitoring of the growth mode, but also provides atomic-scale snapshots of the processes taking place at the surface during deposition [3]. After constructing an oxide MBE system at the Advanced Photon Source [4], we demonstrated that epitaxial growth is not as simple as laying

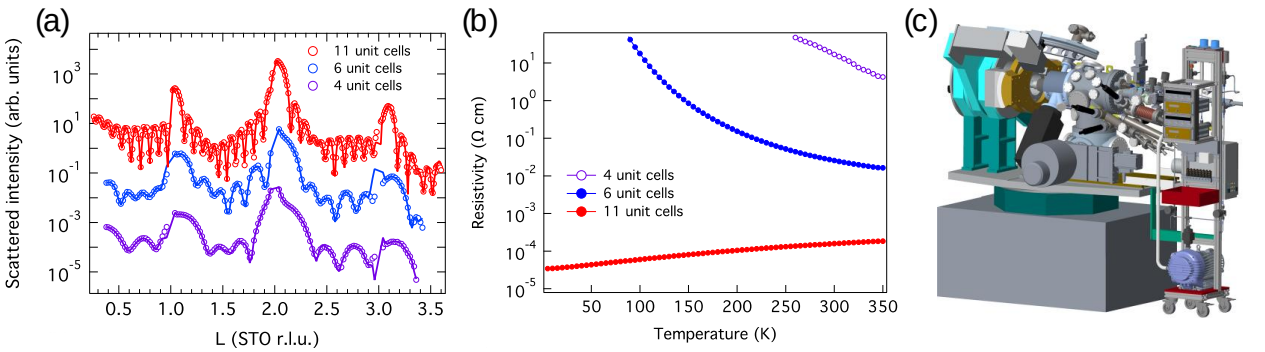

Figure 1 *(a) Scattered intensity along the 00L specular rod, measured for three $LaNiO_3$ films immediately after growth at 590°C. (b) Temperature dependent resistivity, showing that the 11 uc film is metallic while the thinner ones are more insulating [6]. (c) Schematic of the in situ hybrid MBE, showing the vertical rack used to deliver the metalorganic precursors to the chamber [7].*

down one atomic plane at a time on an inert substrate. Rather we found that the atomic layers can dynamically rearrange during deposition [5]. More recently, we discovered that even when grown in a background of ozone and oxygen, the amount of oxygen incorporated into a complex oxide can depend on film thickness [6]. Scans along the specular rod after growth of different thickness $LaNiO_x$ films on $SrTiO_3$ (001) are presented in **Fig. 1a**. The variation in oxygen stoichiometry results in a thickness-dependent insulator-to-metal transition (**Fig. 1b**) [6].

The $LaNiO_x$ films were grown by conventional MBE, alternating between La and Ni sources with the use of shutters. Even when monitoring growth *in situ*, however, maintaining a perfect 1:1 ratio of La:Ni throughout deposition cannot be achieved. To remedy this, we recently extended our *in situ* capability by constructing a "hybrid MBE" system (**Fig. 1c**), where chemical reactions take place during deposition to facilitate the growth of stoichiometric ABO_x materials [7]. Here, we exploit a "growth window," within which chemical reactions take place between the adsorbed A and B species in a certain temperature and pressure range to ensure that the A:B stoichiometry is 1:1. We conducted the first *in situ* X-ray study of hybrid MBE deposition, growing a $SrTiO_3$ film with a titanium isopropoxide precursor. Scattering at the 00½ position showed that at 750°C hybrid deposition takes place in the layer-by-layer growth mode [7].

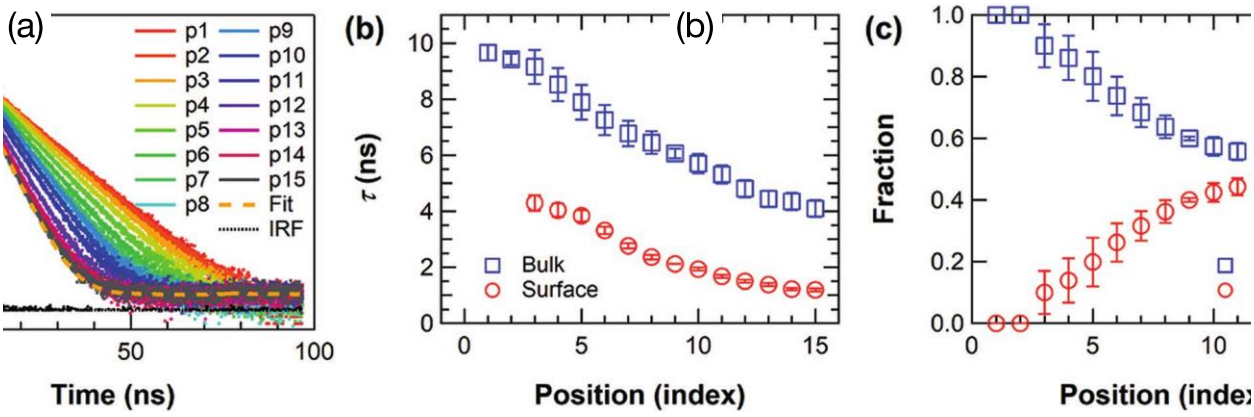

Figure 2 *(a) Illustration of the spatial origins of the two blue luminescence decay components. (b) Electron concentration profiles along the oxygen vacancy gradient for the near-surface and bulk regions [10].*

Point defect control in heterostructures: As described above, defects in oxide heterostructures can strongly impact behavior, and improved control over them can be a powerful means of tailoring electronic properties. We have written extensive reviews on this topic in both *Reports in Progress in Physics* [8], *Surface Science Reports* [9], and *Adv. Phys. X* [10]. We also conducted detailed, quantitative studies on the effect of oxygen vacancies on the electronic structure of $SrTiO_3$ [11]. Here we exploited the fact that oxygen vacancies lead to optical luminescence, and by measuring the time dependence of these spectra (**Fig. 2a**), we can distinguish and quantify the oxygen vacancy concentration at the surface versus that within the bulk (**Fig. 2b**). As such we were able to directly study 2D electron gas (2DEG) formation at the $SrTiO_3$ surface and its dependence on defect concentration. We found that electrons due to the vacancies accumulate within a 3 nm region at the surface, confined there by a ~100 meV potential well.

Future Plans

The goal of future work is to determine how to effectively control both the atomic and electronic structure of materials during synthesis as well as to understand defect dynamics in these systems. In particular, we seek ways to control defects within these heterostructures and explore their behavior over multiple length and time scales. Ultimately, we wish exploit their coupling with different functionalities to arrive at materials with configurable properties. The outcome of this work will be the fundamental scientific understanding that enables advances in defect-controlled, atomically-tailored heterostructures. Below, we describe two areas of interest.

In situ atomic and electronic structure: Much of our prior *in situ* results are based on surface X-ray diffraction (SXRD) and are structural in nature: the equipment necessary for X-ray scattering differs greatly from that required for electronic structure measurements such as angle-resolved photoemission spectroscopy (ARPES). Thus, if one wishes to correlate atomic structure with electronic structure, the samples are often exposed to air, leading to adsorbed contaminants and altered structural and electronic depth profiles.

We address this issue by employing two different strategies. In one, we will perform *in situ* oxide MBE/SXRD/ARPES studies, conducting *in situ* growth and SXRD experiments in the MBE system described above and transferring the film *in vacuo* to another system at the APS for ARPES. The other strategy is to combine scattering with spectroscopy on the same system by mounting a hemispherical electron analyzer onto an X-ray diffractometer. We have done this for a pulsed laser deposition (PLD) system, such that we can now monitor growth of a thin film with X-rays, determine its atomic structure with SXRD, and determine its electronic structure with ARPES prior to continuing growth. We note that the electronic structure determined by photoemission spectroscopy is typically only representative of the topmost unit cells of the thin film, given the limited ability of photoelectrons to exit from deep within the material. However, new ARPES detectors can take advantage of the hard X-rays (up to 12 keV) [12], and such (H)ARPES systems can be used to measure the electronic structure more representative of the thin film. We have constructed the world's first *in situ* PLD/SXRD/HARPES system, with the initial X-ray photoelectron spectroscopy results shown in **Fig. 3** for a $LaAlO_3$ film grown on $SrTiO_3$. We will exploit both of these highly unique MBE and PLD systems for a variety of different epitaxial heterostructures, with the aim of achieving defect-controlled synthesis for the creation and design of new electronic materials.

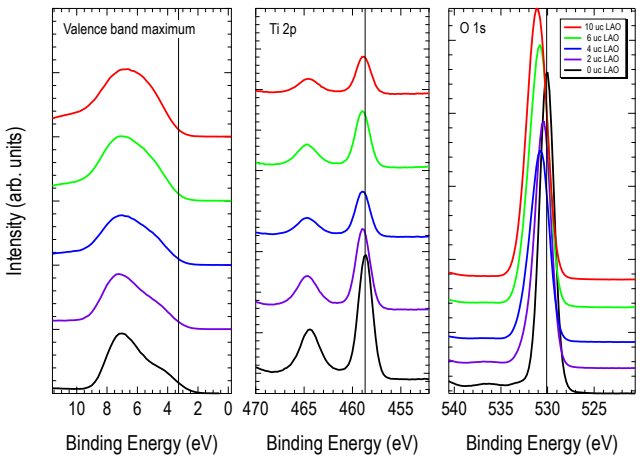

Figure 3 *X-ray photoelectron spectra measured with 10 keV X-rays immediately after growth of $LaAlO_3/SrTiO_3(001)$ at 550°C.*

Defect dynamics: After the APS upgrade, the X-rays will be more coherent in nature – i.e., the incoming X-rays will be more like plane waves, such that the phase can be recovered after the scattering process. This will allow a wealth of remarkable possibilities for science, including improved coherent diffraction imaging (CDI) and greatly improved X-ray photon correlation spectroscopy (XPCS).

XPCS is particularly conducive to *in situ* studies, as it permits the investigation of dynamics during the growth process: that is, one will be able to measure the *time fluctuations* of species as they deposit, migrate, and incorporate into the material.

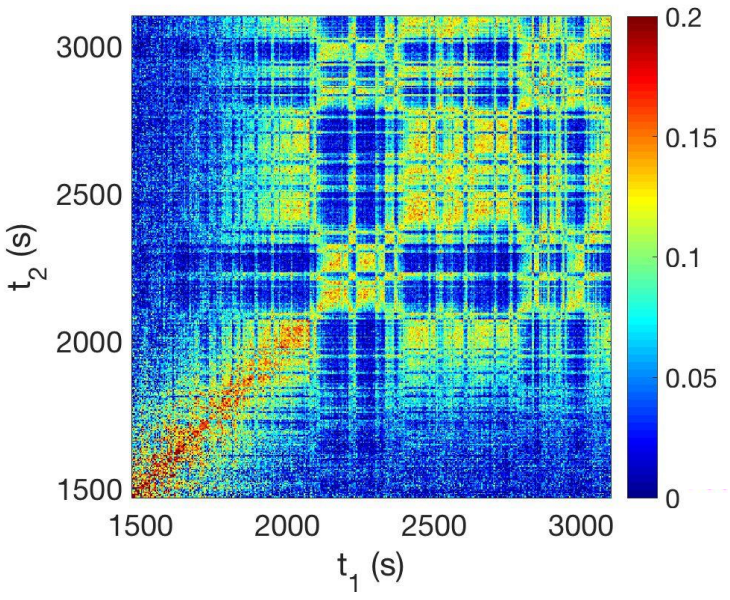

Figure 4 *Two-time correlation map measured at the $SrCoO_x$ 00½ reflection at 360°C. The gas environment was switched from oxygen to nitrogen at 1600 s.*

We have already conducted preliminary studies on the dynamics of oxygen defects in the $SrCoO_x$ system. Here, given a sufficient concentration of oxygen vacancies, the vacancies can order within the crystal lattice. In effect, $SrCoO_x$ changes from the perovskite $SrCoO_3$ phase to the brownmillerite $SrCoO_{2.5}$ in reducing environments. We show a two-time correlation map measured at the 00½ reflection in **Fig. 4**, where the oxygen pressure was switched from high to low at 1600 seconds, leading to nucleation of the brownmillerite (vacancy-ordered) phase. As seen, the two-time correlation map exhibits a checkerboard-like pattern; although the brownmillerite structure is thermodynamically stable, the configuration of vacancies fluctuates with time. Such insight can only be provided by a coherent X-ray beam. In the near term and in preparation for the APS upgrade, we will expand our investigation of defect dynamics in oxide heterostructures and combine XPCS studies with those of *in situ* growth.

References

1. D. G. Schlom, *APL Materials* **3,** 062403 (2015).
2. J. H. Haeni, C. D. Theis, and D. G. Schlom, *J. Electroceram.* **4,** 385 (2000).
3. H. Zhou and D. D. Fong in *Epitaxial Growth of Complex Metal Oxides*. Woodhead Publishing, Elsevier 263 (2015).
4. J. H. Lee et al. *Rev. Sci. Instrum.* **87,** 013901 (2016).
5. J. H. Lee et al. *Nat. Mater.* **13,** 879 (2014).
6. I.-C. Tung et al., *Phys. Rev. Mater.* **1,** 053404 (2017).
7. T. K. Andersen et al., *Rev. Sci. Instrum.* **89,** 033905 (2018).
8. S. V. Kalinin, Y. Kim, D. D. Fong, and A. N. Morozovska, *Rep. Prog. Phys.* **81,** 036502 (2018).
9. T. K. Andersen, D. D. Fong, and L. D. Marks, *Surf. Sci. Rep*. **73,** 213 (2018).
10. H.-T. Zhang et al., *Adv. Phys. X* **4,** 1523686 (2018).
11. S. Y. Cook et al., *Adv. Electron. Mater.* 1800460 (2018).
12. C. S. Fadley, *J. Electron. Spectros. Relat. Phenomena* **190,** 165 (2013).

FWP 58920 Publications (Since 03/2017)

1. *"Polarity Driven Oxygen Vacancy Formation in Ultra-thin $LaNiO_3$ Films on $SrTiO_3$",* I. C. Tung, G. Luo, J. H. Lee, S. H. Chang, J. Moyer, H. Hong, M. J. Bedzyk, H. Zhou, D. Morgan, D. D. Fong, and J. W. Freeland, *Phys. Rev. Mater*. **1,** 053404 (2017).
2. *"Effect of defects on reaction of NiO surface with Pb-contained solution",* J. Kim, B. Hou, C. Park, C. B. Bahn,, J. Hoffman, J. Black, A. Bhattacharya, N. Balke, H. Hong, J. H. Kim, and S. Hong, *Scientific Reports 7*, 44805 (2017).
3. *"Epitaxial growth of high quality $SrFeO_3$ films on (001) oriented $(LaAlO_3)_{0.3}(Sr_2TaAlO_6)_{0.7}$"*, Deshun Hong , Changjiang Liu , John Pearson , and Anand Bhattacharya, *Applied Physics Letters* **111**, 232408 (2017). (Featured Article)
4. *"Nanoscale measurement of Nernst effect in two-dimensional charge density wave material 1T-TaS_2"*, Stephen M. Wu, Adina Luican-Mayer, Anand Bhattacharya, *Applied Physics Letters* **111**, 23109 (2017).
5. *"Surface screening mechanisms in ferroelectric thin films and its effect on polarization dynamics and domain structures"*, S. V. Kalinin, Y. Kim, D. D. Fong, and A. Morozovska, *Rep. Prog. Phys*. **81,** 036502 (2018).
6. *"Development of a Hybrid Molecular Beam Epitaxy Deposition System for In-Situ Surface X-ray Studies"*, T. K. Andersen, S. Y. Cook, E. Benda, H. Hong, L. D. Marks, D. D. Fong, *Review of Scientific Instruments* **89,** 033905 (2018).
7. "*Pauling's rules for oxide surfaces"*, T. K. Andersen, D. D. Fong, L. D. Marks, *Surf. Sci. Rep.* **73,** 213 (2018).
8. "*Quantitative Observation of Threshold Defect Behavior in Memristive Devices with Operando X-ray Microscopy"*, H. Liu, Y. Dong, M. J. Cherukara, K. Sasikumar, B. Narayanan, Z. Cai, B. Lai, L. Stan, S. Hong, M. K. Y. Chan, S. K. R. S. Sankaranarayanan, H. Zhou, and D. D. Fong, *ACS Nano* **12,** 4938 (2018).
9. "*Single-Layer TiOx Reconstructions on SrTiO3 (111): (√7 × √7)R19.1°, (√13 × √13)R13.9°, and Related Structures"*, T. K. Andersen, S. Wang, M. R. Castell, D. D. Fong, L. D. Marks, *Surf. Sci.* **675,** 36 (2018).
10. *"Probing short-range magnetic order in a geometrically frustrated magnet by means of the spin Seebeck effect"*, C. Liu, S. M. Wu, J. E. Pearson, J.S. Jiang, N. d'Ambrumenil, A. Bhattacharya, *Phys. Rev.* B (R) **98**, 060415 (2018). (Editor's Suggestion)
11. *"Unconventional slowing down of electronic and structural dynamics in photoexcited charge-ordered $La_{1/3}Sr_{2/3}FeO_3$."* Yi Zhu, Jason Hoffman, Clare E. Rowland, Hyowon Park, Donald A. Walko, John W. Freeland, Philip J. Ryan, Richard D. Schaller, Anand Bhattacharya, and Haidan Wen. *Nature Communications* **9**, 1799 (2018).
12. *"Tunable Noncollinear Antiferromagnetic Resistive Memory through Oxide Superlattice Design"*, Jason D. Hoffman, Stephen M. Wu, Brian J. Kirby, and Anand Bhattacharya, *Phys. Rev. Applied* **9**, 044041 (2018).
13. *"Image registration of low signal-to-noise cryo-STEM data"*, Benjamin H Savitzky, Ismail El Baggari, Colin B Clement, Emily Waite, Berit H Goodge, David J Baek, John P Sheckelton, Christopher Pasco, Hari Nair, Nathaniel J Schreiber, Jason Hoffman,

Alemayehu S Admasu, Jaewook Kim, Sang-Wook Cheong, Anand Bhattacharya, Darrell G Schlom, Tyrel M McQueen, Robert Hovden, Lena F Kourkoutis, *Ultramicroscopy* **191**, 56 (2018).

14. *"X-Ray magnetic circular dichroism and near-edge X-ray absorption fine structure of buried interfacial magnetism measured by using a scanning tunneling microscope tip"*, H. Chang, N. Shirato, Y. Zhang, J. Hoffman, D. Rosenmann, J. W. Freeland, Anand Bhattacharya, Volker Rose, S-W Hla, *Appl. Phys. Lett.* **113**, 061602 (2018).
15. *"Emergent c-axis magnetic helix in manganite/nickelate superlattices"*, G. Fabbris, N. Jaouen, D. Meyers, J. Feng, J. D. Hoffman, R. Sutarto, S. G. Chiuzbăian, A. Bhattacharya, and M. P. M. Dean, *Phys. Rev.* B **98**, 180401(R) (2018). (Editors' Suggestion)
16. "*Dynamic Field Modulation of the Octahedral Framework in Metal Oxide Heterostructures"*, H. Liu, Y. Dong, D. Xu, E. A. Karapetrova, S. Lee, L. Stan, P. Zapol, H. Zhou, D. D. Fong, *Adv. Mater.* **30,** 1804775 (2018).
17. "*Beyond Electrostatic Modification: Design and discovery of functional materials via ionic-electronic and ionic-lattice coupling"*, H.-T. Zhang, Z. Zhang, H. Zhou, H. Tanaka, D. D. Fong, and S. Ramanathan, *Adv. Phys. X* **4,** 1523686 (2018).
18. "*Engineering $SrSnO_3$ Phases and Electron Mobility at Room Temperature Using Epitaxial Strain"*, T. Wang, A. Prakash, Y. Dong, T. Truttmann, A. Bucsek, R. James, D. D. Fong, J.-W. Kim, P. J. Ryan, H. Zhou, T. Birol, and B. Jalan, *ACS Appl. Mater. Inter.* **10,** 43802 (2018).
19. "*The vacancy-induced electronic structure of the $SrTiO_{3-d}$ surface"*, S. Y. Cook, M. T. Dylla, R. A. Rosenberg, Z. R. Mansley, G. Jeffrey Snyder, L. D. Marks, D. D. Fong, *Adv. Elect. Mater.* **5,** 1800460 (2019).
20. *"Counter-thermal flow of holes in high-mobility $LaNiO_3$ thin films"*, Changjiang Liu, Friederike Wrobel, Jason D. Hoffman, Deshun Hong, John E. Pearson, Eva Benckiser and Anand Bhattacharya, *Phys. Rev.* B (R) **99**, 041114 (2019).
21. *"Parameter transferability, self-doping, and metallicity in $LaNiO_3/LaMnO_3$ superlattices"*, A Lopez-Bezanilla, LF Arsenault, A Bhattacharya, PB Littlewood, AJ Millis, *Phys. Rev.* B **99**, 035133 (2019).
22. *"Atomic layer rearrangement during heteroepitaxial growth on $SrTiO_3$"*,S. Y. Cook, K. Letchworth-Weaver, I.-C. Tung, T. K. Andersen, H. Hong, L. D. Marks, D. D. Fong, to appear in *Science Advances* (2019).
23. *"Dopant-dependent stability of garnet solid electrolyte interfaces with lithium metal"*,Y. Zhu, J. G. Connell, S. Tapavcevic, P. Zapol, A. Sharafi, N. Taylor, J. Sakamoto, L. A. Curtiss, D. D. Fong, J. W Freeland, and N. M. Markovic, to appear in *Advanced Energy Materials* (2019).
24. *"Seeded lateral solid-phase crystallization of the perovskite oxide $SrTiO_3$"*,Y. Chen, J. A. Tilka, Y. Ahn, J. Park, A. Pateras, T. Zhou, D. E. Savage, I. McNulty, M. V. Holt, D. M. Paskiewicz, D. D. Fong, T. F. Kuech, and P. G. Evans, submitted to *J. Phys. Chem. C*

Coherent control of spin states in organic electronics – discovery and investigation of complex room-temperature magnetic quantum excitations

PI: Christoph Boehme, co-PI: John M. Lupton
University of Utah, Department of Physics and Astronomy,
115S 1400E, Salt Lake City, Utah, 84112, boehme@physics.utah.edu
Award # DE-SC0000909

Program Scope

The focus of this program has been to address, in the context of organic semiconductors, the long-term challenges set forward by the Department of Energy's Basic Energy Sciences Advisory Committee, such as "How do we control materials processes at the level of electrons?", "How do we characterize and control matter away - especially very far away - from equilibrium?" and "How do remarkable properties of matter emerge from complex correlations of the atomic or electronic constituents and how can we control these properties?".

Specifically, this program pursues the study of ***complex room-temperature magnetic quantum excitations (CoRMQE)***, which include ***higher-spin systems*** *with* ***s*** > ½ (excitons, exciton-polaron pairs or exciton pairs) [1] as well as ***resonantly induced collective charge-carrier spin pair ensembles*** that emerge under ultrastrong resonant driving fields B_1 as illustrated in Fig. 1 [2,3,6]**.** Central to how these phenomena affect spin-dependent electronic transitions and, thus, physical materials behaviors such as electronic, optoelectronic and magneto-optoelectronic properties are the strengths of ***spin-hyperfine interactions (HFIs)*** as well as ***spin-orbit coupling (SOC)*** [2]**.** While ***HFIs*** are typically strong in organic materials due to the all-abundant hydrogen, SOC is generally weak, yet still not negligible for the behavior of paramagnetic charge carrier states. Therefore, this project will focus in particular on the following questions: ***(i) What is the influence of spin-spin interactions, SOC, and the HFI on charge carriers and thus on the formation of CoRMQEs?*** Using recent demonstrations of differentiation between charge carrier SOC and HFI with electrically detected magnetic resonance (EDMR) spectroscopy [4,5,7-10], the influence of HFI and SOC on CoRMQEs is studied. ***(ii) What is the nature of the dynamics of CoRMQEs?*** Previous pulsed EDMR

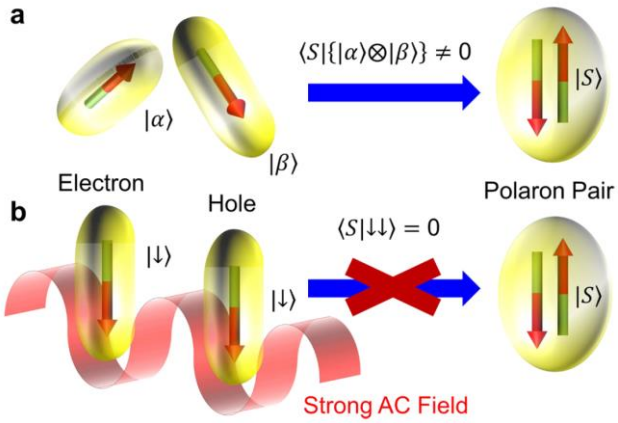

Fig. 1: *Illustration of the emergence of room-temperature magnetic quantum excitations in an organic semiconductor for the example of spin collectivity (the spin-Dicke regime) in organic semiconductors for weak (a) and strong (b) oscillating driving fields B_1 as described by Roundy and Raikh [1] and observed by Waters et al. [2]. (a) Two adjacent, weakly SOC and mutually weakly spin-spin coupled localized singly occupied paramagnetic charge carrier states (an electron and a hole polaron in an organic semiconductor) form a pair whose spin-permutation symmetry governs the probability to yield one doubly occupied state (an exciton) within the singlet spin manifold. When the two charge carriers experience exposure to locally different proton hyperfine fields, their electron spin states will be arbitrary, and thus the pair permutation symmetry will be arbitrary. (b) Under strong AC drive, the two charge carrier states become mutually coherent and form a triplet state and a transition into a doubly occupied singlet state becomes forbidden (adapted from Ref. [3]).*

measurements showed that spin-coherence times (T_2) of paramagnetic charge carrier states in organic semiconductors are typically below 1µs [5,7], due to the random HFI, limiting their utilization for quantum applications. As CoRMQEs can form when B_1 > HFI, it is conceivable that long T_2 emerge under strong drive when coherence is protected by the strong driving fields. ***(iii) What is the quantum mechanics of resonantly induced collective charge-carrier spin ensembles?*** The study of charge-carrier spin collectivity has revealed an unexpected wealth of conductivity effects related to the formation of CoRMQEs, raising questions of whether multi-photon transitions, avoided level crossings, and spin-spin interactions can influence the way collectivity affects the macroscopic materials behaviors.

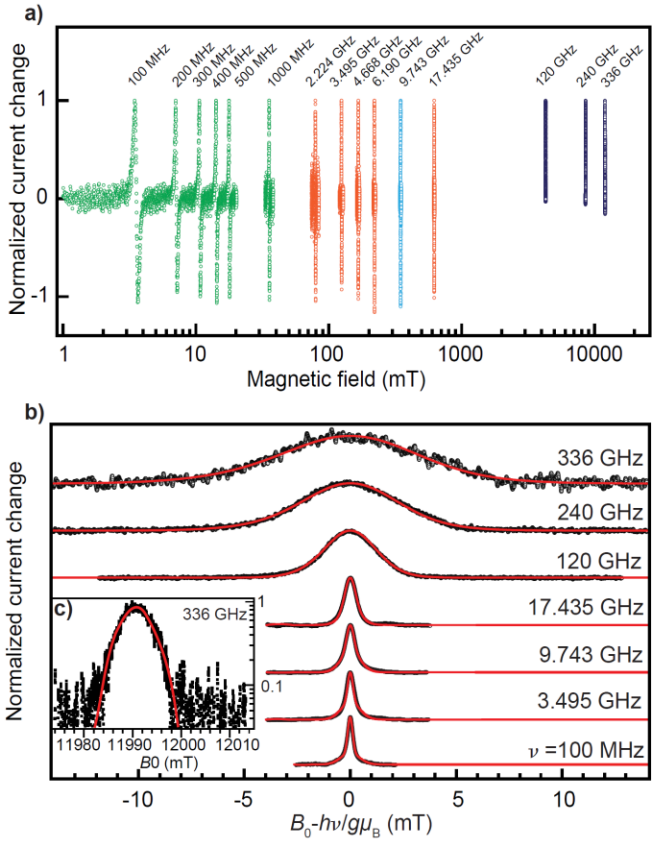

Fig. 2: *Multi-frequency electrically detected magnetic resonance (EDMR) on PEDOT:PSS films. a) EDMR spectra spanning 11 octaves in radiation frequency. The three high-field spectra were measured under modulation of the resonant field, whereas the low-field spectra were obtained by modulating the static magnetic field B_0, resulting in a derivative line shape. Green spectra were obtained using coils as sources of the RF radiation, red spectra used coplanar waveguides, the blue spectrum a commercial X-band resonator, and black spectra a free-space millimeter-wave irradiation. b) Broadening of the resonance spectra with increasing resonance frequency. The red curves show global double-Gaussian fits to the spectra using the same parameter sets for all frequencies. (c) Replot of 336GHz data from (b) on logarithmic scale with single Gaussian fit, illustrating isotropic spectral broadening. (adapted from Ref. [91])*

Recent Progress

During the past 24 months, much progress has been made on the simultaneous measurements and spectroscopic discrimination of SOC induced spin effects such as the distribution of effective *g*-factors and HFI effects, by means of multi-frequency EDMR [8-10]. Following earlier studies of the π-conjugated polymer poly[2-methoxy-5-(2-ethyl-hexyloxy)-1,4-phenylenevinylene] (MEH-PPV) [4] as well as for two morphological phases of the π-conjugated polymer polyfluorene (PFO) [5], the disordered glassy phase as well as the highly ordered β-phase, similar experiments were conducted for the polymer blend poly(3,4-ethylenedioxythiophene) polystyrene sulfonate (PEDOT:PSS) [8,9] as well as the commercial poly-phenylene-vinylene superyellow-PPV (a propriety polymer) [9] in addition to fully deuterated MEH-PPV (yet unpublished). These measurements revealed that SOC affects Zeeman-levels in PEDOT:PSS at much lower magnetic fields of <100mT, compared to MEH-PPV, demonstrating that both the HFI as well as SOC strengths are, in principle, tunable by means of materials preparation parameters. These tuning ranges appear to be narrow, i.e. within one order of magnitude.

In order to study the influence of SOC more sensitively, multifrequency EDMR measurements were extended from a magnetic field range of approximately one order of magnitude all the way into the very low magnetic fields range (~1mT) and the very high magnetic field domain of up to 12T, covering more than 4 orders of magnitude. For each of the polymers discussed above, similar series of multi-frequency electrically detected magnetic resonance (EDMR) measurements were conducted, resulting in sets of EDMR spectra exceeding 11 octaves in frequency range, from less than 100MHz to more than 300GHz.

Figure 2(a) displays plots of the data that was acquired for PEDOT:PSS at low temperatures (~5K) [9]. It shows the current change in PEDOT:PSS layers with Al and indium tin oxide (ITO) contacts under application of a forward bias, as functions of the applied magnetic field, for various applied frequencies. The vertical scales of the displayed data was normalized to the respective resonance maximum currents, with each data set labeled by the frequency under which it was recorded. Figure 2 (b) shows 7 of the 15 normalized data sets in a water fall plot on enhanced magnetic field scales that are centered about the respective on-resonance magnetic fields. This plot reveals how the magnetic resonance lines become monotonically broader as the frequency is increased. The red lines display the result of a global fit of the generated data with two Gaussian functions (for electrons and holes, respectively) whose widths are governed by both the strength of local hyperfine fields as well as the width of SOC induced distributions of Landé-g factors. "Global fit" means that the model to describe ***all*** 15 data sets in (a) requires the same input parameters (the two hyperfine field strengths and two g-factor distribution widths for electrons and holes, respectively) ***at the same time*** – in other words, the model requires that only four parameters must suffice to make this model describe ***all*** 15 data sets at the same time. The excellent agreement of the red fit results and the experimental data is strong evidence for the correctness of this model that is based on the polaron pair recombination mechanism that has been explored in past project years. Thus, the measurements shown in Fig. 2 constitute the, to date, most accurate deconvolution of hyperfine field strength and SOC effects on charge carriers in PEDOT:PSS.

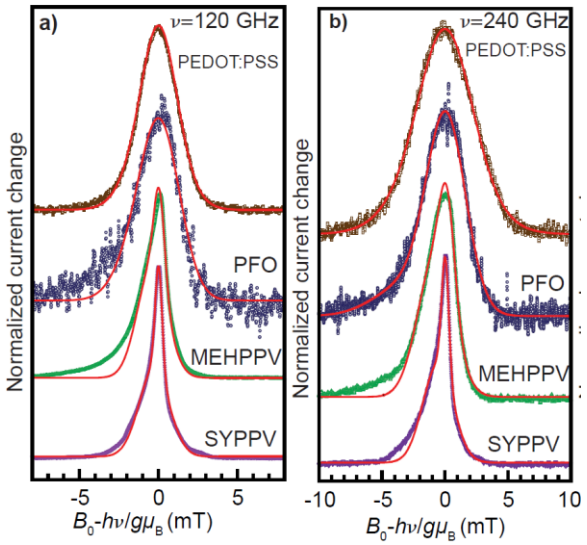

Fig. 3: *Plots of the EDMR signals of PEDOT:PSS, PFO, MEH-PPV, and SY-PPV for applied frequencies of 120GHz and 240GHz, respectively, as well as the results of the global fits of the multi-frequency measurements which were obtained from simultaneous fits of the displayed data as well as EDMR data measured and various high- and low-frequency conditions. The data shows that the assumption that charge carriers possess homogeneously broadened magnetic resonance lines due to isotropic charge carrier states is refuted by the high-magnetic field data obtained for MEH-PPV, PFO, and SY-PPV. The deviations of the global fits (the red lines) show that g-tensors and their anisotropies can be profoundly important for magneto-optoelectronic materials properties of these investigated thin-film layers (adapted from Ref. [9]).*

We have conducted measurements similar to those for PEDOT:PSS for MEH-PPV, SY-PPV, and PFO. Similarly as for PEDOT:PSS, the EDMR spectra at magnetic fields below 4T fit the model predicting two Gaussian lines excellently. However, in contrast to PEDOT:PSS, the

global fit of all other polymers show significant deviations from this spectral shape above 4T as revealed by Fig. 3, which displays the EDMR lines measured for all four polymer materials for an applied frequency of 120GHz (a) and 240GHz (b). This line shape deviation from Gaussian functions is due to the anisotropic g-tensors of the electronic states which cause the observed signals. Since *g*-factor anisotropies are caused by anisotropies of the associated electronic states, the spectra shown in Fig. 3 provide insights into the nature of electron and hole wave functions. In order to reveal these insights, we have used predictions of density functional theory for the wavefunctions of MEH-PPV polaron states in order to calculate the expected EDMR spectra [10]. Using these calculations and the resulting predictions of EDMR spectra, a comparison with experimental EDMR spectra can be made. Thus, experimental EDMR data can be used to scrutinize theoretical models. For the DFT predicted electron and hole states in MEH-PPV that are plotted in Fig. 4, accurate predictions for high-field EDMR spectra could be made and the confirmation of these predictions [10] did not only experimentally confirm the calculations illustrated in Fig. 4, they also allowed for the identification of the observed EDMR resonances with electron (LUMO) and hole (HOMO) polarons states.

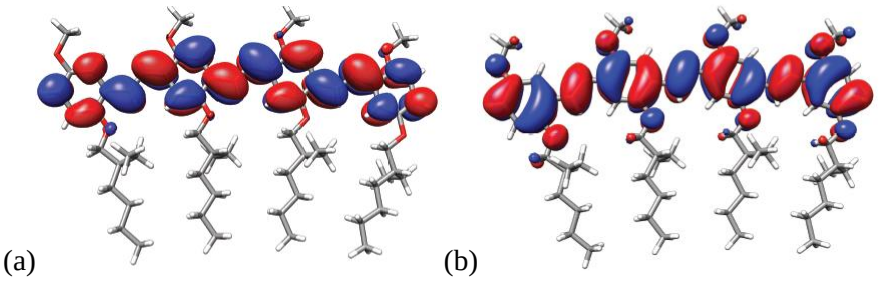

Fig. 4: *Plots of the single-carrier probability density of the LUMO (a) and HOMO (b) of an MEH-PPV model of four monomer units (adapted from Ref. [10]).*

Future Plans

Following the studies described in the context of Figs. 2 through 4, EDMR spectroscopy at different frequencies and magnetic field strengths will be carried out in order to separately determine SOC induced *g*-strain and HFI around CoRMQEs. As for the multi-frequency EDMR study of charge carrier states in MEH-PPV [10], it is aimed to obtain information about the wavefunctions of CoRMQEs such as exciton-polaron complexes and applications of these techniques for the understanding of the electronic and optoelectronic materials behavior [11-13] are anticipated.

For CoRMQEs that emerge under strong drive conditions (when spin-collectivity appears), it is planned to explore the influence that various quantum mechanical effects such as level-crossings, multi-photon transitions, and Bloch-Siegert shifts can have on the measured materials conductivity.

References

[1] W. J. Baker et al., *Phys. Rev. B* **84,** 165205 (2011).

[2] R. C. Roundy & M. E. Raikh, *Phys. Rev. B* **88**, 125206 (2013).

[3] D. P. Waters et al., *Nature Physics* **11** (11), 910 (2015).

[4] G. Joshi et al., *Appl. Phys. Lett.* **109**, 103303 (2016).

[5] R. Miller et al., *Phys. Rev. B* **94**, 214202 (2016).

Published Journal Articles of BES sponsored research in 2017-2019

[6] S. Jamali, G. Joshi, H. Malissa, J. M. Lupton, C. Boehme, Monolithic OLED-microwire devices for ultrastrong magnetic resonant excitation, *Nano Lett.* **17** (8), 4648 (2017). http://dx.doi.org/10.1021/acs.nanolett.7b01135

[7] M. Y. Teferi, J. Ogle, G. Joshi, H. Malissa, S. Jamali, D. L., Baird, J. M. Lupton, L. Whittaker-Brooks, and C. Boehme, Tuning effective hyperfine fields in PEDOT:PSS thin films by doping, Phys. Rev. B 98, 241201(R) (2018). https://dx.doi.org/10.1103/PhysRevB.98.241201

[8] Joshi, M. Y. Teferi, S. Jamali, M. Groesbeck, J. van Tol, R. McLaughlin, Z. V. Vardeny, J. M. Lupton, H. Malissa, C. Boehme, High-Field Magnetoresistance of Organic Semiconductors, *Phys. Rev. Applied* **10** (2), 024008 (2018). https://doi.org/10.1103/PhysRevApplied.10.024008

[9] G. Joshi, M. Y. Teferi, R. Miller, S. Jamali, D. L. Baird, J. v. Tol, H. Malissa, J. M. Lupton, C. Boehme, Isotropic effective charge-carrier g-tensors in PEDOT:PSS, *J. Am. Chem. Soc.* **140**, 6758 (2018). https://doi.org/10.1021/jacs.8b03069

[10] H. Malissa, R. Miller, D. L. Baird, S. Jamali, G. Joshi, M. Bursch, S. Grimme, J. van Tol, J. M. Lupton, and C. Boehme, Revealing weak spin-orbit coupling effects on charge carriers in a π-conjugated polymer, *Phys. Rev, B* **97**, 161201 (R) (2018) (Rapid Communication). https://doi.org/10.1103/PhysRevB.97.161201

[11] H. Kraus, S. Bange, F. Frunder, U. Scherf, C. Boehme, and J. M. Lupton, Visualizing the radical-pair mechanism of molecular magnetic-field effects by magnetic resonance-induced electrofluorescence to electrophosphorescence interconversion, *Phys. Rev. B* **95**, 241201(R) (2017). (Rapid Communication) https://doi.org/10.1103/PhysRevB.95.241201

[12] C. Boehme, H. Malissa, Electrically Detected Magnetic Resonance Spectroscopy, *eMagRes* **6**, 83 (2017).

[13] Z. Zhang, H. Li, R. Miller, S. Jamali, H. Malissa, Q. Zhang, J. Yin, C. Boehme, J. C. Grossman, and S. Ren, Freestanding organic charge-transfer conformal electronics, *Nano Lett.* **18**, 4346 (2018). https://pubs.acs.org/doi/abs/10.1021/acs.nanolett.8b01342

Light-matter interaction phenomena using subwavelength engineering of material properties

PI: Igal Brener
Team members: Michael B. Sinclair, Willie Luk, Sheng Liu, Salvatore Campione, John Klem, Michael Goldflam

Sandia National Laboratories, Albuquerque, NM 87185, USA

Program Scope

Nanostructured materials offer new opportunities to rewrite the laws of light–matter interaction as they are customarily applied to bulk materials. This project focuses on such emergent behavior, with an emphasis on metamaterials coupled to semiconductors. We intend to demonstrate that this combination of nanofabricated structures and materials enables unique new ways to control the flow of energy between photons, phonons, and electrons that are not possible with natural materials and thus will lead to phenomena with broad impact, ranging from fundamental science to technologically relevant applications. For the upcoming period, we propose to focus our efforts on four topics. *Metasurface-Mediated Photon Emission* will utilize dielectric metasurfaces and study the influence of resonator mode structure and resonator–resonator coupling on the emission properties of quantum emitters embedded within the resonators. *Strong Coupling to Metamaterials: Impact on Condensed Matter Excitations* will study how metasurfaces can be used to manipulate the microscopic properties of semiconductor materials, such as phonon energies and carrier distributions. *Optical Nonlinearities from Coupled Metamaterials-Semiconductors* will investigate the rich new nonlinear optical physics that can be obtained when the unique electromagnetic behavior of dielectric metasurfaces is combined with nonlinear semiconductor materials. *Ultrafast and Spatiotemporal Phenomena in Metamaterials* will explore novel transient behavior that can be achieved through ultrafast modulation of constituent material properties. To achieve these goals, our program combines state-of-the-art capabilities in: semiconductor growth in the III-V and III-Nitride systems; semiconductor physics and many-body theory; micro- and nano-lithography; spectroscopic and ultrafast characterization; and full-wave electromagnetic simulation.

1. Linear and Nonlinear Optical Properties of All-Dielectric Metasurfaces

All-dielectric metamaterials consisting of arrays of high-index, subwavelength-size Mie resonators have attracted much attention recently due to their much lower loss at optical frequencies compared with their metallic counterparts. Moreover, these Mie resonators interact strongly with both electric and magnetic fields and therefore enable manipulation of the electromagnetic permittivity and permeability. Great success has been achieved in using these metamaterials for nonlinear optical processes, ultrathin optical components and advanced wavefront engineering. Leveraging our capabilities in the design and nanofabrication of dielectric metasurfaces using III-V semiconductors [1], we have expanded our research using these metasurfaces for nonlinear optics and coupling to emitters.

1.1 Nonlinear Optics with III-V Dielectric Metasurfaces

Previously, we had already demonstrated strong resonantly enhanced second-harmonic generation with conversion efficiencies exceeding 10^{-5} from these III-V metamaterials. [2] Furthermore, due

to the direct bandgap of the constituent semiconductors, photoexcited carriers can also induce other types of strong nonlinearities such as transient saturation and/or resonance shift on an ultrafast timescale. [3] In the last two years we have turned our attention to more "extreme" nonlinear optics, i.e., simultaneous, multi-order nonlinear processes occurring in such dielectric metasurface.

An example of this multiple order nonlinear optical behavior is shown in Fig. 1 [4]. When a GaAs Mie metasurface is pumped near its magnetic and electric dipole resonant wavelengths using two femtosecond pump lasers (1570 and 1240nm), we observe a multitude of peaks in the nonlinear emission spectra. After careful delay and pump power dependence studies, we assign these to the processes specified in Fig. 1(b): some come from harmonic generation from the individual pump beams whereas others arise from second, third or higher dual-pump nonlinear effects. The different nonlinear processes at play are displayed at the bottom of Fig. 1(b). Remarkably, and unlike nonlinear optics in conventional materials, all these processes occur simultaneously and without the need for phase matching, due to the nanoscale thickness of our sample and the moderate Q of the resonances.

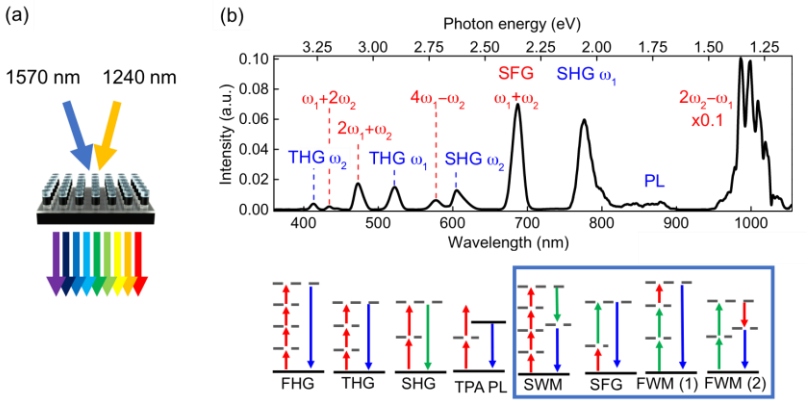

Figure 1: a) Schematic of the GaAs metasurface pumped with two different lasers. (b) top: measured nonlinear spectra; bottom: diagrams showing the different nonlinear optical processes measured.

1.2 Coupling between III-V Dielectric Metasurfaces and Emitters

Embedding high quality emitters *inside* dielectric metasurfaces can enable new directions in light matter interaction as well as provide new paths for emission and far-field control. We have recently created dielectric metasurfaces with both symmetric and symmetry-broken design [5] from III-V heterostructures that contain high-quality epitaxial InAs quantum dots. [6] An electron micrograph of the symmetry-broken version of this metasurface is shown in Fig. 2(a) and a schematic of the layers in Fig. 2(b). Also shown in the latter, is the calculated reflectivity spectra showing two sharp Fano features resulting from the mode coupling between a bright in-plane electric or

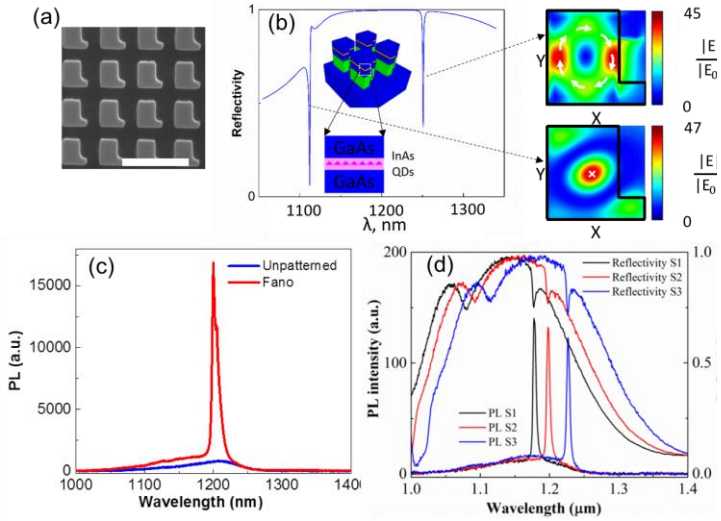

Figure 2. (a) SEM of a GaAs symmetry broken metasurface that couples in and out plane Mie dipole modes. (b) calculated reflectivity spectra. (c) photoluminescence spectra of the QDs with and without spectral overlap to the Fano resonances shown in (b). (d) different scaling factors of the metasurface.

magnetic dipole mode, and the corresponding "dark" out-of-plane dipole mode. When these sharp Fano features spectrally overlap the emission of the quantum dots, the photoluminescence spectra is enhanced significantly at the corresponding narrow spectral feature. This behavior is scalable, as shown in Fig. 2(d). Other interesting phenomena we studied were the far-field radiation pattern reshaping occurring due to the different symmetry of the nanoresonators and the metasurface array configuration. [6]

2. Semiconductor Hyperbolic Metamaterials and Epsilon Near Zero Phenomena

Building on previous studies of epsilon-near-zero material using indium tin oxide, we studied the quantum limit of epsilon-near-zero behavior in two material systems: semiconductor heterostructures and high mobility conductive oxides. For the semiconductor heterostructure, we fabricated a superlattice of highly doped and undoped quantum wells. This structure belongs to a class of metamaterial called hyperbolic metamaterial that exhibit an unbounded constant frequency dispersion curve. The material is highly anisotropic and therefore the epsilon-near-zero energies for in-plane and out-of-plane are at different. On a more fundamental level, what is the proper way to connect the permittivity function of the quantum well system with that of the effective medium model? In a recently published paper [7] we addressed this question and showed that the origin of a prominent absorption feature observed experimentally arises due to an epsilon-near-zero effect of the out-of-plane permittivity. For the conductive oxide system, we have found that the ability to create high mobility oxide samples has created an opportunity to explore nonlocal effects [8] optically, for the first time in a 11nm thick CdO film. Related to this work is our prior work exploiting the perfect absorption property of an epsilon-near-zero mode to enable femtosecond optical switching: using a pump laser at the perfect absorption wavelength we modified the plasma frequency of the electrons on a femtosecond time scale. The sudden change in the plasma frequency allows reflective switch from 0 to near 100% in ~100fs time scale. [9]

Future Plans

Our activities will proceed along the following directions:

i) *Metasurface-Mediated Photon Emission:* we will continue to explore other types of emitters coupled to metasurfaces such as excitons in two dimensional material and conventional III-V quantum wells.

ii) *Strong Coupling to Metamaterials: Impact on Condensed Matter Excitations:* we'll continue to explore the effect of metamaterials on phonons in several condensed matter systems

iii) *Optical Nonlinearities from Coupled Metamaterials-Semiconductors:* We plan on combining Mie metasurfaces and resonant nonlinearities in Intersubband transitions. We also plan on investigating other optical nonlinearities using III-V all-dielectric metamaterials.

iv) *Ultrafast and Spatiotemporal Phenomena in Metamaterials:* using spatially and temporally structured pump beams, we plan tophotoexcite dielectric metamaterials built from direct bandgap semiconductors and study their transient optical behavior.

References

[1] S. Liu, G. A. Keeler, J. L. Reno, M. B. Sinclair, and I. Brener, Advanced Optical Materials **4**, 1457 (2016).

[2] S. Liu, M. B. Sinclair, S. Saravi, G. A. Keeler, Y. Yang, J. Reno, G. M. Peake, F. Setzpfandt, I. Staude, T. Pertsch, and I. Brener, Nano Lett. **16**, 5426 (2016).

[3] M. R. Shcherbakov, S. Liu, V. V. Zubyuk, A. Vaskin, P. P. Vabishchevich, G. Keeler, T. Pertsch, T. V. Dolgova, I. Staude, I. Brener, and A. A. Fedyanin, Nature Communications **8**, 17 (2017).

[4] S. Liu, P. P. Vabishchevich, A. Vaskin, J. L. Reno, G. A. Keeler, M. B. Sinclair, I. Staude, and I. Brener, Nature Communications 1 (2018).

[5] S. Campione, S. Liu, L. I. Basilio, L. K. Warne, W. L. Langston, T. S. Luk, J. R. Wendt, J. L. Reno, G. A. Keeler, I. Brener, and M. B. Sinclair, ACS Photonics **3**, 2362 (2016).

[6] S. Liu, A. Vaskin, S. Addamane, B. Leung, M.-C. Tsai, Y. Yang, P. P. Vabishchevich, G. A. Keeler, G. Wang, X. He, Y. Kim, N. F. Hartmann, H. Htoon, S. K. Doorn, M. Zilk, T. Pertsch, G. Balakrishnan, M. B. Sinclair, I. Staude, and I. Brener, Nano Lett. **18**, 6906 (2018).

[7] I. Montano, S. Campione, J. F. Klem, T. E. Beechem, O. Wolf, M. B. Sinclair, and T. S. Luk, Nature Publishing Group 1 (2018).

[8] D. de Ceglia, M. Scalora, M. A. Vincenti, S. Campione, K. kelley, E. L. Runnerstrom, J.-P. Maria, G. A. Keeler, and T. S. Luk, Nature Publishing Group 1 (2018).

[9] Y. Yang, K. Kelley, E. Sachet, S. Campione, T. S. Luk, J.-P. Maria, M. B. Sinclair, and I. Brener, Nat. Phot. 1 (2017).

Two-year list of publications supported by BES

1. *"Light-Emitting Metasurfaces: Simultaneous Control of Spontaneous Emission and Far-Field Radiation",* Sheng Liu, Aleksandr Vaskin, Sadhvikas Addamane, Benjamin Leung, Miao-Chan Tsai, Yuanmu Yang, Polina P. Vabishchevich, Gordon A. Keeler, George Wang, Xiaowei He, Younghee Kim, Nicolai F. Hartmann, Han Htoon, Stephen K. Doorn, Matthias Zilk, Thomas Pertsch, Ganesh Balakrishnan, Michael B. Sinclair, Isabelle Staude, and Igal Brener, Nano Letters **18,** 6906 **(**2018)
2. "Semiconductor Hyperbolic Metamaterials at the Quantum Limit," I. Montaño, S. Campione, J. F. Klem, T. E. Beechem, O. Wolf, M. B. Sinclair, and T. S. Luk, Scientific Reports **8**, 16694 (2018).
3. *"Nonlinear frequency conversion in optical nanoantennas and metasurfaces: materials evolution and fabrication",* Mohsen Rahmani, Giuseppe Leo, Igal Brener, Anatoly Zayats, Stefan Maier, Costantino De Angelis, Hoe Tan, Valerio Flavio Gili, Fouad Karouta, Rupert Oulton, Kaushal Vora, Mykhaylo Lysevych, Isabelle Staude, Lei Xu, Andrey Miroshnichenko, Chennupati Jagadish, Dragomir Neshev, Opto-Electronic Advances **1**, 180021 (2018)
4. *"A metasurface optical modulator using voltage-controlled population of quantum well states",* Raktim Sarma, Salvatore Campione, Michael Goldflam, Joshua Shank, Jinhyun Noh, Loan T Le, Michael D Lange, Peide D Ye, Joel Wendt, Isaac Ruiz, Stephen W Howell, Michael Sinclair, Michael C Wanke, Igal Brener, Appl. Phys. Lett. **13**, 201101 (2018)
5. *"Difference-Frequency Generation in Polaritonic Intersubband Nonlinear Metasurfaces",* Yingnan Liu, Jongwon Lee, Stephen March, Nishant Nookala, Daniele Palaferri, John F Klem, Seth R Bank, Igal Brener, Mikhail A Belkin, Advanced Optical Materials, 1800681(2018).
6. *"Quenching of Infrared-Active Optical Phonons in Nanolayers of Crystalline Materials by Graphene Surface Plasmons",* Peter Q. Liu, John Reno, Igal Brener, ACS Photonics **5**, 2706 (2018)
7. "*Strongly interacting dipolar-polaritons in optical waveguides",* Itamar Rosenberg, Dror Liran, Yotam Mazuz-Harpaz, Kenneth West, Loren Pfeiffer and Ronen Rapapport, Science Advances 2018, DOI: 10.1126/sciadv.aat8880
8. "*Mid-infrared second-harmonic generation in ultra-thin plasmonic metasurfaces without a full-metal backplane*," Nishant Nookala, Jiaming Xu, Omri Wolf, Stephen March, Raktim Sarma, Seth Bank, John Klem, Igal Brener, and Mikhail Belkin, Applied Physics B **128,** 132 (2018).
9. "*An all-dielectric metasurface as a broadband optical frequency mixer*," Sheng Liu, Polina P, Vabishchevich, Aleksandr Vaskin, John L Reno, Gordon A Keeler, Michael B Sinclair, Isabelle Staude, and Igal Brener, *Nature Communications* **9**, 2507 (2018).
10. *"Viscoelastic optical nonlocality of low-loss epsilon-near-zero nanofilms,"* Domenico de Ceglia, Michael Scalora, Maria A. Vincenti, Salvatore Campione, Kyle Kelley, Evan L. Runnerstrom, Jon-Paul Maria, Gordon A. Keeler & Ting S. Luk, Scientific Reports **8**, 9335 (2018)
11. *"Light Emission by Nonequilibrium Bodies: Local Kirchhoff Law",* J.-J. Greffet, P. Bouchon, G. Brucoli, & F. Marquier, Phys. Rev. X **8,** 021008 (2018).
12. "*Efficient photoconductive terahertz detector with all-dielectric optical metasurface*," O Mitrofanov, T Siday, RJ Thompson, TS Luk, I Brener, and JL Reno, *APL Photonics* 3, 051703 (2018).
13. "*Enhanced Second-Harmonic Generation Using Broken Symmetry III–V Semiconductor Fano Metasurfaces*," Polina P. Vabishchevich, Sheng Liu, Michael B. Sinclair, Gordon A. Keeler, Gregory M. Peake, and Igal Brener *ACS Photonics* 5, 1685 **(**2018).
14. "*Polarization-Dependent Second Harmonic Diffraction from Resonant GaAs Metasurfaces*," Franz J. F. Löchner, Anna N. Fedotova, Sheng Liu, Gordon A. Keeler, Gregory M. Peake, Sina Saravi, Maxim

R. Shcherbakov, Sven Burger, Andrey A. Fedyanin, Igal Brener, Thomas Pertsch, Frank Setzpfandt, and Isabelle Staude, *ACS Photonics* 5, 1786 (2018).

15. "*Near-field spectroscopy and tuning of sub-surface modes in plasmonic terahertz resonators*," O. Mitrofanov, Y. Todorov, D. Gacemi, A. Mottaghizadeh, C. Sirtori, I. Brener, and J. L. Reno, " Opt. Express 26, 7437-7450 (2018).

16. "*Multipolar second harmonic generation in a symmetric nonlinear metamaterial,*" O Wolf, S Campione, Y Yang, and I Brener, Scientific Reports **7** (2017); doi: 10.1038/s41598-017-08039-1

17. *"Huygens' metasurfaces enabled by magnetic dipole resonance tuning in split dielectric nanoresonators*," Sheng Liu, Aleksandr Vaskin, Salvatore Campione, Omri Wolf, Michael B. Sinclair, John L. Reno, Gordon A. Keeler, Isabelle Staude, and Igal Brener, Publication Date (Web): Jun 7, 2017, DOI: 10.1021/acs.nanolett.7b01301

18. "*Solitary Oxygen Dopant Emission from Carbon Nanotubes Modified by Dielectric Metasurfaces*," Xuedan Ma, Anthony R. James, Nicolai F. Hartmann, Jon K. Baldwin, Jason Dominguez, Michael B. Sinclair, Ting S. Luk, Omri Wolf, Sheng Liu, Stephen K. Doorn, Han Htoon, and Igal Brener, ACS Nano, Just Accepted Manuscript, 23May17, DOI: 10.1021/acsnano.7b02951

19. "*Femtosecond optical polarization switching using a cadmium oxide-based perfect absorber*," Yuanmu Yang, Kyle Kelley, Edward Sachet, Salvatore Campione, Ting S. Luk, Jon-Paul Maria, Michael B. Sinclair & Igal Brener, Nature Photonics **11**, 390 (2017)

20. "*Ultrafast all-optical tuning of direct-gap semiconductor metasurfaces*," Maxim R Shcherbakov, Sheng Liu, Varvara V Zubyuk, Aleksandr Vaskin, Polina P Vabishchevich, Gordon Keeler, Thomas Pertsch, Tatyana V Dolgova, Isabelle Staude, Igal Brener, Andrey A Fedyanin, Nature Comm. **8**, 2017

21. *"Design, fabrication and characterization of a hybrid metal-dielectric nanoantenna with a single nanocrystal for directional single photon emission",* Moshe G. Harats, Nitzan Livneh, and Ronen Rapaport, Optical Materials Express **7**, 834 (2017)

22. *"Quantum emitters coupled to circular nanoantennas for high brightness quantum light sources",* Hamza Abudayyeh and Ronen Rapaport, Quantum Sci. Technol. **2** 034004 (2017) doi:10.1088/2058-9565/aa73e4

A Nonlinear Approach to Weyl Transport

Kenneth S. Burch, Boston College

Program Scope

The program focuses on exploring the optoelectronic properties of Weyl semimetals (WSM) to understand their dynamics crucial for energy efficient devices. Various optical techniques are employed: Raman scattering and nonlinear photocurrent generation to separate the role of band structure, phonons, defects, and topology.

Recent Progress

Broadband, efficient and fast conversion of light to electricity is crucial for sensing and clean energy. An alternative means to this is the bulk photo-voltaic effect (BPVE), a second-order non-linear optical effect which intrinsically converts light into electrical current. The PI has developed a new means to probe the intrinsic nonlinearity of Weyl semimetals, resulting from their divergent Berry curvature. Specifically, the Burch group has demonstrated the largest BPVE ever observed. Furthermore, this was in mid-infrared where the BPVE has never been seen and could enable new mid-IR sensors and efficient conversion of thermal radiation to electricity. To enable this, the PI developed new microscopic devices of the Weyl semimetal TaAs, combined with careful study of the symmetry (i.e., polarization and crystallographic direction dependence).

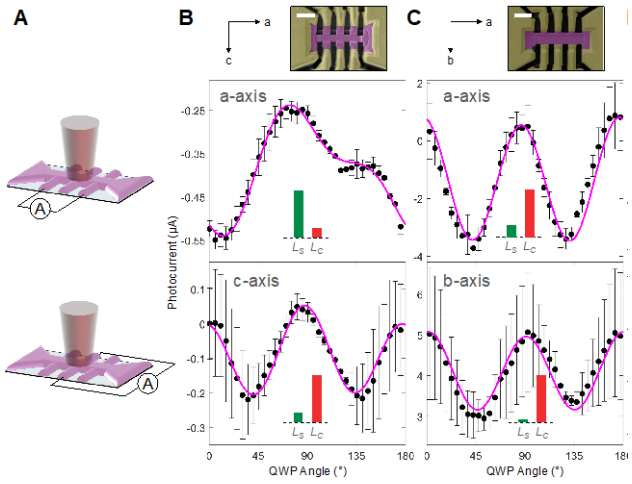

Figure 1: (A) Diagram of the device indicating the axis along which the current is probed. (B,C) Upper panel, SEM image of the measured device and crystal orientation. Scale bars are 5 μm. Middle/Lower panel, data (black dots) for photocurrent measured along the longitudinal/transverse axis of the Hall bar. As expected for devices with c- axis in the plane, the current along the a-axis is dominated by shift current response (sin(4φ) - LS). In all other cases the term due to thermal response (cos(4φ) - LC), is largest.

As shown in Figure 1A, the photocurrent was measured along two distinct crystallographic axes, simultaneously, as the polarization was varied using a quarter wave plate. In Figure 1B the response from a sample with the broken inversion axes in the plane is shown. As expected by symmetry the thermal terms contribute along both axes and depend only on the direction of the linear polarization (i.e., as cosine terms). However, the nonlinear response requires the mixing of

Ex and Ey electric fields, and thus only appears as a sine term. Furthermore, as expected it only is revealed when the broken inversion is in the plane, and the current is normal to it. Figure 1c further demonstrates the difference between BPVE and photothermal effects, where we show the response from a device that does not have the broken inversion in the plane, and thus does not reveal any sine term. Using this we separated the intrinsic nonlinear photocurrent generation from the extrinsic photothermal effects, revealing a colossal BPVE in the Mid-IR. This discovery results from combining recent developments in Weyl semimetals, focused-ion beam fabrication, and theoretical works suggesting a connection between the BPVE and topology. The magnitude and the wavelength range of the assigned shift may impact optical detectors, clean energy, and topology, and demonstrates the utility of Weyl semimetals for practical applications (currently in-press at Nature Materials).

Future Plans

We are currently investigating two different aspects of the transport in Weyl semimetals. First, we have begun studies of the wavelength dependence of the non-linear response in the hopes of uncovering more information about the role of Berry curvature and scattering. Also, we have expanded to measure a similar compound NbAs and a type-II Weyl semimetal WP2. The latter is quite exciting as it appears to reveal hydrodynamic transport as well as an enormous resistance ration exceeding 25000 (see references). Close collaboration with Prineha Narang (Harvard) enables us to carefully separate the different contributions to the Raman and nonlinear response. Indeed, she has developed means to rapidly calculate the phonon-phonon, electron-phonon, and dispersions for both as a function of temperature. By comparing the temperature dependence of the Raman scattering in WP2, NbAs and TaAs we should uncover the origins of the differences in their mobility, as well as provide insights into the hydrodynamic behavior. Also, Narang's group is working to develop new codes to calculate the role of scattering in the shift current (i.e., BPVE) in these materials. By comparing with our measurements (as well as potentially with temperature) and with the insights gained from our studies of their scattering processes, we aim to optimize the materials for future optical devices.

References

J. Coulter et al, Phys. Rev. B 98, 115130 (2018)

J. Gooth et al, arXiv:1706.05925

A. Jaoui et al, npj Quant Mater **3** 64 (2018)

Publications

"Colossal Mid-Infrared Bulk Photovoltaic Effect in a type-I Weyl Semimetal", G. B. Osterhoudt, L. K. Diebel, X. Yang, J. Stanco, X. Huang, B. Shen, N. Ni, P. Moll, Y. Ran, and K. S. Burch, Nature Materials (in press) arXiv:1712.04951, 2019.

Fundamental Studies on Heat Conduction in Polymers

Gang Chen, Mechanical Engineering Department, Massachusetts Institute of Technology

Program Scope

This project aims to investigate the conduction of heat in polymer structures. Although most polymers have a thermal conductivity within a range of 0.1-0.5 W/m-K. Our current fundamental understanding in the underlying mechanism of heat conduction in polymers remains very poor. This project aims to provide insight on such unanswered questions by developing a fundamental understanding of heat conduction along an individual molecular chain as well as in amorphous polymers through both simulations and experiments. Progress made includes (1) achieving high thermal conductivity of P3HT films obtained via organic chemical vapor deposition and controlling molecular structures in processing, (2) improving understanding of the origin of high thermal conductivity of mechanical polyethylene films, and (3) simulation of thermal conductivity of semicrystalline polymers.

Recent Progress

Molecularly Engineered Polymer with High Thermal Conductivity

Conjugated polymers are potential candidates for good thermal conductors, as a result of the rigid conjugated backbone and the strong intermolecular π-π stacking interactions. Whereas the carbon-carbon single bonds (C-C, ~347 kJ/mole)[1] are prevalent in diamond and stretched polyethylene which has shown ultrahigh thermal conductivities (~ 2000 W/m-K for diamond[2] and ~104 W/m-K for stretched polyethylene[3]), the conjugated double bonds (C=C, ~610 kJ/mole) are nearly twice as strong, and thus are expected to dramatically improve phonon transport along the polymer chains[4]. Furthermore, the π-π stacking interaction between the chains is approximately 10-100 times

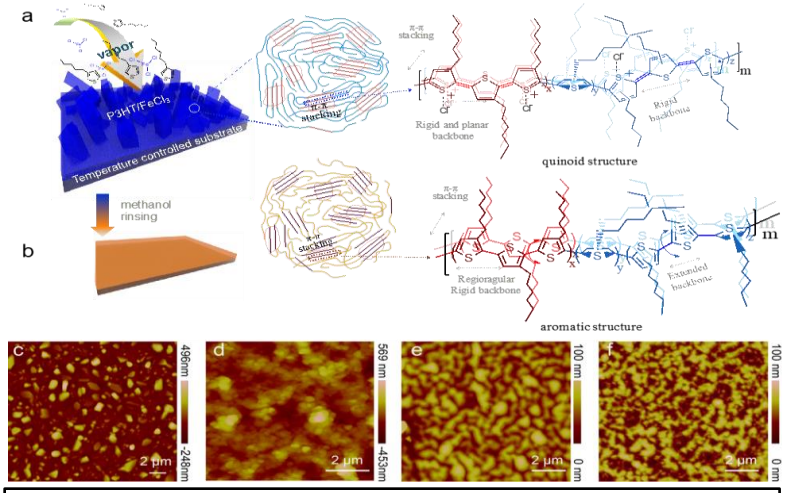

Fig. 1. oCVD synthesis process, molecular structure and film morphology. (a) Left side: the growth process of P3HT/ $FeCl_3$ thin films from vapor phase. Middle: schematics of the microstructure of a doped P3HT film. Right side: the extended chain in quinoid form grown on $FeCl_3$. **(b)** P3HT thin film. Left side: Methanol rinsing dissolve the excess oxidant. Middle: schematics of the microstructure of a dedoped P3HT film. Unlike coiled and entangled chains in common polymers, the extended chain of the dedoped P3HT is shown in right side. **(c-f)** Films morphology characterized by tapping-mode AFM: **(c)** 45 °C-grown P3HT/$FeCl_3$ (40 min-polymerization) **(d)** 85 °C-grown P3HT/$FeCl_3$ (40 min-polymerization). **(e)** De-doped 45 °C-grown P3HT. **(f)** Dedoped 85 °C-grown P3HT[7].

stronger than the vdW interactions (weak vdW, ~0.4-4 kJ/mole)[5], which could substantially enhance phonon transport across the chains. However, traditional conjugated polymers are characterized by low thermal conductivities (~0.2 W/m-K) similar to non-conjugated polymers. Researchers hypothesize that such low thermal conductivity is due to strong phonon scatterings by chain distortions and entanglements, etc[4,6]. To realize the full potential of conjugated polymers, the critical challenge that remains is how to precisely control the conformation of the planar conjugated backbones together with the interchain π-π stacking at the molecular level.

We have achieved significantly higher conductivity in conjugated poly(3-hexylthiophene) (P3HT) thin film fabricated using oxidative chemical vapor deposition (oCVD) by controlling molecular configurations using substrate temperature. This all-dry vapor-phase technique synthesizes monomers directly into a polymeric thin film via step growth polymerization. (Fig. 1). We show that ordered structures with rigid backbones can be produced by oCVD with stacking in the transverse direction via π-π interactions (Fig. 1[GC1][BL2][BL3]). By simultaneously harnessing the strong conjugated bonds along polymer chains and the π-π interactions between them, we obtain a record-high thermal conductivity of 2.2 W/m-K near room temperature in P3HT films.

<u>Understanding Origin of High Thermal Conductivity of Mechanical Stretched Polyethylene Films</u>

Our past studies had suggested that individual polyethylene chains have high, even divergent thermal conductivity. We have demonstrated ultra-drawn polyethylene nanowire with thermal conductivity as high as 104 W/m-K [3] and also have developed a manufacturing process to produce mechanical stretched polyethylene thin films[8] and measured thermal conductivity over 60 W/m-K at 100 draw ratio (Fig. 2a). However, the mechanisms behind the high thermal conductivity were not clear. During the past two years, we further established the reliability of our home built thermal conductivity measurement system, and continued studying thermal conductivity mechanisms leading to such high thermal conductivity. Combining careful structural characterization with modeling (Fig. 2b), we found that the amorphous region after the drawing is no longer composed of random disordered chains, but rather has developed some degrees of the orientation order with more extended and aligned chains. The extracted high thermal conductivity of the amorphous region with some molecular orientation is much higher than that of oriented polythiophene fibers grown in a template[9].

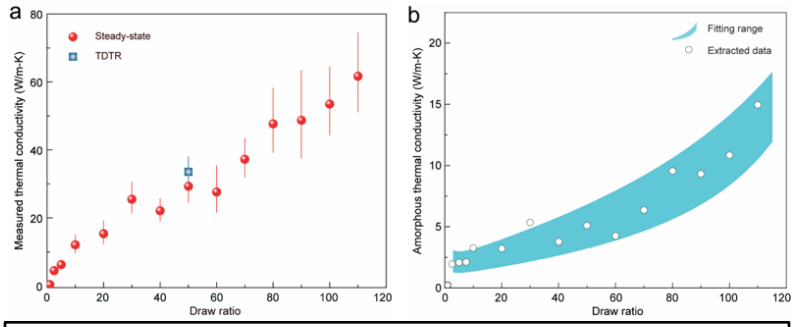

Fig. 2 Measured and computed thermal conductivities for the polymer films. **(a)** Measured total thermal conductivity as a function of the draw ratio. The red spheres were obtained from the steady-state experiments. **(b)** Extracted amorphous thermal conductivity values.

Thermal Transport in Semicrystalline Polymer Using Molecular Dynamics.

To better understand the high thermal conductivity in ultradrawn polyethylene, we study the contribution of amorphous polyethylene in different morphologies to thermal transport using molecular dynamics simulations. The polyethylene in different configurations is generated by the Enhanced Monte Carlo (EMC) method[10]. Thermal conductivity is calculated using nonequilibrium molecular dynamics simulations. An illustration of our calculation domain is shown in Fig. 3a, where we have two crystalline lamellar on the boundaries and the amorphous interlamellar regime. We take into account three types of chain topologies in the interlamellar region, i.e., bridges, loops, and tails. Among these, the bridge is defined as the segments connecting the crystalline stems throughout the interlamellar region; the loop is defined to connect crystalline stems at the same side; and for the tail, one side of it is connected to the crystalline stems while the other side terminates. We group the calculated results into three regions: (I) at a low crystallinity, for example, crystallinity around 18%, their numbers of bridge chains (Bn) are mainly in the range of 1–4. In these configurations, the effective thermal conductivity of the entire amorphous regions can be roughly treated the same as that of the amorphous polymer; (II) at an intermediate crystallinity, i.e., between 50% and 72%, and the Bn is in the range of 3–15. The role of bridges and their interaction with atoms in loops and tails become important, and the effective thermal conductivity increases linearly with the Bn. This regime starts to deviate from previous models assuming a homogenous interlamellar region; (III) at a high crystallinity (more than 83%), the Bn can even achieve 27. Here heat transfer along bridges dominates so that the effective thermal conductivity increases linearly with Bn in a much larger slope. The results are shown in Fig. 3b. These results indicate that not only the crystallinity but also the number of bridges should be considered to estimate the effective thermal conductivity of semicrystalline polymer systems with high crystallinity. These results are in qualitative agreement with our experiment.

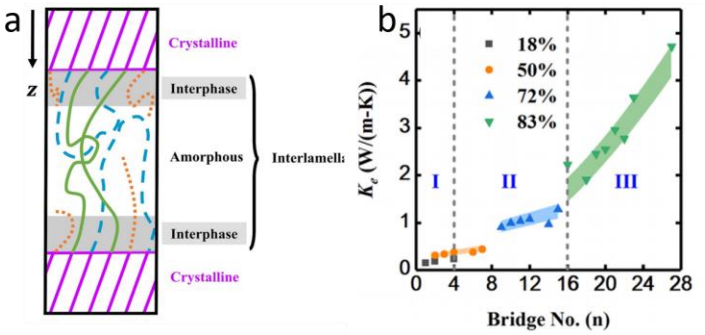

Fig. 3. Thermal conductivity of semicrystalline polyethylene with different crystallinity. (a) Schematic diagram of semicrystalline structure. Crystalline stems are denoted by purple slashes, bridges are denoted by green solid lines, loops are denoted by blue dashed lines, and tails are denoted by orange dotted lines. **(b)** Effective thermal conductivity (Ke) of the semicrystalline PE as a function of bridge number (Bn). Region I is for crystallinity ~18%, where the thermal conductivity of the interlamellar region can be roughly described by the pure amorphous thermal conductivity. Region II is for crystallinity between 50% and 72%, where Ke increases linearly with Bn. Region III for crystallinity above 83%, where Ke increases linearly with Bn in a much larger slope. Shaded regions are given by modified Takayanagi's model[11].

Future Plans

We plan to continue the fundamental theoretical and experimental studies on thermal conductivity of polymers. Simulation wise, we will exam thermal conductivity of different polymer structures, such as block copolymers and polymers with π–π bonds, kinks, and bifurcations in the polymer structure, using a combination of molecular dynamics, lattice dynamics, and density functional theories. Experimentally, we will focus more on improving the thermal conductivity of random polymers and polymer blends. Polymer blends have different channels for thermal transport because of the self-assembling and interaction when two different polymers meet, and their thermal conductivity can be much higher than either one of its components.

References

1. Ouellette, R. J., *Organic Chemistry : Structure, Mechanism, and Synthesis.* Elsevier, (2014).
2. Balandin, A. A., Thermal Properties of Graphene and Nanostructured Carbon Materials. *Nat. Mater.* **10,** 569–581 (2011).
3. Shen, S., Henry, A., Tong, J., Zheng, R. & Chen, G., Polyethylene Nanofibres with very High Thermal Conductivities. *Nat. Nanotechnol.* **5,** 251–255 (2010).
4. Zhang, T., Wu, X. & Luo, T., Polymer Nanofibers with Outstanding Thermal Conductivity and Thermal Stability: Fundamental Linkage between Molecular Characteristics and Macroscopic Thermal Properties. *J. Phys. Chem. C* **118,** 21148–21159 (2014).
5. Frieden, E. Non-covalent Interactions: Key to Biological Flexibility and Specificity. *J. Chem. Educ.* **52,** 754 (1975).
6. Henry, A., Thermal Transport in Polymers, *Annu. Rev. Heat Transf.* **17,** 485–520 (2014).
7. Xu, Y. *et al.* Molecular Engineered Conjugated Polymer with High Thermal Conductivity. *Sci. Adv.* **4,** eaar3031 (2018).
8. Loomis, J. *et al.* Continuous Fabrication Platform for Highly Aligned Polymer Films. Technology **02,** 189–199 (2014).
9. Singh, V. *et al.* High thermal conductivity of chain-oriented amorphous polythiophene. *Nat. Nanotechnol.* **9,** 384–390 (2014).
10. in 't Veld, P. J. & Rutledge, G. C. Temperature-Dependent Elasticity of a Semicrystalline Interphase Composed of Freely Rotating Chains. *Macromolecules* **36,** 7358–7365 (2003).
11. Lu, T. *et al.* Thermal Transport in Semicrystalline Polyethylene by Molecular Dynamics Simulation. *J. Appl. Phys.* **123,** 015107 (2018).

Publications Resulting from This Project

1. Xu, Y., Wang, X., Zhou, J., Song, B., Jiang, Z., Lee, E. M. Y., Huberman, S., Gleason, K. K. & Chen, G. Molecular Engineered Conjugated[GC4] Polymer with High Thermal Conductivity. *Science Advances* 4: eaar3031 (2018).
2. Lu, T., Kim, K., Li, X., Zhou, Jun., Chen, G. & Liu, J., Thermal Transport in Semicrystalline Polyethylene by Molecular Dynamics Simulation. *Journal of Applied Physics* 123: 015107 (2018).

3. Tsurimaki, Yoichiro., Tong, J., Boriskin, V. N., Semenov, A., Ayzatsky, M. I., Machekhin, Y. P., Chen, G. & Boriskina, S. V., Topological Engineering of Interfacial Optical Tamm States for Highly Sensitive Near-singular-phase Optical Detection. *ACS Photonics* 5: 929-938 (2018).
4. Boriskina, S. V., Cooper, T. A., Zeng, L., Ni, G., Tong, J. K., Tsurimaki, Y., Huang, Y., Meroueh, L., Mahan. G. & Chen, G., Losses in Plasmonics: from Mitigating Energy Dissipation to Embracing Loss-enabled Functionalities. *Advances in Optics and Photonics* 9, 775-827 (2018).
5. Boriskina, S. V. & Tsurimaki, Y., Sensitive Singular-phase Optical Detection without Phase Measurements with Tamm Plasmons. *Journal of Physics: Condensed Matter* 30, 224003 (2018).

DOE award # DE-SC0002626, Massachusetts Institute of Technology
DOE award # DE-SC0014435, Rice University

Electrochemically-Driven Phase Transitions in Battery Storage Compounds

PIs: Yet-Ming Chiang[1], Ming Tang[2], co-PI: W. Craig Carter[1]
[1]Massachusetts Institute of Technology, Dept. of Materials Science and Engineering, Cambridge, MA 02139, ychiang@mit.edu
[2]Rice University, Dept. of Materials Science and Nanoengineering, 6100 Main Street, Houston, TX 77005, mt20@rice.edu

Program Scope

This abstract reports on activities conducted under a no-cost extension of the subject grant, during which the focus of this project pivoted from ion storage compounds to ion-conducting compounds (i.e., solid electrolytes) in which structure and phase transitions are central to the physical properties of interest. Specifically, the focus has been on cluster-based anti-perovskite compounds [1-3] for which first-principles calculations (including DFT and MD) at Virginia Commonwealth University (PI: Puru Jena) have been performed, and have revealed exciting transport and other properties. These cluster-ion anti-perovskites have the general formula Li_3AX or Na_3AX in which A=O,S and X=AlH_4, BH_4, BF_4. X can also include partial substitution with the halogens Cl, Br and I, for which anti-perovskite formulations have previously been established. None of the computed cluster-ion anti-perovskites have previously been synthesized experimentally. Thus the main scope of this effort has been to establish synthesis methods for anti-perovskites containing specific cluster-ions of interest, and if successful, to characterize their phase stability and transport properties.

Recent Progress

The hygroscopic nature common to all of the anti-perovskites in this compositional family, combined with the fact that a number of the starting materials are known strong oxidizers, dictated that all synthesis experiments be conducted completely within an argon-filled glove box (~0.1 ppm partial pressure each of oxygen and water), including heat treatments. For some starting materials, violent exothermic reactions were observed upon mixing or heating to <250°C in the inert gas environment; see *Safety Note* at the end of this report.

Previously, successful synthesis of three cluster-ion anti-perovskites have been reported in the literature: Na_2NO_2 [4], Na_3OCN [4], and $Na_2(NH_2)(BH_4)$ [5]. In the present work, we attempted the synthesis of 31 compounds of anti-perovskite stoichiometry. Figure 1 displays the successful/unsuccessful attempts, plotted against the highest phase purity obtained in the samples, characterized on the basis of Rietveld refinement of powder X-ray diffraction data. We were able to confirm the synthesis of Na_2NO_2 and $Na_2(NH_2)(BH_4)$ using similar methods as reported in the literature (Na_3OCN was not attempted). In addition, five new cluster-ion anti-perovskites were synthesized. As shown in Figure 1, a high level of phase purity (>85%) was observed ion all of the successfully synthesized compounds (in some cases, after multiple experiments with systematic improvements in method). More than 20 compositions of the anti-perovskite stoichiometry were attempted that did not crystallize in the anti-perovskite structure. Several trends were observed, as noted below.

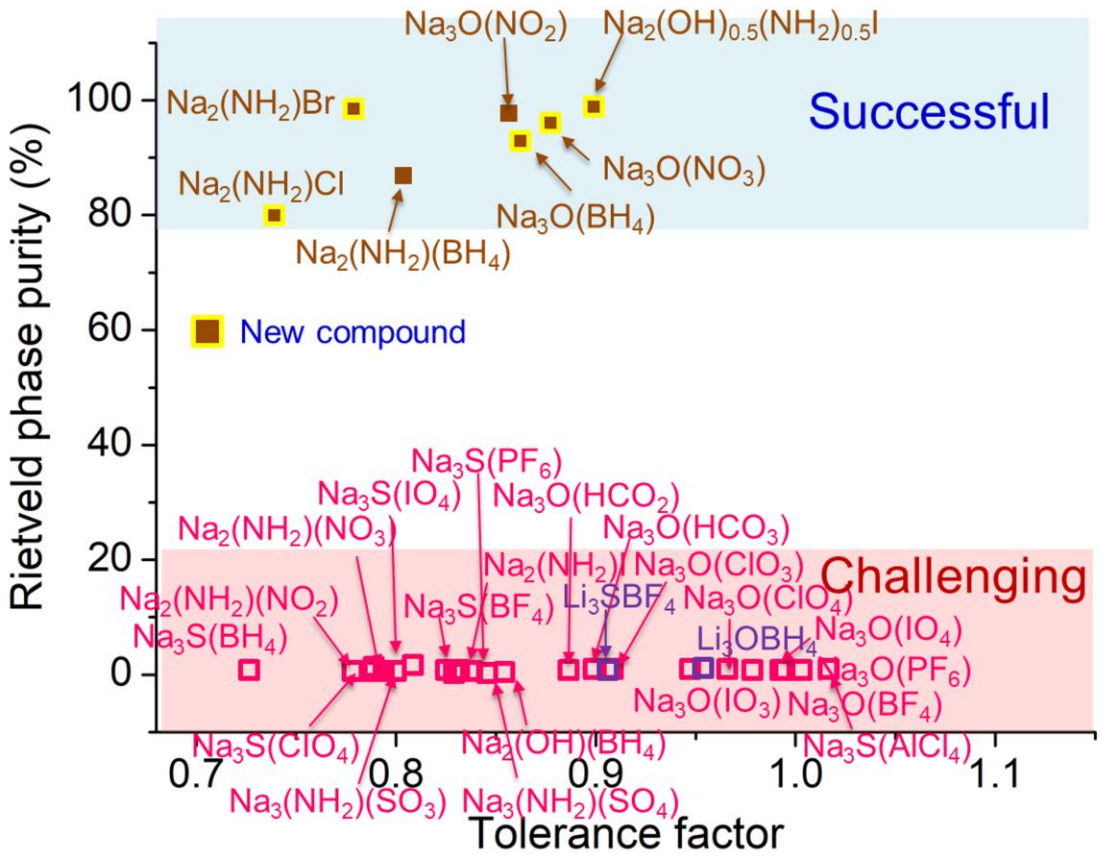

Figure 1. Summary of results for 31 attempted syntheses of cluster-ion anti-perovskites, plotted as anti-perovskite phase purity (from Rietveld refinement of powder XRD) against the computed Goldschmidt tolerance factor of the compound.

In all cases, we used a precursor containing the cluster ion of interest as a starting material in the synthesis reaction: $LiBH_4$, $NaBH_4$, $NaNH_2$ or $NaNO_2$. The synthesis temperatures ranged from 140°C to 260°C. No Li-based cluster-ion anti-perovskites were successfully synthesized using $LiBH_4$, we attempted to produce the compounds described in refs. [1-3]. Below the decomposition of this precursor (275°C), no reactivity was observed (by XRD); near and above its decomposition temperature, Li_3B was observed in all three cases. Li_3B is a known decomposition product of $LiBH_4$. Alternative Li salts and potentially hydrogen atmosphere may be required to stabilize compositions containing both Li and BH_4.

In contrast, all of the 5 new compounds synthesized to date are in the Na family, and include the anions NO_2, NH_2 and BH_4. Two include the BH_4 anion, $Na_3O(BH_4)$ and Na2(NH2)(BH4), and were synthesized using NaBH4 as a starting component. We believe that success with this precursor compared to LiBH4 may be associated with the greater stability of $NaBH_4$ (decomposition temperature 300°C); these two anti-perovskites were synthesized at 220°C. The remaining Na cluster-ion anti-perovskites were synthesized using $NaNH_2$ or $NaNO_2$ as a precursor. An example of an XRD pattern for $Na_3O(BH_4)$ at >99% phase purity is shown in Figure 2.

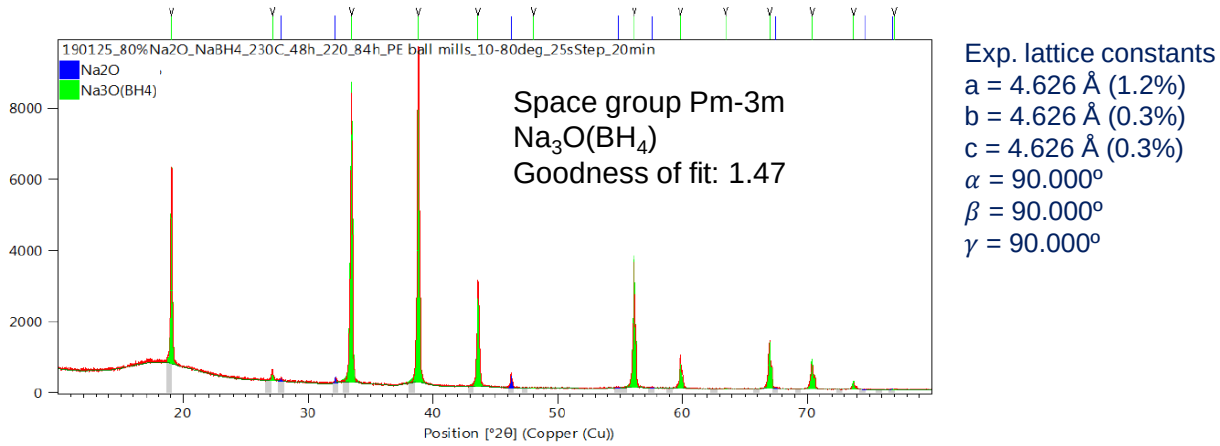

Figure 2. Powder X-ray diffraction pattern for $Na_3O(BH_4)$ showing >99% phase purity.

Future Plans

The successful synthesis of several cluster-ion anti-perovskites is promising, but does not yet allow direct comparison with the first principles modeling, which has to date focused on the Li family. New syntheses are planned using alternative Li precursors that have been identified. Conversely, calculations are planned for those anti-perovskites that have been successfully synthesized in the Na family, seeking similar structure-property correlations. Electrical properties characterization and temperature-dependent X-ray diffraction are planned for the Na anti-perovskites that have been synthesized. Given the prevalence of light elements in all of these compounds, neutron diffraction experiments are also planned for a more detailed characterization of structure. Finally, melting behavior will be characterized, and melt-based single crystal growth will be attempted for those compounds that are determined to be congruently-melting.

References

1. Fang, Hong, Shuo Wang, Junyi Liu, Qiang Sun, and Puru Jena. "Superhalogen-based lithium superionic conductors." Journal of Materials Chemistry A 5, no. 26 (2017): 13373-13381.

2. Fang, Hong, and Puru Jena. "Sodium Superionic Conductors Based on Clusters." ACS applied materials & interfaces 11.1 (2018): 963-972.

3. Fang, Hong, and Puru Jena. "Li-rich antiperovskite superionic conductors based on cluster ions." Proceedings of the National Academy of Sciences 114.42 (2017): 11046-11051.

4. Müller, Winfried, and Martin Jansen. "ONa3, Kristallstruktur und Natriumionenleitfähigkeit." Zeitschrift für anorganische und allgemeine Chemie 591, no. 1 (1990): 41-46.

5. Chater, Philip A., Paul A. Anderson, James W. Prendergast, Allan Walton, Vicky SJ Mann, David Book, William IF David, Simon R. Johnson, and Peter P. Edwards. "Synthesis and characterization of amide–borohydrides: New complex light hydrides for potential hydrogen storage." Journal of Alloys and Compounds 446 (2007): 350-354.

Published and Accepted Journal Publications

1. K. Xiang, K. Yang, W.C. Carter, M. Tang and Y.-M. Chiang, "Mesoscopic Phase Transformation Kinetics in Secondary Particles of Electrode-Active Materials in Lithium-Ion Batteries," *Chem. Mater.*, **30**[13] 4216-4225 (2018), DOI: 10.1021/acs.chemmater.7b05407.
2. L. Cai, M. J. Shearer, Y. Zhao, Z. Hu, F. Wang, Y. Zhang, K. W. Eliceiri, R. J. Hamers, W. Yan, S. Wei, M. Tang, and S. Jin, "Chemically Derived Kirigami of WSe_2", Journal of the American Chemical Society 140, 35 (2018).
3. Q. Meng, L. Wu, D. O. Welch, M. Tang and Y. Zhu, "Non-uniform Stress-free Strains in a Spherically Symmetrical Nanosized Particle and its Applications to Lithium-ion Batteries", Scientific Reports 8, 4936 (2018)
4. X. Wang, W. Zeng, L. Hong, W. Xu, H. Yang, F. Wang, H. Duan*, M. Tang*, and H. Jiang*, "Stress-Driven Lithium Dendrite Growth Mechanism and Dendrite Mitigation by Electroplating on Soft Substrates", Nature Energy 3, 227 (2018)
5. Hong Li, Linsen Li, Yuchen-Karen Chen-Wiegart, Jiajun Wang, Kai Xiang, Liyang Gan, Wenjie Li, Fei Wang, Jun Wang, Yet-Ming Chiang, Song Jin, Ming Tang, "Two-Dimensional Lithium Diffusion Behavior and Probable Hybrid Phase Transition Kinetics in Olivine Lithium Iron Phosphate," *Nature Comm.*, **8**:114 (2017) DOI: 10.1038/s41467-017-01315-8.
6. J. Liu, B. Ludwig, Y. Liu, Z. Zheng, F. Wang, M. Tang, J. Wang, J. Wang, H. Pan, Y. Wang*,"Scalable Dry Printing Manufacturing to Enable Long Life and High Energy Lithium-Ion Batteries", Advanced Materials Technology 2, 1700106 (2017)
7. K. Xiang, W. Xing, D. B. Ravnsbæk, L. Hong, M. Tang, Z. Li, K. M. Wiaderek, O. J. Borkiewicz, K. W. Chapman, P. J. Chupas, Y.-M. Chiang, "Accommodating High Transformation Strains in Battery Electrodes via Formation of Nanoscale Intermediate Phases: Operando Investigation of Olivine $NaFePO_4$", *Nano Letters*, *17*, 1696 (2017). DOI: 10.1021/acs.nanolett.6b04971

Pure Spin Current Phenomena in Heavy Metals

C. L. Chien, Johns Hopkins University

1. Program Scope

Exploration of pure spin current phenomena and devices, including generation, detection, and amplifications of pure spin currents in heavy metals (HMs) with strong spin orbit coupling (SOC), ferromagnetic and antiferromagnetic metals and insulators, and spin-orbit torque (SOT) switching.

2. Recent Progress

A pure spin current can efficiently transport spin angular momentum with minimal Joule heating and no Oersted field. HMs, such as Pt and W, with strong SOC play central roles in pure spin current phenomena and devices. HMs are generators and detectors of pure spin current via spin Hall effects (SHE) and inverse spin Hall effect (ISHE) respectively [1,2]. The spin Hall angle (θ_{SH}) of a HM characterizes the efficiency of the spin-to-charge conversion. In the layer structures of HM/FM/MgO, the HM induces perpendicular magnetic anisotropy (PMA), Dzyaloshinskii-Moriya interaction (DMI), Néel domain walls (DWs) of a single chirality, and generates SOT that can switch the FM layer.

Recently, bismuth (Bi), the heaviest non-radioactive element metal, has attracted a lot of attention for possible pure spin current phenomena. Spin pumping (SP) experiments reported very large voltage signals in Py/Bi (where Py = permalloy) and even larger signals in Bi/Ag [3-8], both have been attributed to large spin-to-charge conversion due to the inverse Rashba-Edelstein effect (IREE) first proposed for 2DEG and a very large θ_{SH} [9]. However, these claims are based on SP experiments using FM metals, which are known to harbor various parasitic effects (e.g., spin rectification, anomalous Nernst effect, spin Hall MR, etc.) due to the conduction electrons in the FM metals [10,11]. Some of these effects (e.g., the anomalous Nernst effect) have the same symmetry as that of ISHE, thus inseparable. We recently use longitudinal spin Seebeck effect (LSSE) to thermally inject spin current into Bi and Bi/Ag from an FM insulator YIG, which, with no charge carriers is not susceptible to the parasitic effects that plague FM metals. With LSSE using YIG, as schematically shown in *Fig. 1a*, we have reached very different conclusions for Bi and Bi/Ag [12].

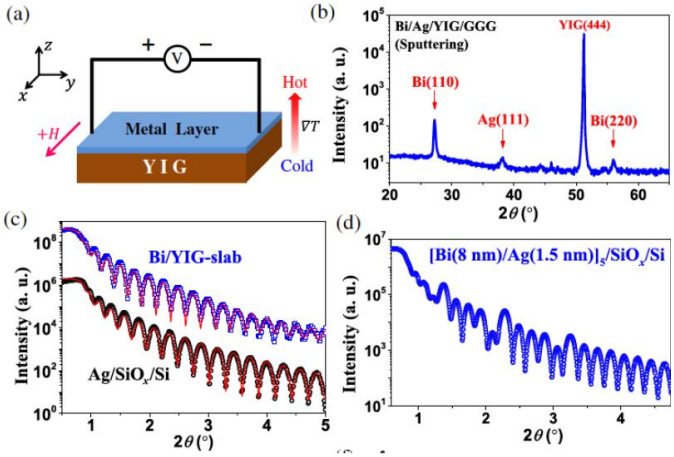

Fig. 1: *(a) Schematic diagram for measuring LSSE in thin film/YIG samples, (b) XRD results of Bi(100 nm)/Ag(100 nm)/YIG/GGG, and low-angle x-ray diffraction results of (c) Bi(30 nm)/YIG (scaled by 10^3) and Ag(30 nm)/SiO_x/Si, and (d) superlattice [Bi(8 nm)/Ag(1.5 nm)]$_5$/SiO_2/Si.*

In any pure spin current experiment the essential question is whether the measured

voltage is due to spin-to-charge conversion in the HM, for which we use the following criteria:

a. the measured voltage must adhere to the ISHE symmetry,

b. the measured voltage must change sign for two HMs with opposite sign of θ_{SH},

c. the measured voltage must vanish when the pure spin current has been blocked,

d. there is no measured voltage without the HM.

We have shown that these criteria are fulfilled in LSSE experiment in Pt/YIG and W/YIG.

Unlike other HMs, fabrication of high quality Bi thin films is more challenging in part because of the low melting point of Bi. Previous reports have shown Bi thin films with large roughness [6]. We resort to three deposition methods for the Bi thin films: magnetron sputtering with substrates held at 77 K, molecular beam epitaxy, and thermal evaporation, resulting in Bi(110)-textured (*Fig. 1b*), epitaxial Bi(111), and polycrystalline Bi thin films, respectively. The sputtered thin films exhibit many orders of low angle x-ray diffraction peaks with low roughness of about 0.4 nm (*Fig. 1c* and *Fig. 1d*). In contrast, the evaporated polycrystalline Bi film show large roughness of about 2 to 4 nm as previously reported [6]. We used two types of YIG materials of epitaxial YIG (5μm)/GGG and bulk 500-μm polycrystalline YIG slab.

The typical ISHE voltage via LSSE for Pt/YIG/GGG is shown in *Fig. 2a*. The ISHE voltage saturates with YIG magnetization, and reverses sign when YIG reverses. When a 3-nm MgO layer has been inserted between HM and YIG to block the pure spin current, the ISHE voltage vanishes. In W/YIG (not shown), the ISHE shows opposite sign as expected because of the opposite sign of θ_{SH} of W. The Pt/YIG and W/YIG results firmly establish the pure spin current phenomena in HM/YIG.

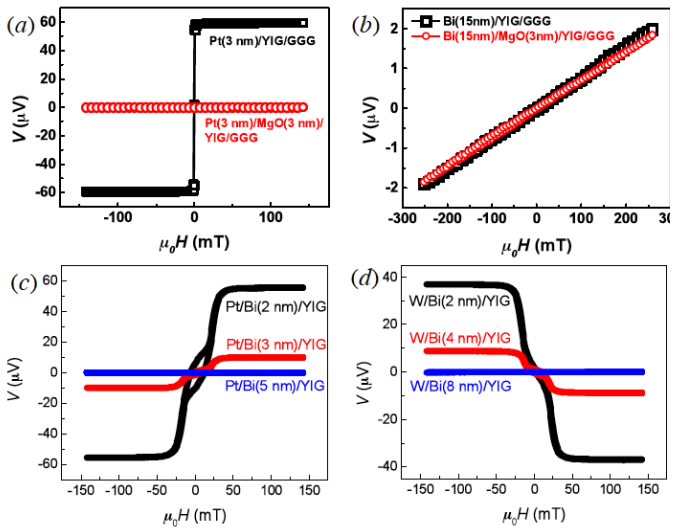

Fig. 2: *Measured voltage as a function of the magnetic field for (a) Pt(3 nm)/YIG/GG and Pt(3 nm)/MgO(3 nm)/YIG/GGG, (b) Bi(15 nm)/YIG/GGG (black) and Bi(15 nm)/MgO(3 nm)/YIG/GGG (red), (c) Pt/Bi/YIG with Bi thickness of 2, 3, and 5 nm, and (d) W/Bi/YIG with Bi thickness of 2, 4, and 8 nm.*

However, in Bi/YIG/GGG and Bi/Ag/YIG/GGG, we found that the measured voltage does not adhere to the ISHE symmetry (*Fig. 2b*). Instead, the measured voltage is linearly proportional to the magnetic field without saturation. We observed the same voltage regardless of whether the pure spin current has been blocked by the 3 nm MgO layer (*Fig. 2b*). These results conclusively show the measured voltage in Bi/YIG is *not* due to spin-to-charge conversion in Bi. This is the telltale sign of ordinary Nernst effect, for which Bi has the largest coefficient.

One might suspect that in Bi/YIG, the pure spin current has been blocked at the

interface between Bi and YIG, therefore has not entered into Bi for spin-to-charge conversion. To test this assertion we placed a HM layer beyond the Bi layer. We observed clear ISHE voltage in Pt/Bi/YIG (*Fig. 2c*) and W/Bi/YIG (*Fig. 2d*) with the expected ISHE symmetry and opposite voltages for Pt and W. Furthermore, as we increase the Bi thickness, the ISHE voltage decreases exponentially. These experiments show conclusively that the pure spin current has been injected into, passed through, the Bi layer, and detected in Pt and W, but with negligible spin-to-charge conversion in Bi. We conclude a very small spin Hall angle for Bi with an upper limit of $\theta_{SH} < 2 \times 10^{-5}$.

We have reached the same conclusion for Bi(110)-textured, epitaxial Bi layer, polycrystalline Bi thin films, with low roughness and with high roughness, on epitaxial YIG thin films and on bulk polycrystalline YIG substrates, that there is *negligible* spin-to-charge conversion Bi and Bi/Ag. There is *no* evidence of the claimed IREE. There is, however, a large voltage due to the ordinary Nernst effect in Bi, linearly proportional to the external magnetic field, and distinctly different from that of the ISHE.

These results have been published in *Di Yue, Weiwei Lin, Jiajia Li, Xiaofeng Jin, and C. L. Chien, "Spin-to-Charge Conversion in Bi Films and Bi/Ag Bilayers," Phys. Rev. Lett.* ***121****, 037201 (2018).*

3. Future Plans

We plan to explore pure spin current phenomena in antiferromagnets with defined order, superconductors including triplet pairing, and quantum materials including Weyl semimetals, as well as SOT switching in ferromagnetic and antiferromagnetic nanostructures.

4. References

[1] *M. I. Dyakonov and V. I. Perel, Possibility of orienting electron spins with current, JETP Lett.* ***13****, 467 (1971),*

[2] *J. E. Hirsch, Spin Hall effect, Phys. Rev. Lett.* ***83****, 1834 (1999).*

[3*] D. Hou, Z. Qiu, K. Harii, Y. Kajiwara, K. Uchida, Y. Fujikawa, H. Nakayama, T. Yoshino, T. An, K. Ando, X. Jin, and E. Saitoh, Interface induced inverse spin Hall effect in bismuth/permalloy bilayer, Appl. Phys. Lett,.* ***101****, 042403 (2012).*

[4] *H. Emoto, Y. Ando, G. Eguchi, R. Ohshima, E. Shikoh, Y. Fuseya, T. Shinjo, and M. Shiraishi, Transport and spin conversion of multicarriers in semimetal bismuth, Phys. Rev. B* ***93****, 174428 (2016).*

[5] *Y. Niimi, Y. Kawanishi, D. H.Wei, C. Deranlot, H. X. Yang, M. Chshiev, T. Valet, A. Fert, and Y. Otani, Giant Spin Hall Effect Induced by Skew Scattering from Bismuth Impurities Inside Thin Film CuBi Alloys, Phys. Rev. Lett.* ***109****, 156602 (2012).*

[6] *J.-C. Rojas-Sánchez, L. Vila, G. Desfonds, S. Gambarelli, J. P. Attan´e, J. M. De Teresa, C. Mag´en, and A. Fert, Spin-to-charge conversion using Rashba coupling at the interfacebetween non-magnetic materials, Nat. Commun.* ***4****, 2944 (2013).*

[7] *W. Zhang, M. B. Jungfleisch,W. Jiang, J. E. Pearson, and A. Hoffmann, Spin pumping and inverse Rashba-Edelstein effect in NiFe/Ag/Bi and NiFe/Ag/Sb, J. Appl. Phys.****117****, 17C727 (2015).*

[8] *Y. Ando and M. Shiraishi, Spin to Charge Interconversion Phenomena in the Interface and Surface States, J. Phys. Soc. Jpn.* ***86****, 011001 (2017).*

[9] *V. M. Edelstein, Spin polarization of conduction electrons induced by electric current in two-dimensional asymmetric electron systems, Solid State Commun.* ***73****, 233 (1990).*

[10] *M. Harder, Y. Gui, and C.-M. Hu, Electrical detection of magnetization dynamics via spin rectification effects, Phys. Rep.* ***661****, 1 (2016).*

[11] *R. Iguchi and E. Saitoh, Measurement of spin pumping voltage separated from extrinsic microwave effects, J. Phys. Soc. Jpn.* ***86****, 011003 (2017).*

[12] *Di Yue, Weiwei Lin, Jiajia Li, Xiaofeng Jin, and C. L. Chien, "Spin-to-Charge Conversion in Bi Films and Bi/Ag Bilayers," Phys. Rev. Lett.* ***121****, 037201 (2018).*

Publications from work supported by the DOE grant over the previous two years

1. *W. Lin and C. L. Chien, "Electrical Detection of Spin Backflow from an Antiferromagnetic Insulator/YIG Interface," Phys. Rev. Lett.* ***118****, 067202 (2017).*
2. *D. Qu, S. Y. Huang, G. Y. Guo, and C. L. Chien, "Inverse spin Hall effect in* Au_xTa_{1-x} *alloy films," Phys. Rev. B* ***97****, 024402 (2018).*
3. *Yufan Li, Qinli Ma, S. X. Huang, C. L. Chien, "Thin films of topological Kondo insulator candidate* SmB_6*: strong spin-orbit torque without exclusive surface conduction," Sci. Adv.* ***4****, eaap8294 (2018).*
4. *Qinli Ma, Yufan Li, D. B. Gopman, Yu. P. Kabanov, R. D. Shull, and C. L. Chien, "Switching a perpendicular ferromagnetic layer by competing spin currents," Phys. Rev. Lett.* ***120****, 117703 (2018).*
5. *T. Liu, Yufan Li, L. Gu, J. J. Ding, H. C. Chang, P. A. P. Janantha, B. Kalinikos, V. Novosad, A. Hoffmann, R. Q. Wu, C. L. Chien, and M. Z. Wu, "Nontrivial Nature and Penetration Depth of Topological Surface States in* SmB_6 *Thin Films," Phys. Rev. Lett.* ***120****, 207206 (2018).*
6. *Yu Wang, Weiwei Lin, Danru Qu, Qinli Ma, Yue Zhang, Yufan Li, Shuming Yang, and C. L. Chien, "Voltage-Controlled Sensitivity of the Spin Seebeck Effect in* $Pt/Y_3Fe_5O_{12}/MgO/(PbMg_{1/3}Nb_{2/3}O_3)_{0.7}(PbTiO_3)_{0.3}$ *Multiferroic Heterostructures," Phys. Rev. Appl.* ***10****, 014004 (2018).*
7. *Di Yue, Weiwei Lin, Jiajia Li, Xiaofeng Jin, and C. L. Chien, "Spin-to-Charge Conversion in Bi Films and Bi/Ag Bilayers," Phys. Rev. Lett.* ***121****, 037201 (2018).*

Spin-Mediated Heat Conduction and Low-Temperature Spin-Seebeck Effect in the Helimagnetic Insulator Cu_2OSeO_3

PI: Joshua L. Cohn, Department of Physics, University of Miami,
P.O. Box 248046, Coral Gables, FL 33124
Contact: (305) 284-7123; jcohn@miami.edu

Program Scope

This program involves experimental transport studies of bulk materials exhibiting *extreme* thermoelectric behavior and/or unusual spin-mediated heat conduction. Our prior work investigated a giant Nernst effect [Phys. Rev. Lett. **108**, 056604 (2012)] at low temperature and very large Seebeck anisotropy above room temperature [Phys. Rev. Lett. **112**, 186602 (2014)] in the quasi-one-dimensional (Q1D) conductor, $Li_{0.9}Mo_6O_{17}$ ("Li-purple bronze" or LiPB); ongoing studies are examining an unusual and highly anisotropic magnetic field-suppressed metallic state below its superconducting transition (T_c=2K). An increasing focus of the program for the past two years is spin transport in the helimagnetic insulator Cu_2OSeO_3 which we showed to have a record-high magnon thermal conductivity at T<10 K. The influence of its novel spin phases on magnon transport and the spin-Seebeck effect are the subject of current and future work.

Recent Progress

Ballistic magnon heat conduction in the helimagnetic insulator Cu_2OSeO_3 [Phys. Rev. B **95**, 224407 (2017), Editor's Suggestion]

We identified a ballistic (boundary-limited) magnon thermal conductivity (κ_m) at T<10K in single crystals of the ferrimagnetic insulator Cu_2OSeO_3 (Fig. 1) – **the largest ever observed for any known ferro- or ferrimagnetic material** — and nearly two orders of magnitude larger than for yttrium-iron garnet (YIG),[1] the best studied system to date. Spin-mediated heat conduction in ferromagnetic materials has been of interest for decades, but a dearth of suitable ferro- or ferrimagnetic insulators exhibiting magnonic heat conduction has limited investigation.

Cu_2OSeO_3 is a cubic material, comprising a distorted pyrochlore lattice of corner-sharing Cu tetrahedra. Inequivalence of copper sites and strong magnetic interactions within tetrahedra lead to a 3-up-1-down, spin S=1 magnetic state [2,3] that persists above the long-range magnetic ordering temperature $T_C \approx 58\,K$. Dzyaloshinsky-Moriya interactions induce a long-wavelength, incommensurate helical spin structure. At low temperatures, the low-field

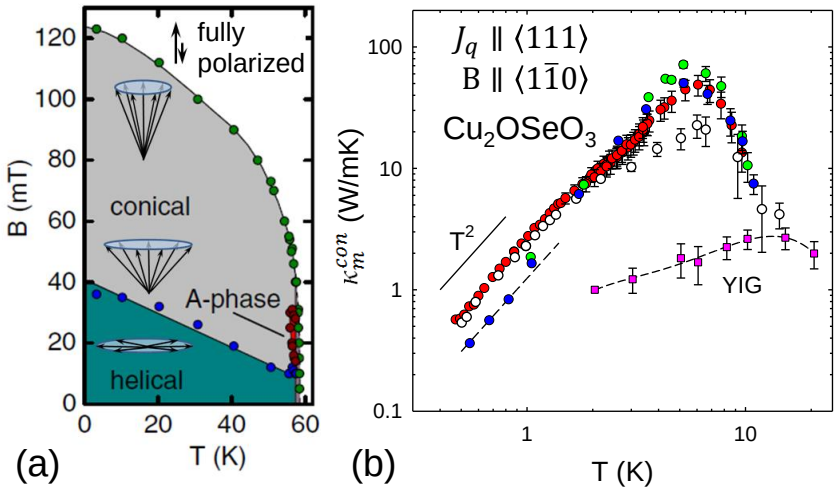

Fig. 1 (a) B-T phase diagram for Cu_2OSeO_3 (Ref. 4), (b) Conical-phase magnon thermal conductivity for four Cu_2OSeO_3 single crystals. Data for YIG are from Ref. 1.

state is helimagnetic[4] wherein the atomic spins rotate within a plane perpendicular to the helical axis with a wavelength of 62 nm; multiple domains with helices aligned along ⟨100⟩ directions characterize this phase. At $H \geq 30\ mT$ the helices of individual domains rotate along the field to form a single-domain, conical (*C*) phase in which spins rotate on the surface of a cone. Further increasing the field narrows the conical angle until $H \geq 100\ mT$ where the ferrimagnetic, fully polarized (*FP*) spin state emerges.

Novel Spin Phases Probed by Magnon Heat Conduction [Phys. Rev. B **99**, 020403, Rapid Commun. (2019)]

Our recent work (Fig. 2) examines magnon heat conduction for applied magnetic fields $H \parallel \langle 100 \rangle$ for for which small-angle neutron scattering (SANS) studies[5,6,7] reveal additional spin phases unique to this field orientation: titled conical (*TC*) and low-temperature skyrmion (*LTS*). A complete suppression of the magnon heat flux in the tilted conical phase is identified for heat current along ⟨110⟩. We interpreted this behavior to imply strong magnon scattering by tilt domain boundaries (Fig. 3). The observation raises the prospect of exploiting this configuration of heat flux and applied field in a field-controllable spin-current switch. The low-temperature skyrmion phase, characterized by long-range skyrmion lattice order, supports maximum magnon heat conduction comparable to that of the fully polarized phase. Suppressed magnon heat conduction characterizes regions of phase coexistence.

Spin-Seebeck Effect in Cu_2OSeO_3 [manuscript in preparation]

We have begun to investigate the longitudinal spin-Seebeck effect (LSSE) using 10-nm thick Pt films deposited on the heater end of our single-crystal specimens [Fig. 4 (a)]. The spin-Seebeck voltage, generated perpendicular to the directions of heat flow and applied magnetic field, is

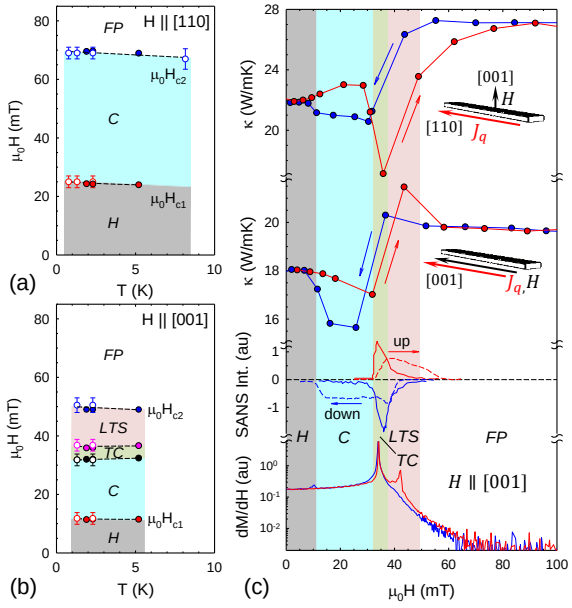

Fig. 2 (a) Low-*T* phase diagrams for Cu_2OSeO_3 with (a) *H*||[110] and (b) *H*||[001]. (c) Upper panels: $\kappa(H)$ for *H*||[001] and two orientations of the heat current. Middle panel: SANS intensities for increasing ("up") and decreasing ("down") fields (from Ref. [7]) for the *TC* (solid curves) and *LTS* (dashed curves) phases. Lower panel: *dM/dH*.

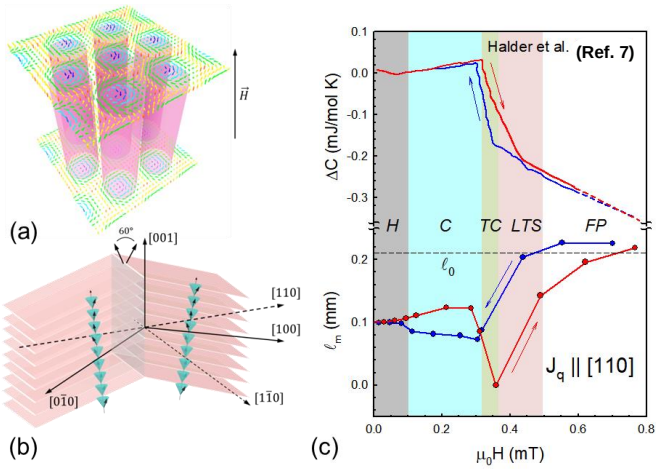

Fig. 3 Skyrmion spin textures in the *LTS* phase, (b) an idealized planar boundary between tilted conical domains of the *TC* phase (the planes represent layers of atomic spins oriented in the direction dictated by the adjacent conical spirals), (c) Change with field in the specific heat (from Ref. [7]) extended to higher field (dashed lines) and magnon mean-free path, ℓ_m computed from kinetic theory. The horizontal dashed line indicates the specimen transverse dimension ℓ_0.

antisymmetric in field [Fig. 4 (b)]. The antisymmetrized SSE signal [Fig. 4 (c)] has features that clearly correspond to the spin-phase transitions (Fig. 1) *H-C* and *C-FP* [shading and labels, Fig. 4 (c)]: rising in the conical phase (where the magnetic domains rotate along the field), and saturating in the fully polarized phase. **The LSSE coefficient** ($\sigma_{LSSE} = E_y/\nabla T_x$) in the fully polarized phase at H=4.5 kOe [Fig. 4 (d)] **is the largest reported to date for any material**, consistent with the magnitude of the magnon thermal conductivity we reported.

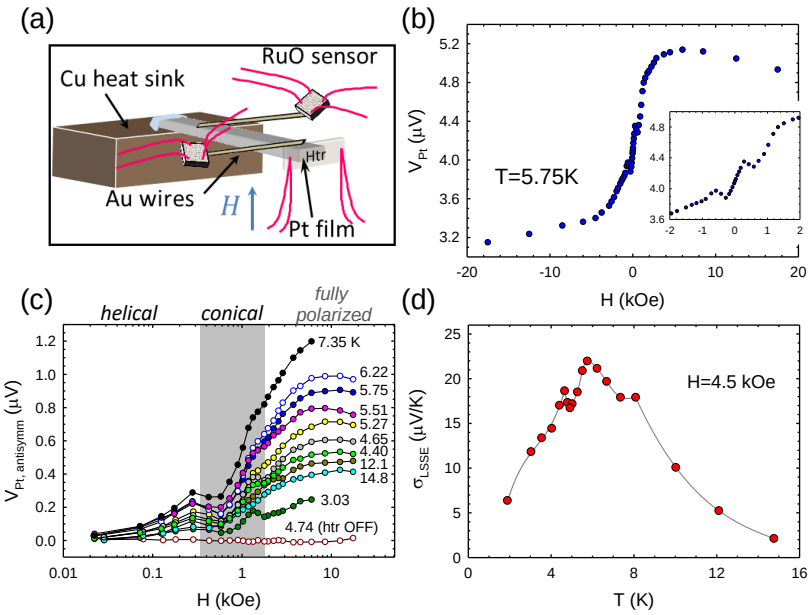

Fig. 4 (a) Schematic of SSE measurement geometry, (b) raw Pt voltage signal at T=5.75 K for $J_q \parallel [111], H \parallel [1\bar{1}0]$, (c) antisymmetric (in field) LSSE signal *vs* applied field at various temperatures, (d) SSE coefficient *vs* T at 4.5 kOe. Solid curves are guides.

Future Plans

We will extend spin-Seebeck measurements on Cu_2OSeO_3 crystals to other orientations of heat current and field, especially to verify the field-controllable spin-current switch concept noted above [Fig. 3 (c)]. Goals include examining the role of the spin phases on interfacial spin current transfer and testing spin-Seebeck models by exploiting the unprecedentedly large and calibrated spin currents available in this compound

References

1. S. R. Boona and J. P. Heremans, *Magnon thermal mean free path in yttrium iron garnet*, Phys. Rev. B **90**, 064421 (2014).
2. Jan-Willem G. Bos, C. V. Colin, and T. T. M. Palstra, *Magnetoelectric coupling in the cubic ferrimagnet Cu_2OSeO_3*, Phys. Rev. B **78**, 094416 (2008).
3. M. Belesi, I. Rousochatzakis, H. C. Wu, H. Berger, I. V. Shvets, F. Mila, and J. P. Ansermet, *Ferrimagnetism of the magnetoelectric compound Cu_2OSeO_3 probed by ^{77}Se NMR*, Phys. Rev. B **82**, 094422 (2010).
4. T. Adams, A. Chacon, M. Wagner, A. Bauer, G. Brandl, B. Pedersen, H. Berger, P. Lemmens, and C. Pfleiderer, Long-Wavelength Helimagnetic Order and Skyrmion Lattice Phase in Cu_2OSeO_3, Phys. Rev. Lett. **108**, 237204 (2012).
5. A. Chacon, L. Heinen, M. Halder, A. Bauer, W. Simeth, S. Mühlbauer, H. Berger, M. Garst, A. Rosch, and C. Pfleiderer, *Observation of two independent skyrmion phases in a chiral magnetic material*, Nat. Phys. **14**, 936 (2018).
6. F. Qian, L. J. Bannenberg, H. Wilhelm, G. Chaboussant, L. M. Debeer-Schmitt, M. P. Schmidt, A. Aqeel, T. T. M. Palstra, E. Brück, A. J. E. Lefering, C. Pappas, M. Mostovoy,

and A. O. Leonov, *New magnetic phase of the chiral skyrmion material Cu_2OSeO_3* Sci. Adv. **4**, 7323 (2018).
7. M. Halder, A. Chacon, A. Bauer, W. Simeth, S. Mühlbauer, H. Berger, L. Heinen, M. Garst, A. Rosch, and C. Pfleiderer, *Thermodynamic evidence of a second skyrmion lattice phase and tilted conical phase in Cu_2OSeO_3,* Phys. Rev. B **98**, 144429 (2018).

Publications 2017-2019

1. D. Shukla, N. Prasai, T. M. Carlino, M. M. A. Mazza, A. M. Scott, and J. L. Cohn, Anisotropic Heat Conduction in the Metal Organic Framework Perovskites $[C(NH_2)_3]X(HCOO)_3$ (X=Cu, Zn), *Appl. Phys. Lett.*, in press (2019).

2. N. Prasai, A. Akopyan, B. A. Trump, G. G. Marcus, S. X. Huang, T. M. McQueen, and J. L. Cohn, Spin phases of the helimagnetic insulator Cu_2OSeO_3 probed by magnon heat conduction, *Phys. Rev.* B **99**, 020403 (Rapid Commun.) (2019).

3. N. Prasai, A. B. Christian, J. J. Neumeier, and J. L. Cohn, Resonant scattering of phonons in the quasi-one-dimensional spin-chain compounds AB_2O_6 (A = Ni, Co; B = Sb, Ta) , *Phys. Rev. B* **98**, 134449 (2018).

4. N. Prasai, B. A. Trump, G. G. Marcus, A. Akopyan, S. X. Huang, T. M. McQueen, and J. L. Cohn, *Ballistic magnon heat conduction and possible Poiseuille flow in the helimagnetic insulator Cu_2OSeO_3,* Phys. Rev. B **95**, 224407 (2017).

Characterization of Functional Nanomachines

PI: Michael F. Crommie
Co-Investig.: A.P. Alivisatos, C. Bustamante, M.L. Cohen, F.R. Fischer, S.G. Louie, A. Zettl
UC Berkeley, Physics Department, 366 LeConte Hall #7300, Berkeley, CA 94720
Materials Sciences Division, Lawrence Berkeley National Laboratory
e-mail: crommie@berkeley.edu

Program Scope: The overarching goal of this program is to explore the fundamental behavior of nanomachines that are engineered at the atomic scale and that can control energy and information through mechanical transduction processes. We are following two paths toward this goal: first, we are exploring naturally occurring biomotors that take advantage of the molecular mechanisms provided by Nature and, second, we are purposefully designing new synthetic molecular machines in a molecule-by-molecule fashion. This research helps to clarify the mechanisms by which nanomachines convert different forms of energy into directed mechanical activity as well as how these processes are affected by different environmental dissipation mechanisms. This program is aimed at creating new categories of functional nanomachines, such as bottom-up fabricated synthetic molecular machines that operate on surfaces, top-down fabricated carbon-based nanomachines that exploit the electromechanical properties of nanotubes and graphene, and hybrid nanomachines composed of integrated synthetic and biological components. This program has seven co-investigators whose expertise span physics, chemistry, and biology. The experimental tools utilized by our collaboration range from synthetic chemistry, electron microscopy, and scanned probe techniques (**Alivisatos, Fischer,** and **Crommie**), to photolithography, wet biology, and laser tweezers (**Zettl** and **Bustamante**). **Cohen** and **Louie** provide theoretical support through the use of *ab initio* density functional techniques and molecular dynamics calculations.

Recent Progress: Here we highlight our activities in the subtask of this program entitled *Imaging Molecular Actuation in Nanodevices*. This subtask involves three main thrusts: (1) Redox-induced single-molecule actuation, (2) Current and electric field-induced molecular actuation, and (3) Bottom-up self-assembly of molecular nanomachines.

(1) Redox-induced single-molecule actuation: This thrust builds upon a recent discovery by Crommie and coworkers[1] that it is possible to reversibly change the groundstate charge of a single molecule adsorbed on the surface of a graphene field effect transistor (FET) (Fig. 1). This concept is similar to conventional electrochemistry but differs in that it can be performed in ultrahigh vacuum (UHV) with no electrolyte solution or ionic double layer. This enables individual molecules having different charge states to be spectroscopically probed and imaged using a scanning tunneling microscope (STM). The main goal of this thrust is to use this technique to reversibly change the *mechanical* state of individual molecules. This is possible, in principle, because the addition or removal of a single charge to a molecule (i.e., a "redox" reaction) often causes the molecule to change shape in response to charge-induced rearrangement of chemical bonds.

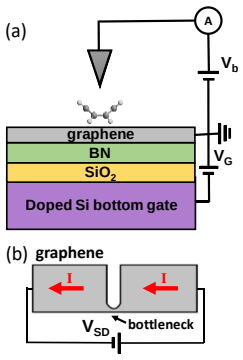

Fig. 1: Gate-tunable graphene devices. (a) Schematic of a graphene FET. (b) A graphene device with a notch patterned by AFM nanolithography.

We have put significant effort into searching for an appropriate molecular candidate to explore this phenomenon (which has never been observed at the single molecule level) and to provide a new platform for fabricating more complex synthetic molecular machines. We currently

believe that cyclooctatetraene (COT), a small molecule composed of only eight carbon atoms (Fig. 2), is ideal for our purposes. COT is stable, easy to deposit from vapor phase, and is known to adopt a "saddle" shape when neutral and to flatten when negatively charged by one additional electron (Figs. 2a,b). Before performing experiments on this molecule we theoretically tested that it would have the proper energy level structure when adsorbed to graphene. These calculations were performed using *ab initio* density functional theory. Our simulations confirm that individual COT molecules adsorbed onto graphene should undergo reversible gate-tunable mechanical transformations for physically achievable device parameters.[2]

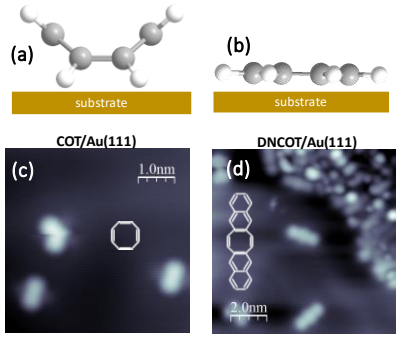

Fig. 2: COT and derived molecules imaged on Au(111). (a) Saddle conformation of a neutral COT molecule. (b) Planar conformation of a charged COT molecule. (c) STM image of COT on Au(111). (d) STM image of DNCOT on Au(111).

We next deposited COT molecules onto the surface of a graphene FET held at T=4K in UHV. Although COT is readily imaged on Au(111) (Fig. 2c), we found that bare COT molecules are unstable on the graphene FET surface under typical STM imaging conditions. As result, we functionalized COT (in collaboration with D. Toste) to strengthen its interaction with graphene. The newly functionalized DNCOT molecules were found to be stable on Au(111) (Fig. 2d) and are currently being tested at the surface of graphene FET devices.

(2) Current and electric field-induced molecular actuation: A second technique for mechanically actuating molecular nanostructures in a device environment is through application of electrical current and/or electric field. This is quite different from the redox-based mechanism described above since current-induced mechanical actuation arises from momentum transfer to molecular structures via scattered electrical current. This effect is called the "wind force" and depends sensitively on the coupling of the molecule to the underlying electronic states of the substrate. Transverse electric fields can also apply mechanical force on molecular structures that are charged or have a dipole moment. This is called the "direct force" and is expected to dominate in graphene devices that have break junction gaps (which decrease current but concentrate potential gradients). The relative contributions of these two forces in electromigration processes are not well understood and these effects have never been probed at the single-atom/single-molecule level using scanned probe microscopy.

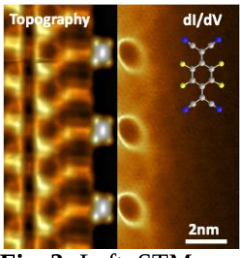

Fig. 3: Left: STM image of a charged F_4TCNQ array. Right: A dI/dV map of the pristine graphene region adjacent to the array showing charging rings from supercritical states.

We have performed direct measurement of molecular coupling to graphene conduction band states in FET devices, a prerequisite for controlling and understanding electromigration-induced nanomechanical processes. This was accomplished by depositing F_4TCNQ molecules onto a graphene FET decorated with PCDA molecular islands. Individual F_4TCNQ molecules attached to PCDA island edges to create atomically-precise 1D molecular arrays (Fig. 3). F_4TCNQ molecules are useful for exploring molecular coupling to graphene charge carriers because their charge state can be modulated via applied gate voltage.[1] We have discovered that the coupling of charged F_4TCNQ molecules to underlying graphene electrons depends sensitively on the intermolecular spacing of the molecular array. In

the dilute limit (intermolecular separation ≥ 20 nm) the molecules act like isolated Coulomb centers and scatter graphene electrons without inducing any significant changes in the graphene electronic structure. At closer intermolecular separation, however, a dramatic change occurs and the molecular array induces new electronic bound states in the underlying graphene (Fig. 3). We have determined that this arises through a new physical process that we call "frustrated supercriticality". This process enables a collection of subcritical charges (e.g., charged molecules) to collectively exhibit supercritical behavior so long as the charge spacing is less than the graphene screening length and the total amount of stationary charge exceeds the supercritical threshold.[3]

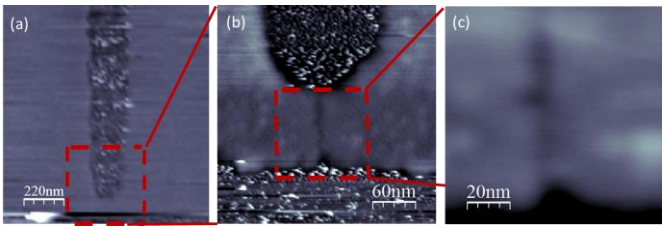

Fig. 4: A graphene bottleneck fabricated by AFM nanolithography. (a) EFM image of a graphene bottleneck obtained at T=4K in UHV. (b) Zoom-in EFM image of the graphene bottleneck. A nanogap is visible at the narrowest part of the bottleneck. (c) Zoom-in EFM image of the nanogap. This graphene device is supported by SiO_2.

The next step in this subproject thrust will be to subject our molecular assemblies to applied current flow and lateral electric fields. We have made significant progress in this direction by attaching source/drain electrodes to our graphene FETs and "necking" them down to increase current density and electric field intensity (Fig. 4). A clean AFM-based cutting technique allows us to create "notches" in graphene flakes that result in bottlenecks with widths less than 100 nm. This increases the current density in our graphene devices by more than an order of magnitude. This also allows us to create high local electric field regions by steadily increasing current through the bottleneck until it "breaks", thus creating break junctions with narrow gaps on the order of 1-10 nm (Figs. 4b,c). Such break junctions impede the flow of current but create regions of extremely high electric field, and have never been imaged via STM until now. We are currently working to deposit molecular nanostructures into these high field regions.

(3) Bottom-up self-assembly of molecular nanomachines: Molecular machines can be synthesized in solution and deposited onto surfaces from liquid, but this process invariably results in extremely dirty surfaces that preclude atomic-scale or single-molecule imaging. An alternative technique for obtaining ultraclean molecular nanostructures that can be imaged down to the atomic-scale is to perform "on-surface" synthesis. Here molecular precursors are vacuum-deposited onto a clean surface and induced to covalently bond in some prearranged manner (covalent bonds are required to give nanomachines cohesive integrity). We have made significant progress exploring a number of different covalent linkage schemes with the goal of assembling molecular machines.

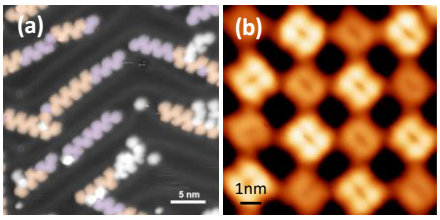

Fig. 5: (a) STM image of nanoribbon heterojunctions formed by hierarchical growth. (b) STM dI/dV map of covalently-bonded TAPP and TFPP molecules forming a 2D "checkerboard" pattern (linked by imine bonds).

The covalent linkage technique that provides the highest degree of on-surface synthesis control is modified Ullmann coupling.[4] Here precursor molecules are terminated with halide atoms that cleave at moderate temperature, resulting in radical formation and polymerization of the precursors. This allows formation of highly targeted bonding geometries, but at the cost of requiring a metal growth substrate to induce halide cleavage. We have demonstrated that it is possible to use new, Ullmann-based hierarchical growth techniques to grow 1D polymers that exhibit a single heterojunction between two dissimilar molecular segments.[5] This is an

unprecedented level of structural control for 1D molecular on-surface synthesis (Fig. 5a). We accomplished this by functionalizing two distinct molecular precursors with different halides (I and Br). I atoms cleave at lower temperature than Br atoms, and so by slowly ramping the temperature it is possible to induce I-functionalized precursors to polymerize before Br-functionalized precursors. Special linker molecules functionalized with Br on one side and I on the other allow the two different segments to link at a *single* interface. Fig. 5a shows an STM image of graphene nanoribbon heterojunctions formed using this new technique.

The requirement of a metallic growth substrate for Ullmann coupling can be limiting since insulating substrates are often desirable to enhance nanomachine functionality. It is thus useful to explore covalent coupling reactions that work on insulators. One such reaction that we have studied recently is the Schiff base reaction[6] which results in an imine bond linkage (C-N=C). Because this is a condensation reaction it can occur on insulating surfaces. We have recently shown that this coupling reaction can be used in UHV to link two different types of porphyrin cores into a 2D covalent organic framework (Fig. 5b). This new type of molecular network has conduction band edge and valence band edge states that are localized on different sublattices, and so it exhibits a "checkerboard" topography. We are currently exploring the use of this reaction scheme to create self-assembled nanomechanical structures on insulating surfaces (e.g., hBN).

Future Plans: We are vigorously developing new molecular nanomachine systems and new device platforms for actuating them. For example, we are developing new types of functionalized COT molecules to bring COT frontier orbitals into better alignment with the graphene Dirac point. We are also developing new molecular systems that can be actuated with light and which self-assemble on insulating substrates. We are additionally developing new techniques to "cut" our graphene devices into precise nanoscale arrangements that better facilitate nanomachine actuation (e.g., through the use of a He focused ion beam).

One of our most exciting new directions, however, is the development of a new instrument that will enable picosecond time-resolved STM characterization with Ångström spatial resolution. This tool will provide a new window into the inner workings of nanomachines. The idea here is to observe the ultrafast dynamical motion of nanomachines at the single-atom/single-molecule level. This will be accomplished by integrating a pump/probe laser system with a cryogenic UHV STM (in collaboration with Feng Wang). STMs have poor bandwidth and so the time resolution here comes from the delay time between coincident optical pulses (this technique has been used previously to image the vibrational dynamics of individual molecules[7]). The probe signal here will be in the infrared (λ = 1 micron) to facilitate a well-defined STM tunneling process, but the pump signal can be "doubled" or "tripled" into the visible or UV regime to facilitate electron-hole induced relaxation processes that are useful for nanomachine functionality.

References:

[1] S. Wickenburg, J. Lu, J. Lischner, H. Tsai, A.A. Omrani, A. Riss, C. Karrasch, A. Bradley, H. Jung, R. Khajeh, D. Wong, K. Watanabe, T. Taniguchi, A. Zettl, A.H. Castro Neto, S.G. Louie, and M.F. Crommie, *Nature Communications* **7**, 13553 (2016).

[2] S. Oh, M.F. Crommie, and M.L. Cohen, *ACS Nano* **13**, 1713 (2019).

[3] J. Lu, H. Tsai, A.N. Tatan, S. Wickenburg, A.A. Omrani, D. Wong, A. Riss, E. Piatti, K. Watanabe, T. Taniguchi, A. Zettl, V.M. Pereira, and M.F. Crommie, *Nature Communications* **10**, 477 (2019).

[4] L. Grill, M. Dyer, L. Lafferentz, M. Persson, M.V. Peters, and S. Hecht, *Nat. Nanotech.* **2**, 687 (2007).

[5] C. Bronner, R.A. Durr, D.J. Rizzo, Y. Lee, T. Marangoni, A.M Kalayjian, H. Rodriguez, W. Zhao, S.G. Louie, F.R. Fischer, and M.F. Crommie, *ACS Nano* **12**, 2193 (2018).

[6] C. Chen, T. Johsi, H. Li, A.D. Chavez, Z. Pedramrazi, P. Liu, H. Li, W.R. Dichtel, J. Bredas, and M.F. Crommie, *ACS Nano* **12**, 395 (2018).

[7] T.L. Cocker, D. Peller, P. Yu, J. Repp, and R. Huber, *Nature* **539**, 263 (2016).

Publications resulting from work supported by DOE grant over previous two years:

1. H. Cho, M. R. Jones, S. Nguyen, M.R. Hauwiller, A. Zettl, and A.P. Alivisatos. The Use of Graphene and Its Derivatives for Liquid Phase Transmission Electron Microscopy of Radiation-Sensitive Specimens. *Nano Letters* **17**, 1, 414 (2017).
2. S. Wickenburg, J. Lu, J. Lischner, H.-Z. Tsai, A. Omrani, A. Riss, C. Karrasch, A. Bradley, H.S. Jung, R. Khajeh, D. Wong, K. Watanabe, T. Taniguchi, A. Zettl, A. Castro Neto, S. Louie, and M. Crommie. Tuning charge and correlation effects for a single molecule on a graphene device. *Nature Commun*. **7,** 131553 (2016).
3. M. M. Ugeda, A.J. Bradley, L. Rodrigo, M. Yu, W. Liu, P. Doak, A. Riss, J. B. Neaton, T. D. Tilley, R. Pérez, and M.F. Crommie. Covalent Functionalization of GaP(110) Surfaces via a Staudinger-Type Reaction with Perfluorophenyl Azide. *J. of Phys. Chem. C* **120**, 26448 (2016).
4. J. Cho, I. V. Pechenezhkiy, L. Berbil-Bautista, S. K. Meier, K. P. C. Vollhardt, and M. F. Crommie. Imaging Structural Transitions in Organometallic Molecules on Ag(100) for Solar Thermal Energy Storage. *J. of the Korean Phys. Soc.* **70**, 586 (2017).
5. G.D. Nguyen, H.-Z. Tsai, A.A. Omrani, T. Marangoni, M. Wu, D.J. Rizzo, G.F. Rodgers, R.R. Cloke, R.A. Durr, Y. Sakai, F. Liou, A.S. Aikawa, J.R. Chelikowsky, S.G. Louie, F.R. Fischer, and M.F. Crommie. Atomically Precise Graphene Nanoribbon Heterojunctions from a Single Molecular Precursor. *Nature Nanotechnology*, **12**, 1077 (2017).
6. H.R. Barzegar, A. Yan, S. Coh, E. Gracia-Espino, G. Dunn, T. Wågberg, S.G. Louie, M.L. Cohen, and A. Zettl. Electrostatically driven nanoballoon actuator. *Nano Letters* **16**, 11, 6787 (2016).
7. H.R. Barzegar, A. Yan, S. Coh, E. Gracia-Espino, C. Ojeda-Aristizabal, G. Dunn, M.L. Cohen, S.G. Louie, T. Wagberg, and A. Zettl. Spontaneous twisting of a collapsed carbon nanotube. *Nano Research* **10**, 6, 1942 (2017).
8. O. Herrera-Asmat, L. Lubkowska, M. Kashlev, C.J. Bustamante, D.G. Guerra, M.L. Kireeva. Production and characterization of a highly pure RNA polymerase holoenzyme from Mycobacterium tuberculosis. *PREP* **134** (2017). doi: 10.1016/j.pep.2017.03.013.
9. San-Martin Á, Rodriguez-Aliaga P, Molina JA, Martin A, Bustamante C, Baez. Knots can Impair Protein Degradation by ATP-dependent Proteases. *PNAS* **114**, 9864 (2017).
10. A. Lee, K. Tsekouras, C. Calderon, C. Bustamante, S. Pressé. Unraveling the Thousand Word Picture: An Introduction to Super-Resolution Data Analysis. *Chem. Rev.* **117**, 11, 7276 (2017).
11. J. Horng, H. B. Balch, A. F. McGuire, H.-Z. Tsai, P. R. Forrester, M.F. Crommie, B. Cui, F. Wang. Imaging Electric Field Dynamics with Graphene Optoelectronics. *Nature Commun*. **7**, 13704 (2016).
12. P. Cao, P. Bai, A. A. Omrani, Y. Xiao, K. L. Meaker, H.-Z. Tsai, A. Yan, H. S. Jung, R. Khajeh, G. F. Rodgers, Y. Kim, A. S. Aikawa, M. A. Kolaczkowski, Y. Liu, A. Zettl, K. Xu, M. F. Crommie, and T. Xu. Preventing Thin Film Dewetting via Graphene Capping. *Advanced Materials* **29**, 1701536 (2017).

13. T. Joshi, J.H. Kang, L. Jiang, S. Wang, T. Tarigo, T. Lyu, S. Kahn, Z. Shi, Y.R. Shen, M.F. Crommie, and F. Wang. Coupled One-Dimensional Plasmons and Two-Dimensional Phonon Polaritons in Hybrid Silver Nanowire/Silicon Carbide Structures. *Nano Letters* **17**, 3662 (2017).

14. C. Bronner, T. Marangoni, D. J. Rizzo, R. A. Durr, J. H. Jørgensen, F. R. Fischer, and M. F. Crommie. Iodine versus Bromine Functionalization for Bottom-Up Graphene Nanoribbon Growth: Role of Diffusion. *Journal of Physical Chemistry C* **121**, 18490 (2017).

15. S. Tafoya, S. Liu, J. Castillo, R. Atz, M. Morais, S. Grimes, P. Jardine, and C. Bustamante. Molecular switch-like regulation enables global subunit coordination in a viral ring ATPase. *PNAS* **115**, 7961 (2018).

16. D.B. Litt, M.R. Jones, M. Henschel, Y. Wang, S. Yang, H.D. Ha, X. Zhang, and A.P. Alivisatos. Hybrid Lithographic and DNA-Directed Assembly of a Configurable Plasmonic Metamaterial that Exhibits Electromagnetically Induced Transparency. *Nano Lett.* **18**, 859 (2018).

17. S. Tafoya and C. Bustamante. Molecular switch-like regulation in motor proteins. *Philos T R Soc* B **373**, 1749 (2018).

18. Z. Pedramrazi, C. Chen, F. Zhao, T. Cao, G.D. Nguyen, A.A. Omrani, H.-Z. Tsai, R.R. Cloke, T. Marangoni, D.J. Rizzo, T. Joshi, C. Bronner, W.-W. Choi, F.R. Fischer, S.G. Louie, and M.F. Crommie. Concentration Dependence of Dopant Electronic Structure in Bottom-Up Graphene Nanoribbons. *Nano Letters* **18**, 3550 (2018).

19. C. Bronner, R.A. Durr, D.J. Rizzo, Y.-L. Lee, T. Marangoni, A.M. Kalayjian, H. Rodriguez, W. Zhao, S.G. Louie, F.R. Fischer, and M.F. Crommie. Hierarchical On-Surface Synthesis of Graphene Nanoribbon Heterojunctions. *ACS Nano* **12**, 2193 (2018).

20. N. Liu, G. Chistol, Y. Cui, and C. Bustamante. Mechanochemical coupling and bi-phasic force-velocity dependence in the ultra-fast ring ATPase SpoIIIE. *eLife* **7**, e32354 (2018).

21. G. Dunn, K. Shen, J.N. Belling, T.N.H. Nguyen, E. Barkovich, K. Chism, M.M. Maharbiz, M.R. DeWeese, and A. Zettl. Selective Insulation of Carbon Nanotubes. *Phys. Status Solidi B* **254**, 1700202 (2017).

22. S.M Gilbert, G. Dunn, A. Azizi, T. Pham, B. Shevitski, E. Dimitrov, S. Liu, S. Aloni, and A. Zettl. Fabrication of Subnanometer-Precision Nanopores in Hexagonal Boron Nitride. *Scientific Reports* **7**, 15096 (2017).

23. S.M. Gilbert, S. Liu, G. Schumm, and A. Zettl. Nanopatterning Hexagonal boron Nitride with Helium Ion Milling: Towards Atomically-Thin, Nanostructured Insulators. *MRS Advances* **3**, 327 (2018).

24. D.J. Rizzo, G. Veber, T. Cao, C. Bronner, T. Chen, F. Zhao, H. Rodriguez, S.G. Louie, M.F. Crommie, and F.R. Fischer. Topological Band Engineering of Graphene Nanoribbons. *Nature* **560**, 204 (2018).

25. C. Chen, T. Joshi, H. Li, A.D. Chavez, Z. Pedramrazi, P.-N. Liu, H. Li, W.R. Dichtel, J.-L. Bredas, and M.F. Crommie. Local Electronic Structure of a Single-Layer Porphyrin-Containing Covalent Organic Framework. *ACS Nano* **12**, 385 (2018).

26. R. Gabizon, A. Lee, H. Vahedian-Movahed, R. Ebright, and C. Bustamante. Pause sequences facilitate entry into long-lived paused states by reducing RNA polymerase transcription rates. *Nature Communications* **9**, 2930 (2018).

27. M. Righini, A. Lee, C. Cañari-Chumpitaz, T. Lionberger, R. Gabizon, Y. Coello, I. Tinoco Jr, and C. Bustamante. Full molecular trajectories of RNA polymerase at single base-pair resolution. *PNAS* **115**, 1286 (2018).

28. A. Bustamante, J. Sotelo-Campos, D.G. Guerra, M. Floor, C.M.A. Wilson, C. Bustamante, and M. Baez. The energy cost of polypeptide knot formation and its folding consequences. *Nature Communications* **8**, 1581 (2017).

Energy Carrier Transport in Functionalized Two-Dimensional Layered Chalcogenides

Principal Investigator: Steve Cronin, University of Southern California

Collaborator: Li Shi, University of Texas at Austin

Program Scope

The goal of this collaborative project is to study two-dimensional (2D) layered chalcogenide materials and tune and improve the electrical, optical, thermal and thermoelectric properties of this class of functional materials. Building on the progress made in our study of phonon and electron transport in pristine 2D layered heterostructures, we investigate both in-plane and cross-plane thermal and thermoelectric transport properties of 2D chalcogenide materials and develop tools and techniques for studying thermal and thermoelectric transport over smaller length scales and larger spectral ranges than was previously possible.

Recent Progress

Cross-Plane Thermoelectric and Thermionic Transport across Au/h-BN/Graphene Heterostructures[1]

The thermoelectric voltage generated at an atomically abrupt interface has not been studied exclusively because of the lack of established measurement tools and techniques. Atomically thin 2D materials provide an excellent platform for studying the thermoelectric transport at these interfaces. The Cronin group has developed a novel technique and device structure to probe the thermoelectric transport across Au/h-BN/graphene heterostructures, as illustrated in Figure 7a. An indium tin oxide (ITO) transparent electrical heater is patterned on top of this heterostructure, enabling Raman spectroscopy and thermometry to be obtained from the graphene top electrode *in situ* under device operating conditions. Here, an AC voltage V(ω) is applied to the ITO heater and the thermoelectric voltage across the Au/h-BN/graphene heterostructure is measured at 2ω using a lock-in amplifier. We report the Seebeck coefficient for our thermoelectric structure to be -215 μV/K. The Au/graphene/h-BN heterostructures enable us to explore thermoelectric and thermal transport on nanometer length scales in a regime of extremely short length scales. The thermoelectric voltage generated at the graphene/h-BN interface is due to thermionic emission rather than bulk diffusive transport. As such, the measured property should be thought of as an interfacial Seebeck coefficient rather than a Seebeck coefficient of the constituent materials.

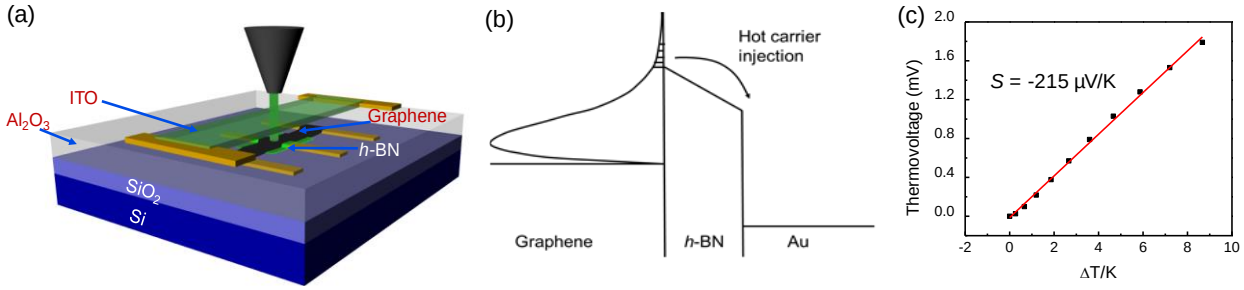

Figure 1. (a) Schematic diagram and (b) energy band diagram of the thermionic emission process for a graphene/*h*-BN/Au heterostructure. (c) Thermoelectric voltage plotted as a function of the temperature difference across the Au/*h*-BN/graphene heterostructure.

Cross-Plane Seebeck Coefficient Measurement of Misfit Layered Compound Superlattices[2]

We have also reported cross-plane thermoelectric measurements of misfit layered compounds $(SnSe)_n(TiSe_2)_n$ (n = 1,3,4,5), approximately 10-50 nm thick (Figure 8). These materials exhibit ultra-low cross-plane thermal conductivities due to the poor phonon-phonon coupling between layers.[3] Here, metal resistance thermometers are fabricated on the top and bottom of the $(SnSe)_n(TiSe_2)_n$ material to measure the temperature difference and heat transport through the material directly. By varying the number of layers in a supercell, n, we vary the interface density while maintaining a constant global stoichiometry. The Seebeck coefficient measured across the $(SnSe)_n(TiSe_2)_n$ samples was found to depend strongly on the number of layers in the supercell (n). When n decreases from 5 to 1, the cross-plane Seebeck coefficient decreases from -31 to -2.5 μV/K, while the cross-plane effective thermal conductivity decreases by a factor of 2, due to increased interfacial phonon scattering. The cross-plane Seebeck coefficients of the $(SnSe)_n(TiSe_2)_n$ are very different from the in-plane Seebeck coefficients, which are higher in magnitude and less sensitive to the number of layers in a supercell, n. We attribute this difference to the different carrier types in the n-SnSe and p-$TiSe_2$ layers and the effect of tunneling on the cross-plane transport.

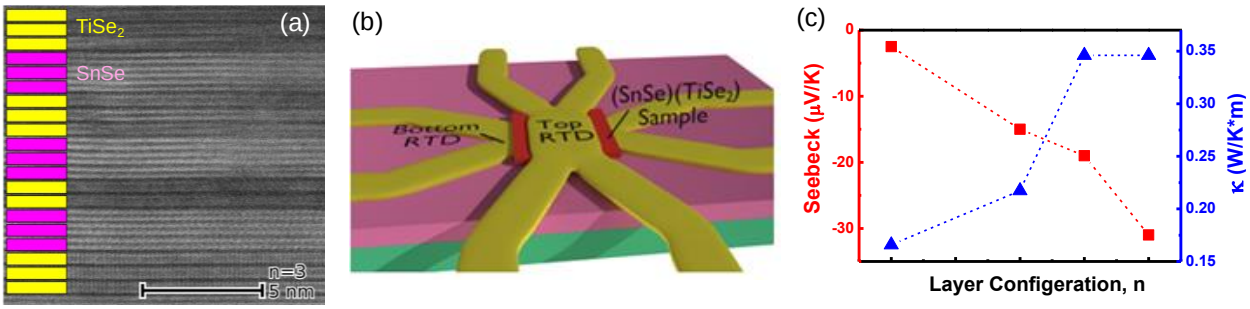

Figure 2. (a) Cross-sectional TEM image of the n = 3 thin film with turbostratic disorder between the layers. Schematic structures overlaid on the n = 3 image highlight the superlattice structure. (b) Schematic diagram of the cross-plane thermoelectric device. (c) Cross-plane Seebeck coefficient and thermal conductivity with different layer configuration n. The Seebeck coefficient is increased from -2.5 to -31 μV/K as n varies from 1 to 5, and the thermal conductivity is increased from 0.17 to 0.34 W/m·K.

Enhanced Cross-plane Thermoelectric Transport of Rotationally-disordered $SnSe_2$ via Se Vapor Annealing[4]

We have also reported a 16-fold increase in the cross-plane Seebeck coefficient of these rotationally-disordered materials (from -38.6 to -631 μV/K) after Se annealing due to both the SnSe-to-$SnSe_2$ transition and the mitigation of unintentional doping by Se vacancies (Fig. 9). Here, the SnSe films were grown by the modulated element reactant (MER) approach in David Johnson's group at University of Oregon. These materials exhibit ultralow cross-plane thermal conductivities, which are advantageous for thermoelectric energy conversion. The initially grown SnSe films have relatively low cross-plane Seebeck coefficients (-38.6 μV/K) due to significant unintentional doping originating from Se vacancies when

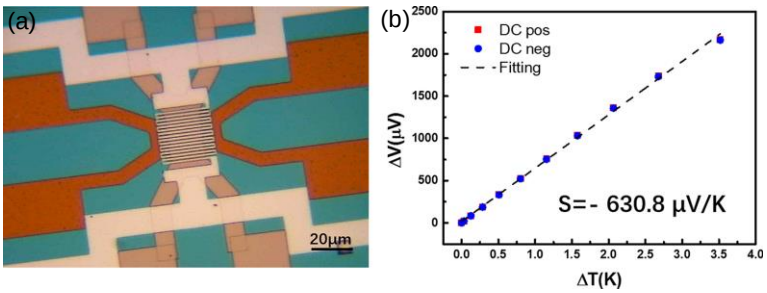

Figure 3. (a) Optical microscope image and (b) cross-plane Seebeck coefficient measurement of rotationally-disordered $SnSe_2$.

annealed in nitrogen, as a result of the relatively high vapor pressure of Se. By performing post-growth annealing at a fixed Se partial pressure (300 °C for 30 min using $SnSe_2$ as the Se source in a sealed tube), a transition from SnSe to $SnSe_2$ is induced, which is evidenced by clear changes in the X-ray diffraction patterns of the films. We also observe a corresponding 6-fold drop in the electrical conductivity (from 3 to 0.5 S/m) after Se annealing, which is consistent with both a drop in the carrier concentration and an increase in band gap. The power factor $S^2\sigma$ increased by a factor of 44 from 4.5 nW/m·K^2 to 0.2 μW/m·K^2 after Se annealing. We believe that these results demonstrate a robust method for mitigating unintentional doping in a promising class of materials for thermoelectric applications.

Enhanced thermoelectric efficiency in topological insulator Bi_2Te_3 nanoplates via atomic layer deposition-based surface passivation[5]

We also reported in-plane thermoelectric measurements of Bi_2Te_3 nanoplates, a topological insulator with Dirac-like metallic surface states, grown by a vapor-solid process in Li Shi's group. The as-grown flakes exposed to ambient conditions exhibit relatively small thermopowers around -34 μV/K due to unintentional surface doping upon gas adsorption and surface oxidation. After removal of the unintentional surface doping and surface passivation by deposition of 30 nm of Al_2O_3 using atomic layer deposition (ALD), the Seebeck coefficient of these flakes increases by a factor of 5 to -169 μV/K (Figure 10). Here, we believe that the ALD-based surface passivation can prevent the degradation of the thermoelectric properties caused by gas adsorption and surface oxidation processes, thus, reducing the unintentional doping in the Bi_2Te_3 and increasing the Seebeck coefficient. The high surface-to-volume ratio of these thin (~10 nm thick) nanoplates make them especially sensitive to surface doping, which is a common problem among nanomaterials in general. An increase in the sample resistance is also observed after the ALD process, which is consistent with the decrease in doping.

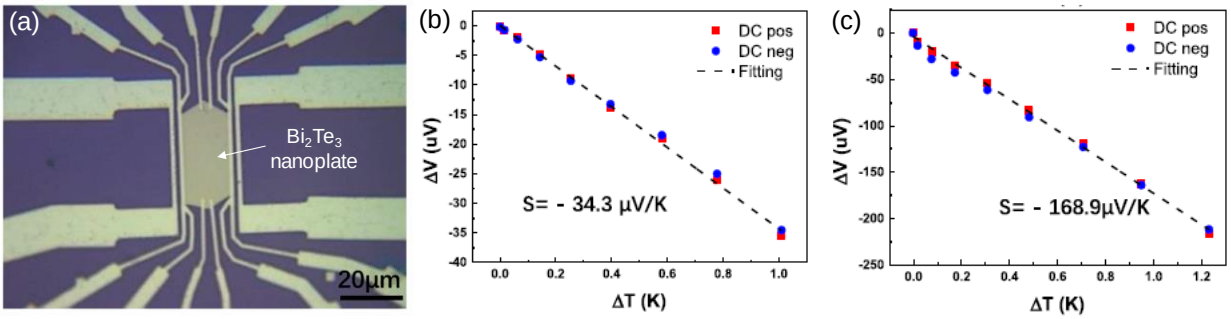

Figure 4. (a) Optical microscope image and Seebeck coefficient measurement (b) before and (c) after ALD passivation.

Future Plans

We plan to measure collective energy transport of excitons (both in-plane and cross-plane) of two-dimensional materials using a combination of electrical, optical, and electron microscopy techniques, and to collaborate with the Shi group measuring the in-plane transport properties of 2D materials using microbridge devices.

References/Publications

1. Poudel, N., S.-J. Liang, D. Choi, B. Hou, L. Shen, H. Shi, L.K. Ang, L. Shi and S. Cronin, *Cross-plane Thermoelectric and Thermionic Transport across Au/h-BN/Graphene Heterostructures.* Scientific Reports, **7**, 14148 (2017).
2. Li, Z., S.R. Bauers, N. Poudel, D. Hamann, X.M. Wang, D.S. Choi, K. Esfarjani, L. Shi, D.C. Johnson and S.B. Cronin, *Cross-Plane Seebeck Coefficient Measurement of Misfit Layered Compounds (SnSe)(n)(TiSe2)(n), (n=1,3,4,5).* Nano Letters, **17**, 1978-1986 (2017).
3. Chiritescu, C., D.G. Cahill, N. Nguyen, D. Johnson, A. Bodapati, P. Keblinski and P. Zschack, *Ultralow thermal conductivity in disordered, layered WSe2 crystals.* Science, **315**, 351-353 (2007).
4. Chen, J., D.M. Hamann, D.S. Choi, N. Poudel, L. Shen, L. Shi, D.C. Johnson and S.B. Cronin, *Enhanced Cross-plane Thermoelectric Transport of Rotationally-disordered $SnSe_2$ via Se Vapor Annealing.* Nano Letters, DOI: 10.1021/acs.nanolett.8b02744 (2018).
5. Chen, J.H., J. Kim, N. Poudel, B.Y. Hou, L. Shen, H.T. Shi, L. Shi and S. Cronin, *Enhanced thermoelectric efficiency in topological insulator Bi_2Te_3 nanoplates via atomic layer deposition-based surface passivation.* Applied Physics Letters, **113**, 083904 (2018).
6. Wang, B., S. Yang, L. Shen and S.B. Cronin, Ultra-Low Power Light Emission via Avalanche and Sub-avalanche Breakdown in Suspended Carbon Nanotubes. ACS Photonics, DOI: 10.1021/acsphotonics.8b00896 (2018).
7. Shen, L., G.N. Gibson, N. Poudel, B. Hou, J. Chen, H. Shi, E. Guignon, N.C. Cady, W.D. Page, A. Pilar and S.B. Cronin, Plasmon resonant amplification of hot electron-driven photocatalysis. Applied Physics Letters, 113, 113104 (2018).
8. Niu, S., G. Joe, H. Zhao, Y. Zhou, T. Orvis, H. Huyan, J. Salman, K. Mahalingam, B. Urwin, S.B. Cronin and J. Wu, Giant optical anisotropy in a quasi-one-dimensional crystal. Nature Photonics, 1 DOI:10.1038/s41566-018-0189-1 (2018).
9. Sarkar, D., W. Wang, M. Mecklenburg, A.J. Clough, M. Yeung, C. Ren, Q. Lin, L. Blankemeier, S. Niu, S.B. Cronin and H. Zhao, Confined Liquid Phase Growth of Crystalline Compound Semiconductors on Any Substrate. ACS Nano, DOI:10.1021/acsnano.8b01819 (2018).
10. Babicheva, V.E., S. Gamage, L. Zhen, S.B. Cronin, V.S. Yakovlev and Y. Abate, ACS Photonics, 5, 2106-2112 (2018).
11. Wang, B., L. Shen, S. Yang, J. Chen, J. Echternach, R. Dhall, D. Kang and S. Cronin, Physical Review Applied, 9 (2018).
12. Choi, D., N. Poudel, S. Park, D. Akinwande, S.B. Cronin, K. Watanabe, T. Taniguchi, Z. Yao and L. Shi, ACS Applied Materials & Interfaces, 10, 11101-11107 (2018).
13. Abate, Y., D. Akinwande, S. Gamage, H. Wang, M. Snure, N. Poudel and S.B. Cronin, Advanced Materials, 1704749 (2018).
14. Zhao, H., Z. Dong, H. Tian, D. DiMarzi, M.G. Han, L. Zhang, X. Yan, F. Liu, L. Shen, S.B. Cronin and S.J. Han, 29, 1703232 (2017).
15. Shen, L., N. Poudel, G.N. Gibson, B. Hou, J. Chen, H. Shi, E. Guignon, W.D. Page, A. Pilar and S.B. Cronin, Nano Research, 11, 2310-2314 (2018).
16. Wang, B., F. Rezaeifar, J. Chen, S. Yang, R. Kapadia and S.B. Cronin, ACS Photonics, 4, 2706-2710 (2017).
17. Wang, Yang, Chen, Mann, Bushmaker and Cronin, Applied Physics Letters, 111, 131101 (2017).
18. Choi, D., N. Poudel, S.B. Cronin and L. Shi, Applied Physics Letters, 110, 073104 (2017).
19. Chatzakis, I., Z. Li, A.V. Benderskii and S.B. Cronin, Nanoscale, 9, 1721-1726 (2017).

Aluminum-graphite batteries using ionic liquid (analog) electrolytes

Hongjie Dai, Department of Chemistry, Stanford University, Stanford, CA 94305

Program Scope

Renewable energy storage on the grid scale is one of today's great challenges, which left unsolved will allow the developed world's dependence on fossil fuels to continue indefinitely. Ideally, devices employed for energy storage should be low-cost, capable of a high rate energy uptake/delivery, environmentally friendly, non-toxic, non-flammable, and have a high cycle life. Batteries utilizing aluminum metal at the anode are very promising for high energy density energy storage devices given its high theoretical volumetric capacity of 8040 $mAh \cdot cm^{-3}$, compared to 2046 for Li $mAh \cdot cm^{-3}$, as a result of its three electron redox. Furthermore, Al is about 1000 times more earth abundant than lithium, and as demonstrated by our group[1] can use graphite as a high-rate cathode material, which is much cheaper and less toxic than lithium battery cathode materials. This Al-graphite battery used an Al metal anode, 3D graphitic foam (or pyrolytic graphite foil) cathode (70 mAh/g capacity), and ionic liquid electrolyte (Aluminum chloride : 1-ethyl-3-methylimidazolium chloride ($AlCl_3$-EMIC) = 1.3 : 1), rendering the battery non-flammable, and thousands of cycles at a rate of 4000 mA/g without capacity decay was easily demonstrated. The research described here involves the further development and characterization of the graphite cathode and improved electrolyte systems (lower cost and toxicity), all with the focus of increasing cathode capacity and elimination of parasitic side reactions from battery charge/discharge.

Recent Progress

While Al-graphite batteries using graphitic foam cathodes exhibited impressive performance (could charge in ~1 min, power density = 3,000 $W \cdot kg^{-1}$), the increased volume of the cathode would hamper future optimization of energy density. Free-standing graphite cathodes prepared from a mixture of graphite powder and PVDF binder were pursued using the same ionic liquid electrolyte, and demonstrated increased capacities of ~110 mAh/g (Fig. 1A) (which increased the energy density of the battery from 40 to 68.7 $Wh \cdot kg^{-1}$) with Coulombic efficiencies (which improved at higher rate) of 98% at 0.9C rate (Fig. 1B). Intercalation of graphite by $AlCl_4^-$ was again confirmed using ex-situ XRD and in-situ Raman of the graphite flake during charge-discharge, confirming the same battery charge-discharge reactions. Furthermore, chlorination of the graphite edges during battery charge/discharge was also demonstrated using XAFS, indicating that minimizing the surface area and defect density of the graphite particles would be important for minimizing irreversible capacity loss involving the oxidation of $AlCl_4^-$ from the electrolyte, which could be catalyzed by graphite edge sites.

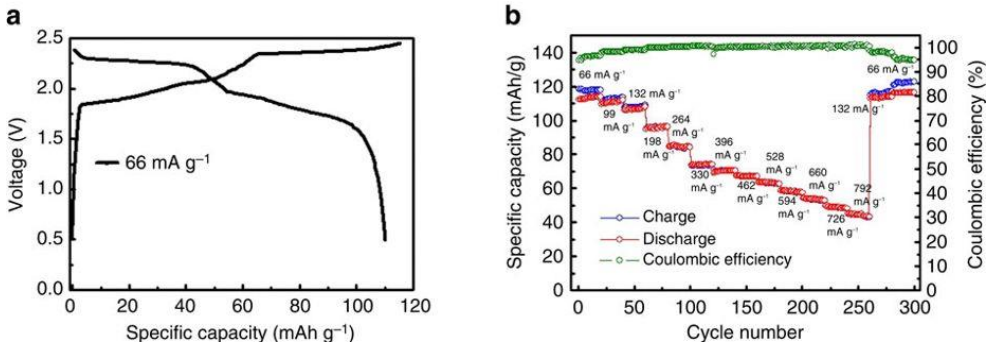

Figure 1. Galvanostatic charge/discharge data for Al-graphite battery using free-standing graphite powder cathode demonstrating increased capacity. A) Charge/discharge curve, B) Rate capability of graphite powder cathode.

Another demonstration of increased capacity, occurring now at even higher voltages than previously accessed by this aluminum battery, came from low temperature studies. For this work, graphite powder cathodes were prepared on a conductive carbon substrate opposed to free-standing form, as described in the paragraph above. At room temperature, the capacity of this Al battery was limited to ~80 mAh/g using a cutoff voltage of 2.4V, above which side reaction would rapidly ensue (irreversible capacity obtained). By changing the electrolyte to $AlCl_3$: EMIC = 1.5 : 1 or 1.7 : 1, which have lower melting points, the battery could easily operate at temperatures of -10°C and -20°C. Graphite intercalation is well known to happen in stages, hence the display of multiple plateaus during charge/discharge of batteries using it as an anode or cathode material.

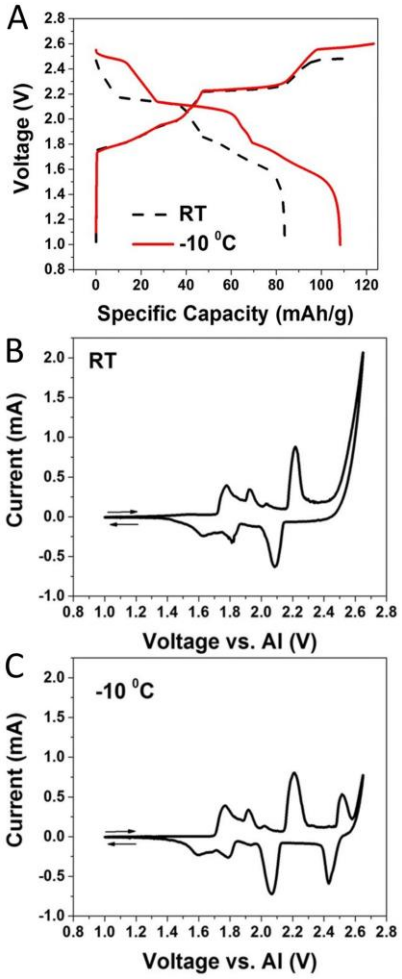

It was demonstrated that by cooling the battery to -10°C, an extra staging event of graphite was obtained, which was confirmed through operando X-ray diffraction measurements (Fig. 3), corresponding to the extra plateau observed around 2.5V during galvanostatic charge/discharge (Fig. 2A). The Al battery studied here displays two main plateaus at room temperature, the first of which can be decomposed into multiple different redox events as shown by cyclic voltammetry (Fig. 2B). When CV is performed at -10°C, a clear new redox couple emerges around 2.5V (Fig. 2C), which corresponds to the new plateau seen in battery charge-discharge. This indicates the stage three graphite intercalation compound is only stable at low temperature.

Figure 2. A) Galvanostatic Charge/discharge curve for Al-graphite battery at room temperature vs. -10C when charged to high voltage; cyclic voltammetry of the graphite cathode at B) room temperature showing irreversible capacity at high voltage and at C) -10C where this redox reaction becomes reversible.

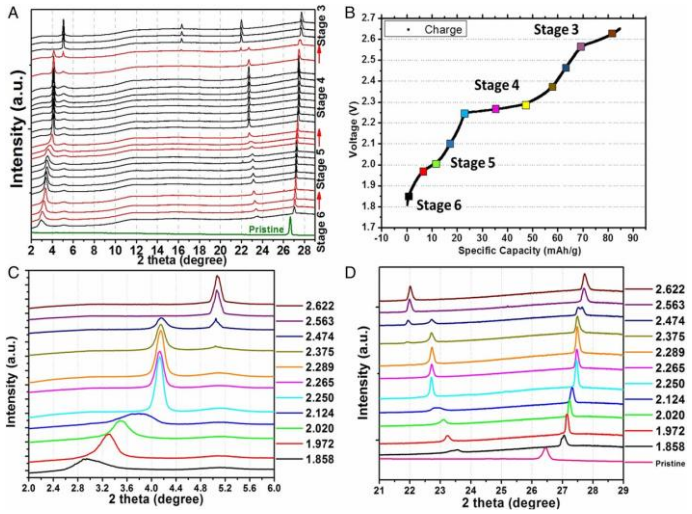

Figure 3. Operando XRD on the graphite positive electrode during galvanostatic charging of the Al-graphite battery. A) Operando XRD spectra, B) corresponding galvanostatic charging curve, C) low angle regime and D) large angle regime of the operando XRD spectra showing details of the spectral evolution.

Another endeavor involved in the development of this Al-graphite battery system was lowering the cost of the electrolyte. As demonstrated by Abood et al.[3], aluminum could be deposited from a 1 : 1 mixture of aluminum chloride and urea, which forms an ionic liquid analog through the heterolytic cleavage of Al_2Cl_6 by the Lewis basic urea ligand. At $0.50/kg, urea would provide for a superior electrolyte in terms of cost over EMIC (estimated $50/kg, given the scale). Our group demonstrated that these ionic liquid analogs (termed analogs since the resulting liquids involve an equilibrium between ionic and neutral species, and are not simply deep eutectics) at a 1.3 : 1 mixture of aluminum chloride to urea was far superior for Al-deposition, meanwhile still allowing highly reversible intercalation of $AlCl_4^-$ at the graphite cathode (70 mAh/g capacity) with an overall Coulombic efficiency of >99.5% during initial cycling at 100 mA/g (Fig. 4A, B). Al deposition therefore appeared to still occur most easily through the $Al_2Cl_7^-$ anion, which was shown to exist in this system using Raman spectroscopy, as is known for the EMIC-$AlCl_3$ system employed previously. The ionic liquid analog was somewhat more viscous than imidazolium based electrolytes, but still maintained reasonable rate capability (Fig. 4C).

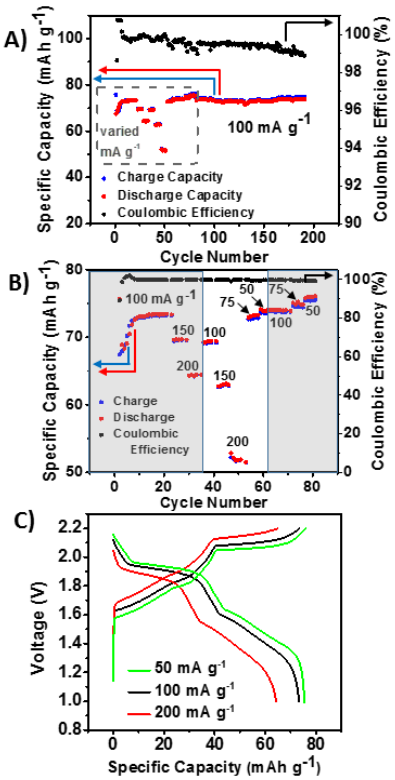

Figure 4. Galvanostatic charge/discharge data for Al-graphite battery employing $AlCl_3$: urea = 1.3 : 1 electrolyte. at various rates at room temperature. A) Cycling data, B) zoom of initial cycling of **A** showing rate capability (gray region represents 2.25V upper cutoff, white region represents 2.20V upper cutoff), and C) Galvanostatic charge/discharge curves.

Future Plans

In order to utilize the high capacity of the Al metal anode, higher capacity cathode materials need to be developed. MC Lin et al. (2018) have demonstrated the use of a sulfur/MWCNT composite cathode that lasts easily for 100 cycles using the $AlCl_3$-urea electrolyte system. While $AlCl_3$-urea electrolyte system has the advantage of low-cost, its ionic conductivity is lower than imidazolium based ionic liquids due to a higher viscosity and lower ionicity. Other mechanisms through which to obtain higher stages of intercalation into graphite will be explored, as well as a search for other types of conversion cathodes for the Al battery utilizing chloride rich electrolytes. Alternative inorganic electrolyte systems will also be pursued.

References

1. Lin, M.; Gong, M.; Lu, B.; Wu, Y.; Wang, D.; Guan, M.; Angell, M.; Chen, C.; Yang, J.; Hwang, B.; Dai, H. An ultrafast rechargeable aluminium-ion battery. *Nature* **2015**, *520*, 325-+.

2. Wang, D.; Wei, C.; Lin, M.; Pan, C.; Chou, H.; Chen, H.; Gong, M.; Wu, Y.; Yuan, C.; Angell, M.; Hsieh, Y.; Chen, Y.; Wen, C.; Chen, C.; Hwang, B.; Chen, C.; Dai, H. Advanced rechargeable aluminium ion battery with a high-quality natural graphite cathode. *Nature Communications* **2017**, *8*, 14283.

3. Abood, H. M. A.; Abbott, A. P.; Ballantyne, A. D.; Ryder, K. S. Do all ionic liquids need organic cations? Characterisation of [AlCl2 center dot nAmide](+) AlCl4- and comparison with imidazolium based systems. *Chemical Communications* **2011**, *47*, 3523-3525.

Publications

1) DY Wang, CY Wei, MC Lin, CJ Pan, HL Chou, HA Chen, M Gong, Y Wu, C Yuan, M Angell, YJ Hsieh, YH Chen, CY Wen, CW Chen, BJ Hwang, CC Chen, and H Dai. "Advanced rechargeable aluminium ion battery with a high-quality natural graphite cathode". *Nat. Commun.* **2017**, 8, 14283.
2) CJ Pan, C Yuan, G Zhu, Q Zhang, CJ Huang, MC Lin, M Angell, BJ Hwang, P Kaghazchi, and H Dai. "An operando X-ray diffraction study of chloroaluminate anion-graphite intercalation in aluminum batteries". *Proc. Natl. Acad. Sci. U. S. A.* **2018**, 115, 5670-5675.
3) M Angell, G Zhu, MC Lin, Y Rong, and H Dai. "High Coulombic efficiency aluminum-ion battery using an $AlCl_3$-urea ionic liquid analog". *Proc. Natl. Acad. Sci. U. S. A.* **2017**, 114, 834-839.

Spin Transport in group IV materials and 2D membranes

Hanan Dery

Depts. of Electrical and Computer Engineering and of Physics, University of Rochester

Program Scope

During the last two years, this program was mainly focused on two studies. The first one dealt with many-body interactions in monolayer transition-metal dichalcogenides (ML-TMDs), manifested through the exciton spectrum. The second study focuses on the effect of localization on optical properties in ML-TMDs. While we have made progress in both fronts [see 2-year list of publications supported by BES], I will focus in this short document only on the progress we have made in understanding the localization effects.

Recent Progress: optical properties of ML-TMDs

Photoluminescence (PL) experiments of ML-TMDs often show that the binding energy of negative trions (a three-body complex made of two electrons and a hole) is conspicuously similar to the energy of optical phonons. This enigmatic coincidence calls into question whether phonons are involved in the radiative recombination process. We have recently addressed this question [1], unraveling an intriguing optical transition mechanism. Its initial state is a localized charge (electron or hole) and delocalized exciton. The final state is the localized charge, phonon and photon. In between, the intermediate state is a virtual trion formed when the localized charge captures the exciton through emission of the phonon. We have analyzed the difference between recombination processes that involve real and virtual trions (i.e., with and without a phonon), and provided useful ways to distinguish between the two in experiment.

To better explain the research question, we use the experimental data in Fig. 1, taken by the group of Xiaodong Xu with whom we collaborated in this project [1]. The top panels show the normalized PL from $MoSe_2$, WSe_2, WS_2, and MoS_2 (left to right), where all the MLs are unintentionally *n*-type and all are supported on Si/SiO2 substrates. In each case, the emission spectra have two peaks where the higher energy one is attributed to neutral excitons (X^0). Typically, it is tempting to attribute the low-energy peak to negative trions because some of these peaks also appear in the absorption spectra when electrons are added to the ML through a gate voltage. However, when performing Raman spectroscopy on the same samples (lower panels of Fig. 1), we find that the energy of the dominant Raman-active phonon mode matches the energy difference between X^0 and the low-energy peak in the PL. This systematic behavior raises the question: Does the low energy peak in the PL stem from recombination of real trions or is it phonon-assisted recombination of excitons? This important question was addressed in our work.

Phonon-assisted optical transitions of neutral excitons, governed by the Fröhlich interaction, are weak in ML-TMDs. It is a result of the charge neutrality and small size of the exciton as well as the similar effective masses of electrons and holes. On the other hand, phonon-assisted recombination that is facilitated by localized electrons is strong. Here, the strong Fröhlich coupling between a localized electron (or hole) and the lattice is used to capture a nearby exciton by emission of a phonon. The capture mechanism is considered virtual during radiative recombination if $\Delta E = E_T + E_\lambda - E_X - E_\ell \neq 0$, where the energies are of the localized trion (E_T), exciton (E_X), localized charge (E_ℓ), and phonon (E_λ). Energy conservation dictates that the exciton is converted to a phonon plus photon. Furthermore, if ΔE is close to zero, the

emission spectrum includes a single dominant phonon-assisted optical transition instead of a series of phonon-replicas that decay according to the standard Huang-Rhys analysis.

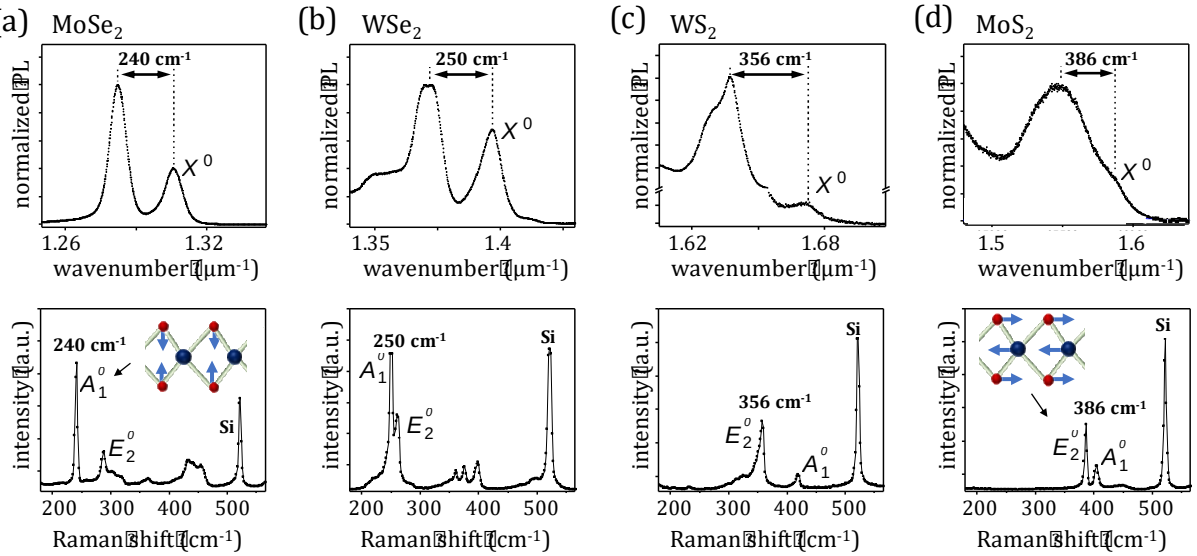

FIG. 1: (a)-(d) Normalized PL (top) and Raman spectra (bottom) of common ML-TMDs supported on Si/SiO_2 substrates. The normalized PL includes the neutral exciton peak (X^0) and a peak that is commonly associated with the negatively-charged trion in *n*-type samples. The energy difference between these peaks matches the energy of the dominant Raman active phonon mode in each of the MLs, as is readily seen in the top and bottom panels. The active Raman phonons are the homopolar and longitudinal-optical modes, denoted by A_1' and E_2', respectively. Their atomic displacements are indicated in the insets of (a) and (d). The Raman spectra also show the active optical phonon mode of the Si substrate around 520 cm^{-1}

Figure 2(a) shows the calculated energies in ML-WSe_2 when a +1e charged defect is embedded in SiO_2. The electron binding energy is largest when the defect is at the surface, $E_\ell(z$ = 0.3 nm) ~200 meV. A similar localization-induced enhancement is seen in the energy of the trion (E_T). On the other hand, excitons are essentially unaffected by the defect, as shown by the inset. The weak dependence stems from the confluence of exciton neutrality and lack of contact between extrinsic defects and electrons or holes in the mid-plane of the ML. Similarly, $E_T - E_\ell$ is also largely independent of z because the defect interacts weakly with the added electron-hole pair in the trion complex. Figure 2(c) shows the value of $\Delta E = E_T + E_\lambda - E_X - E_\ell$, where $E_\lambda =$ 32 meV is the energy of the phonon [2].

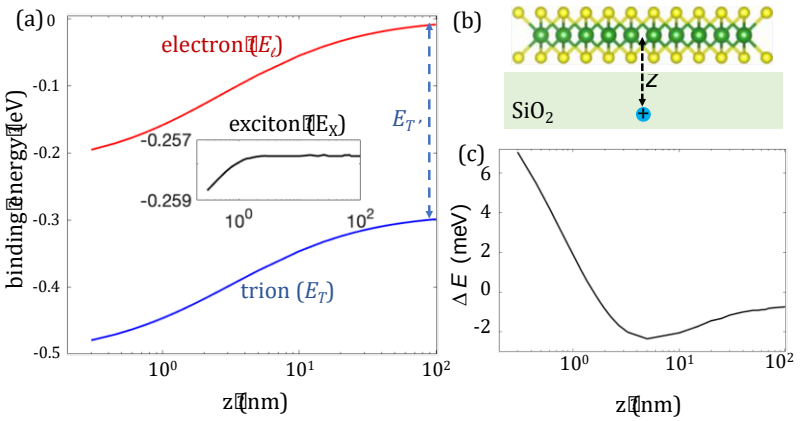

FIG. 2: (a) Ground-state energies of electrons (E_ℓ), excitons (E_X, inset), and negative trions (E_T) in ML-WSe_2 supported on SiO_2 substrate as a function of the distance of a positive point-charge defect from the mid-plane of the ML. E_T' denotes the energy of delocalized trions ($z \to \infty$). (b) A cartoon of the ML, substrate and extrinsic defect. (c) $\Delta E = E_T + E_\lambda - E_X - E_\ell$, where $E_\lambda = 32$ meV is the phonon energy.

We analyze interactions that facilitate the capture process. When the magnitude of their matrix elements is comparable or larger than ΔE, phonon-assisted optical transitions display a strong resonance in the emission spectra. The matrix element reads [1]

$$M_\lambda(K,q) = \left\langle \Psi_T \middle| \sum_j \beta_j D_{j,\lambda}(\boldsymbol{q})\, e^{-i\boldsymbol{q}\boldsymbol{r}_j} \middle| \Psi_X(\boldsymbol{K})\Psi_\ell \right\rangle \quad (1)$$

where $\lambda = \{A_1', E_2'\}$ is the phonon mode (insets of Fig. 1). $\boldsymbol{q}$ and $\boldsymbol{K}$ are the phonon and exciton wavevectors, respectively. The localized electron (trion) state is denoted Ψ_ℓ (Ψ_T). The exciton in the initial state is delocalized, $\Psi_X(\boldsymbol{K}) = \varphi(\boldsymbol{r})e^{-i\boldsymbol{K}\boldsymbol{R}}/\sqrt{A}$, where $\boldsymbol{r} = \boldsymbol{r}_e - \boldsymbol{r}_h$ is the relative coordinate, and $\boldsymbol{R} = (m_e\boldsymbol{r}_e + m_h\boldsymbol{r}_h)/(m_e + m_h)$ is the center-of-mass coordinate. A is the area of ML. The sum over j takes into account the long-range Fröhlich interaction between the j^{th} particle and longitudinal-optical phonons, $D_{j,E_2'}(\boldsymbol{q})$, or the short-range interaction of the particle with homopolar phonons, $D_{j,A_1'}(\boldsymbol{q})$. $\beta_j = 1$ ($\beta_j = -1$) when the j^{th} particle is an electron (hole).

The rate of the phonon-assisted recombination mediated by localized electrons reads [1]

$$\frac{1}{\tau_\lambda(K)} = \left[\frac{1 \pm p_\ell}{2} n_d A \frac{\sum_q |M_\lambda(K,q)|^2 \beta_j D_{j,\lambda}(\boldsymbol{q})}{(\Delta E - E_K)^2 + \Gamma^2}\right] \frac{1}{\tau_\ell} \quad (2)$$

where n_d is the density of localized electrons due to extrinsic defects, Γ is the broadening parameter, and E_K is the exciton kinetic energy. τ_ℓ is the radiative decay time of a localized trion. The term $(1 \pm p_\ell)/2$ denotes the change in the recombination rate when the localized electron system becomes spin-polarized ($p_\ell \neq 0$) because of a strong magnetic field or magnetic proximity effects. In more detail, a delocalized exciton can be captured only if the spin of its electron component is opposite to that of the localized electron (the valley degree of freedom is not a good quantum number for localized electrons, and therefore localized trions can only appear in a singlet-spin configuration [1]). When the localized electrons are spin-polarized, the phonon-assisted recombination rate is enhanced for one exciton branch, $(1 + p_\ell)/2$, while it is suppressed for the other, $(1 - p_\ell)/2$. Below, we focus on the non-magnetic case ($p_\ell = 0$).

The expression inside square brackets in Eq. (2), hereafter denoted by $C_\lambda(K)$, is unit-less and it represents the amplitude of the virtual capture process. Figure 3(a) shows its value when $n_d = 4 \cdot 10^{11}$ cm^{-2} for the Fröhlich interaction, $\lambda = E_2'$, in three different regimes with $\Delta E > 0$, $\Delta E \approx 0$, and $\Delta E < 0$. As shown in Fig. 2(c), ΔE is positive for surface defects ($z < 1.5$ nm). Following Eq. (2), the capture amplitude in this case is optimal when $E_K = \Delta E$. For farther impurities, on the other hand, the capture amplitude decreases monotonically because $\Delta E < 0$. The general trends in Fig. 3(a) are that faster excitons are less prone to the capture process, and that the capture is weaker when the defect is remote. The latter reassures the important role of

localization. It is so because $M_\lambda(K,q)$ is sizable when $q\ell_e \lesssim 1$, where ℓ_e is the characteristic electron localization length. That is, tighter localization enables more phonons to be involved in the capture process and contribute effectively to the sum in Eq. (2). In addition, the overlap between the initial and final states in Eq. (1) is optimal for nearby defects because ℓ_e becomes comparable to both the exciton Bohr radius and the characteristic distances between the particles of the trion complex.

Figure 3(b) shows the calculated normalized PL for a Boltzmann distribution of excitons at T = 5 K. We notice that while the amplitude of the capture process depends on how far the extrinsic defect is from the ML, as shown in Fig. 3(a), the energy of the emitted photon does not, as shown in Fig. 3(b). Namely, the spectral line always appears at E_λ below X^0. Consequently, the resonance photon energies are similar in devices in which the defects are concentrated at a certain distance from the ML, and others in which the defects are uniformly distributed in the substrate. Figure 3(b) shows that the emission from delocalized excitons in the light cone is comparable with the phonon-assisted recombination. The intensity ratio between the phonon-related peak (X^p) and the delocalized exciton peak (X^0) is commensurate with τ_X/τ_ℓ and with the capture efficiency which is governed by the defects' density and distance from the ML. We have considered the Fröhlich interaction and assumed that the density of localized electrons is $n_d = 4\cdot 10^{11}$ cm^{-2}, and that $\tau_\ell = 10\tau_X$ following time-resolved PL experiments [3].

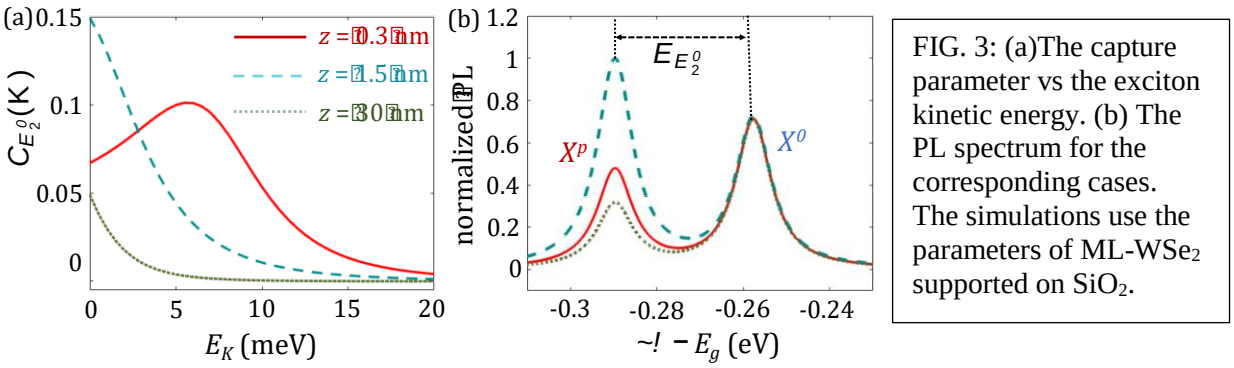

FIG. 3: (a)The capture parameter vs the exciton kinetic energy. (b) The PL spectrum for the corresponding cases. The simulations use the parameters of ML-WSe_2 supported on SiO_2.

In conclusion, we have unraveled an intriguing phonon-assisted radiative process in ML-TMDs. It starts when a localized electron virtually captures a delocalized exciton by emitting a phonon, followed by photon emission from the intermediate virtual trion state. Overall, it is a strong process because $E_T - E_\ell$ nearly resonates with $E_X - E_\lambda$ where $E_T(E_\ell)$ is the energy of a localized trion (electron) and E_X (E_λ) is the energy of an exciton (optical phonon). It is this resonance condition that led to widespread confusion, where the radiative recombination was often attributed to real trions instead of virtual ones; participation of optical phonons in the radiative process was largely ignored. Our work in Ref. [1] discusses ways to distinguish between radiative recombination processes with real and virtual trions based on the energy of the emitted photons. It also discusses ways to probe localization effects by comparing the absorption and emission spectra, as well as by using device quality, gate voltage, temperature, and magnetic field as knobs in PL experiments.

Future Plans

1. We plan to perform a detailed study, showing how the phonon-assisted recombination mechanism supports the findings of recent experiments that probed biexcitons and five-

particle complexes in ML-WSe_2 [4]. Our claim is that the five-particle complex observed in these PL experiments is phonon-assisted recombination of biexcitons mediated by localized electrons.

2. We plan to investigate what causes the circular polarization degree emitted from ML-$MoSe_2$ to be negligible when this material is excited by a circularly polarized light. Of all monolayers in the family, ML-$MoSe_2$ is the only one to show poor optical orientation properties. This open question has not been addressed for nearly a decade.

References

[1] D. Van Tuan, A. M. Jones, M. Yang, X. Xu, and H. Dery, arXiv:1805.08722 (submitted).

[2] Courtade *et al*., Phys. Rev. B **96**, 085302 (2017).

[3] Robert *et al*., Phys. Rev. B **93**, 205423 (2016); Wang *et al*., Phys. Rev. B **90**, 075403 (2014).

[4] Chen *et al*., Nat. Commun. **9**, 3717 (2018); Ye *et al*., Nat. Commun. **9**, 3718 (2018); Li *et al*., Nat. Commun. **9**, 3719 (2018); Barbone *et al*., Nat. Commun. **9**, 3721 (2018).

Publications (2-year list of publications supported by BES)

[1] D. Van Tuan, B. Scharf, I. Žutić, and H. Dery, *Intervlley plasmons in crystals*, arXiv:1901.02567 (to be submitted).

[2] D. Van Tuan, A. M. Jones, M. Yang, X. Xu, and H. Dery, *Virtual trions in the photoluminescence of monolayer transition-metal dichalcogenides*, arXiv:1805.08722 (submitted).

[3] B. Scharf, D. Van Tuan, I. Žutić, and H. Dery, *Dynamical screening in monolayer transition-metal dichalcogenides and its manifestations in the exciton spectrum*, Topical Review in J. Phys. Condens. Matter (in press, https://doi.org/10.1088/1361-648X/ab071f); arXiv:1801.06217.

[4] I. Žutić, A. Matos-Abiague, B. Scharf, H. Dery, and K. Belashchenko, *Proximitized materials*, Materials Today **22**, 85-107 (2019).

[5] D. Van Tuan, B. Scharf, Z. Wang, J. Shan, K. F. Mak, I. Žutić, and Hanan Dery, *Probing many-body interactions in monolayer transition-metal dichalcogenides*, Phys. Rev. B **99**, 085301 (2019).

[6] D. Van Tuan, M. Yang, and H. Dery, *Coulomb interaction in monolayer transition-metal dichalcogenides*, Phys. Rev. B **98**, 125308 (2018).

[7] D. Van Tuan, B. Scharf, I. Žutić, and H. Dery, *Marrying Excitons and Plasmons in Monolayer Transition-Metal Dichalcogenides*, Phys. Rev. X **7**, 041040 (2017).

DOE Award # DE-FG02-07ER46426, Stanford University

Nanophotonics-enhanced solar cells

PI: Shanhui Fan,
Department of Electrical Engineering, Stanford University. Email: shanhui@stanford.edu.

Co-PI: Prof. Mark Brongersma,
Department of Material Science and Engineering, Stanford University, Email: markb29@stanford.edu.

Program Scope or Definition

The overall emphasis of the program is to develop a fundamental understanding of light-matter interaction at nanocale, in the context of renewable energy harvesting, including enhancing the efficiency of solar cells. Towards this goal, we are undertaking substantial efforts on developing the optimal strategy for photonic based thermal management of solar cells, on developing nanophotonic structures for spectrum splitting which is potentially for harvesting the entire solar spectrum efficiently, on developing an understanding of the theoretical potential in renewable for harvesting outgoing thermal radiation, and on new concepts of thermal metamaterials inspired by nanophotonics.

Below we review some of the major progress [1-10] made in this report period.

Recent Progress

Photonic cooling of solar cells. The heating of a solar cell has significant adverse consequences on both its efficiency and its reliability. In a paper published in ACS Photonics [1], we outline a comprehensive photonic strategy for the cooling of silicon solar cells. For this purpose we experimentally characterize the thermal radiation and solar absorption properties of commercial silicon solar cells (Figure 1 a-c). On the basis of such experimental characterization, we propose a comprehensive photonic approach by simultaneously performing radiative cooling while also selectively utilizing sunlight. In particular, we design a photonic cooler made of one-

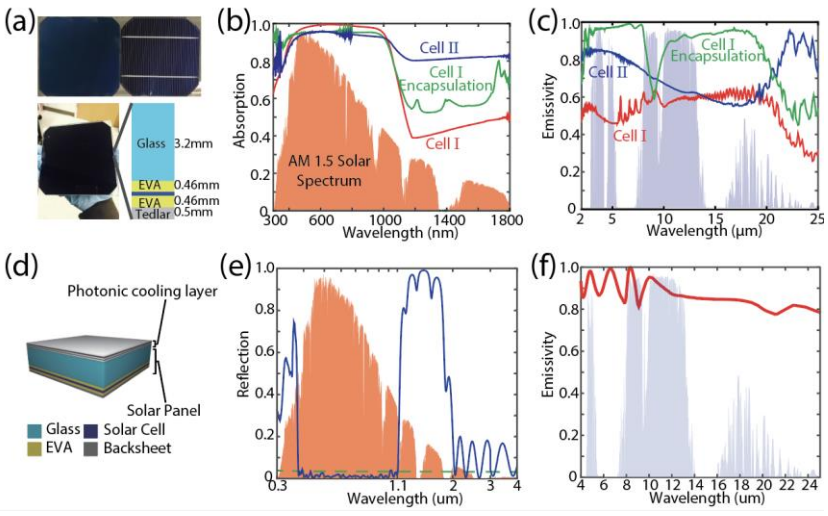

Figure 1. Photonic cooling of solar cells. (a) Photo of typical silicon solar cells (top) and a solar cell with encapsulation (bottom). (b),(c) Experimentally measured absorption (b) and thermal emissivity (c) spectra of the two solar cells and an encapsulated solar cell shown in (a). (d) Schematic of a proposed photonic cooling layer on top of an encapsulated solar panel. (e) Reflection spectrum of the photonic cooling layer in the solar spectrum range, with strong sub-bandgap reflection and broadband above-bandgap anti-reflection. (f) Thermal emissivity spectrum of the photonic cooling layer in the infrared wavelength range.

dimensional photonic films (Figure 1d) that can strongly radiate heat through its thermal emission while also significantly reflecting the solar spectrum in the sub-band-gap and ultraviolet regimes (Figure 1e-f). We show that applying this photonic cooler to a solar panel can lower the cell temperature by over 5.7 °C. We also show that this photonic cooler can be used in a concentrated photovoltaic system to significantly reduce the solar cell temperature or required cooling power. This photonic cooler can be readily implemented in current photovoltaic modules as a retrofit to improve both efficiency and lifetime. Our approach points to an optimal photonic approach for photonic thermal management of solar cells.

Efficient subwavelength photon sorting with an anti-Hermitian photodetector. The ability to split an incident light beam into separate wavelength bands is central to a diverse set of optical applications, including photovoltaics, photocatalysis, imaging, biosensing and communication. Entirely new opportunities are currently emerging with the recently demonstrated possibility to spectrally split light at a subwavelength scale with optical nanostructures. Unfortunately, such small structures offer limited spectral control and are hard to exploit in optoelectronic devices. As a collaboration between Brongersma and Fan groups [6], in a paper published in Nature Communications, we overcome both challenges and demonstrate how within a single-layer metafilm one can laterally sort photons of different wavelengths below the free-space diffraction limit and extract a useful photocurrent (Figure 2). This chipscale demonstration of anti-Hermitian coupling between resonant photodetector elements also facilitates near-unity photon-sorting efficiencies, near-unity absorption, and a narrow spectral response (~ 30 nm) for the different wavelength channels (Figure 2d-e). This work opens up entirely new design paradigms for image sensors and energy harvesting systems in which the active elements both sort and detect photons.

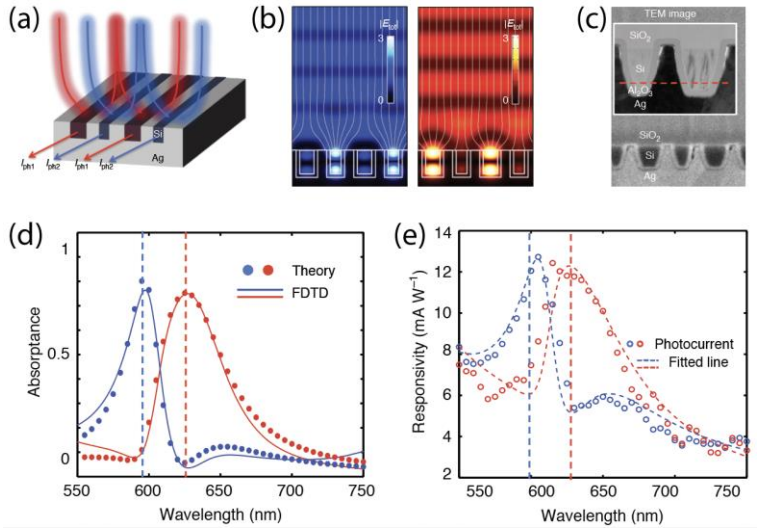

Figure 2. (a) Schematic of a photon sorting, metafilm device that leverages anti-Hermitian coupling. (b) Simulated total electric field with superposed power flow lines at the wavelengths of 595 nm (left) and 625 nm (right) showing that Mie-like resonances are excited selectively in narrow(/wide) beams at shorter(/longer) illumination wavelengths. (c) Cross-sectional SEM image of a fabricated device structure. The inset shows the TEM image of a repeating unit cell of the metafilm with electrically insulated Si beams (light) embedded in an Ag film (dark). (d) Theoretical calculated and simulated absorption spectra of the multi-sized nanobeam array. (e) Experimentally extracted photocurrent spectrum depicted as circled point with the fitted line for an anti-Hermitian coupled system.

Thermodynamic limits of energy harvesting from outgoing thermal radiation. A large part of the research on renewable energy has focused on harvesting power from solar radiation. But, for the Earth to maintain its temperature, it must radiate to the outer space an amount of power approximately equal to that of the incoming solar radiation. However, far less is understood about the theoretical limits of harvesting power from such outgoing radiation. In a paper published in the Proceedings of the National Academy of Sciences [8], we derive the thermodynamic limits of harvesting power from the outgoing thermal radiation from the ambient to the cold outer space. The derivations are based on a duality relation between thermal engines that harvest solar radiation and those that harvest outgoing thermal radiation. In particular, we derive the ultimate limit for harvesting outgoing thermal radiation, which is analogous to the Landsberg limit for solar energy harvesting, and show that the ultimate limit far exceeds what was previously thought to be possible (Table 1). Our results indicate a theoretical limit that far exceeds what was previously thought to be possible and highlight the significant potential for harvesting outgoing thermal radiation for renewable energy applications.

Limit	Positive illumination: efficiency, %	Negative illumination: power, W/m^2
Shockley–Queisser	40.7	54.8
Blackbody	85.4	48.4
Multicolor	86.8	55.0
Landsberg	93.3	153.1

Table 1. Comparison of thermodynamic limits of positive and negative illumination of energy conversion

Thermal meta-device in analogue of zero-index photonics. Inspired by the developments in photonic metamaterials, the concept of thermal metamaterials has promised new avenues for manipulating the flow of heat. In photonics, the existence of natural materials with both positive and negative permittivities has enabled the creation of metamaterials with a very wide range of effective parameters. In contrast, in conductive heat transfer, the available range of thermal conductivities in natural materials is far narrower, strongly restricting the effective parameters of thermal metamaterials and limiting possible applications in extreme environments. In a paper published in Nature Materials [10], Fan in collaboration with Prof. Cheng Wei Qiu at the National University of Singapore identify a rigorous correspondence between zero index in Maxwell's equations and infinite thermal conductivity in Fourier's law (Figure 3a). We also propose a conductive system with an integrated convective element (Figure 3b) that creates an extreme effective thermal conductivity, and hence by correspondence a thermal analogue of photonic near-zero-index metamaterials, a class of metamaterials with crucial importance in controlling light. Synergizing the general properties of zero-index metamaterials and the specific diffusive nature of thermal conduction, we theoretically and experimentally demonstrate a thermal zero-index cloak

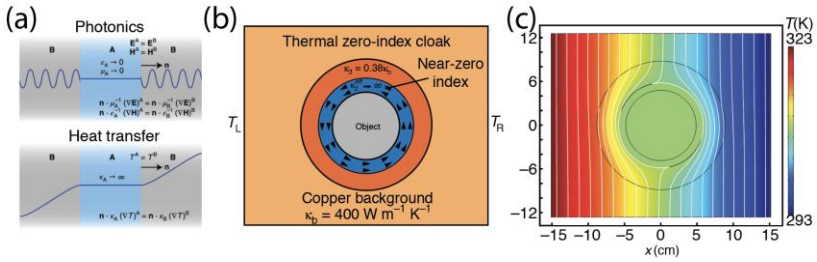

Figure 3. (a) The analogue between electromagnetic wave transport through a zero-index medium and heat conduction through a material with infinite thermal conductivity. (b) Schematic of a thermal zero-index cloak with high effective thermal conductivity achieved through heat conduction. (c) Steady-state temperature profile of the thermal cloak. The object is successfully protected by the thermal zero-index cloak without distortion of the temperature field.

(Figure 3c). In contrast with conventional thermal cloaks, this meta-device can operate in a highly conductive background and the cloaked object preserves great sensitivity to external temperature changes. Our work demonstrates a thermal metamaterial which greatly enhances the capability for molding the flow of heat.

Future Plans

In the near future (the coming year) we plan to focus on continued efforts towards understanding light-matter interaction in nanophotonic structures in the context of energy applications. In particular, building upon our theoretical work in [8] on the theoretical limit for harvesting of outgoing radiation, we plan to undertake a few experiments that provide experimental demonstration of the capability for such energy harvesting. The success of such demonstration could be important for off-grid electricity generation, and for night-time lighting purposes. On the theoretical front, plan to continue to develop the theoretical framework for the understanding of light-matter interaction in resonant optical structures, in particular by developing a temporal coupled mode theory formalism that is applicable in the presence of gain/loss and non-reciprocity. This theoretical framework will be connected with the ongoing experimental work in this area in Prof. Mark Brongersma's lab.

Journal Publications of DOE Sponsored Research in 2017-2019

1. W. Li, Y. Shi, K. Chen, L. Zhu, and S. Fan, "A Comprehensive Photonic Approach for Solar Cell Cooling," ACS Photonics 4, 774–782 (2017).

2. S. Buddhiraju and S. Fan, "Theory of solar cell light trapping through a nonequilibrium Green's function formulation of Maxwell's equations," Phys. Rev. B 96, 035304 (2017).

3. S. Fan, "Thermal Photonics and Energy Applications," Joule 1, 264–273 (2017). (Invited review)

4. Z. Zhao, K. X. Wang, and S. Fan, "Analysis of an anti-reflecting nanowire transparent electrode for solar cells," J. Appl. Phys. 121, 113109 (2017).

5. O. Isabella, R. Vismara, D. N. P. Linssen, K. X. Wang, S. Fan, and M. Zeman, "Advanced light trapping scheme in decoupled front and rear textured thin-film silicon solar cells," Sol. Energy 162, 344–356 (2018).

6. S. J. Kim, J. H. Kang, M. Mutlu, J. Park, W. Park, K. E. Goodson, R. Sinclair, S. Fan, P. G. Kik, and M. L. Brongersma, "Anti-Hermitian photodetector facilitating efficient subwavelength photon sorting," Nat. Commun. 9, 316 (2018).

7. Y. Shi, W. Li, A. Raman, and S. Fan, "Optimization of Multilayer Optical Films with a Memetic Algorithm and Mixed Integer Programming," ACS Photonics 5, 684–691 (2018).

8. S. Buddhiraju, P. Santhanam, and S. Fan, "Thermodynamic Limits of Energy Harvesting from Outgoing Thermal Radiation," Proc. Natl. Acad. Sci. 116, E3609–E3615 (2018).

9. W. Li and S. Fan, "Nanophotonic Control of Thermal Radiation for Energy Applications," Opt. Express 26, 15101–15109 (2018). (Invited review in the 20th anniversary edition of the Optics Express.)

10. Y. Li, K.-J. Zhu, Y.-G. Peng, W. Li, T. Yang, H.-X. Xu, H. Chen, X.-F. Zhu, S. Fan, and C.-W. Qiu, "Thermal meta-device in analogue of zero-index photonics," Nat. Mater. 18, 48–54 (2019).

Atom-defect Hybrid Quantum Systems

Ania Bleszynski Jayich[1], Kunal Mukherjee[2], David Weld[1], Norman Yao[3]

[1] Physics Department UC Santa Barbara, [2]Materials Science Department UC Santa Barbara, and [3]Physics Department UC Berkeley

Program Scope

It has been known since the early twentieth century that quantum mechanics provides a truer description of the world than classical physics, albeit a nonintuitive one. This first quantum revolution revealed that objects can exist in a superposition of many places at once, and that entangled elements separated by thousands of miles can be inextricably linked. A second quantum revolution is now brewing which promises to usher in fundamental changes in the way humans obtain, manipulate, and store information by exploiting the quirky, but delicate, phenomena unique to quantum mechanics.

Individual atoms, both in isolation and as pointlike crystal defects, lie at the heart of many emerging quantum technologies powering this revolution. Isolated atoms are among the most perfect quantum systems; they can retain quantum information coherently for long periods of time, and exhibit spectra guaranteed to be identical to that of other atoms of the same species. Solid-state point defects benefit both practically and quantitatively from the strong trapping provided by their crystal host, while still exhibiting appreciable quantum coherence times even at room temperature (millisecond scale for the nitrogen-vacancy (NV) center in diamond, for example). As in a classical information processor, in which several disparate technologies (e.g. charge-based logic elements and magnetic memory elements) are combined in a single device, it has become clear that future quantum technologies will benefit from incorporating multiple quantum elements, each serving the purpose to which it is best suited.

We are developing a hybrid quantum system combining the benefits of atoms and defects, realizing a composite quantum technology platform with capabilities well beyond those of its constituent parts. Individual adatoms deposited onto a diamond surface in a highly controlled, cryogenic, and ultra-high vacuum environment are coherently coupled to subsurface NV centers, enabling creation and and manipulation of quantum states in strongly-interacting hybrid atom-defect clusters. By leveraging the strengths of its constituent parts, NV centers and individual atoms, this hybrid architecture presents several important advantages that directly address the two primary challenges facing any quantum technology: 1) engineering of robust and scalable interactions and 2) decoherence. Crucially, the proposed quantum system features extreme materials control over both the constituents and the quantum interface between them. Non-invasive probing of adatoms in a metal-free environment should enable the realization of unprecedentedly long coherence times for adatom spins. This will enable quantitative probing and control of surface-mediated decoherence processes which represent a nearly universal challenge to all quantum computing architectures. With its localization at the surface, the NV-

adatom system forms an ideal nanoscale quantum sensor. Leveraging our ability to assemble and address adatoms on a clean 2D surface, a specific metrological application we will pursue is probing novel states of matter in 2D interacting spin systems. The convergent expertise of our team (experimental and theoretical aspects of quantum control of atoms and defect centers, and atom-by-atom materials synthesis) is vital to the success of this ambitious proposal.

Recent Progress

We have assembled a room temperature, ultra-high vacuum (UHV) system (Fig. 1) in which we have measured the properties of NV centers under nominally oxygen-terminated surfaces and under a few nm of adsorbed indium atoms. We observed a large drop in the T_1 spin relaxation time of the NV centers with the layer of indium atoms, but we did not see a change in the T_2 spin coherence time. The optical contrast of the NV spin state also decreased over the time scale of a few weeks while under the In atoms. We have also coupled in a pulsed laser with the goal of removing the In atoms, though have as yet been unsuccessful, most likely due to insufficient power.

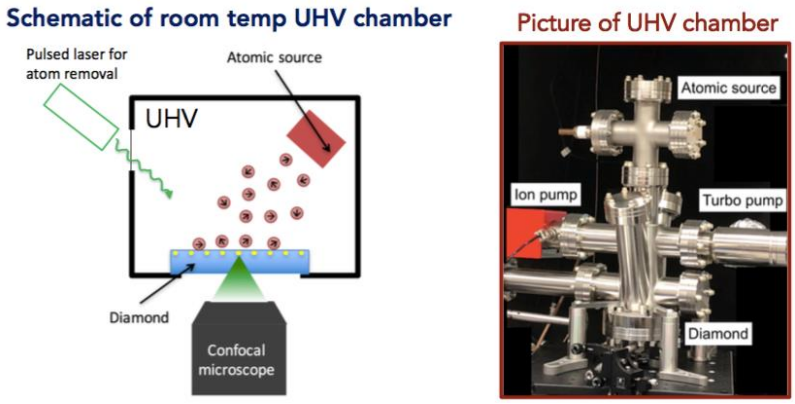

Fig. 1: left: schematic of room temperature UHV chamber for studying NV-adatom hybrid system. Right: assembled UHV chamber.

Future Plans

We are currently assembling a cryogenic UHV system (Fig. 2) with surface preparation tools that would 1) provide higher levels of vacuum to ensure that the only adatoms are the atoms we intentionally deposit on the surface, 2) reduce surface mobility of adatoms to ensure that adatoms stick where they land, and 3) provide surface preparation and surface characterization tools, including heating, electron guns, and oxygen and nitrogen termination.

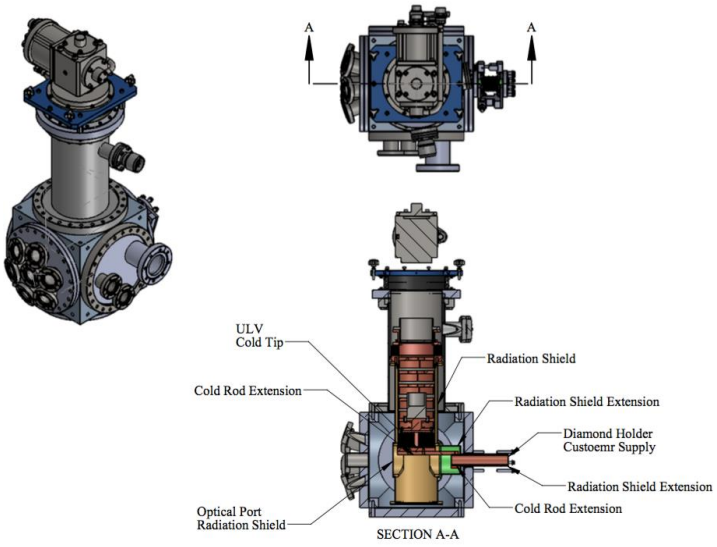

Fig. 2: CAD drawings of the cryogenic UHV system under construction for studying hybrid atom-defect systems.

Abstract

PROJECT TITLE: Superionic Clusters - Structure, Stability, and Energy Applications

PI: Jena, Purusottam
Department of Physics, Virginia Commonwealth University, Richmond, VA 23284-2000
pjena@vcu.edu

PROGRAM SCOPE:

The objective of our project is to provide a fundamental understanding of the structure-property relationships of a novel class of superionic clusters mimicking the chemistry of alkali and halogen atoms and to explore their potential as building blocks of energy materials. Working closely with experimental groups, we not only validate our theoretical predictions but also guide experiments in the focused discovery of energy and magnetic materials.

The project exploits the unique size and composition specific properties of isolated clusters and explores their potential as building blocks of functional materials. Using first-principles theory our approach is an atom-by-atom rational design of a new class of superionic clusters, such as super-alkalis and super-halogens that not only mimic the chemistry of alkali and halogen atoms, respectively, but also are suitable for forming salts with unusual properties. The project deals with three interrelated thematic areas: (1) *Super-ions as building blocks of energy materials:* Realizing that electrolytes in metal-ion batteries and hybrid perovskites solar cell materials are salts composed of complex cations and anions, we study a wide range of super-alkalis and super-halogens as building blocks of these salts and tailor their properties by choosing their size and composition. To address environmental concern, we also study the role of super-alkalis in CO_2 activation. (2) *Stability of multiply charged clusters:* While multiply charged clusters are stabilized in solutions and in the solid phase by compensating cations, they often fragment or auto-eject the extra electron(s) in the gas phase. Although doubly charged anions are well studied, very little is known about the stability of tri-anions. Using various electron-counting rules we study the size and composition of tri-anions and beyond that are stable in the gas phase and explore their potential as building blocks of electrolytes in Al-ion batteries. (3) *Mn_2^+ as a building block of low-dimensional magnetic materials:* Our focus on Mn-based systems is based on the fact that magnetic coupling between Mn atoms is sensitive to inter-atomic distance and charge state. While Mn_2 dimer is antiferromagnetic, removal of a single electron makes it ferromagnetic with a magnetic moment of 11 μ_B. We study magnetic properties of clusters, nanowires, and two-dimensional arrays composed of Mn_2Au cluster which, due to charge transfer from Mn_2 to Au, also has a moment of 11 μ_B. Our studies not only complement recent experiments but also are aimed at guiding experiments in discovery of new materials.

RECENT PROGRESS:

Research over the past two years has resulted in 41 publications, eight of which are featured on the cover of journals [1-8]. These are given in Figs. 1-8. Some of our papers are published in high-impact journals such as Chemical Review, Proceedings of the National Academy of Sciences, Angew. Chem. Int. Ed., Physical Review Letters, Journal of Physical Chemistry Letters, Nano Letters, Chemistry of Materials, etc. The papers cover a wide range of topics dealing with structure-property relationships of zero-dimensional systems (clusters), one-dimensional systems (nano-wires and nano-tubes), two-dimensional systems (topological materials, ψ-graphene, van der Waals Ferroelectrics, Transition-Metal Dichalcogenide Monolayers), and three-dimensional materials based on perovskites for solar cell and optoelectronic applications and anti-perovskites for Li- and Na-ion batteries. The works on clusters involve super-alkali and super-halogen clusters as building blocks of electrolytes in Li-ion batteries, activation of CO_2, organo-Zintl based super-atoms, colossal stability of tri-anions in the gas phase, stability of organo-metallic clusters, and magnetism. A major contribution to this field is our 115-page review article in Chemical Review on "Super-atomic Clusters: Design Rules and Potential for Building Blocks of Materials". The work on one-dimensional materials include CO_2 capture by a metallic peanut-shaped carbon nanotube, how confinement boosts CO oxidation on Ni atom embedded in BN nanotube, and hierarchical electrides composed of Li_3O super-alkalis. Work on 2D materials include topological crystalline quantum spin Hall effect in transition metal intercalated compounds, Ψ-graphene - a new metallic allotrope of planar carbon, thermoelectric properties of layered $GeAs_2$, giant valley splitting in Group III transition metal dichalcogenide monolayers, bipolar magnetic materials based on metal-organic coordination networks, and van der Waal ferroelectrics. Work on three-dimensional materials cover a wide range of topics involving solar cells based on hybrid perovskites, anodes and cathodes for Li- and Na-ion batteries, anti-perovskite based superionic conductors, quantum anomalous Hall effect, topological nodal-line semi-metallic carbon, and Janus nanoparticles for removal of formaldehyde. It is impossible to cover in details the fundamental science and potential for applications of materials studied and we hope that the list of papers published during this period and included in this extended abstrcat will be helpful for the reader.

Fig. 1-8 Papers appearing journal covers published during 2017-2018.

REFERENCES:

1. Driver, N. and Jena, P.: "Electron Affinities of Modified Benzene", Int. J. Quantum. Chem. **118**, e25504 (2018) **DOI:** 10.1002/qua.25504
2. Fang, H., Wang, S., Liu, J., Sun, Q., and Jena, P.: "Superhalogen-based Li-ion Superionic Conductors", J. Mat. Chem. A **5**, 13373 (2017)
3. Zhao, T., Wang, Q., and Jena, P.: "Rational Design of Superalkalis and Their Role in CO_2 Activation", Nanoscale **9**, 4891 (2017)
4. Zhao, T., Zhu, J., Wang, Q., and Jena, P.: "Colossal Stability of Gas-phase Tri-anions: Super-pnictogens," Angew. Chem. Int. Ed. VIP **56**, 13421 (2017)
5. Xue, Q., Wu, M., Zeng, X., Jena, P.: "Co-mixing Hydrogen and Methane May Double the Energy Storage Capacity", J. Mat. Chem. A **6**, 8775 (2018)
6. Wang, S.; Liu, J.; Qie, Y.; Gong, S.; Sun, Q.; and Jena, P.: "Discovery of a High-pressure Phase of Rutile-like CoO_2 and its Potential as a Cathode Material", J. Mat. Chem. A **6**, 18329 (2018)
7. Boateng, D. A., Gutsev, G. L., Jena, P., and Tibbetts, K. M: "Ultrafast Coherent Vibrational Dynamics in Dimethyl Methylphosphonate Radical Cation", Phys. Chem. Chem. Phys. **20**, 4636 (2018)
8. Zhang, Y.; Liu, Y.; Meng, Z.; Ning, C.; Xiao, C.; Deng, K.; Jena, P.; Lu, RF: "Confinement boosts CO oxidation on Ni atom embedded inside boron nitride nanotubes", Phys. Chem. Chem. Phys. **20**, 17599 (2018)

FUTURE PLANS

Our future projects will include design of cluster based materials for energy harvesting, conversion, and storage; stability of multiply charged negative ions such as tetra- and penta-anions in the gas phase; developing new algorithm to search for metastable phases of materials, particularly those based on carbon; and understanding the evolution of the structure and properties of clusters. We plan to work with experimentalists for focused discovery of new cluster-based antiperovskites for Li and Na-ion batteries and hydrogenated C_{60} for Li storage and its potential as a new anode material for Li-ion battery. We will also study magnetism of a new class of salts composed of alkali metal cations (e.g. K^+) and Gd based super-halogens (e.g. $GdCl_3^-$) to explore the effect of Cl vacancies on the magnetic coupling.

PUBLICATIONS (2017-2019):

1. Huang, C., Zhou, J., Wu, H., Deng, K., Jena, P., Kan, K.: "Quantum Anomalous Hall Effect in Ferromagnetic Transition Metal Halides", Phys. Rev. B **95**, 045113 (2017)
2. Cheng, Y., Feng, X., Cao, X., Wen, B., Wang, Q., Kawazoe, Y., and Jena, P.: "Body-Centered Tetragonal C16 : A Novel Topological Node-Line Semi-Metallic Carbon Composed of Tetrarings", Small **13**, 1602894 (2017), DOI: 10.1002/smll.201602894
3. Zhou, J. and Jena, P.: "Two-dimensional Topological Crystalline Quantum Spin Hall Effect in Transition Metal Intercalated Compounds", Phys. Rev. B. **95**, 081102 (R) (2017)
4. Zhao, T., Wang, Q., and Jena, P.: "Rational Design of Superalkalis and Their Role in CO_2 Activation", Nanoscale **9**, 4891 (2017)
5. Hong F. and Jena, P.: "B12(SCN)122-: An Ultra-Stable Weakly-Coordinating Dianion for Electrolyte Salts in Metal-Ion Batteries", J. Phys. Chem. C **121**, 7697 (2017)

6. Li, X., Wang, Q., and Jena, P.: "ψ-graphene: A new metallic allotrope of planar carbon with potential applications as anode materials for lithium-ion batteries", J. Phys. Chem. Letts. **8**, 3234 (2017)
7. Zhong, M-M., Zhou, J., Fang, H., Jena, P.: "Role of ligands on the stability of B_nX_n and $CB_{n-1}X_n$ (n = 5–10; X = H, F, CN) and their potential as building blocks of electrolytes in lithium ion batteries", Phys. Chem. Chem. Phys. **19**, 17937 (2017)
8. Fang, H., Wang, S., Liu, J., Sun, Q., and Jena, P.: "Superhalogen-based Li-ion Superionic Conductors", J. Mat. Chem. A **5**, 13373 (2017)
9. Zhou, J., Sun, Q., Jena, P.: "Valley-Polarized Quantum Anomalous Hall Effect in Ferrimagnetic Honeycomb Lattice", Phys. Rev. Letts. **119**, 046403 (2017)
10. Fang, H. and Jena, P.: "Atomic-level Design of Water-resistant Hybrid Perovskites for Solar Cells", J. Phys. Chem. Letts **8**, 3726 (2017)
11. Zhong, M. M., Jian Zhou, J., and Jena, P.: "Rational Design of Stable Dianions by functionalizing polycyclic aromatic hydrocarbons", Chem. Phys. Chem. **18**, 1937 (2017)
12. Reddy, G. N., Jana, M., Jena, P., and Giri, S.: "Organo−Zintl-Based Superatoms: $[Ge_9(CHO)_3]$ and $[Ge_9(CHO)]$", Chem. Phys. Letters **686**, 195 (2017)
13. Zhao, T., Zhu, J., Wang, Q., and Jena, P.: "Colossal Stability of Gas-phase Tri-anions: Super-pnictogens," Angew. Chem. Int. Ed. VIP **56**, 13421 (2017)
14. Fang, H. and Jena, P.: "Li-rich antiperovskite superionic conductors based on cluster ions", Proc. Nat. Acad. Sci. **14**, 1047 (2017)
15. Wang, F. Q., Guo, Y., Wang, Q., Kawazoe, Y., and Jena, P.: "Exceptional Thermoelectric Properties of Layered $GeAs_2$", Chem. Mat. **29**, 9300 (2017)
16. Zhou, J. and Jena, P.: "Giant Valley Splitting and Valley Polarized Plasmonics in Group-III Transition-Metal Dichalcogenide Monolayers", J. Phys. Chem. Letters **8**, 5764 (2017)
17. Gutsev, G. L., Boateng, D. A., Jena, P., and Tibbetts, K. M.: "A Theoretical and Mass-Spectrometry Study of Dimethyl Methylphosphonate: New Isomers and Cation Decay Channels in an Intense Femtosecond Laser Field", J. Phys. Chem. A **121**, 8414 (2017)
18. Driver, N. and Jena, P.: "Electron Affinities of Modified Benzene", Int. J. Quantum. Chem. **118**, e25504 (2018) **DOI:** 10.1002/qua.25504
19. Wang, D., Li, Z., Zhou, J., Fang, H., He, X., Jena, P., Zeng, J-B., Wei-Ning Wang, W-N.: "Simultaneous Detection and Removal of Formaldehyde at Room Temperature: Janus Au@ZnO@ZIF-8 Nanoparticles" Nano-Micro Letters DOI 10.1007/s40820-017-0158-0 (2018)
20. Feng, X., Wu, Q., Cheng, Y., Wang, Q., Kawazoe, Y., Jena, P.: "Monoclinic C_{16}: sp^2-sp^3 Hybridized Nodal-Line Semimetal Protected by PT-Symmetry", Carbon **127**, 527 (2018)
21. Gutsev, G. L, Belay, K. G., Gutsev, L. G., Ramachandran, B. R., and Jena, P. : "Effect of hydrogenation on the structure and magnetic properties of an iron oxide cluster", Phys. Chem. Chem. Phys. **20**,4546-553 (2018)
22. Boateng, D. A., Gutsev, G. L., Jena, P., and Tibbetts, K. M: "Ultrafast Coherent Vibrational Dynamics in Dimethyl Methylphosphonate Radical Cation", Phys. Chem. Chem. Phys. **20**, 4636 (2018)
23. Chen, Y., Liu, J., Sun, Q., Kawazoe, Y., and Jena, P.: "Bipolar Magnetic Materials Based on Two-Dimensional Ni[TCNE] Metal-organic Coordination Networks", Advanced Electronic Materials **4**, 1700323 (2018)
24. Zhao, T., Wang, Q., and Jena, P.: "A Metallic Peanut-Shaped Carbon Nanotube and its Potential for CO_2 Capture", Carbon **132**, 249 (2018)
25. Boateng, D. A., Gutsev, G., Jena, P. and Tibbetts, K.: "Dissociation dynamics of 3- and 4-nitrotoluene radical cations: Coherently driven C-NO_2 bond hemolysis", J. Chem. Phys. **148**, 134305 (2018)
26. Xue, Q., Wu, M., Zeng, X., Jena, P.: "Co-mixing Hydrogen and Methane May Double the Energy Storage Capacity", J. Mat. Chem. A **6**, 8775 (2018)
27. Huang, C., Zhou, J., Deng, K., Kan, E., Jena, P.: "Effect of Coulomb Correlation on the Magnetic Properties of Mn Clusters", J. Phys. Chem. A **122**, 4350 (2018)

28. Gutsev, L. G., Gutsev, G. L., and Jena, P.: "Collective super-exchange and exchange coupling constants in hydrogenated iron oxide particle $Fe_8O_{12}H_8$", J. Phys. Chem. A **122**, 5043 (2018)
29. Zhong, M-M., Fang, H., Jena, P.: "$B(SCN)_4^-$: A new weakly coordinating anion in the tetracyanoborate family", J. Phys. Chem. C **122**, 133371 (2018)
30. Liu, J.; Li, X.; Wang, Q.; Kawazoe, Y.; and Jena, P.: "A New 3D Dirac Nodal-Line Semi-Metallic Graphene Monolith for Lithium Ion Battery Anode Material", J. Mat. Chem. A **6**, 13816 (2018)
31. Zhang, Y.; Liu, Y.; Meng, Z.; Ning, C.; Xiao, C.; Deng, K.; Jena, P.; Lu, RF: "Confinement boosts CO oxidation on Ni atom embedded inside boron nitride nanotubes", Phys. Chem. Chem. Phys. **20**, 17599 (2018)
32. Wu, M. and Jena, P.: "The Rise of Two-dimensional van der Waals Ferroelectrics", WIREs Computational Molecular Science **8**: e1365 (2018) doi/10.1002/wcms.1365
33. Qie, Y., Liu, J., Li, X., Wang, S., Sun, Q., and Jena, P.: "Interpenetrating Silicene Networks: A Topological Nodal-line Semimetal with Potential as an Anode Material for Sodium Ion Batteries", Phys. Rev. Materials **2**, 084201 (2018)
34. Wang, S.; Liu, J.; Qie, Y.; Gong, S.; Sun, Q.; and Jena, P.: "Discovery of a High-pressure Phase of Rutile-like CoO_2 and its Potential as a Cathode Material", J. Mat. Chem. A **6**, 18329 (2018)
35. Hong Fang, H., Jian Zhou, J., and Jena, P.: "Super-alkalis as Building Blocks of One-Dimensional Hierarchical Electride", Nanoscale **10**, 22963 (2018)
36. Jena, P. and Sun, Q.: "Super Atomic Clusters: Design Rules and Potential for Building Blocks of Materials", Chem. Rev. **118**, 5755-5870 (2018)
37. Fang, H. and Jena, P.: "Sodium Superionic Conductors Based on Clusters", ACS Appl. Mat. and Interfaces **11**, 963 (2019)
38. Qie, Y., Liu, J., Wang, S., Sun, Q., and Jena, P.: "Tetragonal C_{24}: A Topological Nodal-surface Semimetal with Potential as an Anode Material for Sodium Ion Batteries", J. Mat. Chem. A (in press)
39. Boateng, D. A., Word, M. D., Gutsev, L. G., Jena, P., and Tibbetts, K. M.: "Conserved Vibrational Coherence in the Ultrafast Rearrangement of 2-Nitrotoluene Radical Cation", J. Phys. Chem. A (in press)
40. Reddy, G. N., Parida, R., Jena, P., and Giri, S.: "Superhalogens as Building Blocks of Super Lewis Acids", Chem. Phys. Chem. (in press)
41. Zhou, W., Shen, H., Wang, Q., Kawazoe, Y., and Jena P.: "N-doped Peanut-Shaped Carbon Nanotubes for Efficient CO_2 Electrocatalytic Reduction, J. Appl. Physics (in press)

Parametrically Induced QUantum Engineering (PIQUE)

PI: Archana Kamal, University of Massachusetts, Lowell MA

Co-PIs: Leonardo Ranzani, Raytheon-BBN Technologies, Cambridge MA
Diego Risté, Raytheon-BBN Technologies, Cambridge MA
José Aumentado, National Institute of Standards and Technology, Boulder
Raymond W. Simmonds, National Institute of Standards and Technology, Boulder

Program Scope

The research proposed in this work introduces a new and powerful framework, called PIQUE (Parametrically-Induced QUantum Engineering), which employs only continuous parametric interactions between qubits, and between qubits and reservoirs to implement quantum state stabilization, logical control and measurement. Our approach improves the speed and robustness of quantum information systems by providing large, high-fidelity and fully controllable multi-partite entangled states on demand. This research leverages theoretical and experimental expertise in parametric systems and superconducting qubit technology of the PIs at UML and Raytheon-BBN, along with fabrication expertise available at National Institute of Standards and Technology (NIST).

The continuous-wave parametric interactions explored in this work are used to implement multipartite stabilization and parity measurement, and provide an easier-to-implement approach that is complementary to the usual methods based on digital quantum gates and feedback. The experiments proposed also expand the superconducting circuit-based quantum information toolbox by developing novel parametric couplers and tunable resonators, in both distributed and lumped-element designs, enabling immediate and near term practical applications.

Recent Progress

The collaboration has recently communicated a paper [Doucet, 2018] on parametrically-induced autonomous entanglement generation and stabilization in two-qubit systems. This paper, for the first time, highlights that a concurrent scaling of steady-state fidelity and stabilization time in a driven-dissipative system is intimately tied to a balance between dissipation-dominated and drive-dominated dynamics. The importance of such an optimality is not limited to circuit-QED and has implications for open system physics in intermediate coupling regimes beyond the specifics of a particular stabilization protocol. Such behavior is in stark contrast with “classic” schemes that employ dissipation as a resource -- these are limited to perturbative driving and must compromise the achievable state preparation purity in order to stabilize rapidly with respect to the qubit decoherence rates [Reiter, 2012; Shankar, 2013]. These constraints hamper the

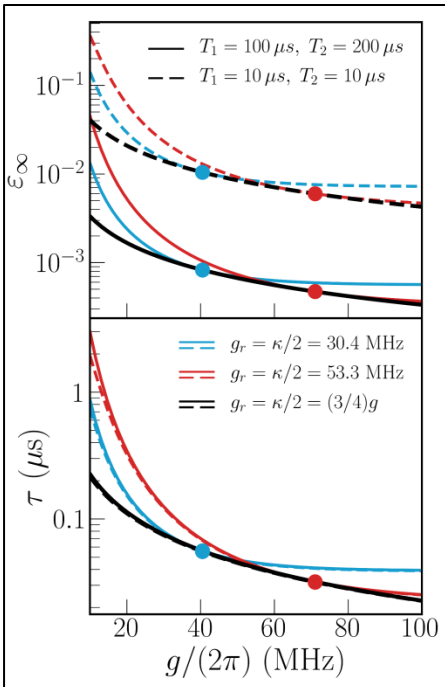

Figure 1: Calculated performance metrics for Bell state stabilization, as a function of parametric coupling strength. The black line shows the results obtained with optimal ratio between coupling and decay rates.

usability of such schemes when they are extended to larger systems, or when they are used to prepare resource states for quantum algorithms.

On the experimental side, the fabrication and initial characterization of first generation devices is being led by the Advanced Microwave Photonics Group at NIST, Boulder. Figure 2(a) shows center of a dual-transmon and linear resonator circuit. In this configuration the three elements are coupled via a SQUID-based tunable coupler. This design has the advantage of having a single coupling element with a small footprint [Zakka-Bajjani, 2011], capable of implementing all three pairwise interactions. This architecture this is appealing both from the point of view of scalability to higher number of qubits, and implementation of higher-order interactions. Continuous wave spectroscopy of this design using parametric drives shows mode-splitting on the order of 50-100 MHz; the qubit frequencies are around 5.3 GHz and coherence times are on the order of few tens of microseconds ($T_1 = 30\ \mu s;\ T_2 = 20\ \mu s$). Theoretical analysis and numerical simulations, presented in Figure 1, predict state stabilization fidelities of greater than 99% within 100 ns for these parameters.

Measurement of these devices is being led by Quantum Engineering and Computing group at Raytheon-BBN Technologies. The measurement and control electronics is in advanced stages of development at Raytheon-BBN Technologies. Figure 2(b) depicts the schematic for experimental setup for the two-qubit Bell state experiment. This effort will directly leverage and build upon existing capabilities at BBN, such as the availability of custom arbitrary pulse generators (APS) [Ryan, 2017] that allow multi-channel, fast quantum control along with low-latency (430ns end-to-end).

Future Plans

The future goals are to extend and study parametrically-controlled dissipation for multipartite entanglement generation. This will include studies of both autonomous and measurement-based schemes for few-qubit systems. One of the important outcomes of this work will be a deeper understanding of the unique advantages enabled by parametric interactions, such as continuous phase-tunability of target states and effects of imposing chirality [Kamal, 2011; Ranzani, 2015] for dissipative state engineering.

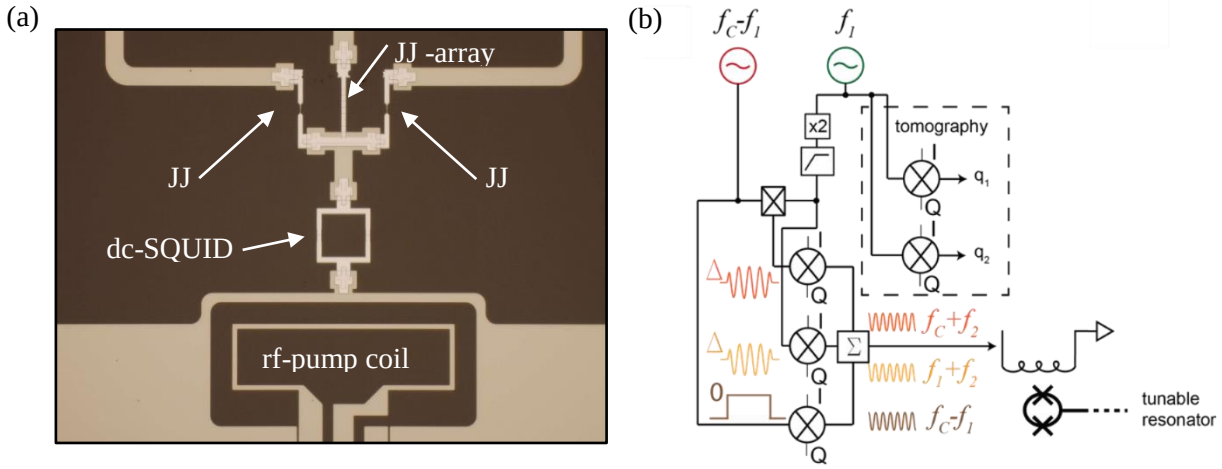

Figure 2: (a) Micrograph of the two-qubit chip with tunable coupler. (b) Control setup for the autonomous stabilization and state tomography of an even-parity Bell state. The simple relation between these frequencies allows generation of all the required tones using only two sources, one at f_1 and the other at $f_C - f_1$.

A parallel and bonus track enabled by these investigations relates to fundamental studies of open quantum system dynamics, such as studying non-perturbative methods for decay of dressed states relevant for strong driving conditions. We will also explore and develop efficient computational techniques, such as those based on engineered disssipators, for extending these studies to multi-qubit systems.

Experimentally, the immediate goal is to demonstrate and characterize the fidelity and speed for autonomous entanglement stabilization in the presence of strong parametric coupling. This will be first done for two-qubit Bell state stabilization, which will set the framework for optimizing designs of parametric couplers, careful quantification of parametrically-mediated couplings on qubit coherence and mitigation strategies, and study of experimental (parameter asymmetries, crosstalk) and theoretical non-idealities (counter-rotating terms, leakage channels). Once this is accomplished, similar architecture and design principles will be leveraged for parametrically-enabled multi-qubit parity measurement. This will allow a direct and powerful platform for comparing autonomous and measurement-based entanglement generation in parametrically-driven platforms.

References

[Kamal, 2011] A. Kamal, J. Clarke, M. H. Devoret, "Noiseless non-reciprocity in a parametric active device", Nature Physics 7(4), 311–315 (2011).

[Ranzani, 2015] L. Ranzani, and J. Aumentado, "Graph-based analysis of nonreciprocity in coupled-mode systems", New Journal of Physics 17, 023024 (2015).

[Reiter, 2012] F. Reiter, M. J. Kastoryano and A. S. Sørensen, “Driving two atoms in an optical cavity into an entangled steady state using engineered decay”, New J. Phys. 14, 053022 (2012).

[Ryan, 2017] C. A. Ryan, B. R. Johnson, D. Ristè, B. Donovan, and T. A. Ohki, “Hardware for Dynamic Quantum Computing”, Review of Scientific Instruments 88, 104703 (2017).

[Shankar, 2013] S. Shankar, M. Hatridge, Z. Leghtas, K. M. Sliwa, A. Narla, U. Vool, S. M. Girvin, L. Frunzio, M. Mirrahimi, and M. H. Devoret, “Autonomously stabilized entanglement between two superconducting quantum bits”, Nature 504, 419–422 (2013).

[Zakka-Bajjani, 2011] E. Zakka-Bajjani, F. Nguyen, M. Lee, L. R. Vale, R. W. Simmonds, and J. Aumentado, “Quantum superposition of a single microwave photon in two different colour states”, Nature Physics 7, 599-603 (2011).

Publications

[Doucet, 2018] E. Doucet, F. Reiter, L. Ranzani, A. Kamal. “High-fidelity dissipative engineering using parametric interactions”. Under review in Phys. Rev. Lett., arXiv:1810.03631 (2018).

Phase-Field Modeling of Materials Interfaces and Nanostructures

Principal Investigator:

Alain Karma
Address: Department of Physics and Center for Interdisciplinary Research on Complex Systems, Northeastern University, 360 Huntington Avenue, Boston, Massachusetts 02115
Email: a.karma@neu.edu

Program Scope

Nanostructured materials offer unique properties for a wide range of energy applications. Liquid metal dealloying (LMD) has recently attracted wide attention in the materials communities as a powerful alternative to electrochemical dealloying to produce topologically complex nanoporous and nanocomposite structures with remarkable properties. Materials applications of LMD range from ultra-high surface area electrolytic capacitors to nanocomposites combining high strength and high ductility to nanoporous Si for battery anodes with high-capacity and very long cycle life. While electrochemical dealloying is limited to a few metallic alloys, LMD can be used to dealloy much more diverse mixtures of both metallic and non-metallic elements, thereby dramatically enhancing the ability to produce novel nanostructures by dealloying. Yet, the fundamental principles that govern structure formation during LMD have just started to be explored. This project exploits the phase-field method to investigate the basic mechanisms that control the morphology and composition of dealloyed nanostructures. This research exploits the unique capability of this method to track simultaneously the geometrically complex evolution of the solid-liquid interface during dealloying and compositional domain formation within the interfacial layer in a thermodynamically consistent way. We are using phase-field simulations to investigate the mechanisms that control the range of alloy and melt compositions yielding nanostructures with desired high-genus connected topologies, the kinetics of dealloying, and the evolution of the structure scale. We are also developing this method to study the formation of nanoporous crystalline Si by dealloying of Si-based alloys (e.g. Si-Mg and Si-Ge) as well as to investigate the chemo-mechanical behavior of nanoporous crystalline Si. The latter study exploits our recently developed phase-field model of chemo-mechanical fracture, which is being extended to include the anisotropic crystall ine Si to amorphous Li_xSi alloy phase transformation. This model is being used to address the outstanding question of why nanopourous Si exhibits superior properties as a Li-ion battery anode material.

Recent progress

Nanoporous and nanocomposite structure formation by liquid metal dealloying

Liquid metal dealloying (LMD) is by now an established technique to produce nanocomposite and open nanoporous structures with ultra-high interfacial area for diverse applications. In its simplest implementation, the technique involves immersing a precursor A-B alloy into a liquid melt of C with B miscible and A immiscible in C. The liquid melt dissolves the miscible element B selectively, and the immiscible element A forms a topologically connected or disconnected bicontinuous structure of interpenetrating A-rich

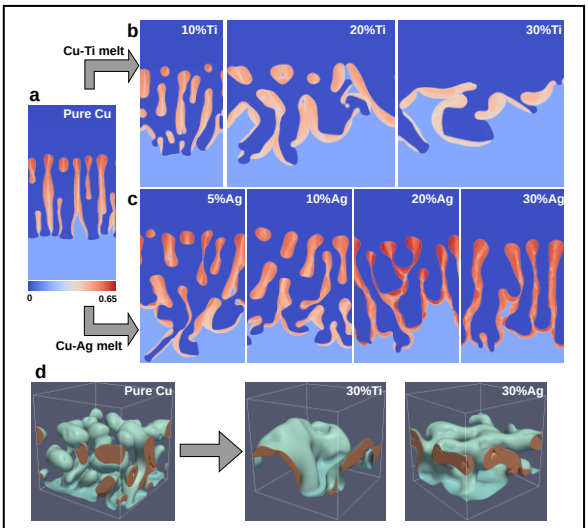

Fig. 1. Results of 2D and 3D phase-field simulations of dealloying of a $Ta_{15}Ti_{85}$ alloy showing the effects of varying the liquid melt composition on structure formation. Addition of different amounts of Ti or Ag to the Cu melt destabilizes eutectic-like coupled growth of Cu-rich liquid channels and Ta-rich lamellae and promotes the formation of a desired topologically connected structure. Dealloying of the same alloy by a pure Cu melt forms a disconnected lamellar structure.

and C-rich phases depending on the alloy composition. When the dealloyed structure is topologically connected, a nanoporous structure of the A-rich or C-rich phases can be further obtained by selective etching of one of those two phases. While electrochemical dealloying can form topologically connected structures for even small concentrations of the immiscible element in the base alloy, LMD yields disconnected structures below a critical composition [1]. The complex interfacial pattern formation mechanism giving rise to this transition from topologically connected and disconnected structures as a function of base alloy composition is not fundamentally understood. We have used phase-field modeling to understand this transition and to explore the possibility that the dealloyed morphology can be controlled by varying the melt composition. We examined the generic cases where the liquid melt contains the miscible element of the base alloy, exemplified by dealloying Ta-Ti alloys by Cu-Ti melts, and where the liquid melt contains a different element that reduces the solubility of the miscible element in the melt, exemplified by dealloying of Ta-Ti alloys by Cu-Ag melts. Morphologies of dealloyed nanoporous structures from the 2D and 3D simulations are shown in Fig. 1. The dealloying front progresses from top to bottom, where immiscible Ta is concentrated and forms nanoporous structures. The system size in 2D simulations is 384×640 nm^2. The system sizes of the 3D simulations are 96×96×128nm^3 for pure Cu and 30%Ag and 128×128×96 nm^3 for 30%Ti. The base alloy of all simulations is $Ta_{15}Ti_{85}$ and the melt is pure Cu in (a), Cu-Ti in (b), Cu-Ag in (c). We find that both Ti and Ag addition in the melt slows down dealloying kinetics and enhance morphological instability at the dealloying front so as to promote the formation of a desired topologically connected structure over a larger range of base alloy composition so as to extend the formation of topologically connected structures to smaller volume fraction of the Ta rich phase. To further understand the role of melt composition on structure formation, we

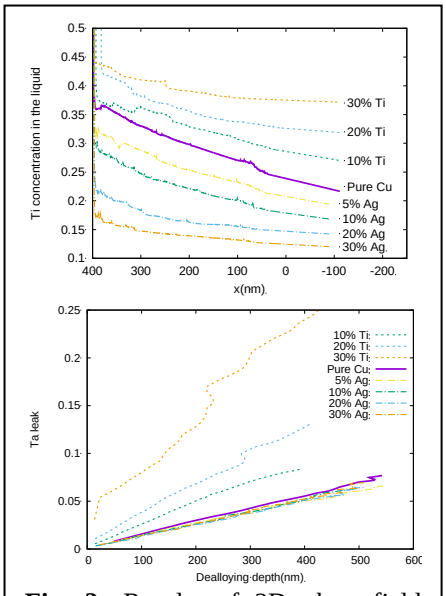

Fig. 2: Results of 2D phase-field simulations characterizing the dealloying kinetics (top) and Ta leak in the melt (bottom).

examined the kinetics of dealloying and the rate of dissolution of Ta. The results shown in Fig. 2 reveal that both Ti and Ag addition to the Cu melt slows down dealloying kinetics by two different mechanisms. Ti addition increases the Ti concentration in the melt outside the dealloyed structure while yielding only a slight increase of Ti concentration at the dealloying front. As a result the Ti concentration gradient is reduced inside the dealloyed structure during dealloying, resulting in a slower velocity of the dealloying front. Ag addition does not affect the Ti concentration in the melt outside the dealloyed structure but strongly decrease the Ti concentration at the dealloying front. As a result the Ti concentration gradient is also reduced inside the dealloyed structure during dealloying, resulting in a slower velocity of the dealloying front. In both cases, the dealloying kinetics remains diffusion-controlled with the dealloying front depth increasing as $t^{1/2}$. We also examined the dissolution of Ta in the melt that is enhanced by Ti addition but left unchanged by Ag addition (Fig. 2) assuming that Ta-Cu and Ta-Ag have equal mixing enthalpy in the melt. The enhancement of Ta dissolution by Ti addition to the melt causes dissolution of the dealloyed structure during dealloying, thereby dramatically reducting the thickness of the final dealloyed layer. In contrast, Ag addition does not produce substantial dissolution of the dealloyed layer during dealloying. Experiments were carried out to validate our modeling predictions (Erlebacher's group at JHU). The results confirm the main phase-field modeling prediction that Ti or Ag addition to the melt promotes the formation of topologically connected structures and further reveal that Ag addition reduces the coarsening rate of the dealloyed structure, yielding a topologically connected structure with a smaller and spatially more uniform ligament size. We carried out additional phase-field simulations showing that this reduction of coarsening rate results from the significantly higher mixing enthalpy of Ta-Ag compared to Ta-Cu, which reduces the Ta concentration in the melt and hence coarsening mediated by bulk liquid state diffusion. In summary, our results show that topologically connected dealloyed structures with smaller and spatially more uniform ligament sizes can be obtained over a wide range of base alloy composition by adding to the melt and element that i) reduces the solubility of the miscible alloy element in the melt so as to reduce the driving force for dealloying and promote a topologically connected structure, and ii) reduces the already small solubility of the immiscible element in the melt so as to suppress coarsening mediated by liquid-state diffusion. Those results open up new possibilities for using melt composition control during LMD to produce nanocomposite and nanoporous structures with desired compositions and morphologies.

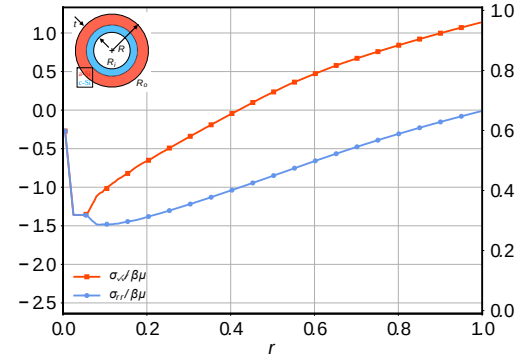

Fig. 3: Evolution of the dimensionless hoop stress and radial stress at different levels of lithiation in a crystalline Si nano-pillar ($t/R = 1$) and $\sigma_y/\beta\mu = 1$.

Chemo-mechanical behavior of Li-ion battery materials

Si and Ge with high theoretical capacity have emerged as strong alternatives for Carbon for use in Li-ion batteries anodes. However, lithiation in both these materials results in a large volumetric expansion which can result in mechanical failure of anodes and hinders their charge carrying capacity. As a result, the design of anodic components to limit the adverse effect of this swelling has emerged as a

major research topic. To extend our basic understanding of the underlying mechanisms associated with phase-change and swelling of these materials, we developed a coupled finite elasto-plastic phase-field model that seamlessly integrates phase change driven swelling and plastic deformation with fracture. The flexible nature of the phase-field fracture model then allows us to model both the initiation and propagation of cracks simultaneously. We chose the hollow nano-pillar geometry (inset of Fig. 3) that has been well studied experimentally as our model system. This model system is attractive in practical terms, as it has already been shown to alleviate mechanical failure [2], and also provides an interesting test case for guiding the geometrical design of more complex anode materials. To shed light on the basic underlying mechanism of failure of this system, we first performed an exhaustive series of axisymmetric simulations at different dimensionless yield stresses $\sigma_y/\mu\beta$ where μ is the shear modulus of the crystalline phase and $\beta = 0.7$ is the linear expansion at full lithiation corresponding to a ~300% volumetric expansion. Our simulations results show that the maximum hoop stress $\sigma_{\theta\theta}$ at the boundary of the annuli is non-monotonic in σ_y and reaches a maximum value. Furthermore, this maximum increases with the ratio $\frac{t}{R}$ of the annulus thickness and outer radius and reaches its maximum value for $\frac{t}{R} = 1$ corresponding to a solid pillar. The existence of this maximum stems from the fact that, as the crystalline core shrinks during lithiation, the stresses decrease on the boundary that originally yielded under compression, thereby causing the originally compressive hoop stress to become tensile.

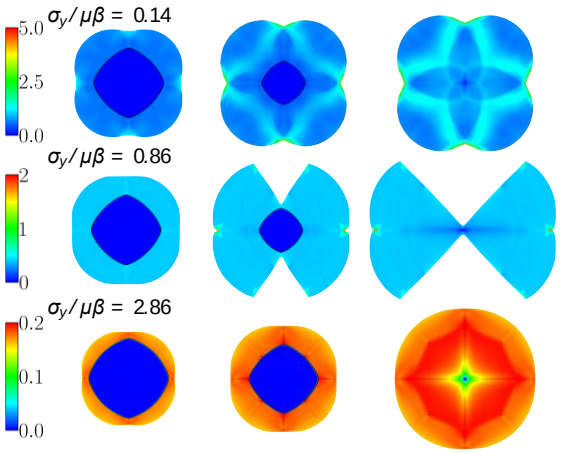

Fig. 4: Evolution of [001] nano-pillar morphology and fracture. The color map depicts the equivalent plastic strain magnitude. The amorphous-crystalline boundary is shown as a black line. **(Top)** For small yield stress σ_y, the magnitude of the hoop stress remains low and forbids crack initiation but allows for the creation of shear-band-mediated V-shaped notches. **(Middle)** In an intermediate range of σ_y, the creation of V-shaped notches enhances the hoop stress and promotes crack initiation. **(Bottom)** At higher σ_y the maximum hoop stress falls below the threshold for crack initiation.

Figure 4 shows the result of full 2D simulations of lithiation of 0.1μm [001] Si nano-pillars. The results show the formation of shear bands that promote fracture. This symmetry breaking is further enhanced by the anisotropic mobility where the corners of the crystalline phase create weak stress singularities. The shear bands are created on the outer boundary of the disk and take the morphology of a V-shaped notch, which in turn concentrate stresses and can further augment the magnitude of the created hoop stresses. Although the magnitude of the hoop stresses is not a precise indicator of crack initiation, the creation of cracks in these components can be reasonably well predicted using its magnitude. In particular, for (i) small yield stresses no fracture initiated but allows for creation of V-shaped notches, (ii) at higher yield stresses a V-shape notch is created that initiates fracture, (iii) increasing the yield stress higher allows for the initiation of a crack without a need for a V-shape notch, (iv) finally, at large enough yield stress no crack can be initiated due to the lack of opening stresses. Fig. 4 shows cases (i), (ii), (iv) for the [001] nano-pillar. In summary, our results reveal the

existence of a critical range of yield stress that promotes fracture in Si based Li-ion battery anode material and distinguishes two regimes of fracture inside this range with and without V-shape notch formation induced by shear-band formation. They further show that the driving force for fracture is dramatically reduced in a thin annulus geometry.

References

1. I. McCue, A. Karma, and J. Erlebacher, MRS Bull. **43**, 27-34 (2018).
2. X.-Y. Zhang et al., J. Mater. Chem. A **5**, 12793-12802 (2017).

Future plans

We will initiate a new theoretical investigation of vapor-phase-dealloying (VPD) that has emerged as a new technique complementary to LMD to produce nanocomposite and open nanoporous structures with ultra-high interfacial area. We will develop complementary phase-field models and kinetic Monte Carlo models of VPD to investigate different diffusion-limited and interface-kinetics dominated regimes of VPD and to investigate quantitatively the role of Knudsen diffusion. Building on the new insights gained from phase-field simulations of lithiation of Si anode materials, we will extend our studies of morphological evolution and fracture to 3D structures including model geometries and topologically connected dealloyed structures of different genus. Furthermore, since the creation of shear band V-shaped notches has emerged as a key phenomenon in understanding the mechanical failure of anodes in the presence of large plastic flow, we plan to further investigate the mechanical instability responsible for their creation.

DOE sponsored publications (2016 to 2019)

3. "Kinetics and morphological evolution of liquid metal dealloying", I. McCue, B. Gaskey, P.A. Geslin, A. Karma, and J. Erlebacher, *Acta Materialia* **115**, 10-23 (2016).
4. Atomistic to continuum modeling of solidification microstructures", A. Karma and D. Tourret, *Current Opinion in Solid State and Materials Science* **20**, 25-36 (2016).
5. "Two-mode Ginzburg-Landau theory of crystalline anisotropy for fcc-liquid interfaces", K.-A. Wu, S.-C. Lin, and A. Karma, *Phys. Rev.* B **93**, 054114 (2016).
6. "Elastically mediated interactions between grain boundaries and precipitates in two-phase coherent solids", Y.-C. Xu, P.-A. Geslin, and A. Karma, *Phys. Rev.* B **94**, 144106 (2016).
7. "Grain growth competition during thin-sample directional solidification of dendritic microstructures: A phase-field study", D. Tourret, Y. Song, A. J. Clarke, and A. Karma, *Acta Materialia* **122**, 220-235 (2017).
8. "Instability in dynamic fracture and the failure of the classical theory of cracks", C-H. Chen, E. Bouchbinder, and A. Karma, *Nature Physics* **13**, 1186 (2017).
9. "Universality and Stability Phase Diagram of Two-Dimensional Brittle Fracture", Y. Lubomirsky, C-H. Chen, A. Karma, and E. Bouchbinder, *Phys. Rev. Lett.* **121,** 134301 (2018).
10. "Pattern formation during electrochemical and liquid metal dealloying", I. McCue, A. Karma, and J. Erlebacher, *MRS Bull.* **43**, 27-34 (2018).
11. "Configurational stability of a crack propagating in a material with mode-dependent fracture energy - Part I: Mixed-mode I + III", J.B. Leblond, A. Karma, L. Ponson, A. Vasudevan, *J. Mech. Phys. Solids* **126**, 187–203 (2019).

Optical, plasmonic, and excitonic phenomena in nanostructures described within a dissipative quantum transport framework

PI: Irena Knezevic, University of Wisconsin – Madison, irena.knezevic@wisc.edu

Program Scope

The objective of this project is to develop versatile theoretical models and computational tools for accurate predictive simulation of the generally far-from-equilibrium and time-dependent dissipative quantum transport in electronic systems interacting with electromagnetic fields inside realistic semiconductor nanostructures

Recent Progress

***Nonlinear response in graphene nanoribbons* [1].** Nonlinear nanophotonics has many potential applications, such as in mode locking, frequency-comb generation, and all-optical switching. The development of materials with large nonlinear susceptibility is key to realizing nonlinear nanophotonics. Nanostructured graphene systems, such as graphene nanoribbons (GNRs) and nanoislands, have been predicted to have a strong plasmon-enhanced nonlinear optical behavior in the nonretarded regime (Fig. 1). Plasmons concentrate the light field down to subwavelength scales and can enhance the nonlinear optical effects; however, plasmon resonances are narrowband and sensitive to the nanostructure geometry. Here we show that graphene nanoribbons, particularly armchair graphene nanoribbons, have a remarkably strong nonlinear optical response in the long-wavelength regime and over a broad frequency range, from terahertz to the near infrared. We use a quantum-mechanical master equation with a detailed treatment of scattering and show that, in the retarded regime, electron scattering has a critical effect on the optical nonlinearity of graphene nanoribbons, which cannot be captured via the commonly used relaxation-time approximation. At terahertz frequencies, where intraband optical transitions dominate, the strong nonlinearity (in particular, third-order Kerr nonlinearity) stems from the jagged shape of the electron energy distribution, caused by the interband electron scattering mechanisms along with the intraband inelastic scattering mechanisms. We show that the relaxation-time approximation (RTA) fails to capture this quantum-mechanical phenomenon and results in a significant underestimation of the intraband nonlinearity. At the midinfrared to near infrared frequencies, where interband optical transitions dominate, the Kerr nonlinearity is significantly overestimated within the relaxation-time approximation (Fig. 2). These findings unveil the critical effect of electron scattering on the optical nonlinearity of nanostructured graphene, and underscore the capability of this class of materials for nonlinear nanophotonics.

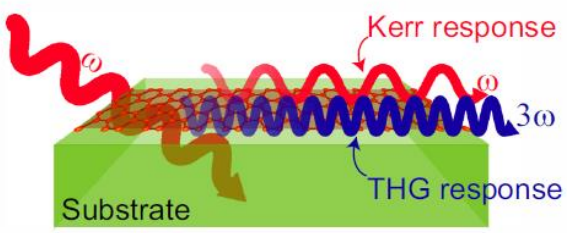

Fig. 1: Schematic of a graphene nanoribbon (GNR) on a substrate. The incident light with frequency ω causes the third-order Kerr response (oscillating with ω) and the third-harmonic (THG) response (oscillating with 3ω). [1].

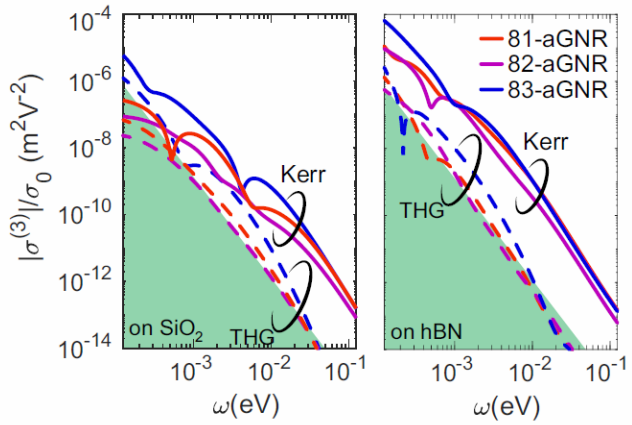

Fig. 2: The absolute value of the the third-order Kerr conductivity (solid) and the THG conductivity (dashed) for three different aGNRs, on two different substrates: SiO2 (left) and hBN (right). The green shaded area shows the third-order conductivity calculated via the common relaxation-time approximation (RTA) dissipator for the relaxation times in the range of 10^{-14}–10^{-11} s. The sheet carrier density is 5×10^{12} cm^{-2} (i.e., the line carrier density is ∼5 × 106 cm−1). The third-order conductivity is normalized to $\sigma_0 = e^2/h$.

***Plasmonis in graphene nanoribbons* [2].** We calculate the dielectric function and plasmonic response of armchair (aGNRs) and zigzag (zGNRs) graphene nanoribbons using the self-consistent-field approach within the Markovian master equation formalism (SCF-MMEF). We accurately account for electron scattering with phonons, ionized impurities, and line-edge roughness and show that electron scattering with surface optical phonons is much more prominent in GNRs than in graphene. We calculate the loss function, plasmon dispersion, and the plasmon propagation length in supported GNRs. Midinfrared plasmons in supported (3N+2)-aGNRs can propagate as far as several microns at room temperature, with 4–5-nm-wide ribbons having the longest propagation length (Fig. 3). In other types of aGNRs and in zGNRs, the plasmon propagation length seldom exceeds 100 nm. Plasmon propagation lengths are much longer on nonpolar (e.g., diamondlike carbon) than on polar substrates (e.g., SiO_2 or hBN),where electrons scatter strongly with surface optical phonons. We also show that the aGNR plasmon density is nearly uniform across the ribbon, while in zGNRs, because of the highly localized edge states, plasmons of different spin polarization are accumulated near the opposite edges.

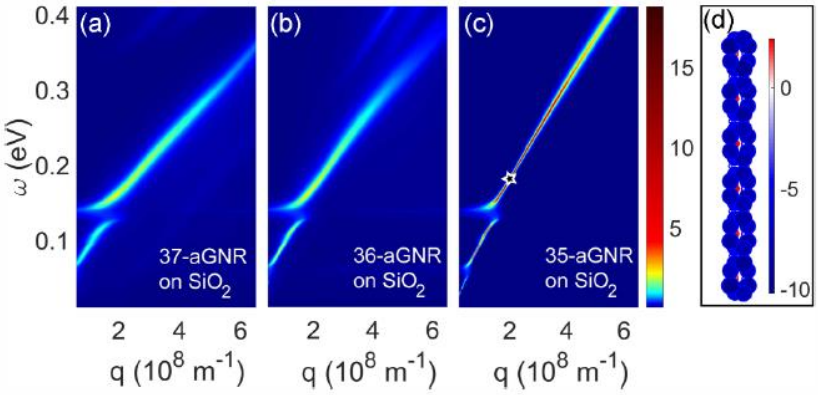

Fig. 3: (a)–(c) Loss functions in 3N+1, 3N, and 3N+2 n-type armchair GNRs of similar widths: (a) 37-aGNR, (b) 36-aGNR, and (c) 35-aGNR. Substrate is SiO_2, the sheet electron density is $n_s = 7 \times 10^{12}$ cm^{-2}, and the impurity density is $N_i = 4 \times 10^{11}$ cm^{-2}. The peak of the loss function gives plasmon dispersion. From the loss-function width along the q-direction we can determine plasmon propagation length. (d) Plasmon spatial distribution (i.e., induced charge density distribution) at different atomic sites throughout a unit cell of the 35-aGNR at the star-marked plasmon resonance from (c). Blue is negative, red is positive, and larger circle radius means greater absolute value of the induced charge density near a site.

Unexpectedly Fast Phonon-Assisted Exciton Hopping between Carbon Nanotubes [3]. Carbon-nanotube (CNT) aggregates are promising light-absorbing materials for photovoltaics. The hopping rate of excitons between CNTs directly affects the efficiency of these devices. We theoretically investigate phonon-assisted exciton hopping (Fig. 4), where excitons scatter with phonons into a same-tube transition state, followed by intertube Coulomb scattering into the final state. Second-order hopping between bright excitonic states is as fast as the first-order process (~1 ps). For perpendicular CNTs, the high rate stems from the high density of phononic states; for parallel CNTs, the reason lies in relaxed selection rules. Moreover, second-order exciton transfer between dark and bright states, facilitated by phonons with large angular momentum, has rates comparable to bright-to-bright transfer, so dark excitons provide an additional pathway for energy transfer in CNT composites. As dark excitons are difficult to probe in experiment, predictive theory is critical for understanding exciton dynamics in CNT composites.

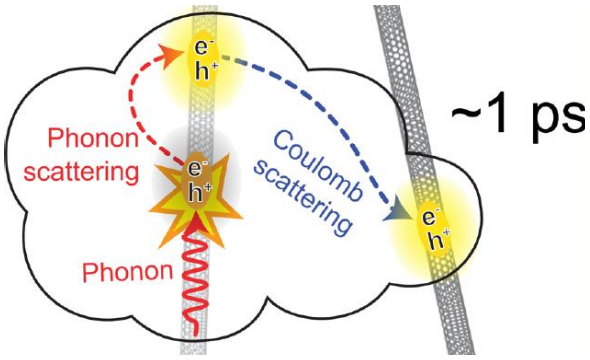

Fig. 4: Phonon-assisted intertube exciton hopping can be very fast, comparable to resonant Coulomb-mediated scattering. In particular, dark-to-bright phonon-assisted exciton scattering is as fast as bright-to-bright scattering [3].

Future Plans

The control of light-matter interaction at the nanoscale is a grand challenge that cuts across modern photonics, plasmonics, and optoelectronics. The development of simulation tools for predictive modeling of nanostructured light emitters and absorbers is critical to successfully tackling this grand challenge. For this purpise, the PI (along with a research scientist and a graduate student) has started to develop a coupled Quantum Transport and Electrodynamics Simulation Tool (QuTEST). This tool be three-dimensional (3D) and capable of handling varied experimental geometries, include both interband and intraband time-dependent electronic quantum transport and properly account for the electron band structure and carrier dissipative processes in all the relevant materials via the density matrix quantum-transport technique, and self-consistently couple the transport kernel and the electrodynamics solver. QuTEST will benefit experimental groups by improving design capability for nanophotonic devices.

References

[1] F. Karimi, A.H. Davoody, and I. Knezevic, "Nonlinear optical response in graphene nanoribbons: The critical role of electron scattering," Phys. Rev. B 97, 245403 (2018).

[2] F. Karimi and I. Knezevic, "Plasmons in graphene nanoribbons," Phys. Rev. B 96, 125417 (2017).

[3] A.H. Davoody, F. Karimi, M. S. Arnold, and I. Knezevic, "Unexpectedly fast phonon-assisted exciton hopping between carbon nanotubes," J. Phys. Chem. C 121, 13084–13091 (2017).

Publications

1. F. Karimi, A.H. Davoody, and I. Knezevic, “Nonlinear optical response in graphene nanoribbons: The critical role of electron scattering,” Phys. Rev. B 97, 245403 (2018).

2. S. Mei and I. Knezevic, “Thermal conductivity of ternary III-V semiconductor alloys: mass-difference scattering versus long-range order,” J. Appl. Phys. 123, 125103 (2018).

3. W. Peng, M. Zamiri, S. A. Scott, F. Cavallo, J. J. Endres, I. Knezevic, M. A. Eriksson, and M. G. Lagally, “Electronic Transport in Hydrogen-Terminated Si(001) Nanomembranes,” Phys. Rev. Applied 9, 024037 (2018).

4. F. Karimi and I. Knezevic, “Plasmons in graphene nanoribbons,” Phys. Rev. B 96, 125417 (2017).

5. S. Soleimanikahnoj and I. Knezevic, “Pseudospin Electronics in Phosphorene Nanoribbons,” Physical Review Applied 8, 064021 (2017).

6. A.H. Davoody, F. Karimi, M. S. Arnold, and I. Knezevic, “Unexpectedly fast phonon-assisted exciton hopping between carbon nanotubes,” J. Phys. Chem. C 121, 13084–13091 (2017).

7. Y. B. Shi, S. Mei, O. Jonasson, and I. Knezevic, “Modeling quantum cascade lasers: Coupled electron and phonon transport far from equilibrium and across disparate spatial scales,” Fortschr. Phys. 65, 1600084 (2017).

8. S. Mei, C. J. Foss, L. N. Maurer, O. Jonasson, Z. Aksamija, and I. Knezevic, "Boundaries, interfaces, point defects, and strain as impediments to thermal transport in nanostructures," 2017 IEEE International Reliability Physics Symposium (IRPS), pp. 6A-1.1-6A-1.10 (2017). https://doi.org/10.1109/IRPS.2017.7936333 (*invited review*)

9. S. Mei, Y. B. Shi, O. Jonasson, and I. Knezevic, “Quantum Cascade Lasers: Electrothermal Simulation Authors,” Handbook of Optoelectronic Device Modeling and Simulation, Ed. Joachim Piprek, CRC Press, Taylor and Francis Books, 2017. (*book chapter*) Preprint at http://arxiv.org/abs/1609.09130

10. L. N. Maurer, S. Mei, and I. Knezevic, “Phonon Monte Carlo: Generating Random Variates for Thermal Transport Simulation,” to appear in Nanophononics, Ed. Z. Aksamija, Pan Stanford Publishing, 2017. (*book chapter*) Preprint at http://arxiv.org/abs/1602.07735

Establishing microscopic photophysics of local cation and anion phase segregation in hybrid perovskite solar cells

Masaru Kuno, Prashant Kamat
University of Notre Dame, Department of Chemistry and Biochemistry

Program Scope

Preventing the realization of hybrid perovskite solar cells is their long-term stability. Intrinsic problems exist with hybrid perovskites wherein they undergo dynamic transformations linked to ion migration. Well known hysteretic behavior in $MAPbI_3$ solar cells is now attributed to both charge and cation migration followed by accumulation at $MAPbI_3$/contact interfaces. Anion migration followed by subsequent accumulation at hybrid perovskite/contact interfaces is also suggested to be the source of unwanted charge injection barriers. In mixed halide perovskites, analogous transformations stem from light-induced anion migration.

We are therefore conducting detailed measurements that will elucidate and quantify limiting factors of hybrid perovskite solar cell performance, stemming from local electronic disorder linked to cation/anion phase segregation. These measurements focus on addressing the origin of local variations in mixed anion/mixed cation perovskite photophysics and aim at providing quantitative (spatially-resolved) modeling for the fate of photogenerated carriers in working devices. More broadly, the study addresses how exactly cation and/or anion phase segregation impacts solar cell performance through changes to underlying charge recombination processes. These studies take advantage of recent measurements we have conducted to microscopically establish hybrid perovskite photophysics in thin films and perovskite solar cells. They also take advantage of work we have done to understand the origin of phase segregation in mixed halide perovskites, wherein we have recently developed a model to describe anion phase segregation in $MAPb(I_{1-x}Br_x)_3$ under optical illumination.[1]

Recent Progress

We have recently been studying cation migration in ~16-20% efficient hybrid perovskite solar cells, having the composition $FA_xMA_yCs_{1-x-y}PbI_3$ (referred to colloquially as FAMACs). This entails use of an infrared absorption technique we have developed, called Infrared Photothermal Heterodyne Imaging (IR-PHI).[2] By monitoring chemically-specific infrared transitions of methylammonium (MA) and formamidinium (FA) cation transitions, we are establishing their migration under applied bias. This information is simultaneously being correlated with local emission measurements wherein spectral changes are being linked to local MA and FA concentrations. Some of this data is shown in **Figure 1** where cation migration in FAMACs lateral devices have been studied.

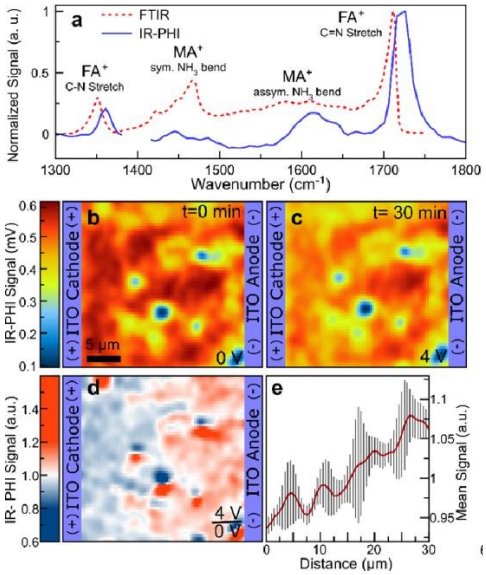

Figure 1. (a) FTIR (dashed blue) and IR-PHI (solid red) spectra of a FAMACs lateral device with relevant FA^+ and MA^+ stretches labeled. IR-PHI maps of the FA^+ 1720 cm^{-1} C=N stretch before (b) and after (**c**) 30 minutes of biasing (V_{bias}= 4 V, |E|= 0.1 V/μm). Associated ratio map (d) before and after biasing along with corresponding averaged IR-PHI signal profile (e).

Future Plans

There are several future avenues of investigation we would like to pursue. (1) We are seeking to establish whether there exist other mixed cation compositions that exhibit suppressed cation migration under bias. This entails both synthetic and theoretical studies tied to experiment. (2) We would like to establish a better connective link between infrared absorption measurements and visible emission measurements to provide the community an easy way to assess cation migration in perovskite materials. (3) We will conduct local, spatially-resolved solar cell measurements of FAMACs and other perovskite solar cells experiencing cation migration. This will establish the fate of photogenerated carriers in perovskite cells undergoing both cation and anion migration. (4) We will also investigate anion migration in mixed cation perovskite materials.

References

[1] *Rationalizing the light-induced phase separation of mixed halide organic-inorganic perovskites*, S. Draguta, O. Sharia, S. Yoon, M. Brennan, Y. V. Morozov, J. Manser, P. Kamat, W. F. Schneider, M. Kuno, Nature Commun. **2017**, 8, 200. DOI: 10.1038/s41467-017-00284-2

[2] *Super-resolution far-field infrared imaging by photothermal heterodyne imaging: Experiment and theory*, Z. Li, K. Aleshire, M. Kuno, G. Hartland, J. Phys. Chem. B **2017**, 121, 8838-8846. DOI: 10.1021/acs.jpcb.7b06065

Publications

1. *Crystal structure of individual $CsPbBr_3$ perovskite nanocubes via high-resolution transmission electron microscopy defocal series analysis*, M. C. Brennan, M. Kuno, S. Rouvimov, Inorg. Chem. **2019**, 58, 1555–1560. DOI: 10.1021/acs.inorgchem.8b03078

2. *Vacancy-mediated anion photosegregation kinetics in mixed halide hybrid perovskites: Coupled kinetic Monte Carlo and optical measurements*, A. Ruth, M. C. Brennan, S. Draguta, Y. V. Morozov, M. Zhukovskyi, B. Janko, P. Zapol, M. Kuno, ACS Energy Lett. **2018**, 3, 2321-2328. DOI:10.1021/acsenergylett.8b01369

3. *To exchange or not to exchange. Suppressing anion exchange in lead halide perovskites with $PbSO_4$-oleate capping*, V. K. Ravi, R. A. Scheidt, A. Nag, M. Kuno, P. V. Kamat, ACS Energy Lett. **2018**, 3, 1049–1055. DOI:10.1021/acsenergylett.8b00380

4. *A quantitative and spatially-resolved accounting of the performance bottleneck in high efficiciency, planar hybrid perovskite solar cells*, S. Draguta, J. A. Christians, Y. V. Morozov, A. Mucunzi, J. S. Manser, P. V. Kamat, J. M. Luther, M. Kuno, Energy Env. Sci, **2018**, 11, 960-969. DOI: 10.1039/C7EE03654J

5. *Subdiffraction infrared imaging of mixed cation perovskites: Probing local cation heterogeneities*, R. Chatterjee, I. M. Pavlovetc, K. Aleshire, G. V. Hartland, M. Kuno, ACS Energy Lett. **2018**, 3, 469-475. DOI: 10.1021/acsenergylett.7b01306

6. *Light-induced anion phase segregation in mixed halide perovskites*, M. C. Brennan, S. Draguta, P. V. Kamat, M. Kuno, ACS Energy Lett. **2018**, 3, 204-213. DOI: 10.1021/acsenergylett.7b01151

7. *Origin of the size-dependent Stokes shift in $CsPbBr_3$ perovskite nanocrystals*, M. C. Brennan, J. E. Herr, T. S. Nguyen-Beck, J. Zinna, S. Rouvimov, J. Parkhill, M. Kuno, J. Am. Chem. Soc. **2017**, 139, 12201-12208. DOI: 10.1021/jacs.7b05683

8. *Shift happens: How halide ion defects influence photoinduced segregation in mixed halide perovskites*, S. J. Yoon, M. Kuno, P. V. Kamat, ACS Energy Lett. **2017**, 2, 1507-1514. DOI: 10.1021/acsenergylett.7b00357

9. *Existence of a size-dependent Stokes shift in $CsPbBr_3$ nanocrystals*, M. C. Brennan, J. Zinna, M. Kuno, ACS Energy Lett. **2017**, 2, 1487-1488. DOI: 10.1021/acsenergylett.7b00383

10. *Rationalizing the light-induced phase separation of mixed halide organic-inorganic perovskites*, S. Draguta, O. Sharia, S. Yoon, M. Brennan, Y. V. Morozov, J. Manser, P. Kamat, W. F. Schneider, M. Kuno, Nature Commun. **2017**, 8, 200. DOI: 10.1038/s41467-017-00284-2

Project Title

Tunable Excitons and Pseudospins in Transition Metal Dichalcogenide Homobilayers

PI and affiliation:

Xiaoqin Elaine Li

Physics Department

University of Texas at Austin

Program Scope:

Transition metal dichalcogenides (TMDs) (MX_2 with M=Mo, W and X=S, Se, and Te) are van der Waals semiconductors which exhibit new and interesting optical properties. While a consistent understanding of exciton and valley pseudospin properties in monolayer TMDs has started to emerge in the last few years, many exciting opportunities to investigate topological exciton bands[1-5], quantum emitters[6], and exciton condensates[7-11] in gated and stacked TMD layers have not been explored experimentally.

We aim to understand fundamental quantum dynamic properties and transport of tunable excitons and pseudospins in homobilayers.

- New exciton resonances and their properties in the presence of a moiré pattern
- Quantum dynamics of excitons and valley pseudospins

Questions of interest to us include the following. Will new excitonic resonances emerge in the presence of moiré superlattice. How do electric gating and twist angle influence exciton and valley lifetime and decoherence time? Do valley pseudospins exhibit improved characteristics as information carriers? Can we control exciton and valley transport in gated and twisted bilayers?

Recent Progress:

Stacking two monolayers of TMDs with the same and different types involves different technical challenges. While we are making good progress learning how to prepare twist angle controlled homobilayers, we continue to investigate exciton properties in heterobilayers. In particular, our group and two other groups have identified new inter-layer excitons (*IXs*) resonances as quantized states confined with the moiré potential[12-14].

Building on this recent discovery, we study *IX* diffusion in $MoSe_2/WSe_2$ heterobilayers using spatially- and time-resolved photoluminescence (PL) measurements. We compare experiments two samples created by chemical vapor deposition and mechanical exfoliation and transfer methods. We found that *IX* diffusions significantly differ in these two types of samples. *We suggest that IXs in the stacked bilayer is largely localized due to the presence of the* moiré potential. These observations provide a different and complementary view of interlayer exciton diffusion from previous experiments on hBLs consisting of TMD monolayers with rather different lattice constants or with larger twist angles[15-17]. We are prepared a manuscript on this result and submitted it for review.

We have performed initial two-dimensional Fourier transform (2DFT) spectroscopy studies on $MoSe_2$ bilayers to understand the quantum dephasing time associated with the excitons. Further analysis is necessary before we can report definitive finding. We plan to report the result in a future meeting.

Future Plans

We plan to work on the following tasks in this coming year.

- Preparation of twisted TMD bilayers with a well-controlled angle.
- Investigation of quantum decoherence times in homobilayers.

Publications:

No publication to report yet.

References

1 Tong, Q., Yu, H., Zhu, Q., Wang, Y., Xu, X. and Yao, W. Topological mosaics in moiré superlattices of van der Waals heterobilayers. *Nature Physics* **13**, 356 (2016).

2 Kundu, A., Fertig, H. A. and Seradjeh, B. Effective Theory of Floquet Topological Transitions. *Physical Review Letters* **113**, 236803 (2014).

3 Dehghani, H., Oka, T. and Mitra, A. Dissipative Floquet topological systems. *Physical Review B* **90**, 195429 (2014).

4 Yuen-Zhou, J., Saikin, S. K., Yao, N. Y. and Aspuru-Guzik, A. Topologically protected excitons in porphyrin thin films. *Nat. Mater.* **13**, 1026 (2014).

5 Claassen, M., Jia, C., Moritz, B. and Devereaux, T. P. All-optical materials design of chiral edge modes in transition-metal dichalcogenides. *Nature communications* **7**, 13074 (2016).

6 Yu, H., Liu, G.-B., Tang, J., Xu, X. and Yao, W. Moiré excitons: From programmable quantum emitter arrays to spin-orbit–coupled artificial lattices. *Science Advances* **3**, e1701696 (2017).

7 Fogler, M. M., Butov, L. V. and Novoselov, K. S. High-temperature superfluidity with indirect excitons in van der Waals heterostructures. *Nat. Commun.* **5**, 4555 (2014).

8 Wu, F.-C., Xue, F. and MacDonald, A. H. Theory of two-dimensional spatially indirect equilibrium exciton condensates. *Physical Review B* **92**, 165121 (2015).

9 Basov, D., Fogler, M. and de Abajo, F. G. Polaritons in van der Waals materials. *Science* **354**, aag1992 (2016).

10 Low, T., Chaves, A., Caldwell, J. D., Kumar, A., Fang, N. X., Avouris, P., Heinz, T. F., Guinea, F., Martin-Moreno, L. and Koppens, F. Polaritons in layered two-dimensional materials. *Nat. Mater.* **16**, 182 (2016).

11 Liu, C.-X. Unconventional Superconductivity in Bilayer Transition Metal Dichalcogenides. *Physical Review Letters* **118**, 087001 (2017).

12 Tran, K., Moody, G., Wu, F., Lu, X., Choi, J., Kim, K., Rai, A., Sanchez, D. A., Quan, J., Singh, A., Embley, J., Zepeda, A., Campbell, M., Autry, T., Taniguchi, T., Watanabe, K., Lu, N., Banerjee, S. K., Silverman, K. L., Kim, S., Tutuc, E., Yang, L., MacDonald, A. H. and Li, X. Evidence for moiré excitons in van der Waals heterostructures. *Nature* **In press** (2019).

13 Seyler, K. L., Rivera, P., Yu, H., Wilson, N. P., Ray, E. L., Mandrus, D. G., Yan, J., Yao, W. and Xu, X. Signatures of moiré-trapped valley excitons in $MoSe_2/WSe_2$ heterobilayers. *Nature* **In press** (2019).

14 Jin, C., Regan, E. C., Yan, A., Iqbal Bakti Utama, M., Wang, D., Zhao, S., Qin, Y., Yang, S., Zheng, Z., Shi, S., Watanabe, K., Taniguchi, T., Tongay, S., Zettl, A. and Wang, F. Observation of moiré excitons in WSe_2/WS_2 heterostructure superlattices. *Nature* **In press** (2019).

15 Rivera, P., Seyler, K. L., Yu, H. Y., Schaibley, J. R., Yan, J. Q., Mandrus, D. G., Yao, W. and Xu, X. D. Valley-polarized exciton dynamics in a 2D semiconductor heterostructure. *Science* **351**, 688-691 (2016).

16 Unuchek, D., Ciarrocchi, A., Avsar, A., Watanabe, K., Taniguchi, T. and Kis, A. Room-temperature electrical control of exciton flux in a van der Waals heterostructure. *Nature* **560**, 340-344 (2018).

17 Jauregui, L., Joe, A. Y., Pistunova, K., Wild, D. S., High, A. A., Zhou, Y., Scuri, G., Greve, K. D., Sushko, A., Yu, C., Taniguchi, T., Watanabe, K., Needleman, D. J., Lukin, M. D., Park, H. and Kim, P. Electrical control of interlayer exciton dynamics in atomically thin heterostructures. *arXiv:1812.08691* (2018).

Understanding and Probing Coherent and Hydrodynamic Phonon Transport in Emerging Energy Materials

Bolin Liao

Department of Mechanical Engineering, University of California, Santa Barbara

Program Scope

The overarching goal of this project is to understand how the phase coherence of phonons and the interaction of phonons with other microscopic degrees of freedom in nanomaterials, such as 2D materials, can affect the energy transport properties and eventually lead to control of energy transport by manipulating phonon interference and phonon scatterings. On the computational side, we are developing and applying first-principles methods to study emerging phonon properties in nanomaterials, including coherent phonons, resonant bonding and gate-tunable phonon-electron scatterings, which hold the promise of enabling significant tunability of energy transport processes with external fields for a wide range of applications. On the experimental side, we are developing ultrafast transient grating spectroscopy and scanning ultrafast electron microscopy (SUEM) to directly probe the coherent phonon transport and phonon-electron interaction processes in nanomaterials with high combined spatial-temporal resolutions. This program will not only provide new insights into the microscopic transport and interaction processes of fundamental energy carriers, but also open new venue towards energy-relevant applications such as thermal switches and coherent energy harvesters.

Recent Progress

1. Coherent phonons in graphene superstructures significantly influence thermal transport properties

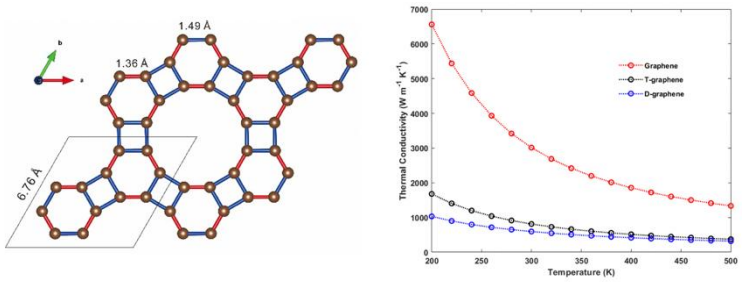

Figure 1 Left: schematic of the D-graphene superstructure. Right: significantly reduced thermal conductivity of D-graphene due to coherent phonon effects.

Coherent wave effects of thermal phonons hold promise of transformative opportunities in thermal transport control, but remain largely unexplored due to the small wavelength of thermal phonons, typically below a few nanometers[1,2]. This small length scale indicates that, instead of artificial phononic crystals, a more promising direction is to examine the coherent phonon effects in natural materials with hierarchical superstructures matching the thermal phonon wavelength. Recently,

we used first-principles simulations to characterize the thermal properties of dodecagraphene (D-graphene)[7], as shown in Fig. 1, a previously unstudied two-dimensional carbon allotrope based upon the traditional graphene structure but containing a secondary, in-plane periodicity. We found that despite very similar atomic structure and bonding strength, D-graphene possesses significantly different thermal properties than that of pristine graphene. At room temperature the calculated thermal conductivity of D-graphene is 600 $Wm^{-1}K^{-1}$ compared to over 3000 $Wm^{-1}K^{-1}$ for graphene. The out of plane acoustic (ZA) mode contribution decreases from 84% in graphene to 47% in D-graphene. We attributed these distinct properties to the presence of three naturally occurring, low frequency optical phonon modes that possess characteristics of phonon coherence and arise from a folding of the acoustic modes and the associated frequency gap opening, a phenomenon also found in superlattices where an out of plane periodicity is introduced. Furthermore, we found that the D-graphene superstructure also significantly suppresses hydrodynamic phonon transport in graphene[3] due to enhanced Umklapp scatterings. The construction of the D-graphene unit cell demonstrates the potential of using coherent phonon effects to significantly modify thermal transport of 2D materials without making drastic changes to their fundamental compositions.

2. Interfacial thermal resistance between hydrodynamic and non-hydrodynamic phonon materials

Hydrodynamic phonon transport occurs when phonon normal scattering dominates the Umklapp scattering. In the hydrodynamic regime, phonons flow like fluid with conserved momentum and reduced dissipation, and thus hydrodynamic phonon transport is promising for low-dissipation energy transport. Furthermore, hydrodynamic phonon transport has been predicted to happen in 2D materials[3] at relatively high temperatures and thus adds to the potential of practical applications of phonon hydrodynamic materials for thermal management and energy transport applications.

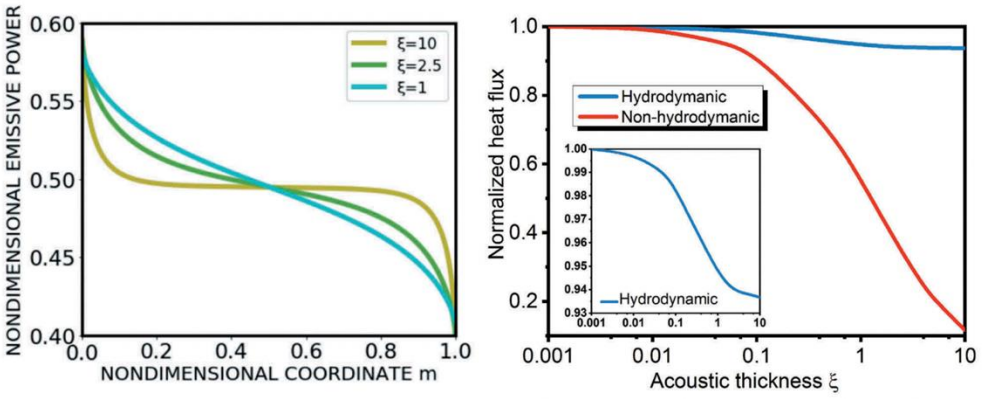

Figure 2 Left: Temperature distribution in a hydrodynamic phonon material, showing the boundary thermal resistance near the hydrodynamic/non-hydrodynamic interface. Right: The normalized heat flux as a function of acoustic thickness for hydrodynamic and non-hydrodynamic phonon transport.

Recently, we developed an integral-equation approach[4] to calculate the local temperature and drift velocity distribution of hydrodynamic phonons when they travel perpendicular to a diffuse-gray boundary. With this framework, we examined the application of an ideal phonon-

hydrodynamic material as the heat transfer medium between two diffuse-gray boundaries with a finite temperature difference. We used the integral-equation approach to solve a modified phonon Boltzmann transport equation with the displaced Bose-Einstein distribution as the equilibrium distribution between two boundaries perpendicular to the heat transfer direction. When the distance between the boundaries is smaller than the phonon normal scattering mean free path, our solution converges to the ballistic limit as expected. In the other limit, we found that, although the local thermal conductivity in the bulk of the hydrodynamic material approaches infinity, the thermal boundary resistance at the interfaces becomes dominant. We identified that this thermal boundary resistance has a new origin: it is caused by the mismatch of the local phonon equilibrium distributions in hydrodynamic and non-hydrodynamic materials. Our study provides insights to both the steady-state thermal characterization of phonon-hydrodynamic materials and the practical application of phonon-hydrodynamic materials for thermal management.

3. Enhanced resonant bonding in 2D materials lead to ultralow thermal conductivity

Crystalline materials with ultralow thermal conductivity are highly desirable for thermoelectric applications. Many known crystalline materials with low thermal conductivity, including PbTe and Bi_2Te_3, possess a special kind of chemical bond called "resonant bond". Resonant bonds consist of superposition of degenerate bonding configurations that leads to structural instability, anomalous long-range interatomic interaction and soft optical phonons, as illustrated in Fig. 3. These factors contribute to large lattice anharmonicity and strong phonon-phonon scattering, which result in low thermal conductivity. Recently, we used first-principles simulation to investigate the effect of resonant bonding in two dimensions (2D), where resonant bonds are in proximity to the surface[5]. We find that the long-range interatomic interaction due to resonant bonding becomes more prominent in 2D due to reduced screening of the atomic-displacement-

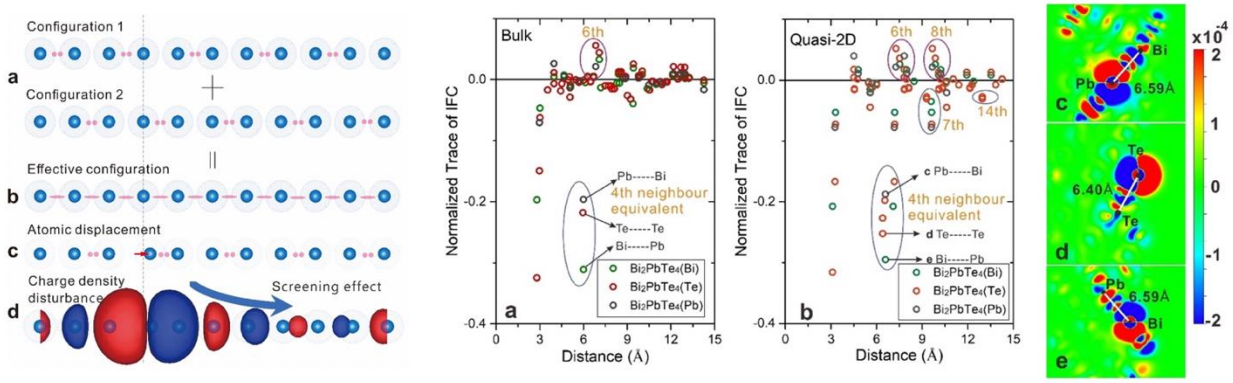

Figure 3 Left: Schematic of the resonant-bond-induced structural instability. Right: The anomalously enhanced interatomic force constants due to resonant bonding in bulk and 2D systems, showing the enhancement of resonant bonding in 2D systems due to reduced electrostatic screening.

induced charge density distortion. To demonstrate this effect, we recently used first-principles simulation to analyze the phonon properties of quasi-2D Bi_2PbTe_4 with an ultralow thermal conductivity of 0.74 W/mK at 300K. By comparing the interatomic force constants of quasi-2D

Bi_2PbTe_4 and its bulk counterpart, and the properties of resonant bonds near the surface and in the bulk, we conclude that resonant bonds are significantly enhanced in reduced dimensions and are more effective in reducing the lattice thermal conductivity. Our results will provide new clues to searching for thermal insulators in low-dimensional materials.

Future Plans

As a relatively new group, we are still in the process of setting up the proposed experiments: transient thermal grating and scanning ultrafast electron microscope. The emphasis for the next year of the program will be on the development of the experimental capabilities and demonstration of experimental measurement of coherent phonons and phonon-electron interaction as detailed in the program proposal. One specific project is to combine three-pulse photoacoustic spectroscopy[6] and transient thermal grating to investigate how coherent flexural phonons in 2D materials interact with photoinduced charge carriers, which can be a promising means of controlling phonon transport with optical excitation or electrostatic gating. On the computational side, we will continue exploring the relationship between phonon coherence and entropy/efficiency of energy transport processes via first-principles simulations.

References

1. Luckyanova, M. N. *et al.* Coherent Phonon Heat Conduction in Superlattices. *Science* **338**, 936–939 (2012).
2. Maldovan, M. Sound and heat revolutions in phononics. *Nature* **503**, 209–217 (2013).
3. Lee, S., Broido, D., Esfarjani, K. & Chen, G. Hydrodynamic phonon transport in suspended graphene. *Nature Communications* **6**, 6290 (2015).
4. Yang, R., Yue, S. & Liao, B. Hydrodynamic Phonon Transport Perpendicular to Diffuse-Gray Boundaries. *Nanoscale and Microscale Thermophysical Engineering* **23**, 25–35 (2019).
5. Yue, S.-Y., Xu, T. & Liao, B. Ultralow thermal conductivity in a two-dimensional material due to surface-enhanced resonant bonding. *Materials Today Physics* **7**, 89–95 (2018).
6. Liao, B., Maznev, A. A., Nelson, K. A. & Chen, G. Photo-excited charge carriers suppress sub-terahertz phonon mode in silicon at room temperature. *Nature Communications* **7**, 13174 (2016).
7. Usama Choudhry, Sheng-Ying Yue and Bolin Liao, Coherent phonon transport in graphene superstructures, submitted.

Publications (DOE Early Career Program started from 09/2018)

Sheng-Ying Yue, Tashi Xu and Bolin Liao, Ultrafast thermal conductivity in a two-dimensional material due to surface-enhanced resonant bonding, Materials Today Physics, **7**, 89, 2018

Runqing Yang, Sheng-Ying Yue and Bolin Liao, Hydrodynamic phonon transport perpendicular to diffuse-gray boundaries, Nanoscale and Microscale Thermophysical Engineering, **23**, 25, 2019 [Cover Article]

Formation of Dirac and Topological States on Semiconductor Surface and Strain Engineering

Feng Liu
University of Utah

Program Scope

This project encompasses a comprehensive study of physical mechanisms that lead to formation of exotic quantum electronic states on semiconductor surfaces and explores a novel approach of strain engineering of such states. It covers four correlated research topics: (1) Mechanistic study of epitaxial growth of an overlayer of Dirac and topological states on semiconductor surfaces, which is atomically bonded but electronic isolated from the underlying substrates. (2) Self-assembled growth of topological states arising from non-conventional lattice symmetry in semiconductor surfaces. (3) Strain engineering of topological surface/edge states and topological nanomechanical architecture. (4) Nanostructured topological materials. The common theme of the proposed research is to understand a new class of "surface-based" 2D Dirac and topological materials chemically supported (i.e., non Van der Waals type) on a substrate. The theoretical studies will be done in collaboration with experiments including Prof. Lagally funded by the DOE-BES "Materials Synthesis and Processing" program.

We will employ a multiscale approach, combining several state-of-the-art theoretical and computational techniques, ranging from first-principles density-functional-theory (DFT) electronic structure calculations to semi-empirical tight-binding (TB) model Hamiltonian analyses and calculations and to classical molecular dynamics (MD) simulations. Specifically, surface equilibrium structure and associated energetics will be calculated by DFT and MD methods. Electronic band structure will be studied using both DFT and TB methods with the TB parameters fit to the DFT band structures in supercells of slab geometry to represent a surface. Band topology will be revealed by analyzing the bulk (thin film) Bloch wavefunctions and the topological surface (edge) states using DFT and TB bands and iterative Green's function and Wannier function method. In addition, DFT as well as classical MD simulations will be carried out to directly simulate topological nanomechanical architectures resulted from the strain induced bending of thin films to study strain engineered topological states and spin manipulation.

Our studies will significantly improve our fundamental understanding of physical origins of surface-based Dirac and topological states in solid material systems, in terms of lattice geometry, spin-orbit coupling (SOC), orbital composition and surface/interface interactions. It will open up a new route towards realizing topological quantum phases in a new class of surface-based 2D materials. It will foster a new field of research by taking the effect of stress/strain to new territories on topological order of materials, beyond strain engineering of self-assembled nanostructures and of electronic properties that we have studied in the past decade within the

DOE-BES program. We believe many of our theoretical findings will provide useful guidance for future experimental efforts in growing surface-based 2D materials as we propose, realizing novel topological phases, strain engineering of topological states and spin texture, and nanostructured topological materials. These studies have also technological impact on advancing electronic and optoelectronic materials for energy applications, to fulfill the mission of Department of Energy.

Recent Progress

During the last two years, we have published 43 journal papers fully or partially supported by this DOE grant, including 8 Physical Review Letters (**3 as Editor's Suggestion and 1 as Featured in Physics**), 3 Nano Letters, 1 Nature Communications, 1 ACS Nano; plus one invited review and one invited book chapter. Two postdoctoral research associates and three graduate students have been fully or partially supported by this DOE project. The PI gave 12 invited talks at national/international conferences, and 18 departmental colloquium/seminar presentations. Below is a brief summary of four topics of research achievements pertaining to this project.

(1) Quantum Spin Hall Effect and Spin Bott Index in Quasicrystal Lattice:[1,2] Despite the rapid progress in the field of the quantum spin Hall (QSH) effect, most of the QSH systems studied up to now are based on crystalline materials. Recently, we propose that the QSH effect can also be realized in quasicrystal lattices (QLs) (See Fig. 1). We show that the electronic topology of aperiodic and amorphous insulators can be characterized by a spin Bott index B_s. The nontrivial QSH state in a QL is identified by a nonzero spin Bott index $B_s = 1$, associated with robust edge states and quantized conductance. We further map out a topological phase diagram in which the QSH state lies in between a normal insulator and a weak metal phase due to the unique wave functions of QLs. Our findings not only provide a better understanding of electronic properties of quasicrystals but also extend the search of the QSH phase to aperiodic and amorphous materials that are experimentally feasible.

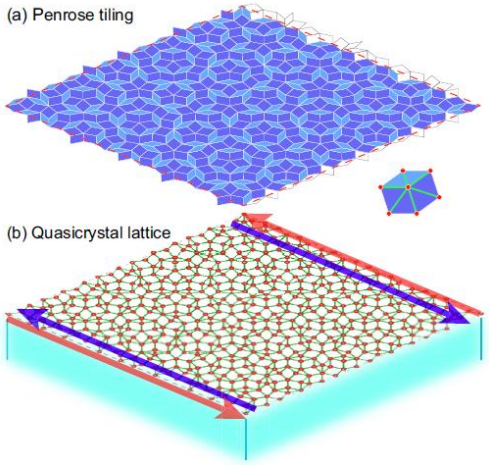

Fig. 1. (a) Penrose tiling of 521 vertices. The red dashed line marks a unit cell under periodic approximation. The inset shows the atomic orbitals on the vertices of rhombuses indicating nearest-neighbor hopping. (b) Illustration of a QSH state in a surface-based 2D QL. The red/blue arrows represent helical edge states with opposite spin polarizations.

Note: This work[1] was selected by PRL editor as "Editor's Suggestion" and published jointly with a PRB "Editor's Suggestion"[2] detailing the theory of Spin Bott index for defining the topology of aperiodic system. As a pleasant surprise, the PRB was converted from the originally submitted Supplementary Information for PRL upon referee and editor's kind recommendation.

(2) Ubiquitous Spin-orbit Coupling in a Screw Dislocation with High Spin Coherency:[3] We theoretically demonstrate that screw dislocation (SD), a 1D topological defect widely present in semiconductors, exhibits ubiquitously a new form of spin-orbit coupling (SOC) effect (see Fig. 2). Differing from the widely known conventional 2D Rashba-Dresselhaus (RD) SOC effect that typically exists at surfaces/interfaces, the deep-level nature of SD-SOC states in semiconductors readily makes it an ideal SOC. Remarkably, the spin texture of 1D SD-SOC, pertaining to the inherent symmetry of SD, exhibits a significantly higher degree of spin coherency than the 2D RD-SOC. Moreover, the 1D SD-SOC can be tuned by ionicity in compound semiconductors to ideally suppress spin relaxation, as demonstrated by comparative first-principles calculations of SDs in Si/Ge, GaAs, and SiC. Our findings therefore open a new door to manipulating spin transport in semiconductors by taking advantage of an otherwise detrimental topological defect.

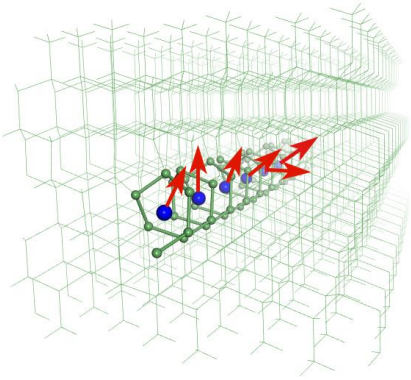

Fig. 2. A schematic diagram of screw dislocation (green balls) in crystal with rotating spin texture (red arrows) due to a ubiquitous SOC effect arising from breaking of local inversion symmetry.

Note: This work was selected by PRL editor as "Editor's Suggestion" and "Featured in Physics" with a nice Viewpoint written by Olena Gomonay in *Physics*, **11**, 78 (2018).

(3) Strain engineering of edge spin currents of quantum spin Hall insulators:[4,5] QSH system can exhibit exotic spin transport phenomena, mediated by its topological edge states. Recently we have demonstrated a new concept of bending strain engineering as an effective means to tune the spin transport properties of a QSH system.[4,5] We show that bending strain can be used to control the spin orientation of counter-propagating edge states of a QSH system to generate a non-zero spin current. This physics mechanism can be applied to effectively tune the spin current and pure spin current decoupled from charge current in a QSH ionsulator by control of its bending curvature. Furthermore, the curved QSH insulator can be achieved by the concept of topological nanomechanical architecture in a controllable way, as demonstrated by the material example of Bi/Cl/Si(111) nanofilm[4] and As-graphane[5] (Fig. 3). This concept of bending strain engineering of spins via topological nanomechanical

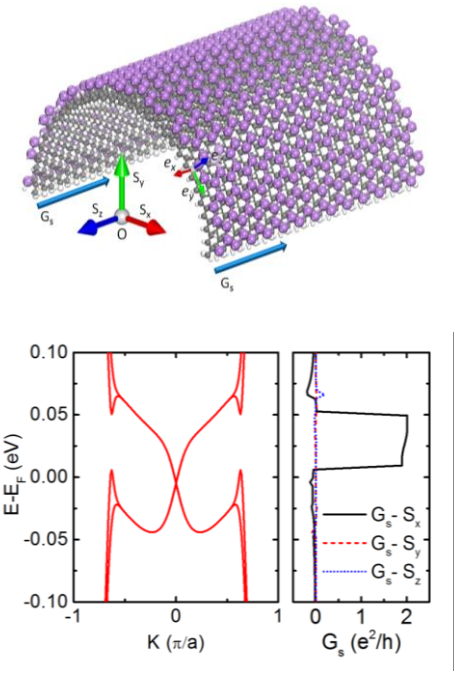

Fig. 3. Upper: A self-bent As-graphane, a curved 2D topological insulator. Lower left: Band structure of the bent As-graphane; lower right: Edge spin conductance.

architecture affords a promising route towards the realization of topological nano mechanospintronics.

Note: This work was highlighted in the DOE SC website (see screen shot on the right), as noted by the DOE Web editor: "The SC tweet about the highlight (https://science.energy.gov/bes/highlights/2017/bes-2017-12-f/) on bending materials was the **top tweet for the last week of December.**"

Future Plans

We plan to expand our current studies in the following areas:

(a) Develop new models for studying quantum materials
(b) Search for new inorganic and organic topological and quantum materials
(c) Continue exploring a new research direction in "topological phases in disordered systems, including quasi-crystalline materials" as recently initiated
(d) Explore different epitaxial growth routes towards formation of topological quantum phases on semiconductor surfaces, especially including studies of defects in topological phases
(e) Initiate a new research direction in flat-band materials
(f) Continue the efforts of experimental collaborations

References

1. "Quantum Spin Hall Effect and Spin Bott Index in a Quasicrystal Lattice", H. Huang and Feng Liu, *Phys. Rev. Lett*., **121**, 126401 (2018). **Editor's Suggestion.**
2. "Theory of spin Bott index for quantum spin Hall states in nonperiodic systems", H. Huang and Feng Liu, *Phys. Rev. B*., **98**, 12513, (2018). **Editor's Suggestion**.
3. "Ubiquitous Spin-Orbit Coupling in a Screw Dislocation with High Spin Coherency", L. Hu, H. Huang, Z. Wang, W. Jiang, X. Ni, Y. Zhou, V. Zielasek, M. G. Lagally, B. Huang and Feng Liu, *Phys. Rev. Lett*, **121**, 066401 (2018). **Editor's Suggestion, Featured in Physics.**
4. "Bending strain engineering in quantum spin Hall system for controlling spin currents", B. Huang, K-H Jin, B. Cui, F. Zhai, J. Mei and Feng Liu. *Nature Commun*., **8**, 15850 (2017).
5. "Quantum Spin Hall Effect and Tunable Spin Transport in As-Graphane", L. Zhang, F. Zhai, K-H Jin, B. Cui, B. Huang, Z. Zhang, J. Lu and Feng Liu. *Nano Lett*., **17**, 4359 (2017).

Publications

1. “Quantum Spin Hall Effect and Spin Bott Index in a Quasicrystal Lattice”, H. Huang and Feng Liu, *Phys. Rev. Lett*., **121**, 126401 (2018). **Editor's Suggestion.**
2. “Theory of spin Bott index for quantum spin Hall states in nonperiodic systems”, H. Huang and Feng Liu, *Phys. Rev. B*., **98**, 12513, (2018). **Editor's Suggestion**.
3. “Ubiquitous Spin-Orbit Coupling in a Screw Dislocation with High Spin Coherency”, L. Hu, H. Huang, Z. Wang, W. Jiang, X. Ni, Y. Zhou, V. Zielasek, M. G. Lagally, B. Huang and Feng Liu, *Phys. Rev. Lett*, **121**, 066401 (2018). **Editor's Suggestion, Featured in Physics.**
4. “Bending strain engineering in quantum spin hall system for controlling spin currents”, B. Huang, K-H Jin, B. Cui, F. Zhai, J. Mei and Feng Liu. *Nature Commun*., **8**, 15850 (2017).
5. “Quantum Spin Hall Effect and Tunable Spin Transport in As-Graphane", L. Zhang, F. Zhai, K-H Jin, B. Cui, B. Huang, Z. Zhang, J. Lu and Feng Liu. *Nano Lett*., **17**, 4359 (2017).
6. “Intrinsic Quantum Anomalous Hall Effect with In-Plane Magnetization: Searching Rule and Material Prediction”, Z. Liu, G. Zhao, B. Liu, Z. F. Wang, J. Yang, and Feng Liu, *Phys. Rev. Lett*. **121**, 246401 (2018). **Editor's Suggestion.**
7. “Significantly Enhanced Magnetoresistance in Monolayer WTe_2 via Heterojunction Engineering: A First-principles Study”, L. Hu, L. Kang, J. Yang, B. Huang and Feng Liu, *Nanoscale* **10**, 22231 (2018). **Nanoscale HOT Article Collection and Editor’s Choice: van der Waals heterostructures.**
8. “Pseudo Dirac nodal sphere semimetal”, J. Wang, Y. Liu, K-H Jin, X. Sui, L. Zhang, W. Duan, Feng Liu and B. Huang, *Phys. Rev. B.*, **98**, 201112(R) (2018).
9. “Incident wavelength and polarization dependence of spectral shifts in β-Ga2O3 UV photoluminescence", Y. Wang, P. T. Dickens, J. B. Varley, X. Ni, E. Lotubai, S. Sprawls, F. Liu, V. Lordi, S. Krishnamoorthy, S. Blair, K. G. Lynn, M. Scarpulla and B. Sensale-Rodriguez, *Sci. Rep*. **8**, 18075 (2018).
10. “Cyano-Based Materials with Giant Optical Anisotropy and Second Harmonic-Generation Effect”, L. Kang, F. Liang, Z. Lin, F. Liu and B. Huang, *Inorg. Chem*. **57**, 15001 (2018).
11. “Black-hole horizon in the Dirac semimetal $Zn_2In_2S_5$”, H. Huang, K-H Jin and Feng Liu, *Phys. Rev. B*., **98**, 121110(R) (2018).
12. “Band gap reduction in van der Waals layered 2D materials via a de-charge transfer mechanism”, C. Zhang, H. Huang, X. Ni, Y. Zhou, L. Kang, W. Jiang, H. Chen, J. Zhang and Feng Liu. *Nanoscale*, **10**, 16759 (2018).
13. “Li doped kagome spin liquid compounds”, W. Jiang, H. Huang, J-W Mei and Feng Liu, *Phys. Chem. Chem. Phys*., **20**, 21693 (2018).
14. “Two Novel Deep-Ultraviolet Nonlinear Optical Crystals with Shorter Phase-Matching Second Harmonic Generation than $KBe_2BO_3F_2$: A First-Principles Prediction”, L. Kang, F. Liang, P. Gong, Z. Lin, Feng Liu and B. Huang, *Phys. Status Solodi RRL*, 1800276 (2018).
15. “Tunable topological semimetal states with ultraflat nodal rings in strained YN”, H. Huang, W. Jiang, K-H, Jin and Feng liu, *Phys. Rev. B* **98**, 045131 (2018).
16. “Intrinsic quantum anomalous hall effect in a two dimensional anilato-based lattice”, X. Ni, W. Jiang, H. Huang, K-H Jin and Feng Liu, *Nanoscale* **10**, 11901 (2018).
17. “Photoinduced nonequilibrium topological states in strained black phosphorus”, H. Liu. J. Sun, C. Cheng, Feng Liu and S. Meng, *Phys. Rev. Lett*. **120**, 237403 (2018).

18. “Prediction of two-dimensional nodal-line semimetals in a carbon nitride covalent network”, H. Chen, S. Zhang, W, Jiang, C. Zhang, H. Guo, Z. Liu, Z. Wang, Feng Liu and X. Niu, *J. Mater. Chem. A*, **6**, 11252 (2018).
19. “Pressure-induced organic topological nodal-line semimetal in the three-dimensional molecular crystal Pd(dddt)2”, Z. Liu, H. Wang, Z. F. Wang, J. Yang and Feng Liu, *Phys. Rev. B*. **97**, 155137 (2018).
20. “Light-Induced Type-II Band Inversion and Quantum Anomalous Hall State in Monolayer FeSe”, Z. F. Wang, Z. Liu, J. Yang and Feng Liu, *Phys. Rev. Lett*. **120**, 156406 (2018).
21. “Alloy Engineering of Topological Semimetal Phase Transition in $MgTa_{2-x}Nb_xN_3$”, H. Huang, K-H Jin and Feng Liu, *Phys. Rev. Lett*. **120**, 136403 (2018).
22. “Formation of a large gap quantum spin Hall phase in a 2D trigonal lattice with three p-orbitals”, C. Li, K-H Jin, S. Zhang, F. Wang, Y. Jia and Feng Liu, *Nanoscale* **10**, 5496-5502 (2018).
23. “Topological Electride Y_2C”, H. Huang, K-H, Jin, S. Zhang and Feng Liu, *Nano Lett*. **18**, 1972 (2018).
24. “Topological states in a two-dimensional metal alloy in Si surface: BiAg/Si(111)-4×4 surface”, X. M. Zhang, B. Cui, M. Zhao and Feng Liu, *Phys. Rev. B*, **97**, 085422 (2018).
25. "Kane Fermion in a Two-Dimensional π Conjugated Bis(iminothiolato)nickel Monolayer”, A. Wang, X. Zhao, M. Zhao, X. Zhao, Y. Feng and Feng Liu, *J. Phys. Chem. Lett*. **9**, 614 (2018).
26. “Prediction of large gap flat Chern band in a two-dimensional metal-organic framework”, N. Su, W. Jiang, Z. F. Wang and Feng Liu, *Appl. Phys. Lett*., **112**, 033301 (2018).
27. “Monte Carlo simulations of electrical percolation in multicomponent thin films with nano fillers”, X. Ni, C. Hui, N. Su, W. Jiang and Feng Liu, *Nanotechnology* **29**, 075401 (2018).
28. “Oxidation-promoted Interfacial Synthesis of Redox-active Bis(diimino)nickel Nanosheet", E. J. H. Phua, K-H Wu, K. Wada, T. Kusamoto, H. Maeda, J. Cao, R. Sakamoto, S. Sasaki, J-W. Mei, W. Jiang, Feng Liu and H. Nishihara, *Chem. Lett*., **47**, 2 (2018).
29. “Prediction of Ideal Topological Semimetals with Triply Degenerate Points in the NaCu3Te2 Family”, J. Wang, X. Sui, W. Shi, J. Pan, S. Zhang, Feng Liu, S.-H. Wei, Q. Yan, and B. Huang, *Phys. Rev. Lett.* **119**, 256402 (2017).
30. “Electronic and spin dynamics in the insulating iron pnictide $NaFe_{0.5}Cu_{0.5}As$”, S. Zhang, Y. He, J.-W. Mei, Feng Liu, and Z. Liu, *Phy. Rev B* **96**, 245128 (2017).
31. “Nanostructured topological state in bismuth nanotube arrays: inverting bonding–antibonding levels of molecular orbitals”, K-H Jin, S-H Jhi and Feng Liu, *Nanoscale*, **9**, 16638 (2017).
32. “Bis(aminothiolato)nickel nanosheet as a redox switch for conductivity and an electrocatalyst for the hydrogen evolution reaction", X. Sun, K. Wu, R. Sakamoto, T. Kusamoto, H. Maeda, X. Ni, W. Jiang, Feng Liu, S. Sasaki, H. Masunage and H. Nishihara. *Chem. Sci*., **8**, 8078 (2017).
33. “Multivalency-Driven Formation of Te-Based Monolayer Materials: A Combined First-Principles and Experimental study”,Z. Zhu, X. Cai, S. Yi, J. Chen, Y. Dai C. Niu, Z. Guo, M. Xie, Feng Liu, J. Cho, Y. Jia and Z. Zhang. *Phys. Rev. Lett*. **119**, 106101 (2017).
34. “Theoretical Discovery of a Superconducting Two-Dimensional Metal−Organic Framework”, X. Zhang, Y. Zhou, B. Cui, M. Zhao and Feng Liu. *Nano Lett*. **17**, 6166 (2017).
35. “Topological nodal-line semimetal in nonsymmorphic Cmce-phase Ag_2S”, H. Huang, K-H Jin and Feng Liu. *Phys. Rev. B* **96**, 115106 (2017).
36. “Atomically Abrupt Topological p−n Junction”, S. Kim, K-H Jin, B. Kho, B. Park Feng Liu J. Kim, H. Yeom. *ACS Nano*, **11**, 9671 (2017).

37. “Creation of half-metallic f-orbital Dirac fermion with superlight elements in orbital-designed molecular lattice”, B. Cui, B. Huang, C. Li, X. Zhang, K-H Jin, L. Zhang, W. Jiang, D. Liu, and Feng Liu. *Phys. Rev. B* **96**, 085134 (2017).
38. “Spin fluctuation induced linear magnetoresistance in ultrathin superconducting FeSe films”, Q. Wang, W. Zhang, W. Chen, Y. Xing, Y. Sun, Z. Wang, J. Mei, Z. Wang, L. Wang, X. Ma, Feng Liu, Q. Xue and J. Wang. *2D Mater*. **4**, 034004 (2017).
39. “Tuning interfacial spin filters from metallic to resistive within a single organic semiconductor family”, J. Wang, A. Deloach, W. Jiang, C. M. Papa, M. Myahkostupov, F. N. Castellano, Feng Liu and D. B. Dougherty. *Phys. Rev. B*, **95**, 241410(R) (2017).
40. “Gapped Spin-1/2 Spinon Excitations in a New Kagome Quantum Spin Liquid Compound Cu3 Zn(OH)6FBr”, Z. Feng, Z. Li, X. Meng, W. Yi, Y. Wei, J. Zhang, Y. C. Wang, W. Jiang, Z. Liu, S. Li, Feng Liu, J. Luo, S. Li, G.Zheng, Z. Y. Meng J. W. Mei and Y. Shi. *Chin. Phys. Lett.*, **34**, 7, 077502 (2017).
41. “π conjugation in the epitaxial Si(111)- ($\sqrt{3}\times\sqrt{3}$) surface: Unconventional “bamboo hat” bonding geometry for Si”, W. Jiang, Z. Liu, M. Zhou, X. Ni and Feng Liu. *Phys. Rev. B*, **95**, 241405(R) (2017).
42. “Tensile strained gray tin: Dirac semimetal for observing negative magnetoresistance with Shubnikov–de Haas oscillations”, H. Huang and Feng Liu. *Phys. Rev. B*, **95**, 201101(R) (2017).
43. "Pulse laser induced graphite-to-diamond phase transition: the role of quantum electronic stress", Z. F. Wang and Feng Liu. *Sci. Chi. Phys.*, **60**, 026811 (2017).
44. “Computational design of two-dimensional topological materials”, Z. F. Wang, K-H Jin and Feng Liu. WIREs Comput Mol Sci 2017, e1304. doi: 10.1002/wcms.1304. (**invited review**).
45. “Organic Topological Insulators” W. Jiang and Feng Liu, in World Scientific Reference on Spin in Organics, Chap 6, pp. 201-224 (2018) (**invited book chapter**).

Universal Parameter to Quantitatively Predict Glass Properties

E. Ma

Department of Materials Science and Engineering, Johns Hopkins University, Baltimore, MD 21218 ema@jhu.edu

Program Scope

Identifying the microscopic mechanisms that control the behavior of glasses is one of the most challenging unresolved problems in physical sciences. Structure-property relationship, in particular, is a central tenet of materials science. For metallic glasses (MGs), the *amorphous* nature of their structures poses major challenges, to a quantitative prediction of the properties. This project is designed to establish "flexibility (volume)" as a universal indicator of the state the MG structure is in, as well as a *quantitative* property correlation derived and confirmed for all MGs.

The flexibility volume will be demonstrated to be universally applicable across various MGs and lengscales from atomic level and up, using molecular dynamics (MD) simulations and synchrotron X-ray experiments, for MGs of all compositions and processing history, enabling a direct comparison of different MG systems to explain the composition dependence often observed for properties. We will illustrate the advantages of flexibility volume over previous phenomenological structural descriptors, such as free volume, liquid-like regions, soft spots and local atomic packing topology.

The advances are expected to help explain the much lowered and variable elastic modulus of MGs with respect to their conventional crystalline counterpart. The availability of a single indicator for a robust property correlation should be of widespread interest to both experimentalists and modelers, particularly useful for formulating mathematical equations about the behavior of the MGs.

Recent Progress

We have used molecular dynamics simulations to demonstrate a quantitative prediction of the shear modulus of amorphous silicon from its structure state [1]. To derive a deterministic correlation, the amorphous structure is described in terms of its flexibility for atomic motion, using a flexibility volume parameter that incorporates both the atomic volume and the vibrational mean square displacement, to combine both static structure and dynamics information [2]. This structure descriptor can be evaluated on the atomic scale and also correlates well with the propensity for thermal relaxations and local shear transformations, providing a metric to map out and explain the mechanical heterogeneity in the amorphous material.

There are several salient features of our results. First of all, the correlation we see in Fig. 1 is an advance over relying solely on the static configuration (often merely a single aspect of the structure) to correlate with properties. Instead, our new flexibility volume parameter, υ_{flex}, purposely incorporates dynamics information via MSD and reflects the overall flexibility that is actually available in the glass internal structure. For a-Si, this descriptor implicitly covers information such as the nature of atomic

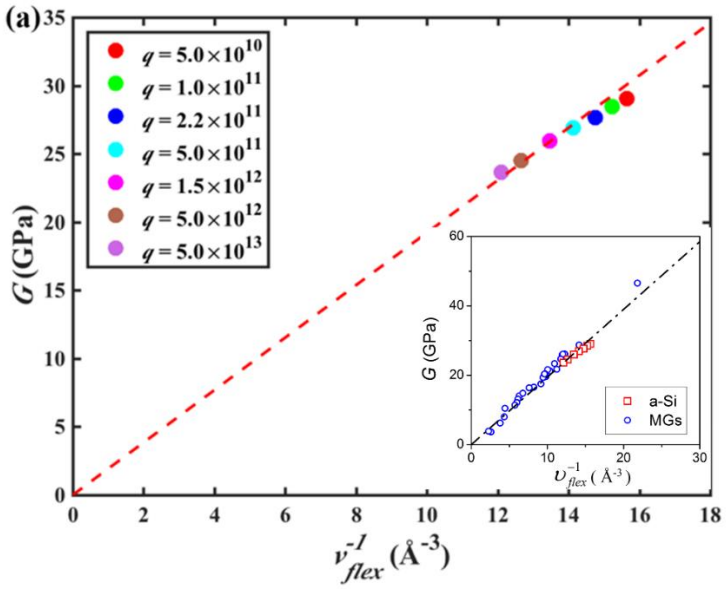

FIG. 1 The quantitative correlation between the shear modulus G and the flexibility volume υ_{flex} for amorphous Si obtained using different quench rate q, in K/s. The dashed straight line is the prediction derived last year for metallic glasses (MGs). The inset includes all the data points of a-Si (in present work) and MGs [2], compared with the dashed line of theoretical prediction [2].

bonding and how liquidlike the environment is. Although υ_{flex} does not directly describe anisotropy, it does reflect the effects of the latter on atomic flexibility. Second, the structural descriptor here arises from Debye theory and enables a quantitative calculation of the shear modulus G, as shown in Fig. 1. The success with a-Si lends support to the universality of the deterministic relationship between the shear modulus and the flexibility volume, for various types of glasses, beyond what has already been demonstrated for metallic glasses [2]. υ_{flex} is thus a good candidate as a single internal variable characterizing the state of the glass in a possible continuum description of mechanical rigidity. Last but not least, different from metallic and polymeric glasses, a-Si is a network glass with directional covalent bonds. The nearest-neighbor coordination number is only four, compared with ~12 for MGs, with abundant excess volume in the first place. a-Si is not ductile normally, so spatial volume is not of fundamental importance in governing the fertile sites where shear transformations tend to take place. We now see that for this open-structure glass, high $\upsilon_{flex,i}$ and its local average remains to be a tell-tale indicator of regions most amenable to imposed local shape change via stress-driven shear transformations, as demonstrated in our simulated a-Si [1]. $\upsilon_{flex,i}$ is thus a prognostic parameter in monitoring the deformability distribution inside a-Si, to explain the spatial heterogeneity of the mechanical response of an amorphous solid. Taken together, the new points made in this study constitute a step-forward in developing mathematically verifiable correlations that link the glassy configuration with properties, for metallically and covalently bonded amorphous solids alike.

Future Plans

In the next stage of this project, we will measure the flexibility volume experimentally, in addition to the computational analyses reported above. The flexibility volume υ_{flex} can be obtained from the MSD, $\langle r^2 \rangle$, or Debye temperature θ_D, both of which can be measured in the laboratory via Inelastic Neutron Scattering (INS) and X-ray/neutron diffraction. We are in the process of applying for beam time at ORNL, and are making MG samples in 5 selected alloy systems. We will first epxerimentally determine their shear modulus using ultrasound velocity measurements, and then measure the flexibility in these very same samples, such that we can quantitatively validate the correaltions.

[1] Fan, Zhao; Ding, Jun; Li, Qing-Jie; Ma, Evan, *Correlating the properties of amorphous silicon with its flexibility volume*, **Physical Review B (2017)** Volume: 95 Issue: 14 DOI: 10.1103/PhysRevB.95.144211

[2] Ding, Jun; Cheng, Y.-Q.; Sheng, Howard; Asta, M; Ritchie, R.; Ma, Evan; *Universal structural parameter to quantitatively predict metallic glass properties*, **Nature Communications** Volume: 7 No: 13733 Published: DEC 12 2016 DOI: 10.1038/ncomms13733

Publications

The most recent (~ past 2 years) papers are listed below.

1. Meng Li, De-Gang Xie, Evan Ma, Ju Li, Xi-Xiang Zhang & Zhi-Wei Shan, *Effect of hydrogen on the integrity of aluminum oxide interface at elevated temperatures*, **Nature Communications** 8 (2017) 14564.

2. Fan, Zhao; Ding, Jun; Li, Qing-Jie; Ma, Evan, *Correlating the properties of amorphous silicon with its flexibility volume*, **Physical Review B** (2017) Volume: 95 Issue: 14 DOI: 10.1103/PhysRevB.95.144211

3. Lihua Wang, Pengfei Guan, Jiao Teng, Pan Liu, Dengke Chen, Weiyu Xie, Deli Kong, Shengbai Zhang, Ting Zhu, Ze Zhang, Evan Ma, Mingwei Chen, Xiaodong Han, *New twinning route in face-centered cubic nanocrystalline metals*, **NATURE COMMUNICATIONS**, Volume: 8 Published: 2017 DOI: 10.1038/s41467-017-02393-4

4. Ding, J; Ma, E, *Computational modeling sheds light on structural evolution in metallic glasses and supercooled liquids*, **npj Computational Materials** Volume: 3 Issue: 9 Published: 2017 doi:10.1038/s41524-017-0007-1

5. Qing-Jie Li, Bin Xu, Shotaro Hara, Ju Li and Evan Ma, *Sample-size-dependent surface dislocation nucleation in nanoscale crystals*, **Acta Mater**. 145(2018) 19-29. doi.org/10.1016/j.actamat.2017.11.048

6. F. Rao, K. Y. Ding, Y. X. Zhou, Y. H. Zheng, M. J. Xia, S. L. Lv, Z. T. Song, S. L. Feng, I. Ronneberger, R. Mazzarello, W. Zhang and E. Ma, *Reducing the stochasticity of crystal nucleation to enable subnanosecond memory writing*, **Science** Vol. 358, Issue 6369, pp. 1423-1427 Published: Nov 8 2017 doi:10.1126/science.aao3212

7. Wang, Zhang-Jie; Li, Qing-Jie; Li, Yao; Huang, H-C; Lu, L; Dao, M ; Li, Ju; Ma, Evan**; S**uresh, Subra; Shan, ZW., *Sliding of coherent twin boundaries*, **Nature Communications** Volume: 8 Published: OCT 24 2017 DOI: 10.1038/s41467-017-01234-8

8. Ma, Evan; Zhu, Ting, *Towards strength-ductility synergy through the design of heterogeneous nanostructures in metals*, **Materials Today** Volume: 20 Issue: 6 Pages: 323-331 Published: JUL-AUG 2017 DOI: 10.1016/j.mattod.2017.02.003

9. J. Yang, Yun-Jiang Wang, E. Ma, A. Zaccone, L. H. Dai and M. Q. Jiang, *Structural Parameter of Orientational Order to Predict the Boson Vibrational Anomaly in Glasses*, **PHYSICAL REVIEW LETTERS** 122, 015501 (2019).

10. Shao-Ping Wang, Evan Ma and Jian Xu, *New ternary equi-atomic refractory medium-entropy alloys with tensile ductility: Hafnium versus titanium into NbTa-based solution*, **Intermetallics** 107 (2019) 15–23

11. Eric Rothchild, Q.-J. Li and Evan Ma, *On the validity of using the Debye model to quantitatively correlate the shear modulus with vibrational properties in cubic metals*, **Scripta Mater**. 158 (2019) 34-37.

12. W. Zhang and E. Ma, *Single element glass to record data*, **Nature Materials** 17 (2018) 654-655.

13. Yuecun Wang, Boyu Liu, X. Zhao, X.H. Zhang, Y.C. Miao, N. Yang, B. Yang, L.Q. Zhang, W.J. Kuang, J. Li, E. Ma and Z.W. Shan, *Turning a native or corroded Mg alloy surface into an anti-corrosion coating in excited CO_2,* **Nature Communications** 9 (2018) 4058.

14. Zhao Fan, Jun Ding & Evan Ma, *Making glassy solids ductile at room temperature by imparting flexibility into their amorphous structure*, **Materials Research Letters** 6:10 (2018) 570-583.

15. Jiang-Jing Wang, Jun Wang, Hongchu Du, Lu Lu, Peter C. Schmit, Johannes Reindl, Antonio M. Mio, Chun-Lin Jia , Evan Ma, Riccardo Mazzarello, Matthias Wuttig, and Wei Zhang, *Genesis and Effects of Swapping Bilayers in Hexagonal GeSb2Te4*, **CHEMISTRY OF MATERIALS,** Volume: 30 Issue: 14 Pages:4770-4777 Published: 2018

16. Muxin Yang, Dingshun Yan, Fuping Yuan, Ping Jiang, Evan Ma, and Xiaolei Wu, *Dynamically reinforced heterogeneous grain structure prolongs ductility in a medium-entropy alloy with gigapascal yield strength*, **PROCEEDINGS**

OF THE NATIONAL ACADEMY OF SCIENCES OF THE UNITED STATES OF AMERICA, Volume: 115 Issue: 28 Pages:7224-7229 Published: 2018

17. Bo-Yu Liu, NanYang, JianWang, Matthew Barnett, Yun-Chang Xin, Di Wu, Ren-Long Xin, Bin Li, R. Lakshmi Narayan, Jian-Feng Nie, JuLi, Evan Ma, Zhi-Wei Shan, *Insight from in situ microscopy into which precipitate morphology can enable high strength in magnesium alloys,* **JOURNAL OF MATERIALS SCIENCE & TECHNOLOGY**, Volume: 34 Issue: 7 Pages:1061-1066 Published: 2018

18. Ma Yan, Yuan Fuping Yang Muxin,Ping Jiang, Evan Ma, Xiaolei Wu, *Dynamic shear deformation of a CrCoNi medium-entropy alloy with heterogeneous grain structures*, **ACTA MATERIALIA**, Volume: 148 Pages:407-418 Published: 2018

19. Li Qing-Jie, Ma Evan, *When 'smaller is stronger' no longer holds,* **MATERIALS RESEARCH LETTERS,** Volume: 6 Issue:5 Pages:283-292 Published: 2018

Magnetic Imaging with Conductive Scanning Probe Microscopy

Sara A. Majetich, Physics Department, Carnegie Mellon University, Pittsburgh, PA 15213

Program Scope

Charge current through a heavy metal (HM) can generate a perpendicular spin current that exerts a spin orbit torque on an adjacent magnetic layer. This program focuses on the questions of transmission efficiency both at a HM/Magnetic Insulator (MI) interface and through the MI. *Addressing such questions requires development and testing of samples and measurement methodology. Specifically, there are needs to grow magnetic insulator thin films on metal substrates, to inject spin current by passing charge current through the metal, and to detect effects unique to spin current transmission.*

Recent Progress

The initial stages of the program are building up each of these capabilities, and at the same time developing a new method to image magnetic nanostructures with conductive atomic force microscopy (C-AFM). Here Pt is used as the metal base layer for charge current injection. A thin film stack that can support either a labyrinth of domain walls or skyrmions, depending on the applied magnetic field, is deposited on the Pt. The layer structure is Si wafer/Ta(3)/Pt(0.5)/$[Co(0.2)/Ni(0.6)]_X$/Pt(1)/Ni(0.48), where the numbers in parentheses indicate the thicknesses in nm, and the number of repeat units ranged between 10 and 20. The multilayer film is exposed to an oxygen plasma to transform the top Ni layer into NiO without reacting with any of the layers below to generate a NiO cap. By varying the amount of Ni in the top layer, the NiO thickness was varied between 0.8 and 2.0 nm. This method yields smooth (~1 nm roughness) polycrystalline NiO films, as determined by scanning probe images of the normal force.

C-AFM was used for 0.8 nm thickness NiO films to probe the electronic uniformity as a function of bias voltage, and to identify the tunneling regime. The I-V response of the Pt-coated tip was measured with in direct contact with a Pt film to verify Ohmic behavior. Next the tip was scanned over the NiO/metal film, where the I-V curve showed tunneling through the NiO barrier. At low bias voltage, pinholes appear as high current pixels. At high bias, above the turn-on threshold, the current as a function of time showed random spikes, indicating undesirable trap-and-release transport through defects in the NiO. For thicknesses at or below 1.5 nm, there was measurable charge tunneling at biases below the turn-on threshold. This means that for future studies of pure magnon current transport through magnetic insulators, greater thicknesses will be necessary.

Using the existing NiO films as a tunnel barrier, a new type of magnetoresistive microscopy was demonstrated. Conductive atomic force microscopy (C-AFM) has previously been used with non-magnetic tips to characterize magnetic tunnel junctions [Bapna 2018]. Here the fixed layer of the tunnel

junction is the C-AFM tip. These tips were prepared by sputtering different thicknesses of Co followed by Pt on the standard conducting tips. The Co introduces a magnetic moment and the Pt on top prevents the Co from oxidizing, and also extends the life of the tip. Too much Pt, however, enables the current to shunt through the non-magnetic metal, and there would be no spin filtering effects. Measurements of the I-V curves with the tips in contact with a Pt film were used to confirm Ohmic behavior. The resulting tips were used both for magnetic force microscopy (MFM), done in non-contact mode, and contact mode conductive AFM of the same regions.

The initial goal is to demonstrate that magnetic C-AFM could reveal the same features as non-contact MFM. Because the origin of the signal from the two methods is different, the magnetic C-AFM tip and sample had to be modified. MFM detects the vertical magnetic fringe field near a sample. The magnitude of the signal depends on the on the force on the magnetic moment of the tip (determined by the relative amount of Co in its coating) due to the local magnetization of the sample, which is proportional to the fringe field it generates. In C-AFM with a magnetic tip, the magnitude of the signal depends on the relative orientation of the tip and sample magnetization, as well as the thickness and band gap of the tunnel barrier. Here the tunnel barrier serves two purposes. First it increases the magnitude of the magnetoresistance signal, relative to that of giant magnetoresistance obtained with an all metal stack. Second, since tunneling is exponentially sensitive to the barrier thickness, the contact area of the tip determines the lateral spatial resolution.

If the sample coercivity (H_c) is low and the magnetic moment of the tip is high, the field of the tip penetrating across the NiO tunnel barrier will be sufficient to reverse the film magnetization. In this case the tip and sample will always have parallel magnetization and no contrast within an image will be observed. Figure 1 illustrates results obtained with a 20 repeat unit stack and a [Co(10)/Pt(4)] tip. Labryinth-like domain walls and dot-like skyrmions are visible due to the spin texture in the metallic stack. The magnetic C-AFM tip was scanned over a 1 μm x 1 μm region with a 1 V bias and ~ 1 nA tunnel current, and most of the domain walls in the region were erased, though the skyrmions remained stable (Fig. 1(a)). After C-AFM scanning in a different region (Figure 1(b)), similar behavior was observed. However, a pulsed magnetic field was sufficient to refresh the sample and to regenerate domain walls in the "erased" regions (Fig. 1(c)).

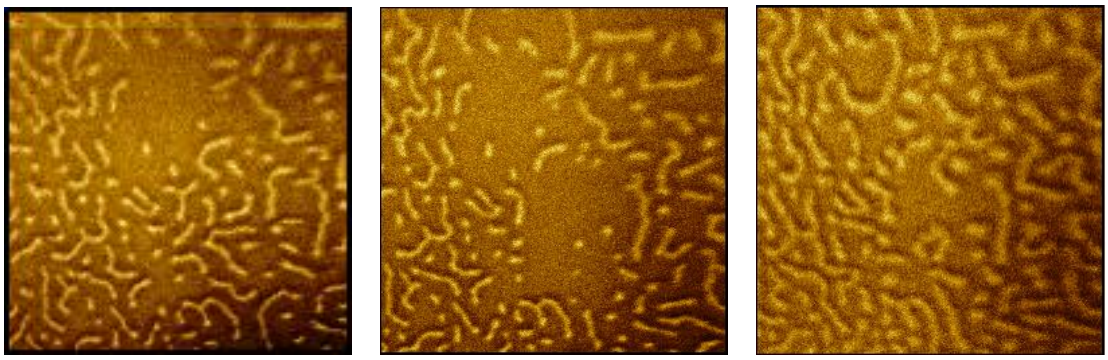

(a) (b) (c)

Fig. 1. (a) 3 μm x 3 μm MFM image recorded in non-contact mode with a +500 Oe vertical field, showing a mixture of labyrinth-like domains and dot-like skyrmions, except in a square region in the top center that was previously scanned by C-AFM. (b) The same region after C-AFM scanning of a second square region in the lower center. Note that the C-AFM scan under these conditions erases the domain walls but not the skyrmions. (c) MFM image after cycling the sample with a -1300 Oe field and returning to the initial conditions.

Future Plans

This work will proceed in two directions in parallel: 1) one taking advantage of the new microscopy technique to demonstrate magnetoresistive reading and spin transfer torque writing of individual skyrmions, and 2) the other focusing on injection and transmission of magnon currents in magnetic insulators.

While it is natural to consider magnetoresistive reading and writing of skyrmions [Fert 2013], so far this has only been achieved using spin polarized scanning tunneling microscopy at low temperature [Romming 2013]. Skyrmions have been successfully imaged in multilayer stacks at room temperature using scanning x-ray transmission microscopy [Woo 2017]. There have been valiant efforts to detect skyrmions using the Hall effect, but those signals are extremely weak [Macciarello 2018]. With the new magnetic C-AFM technique, single skyrmions can be detected with a greater signal-to-noise ratio, and by fabricating channels in the samples, spin transfer torque from a charge current can guide the skyrmion motion. Plans here are first to measure the time-dependent tunnel current as a skyrmion travels underneath the magnetic C-AFM tip, which should show a distinctive signal --- two dips in the magnetoresistance around a peak associated with the skyrmion core. The small dimensions of the tip contact make it feasible to detect such nanoscale (10 nm) variations. To write or erase a skyrmion, the resistance in series with the tip will be reduced and a large tunnel current pulse will be passed through the barrier. The current magnitude will be varied, and afterward the region will be imaged to determine if a skyrmion was created or destroyed. If successful, this would be the first demonstration of magnetoresistive reading and writing of skyrmions.

For the magnon current project, the methodologies developed will be applied to a simpler structure, with only the magnetic insulator film on top of the Pt and no skyrmionic stack. Nanofabrication will be used to form channels in the Pt topped by MI nanopillars, with leads at either end so that a current pulse can be sent through the Pt. Here the interest will be in the magnon current generated by the spin Hall effect in the Pt. A Pt-coated (non-magnetic) C-AFM tip in series with a variable resistor will be used to detect current through the MI. At small thicknesses, as determined in the recent results, direct tunneling is possible. At larger thicknesses transmission occurs only if the charge current through the Pt channel is transformed into a magnon current, the magnon current diffuses through the MI, and it is reconverted into a charge current through the inverse spin Hall effect [Li 2016], [Wesenberg 2017]. Initial experiments will use lock-in techniques to look for enhancement of the tunnel current as a charge current pulse through the Pt passes under a nanopillar. This will enable larger signals, but also checks on the current direction and magnetic field dependence [Lin 2017], which should be difference from those for ordinary tunneling. As the technique is extended to thicker samples, the tunneling contribution should disappear, and the detected signal should provide evidence of the magnon current injection efficiency and diffusion length. With the thicker films a greater degree of antiferromagnetic order in NiO films is expected, and magnetic gating efficiency can be measured.

References

[Bapna 2018] M. Bapna, B. Parks, S. D. Oberdick, S. A. Majetich, H. Almasi, and W.Wang, “Spin Orbit Torque Switching in 20 nm Perpendicular Magnetic Tunnel Junctions”, Phys. Rev. Applied **10**, 024013 (2018).

[Fert 2013] A. Fert, V. Cros, J. Sampaio, “Skyrmions on the track”, Nat. Nanotech. 8 152 (2013).

[Li 2016] J. Li, Y. Xu, M. Aldosary, C. Tang, Z. Lin, S. Zhang, R. Lake, and J. Shi, “Observation of magnon-mediated current drag in Pt/yttrium iron garnet/Pt (Ta) trilayers”, Nat. Commun. **7** 10858 (2016).

[Lin 2017] W. Lin and C. L. Chien, “Electrical Detection of Spin Backflow from an Antiferromagnetic Insulator/$Y_3Fe_5O_{12}$ Interface”, Phys. Rev. Lett. B **118,** 067202 (2017).

[Macciariello 2018] D. Macciarello, W. Legrand, N. Reyren, K. Garcia, K. Bouzehouane, S. Collin, V. Cros, A. Fert, “Electrical detection of single magnetic skyrmions in metallic multilayers at room temperature”, Nat. Nanotech. **13**, 233 (2018).

[Romming 2013] N. Romming, C. Hanneken, M. Menzel, J. E. Bickel, B. Wolter, K. von Bergmann, A. Kubetztka, R. Wiesendanger, “Writing and Deleting Single Magnetic Skyrmions”, Science **341**, 636 (2013).

[Wesenberg 2017] D. Wesenberg, T. Liu, D. Balzar, M. Wu, and B. L. Zink, “Long-distance spin transport in a disordered magnetic insulator”, Nat. Phys. **13**, 987 (2017).

[Woo 2017] S. Woo S, K. M. Song, H. S. Han, M. S. Jung, M. Y. Im, K. S. Lee, K. S. Song, P. Fischer, J.-I. Hong, J. W. Choi, B.-C.Min, H. C. Koo, J. Chang, “Spin-orbit torque-driven skyrmion dynamics revealed by time-resolved X-ray microscopy”, Nat. Commun. **8**, 15573 (2017).

Publications

(None yet)

Energy and Photon Conversion with Nanocrystals and Optically Active Media

(Project # DE-SC0010697)

PIs: Anton Malko, Yves Chabal, and Yuri Gartstein (The University of Texas at Dallas)

Program Scope

Photon management and exciton conversion represent transformative opportunities for improved operational and functional performances, providing the fields of optoelectronics, nanophotonics and energy materials with new functionalities. This project explores the underlying scientific questions for such opportunities arising in hybrid nanostructures comprised of different materials components that are coupled *via* near-field electromagnetic interactions mediating radiative and nonradiative energy transfer (ET) [1,2]. We specifically focus on structures that would contain hierarchically ordered nanocrystal (NC) solids and various semiconductors such as crystalline Si, 2D transition metal dichalcogenides (TMDs) and lead halide perovskites (LHPs). We explore applications of different nanocrystal quantum dots (NQDs): from well-known smaller-size CdSe/ZnS dots to novel "giant" dots (gNQDs) and LHP NCs [3].

Recent Progress

Development of advanced colloidal semiconductor nanocrystals [4-6]. In collaboration with Dr. Hollingsworth at LANL, PbSe/CdSe/CdSe and PbS/CdS/CdS core/shell gNQDs have been prepared using a modified SILAR approach resulting in improved photostability with PL emission in the range of 1-1.2 μm and 1.2-1.5 μm, respectively. Growth of stable and (largely) non-blinking PbSe- and PbS-core nanocrystals has been achieved with the initial application of the low-temperature cation exchange technique to grow first 1-2 monolayer of CdSe (or CdS) shells followed by the traditional SILAR to complete the thick shell growth of gNQDs. We further demonstrated that crystal structure (cubic zinc-blende or hexagonal wurtzite), the particle shape (cubic, spherical or tetrapodal) and the emission

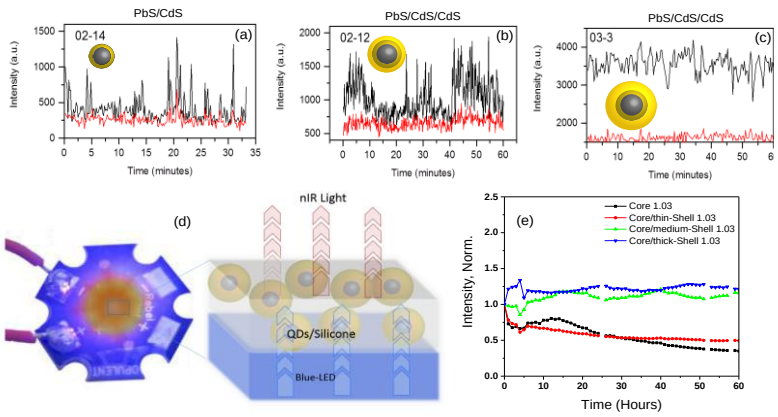

Figure 1: (a-c) Single particle intensity trajectories (blinking traces) for thin, medium and thick shell PbS/CdS nanocrystals respectively. (d) Top view and schematics of the fluorescence downconversion device that employs PbS/CdS/CdS near-IR emitting dots dispersed in a silicone matrix and pumped by blue light emitting diode (e) Near-infrared light emission stability study for downconversion devices with gNQDs of different shell thicknesses.

properties can be tuned by manipulation of the coordinating ligand (TOPO) during the SILAR component of the growth. PbSe/CdSe and PbS/CdS NIR-emitting gNQDs have been studied at the single particle level (blinking traces, attesting to much improved QY and photostability) and have been employed in light down-conversion device schemes with enhanced light output, **Figure 1 (a-e)**. Furthermore, several unique synthesis approaches have been also used to prepare CdSe/CdS core/arm tetrapods and core/shell nanocrystals with enhanced multiexciton properties and demonstrated efficient ET to Si substrates.

Integration of 2D semiconductors and their patterns into photonic structures [7,8]. Our computational studies showed that more involved photonic structures (waveguiding and microcavity configurations) could take advantage of the strong optical responses of 2D semiconductors like TMDs for prospective applications in optoelectronics and photonics. The high in-plane polarizability of 2D layers integrated into the planar waveguide can substantially alter the dispersion of waveguided modes and also results in the appearance of new polaritonic states spatially confined to TMD layers. In addition, the absorption of the light waveguided along the 2D layers could be exploited in 3D structures for light harvesting applications. Conceptually new opportunities also arise to utilize the high polarizability of TMD materials in the dissipation-free spectral region below their optical gaps. This is achieved via integration of *patterned* 2D semiconductors in optical microcavities. While the cavity confines fields to its interior, the high polarizability of 2D materials leads to new cavity modes that are bound to the patterned pieces. A TMD strip can guide such bound cavity photons, while a pair of neighboring strips behaves similar to a photonic waveguide coupler (**Figure 2**). Optical properties of the 2D semiconductors can be strongly modulated *via* light absorption indicating an opportunity for an all-optical control of bound modes. Our analysis thus suggests that embedding patterned 2D TMDs within microcavities can be an attractive prospect for engineering photonic cavity modes and for realization of integrated photonics functionalities on a very different material platform.

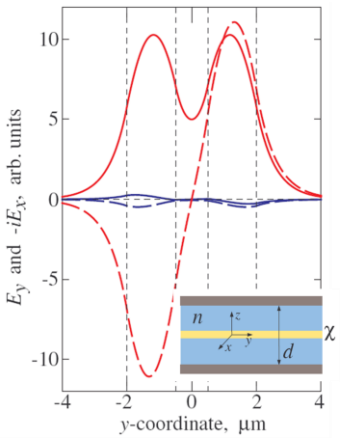

Figure 2: Spatial profiles of the electric field components in bound cavity modes. Red lines are for the E_y component, blue for E_x. Waves with the wave vector k_x=2 μm^{-1} are running along a pair of strips, each of width w=1.5 μm, separated by distance of 1 μm, strips' edges are shown by vertical dashed lines. Solid lines show symmetric and dashed antisymmetric modes of the predominant field polarization. The inset is a schematics of the microcavity geometry, the numerical **e**xample is for d=270 nm, index n=1.5 and χ=10 nm.

Versatile atomic layer deposition of metal oxides to preserve and improve emissive properties of NQD assemblies [9]. To fabricate functional NQD solids, it is vitally important to be able to protect NQDs from the environment and retain their high PL yields in assemblies. We explored chemical, optical and structural changes which occur during the atomic layer deposition (ALD) of aluminum oxide (Al_2O_3) on CdSe/ZnS NQD monolayer films and showed that the process is accompanied

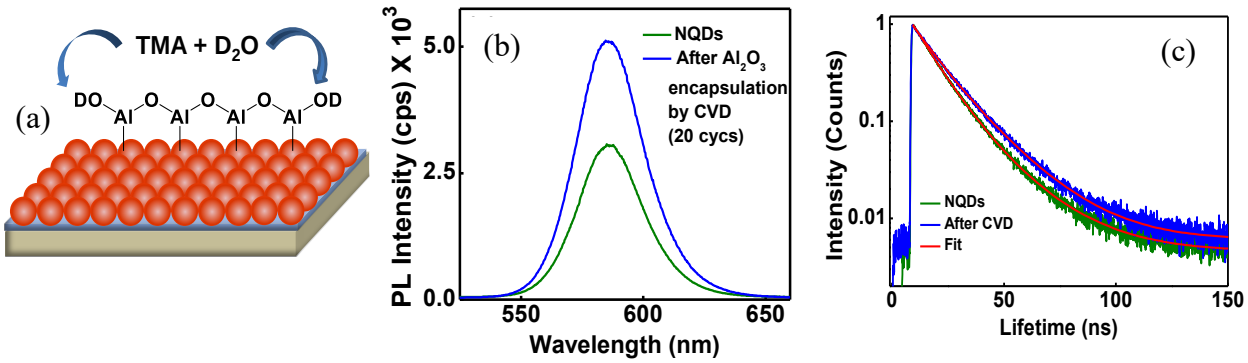

Figure 3: (a) Schematics of the room temperature CVD-like process. (b, c) PL intensity and lifetime enhancement of CdSe/ZnS NQDs before (green) and after (blue) CVD encapsulation.

by reorganization of ligands and replacement of Zn atoms by Al. This deterioration explains the observed NQD PL quenching (both intensity and lifetime). To avoid these detrimental effects, we developed a pulsed co-deposition of both metal and oxidant precursors at room temperature (thus resembling chemical vapor deposition (CVD) method), wherein Al_2O_3 forming reactions take place in the gas phase in the vicinity of the NQD layer at pressures compatible with long diffusion mean free paths (~10 cm). The FTIR and XPS spectra of the resulting oxide-covered assemblies derived by this CVD-like gas phase process reveal much smaller changes in ligand coordination and negligible Al to Zn replacement (~2% change), while TEM images and elemental mapping of encapsulated NQD thin films confirm conformal overcoating by alumina (AlO_x) of the surface of the NQDs, with thicknesses of the oxide layer that can be varied from 3-7 nm. We employed this technique to prepare overcoated NQD/Alumina structures and demonstrated that NQD PL emission intensity and lifetimes are not only preserved but may even be enhanced, **Figure 3 (b, c)**. The films encapsulated this way can thus constitute a basis for the development of well-defined hierarchical multilayer structures through consecutive assembly and encapsulation steps that can be utilized for optoelectronic applications. Moreover, this new deposition method appears to be applicable with other types of NCs for encapsulation that does not worsen their optical properties.

Photon recycling and studies of photophysics in perovskite materials [10]. In collaboration with Prof. Mohammed at KAUST, we have been exploring optical and electronic properties of novel LHPs known for their potential optoelectronic applications. One line of our inquiry concerned an important and debated question of photon recycling in LHPs, which we were able to directly probe taking advantage of the microwire-waveguide geometry of synthesized samples, in particular of

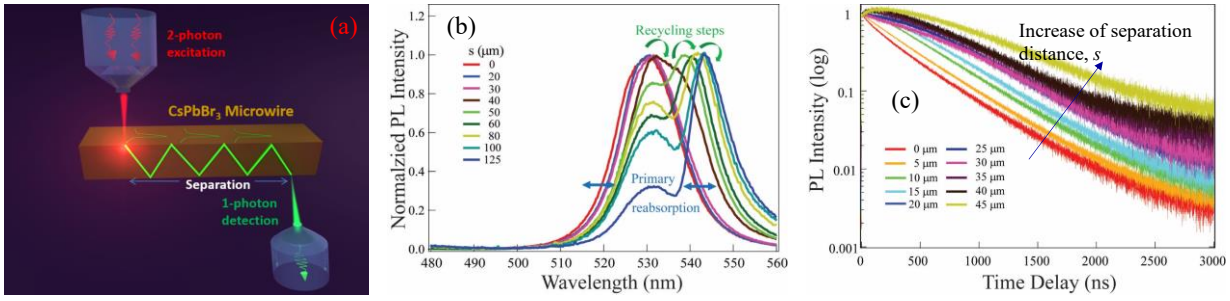

Figure 4: (a) Schematics of photon recycling experiment (b) Normalized PL spectra as function of separation *s*. (c) Normalized PL dynamics of the $CsPbBr_3$ perovskite microwires as function of separation between excitation and collection positions *s*. Consecutive appearance of emission rise times is a signature of photon recycling.

$CsPbBr_3$ material. We performed a detailed time- and spectrally-resolved study of waveguide-assisted photon re-absorption/re-emission in such microwires by tracking the evolution of PL signals as a function of the lateral separation between excitation and collection spots (**Figure 4**). The delayed PL was observed at distances exceeding 100 μm and exhibiting characteristic distance-dependent rise time patterns in PL kinetics, while charge carrier diffusion length was measured just at fractions of μm. The experimental data was rationalized within a modeling framework accounting for recombination and emission processes as well as waveguide-assisted re-absorption. Analysis of the data indicates that intrinsic radiative efficiency of elementary recombination events in $CsPbBr_3$ microwires is close to unity, rendering them useful for light-emitting applications. The observed spectral re-distribution of the PL signal towards lower energy (**Figure 4 (b)**) is consistent with repetitive photon recycling steps taking place under inhomogeneous broadening. The importance of photon reabsorption for long-range spatial propagation of photoexcitations in LHPs has been further confirmed by observing and quantifying the rise time patterns in microwires made of a very different perovskite, $MA(en)PbBr_4$, with 2D internal compositional dimensionality.

Future Plans

The progress described above enables us to make inroads towards building more involved hybrid and photonic structures that could take advantage of enhanced near-field interactions in waveguiding and microcavity configurations with the longer-term goal of achieving effective control of light-matter coupling in such systems. These structures will be utilizing combinations of various nanomaterials of different dimensionalities. Among them, we plan to explore new classes of LHP NCs that have been recently synthesized as well as the preservation/enhancement of their optical properties, individually and in assemblies, as needed for practical optoelectronic and photonic applications. These studies will include extensions to low temperatures as well as to electrical measurements.

References

[1] Agranovich, V. M.; Gartstein, Y. N.; Litinskaya, M. *Chem. Rev.* **2011**, 111, 5179.
[2] Peng, W.; Rupich, S. M.; Shafiq, N.; et al. *Chem. Rev.* **2015**, 115, 12764.
[3] Akkerman, Q. A.; Rainò, G.; Kovalenko, M. V.; Manna, L.V. *Nat. Mater.* **2018**, 17, 394.
[4] Hanson, C. J.; Hartmann, N. F.; Singh, A.; et al. *J. Am. Chem. Soc.* **2017**, 139, 11081.
[5] Mishra, C. N.; Orfield, N. J.; Wang, F.; et al. *Nat. Commun.* **2017**, 8, 15083.
[6] Krishnamurthy, S.; Hu, Z.; Singh, A.; et al. **2019** (submitted).
[7] Gartstein, Y. N.; Malko, A. V. *Optics Express* **2017**, 25, 23128.
[8] Gartstein, Y. N.; Malko, A. V. *Optics Express* **2018**, 26, 20823.
[9] Bose, R.; Dangerfield, A.; Rupich, S. M.; et al. *ACS Appl. Nano Mater.* **2018**, 1, 6782.
[10] Dursun, I.; Zheng, Y.; Guo, T.; et al. *ACS Energy Lett.* **2018**, 3, 1492.

All project publications within past 2 years (2017-2019)

1. T. Guo, S. Sampat, K. Zhang, J. A. Robinson, S. M. Rupich, Y. J. Chabal, Y. N. Gartstein, and A. V. Malko, "*Order of magnitude enhancement of monolayer MoS_2 photoluminescence due to near-field energy influx from nanocrystal films", **Sci. Rep**.* 7, 41967 (2017); **doi**: 10.1038/srep41967.
2. C. N. Mishra, N. J. Orfield, F. Wang, Z. Hu, S. Krishnamurthy, A. V. Malko, J. L. Casson, H. Htoon, M. Sykora, J. A. Hollingsworth, "*Using shape to turn off blinking for two-colour multiexciton emission in CdSe/CdS tetrapods*", ***Nat. Commun.* 8**, 15083 (2017); **doi**: 10.1038/ncomms15083
3. C. J. Hanson, N. F. Hartmann, A. Singh, X. Ma, W. J. I. DeBenedetti, J. L. Casson, J. K. Grey, Y. J. Chabal, A. V. Malko, M. Sykora, A. Piryatinksi, H. Htoon, and J. A. Hollingsworth, "*Giant PbSe/CdSe/CdSe Quantum Dots: Crystal Structure-limited Ultrastable Near-infrared Photoluminescence from Single Nanocrystals*", ***J. Am. Chem. Soc.* 139** (32), 11081–11088 (2017); **doi**: 10.1021/jacs.7b03705
4. T. Guo, S. Sampat, S. M. Rupich, J. A. Hollingsworth, M. Buck, H. Htoon, Y. J. Chabal, Yu. N. Gartstein, and A. V. Malko, "*Biexciton and Trion Energy Transfer from CdSe/CdS Giant Nanocrystals to Si Substrates*", ***Nanoscale* 9**, 19398 – 19407 (2017); **doi**: 10.1039/C7NR06272A
5. Y. N. Gartstein and A. V. Malko, "*Propagation and absorption of light in planar dielectric waveguides with two-dimensional semiconduc*tors", ***Optics Express* 25** (19), 23128-23136 (2017); **doi**: 10.1364/OE.25.023128
6. I. Dursun, Y. Zheng, T. Guo, M. de Bastiani, B. Turedi, L. Sinatra, Md. A. Haque, B. Sun, A. A. Zhumekenov, M. Saidaminov, G. de Arquer, F. Pelayo, E. Sargent, T. Wu, Y. N. Gartstein, O. M. Bakr, O. F. Mohammed and A. V. Malko, "*Efficient photon recycling and radiation trapping in cesium lead halide perovskite waveguides*", ***ACS Energy Letters* 3**, 1492-1498 (2018); **doi**:10.1021/acsenergylett.8b00758
7. Y. N. Gartstein and A. V. Malko, "*Guiding and binding of cavity photons with patterned two-dimensional semiconductors*", ***Optics Express* 26** (16), 20823-20834 (2018); **doi**: 10.1364/OE.26.020823
8. H. T. Yi, P. Irkhin, P. P. Joshi, Y. N. Gartstein, X. Zhu and V. Podzorov, "*Experimental demonstration of correlated flux scaling in photoconductivity and photoluminescence of lead-halide perovskites*", ***Phys. Rev. Applied* 10**, 054016 (2018).
9. R. Bose, A. Dangerfield, S. M. Rupich, T. Guo, Y. Zheng, S. Kwoon, M. J. Kim, Y. N. Gartstein, A. Esteve, Y. J. Chabal and A. V. Malko, "*Engineering Multilayered Nanocrystal Solids with Enhanced Optical Properties Using Metal Oxides for Photonic Applications*", ***ACS Appl. Nano Mater.* 1**, 6782−6789 (2018); **doi**: 10.1021/acsanm.8b01577
10. H. T. Yi, S. Rangan, B. Tang, C. D. Frisbie, R. A. Bartynski, Y. N. Gartstein and V. Podzorov, "*Electric-field effect on photoluminescence of lead-halide perovskites*", **Materials Today** (2019); **doi**:10.1016/j.mattod.2019.01.003

11. Y. Zhang, L. Liu, T. Guo, J. Yin, Y. Han, O. M. Bakr, O. F. Mohammed and A. V. Malko, "*Emergence of Multiple Fluorophores in Individual Cesium Lead Bromide Nanocrystals*", ***Nature Comm***. (submitted).
12. S. Krishnamurthy, Z. Hu, A. Singh, A. E. King, M. Sykora, A. Piryatinski, J. L. Casson, D. J. Williams, H. Htoon, A. V. Malko and J. A. Hollingsworth, "*Engineering blinking and device performance of shelled quantum dots at telecom wavelengths*", (submitted).

Interfaces in Electronic and Structural Materials

Yuri Mishin, PI

Department of Physics and Astronomy
George Mason University, MSN 3F3
4400 University Drive, Fairfax, VA

Phone: 703-993-3984
Fax: 703-993-1269
Email: ymishin@gmu.edu

Program Scope

The Program pursues the following goals: (1) Conduct a systematic atomistic-scale simulation study of a large set of grain boundaries in Si, Ge, Si-Ge alloys and other functional materials. (2) Determine the equilibrium structures of the boundaries as a function of their bicrystallography, temperature and chemical composition. (3) Identify a set of grain boundary phases, investigate their reversible phase transformations, and construct grain boundary phase diagrams. (4) Calculate the Kapitza resistance of the grain boundaries and establish relationships between the Kapitza resistance and the grain boundary crystallographic characteristics, atomic structure, temperature and chemical composition. (5) Develop a fundamental understanding of phonon scattering at Si, Ge and Si-Ge grain boundaries.

These goals will be achieved by atomistic computer simulations using molecular dynamics and a variety of Monte Carlo techniques. The Kapitza resistance of the grain boundaries will be calculated by non-equilibrium molecular dynamics, combined in some cases with the wave-packet method. To ensure the accuracy of the predictions, a new machine-learning (neural-network) interatomic potential will be constructed for the Si-Ge system by training the potential parameters on a massive database of first-principles energies. The project is expected to make a significant impact on the state of knowledge in interface science by improving the fundamental understanding of structure and thermal resistance of grain boundaries in semiconductor materials. It is relevant to the BES mission and is aligned with DOE's Grand Challenge of controlling matter away from equilibrium and the Basic Research Needs for solar energy utilization and electrical energy storage.

Recent Progress

1. In addition to addressing specifically Si, we found it important to finish the work on the bismuth telluride Bi_2Te_3 alloys that was started during the previous funding period, since this work is also related to internal interfaces in thermoelectric materials. Tetradymite-structured chalcogenides, such as Bi_2Te_3, present significant interest as technological materials for thermoelectric energy conversion and as examples of topological insulators. Dislocations in such materials play a critical role during synthesis and processing and can strongly affect functional properties. For example, recent work has suggested that dislocations present at low angle grain boundaries in Bi_2Te_3-based alloys effectively scatter phonons in the mid-frequency range, providing a grain-boundary design strategy for engineering new materials with improved thermoelectric energy conversion efficiency. Scanning tunneling microscopy measurements have demonstrated shifts in the energy of the Dirac state, which were attributed to the large strain fields near the individual dislocation cores. The dislocations existing between the quintuple layers present special interest as their core structure is controlled by the van der Waals interactions between the layers. Although the discovery of such dislocations by electron microscopy in the early 1960s was one of the first direct observations of dislocations in non-metallic materials, their atomic-level core structure has remained elusive for decades. We have finally resolved the basal dislocation core structure in Bi_2Te_3 and quantified the disregistry of the atomic planes by atomic-resolution electron microscopy (Figure 1). We have shown that, in spite of the existence of a

stable stacking fault, the dislocation core spreading is not caused by dissociation into two discrete partials as one would expect. Instead, the wide spreading of the core is mainly due to the weak bonding between the layers, leading to the relatively small energy penalty for layer sliding parallel to the van der Waals gap. The experimental findings are supported by calculations within a semidiscrete variational Peierls-Nabarro model informed by first-principles calculations, showing excellent agreement with experiment (Figure 2). The methodology and conclusions of this work can be extended to other quasi-2D materials with van der Waals bonding between layers.

2. A new machine-learning (ML) interatomic potential has been constructed for Si using the recently proposed Physically-Informed Neural Network (PINN) format. PINN is a new approach that can drastically improve the transferability of ML potentials by informing them of the physical nature of interatomic bonding. This is achieved by combining a rather general physics-based model, namely, an analytical bond-order potential (BOP), with a neural-network regression. The network adjusts the BOP parameters on the fly during the simulations according to the local environments of individual atoms. This approach has recently been demonstrated by developing a general-purpose PINN potential for Al (https://arxiv.org/abs/1808.01696).

For training the potential parameters, a massive database of DFT energies has been generated. The supercells represent over a dozen crystal structures of Si, point defects such as vacancies and interstitials, surfaces with different crystallographic orientations, gamma-surfaces representing generalized stacking faults, a set of clusters containing from two atoms (dimer) to about a hundred atoms, and single-layer and double-layer 2D structures (silicenes). Each supercell was included for a large set of volumes and various shape distortions. For most of the supercells, ab initio MD simulations were run at different temperatures and densities and multiple snapshots were included in the training database. In total, the DFT database represent over 150,000 different atomic environments. The neural network parameters were optimized to achieve the root-mean-square deviation from the DFT data of about 3 meV/atom, which is essentially the DFT accuracy. The new potential has been tested against additional DFT data that was not included in the training set. The potential accurately reproduces a wide range of physical properties at the DFT level, including the phonon spectrum, thermal expansion, defect formation energies, 2D structures, clusters and many others. We currently finishing to test the new potential for more properties before applying it for the grain boundary simulations as planned in this project.

3. Thermal resistance of GBs can affect heat removal in electronic devices and performance of thermoelectric materials. The Kapitza resistance of a series of [001] tilt GBs in Si has been studied using the new potential and the non-equilibrium MD method. The Kapitza conductance $\square_K$ was found to decrease with the misorientation angle and slightly increase with temperature. For high-angle GBs, $\square_K$ is much lower than the bulk conductivity at low temperatures but the two tend to converge at high temperatures. An interesting effect was found wherein $\square_K$ suddenly decreases when the GB dislocations become disordered due to premelting (Fig.3). Structural phase transformations in GBs have a significant effect on their thermal conductivity. One of the fundamental issues in nano-scale thermal conductivity is the definition, or even existence, of the local temperature. This issue has been addressed in two publication under this project.

Future Plans

(1) To further improve the reliability of the atomistic simulations, a hybrid machine-learning interatomic potential will be developed for Si and the Si-Ge system using the neural network approach.

(2) The new potential will be applied to study the thermal resistance of interfaces in Si, Ge, and Si-Ge alloys. The interfaces will include individual GBs and heterostructures composed of parallel GBs or alternating Si-Ge layers. The goal will be to establish relations between the phonon scattering and their atomic structure of the interfaces, the feature size (e.g. layer spacing), chemical composition, temperature and other factors.

Publications of DOE sponsored research (past 2 years)

1. G. P. Purja Pun and Y. Mishin: Optimized interatomic potential for silicon and its application to thermal stability of silicene, *Physical Review* B, **95** (22), 224103 (2017).
2. J. Hickman and Y. Mishin: Extra variable in grain boundary description, *Physical Review Materials* **1**, 010601 (2017).
3. D. L. Medlin, N. Yang, C. D. Spataru, L. M. Hale and Y. Mishin: Unraveling the dislocation core structure at a van der Waals gap: Bismuth telluride as a prototype, *Nature Communications*, in review (2018) (preprint **arXiv:1902.09363**)
4. J. Hickman and Y. Mishin: Thermal resistance of tilt grain boundaries in silicon, *Physical Review Materials*, in review (2018).
5. J. Hickman, G. P. Purja Pun, V. Yamakov and Y. Mishin: Physically-informed artificial neural network potential for silicon, npj Computational Materials, in preparation.

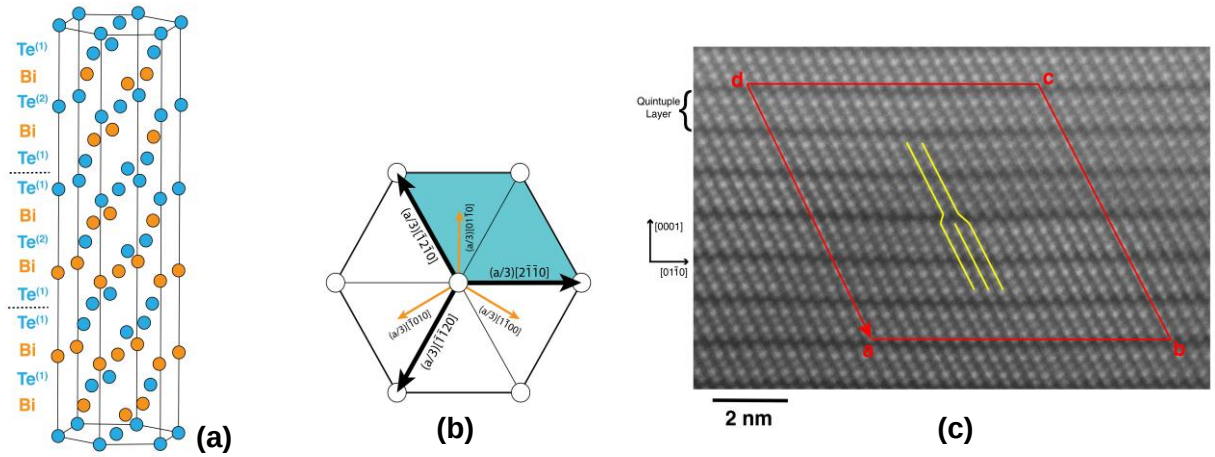

Figure 1: **(a)** Atomic arrangements in Bi_2Te_3. The space between the Te(1)-Te(1) planes is the van der Waals gap. **(b)** Projection of the structure on the basal plane showing the Burgers vectors of dislocations. The unit cell is shaded in blue. The heavy black arrows show the Burgers vectors for the 1/3 <2110> type perfect lattice dislocations, whereas the smaller orange arrows show the (1/3)<1010> type Burgers vectors that would result if Shockley partial dislocations were to form. **(c)** HRTEM image of Bi_2Te_3 projected along the <2110> direction, showing the quintuple layers and the Burgers circuit construction for calculation of the dislocation Burgers vector. The basal planes are horizontal and the yellow lines trace {1015} crystal planes one of which terminates at the dislocation core.

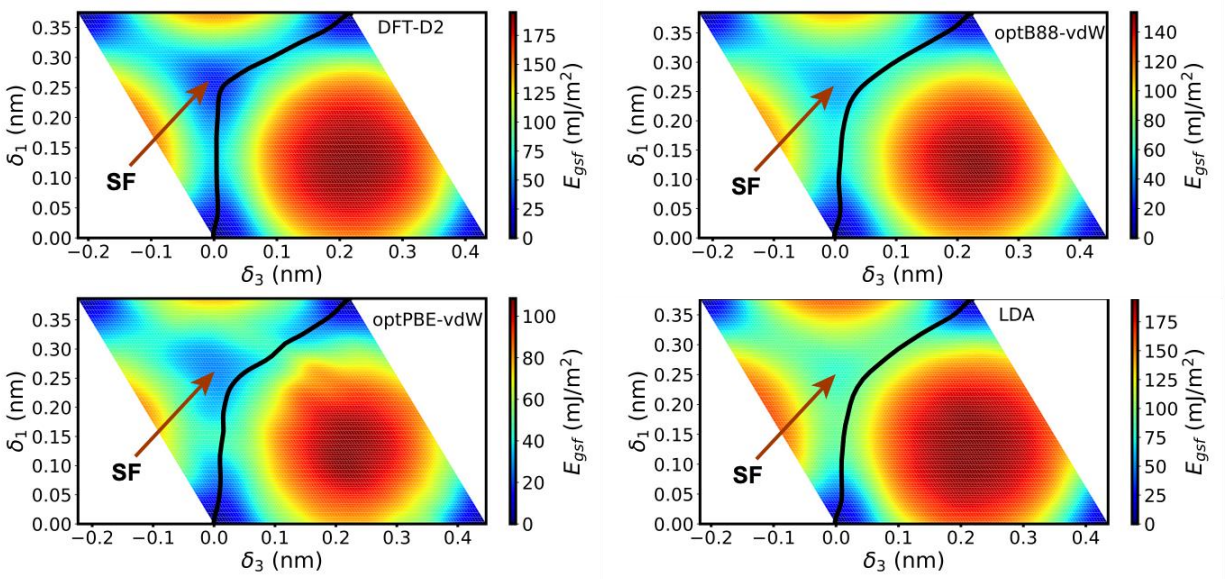

Figure 2: Gamma-surfaces computed with different DFT functionals. The generalized stacking fault energy is only shown within a repeat unit parallel to the basal plane. The stable stacking fault position (local minimum on the gamma-surface) is indicated. The black line shows the disregistry path within the dislocation core region predicted by the semidiscrete Peierls-Nabarro model using the respective gamma-surface.

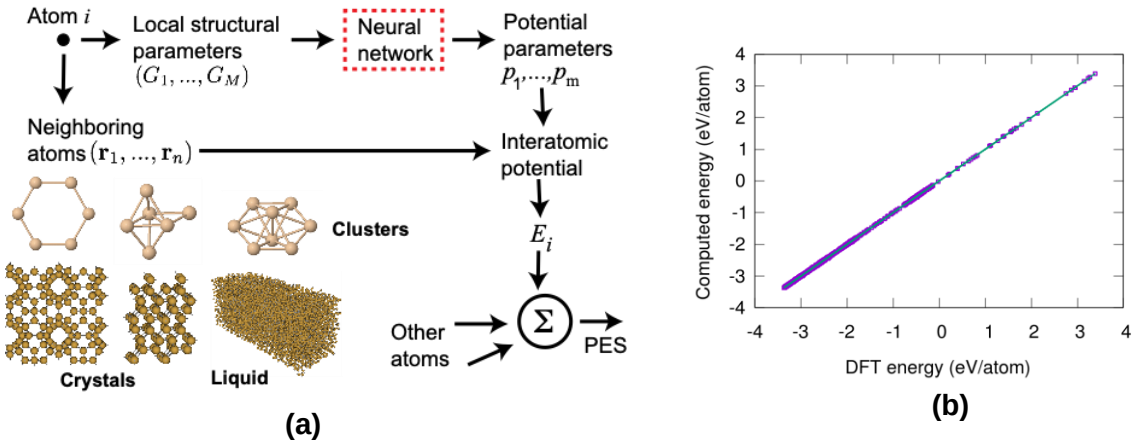

Figure 3: **(a)** Conceptual diagram of the PINN method. Descriptors (G_1,…,G_M) of the local environment of every atom *i* are fed into an artificial neural network, which generate the set of interatomic potential (BOP) parameters p_1,…,p_m. These parameters are used to predict the energy of atom *i* within the local BOP model. The neural network is trained using a large set of DFT energies for multiple crystal structures, liquid, 2D structures, clusters and other atomic configurations. The combination of the physics-based BOP model with neural-network regression ensures DFT-level accuracy of the fit combined with drastically improved transferability to unknown environments. **(b)** Energies of atomic configurations of Si predicted by the new Si PINN potential in comparison with DFT calculations. The straight line represents the perfect fit.

Phase Transitions in Mesoscopic Systems

P.I. Raymond L. Orbach
(The University of Texas at Austin)

Co-P.I. Gregory G. Kenning
(Indiana University of Pennsylvania)

Co-P.I. E. Dan Dahlberg
(University of Minnesota)

Program Scope

Our research focuses on the dynamical properties of glassy systems constrained to the mesoscale. Included are the consequences of the lower critical dimension on spin glass dynamics between two and three dimensions; the observation and analysis of temperature chaos in spin glasses; the magnitude of the correlation length in glassy systems and its time dependence; the impact of approaching the transition temperature on spin glass correlations; the relationship between the onset of 1/f noise and the spin glass transition temperature; the effect of increased anisotropy on 1/f noise; and the effect of metallic or insulating boundary conditions on the coupling between magnetic moments in a metal and consequences for the spin glass transition temperature. Our studies at the mesoscale, combined with recent glass forming liquids correlation studies, will couple the dynamical properties of spin glasses and structural glasses.

The three laboratories involved in the program collaborate in a complementary manner. The group at The University of Texas at Austin provides theoretical guidance and SQUID magnetization measurements of spin glass dynamics over a large time scale; the Indiana University of Pennsylvania group utilizes an ultra-sensitive home-built SQUID magnetometer to measure properties in the vicinity of the spin glass transition temperature; and the University of Minnesota group grows the thin film multilayer structures and performs the 1/f noise electrical resistance measurements arising from spin glass fluctuations. A weekly Skype call coordinates the research programs of the three laboratories, and the publications reflect their close collaboration.

An additional feature of the program is the interaction with the Janus-II group in Spain and Italy. The use of a special-built computer for Ising-like spin glasses has progressed to the point where direct comparison is now possible between their simulations and our thin film experiments. The collaboration has proven so fruitful that our experimental program is developing protocols inspired by the simulations, whereas initially it was reversed: the simulations were working to mimic experiment. The beauty of this synergy will become apparent in future joint publications displaying the “two way street” of this collaboration.

Recent Progress

A unique aspect of our research is the use of spin glass electronic noise to probe the dynamics of spin glasses. The low frequency noise is independent of magnetic field history, and its presence in zero magnetic field allows dynamical studies not possible through any other measurement.

We record the sample voltage with an applied current as a function of time. This record provides the raw data for analyzing the noise. In the analysis one can either consider the entire time record or parse the data into time intervals to compare the noise signals or measure the evolution of 1/f noise as a function of time.

The Mn ions in Cu may be expected to be Heisenberg like but if this were true the spin glass transition temperature is predicted to be close to T = 0. We surmise this is not the case because of the weak anisotropy induced by the Dzyaloshinsky-Moriya interaction arising from the spin orbit coupling of the Mn itself, or high Z non-magnetic impurities co-doped into the spin glass. The same theoretical understanding predicts the glass transition to be Ising like, freezing out the longitudinal component of the Mn spins, and is consistent with magnetization studies. A transition at lower temperatures is predicted to freeze out the transverse components of the Mn spins. The difference in temperature between the longitudinal and transverse freezing temperatures is predicted to increase with increasing anisotropy. Given the long history of magnetization measurements that do not reveal the lower temperature transverse freezing, we explored the effect of an induced anisotropy in the 1/f noise. By co-doping CuMn spin glasses with Au that has a much larger spin orbit coupling than Mn, we have explored the onset temperature of the 1/f noise to determine if we can see the predicted effects for transverse freezing. Using unpatterned large area "witness samples" made at the same time as the noise samples, we are able to independently measure the freezing temperature and the 1/f onset temperature of the spin glass.

From the time record of the measured voltages we can generate the noise voltage spectrum $S_V(f)$. From the noise voltage $S_V(f)$, we can determine the "Hooge" parameter α_H through $S_V(f) = \alpha_H(V^2/N_A)(1/f^\gamma)$, where V is the voltage applied across the sample, N_A the number of atoms in the sample, and $0.8 < \gamma < 1.3$. Our measurements of α_H for the spin glasses CuMn, and CuMn doped with Au are exhibited in Fig. 1 below.

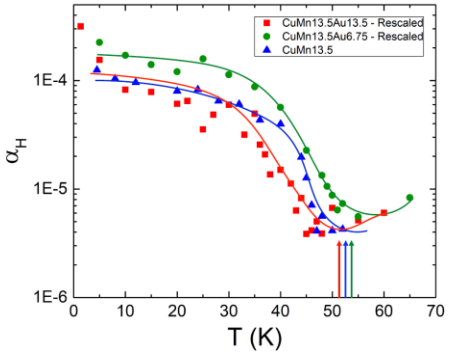

Fig. 1. A plot of the "Hooge" parameter for CuMn and CuMn doped with Au. The vertical arrows denote the onset temperature for the 1/f noise voltage.

Because of the witness sample, we can compare directly the onset temperature for the 1/f noise spectrum arising from spin glass magnetization fluctuations with the freezing temperature associated with the transition from paramagnetic to spin glass dynamics. We find that the onset temperature is, within our error bars, equal to the freezing temperature, even in the presence of increased anisotropy. Our results are exhibited below in Fig. 2.

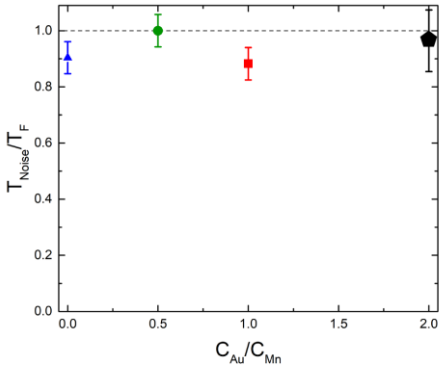

Fig. 2. The ratio of the 1/f noise onset temperature T_{noise} to the spin glass freezing temperature T_f as a function of the anisotropy expressed as the ratio of concentrations C_{Au}/C_{Mn}.

These results should be compared with the findings of Israeloff et al.[1] for pure CuMn, and are at odds with the theoretical predictions of the Sherrington group[2] for uniaxial anisotropy. It should be noted that the Dzyaloshinsky-Moriya anisotropy is unidirectional, accounting perhaps for the different behavior as compared to the predictions for uniaxial anisotropy.

Future Plans

Measurements of the low frequency noise will be used to investigate spin glass state dynamics when crossing from 3D to 2D as a function of time, t, and temperature, T, for various sample thicknesses. The spin glass coherence length is both time and temperature dependent. When, at a given temperature, the time-temperature dependent coherence length, $\xi(t,T)$, reaches the film thickness, $\mathscr{L}$, the sample crosses over to a 2D state, below the spin glass critical dimension $D_L = 2.5$. The sample now consists of a spin glass with correlated pancake-like shaped regions.[3] The film's finite thickness $\mathscr{L}$ results in a maximum barrier height Δ_{max} that varies as $\ell n\, \mathscr{L}$.

From our other studies[4] we know that 1/f noise can arise from collections of two level system oscillators, also known as random telegraph noise (RTN) oscillators. In a system exhibiting RTN, the $S_V(f)$ of the previous section is given by $S_V(f) = (\Delta V)^2(f_{RTN}/2\pi)[(2f_{RTN})^2 + f^2]^{-1}$ where $(\Delta V)^2$ is the noise magnitude and f_{RTN} is a characteristic noise frequency given by $f_{RTN} = f_A \exp(-\Delta/k_BT)$ where f_A is an "attempt frequency," approximately given by the exchange frequency $k_BT_g/\hbar$ where T_g is the bulk spin glass transition temperature.

This expression for $S_V(f)$ has a "knee" at f_{RTN} and is a direct measure of Δ *independent of magnetic field history* and *at zero magnetic field*. The expected frequency dependence of $S_V(f)$ is exhibited in Fig. 3 below for a thin film, and differs from the more conventional ($\mathscr{L}$ large) forms exhibited in Fig. 1.

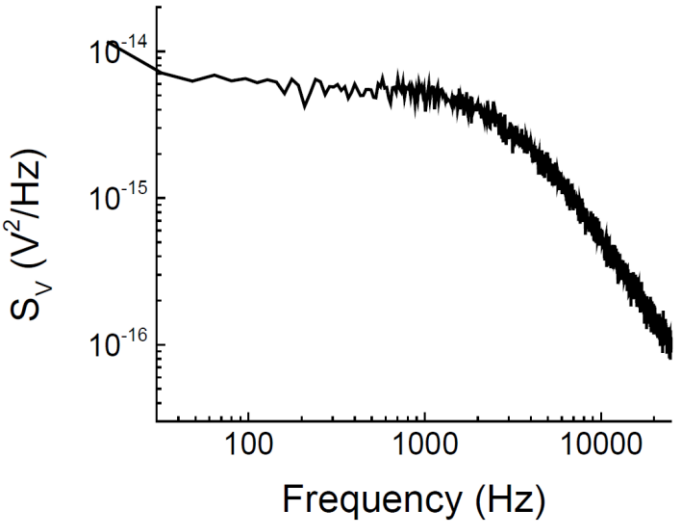

Fig. 3. The power spectral density for a single random telegraph noise (RTN) oscillator. The key feature is the transition to frequency independent noise below about 1000 Hz which is the approximate f_{RTN} for this data.

These experiments, exhibiting the frequency associated with Δ_{max} , will open up a powerful experimental technique for exploration of both temperature and magnetic field chaos, complementing our SQUID magnetization measurements.

References

1. N. E. Israeloff, M. B. Weissman, G. J. Nieuwenhuys, and J. Kosiorowska, Phys. Rev. Lett. **63**, 794 (1989).

2. D. M. Cragg and D. Sherrington, Phys. Rev. Lett. **69**, 1190 (1982).

3. Q. Zhai, D. C. Harrison, and R. L. Orbach, Phys. Rev. B **96**, 054408 (2017).

4. P. R. T. Ribeiro, J. M. M. Ramirez, R. Vidyasagar, F. L. A. Machado, S. M. Rezende, and E. D. Dahlberg, Appl. Phys. Lett. **109**, 102404 (2016).

Publications

"Glassy dynamics in CuMn thin-film multilayers," Q. Zhai, D.C. Harrison, D.M. Tennant, E.D. Dahlberg, G.G. Kenning, and R.L. Orbach, Phys. Rev. B **95**, 054304 (2017).

"Magnetic Field Dependence of Spin Glass Free Energy Barriers," S. Guchhait and R.L. Orbach, Phys. Rev. Lett. **118**, 157203 (2017).

"Effect of magnetic fields on spin glass dynamics," Q. Zhai, D.C. Harrison, and R.L. Orbach, Phys. Rev. B **96**, 054408 (2017).

"End of aging as a probe of finite-size effects near the spin-glass transition temperature," G.G. Kenning, D.M. Tennant, C.M Rost, F.G. da Silva, B.J. Walters, Q. Zhai, D.C. Harrison, E.D. Dahlberg, and R.L. Orbach, Phys. Rev. B **98**, 104436 (2018).

Exploring the impact of the local environment on charge transfer states at molecular donor-acceptor heterojunctions

Barry P. Rand,[1,2] Antoine Kahn,[1] and Noel C. Giebink[3]

[1] Department of Electrical Engineering, Princeton University, Princeton, NJ 08544
[2] Andlinger Center for Energy and the Environment, Princeton University, Princeton, NJ 08544
[3] Department of Electrical Engineering, The Pennsylvania State University, University Park, PA 16802

Program Scope

Charge transfer from a donor-type to an acceptor-type system forms the basis for the photovoltaic effect observed within excitonic systems. The charge transfer (CT) state is a bound geminate charge pair that defines an intermediate state in both charge generation and recombination processes. As such, the CT state possesses a binding energy ($\sim 10 k_b T$) that still needs to be overcome in order to produce a free charge pair. While some important realizations have been made concerning CT states recently regarding their role in limiting open-circuit voltage, there still remains a lack of fundamental knowledge regarding what controls CT state energy and the efficiency by which they may be dissociated, and whether or not Frenkel excitons become free charge via the formation of CT states. This research program sets out to comprehensively investigate the various nanoscale environmental factors that determine CT state behavior (dielectric, structural, dynamic, and energetic), as well as to quantify their spatial extent and density of states (DOS) energetic distribution.

We will utilize sensitive spectral response measurements, impedance spectroscopy, X-ray scattering, and spectroscopic ellipsometry to probe the structure and optical response of thin films, as well as to extract dielectric properties. Surface-sensitive techniques such as ultraviolet photoelectron spectroscopy (UPS), inverse photoelectron spectroscopy (IPES), and X-ray photoelectron spectroscopy (XPS) will be utilized to probe energy levels. Finally, time-resolved and steady-state photoluminescence (PL), electroluminescence (EL), electroabsorption, and pump-probe spectroscopy measurements will be used to probe CT state energetics and dynamics. In this way, the PIs assembled in this collaborative proposal represent a complementary team uniquely suited with the ability to transform our understanding of CT states.

Recent Progress

Recent work has focused on exploring the nature of non-thermal charge carrier occupation in organic solar cells. Like most other solar cells, electrons and holes in organic photovoltaics are usually assumed to be described by a Fermi-Dirac function set by the ambient temperature of the

cell. It has been suggested, however, that electrons and holes in organic solar cells may not fully relax due to energetic disorder and geometric frustration in their active layers, which would have a number of important implications for charge separation and voltage loss in these devices.

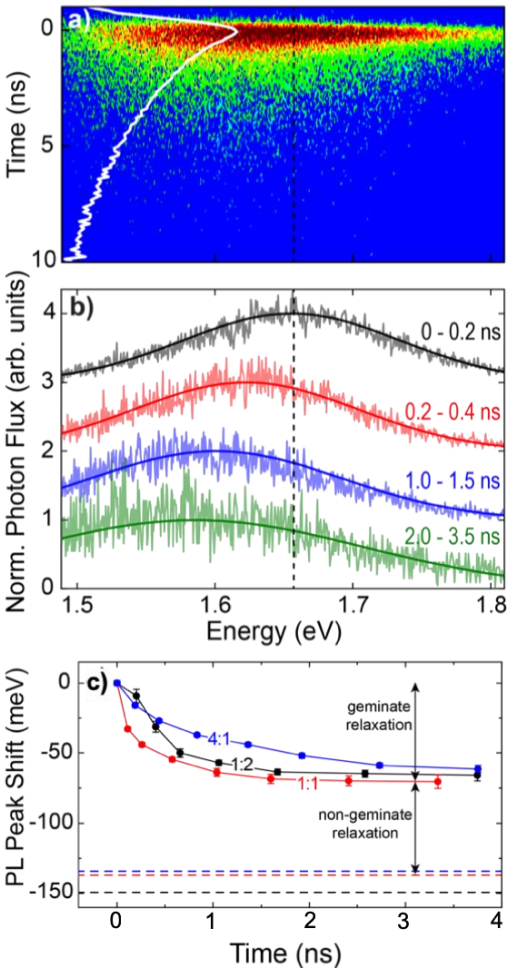

Figure 1. (a) Streak camera image of CT PL showing a dynamic red-shift **(b)** that is summarized with in **(c)**.

We uncovered direct spectroscopic evidence of non-thermal occupation in the charge transfer (CT) density of states (DOS) for organic solar cells involving the donor boron subphthalocyanine chloride (SubPc) and acceptor C_{60}. In transient photoluminescence (PL) measurements shown in Fig. 1(a,b), a dynamic redshift in the transient CT emission attests to geminate CT state relaxation on a sub-ns time scale. Although the CT PL peak appears to have settled at the end of the ns-scale time window in Fig. 1(c), the steady-state CT PL spectrum of each different blend film is further redshifted (with a peak indicated by the dashed lines in Fig. 1(c)), pointing to additional, non-geminate relaxation in the intervening μs-ms time range.

Given the substantial relaxation that takes place between early times and steady-state, it is important to determine whether or not relaxation is complete, that is, whether steady-state CT occupation of the DOS is described by a thermal equilibrium Boltzmann factor set by the CT state chemical potential and ambient temperature. The answer according to Fig. 2 is no: the separation between early time and steady-state CT PL, which is an exclusive measure of how much the distribution has thermalized (since any intrinsic temperature shift in CT energy or DOS should already be accounted for in the early time spectra), trends smaller with decreasing temperature, which is opposite to the expectation of a steepening Boltzmann tail. Instead, these data suggest that relaxation is a thermally-assisted process where carriers must hop through higher energy sites to ultimately reach those with the lowest energy in the DOS tail (which are small in number and far apart by definition).

Although the form of the non-equilibrium CT state distribution is not explicitly known, a reasonable starting point is to assume it is Boltzmann-like and interpret the PL spectrum within the framework of the generalized Planck equation for luminescent radiation, which is commonly used to determine the temperature of inorganic semiconductors and is the basis for the photovoltaic reciprocity relations that have been widely applied to organic solar cells. Using this approach, it is possible to compare the CT PL spectra obtained at different substrate temperatures (e.g. in Fig.

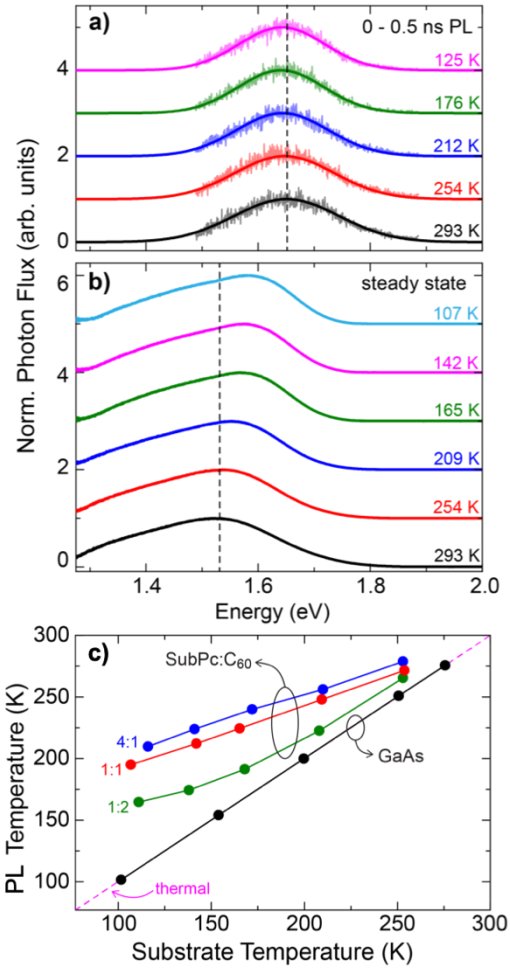

Figure 2. (a) Early-time and steady-state **(b)** CT PL spectra for a 1:1 SubPc:C_{60} blend at different temperatures. **(c)** The luminescence temperature of the blends lies above the actual sample temperature for various different blends, in contrast to the GaAs control case.

2(b)) and determine whether the difference in their corresponding luminescence temperatures is consistent. In control experiments on a GaAs wafer, the two are identical as expected (see Fig. 2(c)). However, in all of the organic solar cell blends, the luminescence temperature increasingly exceeds the substrate temperature as the latter is decreased, confirming that electron and hole populations can be far from equilibrium in organic solar cells.

In other work, we recently expanded our CT research from organic/organic semiconductor interfaces to hybrid metal halide perovskite (MHP)/organic semiconductor interfaces. MHP semiconductors with small exciton binding energy have been widely used in perovskite solar cells and achieved rapid progress in terms of device performance. However, the strong excitonic nature of two-dimensional (2D) perovskites with small *n* values remains underexploited (*n* represents the number of inorganic monolayer sheets sandwiched between bulky organic cation layers).

We observed CT features for the first time when excitonic 2D perovskites are paired with strong electron accepting molecule 1,4,5,8,9,11-hexaazatriphenylenehexacarbonitrile (HATCN) (Fig. 3(a)). The external quantum efficiency (EQE) spectrum contains a Gaussian feature in the spectral region below 2.25 eV that lies below the absorption cutoffs of HATCN and 2D perovskites. We assign this photocurrent contribution to direct absorption from an interfacial CT state based on its qualitative similarity to the intermolecular CT state absorption band commonly observed in organic photovoltaic cells. Additionally, we confirm that CT features are not found at interfaces with insufficient orbital energy offsets, where the orbital energy offset is insufficient to drive charge transfer across the interface, such as when 2D perovskite is paired with tris(8-hydroxyquinoline)aluminum (Alq_3). Furthermore, the photocurrent output is enhanced in the presence of the CT feature compared to the 2D perovskite single layer and 2D perovskite/Alq_3 devices. This observation is consistent with our expectation that, in the same manner as organic solar cells, for highly excitonic 2D perovskites, the presence of a donor/acceptor junction facilitates exciton dissociation and charge generation.

We have further identified several factors that affect the strength of the CT transition. In particular, we have found that the size of the organic cation in the 2D perovskite plays a critical role. CT features were observed in EQE spectra of donor/acceptor solar cells composed of 2D perovskite with relatively small organic cations (e.g., ethylammonium (EA) and butylammonium (BA) cations), whereas no CT features are present when the 2D perovskite layer contains bulkier aromatic phenethylammonium (PEA) cations (Fig. 3(b)). Bulkier cations prevent contact between the 2D perovskite metal halide sheet and the organic layer, inhibiting CT processes at the donor/acceptor interface. Furthermore, the ability to form CT states decreases with increasing *n* value of the 2D perovskite, which is linked to reduced excitonic character.

We have also investigated the electronic structure of the tetracene/Si heterojunction with an ultra-thin (2 nm) interlayer of hafnium nitride. This system is perceived as a good candidate for sensitization of silicon by singlet fission in tetracene. The electronic structure of the interface is important for understanding CT state and triplet transfer in this system.

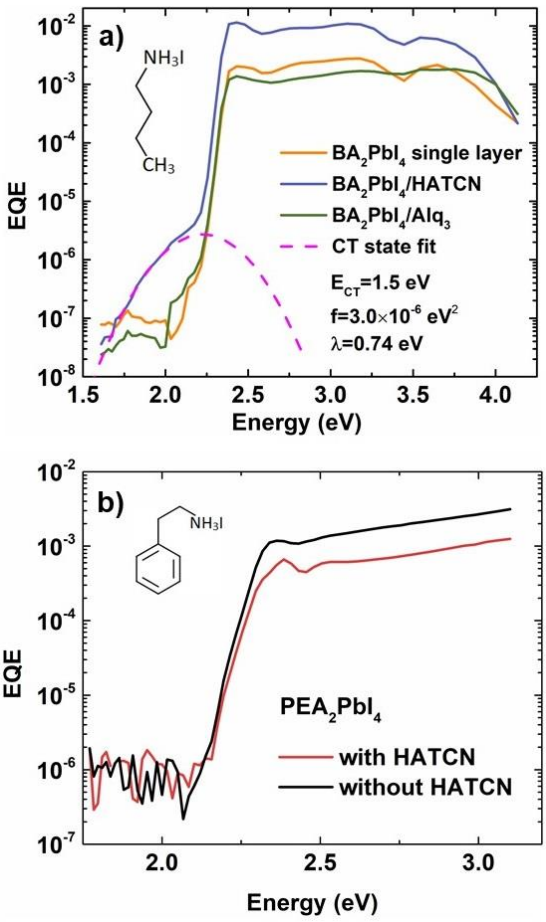

Figure 3. (a) External quantum efficiency (EQE) spectra of BA_2PbI_4 single layer, BA_2PbI_4/HATCN and BA_2PbI_4/Alq_3 heterojunction devices. **(b)** EQE spectra of PEA_2PbI_4 single layer and PEA_2PbI_4/HATCN heterojunction devices.

Future Plans

Our future work will explore the implications of the non-thermal behavior on open-circuit voltage (V_{oc}) in organic solar cells and also prompts us to re-evaluate trends in V_{oc} (such as the slope of V_{oc} versus temperature or the ideality factor deduced from its intensity dependence) that implicitly assume charge carriers to be at the ambient cell temperature. Additionally, we are working on donor/acceptor systems with very large energy offsets to learn about the width of CT state distributions and their role in charge generation. We are also exploring surface termination at 2D perovskite surfaces to control CT state intensity and energetics to understand if such interfaces have the capacity to influence material response. Finally, we are using direct and inverse photoemission spectroscopy to determine the electronic structure and energy level alignment at several donor:acceptor interfaces, namely Si/HATCN and poly(9-vinylcarbazole (PVK)/HATCN. These data are to be coupled with investigation of CT states at these interfaces. Similarly, we are looking at the impact of molecular order and morphology on the electronic structure (transport and optical gaps) of molecular systems (e.g., a-NPB).

2-Year Publications Supported by this BES Award

A.N. Brigeman, M.A. Fusella, B.P. Rand, and N.C. Giebink, "Non-thermal site occupation at the donor-acceptor interface of organic solar cells", *Phys. Rev. Appl.* **10**, 034034 (2018).

L. Zhao, Y.L. Lin, H. Kim, N.C. Giebink, B.P. Rand, "Donor/acceptor charge-transfer states at two-dimensional metal halide perovskite and organic semiconductor interfaces," *ACS Energy Lett.*, **3**, 2708 (2018).

K. Abbasi, D. Wang, M.A. Fusella, B.P. Rand, A. Avishai, "Methods for conducting electron backscattered diffraction (EBSD) on polycrystalline organic molecular thin films," *Microsc. Microanal.*, **24**, 420 (2018).

M.A. Fusella, A.N. Brigeman, M. Welborn, G.E. Purdum, Y. Yan, R.D. Schaller, Y.L. Lin, Y.-L. Loo, T. Van Voorhis, N.C. Giebink, B.P. Rand, "Band-like charge photogeneration at a crystalline organic donor/acceptor interface," *Adv. Energy Mater.*, **8**, 1701494 (2018).

Y.L. Lin, M.A. Fusella, B.P. Rand, "The impact of local morphology on organic donor/acceptor charge transfer states," *Adv. Energy Mater.*, **8**, 1702816 (2018).

Y.L. Lin, F. Zhang, R.A. Kerner, T.C.-J. Yang, A. Kahn, B.P. Rand, "Variable charge transfer state energies at nanostructured pentacene/C_{60} interfaces," *Appl. Phys. Lett.*, **112**, 213302 (2018).

R. Dhanker, C.L. Gray, S. Mukhopadhyay, S. Nunez, C. Cheng, A. Sokolov, and N.C. Giebink, "Large bipolaron density at organic semiconductor/electrode interfaces", *Nat. Comm.* **8**, 2252 (2017).

X. Lin, B. Wegner, K.M. Lee, M.A. Fusella, F. Zhang, K. Moudgil, B.P. Rand, S. Barlow, S.R. Marder, N. Koch, A. Kahn, "Beating the thermodynamic limit with photo-activation of n-doping in organic semiconductors," *Nat. Mater.* **16**, 1209 (2017).

M.A. Fusella, S. Yang, K. Abbasi, H.H. Choi, Z. Yao, V. Podzorov, A. Avishai, B.P. Rand, "Use of an underlayer for large area crystallization of rubrene thin films," *Chem. Mater.*, **29**, 6666 (2017).

Y.L. Lin, M. Koch, A.N. Brigeman, D.M.E. Freeman, L. Zhao, H. Bronstein, N.C. Giebink, G.D. Scholes, B.P. Rand, "Enhanced sub-bandgap efficiency of a solid-state organic intermediate band solar cell using triplet-triplet annihilation," *Energy Environ. Sci.*, **10**, 1465 (2017).

M.A. Fusella, F. Schreiber, K. Abbasi, J.J. Kim, A.L. Briseno, B.P. Rand, "Homoepitaxy of crystalline rubrene thin films," *Nano Lett.*, **17**, 3040 (2017).

Hot Carrier Dynamics in Low Dimensional Systems

Ian R. Sellers, Department of Physics & Astronomy, University of Oklahoma, Norman OK

Matthew Beard, National Renewable Energy Laboratory (NREL), Golden CO

Program Scope

This program is focused on understanding the physics and structural properties of materials that influence hot carrier dynamics and carrier relaxation processes in quantum confined structures. There are two complementary thrusts: hot carrier relaxation and control in III-V type-I and type-II quantum well (QW) systems; and the role of localization and carrier-carrier interactions in perovskite systems. Both these systems have been shown to display unique hot carrier dynamics, which are intimately related to the carrier-carrier, carrier-phonon, and structural architecture. Here, a complementary suite of optical spectroscopist techniques including both continuous wave and ultrafast spectroscopy are used to probe the fundamental properties of hot carriers in these systems.

Recent Progress

Recent work on the two systems under investigation has proceeded in parallel. The first, related to investigating the hot carrier relaxation processes in type-II InAs/$AlAs_{0.14}Sb_{0.86}$ multiple quantum wells, has focused on further understanding the role of phonons in the thermalization of hot carriers in such structures [1]. Specifically, in these architectures, the

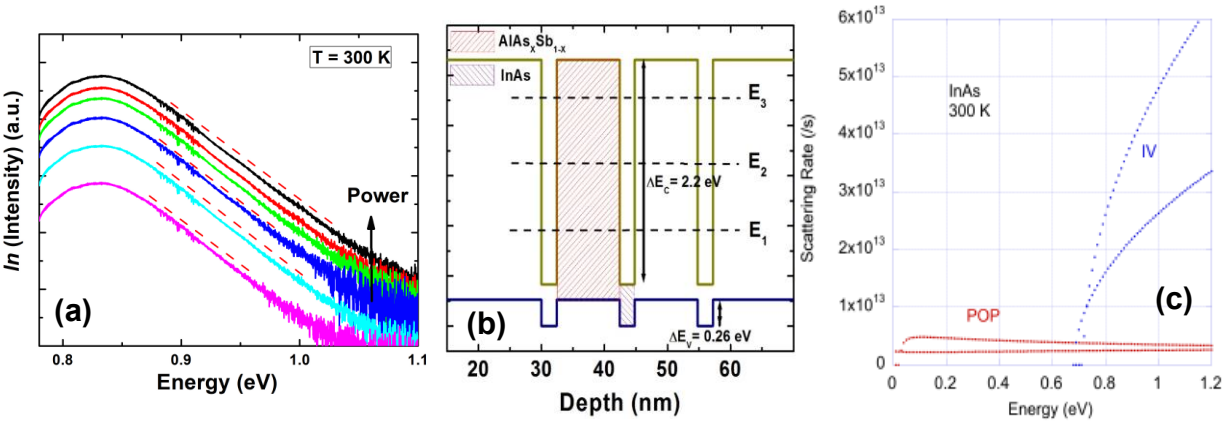

Figure 1: (a) Schematic structure of the band alignment of type-II InAs/AlAsSb QWs. (b) Power dependent PL at 150 K. (c) Comparison of the relative scattering rate of polar optical (POP) and intervalley (IV) phonons as a function of photo-excitation energy.

recombination losses are reduced over typical type-I quantum wells since, the photogenerated electrons are strongly localized in the quantum well; while, the holes rapidly transfer to the lower

energy AlAsSb barrier material (see Figure 1(b)). As a consequence of these characteristics, robust hot carriers have been the observed in CW photoluminescence, where a board high energy tail in the luminescence (indicative of hot carriers [1, 2]) is evident - even at relatively low excitation powers. An example of this data is shown in Figure 1(a), where the high energy tail is essentially constant (and at non-equilibrium temperatures) with increasing excitation power, rather than displaying a broadening (decreasing slope) as has been observed in other QW systems [3, 4].

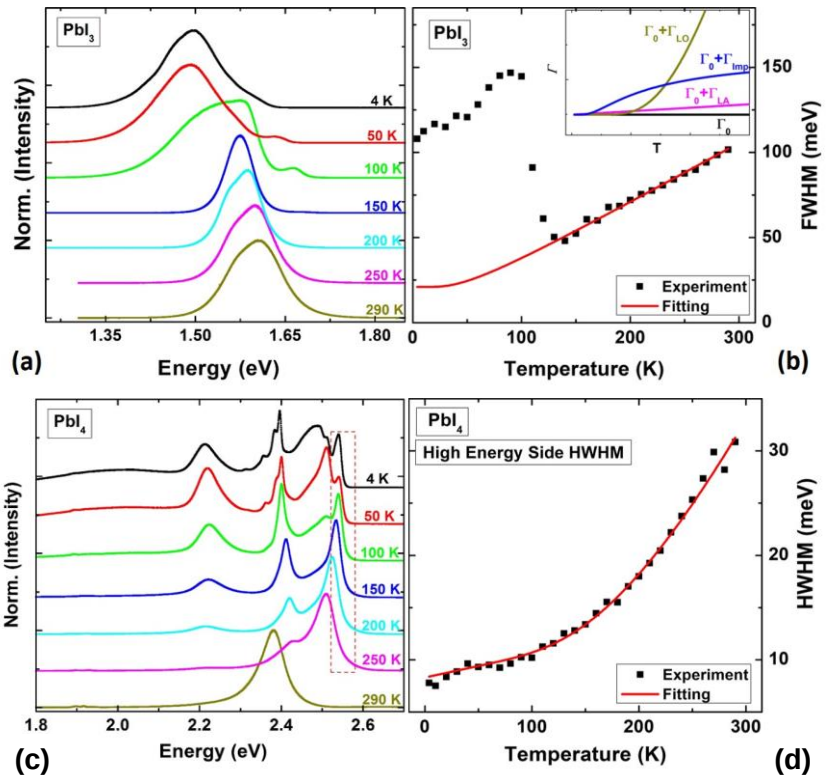

Figure 2: Temperature dependent PL for a thin film of (a) the 3D perovskite MAPbI3 and (c) 2D Schematic structure of the band alignment of type-II InAs/AlAsSb QWs. (b) Power dependent PL at 150 K. (c)

Here, the specific role of carrier-phonon interaction and the temporal dynamics are described. Our data indicates that high energy carriers are scattered from the Γ-valley into higher order (X and L) valleys rather than thermalized via LO phonon emission. This process is very efficient in InAs due to the combination of the large effective mass differences in the bands and the relatively narrow band gap of this semiconductor [5]. As such, the relaxation, (i.e. thermalization of hot carriers) is limited by the scattering *back* of the metastable photogenerated electrons from the higher order valleys to the Γ-point. However, while scattering due to emission of intervalley phonons efficiently transfers high energy carriers to the upper valleys, the reabsorption of these intervalley phonons (therefore back scattering) is a much less prevalent process; since, the density of states of the Γ-valley is much smaller than the L and X valleys. Figure 1(c) shows the scattering rates of the Intervalley (IV) phonons relative to the polar optical phonons (POP) as a function of energy for InAs at 300 K. These ensemble Monte Carlo simulations [6] clearly indicate the preferences of high energy photogenerated carriers to transfer and reside in higher order metastable valleys, rather than thermalize directly via LO phonon emission. Here, we will also present our recent monochromatic PL measurements that excite above (442 nm) and below (1064 nm) the L/X valleys; as well as, the effect this has on the hot carrier temperature and its power dependence, which further supports our hypothesis.

The second facet of this program involves investigating the novel hot carrier effects and electron-phonon interactions in perovskites, which display several of the features observed in our type-II III-V systems. Here, we aim to bring together the respective expertise of the PI's to deconvolve some of the interesting physics occurring in perovskites based upon a strong understanding of reference III-V systems. Although several recent papers have suggested stable hot carriers in perovskites, the exact mechanism remains unclear [7, 8]. In the initial few months of our program, we have focused on investigating the relative properties of the well-studied 3D (bulk) perovskite Methyl ammonium lead triiodide ($MAPbI_3$) with respect to 2D perovskites based on n-butyl ammonium (BA), a so-called Ruddleson-Popper system. Replacing MA with bulkier BA results in layered structures ($BA_2MA_{n-1}Pb_nI_{3n+1}$) that mimic the properties of QWs resulting in large increases in the excitonic properties of the material and a large blueshift in the band gap.

To date, we have focused on investigating BA_2PbI_4 (n = 1) single layer 2D perovskites with respect to $MAPbI_3$. Figure 2(a) and (c) show the temperature dependent PL of the 3D $MAPbI_3$ and 2D (n =1) $BAPbI_4$ films, respectively. In the case of the $MAPbI_3$, broad luminescence is observed at low temperature, which has been attributed to several inhomogeneities in the structural and phase configuration of the structure, along with the contributions of impurity and defect states in this material [11]. As the temperature increases the material undergoes a macroscopic phase transition from orthorhombic to tetragonal with a subsequent blueshift in the PL energy and narrowing of the linewidth. This is more evident in Figure 2(b) which plots the half width at half maximum (HWHM) of the peak PL shown in Figure 2(a). In performing this analysis the relative contribution of impurities and phonons can be determined.

Although the dependence of the $MAPbI_3$ does not follow a simple linear behavior below ~ 100 K (see Figure 2b), once it transitions into the tetragonal phase the broadening (and contribution of inhomogeneities) has a more conventional behavior (decreases) [9]. As is expected from a polar semiconductor, the phonon broadening is dominated by LO phonons with energy of ~ 11 meV, which is consistent with the energy determined by others for optical phonons in these systems [9]. The PL from the 2D perovskite shown in Figure 2(c) displays significantly more structure at lower temperature than the 3D film, which is attributed to the contribution of several excitonic complexes including: Frenkel and Wannier-Mott excitons, bound and free impurity states, and phonon replicas, all of which will be discussed here. When assessing the broadening mechanisms in this 2D system, the fitting of the HWHM was confined to PL related to the continuum-band structure (shown by the region in the dashed box), the origin of which was confirmed by complementary absorption measurements; this will also be presented.

On assessing the relative contributions of the broadening in the BA_2Pb_4 film, significant enhancements in the interaction with LO phonons were observed relative to $MAPbI_3$, with a LO phonon energy in excess of ~ 50 meV. Since much of the recent work in these systems has suggested LO phonon energies in the 5 – 25 meV range, we discuss the possibility of the large values extracted here as the result of the contribution of polaron formation, which causes

considerably more scattering/broadening in more extended (or weakly bound) excitons close to the continuum.

Future Plans

To further investigate the role of intervalley scattering and hot carrier lifetimes in the type-II systems we have booked time at NREL to perform TRPL excited above and below the L and X valleys (March 2019). In addition, we are planning to perform complementary Raman measurements under similar conditions of power and temperature (summer 2019). These measurements will allow us to correlate the radiative lifetime, hot carrier dynamics, and LO phonon signal to intervalley scattering.

In terms of the perovskite work, our plan is to perform complementary Raman measurements at NREL to search for the signature of additional phonon resonances and the effect of polarons in the 2D films, such as to further improve our understanding of these systems. Moreover, we plan to investigate alternative 2D systems in which the effect of structural distortion are investigated and correlated to the optical properties.

References

1. H. Esmaielpour *et al*. Progress in PV: Res. & Apps., **24**, 591 (2016)
2. H. Esmaielpour *et al*. Scientific Reports, **8**, 12473 (2018)
3. A. Le Bris *et al*. Energy & Environmental Science, **5**, 6225 (2012)
4. J. Shah et al. Physical Review Letters, **54**, 2045 (1985)
5. E. D. Grann *et al*. Physical Review B. **53**, 9847 (1996)
6. Acknowledgment: D. K. Ferry *Arizona State University*
7. Y. Yang *et al*. Nature Communications, **8**, 14120 (2016)
8. Y. Yang *et al.* Nature Photonics, **10,** 53 (2016)
9. A. D. Wright *et al.* Nature Communications, **7,** 11755 (2016)

Publications

1. Enhanced LO phonon broadening in BA_2PbI_3 films Ruddleson-Popper 2D Perovskite Films, H. Esmaielpour, V. R. Whiteside, S. Sourabh, G. E. Eperon, and I. R. Sellers. *In preparation for ACS Energy Letters*

Magnetic and Spin Transport Properties in Heterostructures with Atomically Layered Magnetic Materials

Jing Shi, Department of Physics and Astronomy, University of California, Riverside

Program Scope

The current research program explores novel electrical and spin transport properties arising from quantum mechanical interactions at the interfaces of dissimilar materials. Specifically, electron wave-function hybridization at interfaces leads to new interactions such as exchange and spin-orbit interactions which consequently produce phenomena in the individual constituents. The research also aims to manipulate these interactions via new materials and heterostructures. Recent discoveries of atomically layered van der Waals materials such as graphene, transition metal dichalcogenides or TMD (MoS_2, WSe_2), layered ferromagnets (CrI_3, $Cr_2Ge_2Te_6$, Fe_3GeTe_2) and topological insulators (Bi_2Se_3, Bi_2Te_3) offer an unprecedented opportunity to create new heterostructures with desired interactions. One example is to tailor an interface layer with strong exchange and strong spin-orbit interactions using atomically layered materials.

Recent Progress

In this and previous award periods, the PI has demonstrated strong proximity effects at the interfaces of graphene with ferrimagnetic insulators (FMI), graphene and TMD, which manifest themselves in the anomalous Hall effect or weak anti-localization effect in these heterostructures [1-4]. To ensure high-quality interfaces, the PI has improved the fabrication method using glovebox so that more air-sensitive layered materials can be fabricated. Various heterostructures have been fabricated and their transport properties are being investigated.

Future Plans

The PI will take advantage of the newly constructed glovebox and continue fabricating new heterostructures especially with atomically layered ferromagnets. Besides exploring different material combinations, we will apply various experimental knobs to control the strength of the interactions including the hydrostatic pressure and electrostatic gating. Systematic structural (XRD, AFM, Raman, HRTEM, etc.) and magnetic (FMR) property characterizations will be carried out to assess the interface quality and interaction strength. Both electrical (anomalous Hall, phase-coherent quantum transport) and spin (spin Seebeck effect, spin pumping, etc.) transport properties will be investigated to discover new phenomena and develop an in-depth understanding of underlying physics.

References

[1] Z.Y. Wang, C. Tang, R. Sachs, Y. Barlas, and Jing Shi, Proximity-induced ferromagnetism in graphene revealed by the anomalous Hall effect, Phys. Rev. Lett. 114, 016603 (2015); https://doi.org/10.1103/PhysRevLett.114.016603.

[2] Chi Tang, Bin Cheng, Mohammed Aldosary, Zhiyong Wang, Zilong Jiang, K. Watanabe, T. Taniguchi, Marc Bockrath, and Jing Shi, Approaching quantum anomalous Hall effect in proximity-coupled YIG/graphene/h-BN sandwich structure, APL MATERIALS 6, 026401 (2018); DOI: 10.1063/1.5001318.

[3] B.W. Yang, M.-F. Tu, J.W. Kim, Y. Wu, H. Wang, J. Alicea, R.Q. Wu, M. Bockrath and Jing Shi, Tunable spin–orbit coupling and symmetry-protected edge states in graphene/WS¬2, 2D Materials 3, 031012 (2016); DOI:10.1088/2053-1583/3/3/031012.

[4] Bowen Yang, Mark Lohmann, David Barroso, Ingrid Liao, Zhisheng Lin, Yawen Liu, Ludwig Bartels, Kenji Watanabe, Takashi Taniguchi, and Jing Shi, Strong electron-hole symmetric Rashba spin-orbit coupling in graphene/monolayer transition metal dichalcogenide heterostructures, Phys. Rev. B (Rapid Comm) 96, 041409 (R) (2017); DOI: 10.1103/PhysRevB.96.041409.

High-Coherence Multilayer Superconducting Structures for Large Scale Qubit Integration and Photonic Transduction

Irfan Siddiqi, Stefano Cabrini, Frank Ogletree, Alex Weber-Bragioni, Andrew Minor, and Norman Yao
Lawrence Berkeley National Laboratory (LBNL)

William Oliver
Massachusetts Institute of Technology (MIT)

Program Scope

Our project is a joint experiment/theory collaboration to develop next generation quantum systems, targeting new paradigms for the creation and control of coherent phenomena in superconducting materials with an emphasis on elucidating and enhancing entanglement generation and characterization, as well as the transduction of quantum information between disparate modalities, specifically microwave photons and solid matter. We will focus on the tool set afforded by thin films and tunneling junctions as a laboratory to (i) control decoherence channels within novel 3D material architectures, varying material type and defect/doping density, (ii) apply advanced imaging, spectroscopy, and noise sensing techniques to characterize static structural disorder as well as dynamic fluctuations in metallic and dielectric layers, (iii) develop functional quantum interfaces based on linear and nonlinear waveguides to efficiently transmit and receive coherent quantum information, and (iv) develop new theoretical and computational tools to efficiently characterize large scale entanglement in such systems.

Our materials development effort will focus on fabricating novel multi-layer qubit structures using thin film membranes produced by chemical vapor deposition (CVD) and atomic layer deposition (ALD) to realize qubits and their respective wiring layers on (i) opposite sides of a single membranes or (ii) different terraces of a multi-layer stack. As a baseline, we will flip-chip bond two separate chips containing these circuits with an air dielectric. We will vary the choice of metals (Al, Nb, TiN, NbTiN, and transition metal dichalcogenides) and dielectrics (alumina, cobalt oxide, silicon nitride, molybdenum oxide, and tungsten oxide) to minimize decoherence due to parasitic oxides, polymer residues, and non-equilibrium phononic and quasi-particle excitations. These structures will be characterized both electrically using standard qubit coherence benchmarks, and structurally using a suite of multi-modal imaging techniques including transmission electron, scanning tunneling, and atomic force microscopy in combination with spectroscopic probes such as Auger, FTIR, and XPS with depth profiling to fully characterize the metal/dielectric/substrate landscape and topography. Combining these data with photonic probes and theoretical analyses, we aim to develop comprehensive models of the quantum dynamics in functionalized high coherence materials, paving the way for future quantum information technologies.

Recent Progress

We have started tackling the challenge of creating and analyzing the coherence properties of quantum interfaces by way of four parallel and synergistic directions: (i) structural characterization of existing quantum devices, (ii) baseline characterization of coherence in 3D structures, (iii) baseline characterization of coherence of ALD films and structures, and (iv) photonic transduction. The current status of each of these is summarized below.

Structural Characterization

A current materials challenge related to superconducting tunnel junction fabrication revolves around the spread of resistance values obtained for nominally identical structures. This spread, which typically spans around 5-10% for devices that have micron sized and smaller lateral dimensions, is several times larger than the variation in the junction area ascertained by imaging. As a first step in elucidating the mechanism behind this discrepancy, we have taken cross-sectional SEM images with the aid of FIB slicing as shown in Figure 1. We see that there is significant interface roughness associated with the aluminum oxide tunnel barrier, giving us a natural target to investigate further and improve.

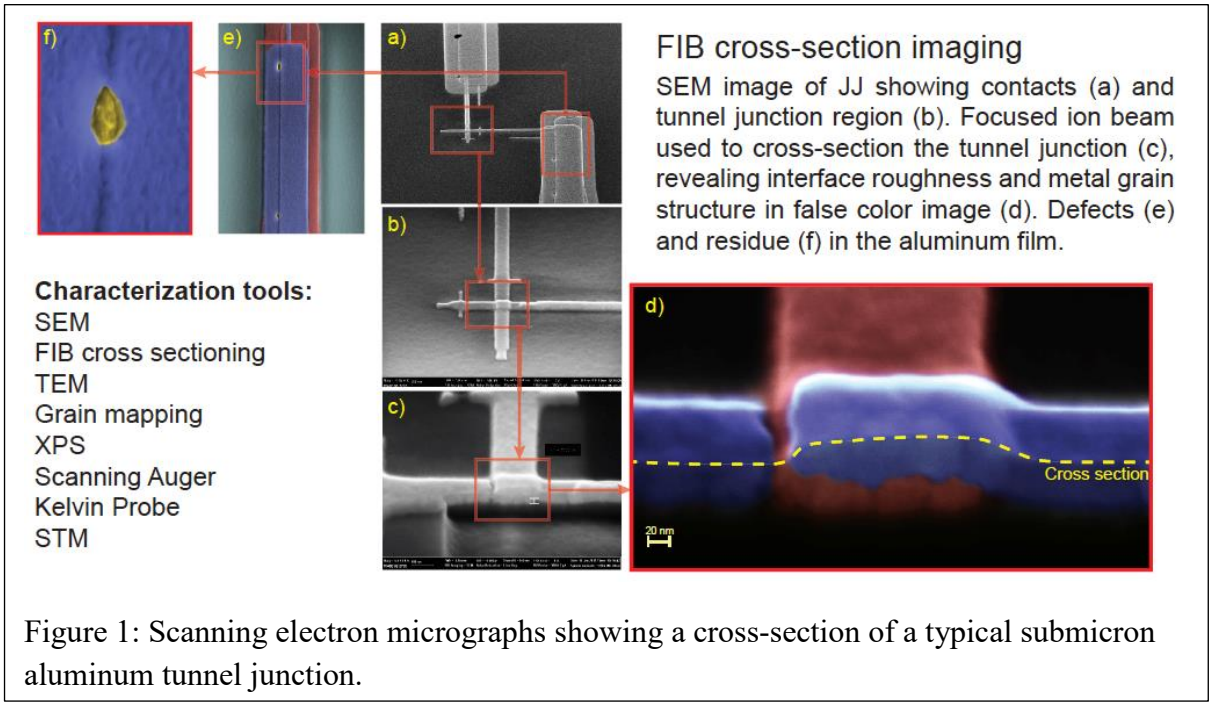

Figure 1: Scanning electron micrographs showing a cross-section of a typical submicron aluminum tunnel junction.

Coherence in 3D Structures

We have developed a series of experiments to benchmark coherence variations when transitioning 2D structures onto a 3D platform. Specifically, we will produce a 3D version of our current 8 qubit design which involves transmon qubits with nearest neighbor coupling on a ring. We will split this structure into two chips that will be mechanically joined with micron sized

spherical spacers to establish capacitive coupling. This set of experiments will allow us to probe coherence times in uncoupled qubits, and then to move on to introducing the coupling resonators by way of the second chip. For both of these measurements, we will have the original 2D planar device and its quantum lifetimes as a reference standard. This first measurement will guide the design of the next stages of 3D devices that will incorporate thin film membranes, and also serve as a dielectric-free reference for those devices.

Coherence in ALD Films

While we characterize losses incurred in transitioning from a 2D to 3D geometry, we are also starting to test the dielectric loss associated with thin ALD membranes. We have designed a set of microwave resonant structures whose quality (Q) factor will be measured at mK temperatures, followed by a deposition of ALD grown material across the entire chip, and then completed with a final characterization step to ascertain the now loaded Q values. This vehicle will allow for the rapid optimization of ALD films vis-à-vis microwave loss, and such materials will then be integrated into 3D qubit devices.

Photonic Transduction

We have now successfully operated the first multiqubit based single photon detector. The device has four transmon qubits in a transmission line and uses subradiant dark states formed by quantum absorbers. We also designed and fabricated a single photon source, also based on superconducting qubits, to test the detector and observed a clear difference in presence of a single microwave photon.

Future Plans

- Multimodal characterization of sub-micron tunnel junctions using TEM, Auger, AFM, STM, and XPS to determine the uniformity of the tunnel barrier and pinpoint defects
- Fabrication, assembly, and testing of 3D wafer bonded quantum devices
- Benchmarking the coherence properties of ALD films using loaded microwave resonators and the optimization of growth conditions to maximize quality factor
- Complete characterization of the first generation of traveling wave photon detectors

Publications

We have just started our first BES grant.

Stimuli-Responsive Mesostructured Hybrid Materials

Ivan I. Smalyukh, University of Colorado at Boulder

Program Scope.

Self-assembly of organic molecules and colloidal nanoparticles is also an exceptionally promising way of designing and fabricating inexpensive synthetic composite materials with new macroscopic physical behavior and properties. The main objective of this project is to explore self-organization of pre-engineered anisotropic functional units into colloidal composites with ordered mesoscopic structures that can be tuned and switched by weak external stimuli, such as light and low-voltage electric fields. Tunable composite materials with interesting physical behavior are designed through integrating unique properties of solid nanostructures with the facile responses of soft matter to weak external stimuli. The research focuses on understanding and control of self-assembly of metal and semiconductor nanoparticles, as well as on material behavior arising from their ordered self-organization and alignment. The design and realization of desired physical properties in these composites are based on the following three strategies: (1) discovery of new condensed matter phases of hybrid molecular-colloidal systems enriched by diversity of colloidal particle's geometric shapes, surface charging, boundary conditions for molecular alignment and chirality; (2) topology of continuous & singular field configurations in the molecular-colloidal systems; (3) effective medium behavior and plasmon-exciton interactions in colloidal assemblies formed by different types of nanoparticles co-assembled at the mesoscopic scales. The fundamental studies of interactions and ordering of nanoparticles reveal underpinning physical mechanisms that guide mesoscale morphology and ultimately determine material properties of the self-assembled composites. PI explores mesoscale self-assembly of anisotropic nanoparticles dispersed in responsive liquid crystalline host media that will enable new composites with properties controlled by applying fields, changing temperature, and using other external stimuli. The focus is on fundamental understanding and control of nanoscale self-assembly and alignment of metal and semiconductor nanoparticles that enable new material behavior arising from orientationally and positionally ordered self-organization of anisotropic molecules and nanoparticles into tunable long-range structures. Electrical realignment of the liquid crystal host, like that used in displays, allows for rearrangement and reorientation of anisotropic nanoparticles, leading to an unprecedented control over self-assembled nanostructures and to dramatic changes in the material emergent behavior and properties. The effective-medium optical properties are characterized and correlated with the hierarchical structure and composition of self-assembled configurations, as well as with plasmon-excition and other interactions separately studied at the level of individual nanoparticles. Experiments are conducted in parallel with analytical and numerical modeling of interactions and effective-medium optical properties, which provide important insights. PI explores how the ensuing novel composite materials can be used to control transmission and directional scattering of light, as needed for applications in smart windows, displays and electro-optic devices. This research transcends traditional disciplinary boundaries of physics, topology, chemistry, engineering, and

materials science. The research in this project broadly advances our knowledge of the nanoscale self-organization phenomena and the ensuing physical behavior.

Recent Progress.

The main recent progress in our research includes the optically biaxial molecular-colloidal liquid crystals [1], elastic colloidal monopoles and multipoles [2,3], as well as the discovery of electrostatically controlled surface anchoring [4], which I briefly describe.

Optically biaxial molecular-colloidal fluids. Order and fluidity often coexist, with examples ranging from biological membranes to liquid crystals, but only a few of many possible distinct realizations of such ordered fluid states have been demonstrated. In our 2018 Science article [1], we have dispersed micrometer-long inorganic photon-upconverting colloidal rods in a fluid host of nanometer-long organic molecular rods. Both types of building blocks, while freely diffusing around, interact to form an orthorhombic nematic fluid, in which like-sized rods are roughly parallel and the molecular ordering direction is orthogonal to that of colloidal rods. A coarse-grained model explains the experimental temperature-concentration phase diagram (Fig. 1) with two uniaxial and one biaxial nematic phases, as well as the orientational distributions of rods. Displaying properties of biaxial optical crystals, these hybrid molecular-colloidal fluids can be switched by electric and magnetic fields and exhibit facile responses to other external stimuli.

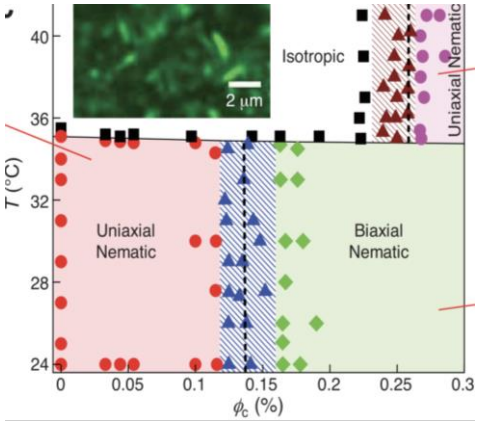

Fig. 1. Temperature-concentration phase diagram of the molecular-colloidal liquid crystal exhibiting a biaxial nematic phase, along with 2 uniaxial phases and 1 isotropic phase. The dashed vertical lines correspond to theoretical model predictions. For details, see Ref. [1].

Optically reconfigurable elastic colloidal monopoles. Monopole-like electrostatic interactions are ubiquitous in biology and condensed matter, enabling colloidal crystals and plastic crystals, but they are typically screened by counterions and cannot be switched from attractive to repulsive due to the nature of charging. On the other hand, monopole-like interactions between colloidal inclusions mediated by orientational elasticity in liquid crystal host fluids have been considered impossible. In a manuscript currently under review [2], we have introduced liquid crystal colloids with strong optically switchable elastic monopole moments. Differently from electrostatics, like-charged elastic monopoles attract and oppositely charged ones repel. The sign and magnitude of elastic charges can be switched by ambient-intensity unstructured light and the monopoles can even be transformed to quadrupoles at will. These findings echo self-assembly of excited-state atoms and may enable reconfigurable colloidal Rydberg matter.

High-order nematic colloidal multipoles. Achieving and exceeding the diversity of colloidal analogs of chemical elements and molecules as building blocks of matter has been the central goal and challenge of colloidal science ever since Einstein introduced the colloidal atom paradigm. Recent significant advances have been achieved by exploiting the powerful machinery of DNA hybridization to assemble colloidal particles, but robust physical means of defining colloidal atoms

and molecules remain limited. In a just accepted Nature Communications article [3], we have introduced the physical design principles that allow for defining high-order elastic nematic colloidal multipoles that emerge when particles with controlled shapes and surface boundary conditions are introduced into a nematic host fluid. Combination of experiments and numerical modeling of equilibrium field configurations, with a subsequent spherical harmonic expansion, allows us to systematically probe elastic multipole moments, bringing analogies with electromagnetism and structure of outmost occupied shells of atomic orbitals. We show that, at least in view of the symmetry of the "director wiggle wave functions", the diversity of elastic colloidal atoms can far exceed that of known chemical elements.

Electrostatic anchoring physical behavior. Differing from isotropic fluids, liquid crystals exhibit highly anisotropic interactions with surfaces, which define boundary conditions for the alignment of constituent rod-like molecules at interfaces with colloidal inclusions and confining substrates. In our recent article (to be published in *Phys Rev Lett*) [4], we have shown that surface alignment of the nematic molecules can be controlled by harnessing the competing aligning effects of surface functionalization and electric field arising from surface charging and bulk counterions. The control of ionic content in the bulk and at surfaces allows for tuning orientations of shape-anisotropic particles like platelets within an aligned nematic host and for changing the orientation of director relative to confining substrates. The ensuing anisotropic elastic and electrostatic interactions enable colloidal crystals with reconfigurable symmetries and orientations of inclusions.

Topological solitonic phases in soft condensed matter. Liquid crystals are widely known for their facile responses to external fields, which forms a basis of the modern information display technology. However, switching of molecular alignment field configurations typically involves topologically trivial structures, though singular line and point defects often appear as short-lived transient states. We have demonstrated [5] electric and magnetic switching of nonsingular solitonic structures in chiral nematic and ferromagnetic liquid crystals. These topological soliton structures are characterized by Hopf indices, integers corresponding to the numbers of times that closed-loop-like spatial regions (dubbed "preimages") of two different single orientations of rod-like molecules or magnetization are linked with each other. We showed that both dielectric and ferromagnetic response of the studied material systems allow for stabilizing a host of topological solitons with different Hopf indices. The field transformations during such switching are continuous when Hopf indices remain unchanged, even when involving transformations of preimages, but discontinuous otherwise [5]. While arising in theories in many branches of science, from particle physics to condensed matter and cosmology, stable three-dimensional topological solitons remained experimentally elusive until very recently. We were able to show that such solitons can be electrically and magnetically switched between states with the same or different Hopf indices. Richness and robustness of this switching promise technological applications in the new breeds of information displays and data storage devices, as well as may provide a test ground and new inspirations for the mathematical knot theory.

Chiral nematic colloidal self-assembly. Colloidal particles disturb the alignment of rod-like molecules of liquid crystals, giving rise to long-range interactions that minimize the free energy

of distorted regions. Particle shape and topology are known to guide this self-assembly process. However, how chirality of colloidal inclusions affects these long-range interactions is unclear. We have explored [6] the effects of distortions caused by chiral springs and helices on the colloidal self-organization in a nematic liquid crystal using laser tweezers, particle tracking and optical imaging. We showed that chirality of colloidal particles interacts with the nematic elasticity to predefine chiral or racemic colloidal superstructures in nematic colloids. These findings are consistent with numerical modelling based on the minimization of Landau–de Gennes free energy. Our study uncovers the role of chirality in defining the mesoscopic order of liquid crystal colloids, suggesting that this feature may be a potential tool to modulate the global orientated self-organization of these systems.

Future Plans. The PI and his team will continue developing mesostructured stimuli-responsive materials that combine unique properties of soft matter and solid nanostructures, along with emergent new behavior enabled by various aspects of topology. PI and his research group are conducting in-depth studies of how this mesoscale self-organization, which can yield centimeter-large mono-crystals of colloidal nanoparticles with tunable center-to-center separations, leads to new physical behavior and material properties arising from a combination of unique properties of nanoparticles as well as structural organization at nanometer to macroscopic scales. The PI is also planning to develop LC co-dispersions of quantum and plasmonic nanoparticles that have their surfaces functionalized with photo-responsive dye molecules containing azobenzene. In these systems, the PI will probe how plasmon-exciton interactions can lead to new physical behavior when the nanoparticle-scale interactions are combined with different forms of long-range orientational and positional ordering that can be tuned by weak external stimuli applied to soft matter host media. More broadly, by exploiting unique properties of solid nanostructures in the forms of their colloidal dispersions and by combining them with the facile response of soft matter to external stimuli, the PI intends to develop a new breed of composites with novel physical behavior, pre-engineered properties, and facile response to external fields. Recent preliminary studies in the PI's group (unpublished) show that perovskite and photon-upconverting nanoparticles dispersed in thermotropic LCs and with their surface functionalized with azobenzene dyes can exhibit active-matter-like physical behavior with ultra-strong responses to light.

References

1. H. Mundoor, S. Park, B. Senyuk, H. Wensink and **I. I. Smalyukh**. "Hybrid molecular-colloidal liquid crystals." *Science* **360**, 768-771 (2018).
2. Y. Yuan, Q. Liu, B. Senyuk and **I.I. Smalyukh**. "Elastic colloidal monopoles and out of equilibrium interactions in liquid crystals." *Under review.* (2019).
3. B. Senyuk, J. Aplinc, M. Ravnik and **I.I. Smalyukh**. "High-order elastic multipoles as colloidal atoms." *Nature Communications* (2019).
4. H. Mundoor, B. Senyuk, S. Park, M. Almansouri, B. Fleury and **I.I. Smalyukh**. "Electrostatically controlled surface boundary conditions in nematic liquid crystals and colloids." *Phys Rev Lett* (2019).

5. J-S. Tai, P.J. Ackerman and **I.I. Smalyukh**. Topological transformations of Hopf solitons realized in chiral ferromagnets and liquid crystals. *Proc. Natl. Acad. Sci. U.S.A.* **115**, 921-926 (2018).
6. Y. Yuan, A. Martinez, B. Senyuk, M. Tasinkevych, and **I. I. Smalyukh**. "Effects of chirality on elastic interactions and colloidal self-assembly in nematic liquid crystals." *Nature Mater.* **17**, 71–78 (2018).

Publications within 2 years (articles acknowledging the DOE award, either the current or the one before its renewal in July 2018):

1. H. Mundoor, S. Park, B. Senyuk, H. Wensink and **I. I. Smalyukh**. "Hybrid molecular-colloidal liquid crystals." *Science* **360**, 768-771 (2018).
2. Y. Yuan, Q. Liu, B. Senyuk and **I.I. Smalyukh**. "Elastic colloidal monopoles and out of equilibrium interactions in liquid crystals." *Under review.* (2019).
3. B. Senyuk, J. Aplinc, M. Ravnik and **I.I. Smalyukh**. "High-order elastic multipoles as colloidal atoms." *Nature Communications* (2019).
4. H. Mundoor, B. Senyuk, S. Park, M. Almansouri, B. Fleury and **I.I. Smalyukh**. "Electrostatically controlled surface boundary conditions in nematic liquid crystals and colloids." *Phys Rev Lett* (2019).
5. J-S. Tai, P.J. Ackerman and **I.I. Smalyukh**. Topological transformations of Hopf solitons realized in chiral ferromagnets and liquid crystals. *Proc. Natl. Acad. Sci. U.S.A.* **115**, 921-926 (2018).
6. Y. Yuan, A. Martinez, B. Senyuk, M. Tasinkevych, and **I. I. Smalyukh**. "Effects of chirality on elastic interactions and colloidal self-assembly in nematic liquid crystals." *Nature Mater.* **17**, 71–78 (2018).
7. Y. Xie, Y. Li, G. Wei, Q. Liu, H. Mundoor, Z. Chen and **I. I. Smalyukh**. "Liquid crystal self-assembly of upconversion nanorods enriched by depletion forces for mesostructured material preparation." *Nanoscale* **10**, 4218 - 4227 (2018).
8. J.-S. B. Tai and **I. I. Smalyukh**. "Static Hopf solitons and knotted emergent fields in solid-state chiral ferromagnetic nanostructures." *Phys Rev Lett* **121**, 187201 (2018).
9. G. H. Sheetah, Q. Liu, B. Senyuk, B. Fleury and **I. I Smalyukh**. Electric switching of visible and infrared transmission using liquid crystals co-doped with plasmonic gold nanorods and dichroic dyes. *Optics Express* **26**, 22264-22272 (2018).
10. P. Rofouie, M. Alizadehgiashi, H. Mundoor, **I. I Smalyukh** and E. Kumacheva. Semi-Spherical Cholesteric Films Formed by Cellulose Nanocrystals. *Advanced Functional Materials* **28**, 1803852 (2018).
11. S. Mi, Y. Xie, Y. Li, R. Liu, X. Liu, I. I. Smalyukh and Z. Chen. The Effect of Thickness-Tunable ZrO2 Shell on Enhancing the Tunneling Magnetoresistance of Fe3O4 Supraparticles. Adv. Mater. Interfaces 5, 1800236 (2018).
12. H. Ruan, G. Chen, X. Zhao, Y. Wang, Y. Liao, H. Peng, C.-L. Feng, X. Xie, **I.I. Smalyukh**. Chirality Enabled Liquid Crystalline Physical Gels with High Modulus but Low Driving Voltage. ACS Applied Materials & Interfaces 10, 43184-43191 (2018).
13. H. Peng, L. Yu, G. Chen, Z. Xue, Y. Liao, J. Zhu, X. Xie, **I.I. Smalyukh**, Y. Wei. Liquid Crystalline Nanocolloids for Storage of Electro-Optic Responsive Images. *ACS applied materials & interfaces*, DOI:10.1021/acsami.8b22636 (2019).

14. Y. Liang, Y. Xie, D. Chen, S. Hou, T. Wen, K. Deng, X. Wu, **I. I. Smalyukh** and Q. Liu. Counterintuitive nanorod assembly driven by strong directional forces and its unusual thermostability. *Nature Comm.* **8**, 1410 (2017).
15. H. Mundoor, B. Senyuk, and I. I. Smalyukh. "Triclinic colloidal crystals from competing elastic and electrostatic interactions." ***Science*** 352, 69-73 (2016).

Metamaterials

Costas M. Soukoulis, Thomas Koschny, Jigang Wang
Ames Laboratory, Iowa State University, Ames, Iowa

Program Scope

Metamaterials are novel artificial materials that enable the realization of innovative properties unattainable in naturally existing materials. We will exploit coherence in light and matter which will significantly advance the photonic technologies our modern societies so vitally rely on. This will be accomplished through fundamental theoretical understanding, analysis, development, fabrication, and experimental characterization of metamaterials and investigate their feasibility for various applications. Our work targets current, fundamental problems and opportunities in controlling light with matter and matter with light. We will find new ways to mitigate dissipative losses in optical metamaterials, specifically in active optical metasurfaces and plasmonic structures coupled to quantum-emitters, and will develop novel lasing systems with non-trivial out-coupling, coherent surface plasmon sources and dark near-field sources, e.g., for Surface Enhanced Raman Spectroscopy sensing. We will expand the control afforded by metasurfaces over the radiative vacuum and radiation damping of resonant nanoparticles and enable new, fundamental improvements to metasurface-based difference-frequency generations for coherent THz sources as well as photon energy-conversion by higher harmonic generation. We will demonstrate constructive ways to increase the operational bandwidth of metasurfaces. We will explore non-trivial optical forces and novel avenues for implementing opto-mechanical coupling and coherent manipulation of the mechanical state of matter with light.

Recent Progress

Dark dielectric surface-state based lasing metasurfaces: We developed a theory of novel dark dielectric surface-state based lasing metasurfaces. This lasing, i.e. stimulated emission into a macroscopically populated dark electromagnetic surface state, constitutes a dielectric analog of lasing into dark plasmon-polaritons and allows to design ultra-thin, large-aperture lasing dielectric surface, which control over directionality and shape of the out-coupled laser beam. We developed a theory for experimentally relevant finite emitting apertures and explain the interplay between lasing mode structure, intended outcoupling of radiation and edge leakage. This provides important guidance for experimental implementations [1]. The high Q-factor afforded by dielectric dark resonant states together with the deeply sub-wavelength sickness of the metasurface provides a route to miniaturization of laser systems. Especially if surface emitting lasers with non-trivial beam characteristics and/or large apertures are desired, we can design metasurfaces that combine tight

near-field coupling between quantum emitters (the gain medium) with resonant dark states, leading to "lasing" directly into the bound photonic modes of the dark states rather than propagating waves of light. Then, coupling to the free-space radiation field can be managed by a metasurface that allows precise control over the amount of radiation damping as well as the precise nature of the generated beam (beam profile, direction, polarization, etc.). These structures are the conceptional analog to spasers but al low for more control, higher Q-factors, and lower lasing thresholds. For example, a macroscopically populated dark state may evanescently couple to both electric and magnetic currents of the metasurface, providing directional emission only to the air side, not back into the structure, without a lossy mirror and without a "vertical cavity", enabling the thickness of the lasing structure to be substantially smaller than the wavelength of the emitted radiation. The metamaterial laser system offers radiation damping tunability, along with many other features, such as directionality, sub-wavelength integration, and simple layer-by-layer fabrication.

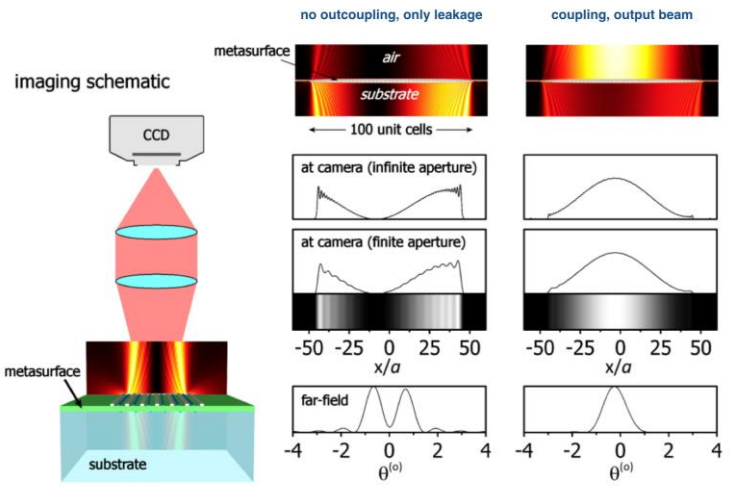

Fig. 1. Competition of radiative out coupling and leakage in realistic finite-size dark surface state lasers [1].

Broadband multi-resonant metasurfaces: We developed a theory for Multi-resonant metasurfaces, which enable broadband, arbitrarily large monotonic phase manipulation while maintaining perfect reflection. This solves the old problem of how to get broadband response from narrow metasurface resonances and can enable arbitrary time-shift modulation of pulsed signals with perfectly reflective metasurface, e.g. for broadband communication technology. Most non-trivial metasurfaces need to be resonant and are therefore inherently n arrow-band, leading to pulse distortion. Large group delays & monotonic phase delays exceeding 2π are not possible with conventional metasurfaces. Multiple, properly arranged alternating electric and magnetic resonances can overcome these problems. Metasurfaces impart phase discontinuities on impinging electromagnetic waves that are typically limited to $0-2\pi$. Here, we demonstrate that multi-resonant metasurfaces can break free from this limitation and supply arbitrarily large, tunable time delays over ultra-wide bandwidths. As such, ultra-thin metasurfaces can act as the equivalent of thick bulk structures by emulating the multiple geometric resonances of three-dimensional systems that originate from phase accumulation with effective material resonances implemented on the surface itself via suitable subwavelength meta-atoms. We describe a constructive procedure for defining the required sheet admittivities of such metasurfaces. Importantly, the proposed approach provides an exactly linear phase response so that broadband pulses can experience the desired group delay

without any distortion of the pulse shape. We focus on operation in reflection by exploiting an antimatching condition, satisfied by interleaved electric and magnetic Lorentzian resonances in the surface admittivities, which completely zeroes out transmission through the metasurface. As a result, the proposed metasurfaces can perfectly reflect a broadband pulse imparting a prescribed group delay. The group delay can be tuned by modifying the implemented resonances, thus opening up diverse possibilities in the temporal applications of metasurfaces. High-fidelity, arbitrary time-shift modulation of pulsed signals with ultra thin metasurfaces, e.g., for broadband communications technology.

We also explored resonant photonic crystal surface modes and demonstrated dielectric metasurfaces pairing toroidal and magnetic dipole resonances for low-loss and dynamically reconfigurable waveform manipulation. [3]

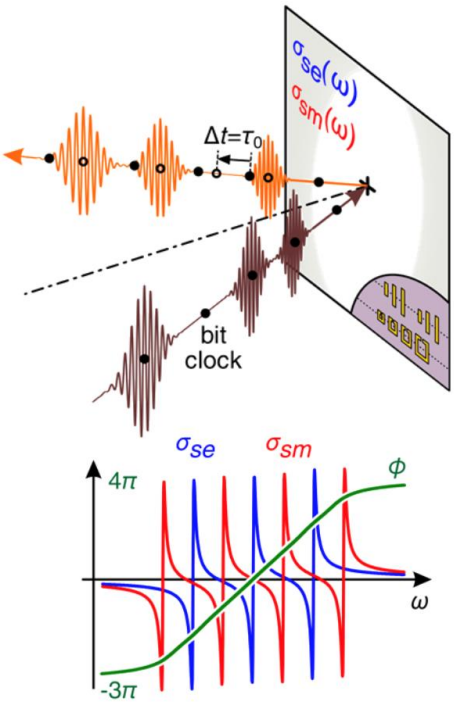

Fig. 2. An arbitrary broadband signal can be perfectly reflected and arbitrarily time shifted by a metasurface with specific trains of alternating electric and magnetic resonances in their sheet conductivities that implement a broadband *linear* phase shift. [2]

Optical force and opto-mechanical coupling in plasmonic metasurfaces: We develop opto-mechanical dynamic control of the electromagnetic properties of metasurfaces with wide modulation bandwidth. We showed that the optical force in suspended graphene plasmonic cavities can implement strong opto-mechanical coupling, mechanical state switching and non-linearity. We explored NEMS-based tunable IR metasurfaces embedding nano-cantilevers into complementary SRRs suspended over individual wells. The cantilevers can be mechanically actuated by electrostatic force, crating a tunable metamaterial, but also constitute the first step towards implementing nonlinearity and opto-mechanical coupling mediated by the dynamic optical force resulting from the strong local resonant fields in the metasurface. [4]

Future Plans

Dark surface state lasers: Experimental realization of NIR and VIS dark-mode surface lasers with collaborators and analyze their behavior validating our theory. Develop theory for finite systems and nontrivial finite-width functionalized lasing output beams. Explore theory for electrically pumped dark-state surface lasers.

Exploration of broadband multi-resonant metasurfaces: We will further explore theory of multi-resonant broadband metasurfaces for arbitrary large phase- and group-delay wavefront manipulations, especially extending to combined spatio-temporal broadband phase control.

Enhanced nonlinearity by radiation control: Metal-based metasurfaces can have huge nonlinearities, which are tunable in frequency. We design metasurfaces that separately control linear and nonlinear radiation damping, enabling tailored optical nonlinearities and enhanced THz generation by metasurfaces with managed radiation damping (maximizing Q-factor by suppressing linear radiation damping) and critical coupling to pump radiation (perfectly absorbing).

Opto-mechanical coupling in metasurfaces: Develop theory and possible realistic designs for graphene based nonlinear metasurfaces based on opto-mechanical coupling of graphene plasmons and cavity phonons. Explore theory of chiral surface modes for lateral optical force.

Development of computational tools: We will continue to develop our self-consistent FDTD calculations for non-linear and gain materials, enabling realistic simulations that include spontaneous emission and noise to model luminescence and the transition from luminescence to lasing and allow comparison with experimental data.

References

1. S. Droulias, T. Koschny, C. M. Soukoulis, ACS Photonics 5, 3788 (2018);
   S. Droulias, A. Jain, T. Koschny, C. M. Soukoulis, Phys. Rev. Lett. 180, 073901 (2017).

2. O. Tsilipakos, T. Koschny, C. M. Soukoulis, ACS Photonics, 5, 1101 (2018);
   V. Ginis, P. Tassin, T. Koschny, C. M. Soukoulis, Appl. Phys. Lett. 108, 031601 (2016).

3. O Tsilipakos, A. C. Tasolamprou, T. Koschny, M. Kafesaki, E. N. Economou, and C. M. Soukoulis, Advanced Optical Materials, 6, 1800633 (2018);
   A. Tasolamprou, T. Koschny, M. Kafesaki, C. M. Soukoulis, ACS Photonics, 4, 2782 (2017).

4. P. Zhang, N. H. Shen, T. Koschny, C. M. Soukoulis, ACS Photonics 4, 181 (2017);
   Q. Wang, D. Mao, P. Liu, T. Koschny, C. M. Soukoulis, L. Dong,
   J. Microelectromechanical Systems 26, 1371 (2017).

Publications

1. R. G. Peng, Z. Q. Xiao, Q. Zhao, F. L. Zhang, Y. G. Meng, B. Li, J. Zhou, Y. C. Fan, P. Zhang, N. H. Shen, T. Koschny, and C. M. Soukoulis, "Temperature-Controlled Chameleonlike Cloak," Physical Review X, 7, 011033 (2017).
2. S. Droulias, A. Jain, Th. Koschny, and C. M. Soukoulis, "Novel Lasers Based on Resonant Dark States," Physical Review Letters, 118, 073901 (2017).
3. S. Droulias, A. Jain, Th. Koschny, and C. M. Soukoulis, "Fundamentals of Metasurface Lasers Based on Resonant Dark States," Physical Review B, 96, 155143 (2017).
4. G. Georgiou, N. H. Shen, J. G. Rivas, Th. Koschny, and C. M. Soukoulis, "Photoimprinted Controllable Fano Resonance in the Terahertz Regime," ACS Photonics, 4, 1785-1789 (2017).
5. Th. Koschny, C. M. Soukoulis, and M. Wegener, "Metamaterials in Microwaves, Optics, Mechanics, Thermodynamics, and Transport," Journal of Optics, 19, 084005 (2017).
6. A. Tasolamprou, Th. Koschny, M. Kafesaki, C. M. Soukoulis, "Near-Infrared and Optical Beam Steering and Frequency Splitting in Air-Holes-in-Silicon Inverse Photonic Crystals," ACS Photonics, 4, 2782 (2017).
7. P. Zhang, N. H. Shen, Th. Koschny, and C. M. Soukoulis, "Surface-Plasmon-Mediated Gradient Force Enhancement and Mechanical State Transitions of Graphene Sheets," ACS Photonics, 4, 181- 187 (2017).
8. G. Kenanakis, C. P. Mavidis, E. Vasilaki, N. Katsarakis, M. Kafesaki, E. N. Economou, and C. M. Soukoulis, "Perfect Absorbers Based on Metal-Insulator-Metal Structures in the Visible Region: A Simple Approach for Practical Applications," Applied Physics A-Materials Science & Processing, 123, 77 (2017).
9. E. Ozgun, A. E. Serebryannikov, E. Ozbay, C. M. Soukoulis, "Broadband Mixing of PT-symmetric and PT-broken Phases in Photonic Heterostructures with a One-dimensional Loss/Gain Bilayer," Scientific Reports, 7, 15504 (2017).
10. O. Tsilipakos, A. C. Tasolamprou, Th. Koschny, M. Kafesaki, E. N. Economou, and C. M. Soukoulis, "Dielectric Rod Metasurfaces: Exploiting Toroidal and Magnetic Dipole Resonances," 2017 11th International Congress on Engineered Materials Platforms for Novel Wave Phenomena, 355-357 (2017).
11. Z. Viskadourakis, K. C. Vasilopoulos, E. N. Economou, C. M. Soukoulis, and G. Kenanakis, "Electromagnetic Shielding Effectiveness of 3D Printed Polymer Composites," Applied Physics A- Materials Science & Processing, 123, 736 (2017).
12. Q. Wang, D. Mao, P. Liu, Th. Koschny, C. M. Soukoulis, and L. Dong, "NEMS-Based Infrared Metamaterial via Tuning Nanocantilevers Within Complementary Split Ring Resonators," J. Microelectromechanical Systems, 26, 1371 (2017).
13. Z. J. Wang, L. Q. Jing, K. Yao, Y. H. Yang, B. Zheng, C. M. Soukoulis, H. S. Chen, and Y. M. Liu, "Origami-Based Reconfigurable Metamaterials for Tunable Chirality," Advanced Materials, 29, 1700412 (2017).
14. Y. H. Yang, L. Q. Jing, L. Shen, Z. J. Wang, B. Zheng, H. P. Wang, E. P. Li, N. H. Shen, Th. Koschny, C. M. Soukoulis, and H. S. Chen, "Hyperbolic Spoof Plasmonic Metasurfaces," NPG Asia Materials, 9, e428 (2017).
15. O. Tsilipakos, Th. Koschny, and C. M. Soukoulis, "Antimatched Electromagnetic Metasurfaces for Broadband Arbitrary Phase Manipulation in Reflection," ACS Photonics, 5, 1101 (2018).

16. M. Fang, K. K. Niu, Z. X. Huang, W. E. I. Sha, X. L. Wu, T. Koschny, and C. M. Soukoulis, “Investigation of Broadband Terahertz Generation from Metasurface,” Optics Express, 26, 14241-14250 (2018).
17. S. Droulias, T. Koschny, and C. M. Soukoulis, “Finite-Size Effects in Metasurface Lasers Based on Resonant Dark States,” ACS Photonics, 5, 3788-3793 (2018).
18. Y. Fan, F. Zhang, N.-H. Shen, Q. Fu, Z. Wei, H. Li, and C. M. Soukoulis, “Achieving a High-Q Response in Metamaterials by Manipulating the Toroidal Excitations,” Physical Review A, 97, 033816 (2018).
19. B. Peng, H. Zhang, H. Z. Zhao, K. Xu, G. Ni, J. Li, H. Y. Zhu, and C. M. Soukoulis, “Chemical Intuition for High Thermoelectric Performance in Monolayer Black Phosphorus, α-Arsenene and aW- Antimonene,” Journal of Materials Chemistry A, 6, 2018-2033 (2018).
20. C. M. Soukoulis, “Back to Basics: History of Photonic Crystals and Metamaterials,” Photoniques, 50-56 (March-April 2018).
21. Y. C. Fan, N. H. Shen, F. L. Zhang, Q. Zhao, Z. Y. Wei, P. Zhang, J. J. Dong, Q. H. Fu, H. Q. Li, and C. M. Soukoulis, “Photoexcited Graphene Metasurfaces: Significantly Enhanced and Tunable Magnetic Resonances,” ACS Photonics, 5, 1612-1618 (2018).
22. L. Peng, Y. T. Chen, Y. H. Yang, Z. Y. Wang, F. X. Yu, G. F. Wang, N. H. Shen, B. L. Zhang, C. M. Soukoulis, and H. S. Chen, “Spin Momentum-Locked Surface States in Metamaterials without Topological Transition,” Laser & Photonics Reviews, 12, 1800002 (2018).
23. B. Peng, K. Xu, H. Zhang, Z. Ning, H. Shao, G. Ni, J. Li, Y. Zhu, H. Zhu, and C. M. Soukoulis, “1D Nanostructures: 1D SbSeI, SbSI, and SbSBr with High Stability and Novel Properties for Microelectronic, Optoelectronic, and Thermoelectric Applications,” Advanced Theory and Simulations, 1, 170000 (2018).
24. O Tsilipakos, A. C. Tasolamprou, T. Koschny, M. Kafesaki, E. N. Economou, and C. M. Soukoulis, “Pairing Toroidal and Magnetic Dipole Resonances in Elliptic Dielectric Rod Metasurfaces for Reconfigurable Wavefront Manipulation in Reflection, Advanced Optical Materials, 6, 1800633 (2018).
25. S. Droulias, T. Koschny, M. Kafesaki, C. M. Soukoulis, “On loss compensation, amplification and lasing in metallic metamaterials,” Nanomaterials and Nanotechnology, 9, 1-12 (2019).
26. M. Fang, N. H. Shen, W. E. I. Sha, Z. X. Huang, T. Koschny and C. M. Soukoulis, "Nonlinearity in the Dark: Broadband Terahertz Generation with Extremely High Efficiency,” Physical Review Letters, 122, 027401 (2019).

Project Title: Complex magnetism and emergent phenomena in correlated electron oxide materials

Principal Investigator: Prof. Hari Srikanth
University of South Florida, Department of Physics, PHY 114
4202 East Fowler Ave, Tampa, FL 33620
E-mail: sharihar@usf.edu

Co-Principal Investigator: Prof. Manh-Huong Phan
University of South Florida, Department of Physics, PHY 114
4202 East Fowler Ave, Tampa, FL 33620
E-mail: phanm@usf.edu

Project Participants (USF): Eleanor Clements (Ph.D. student), Richa Pokharel Madhogaria (Ph.D. student), Joshua Robles-Garcia (Ph.D. student), and Vijaysankar Kalappattil (Postdoctoral fellow).

Project Collaborators: Prof. David Mandrus (The University of Tennessee) and Prof. Sang-Wook Cheong (Rutgers University)

Other Collaborators: Dr. Xavier Moya (Cambridge University, UK), Prof. Dang Toan, Duytan University, Vietnam), Prof. Matthias Batzill (University of South Florida)

Program Scope:

Transition-metal oxides exhibit rich complexity in their fundamental physical properties determined by the intricate interplay between structural, electronic and magnetic degrees of freedom. The overall goal of our DOE funded project is to employ a unique approach that combines DC and AC magnetic susceptibility measurements, neutron diffraction, synchrotron X-ray diffraction with relatively unconventional RF transverse susceptibility (TS), magnetocaloric effect (MCE) and spin Seebeck effect (SSE) to yield new insights into the ground state magnetism in a wide variety of complex oxides and emerging systems. In particular, we have demonstrated the important impacts of phase coexistence, reduced dimensionality, magnetic proximity, strain, and anisotropy on the exotic magnetic properties in quasi-one-dimensional (1D) spin chain compounds of $Ca_3Co_{2-x}T_xO_6$ (T = Mn or Fe, x=0, 0.05, ...1), multicaloric double perovskites (La_2CoMnO_6, Y_2CoMnO_6, Pb_2CoWO_6), strain-mediated $La_{0.7}R_{0.3}MnO_3/BaTiO_3$ (R=Ca and Sr) and $[Fe_3O_4/Cu]n$ heterostructured films, $Y_3Fe_5O_{12}$ (YIG)/C_{60}/Pt multilayers, exchange-coupled $Fe_3O_4/CoFe_2O_4$ core/shell nanoparticles, and Fe_3O_4 nanorods grown on $SrTiO_3$ films. Other research efforts include the exploration of exotic magnetism in strongly correlated systems that host topologically nontrivial states of varying dimensionality and topological winding number: the chiral soliton lattice in $Cr_{1/3}NbS_2$, the Bloch-type SkL in MnSi, and the Neel SkL in GaV_4S_8, as well as the new discovery of strong room-temperature ferromagnetism in VSe_2 at the single layer limit.

We present here selective results from $Ca_3Co_2O_6$, La_2CoMnO_6, and $Cr_{1/3}NbS_2$, highlighting the important effects of reduced dimensionality, strain, phase coexistence, magnetic anisotropy, and magnetic proximity in correlated electron materials.

Recent Progress:

1. Emergence of a new magnetic phase in the spin chain compound $Ca_3Co_2O_6$ under high pressure

Quasi-one-dimensional (1D) spin chain $Ca_3Co_2O_6$, which combines geometric frustration with intrinsic low-dimensionality giving rise to complex magnetism (Fig. 1a), continues to attract a great deal of interest. Our MCE study has established a new and comprehensive magnetic phase diagram for a single crystal of $Ca_3Co_2O_6$ (grown by Prof. Cheong's group at RU) consistent with recently identified spin-density wave and short-range order phases (*Phys. Rev. B 89, 144414, 2014*). A systematic magnetic study on $Ca_3Co_2O_6$ nanocrystaline samples synthesized by our advanced sol-gel method has shown that grain size reduction to just below the maximum correlation length has no significant effect on the appearance of the low-temperature magnetization steps (Fig. 1b). Our finding indicates that correlations in the *ab*-plane are more important than correlations along the *c*-axis in the appearance of the plateaus, resolving issues that remained unexplained in the literature (*Phys. Rev. B*, submitted).

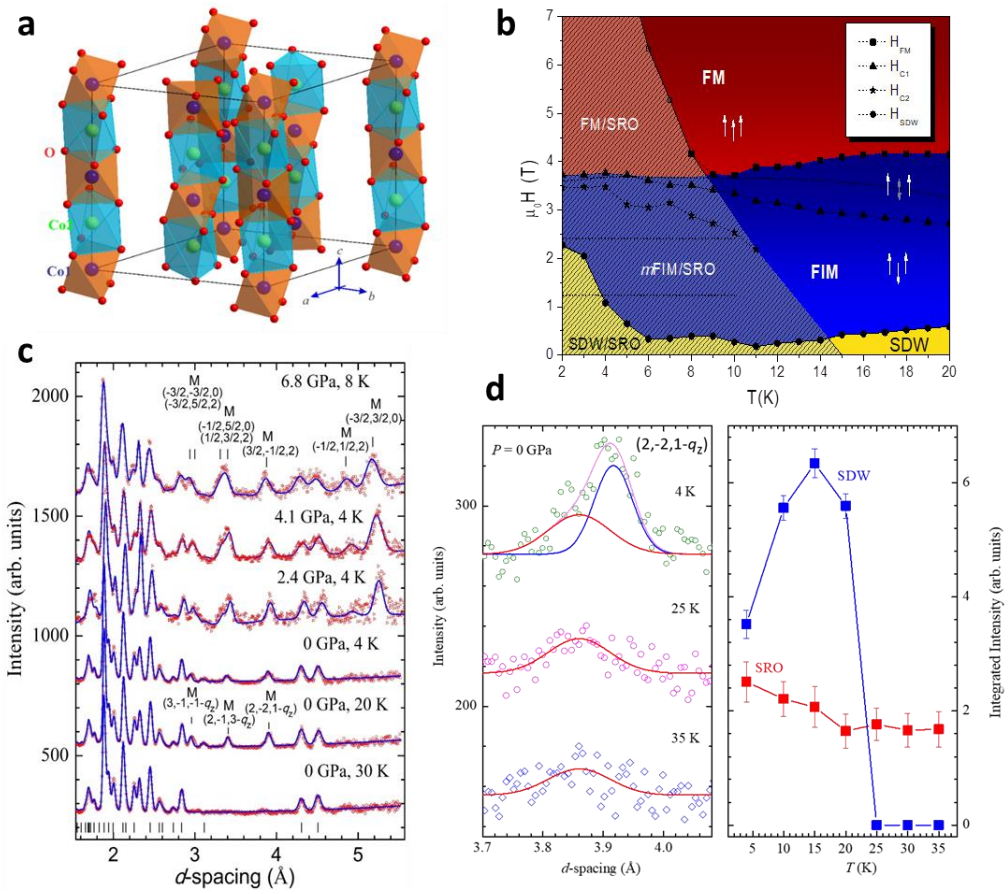

Figure 1: (a) A rhombohedral crystal structure of $Ca_3Co_2O_6$; (b) Magnetic phase diagram including ferromagnetic (FM), ferrimagnetic (FIM), metastable FIM (*m*FIM), short-range-order (SRO), and spin-density wave (SDW) phases for polycrystalline $Ca_3Co_2O_6$. (b) Neutron diffraction patterns of the same $Ca_3Co_2O_6$, measured at selected pressures up to 6.8 GPa and low temperatures, and processed by the Rietveld method. The experimental points and calculated profiles are shown. The ticks below represent the calculated positions of the structural peaks. The positions of the characteristic magnetic peaks of the SDW phase at ambient pressure and collinear AFM phase at high pressure are marked as "M" and relevant peak indexes are given. (d) The sections of the diffraction patterns demonstrating evolution of the peaks associated with the long rage SDW and short range magnetic order (left) and temperature dependences of their intensities (right).

In our recent collaboration with Prof. Toan Dang of Duy Tan University, we have demonstrated for the first time that the symmetry of the long range magnetic order in a quasi-one-dimensional spin chain compound such as $Ca_3Co_2O_6$ is highly sensitive to application of high pressure (*Phys. Rev. B 98, 134435, 2018*). The lattice compression leads to the suppression of the spin density wave magnetic phase and the stabilization of the collinear commensurate antiferromagnetic phase. The role of the competing intra- and interchain magnetic interactions mediated by variation of interatomic distances has been analyzed, pointing to more significant increase of intrachain ones upon compression. The subsequent raise of the J_1/J_{23} magnetic interaction parameters ratio is a possible reason for the observed pressure-induced magnetic phase transformation. The pressure evolution of the Néel temperature of the pressure-induced AFM phase has been analyzed and found a good agreement with the experimental value. We are currently investigating the effects of reduced dimentionality and high pressure on the low-temperature spin dynamics and related magnetization relaxation processes in $Ca_3Co_{2-x}T_xO_6$ (T = Mn or Fe, x=0, 0.05, ...1).

2. A new magnetic phase digram of La_2CoMnO_6: Evidence for long-range ferromagnetic order and spin frustration

Double perovskite oxides ($A_2BB'O_6$) have generated growing interest in the scientific community due to their outstanding physical properties with composition variations. Among them, La_2CoMnO_6 (LCMO) emerges as an insulating ferromagnet with strong magnetodielectric coupling, but its ground state magnetic properties are not well understood.

Using complementary magnetic studies, we have revealed, for the first time, the underlying ground state magnetism and critical behavior in LCMO (*Phys. Rev. B, accepted*). Neutron diffraction evidences a long-range ferromagnetic ordering, which is also corroborated by a critical exponents analysis. An analysis of the magnetization dynamics by means of linear and nonlinear ac magnetic susceptibilities marks the presence of two distinct cluster glass-like states that emerge at low temperatures. The isothermal entropy change as a function of temperature and magnetic field (H) is exploited to investigate the mechanism of stabilization of the magnetic phases across the H-T phase diagram. In the regime of the phase diagram where thermal energy is sufficiently low, regions of competing interactions due to local disorder become stabilized and display glass-like dynamics. The freezing mechanism of clusters is illustrated using a unique probe of transverse susceptibility that isolates the effects of the local anisotropy of the spin clusters. A comparative study for annealed LCMO shows the increase in the grain boundaries and antiphase, however, magnetic transitions remain preserved.

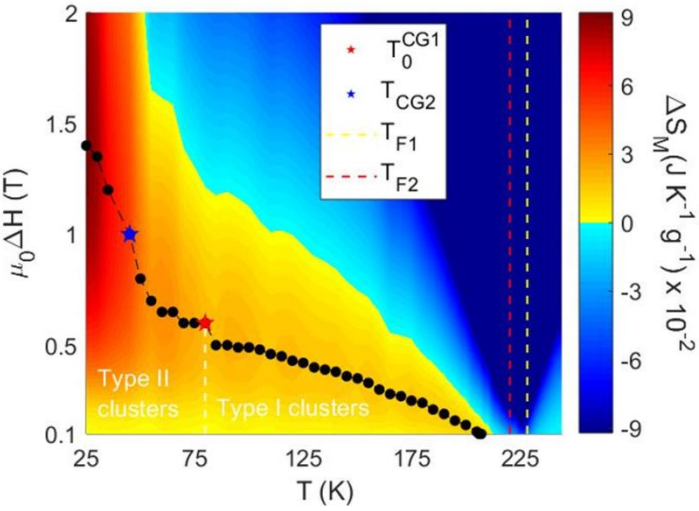

Figure 2: A new magnetic phase diagram is established from the MCE study. Surface plot showing the change in ΔS_M at all temperature and field range. All four phases are shown: T_{F1}= first FM transition temperature, T_{F2} = second FM transition temperature, T_0^{CG1} = freezing point of type I clusters and T_{CG2} = marks the presence of type II clusters.

3. A new magnetic phase diagram and spin dynamics in the chiral helimagnet $Cr_{1/3}NbS_2$

$Cr_{1/3}NbS_2$ is a unique example of a hexagonal chiral helimagnet with high crystalline anisotropy, and has generated growing interest for a possible magnetic field control of the incommensurate spin spiral. However, a clear understanding of the ground state magnetism, critical behavior and spin dynamics in this system is lacking.

In collaboration with Prof. Mandrus' group at the University of Tennessee, we have studied the static and dynamic magnetic properties of single crystalline $Cr_{1/3}NbS_2$. We have found that at magnetic fields above the critical field for the IC-C phase transition, a second-order transition to an FFM state occurs at T_C. This transition is described by the 3D Heisenberg model. At moderate and low magnetic fields, ΔS_M clearly defines the critical fields of the onset of the chiral and ferromagnetic states, including crossovers within the CSL phase. A new comprehensive phase diagram (Fig. 3a) has been constructed for the first time from the magnetization and MCE data (*Nature: Scientific Reports* 7, 6545 (2017)).

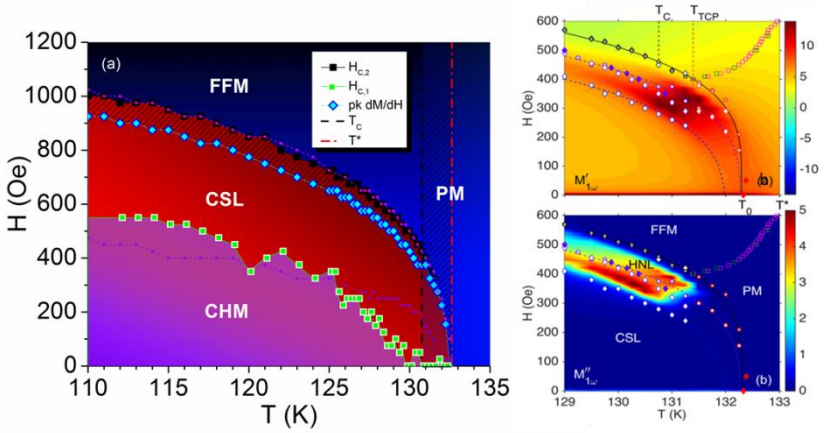

Figure 3: (a) *H-T* phase diagram from $\Delta S_M(T,H)$ and magnetization data. The shaded region between T_C and T^* indicates strong FM correlations in the PM phase. The hashed area between $H_{C,2}$ and H_{peak} defines the highly non-linear CSL. $H_{C,1}$ and $H_{A,1}$ (purple line) form a phase pocket of the linear CSL. $H_{A,2}$ (pink line) corresponds exactly to $H_{C,2}$. (b) *H-T* phase diagram determined from the linear and nonlinear components of the ac magnetic response plotted onto $M'_{1\omega}(H,T)$ and $M''_{1\omega}(H,T)$ for (n = 2 – 5) at f = 10,000 Hz.

Since the behavior of the magnetic response of long-wavelength structures includes contributions from spins on atomic length-scales and from the macroscopic spin structure, we have studied the frequency dependence of the ac magnetic response of $Cr_{1/3}NbS_2$ to identify the onset of the collective response of a spin structure that is coherent over large length-scales (Fig. 3b). For the first time, we have experimentally resolved the tricritical point at T_{TCP} in a temperature regime above the ferromagnetic Curie temperature which separates the linear and nonlinear magnetic regimes of the CSL at the phase transition (*Phys. Rev. B 97, 214438 (2018)).*

Future plans:

Several multicaloric double perovskites ($A_2BB'O_6$: A=La, Y, Pb; B=Co, Fe; B'=Mn, W), exchange-coupled $Fe_3O_4/CoFe_2O_4$ core/shell nanoparticles, $[Fe_3O_4/Cu]_n$ and $Y_3Fe_5O_{12}$ (YIG)/C_{60}/Pt multilayer films, and systems that host noncollinear spin textures ($Cr_{1/3}NbS_2$, MnSi, GaV_4S_8), are identified in which our combined analytical method will continue to yield new insights into the magnetic ground states, phase evolution and spin dynamics. To understand the reduced dimensionality and confinement effects in 2D van der Waals magnetic systems which are of topical interest, we will investigate the magnetic and magneto-transport properties of transition metal dichalcogenides such as XM_2 (X=V, Mn, W, Ti; M=Se, S, Te) at the single layer limit. Our research efforts over the next years will be targeted towards elucidating these emergent aspects of correlated magnetic systems that could have important impacts on future quantum devices and computing technology.

Publications:

List of papers acknowledging DoE grant support during the 2-year period (2017-2018):

(Students and postdocs' names are italicized, PI and co-PI names are in bold)

1. "Field-dependence of the Nonlinear Magnetic Response and Tricritical Point in the Monoaxial Chiral Helimagnet $Cr_{1/3}NbS_2$" - *E. Clements*, ***R. Das***, **M.H. Phan**, L. Li, V. Keppens, D. Mandrus, M. Osofsky, and **H. Srikanth**, ***Physical Review B*** 97, 214438 (2018)
2. "Emergent magnetic phase transformations in the spin chain compound $Ca_3Co_2O_6$ under high pressure" - D. P. Kozlenko, N. T. Dang, N.O. Golosova, S. E. Kichanov, E. V. Lukin, H.-P. Liermann, K. V. Glazyrin, S. H. Jabarov, T.L. Phan, B. N. Savenko, *P. Lampen-Kelley*, *E. Clements*, **H. Srikanth**, and **M.H. Phan**, ***Physical Review B*** 98, 134435 (2018)
3. "Strong Room Temperature Ferromagnetism in VSe_2 Monolayers on van der Waals substrates" - M. Bonilla, S. Kolekar, Y. Ma, H. Coy Diaz, *V. Kalappattil*, ***R. Das***, *T. Eggers*, **M.H. Phan**, and M. Batzill, ***Nature Nanotechnology*** 13, 289 (2018)
4. "Critical Behavior and Macroscopic Phase Diagram of the Monoaxial Chiral Helimagnet $Cr_{1/3}NbS_2$" - *E. Clements*, ***R. Das***, L. Li, Paula J. L. Kelley, **M.H. Phan**, V. Keppens, D. Mandrus, and **H. Srikanth**, ***Nature: Scientific Reports*** 7, 6545 (2017)
5. "Epitaxial Magnetite Nanorods with Enhanced Room Temperature Magnetic Anisotropy" - S. Chandra, ***R. Das***, *V. Kalappattil*, C. Harnegea, R. Nechache, **M.H. Phan**, F. Rosei, and **H. Srikanth**, ***Nanoscale*** 9, 7858 (2017)
6. "Coexistence of long-range ferromagnetism and glassy behavior in the double perovskite La_2CoMnO_6," *R.P. Madhogaria*, ***R. Das***, N.T. Dang, *E. Clements*, ***V. Vijaysankar***, D.P. Kozlenko, **M.H. Phan**, H. Srikanth, ***Physical Review B*** (revised)
7. "Giant Low-field Magnetocaloric Effect and Refrigerant Capacity in Reduced Dimensionality $EuTiO_3$ Multiferroics" - R. Das, R. Prabhu, N. Venkataramani, S. Prasad, L. Li, M.H. Phan, V. Keppens, D. Mandrus, and H. Srikanth, ***Nature: Scientific Reports*** (revised)
8. "Magnetic anisotropy and switching behavior of $Fe_3O_4/CoFe_2O_4$ core/shell nanoparticles" - ***R. Das***, *J. Robles*, *M. Glassell*, *V. Kalappattil*, **M.H. Phan**, **H. Srikanth**, ***Journal of Electronic Materials*** 48, 1461 (2018)
9. "Improving the heating efficiency of iron oxide nanoparticles by tuning their shape and size" - *Z. Nemati*, ***J. Alonso***, I. Rodrigo, ***R. Das***, E. Garaio, J.A. Garcia, I. Orue, **M.H. Phan**, and **H. Srikanth**, ***The Journal of Physical Chemistry C*** 122, 2367 (2018)
10. "Exchange-coupled $Fe_3O_4/CoFe_2O_4$ nanoparticles for advanced magnetic hyperthermia" - *J. Robles*, ***R. Das***, M. Glassell, **M.H. Phan**, **H. Srikanth**, ***AIP Advances*** 8, 056719 (2018)
11. "Role of the magnetic anisotropy in organic spin valves" - *V. Kalappattil*, R. Geng, S. H. Liang, R. C. Subedi, T. D. Nguyen, W. B. Zhao, X. G. Li, ***R. Das***, D. Mukherjee, S. Chandra, **H. Srikanth**, and **M.H. Phan**, ***Journal of Science: Advanced Materials and Devices*** 2, 378 (2017)

12. "Crystal structure and magnetic coupling of Ti-doped $Bi_{0.84}La_{0.16}FeO_3$ at morphotropic phase boundary" - P.T. Tho, *E.M. Clements*, D.H. Kim, N. Tran, M.S. Osofsky, **M.H. Phan**, T. L. Phan, and B. W. Lee, ***Journal of Alloys and Compounds*** 741, 59 (2018)

13. "Superparamagnetic Iron Oxide Nanodiscs for Hyperthermia Therapy: Does Size Matter?" - *Z.N. Porshokouh*, S. M. Salili, ***J.A. Masa***, A. Ataie, ***R. Das***, **M.H. Phan,** and **H. Srikanth**, ***Journal of Alloys and Compounds*** 714, 709 (2017)

14. "Iron oxide nanospheres and nanocubes for hyperthermia therapy: A comparative study" - *Z. Nemati*, ***R. Das***, ***J. Alonso***, *E. Clements*, **M.H. Phan**, and **H. Srikan**th, ***Journal of Electronic Materials*** 46, 3764 (2017)

15. "Photopolymerization-based synthesis of iron oxide nanoparticle embedded PNIPAM nanogels for biomedical applications" - D.J. Denmark, R.H. Hyde, C.Gladney, **M.H. Phan**, K.S. Bisht, **H. Srikanth**, P. Mukherjee, and S. Witanachchia, Drug Delivery 24, 1317 (2017)

16. "A novel contactless magneto-LC resonance technology for real-time respiratory motion monitoring" - *O. Thiabgoh*, *T. Eggers*, and **M.H. Phan**, ***Sensors and Actuators A*** 265, 120 (2017)

17. "Impact of the transverse magnetocrystalline anisotropy of a Co coating layer on the magnetoimpedance response of FeNi-rich nanocrystalline ribbon" - *T. Eggers*, D.S. Lam, *O. Thiabgoh*, J. Marcin, P. Švec, N.T. Huong, I. Škorvánek, and **M.H. Phan**, ***Journal of Alloys and Compounds*** 741, 1105 (2018)

18. "Real-time monitoring of position and motion of a non-stationary object with a highly sensitive magnetic impedance sensor" - *O. Thiabgoh, T. Eggers*, *V.O. Jimenez*, S.D. Jiang, J.F. Sun, and **M.H. Phan**, ***Journal of Science: Advanced Materials and Devices*** 3, 122 (2018)

19. "Relating surface roughness and magnetic domain structure to giant magneto-impedance of Co-rich melt-extracted microwires" - S.D. Jiang, *T. Eggers*, *O. Thiabgoh*, D.W. Xing, W. D. Fei, H. X. Shen, J. S. Liu, J.R. Zhang, W.B. Fang, J.F. Sun, **H. Srikanth**, and **M.H. Phan**, ***Nature: Scientific Reports*** 7, 46253 (2017)

20. "Enhanced Curie temperature and cooling efficiency in melt-extracted $Gd_{50}(Co_{69.25}Fe_{4.25}Si_{13}B_{13.5})_{50}$ microwires" - Y. Bao, H.X. Shen, D.W. Xing, S. Jiang, J.F. Sun, **M.H. Phan**, ***Journal of Alloys and Compounds*** 692, 658 (2017)

21. "Enhancement of giant magneto-impedance in series Co-rich microwires for low field sensing applications" - *S. D. Jiang*, *T. Eggers*, *O. Thiabgoh*, D. W. Xing, W. B. Fang, J. F. Sun, **H. Srikanth**, and **M.H. Phan,** ***Journal of Electronic Materials*** 47, 2667 (2018)

22. "Magnetic iron oxide-carbon nanocomposites: Impacts of carbon coating on the adsorption and inductive heating responses," T.L.H. Pham, T.H. Le, L. Hoang, H.T. Le, T.A. Tran, V.Q. Nguyen, A. Javier, **M.H. Phan**, A.T. Pham, ***Journal of Alloys and Compounds*** 739, 139 (2018)

Effects of Pressure and Field on Magnetostructural Phase Transitions

Shane Stadler, Louisiana State University, Department of Physics and Astronomy

Naushad Ali, Southern Illinois University, Department of Physics

Program Scope

The objective of this project is to discover and explore new solid-state caloric materials, and to understand the origins of their physical behaviors including magnetocaloric effects, barocaloric effects, and transport properties. Materials that exhibit extreme changes in magnetostructural and transport properties linked to magnetostructural phase transitions near room temperature are relatively rare, and often lead to multifunctional properties important for modern technologies. In this project we study multifunctional materials including multicaloric materials with the goal of improving our understanding of the magnetostructural phase transitions that are responsible for their novel physical behaviors.

Recent Progress

Multicaloric effects and reversibility in MnTX systems: MnTX based (T = Co, Ni, Fe; X = Ge, Si) intermetallic compounds can be formed that exhibit temperature and field induced magnetostructural transitions (MSTs) that lead to shape-memory phenomena, magnetocaloric effects (MCEs), and volume anomalies near room temperature.[1-3] We had previously found two isostructurally substituted MnTX compounds that exhibit large magnetocaloric effects at a magnetostructural transition near room temperature, namely, $(MnNiSi)_{1-x}(MnFeGe)_x$ and $(MnNiSi)_{1-x}(FeCoGe)_x$.[4,5] These materials exhibit magnetostructural transitions in temperature ranges that span room temperature, and can be tuned by varying the compositions or by applying hydrostatic pressure. Of particular importance was the observation of pronounced pressure-induced temperature shifts of the magnetostructural transitions in these materials by up to -10 K/kbar (in $(MnNiSi)_{1-x}(FeCoGe)_x$).[5]

The large pressure-induced temperature shifts led to a study of the barocaloric effects in these materials, resulting in impressive entropy changes (greater than 70 J/kgK) and refrigeration cooling powers (RCP) that approached 1500 J/kg for an applied pressure of 2.7 kbar (see Fig. 1 for x = 0.38 for decompression).[6] To note, this system shows *inverse* barocaloric effects,

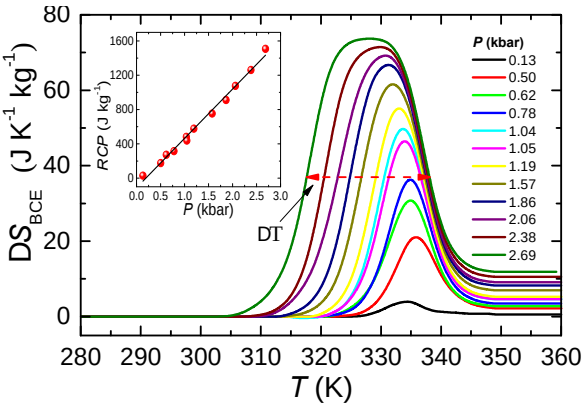

Fig. 1. The entropy change (ΔS) as a function of temperature and pressure for the compound with x = 0.38. ΔT ~ 25 K is the full width at half max (dashed arrow) of the ΔS curve with P = 2.69 kbar. The inset shows the RCP as a function of pressure (P). [Ref. 6]

meaning that the entropy change is positive and the temperature change is negative with compression. This system also shows a large magnetocaloric effect at the same transition.[5] These results were very encouraging, yet there are many questions yet to be answered, the most important of which pertain to the temperature change in this system, and the reversibility.

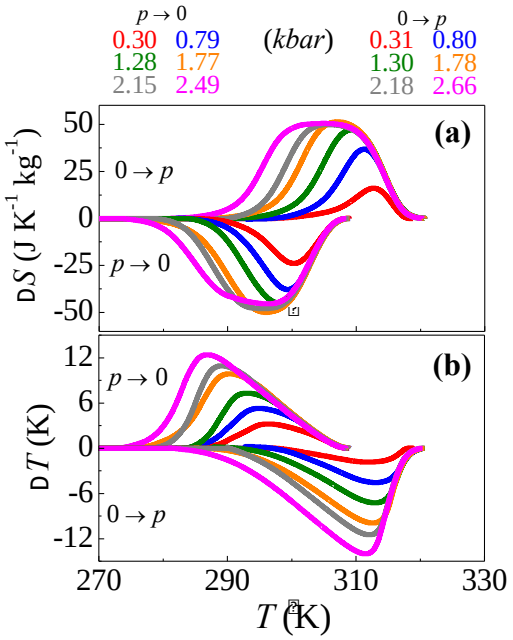

Fig. 2. Barocaloric effects of $(MnNiSi)_{1-x}(FeCoGe)_x$ (x = 0.39) as a function of temperature: **(a)** Isothermal entropy change and **(b)** adiabatic temperature change. Each curve represents a different starting temperature. Changes on applying pressure are calculated from heating runs and changes on removing pressure are calculated from cooling curves.

The thermal hysteresis of the magnetostructural transitions in $(MnNiSi)_{1-x}(FeCoGe)_x$, as determined from magnetization measurements, ranges from 10-15 K. This is a detrimental effect in regard to the usefulness of the material in solid state cooling applications, and we have therefore conducted a study of the reversibility of the barocaloric properties. Calorimetry (heat flow) measurements under hydrostatic pressure were performed with a custom-built Cu-Be calorimeter and methods as described in Ref. 7. Barocaloric effects were calculated via the quasi-direct method as the difference between isobaric curves at different pressures following proper paths, i.e. isothermal entropy changes were calculated as $\Delta S(T, \Delta p) = S(T, p_f) - S(T, p_0)$, and adiabatic temperature changes as $\Delta T(S, \Delta p) = T(S, p_f) - T(S, p_0)$, where the lower pressure value was always taken as the normal pressure. Because of the inverse BCE ($dT_i/dp < 0$) and the athermal (hysteresis rate-independent) character of the transition, the transition line crossed on compression (decompression) coincides with the transition line crossed on heating (cooling). Consequently, both ΔS and ΔT on compression (decompression) have been calculated from the isobaric curves on heating (cooling) and are shown in Fig. 2 for $x = 0.39$ (samples with $x = 0.40$ and 0.41 showed similar results but their transitions are shifted to lower temperatures by about 30 K and 60 K, respectively).[8] The maximum temperature change for the $x = 0.39$ was about 14 K and the entropy change was 52 J $kg^{-1}K^{-1}$. Although these are relatively impressive values, it is the reversible components that that are most important for cooling cycles employed in applications.

Reversible entropy changes (ΔS_{rev}), can be computed from the overlap between the irreversible heating and cooling ΔS curves (Fig. 2a) on compression and decompression.[9] It can be seen that there is appreciable overlap at even relatively low pressures $p \geq 0.3$ kbar (see Fig. 3a). The overlap becomes progressively larger with increasing pressure, and achieves giant values (~44 J $kg^{-1}K^{-1}$) at higher pressures ($p >$ ~2 kbar). These values become even more relevant when normalized per unit volume (see Table 1) given the high mass density of the compounds (ρ ~ 7.2 g/cm^3).

Table 1 Summary of barocaloric parameters for $(MnNiSi)_{1-x}(FeCoGe)_x$ compounds.

x	$\|\Delta S\|$	$\|\Delta S\|$	$\|\Delta T\|$	$\|\Delta S_{rev}\|$	$\|\Delta S_{rev}\|$	$\|\Delta T_{rev}\|$	p
	J K^{-1} kg^{-1}	J K^{-1} cm^{-3}	K	J K^{-1} cm^{-3}	J K^{-1} kg^{-1}	K	kbar
0.39	52±5	0.37±0.04	14±2	0.31±0.04	44±5	6±2	2.6
0.40	54±5	0.38±0.04	17±2	0.33±0.04	47±5	4±2	2.3
0.41	40±5	0.28±0.04	10±2	0.17±0.04	24±5	1.8±2	2.3

Reversible adiabatic temperature changes $|\Delta T|_{rev}$ were computed from the subtraction of the isobaric curve on heating at high pressure from the isobaric curve on cooling at normal pressure following adiabatic paths (see Fig. 3b).[10] The reversible temperature change reaches 6 K for a pressure of 2.6 kbar. Previous studies on this material show that the effect is not saturated at this pressure.[6] This reversible value of $|\Delta T|_{rev}$ is in line with direct measurements (i.e., measured with a thermocouple embedded directly in the sample while undergoing compression). Directly measured temperature changes reached up to 4.6 K for an applied hydrostatic pressure of 2.5 kbar.[11]

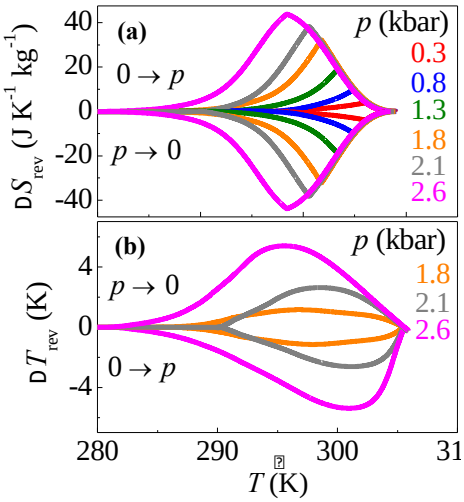

Fig. 3. **(a)** Reversible entropy change (ΔS_{rev}) and **(b)** reversible temperature change (ΔT_{rev}) as a function of temperature and pressure.

This study has shown that the thermal hysteresis in these materials can be overcome to some degree with sufficiently large applied pressures. It would be greatly beneficial, however, to find a way to reduce the thermal hysteresis in these systems through either varying the composition or exploring new synthesis methods or post-melt treatments. We have recently explored the effects of quenching temperature on the magnetostructural transitions and magnetocaloric properties of $(MnNiSi)_{0.62}(FeCoGe)_{0.38}$.[12] As-cast samples were annealed and quenched at temperatures that ranged from 700 ^{o}C (see curve AQ700 in Fig. 4) to 1050 ^{o}C (sample AQ1050). Two trends have been observed with increasing quenching temperature (Fig. 4): the transition shifts to lower temperature, and the thermal hysteresis decreases until the transition becomes quasi-second-order for AQ1050. Applied pressure shifts the transitions to lower temperatures, consistent with the previously reported behavior of this system.[6] However, for all but AQ700, the transition becomes second order for applied pressure on the order of ~1 GPa (or less). The entropy changes remain relatively large from 35 J kg^{-1}K^{-1} for AQ700 to ~22 J kg^{-1}K^{-1} for AQ1050, despite the latter being a quasi-second-order transition. These properties need to be further explored in the context of barocaloric effects and reversibility.

These studies demonstrate the tremendous barocaloric potential near room temperature of some intermetallic magnetic alloys (devoid of rare earth elements) at moderate pressures. The values of the barocaloric effects in these MnNiSi-FeCoGe alloys are amongst the largest reported for magnetic materials. Although they are smaller than the largest effects observed in nonmagnetic

materials, they compare favorably to other systems with larger barocaloric effects, as clearly set out by our work. For one, their operational temperatures span a very wide range and can be precisely controlled by doping. Second, their high mass density which improves their compactness (e.g., see in Table 1 for volume entropy change). Third, their large thermal conductivities improve heat transfer efficiency. Finally, these systems also exhibit large magnetocaloric effects at the same transitions. The possibility of **multicaloric effects** through the simultaneous or successive application of mechanical and magnetic fields allows for the enhancement of the reversible operational range and other multicaloric advantages.

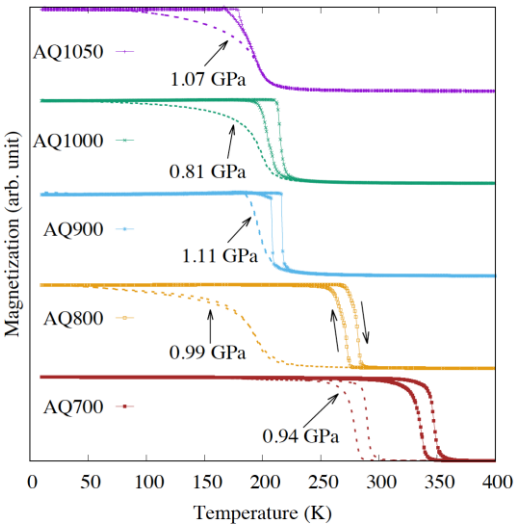

Fig. 4. Magnetization of as a function of temperature, pressure, and quenching temperature of $(MnNiSi)_{0.62}(FeCoGe)_{0.38}$.

Future Plans

We plan take our studies of Mn*TX* multicaloric compounds and Heusler alloys into new directions. The synthesis parameter space will be expanded to include **high-pressure synthesis** (we recently acquired a high-pressure furnace) and thermal quenching to form metastable high-temperature/pressure phases near room temperature. Second, we will synthesize new **magnetic high-entropy alloys** (HEAs) and investigate their phase transitions, and corresponding magnetic and magnetocaloric properties. The Mn*TX* and HEA materials will be fabricated using conventional melting/quenching techniques, as well as under high pressure conditions (~8 GPa) in a high pressure/temperature furnace. The resulting materials will be investigated using magnetometry, transport, thermal, compositional, and structural techniques.

References

[1]E. Liu *et al.*, Nature Commun. **3**, 873 (2012).
[2]T. Samanta *et al.*, Appl. Phys. Lett. **100**, 052404 (2012).
[3]C. L. Zhang *et al.*, Appl. Phys. Lett. **103**, 132411 (2013).
[4]T. Samanta *et al.*, Phys. Rev. B **91**, 020401(R) (2015).
[5]T. Samanta *et al.* J. Appl. Phys. **117** (12), 123911 (2015).
[6]T. Samanta *et al.*, Appl. Phys. Lett. **112**, 021907 (2018).
[7]L. Mañosa *et al.*, Nat. Mater. **9**, 478 (2010).
[8]P. Lloveras et al., Under review.
[9]B. Emre *et al.*, J. Appl. Phys. **113,** 213905 (2013).
[10] A. Aznar *et al.*, Nat. Commun. **8**, 1851 (2017).
[11] A. Us Saleheen, Ph.D. Dissertation (LSU).
[12] Jing-Han Chen *et al.*, Under review.

Publications (2017 – present)

[1] Sudip Pandey, Abdiel Quetz, Anil Aryal, Igor Dubenko, Dipanjan Mazumdar, Shane Stadler, and Naushad Ali, "Magnetocaloric, thermal, and magnetotransport properties of $Ni_{50}Mn_{35}In_{13.9}B_{1.1}$ Heusler alloy," J. Magn. Magn. Mater. **444**, 98 (2017). [DOI: 10.1016/j.jmmm.2017.08.009]

[2], Yury Koshkid'ko, Sudip Pandey, Abdiel Quetz, Anil Aryal, Igor Dubenko, Jacek Cwik, Elvina Dilmieva, Alexander Granovsky, Erkki Lähderanta, Shane Stadler, and Naushad Ali, "Kinetic effects in the magnetic and magnetocaloric properties of metamagnetic $Ni_{50}Mn_{35}In_{14.25}B_{0.75,}$" J. Magn. Magn. Mater. **459**, 98 (2017). [DOI: 10.1016/j.jmmm.2017.11.125]

[3] A. Us Saleheen, T. Samanta, M. Khan, P. W. Adams, D. P. Young, I. Dubenko, N. Ali, and Shane Stadler, "The influence of hydrostatic pressure on the magnetic and magnetocaloric properties of $DyRu_2Si_2$," J. Appl. Phys. **121**, 045101 (2017). [DOI: 10.1063/1.4874466]

[4] S. Pandey, A Quetz, A. Aryal, I. Dubenko, D. Mazumdar, S. Stadler, and N. Ali, "Thermosensitive Ni-based magnetic particles for self-controlled hyperthermia applications," J. Magn. Magn. Mater. **427**, 200 (2017). [DOI: 10.1016/j.jmmm.2016.11.049]

[5] Anil Aryal, Abdiel Quetz, Sudip Pandey, Igor Dubenko, Shane Stadler, and Naushad Ali, "Magnetocaloric effects and transport properties of rare-earth (R= La, Pr, Sm) doped $Ni_{50-x}R_xMn_{35}Sn_{15}$ Heusler alloys," J. Alloys Compd. **717**, 254 (2017). [DOI: 10.1016/j.jallcom.2017.05.096]

[6] Sudip Pandey, Ahmad Us Saleheen, Abdiel Quetz, Jing-Han Chen, Anil Aryal, Igor Dubenko, Philip W. Adams, Shane Stadler, and Naushad Ali, "The effects of hydrostatic pressure on the martensitic transition, magnetic, and magnetocaloric effects of $Ni_{45}Mn_{43}CoSn_{11}$," MRS Comm. **7**(4), 885 (2017). [DOI: 10.1557/mrc.2017.110]

[7] Sudip Pandey, Abdiel Quetz, Anil Aryal, Igor Dubenko, Dipanjan Mazumdar, Shane Stadler, and Naushad Ali, "Magnetic, structural, and magnetocaloric properties of Ni-Si and Ni-Al thermoseeds for self-controlled hyperthermia," *International Journal of Hyperthermia* **33** (7), 779 (2017) [DOI: 10.1080/02656736.2017.1312562]

[8] Anil Aryal, Abdiel Quetz, Sudip Pandey, Tapas Samanta, Igor Dubenko, Margaret Hill, Dipanjan Mazumdar, Shane Stadler, and Naushad Ali, "Magnetostructural phase transitions and magnetocaloric effects in as-cast $Mn_{1-x}Al_xCoGe$ compounds," J. Alloys Compd. **709**, 142 (2017). [DOI: 10.1016/j.jallcom.2017.03.149]

[9] Sudip Pandey, Abdiel Quetz, Anil Aryal, Igor Dubenko, Mikhail Blinov, Igor Rodionov, Valerii Prudnikov, Dipanjan Mazumdar, Alexander Granovsky, Shane Stadler, and Naushad Ali, "Giant field-induced adiabatic temperature changes in In-based off-stoichiometric Heusler alloys," J. Appl. Phys. **121** (13), 133901 (2017). [DOI: 10.1063/1.4979475]

[10] Anil Aryal, Abdiel Quetz, Sudip Pandey, Igor Dubenko, Shane Stadler, and Naushad Ali, "Phase Transitions and Magnetocaloric Properties in $MnCo_{1-x}Zr_xGe$ Compounds," Adv. Condens. Matter Phys. **2017**, 2683789 (2017). [DOI: 10.1155/2017/2683789]

[11] A. Novikov, A. Solokov, E. A. Gan'shina, A. Quetz, I. S. Dubenko, S. Stadler, N. Ali, I. S. Titov, I. D. Rodionov, E. Lähderanta, A. Zhukov, A. B. Granovsky, and R. Sabirianov, "Probing the electronic structure of Ni-Mn-In-Si based Heusler alloy thin films using magneto-optical spectra in martensitic and austenitic phases," J. Magn. Magn. Mater. **432**, 455 (2017) [DOI: 10.1016/j.jmmm.2017.02.012]

[12] Y. Koshkid'ko, S. Pandey, A Quetz, A. Aryal, I. Dubenko, J. Cwik, E. Dilmieva, A. Granovsky, E. Lähderanta, A. Zhukov, S. Stadler, and N. Ali, "Inverse magnetocaloric effects in metamagnetic Ni-Mn-In-based alloys in high magnetic fields," J. Alloys Compnd. **695**, 3348 (2017) [DOI: 10.1016/j/jallcom.2016.12.032]

[13] S. Pandey, A. Quetz, P. J. Ibarra Gaytan, C. F. Sanchez-Valdes, A. Aryal, I. Dubenko, D. Mazumdar, J. L. Sanchez-Llamazares, S. Stadler, and N. Ali, "Magnetic, thermal, and magnetocaloric properties of $Ni_{50}In_{14.5}B_{0.5}$ ribbons," Adv. Mater. Lett. **8**, 1 (2017). [DOI: 10.5185/amlett.2017.1452]

[14] S. Pandey, A. Quetz, A. Aryal, A. Us Saleheen, I. Dubenko, D. Mazumdar, S. Stadler, and N. Ali, "Enhancement of ferromagnetism by substituting Cu for Mn in Ni-Mn-In-B Heusler alloys," Adv. Mater. Lett. **8**, 2 (2017). [DOI: 10.5185/amlett.2017.1403]

[15] M. Khan, O. Alshammari, B. Balasubramanian, B. Das, D. J. Sellmyer, A. Us Saleheen, and S. Stadler, "Controlling the microstructure and associated magnetic properties of $Ni_{0.2}Mn_{3.2}Ga_{0.6}$ melt-spun ribbons by annealing," AIP Adv. **7**, 056230 (2017). [DOI: 10.1063/1.4977892]

[16] S. Pandey, A. Quetz, A. Aryal, I. Dubenko, D. Mazumdar, S. Stadler, and N. Ali, "Large inverse magnetocaloric effects and giant magnetoresistance in Ni-Mn-Cr-Sn Heusler alloys," Magnetochemistry **3**, 3 (2017). [DOI: 10.3390/magnetochemistry3010003]

[17] S. Pandey, A. Quetz, A. Aryal, A. Us Saleheen, I. Rodionov, M. Blinov, M. Prudnikova, I. Dubenko, V. Prudnikov, D. Mazumdar, A. Granovsky, S. Stadler, and N. Ali, "Effects of the partial substitution of Ni by Cr on the transport, magnetic, and magnetocaloric properties of $Ni_{50}Mn_{37}In_{13}$," AIP Advances **7**, 056433 (2017) [DOI: 10.1063/1.4978909]

[18] Tapas Samanta, Pol Lloveras, Ahmad Us Saleheen, Daniel L Lepkowski, Emily Kramer, Igor Dubenko, Philip W Adams, David P Young, Maria Barrio, Josep Ll Tamarit, Naushad Ali, and Shane Stadler, "Barocaloric and magnetocaloric effects in $(MnNiSi)_{1-x}(FeCoGe)_x$," Appl. Phys. Lett. **112** (2), 021907 (2018). [DOI: 10.1063/1.5011743]

[19] Ahmad Us Saleheen, Jing-Han Chen, David P. Young, Igor Dubenko, Naushad Ali, and Shane Stadler, "Critical behavior in Ni_2MnGa and $Ni_2Mn_{0.85}Cu_{0.15}Ga$," J. Appl. Phys. **123**, 203904 (2018). [DOI: doi.org/10.1063/1.5025196]

[20] Jing-Han Chen, Ahmad Us Saleheen, Philip W Adams, David P Young, Naushad Ali, and Shane Stadler, "On entropy determination from magnetic and calorimetric experiments in conventional giant magnetocaloric materials," J. Appl. Phys. **123** (14), 145101 (2018). [DOI: 10.1063/1.5016858]

[21] Sudip Pandey, Jing-Han Chen, Ahmad Us Saleheen, Igor Dubenko, Anil Aryal, Philip W Adams, Shane Stadler, and Naushad Ali, "Specific heat and the influence of hydrostatic pressure on the phase transitions in $Ni_{50}Mn_{35}In_{14.25}B_{0.75}$," J. Magn. Magn. Mater. **463**, 19 (2018). [DOI: 10.1016/j.jmmm.2018.05.029]

[22] Yury Koshkid'ko, Sudip Pandey, Abdiel Quetz, Anil Aryal, Igor Dubenko, Jacek Cwik, Elvina Dilmieva, Alexander Granovsky, Erkki Lähderanta, Shane Stadler, Naushad Ali, "Kinetic effects in the magnetic and magnetocaloric properties of metamagnetic $Ni_{50}Mn_{35}In_{14.25}B_{0.75}$," J. Magn. Magn. Mater. **459**, 98 (2018). [DOI: 10.1016/j.jmmm.2017.11.125]

[23] Sudip Pandey, Abdiel Quetz, PJ Ibarra-Gaytan, CF Sánchez-Valdés, Anil Aryal, Igor Dubenko, Jose Luis Sanchez Llamazares, Shane Stadler, and Naushad Ali, "Magnetostructural transitions and magnetocaloric effects in $Ni_{50}Mn_{35}In_{14.25}B_{0.75}$ ribbons," *AIP Advances* **8** (5), 056434 (2018). [DOI: 10.1063/1.5006467]

[24] Anil Aryal, Abdiel Quetz, CF Sánchez-Valdés, PJ Ibarra-Gaytán, Sudip Pandey, Igor Dubenko, JL Sánchez Llamazares, Shane Stadler, Naushad Ali, "Large reversible magnetic entropy change in rapidly solidified $Ni_{0.895}Cr_{0.105}MnGe_{1.05}$ melt-spun ribbons," *Intermetallics* **97**, 89 (2018). [DOI: 10.1016/j.intermet.2018.04.003]

[25] Sudip Pandey, Ahmad Us Saleheen, Abdiel Quetz, Jing-Han Chen, Anil Aryal, Igor Dubenko, Shane Stadler, and Naushad Ali, "Magnetic and magnetocaloric properties of Ni-Mn-Cr-Sn Heusler alloys under the effects of hydrostatic pressure," *AIP Advances* **8** (5), 056408 (2018). [DOI: 10.1063/1.5005802]

[26] Jing-Han Chen, Ahmad Us Saleheen, Sunil K. Karna, David P. Young, Naushad Ali, and Shane Stadler, "Tuning martensitic transitions in $(NiMnSi)_{0.65}(Fe_2Ge)_{0.35}$ through heat treatment and hydrostatic pressure," J. Appl. Phys. **124**, 203903 (2018). [DOI: 10.1063/1.5051551]

[27] Sudip Pandey, Abdiel Quetz, PJ Ibarra-Gaytan, CF Sanchez-Valdes, Anil Aryal, Igor Dubenko, Dipanjan Mazumdar, JL Sanchez Llamazares, Shane Stadler, and Naushad Ali, "Effects of annealing on the magnetic properties and magnetocaloric effects of B doped Ni-Mn-In melt-spun ribbons," J. Alloys Compd. **731**, 678 (2018). [DOI: 10.1016/j.jallcom.2017.10.063]

[28] Anil Aryal, Abdiel Quetz, Sudip Pandey, Igor Dubenko, Shane Stadler, and Naushad Ali, "Effect of Bi substitution on the magnetic and magnetocaloric properties of $Ni_{50}Mn_{35}In_{15-x}Bi_x$ Heusler alloys," *AIP Advances* **8** (5), 056409 (2018). [DOI: 10.1063/1.5004694]

[29] Sudip Pandey, Sergey Vyzulin, Abdiel Quetz, Anil Aryal, Igor Dubenko, Alexander Granovsky, Shane Stadler, and Naushad Ali, "Microwave absorption through the martensitic and

Curie transitions in $Ni_{45}Cr_5Mn_{37}In_{13}$," *AIP Advances* **8** (5), 056707 (2018). [DOI: 10.1063/1.5006440]

[30] Sudip Pandey, Abdiel Quetz, PJ Ibarra-Gaytan, CF Sanchez-Valdes, Anil Aryal, Igor Dubenko, JL Sanchez Llamazares, Shane Stadler, and Naushad Ali, "Magnetic and martensitic transformations in $Ni_{48}Co_2Mn_{35}In_{15}$ melt-spun ribbons," AIP Advances **8** (10), 101410 (2018). [DOI: 10.1063/1.5041954]

[31] Sudip Pandey, Yury Koshkid'ko, Igor Dubenko, Jacek Cwik, Anil Aryal, Alexander Granovsky, Erkki Lähderanta, Shane Stadler, and Naushad Ali, "Adiabatic Temperature Changes at Structural and Magnetic Phase Transitions in $Ni_{45}Mn_{43}CoSn_{11}$ at High Magnetic Fields," IEEE Trans. Mag. **55** (2), 2500604 (2019). [DOI: 10.1109/TMAG.2018.2866430

[32] Anil Aryal, Sudip Pandey, Igor Dubenko, Dipanjan Mazumdar, Shane Stadler, and Naushad Ali, "Effects of Rare-Earth (R = Pr, Gd, Ho, Er) Doping on Magnetostructural Phase Transitions and Magnetocaloric Properties in $Ni_{43-x}R_xMn_{46}Sn_{11}$ Shape Memory Alloys," IEEE Trans. Mag. **55** (2), 2500505 (2019). [DOI: 10.1109/TMAG.2018.2868134]

[33] Kuei-Chung Cheng, Jing-Han Chen, Shane Stadler, Shih-Hsun Chen, "Properties of atomized AlCoCrFeNi high-entropy alloy powders and their phase-adjustable coatings prepared via plasma spray process," Appl. Surf. Sci. **478**, 478 (2019). [DOI: 10.1016/j.apsusc.2019.01.203]

[34] Anil Aryal, Sudip Pandey, Igor Dubenko, Dipanjan Mazumdar, Shane Stadler, and Naushad Ali, "Magnetostructural phase transitions and large magnetic entropy changes in Ag-doped $Mn_{1-x}Ag_xCoGe$ intermetallic compounds," MRS. Comm. 1-6 (2019). [DOI: 10.1557/mrc.2018.228] (**Accepted** January 2019, no volume assigned)

[35] Sudip Pandey, Mikhail Blinov, Anil Aryal, Igor Dubenko, Valerii Prudnikov, E. Lähderanta, Alexander Granovsky, Nina Pristinskaya, Shane Stadler, and Naushad Ali, "Hall effect in $Ni_{45}Cr_5Mn_{37}In_{13}$ Heusler alloy: drastic violation of correlation between anomalous Hall effect coefficient and resistivity," J. Magn. Magn. Mater. (2019) (**Accepted**)

* Four additional manuscripts are under review.

Probing Coherent States of Light and Matter in Two-Dimensional Semiconductors

Nathaniel P. Stern, Department of Physics and Astronomy, Northwestern University

Program Scope

The ability to enhance light-matter interactions in engineered optical environments is well-established in micro- and nano-photonics. New classes if materials bring new rich correlations between spin, momentum, and light polarization that can be exploited in these photonic systems for information processing and low-power electronics. Interfacing these novel material features with strong optical interactions in intense optical fields suggests the compelling capability to create hybrid light-matter systems harnessing low-energy and protected properties such as spin and pseudospin. The long-term objective of this program is to investigate the interplay between pseudospin in 2D materials and light, revealing new coherent phenomena. The materials studied are the monolayer transition metal dichalcogenides (TMDs), which support polarization-sensitive optical transitions when isolated to a single sub-nanometer crystal layer in thickness. In particular, monolayer TMD semiconductors such as MoS_2 exhibit degenerate valleys in momentum space which have topologically distinct Berry curvature [1]. These valleys can be separately addressed by circularly polarized light, providing a tool for manipulation of carriers in momentum space. Integrating this valley pseudospin property of excitons in monolayer TMDs with engineered strong optical excitations to create novel coherent phenomena represents the key goal of this research.

The scope of this research program primarily focuses on studying light-matter interactions of valley-sensitive excitations in monolayer TMDs. Tuning using microcavity engineering is of primary interest. Polarization-sensitive photoexcitation is also used to study how the subtle details of these optical excitations influence charge transport in optoelectronics. Recently, the research scope has shifted to emphasize the integration of monolayer materials that support valley-polarized emission into photonic devices. This extends the prior work on exciton-polaritons in 2D materials [2] by seeking to implement a system with far more control over optical interactions and improved light input and output characteristics for scalability of these polarization-sensitive phenomena to many-body, long-range optical networks.

Recent Progress

Engineering Valley Polarization of Hybrid Light-Matter Polaritons: Strong coupling between photons in a cavity and excitons in a material result in quasiparticle excitations known as exciton-polaritons that have been observed in traditional semiconductor quantum wells and monolayer TMDs as well [3]. In monolayer TMD exciton-polaritons, the polarization properties

of the emitted light are connected to the valley degree of freedom of carriers arising from the spin-valley selection rules for optical transitions in a TMD [2,4]. In bare monolayer MoS_2 this emission is typically unpolarized at room temperature, but microcavity exciton-polaritons exhibit cavity-modified valley dynamics with polarized emission persisting up to room temperature [2]. In this research, we studied how controlling cavity and optical coupling parameters modifies the valley polarization dynamics of exciton-polaritons in monolayer MoS_2.

A typical dielectric microcavity sample is shown in Fig. 1a. These samples consist of two distributed Bragg reflectors (DBR) made from alternative layers of silicon dioxide (SiO_2) and silicon nitride (Si_3N_4) using plasma-enhanced chemical vapor deposition. A monolayer of molybdenum disulfide (MoS_2) is synthesized by chemical vapor deposition and transferred to the bottom DBR before the top DBR is deposited. Polaritonic states are confirmed from the anticrossing of the upper (UP) and lower (LP) polaritons in angle-resolved reflectivity (Fig. 1a inset). Fitting this anticrossing yields a coupling strength of $g \sim 23$ meV, which is larger than the homogeneous and inhomogeneous linewidths of exciton and microcavity. By experimentally tuning the cavity parameters such as coupling strength (g), cavity decay rate (Γ_c), and detuning (Δ), we found that the valley polarization of the exciton-polaritons can be controlled. Fig. 1b shows the room-temperature emission spectra of valley-polarized exciton-polaritons in cavities with different decay rates achieved by varying the number of DBR pairs from 6 to 10. Both the UP and LP show polarization. Temperature-dependent data (Fig. 2a) show a trend of enhanced valley polarization with increasing cavity decay rates (smaller number of DBR pairs). We extended a cavity model from Ref. [5] to include valley-specific interactions. This phenomenological model incorporates coherent exciton-photon coupling, incoherent pumping, incoherent intervalley scattering, and dissipation, leading to good agreement between data and model (Fig. 2a). The combined

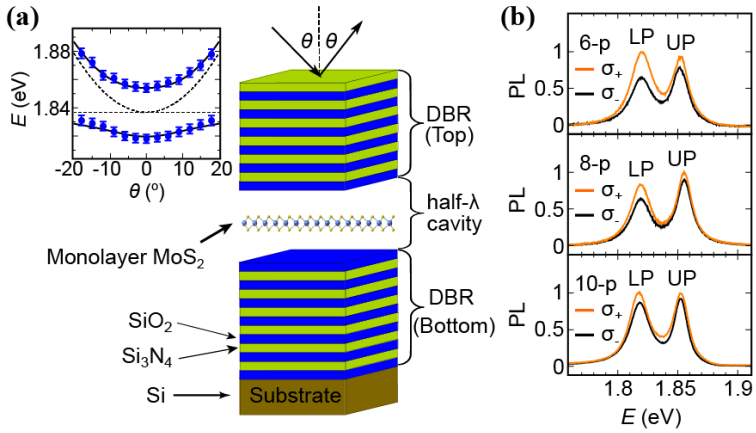

Figure 1: (a) Schematic of the MC-MoS_2 structure. Inset: anticrossing energy dispersion of UP and LP from angle-reflectivity measurements. (b) Emission spectra of valley-polarized exciton-polaritons with different cavity decay rates.

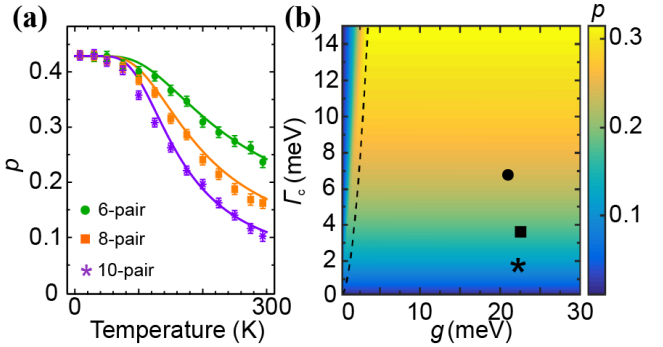

Figure 2: (a) Normalized temperature-dependent polarization for different cavity decay rates. (b) Predicted room-temperature polarization, with points corresponding to the T=300 K results in (a) This shows the ability to engineer valley polarization.

experimental and theoretical picture that we present demonstrates how spin-valley dynamics in monolayer TMD polaritonics can be manipulated through microcavity engineering.

Valley-Sensitive 2D Material Integrated Photonics: Although DBR microcavities are a natural platform for realizing new phenomena, they are not well-suited for scaling to larger optical networks where light acts as an information carrier. This research thrust is timely, as interest in quantum information science grows. It is known that TMDs are excellent candidate materials for strong nonlinear optical phenomena, but practical harnessing of these phenomena in devices would benefit from optical networks. The technology of silicon-based photonics is more suited toward these applications than DBR microcavities. Bringing the non-trivial coherent optical phenomena of 2D materials to a photonic platform is an important advance. Since its inception, our work has sought to tackle this challenge [6]. Recent successes include fiber packaging of an integrated photonics chip for low-temperature study of valley-polarized emission (Fig. 3). Combining the many fabrication steps of photonics processing with nanomaterial integration is a non-trivial task requiring development of new protocols. Our existing realizations demonstrate the main requirements of our goals. These devices, once optimized, will lead to studies of how to excite and measure valley phenomena in integrated photonic circuits, which would be a major advance in the state-of-the-art.

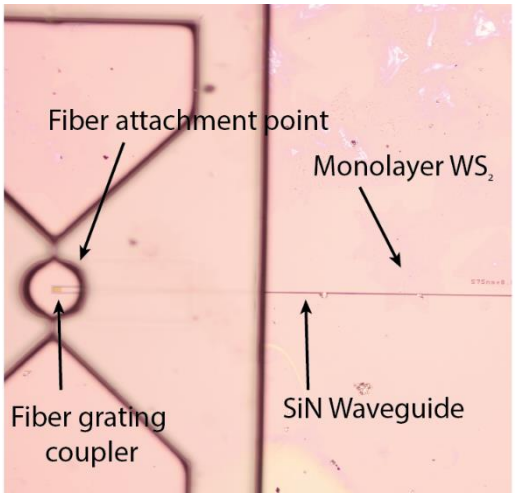

Figure 3: A fiber packaging scheme for low-temperature silicon nitride integrated photonics. A patterned polymer hole aligns an optical fiber to a grating coupler for photonic input/output. Developed monolayer transfer protocols are compatible with the photonics packaging methods.

Future Plans

Building on recent achievements, future directions for this program will focus on realizing new light-matter phenomena with features unique to the 2D semiconductors. Our discovery of valley-polarized exciton-polaritons in 2017 [2] is a key enabler for these new investigations into pseudospin manipulation and integration into a scalable quantum photonics platform [6] that will be the outcomes represent the next phase of this research program.

Valley-Sensitive Stark shift of Exciton-Polaritons: The ability to manipulate spin states is vital for quantum information processing. Extending this possibility to 2D semiconductors is typically done with ultrafast coherent manipulation of valleys using a sub-resonant polarized optical pulse to cause a Stark shift [7]. This can induce valley pseudospin precssion and intentional manipulation of valley polarization. The advantages for valley coherence and optical addressability provided by exciton-poalritons suggests the need for coherent manipulation of these light-matter quasiparticles. We will explore the valley Stark shift of microcavity exciton-

polaritons, which has so far not been observed in 2D materials. Successful observation of this Stark shift, coupled with our observation of room temperature valley coherence, are the prerequisites for demonstrating room temperature coherent valley manipulation in exciton-polaritons. This research direction will leverage ultrafast measurements of the Stark shift to measure picosecond valley dynamics in monolayer nanostructures. We will adopt this approach for manipulating microcavity exciton-polaritons, which has advantages for valley coherence times and extraction of information through light. We will also continue collaborations with material science groups to study these phenomena in high quality large area monolayer samples.

Circular polarization coupling to photonics: With our discovery of valley-polarized exciton-polaritons in MoS_2, we are working to extend this phenomena to integrated photonics devices. This approach provides advantages for long-range many-body interactions and scalable optical networks, but several challenges such as material integration and circular polarization coupling need to be solved. Upcoming research will focus on observing valley-polarized phenomena in waveguides with monolayers transferred on them. We will study the preservation of valley polarization through the emission of circularly-polarized light induced by the near-field electromagnetic field structure. This idea is established in quantum dots, and can lead to direction-sensitive on-chip nonlinear logic devices. Bringing this polarization-sensitivity to an integrated photonics platform will allow engineering of local fields not possible with planar DBR cavities. Our photonics capabilities utilize the capabilities of the Center for Nanoscale Materials at Argonne National Laboratory, a DOE funded national laboratory.

References

[1] D. Xiao, G.-B. Liu, W. Feng, X. Xu, and W. Yao. "Coupled Spin and Valley Physics in Monolayers of MoS_2 and Other Group-VI Dichalcogenides" *Phys. Rev. Lett.* **108**, 196802 (2012).

[2] Y.-J. Chen, J. D. Cain, T. K. Stanev, V. P. Dravid, N. P. Stern. "Valley-Polarized Exciton-Polaritons in a Monolayer Semiconductor." *Nature Photonics* **11**, 431–435, (2017).

[3] X. Liu, T. Galfsky, Z. Sun, F. Xia, E. Lin, Y. Lee, S. Kena-Cohen, and V. M. Menon. "Strong light-matter coupling in two-dimensional atomic crystals." *Nature Photonics* **9**, 20 (2015).

[4] Z. Sun, J. Gu, A. Ghazaryan, Z. Shotan, C. R. Considine, M. Dollar, B. Chakraborty, X. Liu, P. Ghaemi, S. Kena-Cohen and V. Menon. "Optical control of room-temperature valley polaritons," *Nature Photonics* **11**, 491–496 (2017).

[5] F. P. Laussy, E. Del Valle, and C. Tejedor, "Luminescence spectra of quantum dots in microcavities. I. bosons," *Phys. Rev. B* **79**, 235,325 (2009).

[6] G. Wei, T. K. Stanev, D. A. Czaplewski, I. W. Jung, and N. P. Stern. "Silicon-nitride photonic circuits interfaced with monolayer MoS_2." *Appl. Phys. Lett.* **107**, 091112 (2015).

[7] T. LaMountain, H. Bergeron, I. Balla, T. K. Stanev, M. C. Hersam, and N. P. Stern. "Valley-selective optical Stark effect probed by Kerr rotation." *Phys. Rev. B* **97,** 045307 (2018).

Publications

Sponsored by BES 2017 - 2019

1. L Liu, E. J. Lenferink, G. Wei, T. K. Stanev, N. Speiser, and N. P. Stern. “Electrical Control of Circular Photogalvanic Spin-Valley Photocurrent in a Monolayer Semiconductor.” *ACS Appl. Mater. Interfaces* **11**, 3334–3341 (2019). DOI: 10.1021/acsami.8b17476

2. Y.-J. Chen, I. Balla, H. Bergeron, L. Liu, M. C. Hersam, and N. P. Stern. “Dynamics of Valley-Polarized Exciton-Polaritons in Monolayer MoS_2.” *OSA Technical Digest* STu4N.4 (2018). DOI: 10.1364/CLEO_SI.2018.STu4N.4

3. T. LaMountain, E. J. Lenferink, Y.-J. Chen, T. K. Stanev, and N. P. Stern, “Environmental Engineering of Transition Metal Dichalcogenide Optoelectronics.” *Frontiers of Physics* **13**, 138114 (2018). DOI: 10.1007/s11467-018-0795-x

4. T. LaMountain, Yen-Jung Chen, Teodor K. Stanev, Nathaniel P. Stern. "Valley-selective photon-dressed states in transition metal dichalcogenides." *Proc. SPIE 10530, Ultrafast Phenomena and Nanophotonics XXII*, 1053016 (2018). DOI: 10.1117/12.2285666

5. S. C. Ellis, S. Kuhlmann, K. Kuehn, H. Spinka, D. Underwood, R. R. Gupta, L. Ocola, P. Liu, G. Wei, N. P. Stern, J. Bland-Hawthorn, and P. Tuthill "Astrophotonics: the application of photonic technology to astronomy", *Proc. SPIE 10242, Integrated Optics: Physics and Simulations III*, 102420O (2017). DOI: 10.1117/12.2265958

6. S. C. Ellis, S. Kuhlmann, K. Kuehn, H. Spinka, D. Underwood, R. R. Gupta, L. E. Ocola, P. Liu, G. Wei, N. P. Stern, J. Bland-Hawthorn, and P. Tuthill. “Photonic ring resonator filters for astronomical OH suppression.” *Optics Express* **25**, 15868-15889 (2017). DOI: 10.1364/OE.25.015868

7. G. Wei, D. A. Czaplewski, E. J. Lenferink, T. K. Stanev, I. W. Jung, and N. P. Stern. “Size-tunable Lateral Confinement in Monolayer Semiconductors.” *Scientific Reports* **7**, 3324 (2017). DOI: 10.1038/s41598-017-03594-z

8. Y.-J. Chen, J. D. Cain, T. K. Stanev, V. P. Dravid, N. P. Stern. “Valley-Polarized Exciton-Polaritons in a Monolayer Semiconductor.” *Nature Photonics* **11**, 431–435, (2017). DOI: 10.1038/nphoton.2017.86

9. Y. Jia, T. K. Stanev, E. J. Lenferink, N. P. Stern. “Enhanced Conductivity Along Lateral Homojunction Interfaces of Atomically Thin Semiconductors.” *2D Materials* **4**, 021012 (2017). DOI: 10.1088/2053-1583/4/2/021012

Spin Functionality at Interfaces through Complex Oxide Heteroepitaxy

PI: Yuri Suzuki
Department of Applied Physics, Stanford University

Program Scope

The *main research objective* of the program is to develop novel paradigms for *static and dynamic tuning* of quasi-two-dimensional magnetic functionality and, more recently, for *efficient spin current generation, propagation and detection* in complex oxide thin films and heterostructures. In this program, we have focused on the synthesis and characterization of atomically precise complex oxide thin films and heterostructures with spin functionality that may form the basis for the development of a more energy efficient spin-based electronics. In particular, we have focused on the role of octahedral rotations at interfaces due to lattice strain as well as electrical gating to tune the magnetic functionality in complex oxide thin films and heterostructures and the development of a new class of low loss ferrite thin films and heterostructures.

Our recent focus has been on two categories of materials based on *transition metal oxide compounds*:

(i) heterostructures in which octahedral rotations at the interfaces generate unexpected spin functionality not observed in the bulk;

(ii) low damping oxide spinel ferrite thin films (in which ferromagnetism comes from L=0 Fe^{3+} cations exchange coupled via superexchange interactions for efficient spin current generation) and associated heterostructures with strongly spin-orbit coupled complex oxides for spin current detection

Recent Progress

Highlights of recent work include (i) demonstrating interfacial ferromagnetism that is stabilized by non-equilibrium crystal symmetry in (001) $LaNiO_3/CaMnO_3$ superlattices, (ii) demonstrating interfacial ferromagnetism that is induced by polar compensation in (001) $LaNiO_3/CaMnO_3$ superlattices, (iii) demonstrating enhanced ferromagnetism and exchange bias in (111) $LaNiO_3/CaMnO_3$ superlattices and (iv) the evolution of low damping in $Mg(Al,Fe)_2O_4$ films.

Interfacial Ferromagnetism Stabilized by Non-equilibrium Crystal Symmetry.[1] Emergent phenomena at the interface of two different materials have been attributed to electronic, magnetic or other types of reconstruction at the interface. These reconstructions are driven by mismatch in bands, valence, interaction lengths etc. While there have been theoretical predictions about electronic reconstruction giving rise to localized electronic behavior at the interface, there have been many fewer predictions and demonstration of emergent magnetic phenomena at interfaces. In particular, generating ferromagnetism localized at the interface of two non-ferromagnetic materials is of fundamental and technological interest.

We have previously demonstrated that interfacial ferromagnetism emerges in just one unit cell of $CaMnO_3$ at each interface in $CaMnO_3$-based superlattices.[2,3] The confinement of the ferromagnetism to one unit cell was predicted by theory but only demonstrated by our experimental study through a combination of neutron reflectivity, exchange biased hysteresis loops, scanning transmission electron microscopy/ electron energy loss spectroscopy and x-ray magnetic circular dichroism. The interfacial ferromagnetism was explained in terms of Mn double exchange interactions in a single unit cell of $CaMnO_3$ at the interface mediated by itinerant electrons from the adjacent $CaRuO_3$ layer.

A more surprising result that we obtained was that the interfacial ferromagnetism appeared to be switched on and off at interfaces depending on the symmetry of the oxygen octahedra connectivity at the boundary.[4] The crystallographic symmetry-mismatch across the interfaces, associated with

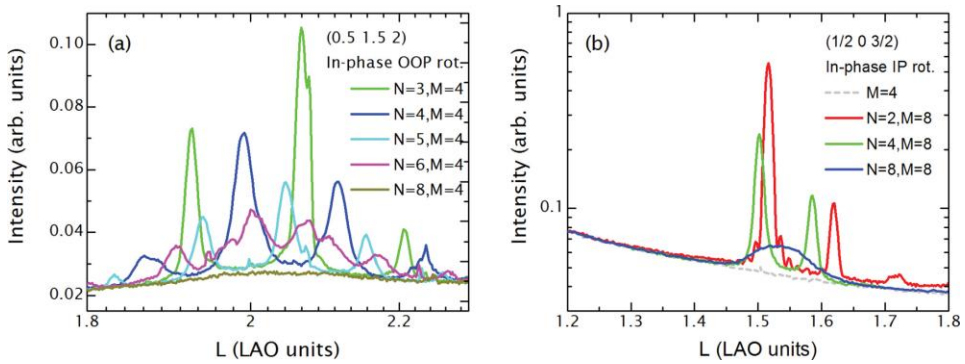

Figure 1. (a) In superlattices with 4 layers of $CaMnO_3$, out-of-plane in-phase $CaMnO_3$ rotations (indicated by (1/2 3/2 2) peaks) decrease and eventually disappear with increasing $LaNiO_3$ layers. (b) In superlattices with 8 layers of $CaMnO_3$, in-plane, in-phase rotations (indicated by (0.5, 0, 1.5) peaks) decrease and nearly disappear by 8 layers of $LaNiO_3$.

incommensurate tilt and rotation of the MnO_6 and RuO_6 octahedra, modulated and even entirely suppressed the interfacial ferromagnetism residing within a single unit cell of the $CaMnO_3$ layer.

In this current review cycle, we have demonstrated that octahedral connectivity can be carefully tuned to generate and modulate emergent ferromagnetism via the choice of constituent materials. These results provide general design rules for predicting the nature of the emergent interfacial ferromagnetism in $CaMnO_3$- based superlattices. We substituted $CaRuO_3$ (orthorhombic in the bulk) with $LaNiO_3$ (rhombohedral in the bulk) as the itinerant layer. By replacing the $CaRuO_3$ with $LaNiO_3$, we introduced a different set of octahedral rotations when combined with nominally orthorhombic $CaMnO_3$ that demonstrated how sensitively the interfacial ferromagnetism depended on both layer materials.

Synchrotron X-ray diffraction measurements indicate out-of-plane in-phase rotations of the oxygen octahedra are observed for thin $LaNiO_3$ layers and 4 layers of $CaMnO_3$ while in-plane in-phase rotations of the oxygen octahedra are observed for thin $LaNiO_3$ layers and 8 layers of $CaMnO_3$. These trends are evident in Figure 1 where relevant half-order peaks of the x-ray diffraction are measured for different superlattices. The evolution of the x-ray diffraction peaks is summarized in Figure 2(a) and (b) for 4 and 8 $CaMnO_3$ layer superlattices respectively. These two in-phase rotations generate distinctly different effects on the interfacial ferromagnetism as shown in the magnetization data in these same figures. For 4 $CaMnO_3$ layer superlattices, a decrease in out-of-plane in-phase rotations for thicker $LaNiO_3$ layers is correlated with an enhanced interfacial ferromagnetism attributed to double exchange interaction among Mn^{3+} and Mn^{4+} cations in the interfacial payer of $CaMnO_3$. For 8 $CaMnO_3$ layer superlattices, a decrease in in-plane in-phase rotations for thicker $LaNiO_3$ layers appears to suppress the double exchange interaction. Together these results emphasize the power of using crystal symmetry mismatch to control an interfacial property such as ferromagnetism.

Role of Polar Compensation in Interfacial Ferromagnetism.[5] Polar compensation can be a strong driving force for the emergence of unexpected electronic and magnetic properties at oxide interfaces. By incorporating perovskite oxides with different A- and B-site cation valences, one can introduce interface electric field in the system. Polar mismatch has been identified as a determining factor in the generation of metallicity in the most famous example of $LaAlO_3/SrTiO_3$. Although emergent ferromagnetism at interfaces has been associated with superexchange interactions or charge transfer driven exchange interactions, there has been very little understanding of the role of polar compensation in the interfacial magnetism. Through polar $LaNiO_3/CaMnO_3$ superlattices, we have been able to identify two key mechanisms driving emergent ferromagnetism. Since $LaNiO_3$ exhibits a thickness dependent metal-insulator transition, $LaNiO_3$ is a promising material to explore the role

of delocalized electrons, as well as polar compensation, in driving charge transfer in oxide heterostructures.

We have discovered that interfacial charge redistribution via polar compensation is essential for explaining the evolution of interfacial ferromagnetism in $LaNiO_3/CaMnO_3$ superlattices as a function of $LaNiO_3$layer thickness. In insulating superlattices (4 unit cells or less of $LaNiO_3$), magnetism is dominated by Ni-Mn superexchange, while itinerant electron-based Mn-Mn double-exchange plays a significant role in thicker metallic superlattices. X-ray absorption spectroscopy and x-ray magnetic circular dichroism studies are consistent with interfacial Ni^{2+} due to polar compensation arising at the $LaNiO_3/CaMnO_3$ interfaces. Additional resonant x-ray scattering measurements, combined with x-ray reflectivity measurements, we find primarily Ni^{3+} in the interior and Ni^{2+} at the interfaces of the $LaNiO_3$ layers. Together these results concusively confirm the presence of interfacial Ni^{2+}, which is consistent with a ferromagnetic Ni-Mn superexchange interaction even in metallic superlattices. We have combined these x-ray spectroscopies with bulk magnetometry and transport measurements to obtain a comprehensive picture of the factors

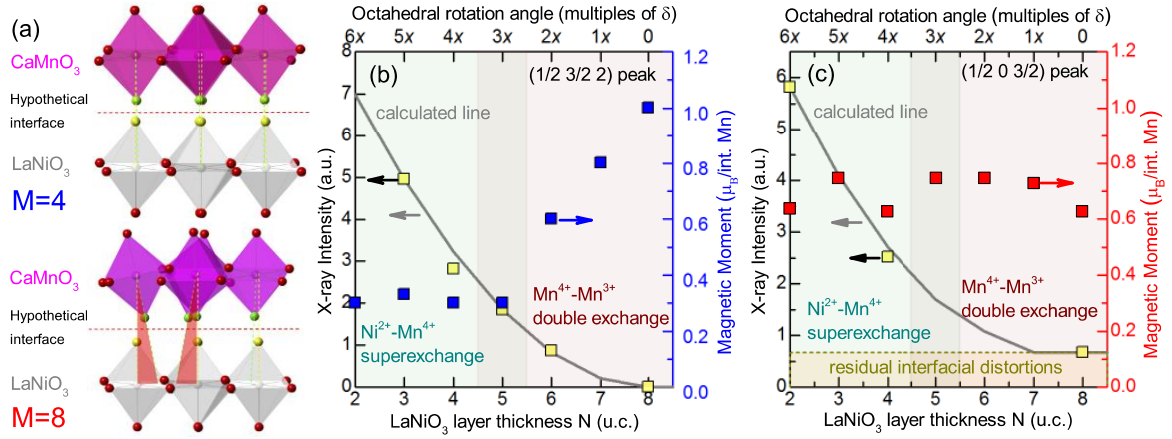

Figure 2. (a) Hypothetical interfacial alignment for M=4 and M=8 superlattices demonstrating M=8 mismatch due to in-plane orthorhombic orientation. (b) X-ray intensity of (0.5, 1.5, 2) half-order Bragg peak due to out-of-plane, in-phase rotations in $CaMnO_3$ = 4 u.c. superlattices (left axis). As $LaNiO_3$ layer thickness N increases, in-phase $CaMnO_3$ rotations decrease and eventually disappear. The calculated line shows expected intensity for a constant decrease in the rotation angle with increasing $LaNiO_3$ layer thickness. Saturated magnetic moment (right axis) increases once the double-exchange interaction is dominant. (b) X-ray intensity of (0) half-order Bragg peak due to in-plane, in-phase rotations in $CaMnO_3$=8 u.c. superlattices (left axis). As $LaNiO_3$ layer thickness N increases, in-phase $CaMnO_3$rotations decrease and nearly disappear by N=8. The calculated line shows the experimental data is well fit to the same model as M=4, with the addition of a constant intensity offset due to interfacial mismatch.

determining emergent interfacial ferromagnetism.

Enhanced Interfacial Ferromagnetism at (111) Interfaces.[6] With advances in the growth of perovskite oxide thin films superlattices, the opportunity for exploring these oxide materials at higher energy surfaces and interfaces has led to the discovery of new emergent and exotic states. We have demonstrated that the (111)-oriented $CaMnO_3/LaNiO_3$ interface gives rise to strong interfacial ferromagnetism based on Ni^{2+}-Mn^{4+} superexchange interactions associated with screening effects caused by polar mismatch. The (111) interface maximizes emergent interfacial moments and exchange interactions. These experiments are possible due to our recent success in synthesizing atomically precise $CaMnO_3/LaNiO_3$ superlattices with (111) orientation by interval pulsed laser deposition. The (111) interface gives rise to strong exchange interactions, beyond those found in (001) $CaMnO_3/LaNiO_3$ superlattices, resulting in a ferromagnetic ordering temperature of 200 K, which is much higher than the bulk antiferromagnetic $CaMnO_3$ ordering temperature of 140 K. The significant

saturated interfacial moment is attributed to the fully uncompensated (111) $CaMnO_3$surface. The strong exchange interaction in our superlattices grown along the (111) direction is also manifest in the observed exchange bias associated with the coupling between the interfacial $CaMnO_3$ and the interior antiferromagnetic $CaMnO_3$.

Low Damping in Epitaxial Spinel Ferrite Thin Films.[9] One of the new directions that we have explored in this current review cycle is the development of new low damping ferromagnetic insulating thin films for spin-current-based electronics. Building on our recent success in identifying and demonstrating low loss epitaxial $Ni_{0.65}Zn_{0.35}Al_{0.8}Fe_{1.2}O_4$[7] and $MgAl_{0.5}Fe_{1.5}O_4$[8] films for spin current generation, we have stabilized a series of ferrite compounds whose magnetism is solely attributed to L=0 Fe^{3+} cations. Low damping is demonstrated via ferromagnetic resonance and correlated with microstructure and cation doping.

Future Plans

In order to understand the underlying mechanism for emergent ferromagnetism in (111) $CaMnO_3$-based superlattices, we have initiated studies on the development of interfacial ferromagnetism in (111) $CaRuO_3/CaMnO_3$ superlattices where the constituent materials have the same orthorhombic symmetry, thus eliminating crystal symmetry mismatch and therefore any non-equilibrium crystal symmetry effects.

We also plan to explore the more Fe rich parts of the $Mg(Al,Fe)_2O_4$ phase diagram and lithium ferrite films in search of low damping ferromagnetic insulating thin films for spin-current-based electronics.

References

1. C. Flint, A. Vailionis, H. Zhou, and Y. Suzuki, *Physical Review B* **96** 144438 (2017).
2. C. He, A.J. Grutter, M. Gu, N.D. Browning, Y. Takamura, B.J. Kirby, J.A. Borchers, J.W. Kim, M.R. Fitzsimmons, X. Zhai, V.V. Mehta, F.J. Wong, and Y. Suzuki, *Physical Review Letters* **109** 197202 (2012).
3. A. J. Grutter, C. He, B. J. Kirby, J. A. Borchers, C. L. Flint, E. Arenholz, and Y. Suzuki, *Physical Review Letters* **115** 047601 (2015).
4. A. J. Grutter, A. Vailionis. J.A. Borchers, B. J. Kirby, C. L. Flint, C. He, E. Arenholz, and Y. Suzuki, *Nano Letters* **16** 5647−5651 (2016).
5. C. L. Flint, A. N'Diaye, P. Shafer, E. Arenholz, and Y. Suzuki, *Physical Review Materials* **1** 02404 (2017).
6. C.L. Flint, D. Yi, E. Karapetrova, A. T. N'Diaye, P. Shafer, E. Arenholz, and Y. Suzuki, "Enhanced Interfacial Magnetism and Exchange Bias in (111)-oriented $LaNiO_3/CaMnO_3$ Superlattices," submitted to *Physical Review Materials* (2018).
7. Satoru Emori, Benjamin A. Gray, Hyung-Min Jeon, Joseph Peoples, Maxwell Schmitt, Krishnamurthy Mahalingam, Madelyn Hill, Michael E. McConney, Matthew T. Gray, Urusa S. Alaan, Alexander C. Bornstein, Padraic Shafer, Alpha T. N'Diaye, Elke Arenholz, Greg Haugstad, Keng-Yuan Meng, Fengyuan Yang, Dongyao Li, Sushant Mahat, David G. Cahill, Pallavi Dhagat, Albrecht Jander, Nian X. Sun, Yuri Suzuki, and Brandon M. Howe, *Advanced Materials* **29** 1701130: 1-8 (2017).
8. Satoru Emori, Di Yi, Sam Crossley, Jake J. Wisser, Purnima Balakrishnan, Padraic Shafer, Christoph Klewe, Alpha T. N'Diaye, Brittany T. Urwin, Krishnamurthy Mahalingam, Harold Y. Hwang, Elke Arenholz, Brandon M. Howe, Yuri Suzuki, *Nano Letters* **18** 4273 (2018).
9. J.J. Wisser, S. Emori, L.J. Riddiford, A. Altman, P. Li, K. Mahalingham, B. T. Urwin, B.M. Howe, A. J. Grutter, B. J. Kirby, Y. Suzuki, in preparation (2019).

Publications

1. C. Flint, A. Vailionis, H. Zhou, and Y. Suzuki, "Tuning interfacial ferromagnetism in $LaNiO_3/CaMnO_3$ superlattices by Stabilizing Non-Equilibrium Crystal Symmetry," *Physical Review B* **96** 144438 (2017).

2. C. L. Flint, A. N'Diaye, P. Shafer, E. Arenholz, and Y. Suzuki, "The Role of Polar Compensation in Interfacial Ferromagnetism of $LaNiO_3/CaMnO_3$ Superlattices," *Physical Review Materials* **1** 02404 (2017).

3. Di Yi, Charles Flint, Purnima Balankrishnan, Krishnamurthy Mahalingam, Brittany Urwin, Arturas Vailionis, Alpha T. N'Diaye, Padraic Shafer, Elke Arenholz, Yongseong Choi, Kevin H. Stone, Jiunhaw Chu, Brandon M. Howe, Jian Liu, Ian Fisher, Yuri Suzuki, "Tuning perpendicular magnetic anisotropy by oxygen octahedral rotations in $(La_{1-x}Sr_xMnO_3)/(SrIrO_3)$ superlattices," *Physical Review Letters* **119** 077201 (2017).

4. Ted D. Sanders, Urusa S. Alaan, Matthew T. Gray, Shameek Bose, Matthew Taylor, Mariona Cabero, Virat Mehta, Maria Varela, Chris Leighton, Yuri Suzuki, "Magnetism in Epitaxial $PrCoO_3$ and $Pr_{0.7}Y_{0.3}CoO_3$ Films," *Journal of Magnetism and Magnetic Materials* **451** 654–659 (2018).

5. R. U. Chandrasena, C. L. Flint, W. Yang, A. Arab, S. Nemšák, M. Gehlmann, V. B. Özdöl, F. Bisti, K. D. Wijesekara, J. Meyer-Ilse, E. Gullikson, E. Arenholz, J. Ciston, C. M. Schneider, V. N. Strocov, Y. Suzuki, and A. X. Gray, "Depth-resolved charge reconstruction at the $LaNiO_3/CaMnO_3$ interface," *Physical Review B* **98** 155103 (2018).

6. C.L. Flint, D. Yi, E. Karapetrova, A. T. N'Diaye, P. Shafer, E. Arenholz, and Y. Suzuki, "Enhanced Interfacial Magnetism and Exchange Bias in (111)-oriented $LaNiO_3/CaMnO_3$ Superlattices," submitted to *Physical Review Materials* (2018).

Hybrid quantum systems: spins, photons and superconducting qubits

Yale University (Lead):
Hong Tang (PI), Steven Girvin, Liang Jiang, Peter Rakich, Robert Schoelkopf – (Co-PIs)
Montana State University:
Rufus Cone (Sub PI), Charles Thiel (Sub Co-PI)

Project Summary

Materials of strong polarization such as piezoelectric materials have important uses in the classical and quantum worlds: they are efficient energy harvesting materials and they have recently emerged as coherent transduction media for transferring quantum information across different physical domains such as microwave phonons, microwave photons and superconducting qubits.

Piezoelectric crystals offer yet another special trait for quantum information processing—the Pockels effect—an electro-optic effect known to go hand-in-hand with piezoelectricity arising from the piezocrystal's broken inversion symmetry. While piezoelectricity couples excitations at low frequencies (phonon and microwave fields), the Pockels effect allows signal conversion between microwave and optical frequencies. In bulk crystals, the Pockels effect is generally considered weak; however, in an integrated platform, high-Q microresonators can be used to drastically enhance electro-optic coupling, and a highly efficient microwave-to-optical quantum interface can be realized for the coherent coupling of hybrid quantum systems.

We propose experimental and theoretical efforts to develop such a hybrid quantum platform. The aim is to marry two quantum technologies: superconducting qubits and spin-systems, based on the thin film Lithium Niobate (LN) and Lithium Tantalate (LT). In addition to having famously strong piezoelectric and Pockels responses and superb optical properties, LN & LT crystals are a particularly promising host for rare-earth-ion (REI) spin centers; spin centers in LN & LT crystals have exhibited remarkably long spin coherence and strong optical and microwave transition strengths. In this three-year program, our goal is to exploit the inherent piezoelectric and Pockels effect in LN to achieve coherent coupling between spins, photons and superconducting qubits.

Through this program, we leverage our team's world-class expertise in circuit QED (Yale) and spin systems (Montana State) to tackle the non-trivial task of harnessing and controlling disparate superconducting, spin, and photonic degrees of freedom on the same chip. Because these systems have ostensibly orthogonal environmental requirements, creative new strategies are needed to marry and control these systems. For example, magnetic fields—typically used to control spin systems—can be detrimental to the superconducting state. Moreover, piezoelectricity—which couples microwave photons to acoustic phonons—can cause the microwaves to radiate as acoustic energy, reducing the coherence time of a superconducting qubit. In this program, we will apply new phonon, microwave and optical spectroscopic tools—unique to the Yale/MSU teams—to pinpoint the material origins of both transmon- and spin-qubit decoherence over a range of energy scales (micro eV-eV). Using different methods to perturb the material matrix and tune spin ensembles, we devise strategies to preserved coherence of these disparate quantum systems when brought together at millikelvin temperatures.
This hybrid quantum system, if realized, will enable ground-breaking advances in quantum information processing: it will empower superconducting circuit QED systems with long-lived quantum memory for achieving advanced quantum computing capabilities, and for the first time will allow high-fidelity optical readout of circuit QED systems through spin qubits. This scalable platform therefore enables critical functionalities of quantum transceivers and will likely play an important role in future distributed quantum computation and secure quantum networks.

Excitons in Low-Dimensional Perovskites

William A. Tisdale, Massachusetts Institute of Technology

Program Scope

The goal of this research effort is to obtain a deeper understanding of strongly bound excitonic states in low-dimensional halide perovskites. Experiments will address how excitons in these quantum-confined materials move, how they interact with the polar lattice, and how their behavior can be manipulated through chemical or structural modification. Specific research activities include synthesis and structural characterization of 2D perovskite quantum wells, direct imaging of exciton and charge carrier transport, and ultrafast electronic and vibrational spectroscopy.

Recent Progress

Interpretation of excitonic and vibrational dynamics in low-dimensional perovskites requires detailed knowledge of their structure, purity, and phase transitions. Because existing knowledge is limited and because materials quality can vary from lab to lab, we first set out to synthesize and characterize a comprehensive series of 2D perovskite crystals, including variation of the octahedral layer thickness (n = 1,2,3,4), alkylammonium chain length (butyl, pentyl, hexyl), and identity of the small organic cation (methylammonium, formamidinium), see Fig. 1.

Synthesis and Structural Trends in Layered 2D Alkylammonium Lead Halide Perovskites

In a forthcoming report, we describe cooling-induced crystallization of layered two-dimensional lead halide perovskites with various layer thicknesses, organic spacer chain lengths, A-site cations, and halide anions. Using X-ray diffraction, we studied the effects of each chemical constituent on the structures and phase transitions. We observed a trend of lower crystal symmetry at low temperature, higher structural distortion on surfaces, alternations of lead iodide bond lengths, splits in bond angles, changes in tilting angles, and increases in the extents of interdigitation and corrugation tilts of organic spacer molecules. We also found that the number of phase transitions was dependent on the lengths of organic spacer molecules, whereas substitution of methylammonium by formamidinium resulted in small structural changes. These results form the foundation for designing layered two-dimensional lead halide perovskites with novel compositions as well as for elucidating structural relationships to thermal, electrical, and optical properties of these materials.

Melting Transitions of the Organic Subphase in Layered Two-Dimensional Halide Perovskites

We investigated the phase behavior of 2D $(C_xH_{2x+1}NH_3)_2[(MA,FA)PbI_3]_{n-1}PbI_4$ layered perovskites near room temperature (-10ºC to +100ºC) as a function of the octahedral layer thickness (n = 1,2,3,4), alkylammonium chain length (butyl, pentyl, hexyl), and identity of the

small organic cation (methylammonium, formamidinium), see Fig. 1. Using differential scanning calorimetry and X-ray diffraction, we observed a prominent and reversible first-order phase transition in each of these compounds corresponding to a melting transition of the alkylammonium chains separating the lead halide perovskite layers. The melting temperature, T_m, monotonically increases from 10ºC to 77.9ºC to 95.9ºC as the carbon chain length increases from C_4 to C_5 to C_6, but is insensitive to the octahedral layer thickness, n. The latent heat of melting, ΔH_m, was found to be in the range 3–5 kJ/mol-spacer, indicating only partial disordering of the carbon chain. We discussed these findings in the context of melting in other 2D molecular systems, including Langmuir-Blodgett films and self-assembled monolayers on metal surfaces, and implications for tuning properties of 2D layered perovskites through molecular engineering of the organic subphase.

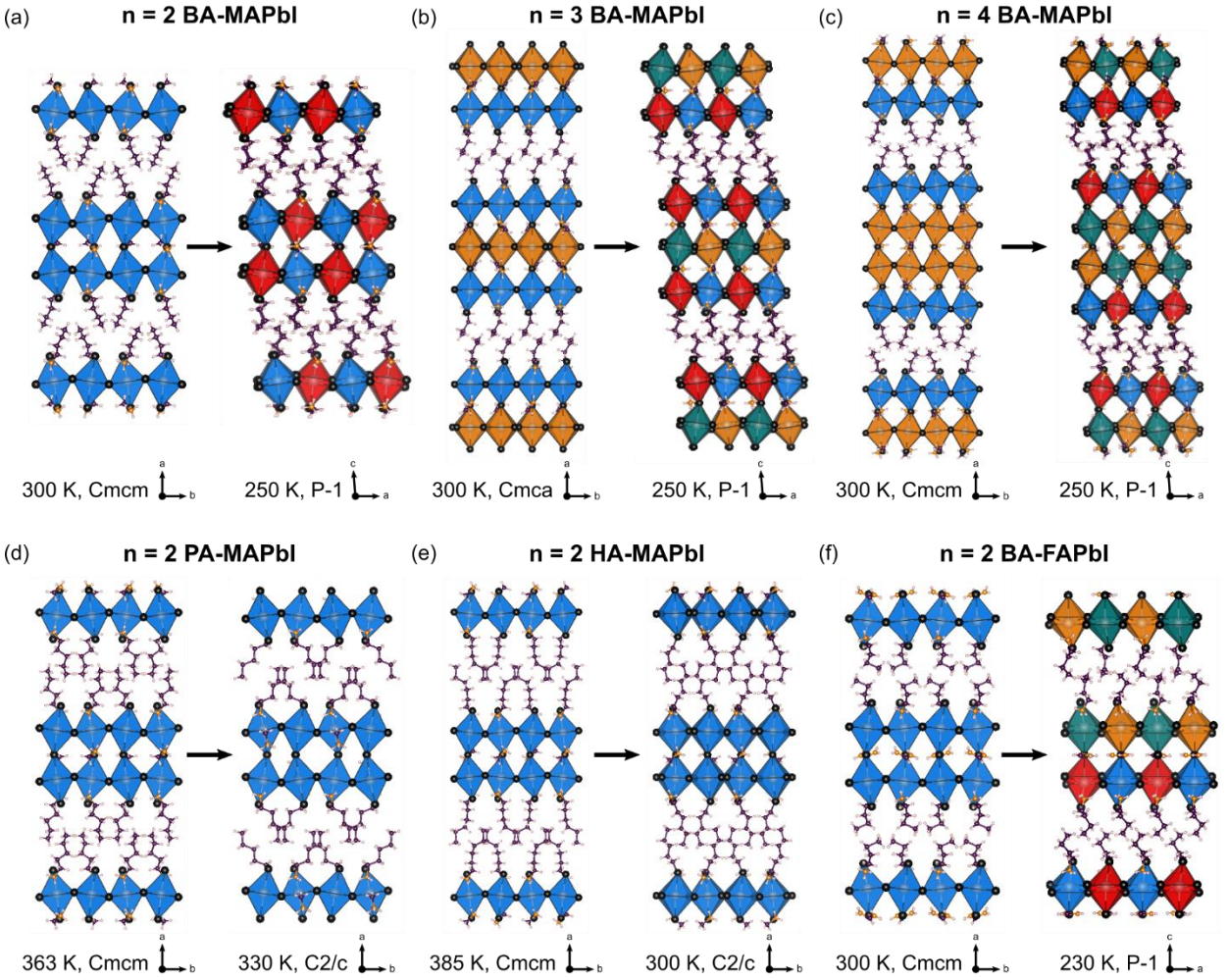

Figure 1. Structural phase transitions in layered 2D alkylammonium lead halide perovskites. MA = methylammonium, BA = butylammonium, PA = pentylammonium, HA = hexylammonium, FA = formamidinium.

Markov Chain Monte Carlo Sampling for Target Analysis of Transient Absorption Spectra

Global and target analysis techniques are ubiquitous tools for interpreting transient absorption (TA) spectra. However, characterizing uncertainty in the kinetic parameters and component spectra derived from these fitting procedures can be challenging. Furthermore, fitting TA spectra of inorganic nanomaterials where the component spectra of different excited states are nearly or completely overlapped is particularly problematic. This limitation has proved particularly challenging for the interpretation of excited state feature in perovskite TA spectra.

In a forthcoming report, we present a target analysis model for extracting excited state spectra and dynamics from TA data using a Markov chain Monte Carlo (MCMC) sampler to visualize and understand uncertainty in the model fits. We demonstrate the utility of this approach by extracting the overlapping component spectra and dynamics of single- and biexciton states in $CsPbBr_3$ nanocrystals. Significantly, refinement of the component spectra is accomplished by fitting the entire fluence-dependent series of ensemble TA data using the Poisson statistics of photon absorption, providing multiple checks for internal consistency. The MCMC method itself is highly general and can be applied to any dataset or model framework to accurately characterize uncertainty in the fit and aid model selection when choosing between different models (Fig. 2).

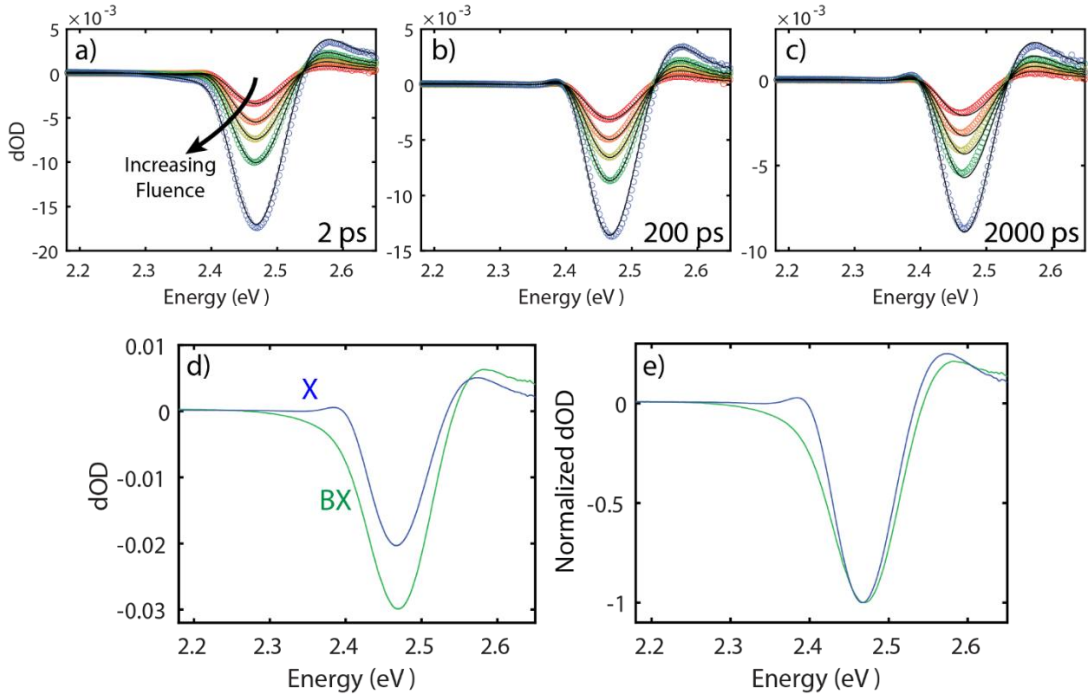

Figure 2. MCMC fitting results for $CsPbBr_3$ nanocrystals at varying laser excitation fluence. (a)-(c) Comparison of the fitted and raw data. The colored circles are raw TA spectra at a pump-probe time delay of 2, 200, and 2000 ps respectively, and the colors indicate differing pump powers from low (red) to high (blue). The black lines are the fitted spectra extracted from 100 random states of the Markov chain overlaid with some transparency. (d) Component spectra of the biexciton (green) and exciton (blue) states extracted from 100 random states of the Markov chain overlaid with some transparency. (e) Component spectra normalized to have the same bleach amplitude for visual comparison.

Future Plans

Our immediate future focus is on performing temperature-dependent spectroscopic studies of the suite of 2D perovskites we have synthesized. This work will be aided in great part by the recent acquisition of a new cry-microscope with superior vibration damping and drift stability, which will be installed in our laboratory in March 2019.

Publications

There are no publications to report because this is a new award with a start date of Sep. 1, 2018.

Uncovering and surmounting loss mechanisms in light emitters

Principal Investigator: Chris G. Van de Walle, University of California, Santa Barbara

Program Scope

The overarching aim of this project is to build an understanding of loss mechanisms in optoelectronic devices and devise methods of overcoming them. Our initial focus was on nitride light emitting diodes (LEDs), because of the crucial impact on technology, and because a great deal of experimental work was concentrated in that area. However, the first-principles methodology that we have been putting in place is general and can be applied to other materials as well as other types of devices.

Our approach for calculating radiative and nonradiative recombination is based on advanced first-principles techniques, taking full account of accurate electronic structure and electron-phonon interactions without any fitting to experiment. We address Auger recombination as well as point-defect assisted Shockley-Read-Hall recombination. For nitride semiconductors, we focus on identifying point defects that detrimentally impact efficiency of LEDs. We have also started applying our capabilities to other materials systems, notably the hybrid perovskites that display high efficiency for photovoltaics and are being considered for light-emitting applications. Our overall goal is to generate the fundamental knowledge that is essential for improving efficiencies, and to provide guidelines for overcoming the limitations.

Recent Progress

In the present phase of the project we continued our efforts on identifying point defects that detrimentally impact the efficiency of nitride devices [P1, P2]. In addition, we investigated defect-related processes in other wide-band-gap semiconductors [P3, P4, P5, P6, P7]. We also continued developing methodology for first-principles calculations of nonradiative processes [P8, P9]. It is our goal to share the software that is developed as part of the project with other scientists. We have made our code to calculate direct and indirect Auger recombination available online. The code is hosted at [https://github.com/jmmshn/bf_auger]. It contains scripts to help the user set up calculations to obtain the eigenvalues, wave functions, and electron-phonon matrix elements. The program then follows the overall formalism of Ref. [1] and computes all the matrix elements needed to obtain the final Auger recombination rate.

For the purposes of this Extended Abstract, we will focus on our recent work on **radiative and nonradiative recombination in hybrid perovskites**. Hybrid perovskites, such as methylammonium lead iodide ($MAPbI_3$), have emerged as promising materials for highly efficient photovoltaics [2, 3] and light emitters [4]. Despite the remarkable success, the fundamental mechanisms that are responsible for the high efficiency are still vigorously debated.

A number of research groups have attributed the high efficiency of the hybrid perovskites to low radiative recombination rates due to the Rashba effect, which is caused by strong spin-orbit coupling and leads to mismatched spins and momenta between the band edges [5, 6]. However, these results were obtained from phenomenological models. We have developed a fully first-principles approach to calculate the three-dimensional spin texture in $MAPbI_3$. As shown in **Figure 1**, we find that the band edges have consistent spin orientations, leading to efficient optical transitions [P10]. These insights call for a reconsideration of the scenario that radiative recombination is suppressed by mismatched spins and provide an in-depth understanding of the origin of the spin texture in hybrid perovskites, which is crucial for designing spintronic devices.

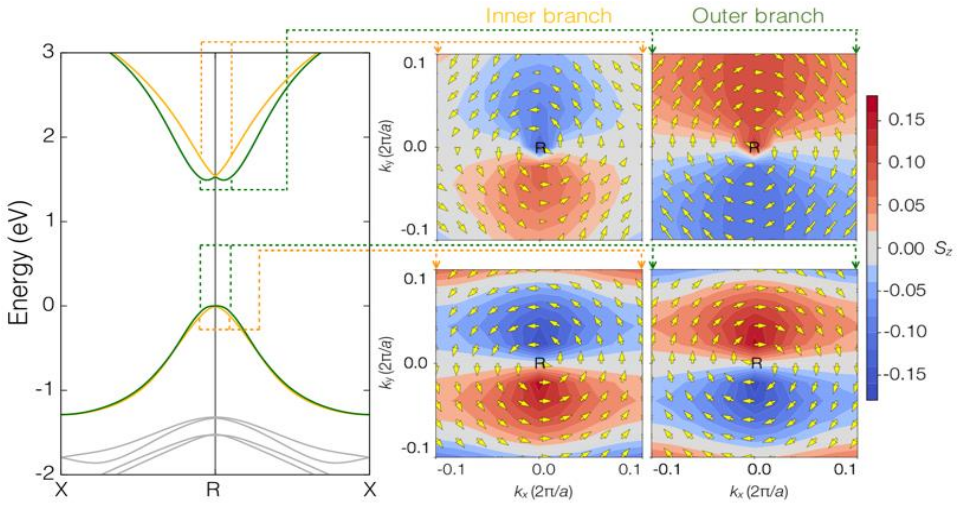

Figure 1. Band structure and spin texture of the band edges of $MAPbI_3$ computed from first principles. The expectation values of the first two components (S_x, S_y) of the spinors are shown by the arrows and that of the third component (S_z) is shown by the background color. From [P10].

We have also investigated the impact of momentum mismatch on the radiative recombination. Even though the band edges have consistent spins, the slight momentum mismatch might still suppress the radiative recombination. While the momentum mismatch can be quantified, the challenge here is that the MA molecule is rotating at room temperature, resulting in a dynamic band structure and momentum splitting. We have accurately computed the radiative recombination coefficient, taking into account the momentum mismatch originating from the rotation of the MA molecule. Our calculations clearly show that the radiative recombination coefficient in $MAPbI_3$ is as high as in traditional direct-gap semiconductors; the indirect nature of the $MAPbI_3$ band gap suppresses radiative recombination by less than a factor of two [P11]. This insight helps to avoid misguided attempts to analyze and design device characteristics based on erroneous assumptions about the recombination rate.

Strong radiative recombination opens the possibility of making efficient light emitters with hybrid perovskites. However, the operation of LEDs requires much higher carrier densities at which Au-

ger recombination might be a concern. Analysis of experimental results has produced some trimolecular recombination coefficients, but it is unclear if they really stem from Auger recombination. We have used our methodology to accurately compute the Auger recombination coefficient in $MAPbI_3$. We find the Auger coefficient to be exceptionally high (~10^{-28} cm^6s^{-1}) when compared to traditional semiconductors with similar band gaps (~10^{-30} cm^6s^{-1}). As shown in **Figure 2**, our methodology allows us to inspect the contributions of different bands to the total Auger coefficients. We can attribute the large Auger coefficient to a resonance in the band structure, as well as to significant lattice distortions [P12]. Based on these insights, we have identified the crucial factors that limit the efficiency of $MAPbI_3$ in light-emitting applications, and we have been able to provide guidelines for design of better hybrid-perovskites-based light emitters.

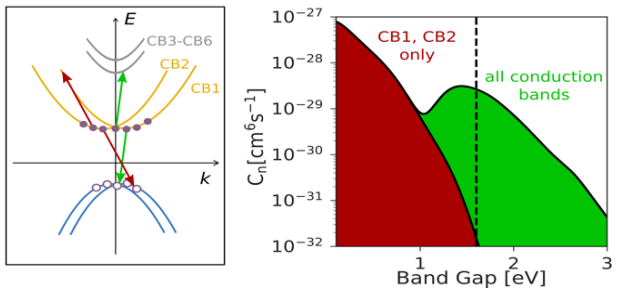

Figure 2. Left: Schematic of Auger processes involving only the CB1-CB2 bands vs. processes with transitions to the CB3-CB6 bands. Right: Computed Auger coefficients as a function of band gap at a carrier density $n=10^{18}$ cm^{-3}, for processes restricted to CB1-CB2 vs. processes with transitions to all CBs. The dashed line represents the experimental gap (1.60 eV). From [P12].

Future Plans

We plan to exploit our capabilities for calculating defect-assisted recombination to continue exploring potential efficiency-reducing defects, impurities, or complexes. For nitride semiconductors, this is particularly important at longer wavelengths, where the "green gap" is still an important concern, as well as at shorter wavelengths, in AlGaN-based UV emitters. We also plan to build on our experience in hybrid perovskites to address defect-assisted recombination and to study Auger recombination in IV-VI semiconductors.

References

[1] E. Kioupakis, D. Steiauf, P. Rinke, K. T. Delaney, and C. G. Van de Walle, Phys. Rev. B, **92**, 035207 (2015).

[2] S. Luo and W. A. Daoud, J. Mater. Chem. A **3**, 8992 (2015).

[3] W. J. Yin, J.-H. Yang, J. Kang, Y. Yan and S.-H. Wei, J. Mater. Chem. A **3**, 8926 (2015).

[4] X. Gong *et al.*, Nat. Mater. **17**, 550 (2018).

[5] F. Zheng, L. Z. Tan, S. Liu, and A. M. Rappe, Nano Lett. **15**, 7794 (2015).

[6] P. Azarhoosh, S. McKechnie, J. M. Frost, A. Walsh, and M. Van Schilfgaarde, APL Mater. **4**, 091501 (2016).

Publications

[P1] J. L. Lyons and C. G. Van de Walle, "Computationally predicted energies and properties of defects in GaN", NPJ Comput. Mat. **3**, 12 (2017). [doi: 10.1038/s41524-017-0014-2]

[P2] C. E. Dreyer, A. Alkauskas, J. L. Lyons, A. Janotti, and C. G. Van de Walle, "First-principles calculations of point defects for quantum technologies", Annu. Rev. Mater. Res. **48**, 1 (2018). [doi: 10.1146/annurev-matsci-070317-124453]

[P3] J. L. Lyons, A. Alkauskas, A. Janotti, and C. G. Van de Walle, "Deep donor state of the copper acceptor as a source of green luminescence in ZnO", Appl. Phys. Lett. **111**, 042101 (2017). [doi: 10.1063/1.4995404]

[P4] H. Peelaers and C. G. Van de Walle, "Sub-band-gap absorption in Ga_2O_3 ", Appl. Phys. Lett. **111**, 182104 (2017). [doi: 10.1063/1.5001323]

[P5] J.-X. Shen, D. Wickramaratne, and C. G. Van de Walle, "Band bowing and the direct-to-indirect crossover in random BAlN alloys", Phys. Rev. Mater. **1**, 065001 (2017). [doi: 10.1103/PhysRevMaterials.1.065001]

[P6] L. Weston, D. Wickramaratne, M. Mackoit, A. Alkauskas, and C. G. Van de Walle, "Native point defects and impurities in hexagonal boron nitride", Phys. Rev. B **97**, 214104 (2018). [doi: 10.1103/PhysRevB.97.214104]

[P7] N. L. Adamski, Z. Zhu, D. Wickramaratne, and C. G. Van de Walle, "Strategies for *p*-type doping of $ZnGeN_2$", Appl. Phys. Lett. **114**, 032101 (2019). [doi:10.1063/1.5063581]

[P8] D. Wickramaratne, J.-X. Shen, A. Alkauskas, and C. G. Van de Walle, "Comment on "Comparative study of *ab initio* nonradiative recombination rate calculations under different formalisms"", Phys. Rev. B **97**, 077301 (2018). [doi: 10.1103/PhysRevB.97.077301]

[P9] D. Wickramaratne, C. E. Dreyer, B. Monserrat, J.-X. Shen, J. L. Lyons, A. Alkauskas, and C. G. Van de Walle, "Defect identification based on first-principles calculations for deep level transient spectroscopy", Appl. Phys. Lett. **113**, 192106 (2018). [doi: 10.1063/1.5047808]

[P10] X. Zhang, J.-X. Shen, and C. G. Van de Walle, "Three-dimensional spin texture in hybrid perovskites and its impact on optical transitions", J. Phys. Chem. Lett. **9**, 2903 (2018). [doi**:** 10.1021/acs.jpclett.8b01004]

[P11] X. Zhang, J.-X. Shen, W. Wang, and C. G. Van de Walle, "First-principles analysis of radiative recombination in lead-halide perovskites", ACS Energy Lett. **3**, 2329 (2018). [doi: 10.1021/acsenergylett.8b01297]

[P12] J.-X. Shen, X. Zhang, S. Das, E. Kioupakis, and C. G. Van de Walle, "Unexpectedly strong Auger recombination in halide perovskites", Adv. Energy Mater. **8**, 1801027 (2018). [doi: 10.1002/aenm.201801027]

Optical, Electrical and Magnetic Studies of Hybrid Organic-Inorganic Perovskite Semiconductors

PI: Z. Valy Vardeny; Physics & Astronomy Department, University of Utah

Program Scope

Magneto-Optical and Spin responses of carriers in organic inorganic perovskite semiconductors
(i) During the last two years we have investigated carrier spin injection into various hybrid organometal trihalide perovskites (OTP) by fabricating spin-related devices such as spin-LEDs and spin-valves. (ii) We have also studied the magneto-optic response of these materials using the high magnetic field national laboratory (NHMFL) in Tallahassee Florida.

Recent Progress

(i) Spin injection into OTP

The family of OTP, namely $CH_3NH_3PbX_3$ (where X is halogen) has recently revolutionized the photovoltaic field [1], and also has shown promise in a variety of other optoelectronic applications [2, 3]. The characteristic spin and magneto-optical properties of charge and neutral excitations in the OTP are influenced by the large SOC of the Pb atoms, which may lead to spin-based device applications. Whereas the concept of OTP spintronics had been initially presented in 2016, our recent work published in *Nature Communication* in 2019 [4] is the first experimental demonstration of hybrid perovskite spintronics *device applications*. This opens up a new avenue in a field that has already attracted great attention in the research community.

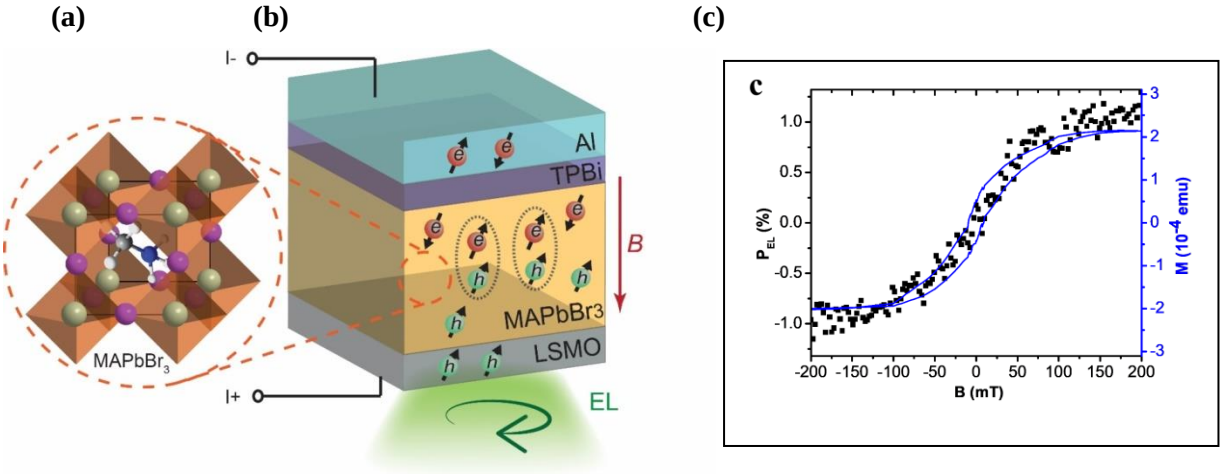

Figure 1: **Demonstration of spin-LED based on $MAPbBr_3$ interlayer**. **(a)** The $MAPbBr_3$ unit cell. **(b)** Schematic of the spin LED device, where the holes, which are spin-polarized due to injection into the OTP layer from the FM electrode (LSMO), recombine with electrons injected from the Al electrode, producing circularly polarized electroluminescence (EL). **(c)** Typical EL polarization degree response ($P_{EL}(B)$) of a spin-LED based on LSMO/$MAPbBr_3$/Al device. From Wang *et al.*, *Nature Communication* 10, 129 (2019); supported by the present DOE grant.

In the published work, we describe our successful fabrication of two prototype spin-related optoelectronic devices, namely the spin light-emitting diode (spin-LED) and spin-valve based on $MAPbBr_3$ with various morphologies, in which we demonstrated spin-aligned carrier injection

into the perovskite interlayers using, respectively the *circularly polarized electroluminescence* technique (see **Fig. 1**) and *giant-magnetoresistance* (GMR) (see **Fig. 2**). This assignment is strongly supported by our measurements of the optical and electrical *Hanle effect***,** which have been the hallmark of spin alignment in, and spin transport through the perovskite interlayer. Surprisingly, from both Hanle effect responses we measured a long spin relaxation time (~300 ps) for the spin polarized carriers and excitons in $MAPbBr_3$ that is similar in magnitude to that in graphene, although the spin-orbit coupling in the perovskites is much stronger than in graphene. The explanation of this discovery may be a puzzle that needs be thoroughly understood. In the meantime, this adds to the miraculous properties of the hybrid perovskites that make them very attractive for spintronics and spin-optoelectronic applications. On the one hand, the large spin-orbit coupling in $MAPbBr_3$ is an imperative property that allows spin manipulation; and, on the other hand, the spin lifetime is sufficiently long to allow spin manipulation. Indeed an unusual compound with promising applications and underlying science [5]. We also note that the OTP compounds contain both organic and inorganic components, and thus they do not belong to any previous class of materials that show potential optoelectronics and spintronics applications. Therefore our studies supported by the present DOE grant have open a new class of materials for spintronics applications.

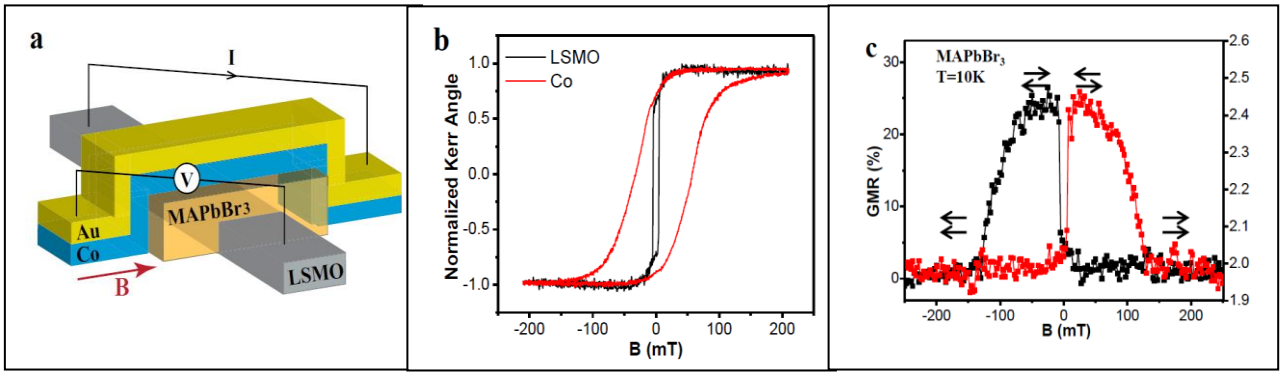

<u>Figure 2</u>: Giant Magnetoresistance (GMR) in $MAPbBr_3$-based spin valve. (a) Schematic of the OTP-based spin-valve. The perovskite layer is positioned in between the LSMO and Co feromagnetic layers having two different cohersive fields (see (b)), where the resistance vs field is measured using 'four probes' geometry. The LSMO injects spin aligned current, J_S into the OTP interlayer in a parallel magnetization direction of the two FM electrodes (low resistance). **(b)** The MOKE(*B*) response of the two FM electrodes (LSMO and Co) measured at 10K that show two different coesive fields. **(c)** Magnetoresistance(*B*) response (given in %) of $MAPbBr_3$-based spin valve measured at *T*=10K. The relative magnetization directions of the FM electrodes are shown for clarity, where the high resistance occurs at antiparallel magnetization configuration. From Wang *et al*. [ref. 4].

Figure 2 demonstrates spin aligned carriers injection into OTP film [4]. The measurements were done using a spin-valve device, where the OTP layer was deposited in between two FM electrodes having two different coercive fields. The GMR(*B*) response follows a well-known pattern, where the device resistance, R is higher when the two magnetization direction are antiparallel to each other. We fabricated spin-valves using $MAPbBr_3$, as well as other OTP's. These GMR(B) responses are very similar to those measured in organic spin-valves [6]. However in contrast to organic spin valves [7] we have succeeded in measuring the 'Hanle effect' in the OTP-based spin-valves [4]. In this kind of measurements we applied a perpendicular field, $B_\perp$ to the injection spin direction that causes the spin to precess about the

applied $B_\perp$ and thus lose their preferred alignment upon injection. This entails the 'smoking gun' experiment that shows spin injection into the OTP interlayer. From the MR($B_\perp$) response we could obtain the spin relaxation time, τ_S in the OTP. We obtained τ_S of order few hundreds ps at 10K [4], which is surprising, considering the strong SOC in these compounds.

(ii) <u>Magneto-optical studies of OTP at high magnetic field in NHMFL at Tallahassee FL</u>

Field-induced spin splitting and anomalous photoluminescence circular polarization in $CH_3NH_3PbI_3$ films at high magnetic field (Phys. Rev. B 97, 134412 (2018))

Using high-field magneto-optical measurements up to 17.5 Tesla at cryogenic temperatures, we have studied the spin-dependent optical transitions in the prototype OTP, namely $CH_3NH_3PbI_3$, which are manifested in the field-induced circularly polarized photoluminescence (FICPO) (see **Fig. 3**) [8]. The energy splitting between left and right circularly polarized emission bands was measured to be ~1.5 meV at 17.5 Tesla, from which we obtained an exciton effective *g*-factor of ~1.32 [8]. Also from the photoluminescence diamagnetic shift we estimate the exciton binding energy to be ~17 meV at low temperature. Surprisingly, the corresponding FICPO is 'anomalous' in that the photoluminescence emission of the *higher* split energy band is stronger than that of the *lower* split band (Fig. 3b). This 'reversed' intensity ratio originates from the combination of long electron spin relaxation time and hole negative *g*-factor in $CH_3NH_3PbI_3$, which are in agreement with a model based on the **k·p** effective-mass approximation.

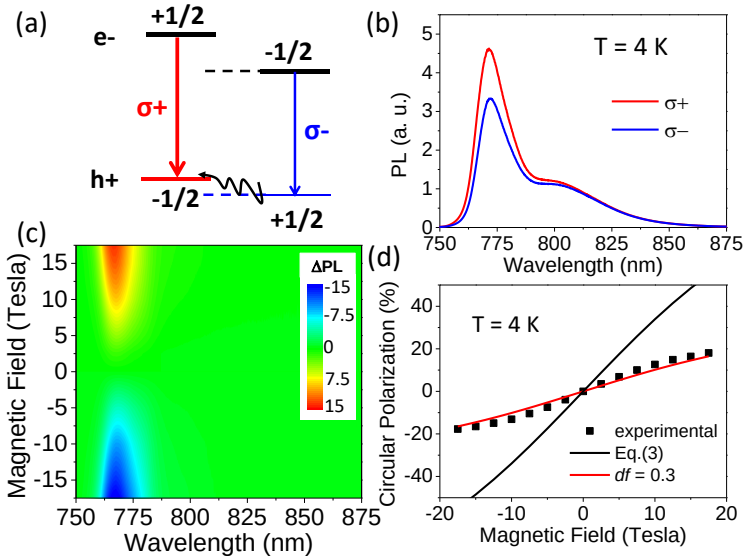

<u>Figure 3;</u> Field-induced circular polarization (FICPO) in the PL emission of $CH_3NH_3PbI_3$ film. (a) Schematic illustration of the relaxation and recombination processes between spin sublevels of electrons in the CB and holes in the VB. The thermal spin distribution of holes in the VB introduces unequal PL intensities with left, σ- and right, σ+ polarizations. Note that the hole *g*-factor is negative in $CH_3NH_3PbI_3$. (b) Field-induced circularly polarized PL emission bands (σ+ and σ-, red and blue lines, respectively) from $CH_3NH_3PbI_3$ film measured at 4 K and B=17.5 T. (c) False color plot of the difference, ΔPL of the circular polarized PL spectra (ΔPL= PL(σ+)-PL(σ-)) at various B fields. (d) The circular polarization value, P vs. B for the free exciton band (black squares), and a fit using a Boltzmann distribution model without (black line) or with (red line) a decreasing factor, D = 0.3, caused by the finite spin relaxation time relative to the PL lifetime. From ref. [8].

Future Plans

In the 4th support year of our program we work on several projects at the NHMFL that involve not only FICPO of the PL emission, but also circular dichroism (CD) and magneto-circular dichroism (MCD) of 3D and 2D organic/inorganic perovskites. In this case we will not be prone to charged traps that produced trion PL upon exciton trapping, but we will study the absorption spectrum instead. We have already preliminary data that show MCD of excitons in $MAPbI_3$ and $MAPbBr_3$, as well as in 2D OTP. Because the exciton binding energy is relatively large in the latter compound we are able to study the interband transition upon the application of an external magnetic field which show the formation of Landau levels; an exciting discovery for 2D organic/inorganic semiconductors.

References

[1] Jeon, N. J. *et al*., *Nature* **517**, 476-480 (2015) (OTP Solar Cells).

[2] Xing, G. *et al*. *Nat. Mater.* **13**, (2014) (OTP Laser action).

[3] Tan, Z.-K. *et al*. *Nat. Nano*. **9**, 687-692 (2014) (OTP LEDs).

[4] Wang, J. *et al.*, *Nature Communication* **10**, 129 (2019) (spin-related devices based on OTP).

[5] P. Odenthal, P. *et al*, *Nature Physics* **13**, 894 (2017) (spin response in $MAPbI_3$).

[6] Xiong, Z. H. et al., *Nature* **427**, 821-824 (2004) [spin-valve based on organic compounds].

[7] Szulczewski, G., *et al*., *Nat. Mater.* **8**, 693 (2009) [Spinterface in organic].

[8] Zhang, C.,*et al., Phys. Rev. B* **97**, 134412 (2018) [FICPO in $MAPbI_3$].

Publications that resulted from the present DOE grant (06.2016-01.2019)

[1] "On the role of intrinsic ions accumulation in the photocurrent and photo-capacitive responses of $MAPbBr_3$ photodetectors", E. Lafalce, C. Zhang, X. Liu, and Z. V. Vardeny, ***Applied Materials and Interfaces***, **8,** 51, 35447 (2016); 10.1021/acsami.6b11925.

[2] "Enhanced emission, reduced lasing thresholds and increased optical gain of nano-crystalline $MAPbBr_3$ films via anti-solvent treatment", E. Lafalce, C. Zhang, Y. Zhai, D. Sun and Z.V. Vardeny, ***J. Appl. Phys***. **120**, 143101 (2016); doi: 10.1063/1.4964417 2016.

[3] "Spin-polarized exciton quantum beats in hybrid organic-inorganic perovskites", P. Odenthal, W. Talmadge, N. Gundlach, R. Wang, C. Zhang, D. Sun, Z.-G. Yu, Z. V. Vardeny, and Y. S. Li, ***Nature Physics*** **13**, 894 (2017).

[4] "Giant Rashba-Splitting in 2D organic-inorganic halide perovskites measured by transient spectroscopies", Yaxin Zhai, S. Baniya, C. Zhang, C.-X. Sheng, E. Ehrenfreund, Z.V. Vardeny, ***Science Advances*** **3,** e1700704 (2017).

[5] "Multi-Functional Optoelectronic-Spintronics Device Based on Hybrid Organometal Trihalide Perovskites", C. Zhang, D. Sun, Z. V. Vardeny, ***Adv. Electron. Mater.*** **3,** 2 (2017); DOI: 10.1002/ aelm.201600426 (2017).

[6] "Electroabsorption spectroscopy studies of $(C_4H_9NH_3)_2PbI_4$ organic-inorganic hybrid perovskite multiple quantum-wells", Eric Amerling, Sangita Baniya, Evan Lafalce, Chuang Zhang, Zeev Valy Vardeny, and Luisa Whittaker-Brooks, ***Jour. of Physical Chemistry Letters*** **8**, 4557-4564 (2017). DOI: 10.1021/acs.jpclett.7b01741

[7] “Temperature-Dependent Electric Field Poling Effects in $CH_3NH_3PbI_3$ Optoelectronic Devices”, Chuang Zhang, Dali Sun, Xiaojie Liu, Chuan-Xiang Sheng and Zeev Valy Vardeny ***Journal of Physical Chemistry Letters*** **8**, 1429 (2017) 10.1021/acs.jpclett.7b00353 (2017).

[8] “Effects of Non-Hydrostatic Stress on Structural and Optoelectronic Properties of Methylammonium Lead Bromide Perovskite”, Rong Zhang, Weizhao Cai, Tiange Bi, Niloofar Zarifi, Tyson Terpstra, Chuang Zhang, Z. Valy Verdeny, Eva Zurek and Shanti Deemyad, accepted in ***Jour. Physical Chemistry Letters*** **8**, 3457-3465 (2017).

[9] "Light-controlled spintronic device based on hybrid organic/inorganic perovskites,"Jingying Wang, Xin Pan, Chuang Zhang, Hangwen Guo, Zeev Valy Vardeny, ***J. Photon. Energy*** **8**(3), 032207 (2018), doi: 10.1117/1.JPE.8.032207.

[10] “Magnetic field effect in organometal trihalide perovskite”, Chuang Zhang, Dali Sun, and Z. Valy Vardeny, chapter #9 in *Spins in Organic*, World Scientific, Ed. Markus Wohlgenannt, published in October 2018. ISBN 978-981-3229-06-8

[11] “Novel Spin Physics in Organic-Inorganic Perovskites”, Chuang Zhang, Dali Sun, and Z. Valy Vardeny, chapter 4.1 in “Halide Perovskites; Photovoltaics, Light Emitting Devices and Beyond”, Willey-VCH, Ed. T.C. Sum and N. Mathews, pp 251-272 (2019); ISBN 978-3-527-34111-5.

[12] “Field-induced spin splitting and anomalous photoluminescence circular polarization in $CH_3NH_3PbI_3$ films at high magnetic field”, Chuang Zhang, Dali Sun, Zhi-Gang Yu, Chuan-Xiang Sheng, Stephen McGill, Dmitry Semenov, and Zeev Valy Vardeny, ***Physical Rev***. B **97**, 134412 (2018). DOI: 10.1103/PhysRevB.97.134412

[13] “Spin-Optoelectronic Devices Based on Hybrid Organic-Inorganic Trihalide Perovskites”, Jingying Wang, Chuang Zhang, Haoliang Liu, Ryan McLaughlin, Yaxin Zhai, Shai R. Vardeny, Xiaojie Liu, Stephen McGill, Dmitry Semenov, Hangwen Guo, Ryuichi Tsuchikawa, Vikram V. Deshpande, Dali Sun, Z. Valy Vardeny, ***Nature Communications*** **10**, 129 (2019) https://doi.org/10.1038/s41467-018-07952-x

Title: Thermodynamic, Kinetic and Electrochemical Studies on Mixed Proton, Oxygen Ion and Electron (Hole) Conductors

PI: Anil V. Virkar, University of Utah

Program Scope

The principal objective of the project is to investigate multi-species transport in predominantly ionic conductors which have applications in fuel cells, electrolyzers, oxygen separators, hydrogen separators, and in sodium and lithium batteries. This includes all solid-state batteries. The work also includes proton exchange membrane (PEM) fuel cells. The literature is primarily focused on transport properties (e.g. conductivities) of such materials or charge transfer at electrode/electrolyte interfaces. In predominantly ionic conductors, the focus has been on ionic conductivity, the effects of which are measureable – e.g. current flowing through a device or electrocatalytic activity of electrodes. Local thermodynamic equilibrium (even when a system is away from thermodynamic equilibrium), however, determines stability [1-3]. Our work is on the measurement of electrode polarizations and their effects on both performance and stability of electrochemical devices and systems. Stability is governed by chemical potentials of electrically neutral species. Thus, local thermodynamic equilibrium in an oxygen ion conductor is primarily dictated by the chemical potential of neutral oxygen, μ_{O_2}; that in a proton conductor by μ_{H_2}; that in a lithium ion conductor by μ_{Li}, etc., or in general chemical potentials of all neutral species comprising the system. This requires the knowledge of local electrochemical potential of electrons. Concepts from non-equilibrium thermodynamics lead to an important result which shows that even in a predominantly ionic conductor, the electronic conductivity, no matter how small, cannot be ignored since it has a profound effect on the local equilibrium [4-6]. Thus, to investigate multi-species transport, electronic transport must be included in the general equations of transport [5-8]. It is equally important to include the role of electrode polarizations in the transport equations. Conductivities of electrolyte materials can be readily determined. However, it is not possible to easily determine electrode polarizations separately. This is because of the difficulty in de-convoluting electrochemical impedance spectra (EIS). We have been developing methods of embedding reference electrodes inside an electrolyte such that the spectra of cathode and anode can be obtained separately. Additionally, we have been developing methods to measure electrode polarizations using a fully DC method. This is important since EIS is an AC method, but electrochemical devices operate in a DC mode. In terms of transport, the relevant mathematical formulas must include the electronic conductivity, however small. The overall transport equations must include Onsager coupling. The Onsager coefficients of the electrochemical device include transport properties of the electrolyte as well as electrode polarizations and interface electron/hole transport paramaters. Our prior work has examined the effect of electrolytic and galvanic operations on stability. [6-9]. The fuel cell mode (or the battery discharge) is the galvanic mode. The electrolysis mode (or the battery charging mode) is the electrolytic mode. The electrochemical devices exhibit greater tendency to degradation in the electrolytic mode. Experimental evidence [10,11] of this behavior has been reported in the literature which confirms our theoretical predictions [5-8]. The origin of this result lies in non-equilibrium thermodynamics and Onsager coupling. The focus of our work is on predominantly

oxygen ion conductors, proton conductors, and monovalent cation conductors and their behavior when removed from thermodynamic equilibrium.

Figure 1

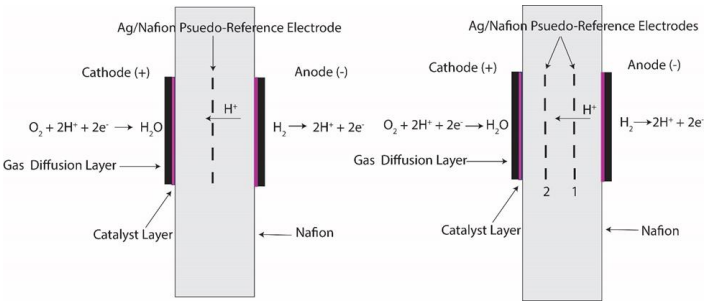

Figure 1: A schematic of a one (left) and a two (right) embedded pseudo-reference electrode MEA.

Figure 2: EIS of Z_{cell}^{sum} and Z_{cell} at (a) open circuit, using (b) 10.3 Ω, (c) 2.65 Ω, and (d) 1.58 Ω resistor.

Figure 2

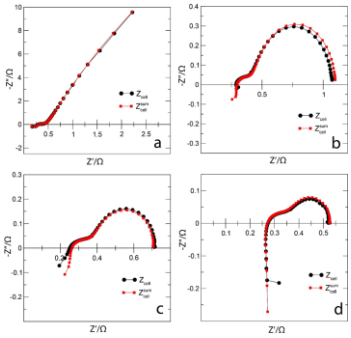

By embedding reference electrodes, we conducted EIS across the embedded probe and the two electrodes separately. We also measured EIS across the cathode and the anode (the entire cell). Figure 2 shows that the sum of the cathode – reference and the anode –reference (red points) EIS spectra exactly match the one across the cathode-anode (that is the entire cell) (black points). Use of reference electrodes allows one to measure the cathode polarization and the anode polarization separately. The one across the entire cell cannot be uniquely de-convoluted to obtain cathode and anode polarizations separately.

Recent Progress

Recent work has been on the following topics: **(1)** Measurement of Electrode Polarizations in PEM Fuel Cells by Embedded Electrodes: PEM fuel cells with one and two embedded Ag-reference electrodes were synthesized. EIS spectra were obtained across the entire cell, as well as between the reference electrodes and anode/cathode and also across the reference electrodes (membrane with two reference electrodes). This made it possible to separately measure cathode and anode electrode polarizations over a range of loads (operating cell). With the two reference electrodes cell, we were also able to fully separate the anode reaction, without any effects of the electrolyte. These measurements will allow us to determine Onsager transport coefficients in terms of electrolyte transport properties and electrode polarization resistances as a function of load. Graduate student Alex Szendrei presented a paper at the Electrochemical Society Meeting in Seattle, WA in May 2018 **(2)** Measurement of Electrode Polarization Resistance of LSM + YSZ electrodes by DC and EIS methods: A cylinder of YSZ was made by powder pressing and sintering. Four Pt strip electrodes were applied at equal distances along the cylinder. Polarization measurements were made in a DC mode under various loads. From these studies, electrode polarization measurements were made. It was observed that even though the two electrodes were identical in composition, their polarization resistances were different. This shows that the usual assumption of using a symmetric cell in EIS to determine polarization resistance is not valid.

Small differences in electrode microstructures, possible unintended differences in the application of electrodes, can make a large difference. Also, the Butler-Volmer equation was found to be applicable. At higher polarization, we were also able to observe the Tafel limit. Alex Szendrei presented a paper at the American Ceramic Society meeting in Daytona Beach, FL in January 2019 **(3)** Synthesis of Li-Ion Conducting Beta"-alumina and a Solid State Lithium Battery: We have conducted preliminary work on the fabrication of Li-ion conducting beta"-alumina and have demonstrated a room temperature solid state battery. Na-beta"-alumina + YSZ composite discs were fabricated by vapor phase conversion of sintered alumina + YSZ discs. These were then ion-exchanged in molten $LiNO_3$ to replace Na^+ by Li^+. Lithium ion conductivity is lower than that of Na-beta"-alumina, but is still quite high and comparable to some other lithium ion conductors. At low temperatures, oxygen ion conductivity of YSZ is much lower than that for alkali ion. A solid state lithium battery was demonstrated [12]. **(4)** Carbon Monoxide Poisoning of Platinum by Electrical Resistance Measurements: One of the modes of degradation of PEMFC anodes is by adsorption of trace levels of CO from the fuel on the anode catalyst thus blocking the active sites where hydrogen oxidation reaction occurs. Carbon monoxide (CO) poisoning of platinum catalysts in proton exchange membrane fuel cells (PEMFC) substantially affects cell performance. Many studies have been reported on performance degradation even with very small concentrations of CO in hydrogen. The present work investigated carbon monoxide adsorption/desorption in situ on a 1 nm thick platinum film deposited on a sapphire substrate by measuring the electrical resistance of the film as a function of CO concentration, exposure time and testing temperature. The experimental data showed an increase in the film resistance upon exposure to CO containing gases. The film resistance was sensitive to CO exposure at a concentration as low as 1 ppm. A model was developed to determine rate constants and activation energies for CO adsorption/desorption on Pt surface using the measurement of electrical resistance as a function of time [13]. **(5)** Effect of Electronic Conductivity on Oxygen Chemical Potential in Oxygen Ion Conductors: Our theoretical work has shown that low level electronic conductivity in predominantly ionic conductors can have a large effect on the chemical potential of the neutral species corresponding to the mobile ion; that is on μ_{O_2} in oxygen ion conductors. Experimental results have also confirmed the consequences of this; namely oxygen electrode delamination in solid oxide electrolysis cells [14]. Laguna-Bercero et al. have actually demonstrated both electrode delamination as well as change in oxygen concentration through the thickness of a YSZ electrolyte –based cell, and the formation of multiple cracks inside the electrolyte [10]. Since YSZ has a very low electronic conductivity, a large variation in oxygen concentration was observed (which corresponds to a large variation in μ_{O_2}). We have recently made samples of 8YSZ and samples containing 5% CeO_2 (5Ce8YSZ). CeO_2 was added to one set of samples to increase the electronic conductivity. Both electrodes were LSM + YSZ composites. The discs were heated to 700°C and a DC voltage was applied to pass ~0.2 to ~0.25 Acm^{-2}. After 24 h, the voltage was removed, and the discs were cooled to room temperature. The discs were then examined under an SEM and EDS scans of O, Zr and Y were obtained through the thicknesses of the discs.

Future Plans

1) To synthesize and characterize ion conducting materials far removed from global thermodynamic equilibrium.
2) To synthesize membranes with embedded screen electrodes. Make measurements under conditions far removed from equilibrium. This will also involve the development of equations that can describe local chemical potentials as functions of position and time in terms of transport.
3) To investigate local thermodynamics and transport in single phase and multi-phase, predominantly ion-conducting materials in systems away from equilibrium. Materials of interest include mixed H^+ and O^{2-}-ion conductors, Na^+-ion conductors, Li^+-ion conductors, and multi-phase composite materials.

References

1) D. Kondepudi and I. Prigogine, 'Modern Thermodynamics: From Heat Engines to Dissipative Structures', John Wiley, New York (1998).
2) S. Kjelstrup and D. Bedeaux, 'Non-Equilibrium Thermodynamics of Heterogeneous Systems', World Scientific, (2008).
3) R. Haase, 'Thermodynamics of Irreversible Processes', Dover Publications, (1990).
4) A. V. Virkar, *J. Electrochem. Soc*., **138** (5) 1481-1487 (1991).
5) A. V. Virkar, *J. Power Sources*, **147** 8-31 (2005).
6) A. V. Virkar, *Int. J. Hyd. Energy*, **35** 9527-9543 (2010).
7) A. V. Virkar, *J. Power Sources*, **196** 5970-5984 (2011).
8) A. V. Virkar, *Int. J. Hyd. Energy*, **37** 12609-12628 (2012).
9) A. V. Virkar, in 'Engineered Ceramics: Current Status and Future Prospects', edited T. Ohji and M. Singh, p. 59-76, Wiley-Am. Ceramic Soc. (2016).
10) M. A. Laguna-Bercero, R. Campana, A. Larrea, J. A. Kilner, and V. M. Orera, *J. Power Sources*, **196** 8942-8947 (2011).
11) J. R. Mawdsley, J. D. Carter, A. J. Kropf, B. Yildiz, and V. A. Maroni, *Int. J. Hyd. Energy*, **34** 4198-4207 (2009).
12) L. Zhu and A. V. Virkar, *ECS Transactions*, **80** (9) 35-44 (2017).
13) L. Zhu, L. Zhang and A. V. Virkar, *J. Electrochem. Soc*., **165** (3) F232-F237 (2018).
14) L. Zhu, L. Zhang and A. V. Virkar, *ECS Transactions*, **80** (9), 81-89 (2017).

Publications

1 'Role of Electronic Conductivity in Stability of Solid Oxide Electrolyzer Cells', L. Zhu, L. Zhang and A. V. Virkar, *ECS Transactions*, **80** (9), 81-89 (2017).
http://dx.doi.org/10.1049/08009.0081ecst

2 'Measurement of Ionic Conductivity and Electrode Polarization at Low Temperatures on 8YSZ by a DC Technique', A. Szendrei, T. D. Sparks and A. V. Virkar, *J. Electrochem. Soc*., **164** (14) F1543-F1550 (2017). http://dx.doi.org/10.1149/2.033174jes

3 'Anode Concentration Polarization in Solid Oxide Fuel Cells as a Dissipative Process', A. V. Virkar, *ECS Transactions*, **78**(1) 1095-1105 (2017). http://dx.doi.org/10.1149/07801.1095ecst

4 'On Space Charge and Spatial Distribution of Defects in Yttria-Stabilized Zirconia', L. Zhang and A. V. Virkar, *J. Electrochem. Soc*., **164** (3) F1506-F1523 (2017).
http://dx.doi.org/10.1149/2.1801713jes

5 'Fabrication of Li-β"-alumina + Yttria-Stabilized Zirconia Composites and Their Application in Lithium Battery', L. Zhu and A. V. Virkar, *ECS Transactions*, **80** (9) 35-44 (2017).
http://dx.doi.org/10.1149/08009.0035ecst

6 ‘A Study of CO Adsorption/Desorption on Thin Platinum Film by the Measurement of Electrical Resistance’, L. Zhu, L. Zhang and A. V. Virkar, *J. Electrochem. Soc.*, **165** (3) F232-F237 (2018). http://dx.doi.org/10.1049/2.0011805jes

Nanocrystal-based Dyads for Solar to Electric Energy Conversion

David N. Beratan, Departments of Chemistry, Biochemistry, and Physics, Duke University, Durham NC 27708
Ron Naaman, Department of Chemical and Biological Physics, Weizmann Institute, Rehovot, Israel 76100
David H. Waldeck, Chemistry Department, University of Pittsburgh, Pittsburgh PA 15260

Program Scope

The optical and electronic properties of semiconductor quantum dots (QDs) make them attractive candidates for applications in photovoltaics, spintronics, photocatalysis, and optoelectronics. Understanding how to control the flow of charge in QD assemblies is essential for realizing novel applications. We are exploring how to manipulate the structural and energetic features of semiconductor nanoparticle (quantum dots, QD) assemblies for promoting charge separation and for inhibiting charge recombination, as well as other energy applications.[1] Our team uses experimental and computational studies to explore the importance of QD-ligand interactions, QD-QD interactions, and QD-electrode interactions that affect electron transfer and to examine the roles played by energy-level gradients, built-in electrostatic potentials, and symmetry/chirality properties. To date we have focused our efforts on exploring how the charge-transfer rate between an electron donor QD and an electron acceptor QD correlates with the QD size, and on special optical, charge transfer, and magnetic properties that appear in chiral QDs.

Recent Progress

QD Charge Transfer, Energy band alignment: We developed a theoretical model to describe electron transfer between pairs of quantum dots[2] and extended it to modeling charge transfer in assemblies of three quantum dots.[3] Our model predicts that the triad systems can improve the charge transfer efficiency by inhibiting charge recombination processes. We developed kinetic models to explore the current−voltage, power−voltage, and power conversion efficiency characteristics of QD dyads and triads as possible light absorption and charge separation 'engines', in bulk heterojunction solar cells. The external and internal power conversion quantum efficiencies were significantly enhanced by introducing a third QD between the donor and acceptor QDs. Given the constraint of comparable charge-recombination and charge separation rates, open-circuit voltages were found to be 10%−17% larger for triads than for dyads, and short-circuit currents

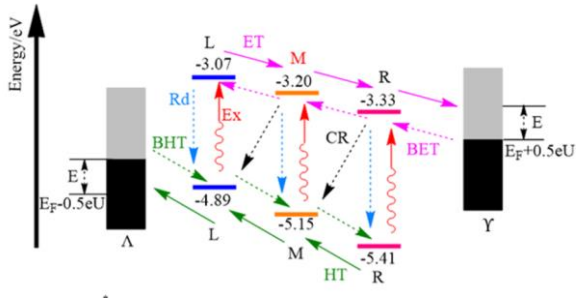

Figure 1. The image shows an energy diagram for a QD triad structure between two electrodes; all of the photoexcitation (Ex)/radiative decay (Rd), ET/back ET (BET), HT/back HT (BHT), and charge recombination (CR) processes in the triad solar cell of the QD triad are indicated. Taken from reference 3.

were about 400% larger for triads than for dyads. These improvements in the efficiencies can be further enhanced by tuning the band-edge energy offset of the middle-position QD; see Figure 1. The triad performance is most favorable when the band-edge energies of the middle QD create an energy cascade of band-edge energies across the QD assembly. To produce the most favorable solar cell performance, the middle QD's conduction (valence) band edge should be closer to the right QD's band edge when the charge recombination rates are low (high) and near the conduction (valence) band edge of the left QD when the charge recombination rates are high (low). This analysis identifies strategies to design multi-QD assemblies for solar energy harvesting and conversion.

Charge Transport, Electric-field effects: We completed theoretical explorations of how electric fields impact charge transport mechanisms in the regime of low tunneling barriers.[4] A growing number of experiments find limited temperature dependence for electron transfer over tens of nanometers. To account for these observations, we developed a transport model based on the electric potential difference that builds up along the molecule as a precursor for electron transfer. Specifically, the voltage changes the nature of the electronic state delocalization, so that efficient resonant tunneling across long distances becomes possible without thermal assistance. This mechanism is general, and is expected to be operative in molecules where the electronic states densely fill a wide energy window (on the scale of electron Volts) above or below the HOMO-LUMO gap. We showed that this effect can explain the temperature and voltage dependence of charge transport through biomacromolecules and organic semiconductors.

QD Charge Transfer, Chiral symmetry effects: Chirality at the nanoscale can induce spin selective charge transport, providing new ways to direct charge (and spin) flow in QD assemblies. Recently, we showed that chiral symmetry of QDs affects the electron-transfer rate for different electron spins.[5] In these studies we used circular polarized light to excite an electron donor with a preferred spin polarization and then monitored the electron transfer rate to a chiral acceptor QD. Furthermore, we showed that the chiral effect on the electron-transfer rate constant correlated with the strength of the acceptor QD circular dichroism (CD) spectrum. These findings imply that the CD strength of the QD exciton transition(s) may be used as a predictor for the spin dependent electron transfer, indicating that chiral

Chiral Imprinting on QD Excitons: We demonstrated the direct synthesis of chiroptical organic–inorganic methylammonium lead bromide perovskite nanoplatelets that is controlled by the chirality of their surface ligands.[6] The circular dichroism spectra display two components strong features, (1) a feature in the 300–350 nm and (2) a feature near the excitonic absorption maximum of the perovskite, 400–450 nm. Based on the energy shifts in these transitions with the perovskite composition (Cl, Br, and I content), we have assigned these transitions to the M and R points, respectively, in the perovskite lattice. The temperature- and concentration-dependent circular dichroism spectra indicate that the chiro-optical response arises from chiral imprinting by the ligand on the electronic states of the quantum-confined perovskite rather than chiral ligand-induced stereoselective aggregation.

Chiral imprinting of ferromagnetism: Recently we showed that chiral molecules can be used to imprint a preferred magnetization on iron oxide nanomaterials.[7] Magnetic memory devices rely on ferromagnets, a requirement which limits size reduction to 30–50 nm. Reducing the size even further, to the ≈10–20 nm scale, destabilizes the magnetization and its magnetic orientation becomes susceptible to thermal fluctuations and stray magnetic fields. Recently, we showed that chiral molecules can imprint ferromagnetism on 10 nm single domain iron oxide nanoparticles. Using asymmetric adsorption of chiral molecules, superparamagnetic iron oxide nanoparticles become ferromagnetic with an average coercive field of ≈80 Oe. The asymmetric adsorption of molecules stabilizes the magnetization direction at room temperature and its orientation depends on the handedness of the chiral molecules.

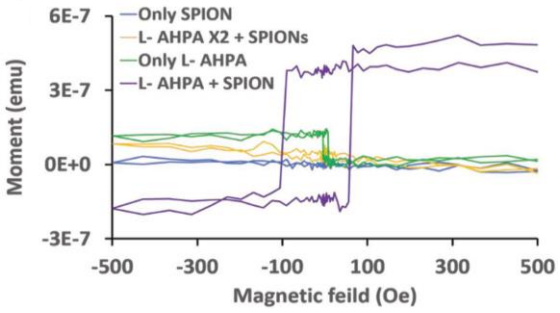

Figure 2. SQUID measurements of the magnetization hysteresis loop for iron oxide nanoparticles (SPIONs) on a chiral peptide (L-AHPA) film. The sample of L-AHPA with iron oxide nanoparticles (purple line) shows a hysteresis loop with an average coercive field of ≈80 Oe. The figure also shows three reference samples: L-AHPA X2 which has chiral molecules adsorbed on both sides of the SPIONS (orange line), a film of L-AHPA molecules (without nanoparticles, green line), and only iron oxide nanoparticles (without AHPA, blue line). Taken from reference 7.

Voltage-controlled magnetization of molecule films: We used GaAs/AlGaAs devices, which host a two-dimensional electron gas, to measure the magnetization that is induced in a monolayer of chiral organic molecules by an applied voltage. We observe clear signatures of room temperature magnetism, which is induced in these systems by applying a gate voltage. We explain this phenomenon as a consequence of the spin-polarized charges that are injected into the semiconductor through the chiral molecules. The orientation of the magnetic moment can be manipulated by low gate voltages, with a switching rate in the MHz range. These devices allow for an efficient, electric field-controlled magnetization.

.

Future Plans

We are extending the studies described above under several different avenues. Our theoretical studies will focus on the (1) the transition from through-bond to through-solvent electron tunneling between coupled NPs as the NP radii and electronic structure are varied and (2) the influence of chiral adsorbates on photoinduced electron transfer between NP pairs. We are extending the chiral nanoparticle and nanoplatelet synthesis studies to other material compositions and will begin to examine their electron spin-filtering properties in films and assemblies, through both optical and dark measurements. We will extend our studies of chiral imprinting on iron oxide nanoparticles and the novel electric and magnetic properties that may arise with changes in the

chiral ligands and the nanoparticle properties, such as size. These studies aim to place our novel findings on a firm theoretical footing and to guide next generation experimental system design.

References

1. B.P. Bloom, R. Liu, P. Zhang, S. Ghosh, R. Naaman, D.N. Beratan, and D.H. Waldeck, "*Directing charge transfer in quantum dot assemblies"* Acc. Chem. Res. **51** (2018) 2565-2573.
2. R. Liu, B.P. Bloom, D.H. Waldeck, P. Zhang, and D.N. Beratan, "*Controlling electron-transfer kinetics of quantum-dot assemblies*", J. Phys. Chem. C **121** (2017) 14401-14412.
3. R. Liu, B.P. Bloom, D.H. Waldeck, P. Zhang, and D.N. Beratan, "*Improving solar cell performance using quantum dot triad charge-separation engines*" J. Phys. Chem. C **122** (2018) 5924-5934.
4. K. Michaeli, D.N. Beratan, D.H. Waldeck and R. Naaman, "*Voltage induced long-range coherent electron transfer through organic molecules*" Proc. Natl. Acad. Sci., in press (2019).
5. B.P. Bloom, B.M. Graff, S. Ghosh, D.N. Beratan and D.H. Waldeck, "*Chirality control of electron transfer in quantum dot assemblies*" J. Am. Chem. Soc. **139** (2017) 9038-9043 (2017).
6. Z. N. Georgieva, B.P. Bloom, S.Ghosh, and D. H. Waldeck "*Imprinting Chirality onto the Electronic States of Colloidal Perovskite Nanoplatelets*" Adv. Mater. (2018) 1800097.
7. G. Koplovitz, G. Leitus, S. Ghosh, B. P. Bloom, S. Yochelis, D. Rotem, F. Vischio, M. Striccoli, E. Fanizza, R. Naaman, D. H. Waldeck, D. Porath and Y. Paltiel "*Single Domain 10 nm Ferromagnetism Imprinted on Superparamagnetic Nanoparticles Using Chiral Molecules*" Small **15** (2019) 1804557.

Publications

E. Z. B. Smolinsky, A. Neubauer, A. Kumar, S. Yochelis, E. Capua, R. Carmieli, Y. Paltiel, R. Naaman, and K. Michaeli "*Electric field controlled magnetization in GaAs/AlGaAs heterostructures-chiral organic molecules hybrids*" submitted (2019).

K. Michaeli, D.N. Beratan, D.H. Waldeck and R. Naaman, "*Voltage induced long-range coherent electron transfer through organic molecules*" Proc. Natl. Acad. Sci., in press (2019).

G. Koplovitz, G. Leitus, S. Ghosh, B. P. Bloom, S. Yochelis, D. Rotem, F. Vischio, M. Striccoli, E. Fanizza, R. Naaman, D. H. Waldeck, D. Porath and Y. Paltiel "*Single Domain 10 nm Ferromagnetism Imprinted on Superparamagnetic Nanoparticles Using Chiral Molecules"* Small **15** (2019) 1804557.

R. Liu, B.P. Bloom, D.H. Waldeck, P. Zhang, and D.N. Beratan, "*Improving solar cell performance using quantum dot triad charge-separation engines*" J. Phys. Chem. C **122** (2018) 5924-5934.

B.P. Bloom, R. Liu, P. Zhang, S. Ghosh, R. Naaman, D.N. Beratan, and D.H. Waldeck, "*Directing charge transfer in quantum dot assemblies*" Acc. Chem. Res., **51** (2018) 2565-2573.

Z.N. Georgieva, B. P. Bloom, S. Ghosh, and D.H. Waldeck "*Imprinting Chirality onto the Electronic States of Colloidal Perovskite Nanoplatelets*" Adv. Mater. (2018) 1800097.

Y. Liu, Z. Zeng, B. Bloom, D.H. Waldeck, and J. Wei "*Low-Current Electrodeposition of α-MnO2 on Superaligned Electrospun Carbon Nanofibers for High-Performance Energy Storage*" Small **14** (2018) 1703237.

B.P. Bloom, B.M. Graff, S. Ghosh, D.N. Beratan, and D.H. Waldeck, "*Chirality control of electron transfer in quantum dot assemblies*" J. Am. Chem. Soc. **139** (2017) 9038-9043.

R. Liu, B.P. Bloom, D.H. Waldeck, P. Zhang, and D.N. Beratan, "*Controlling electron-transfer kinetics of quantum-dot assemblies*" J. Phys. Chem. C **121** (2017) 14401-14412.

Z. Zeng, W. D. Zhang, D. M. Arvapalli, B. Bloom, A. Sheardy, T. Mabe, Y.Y. Liu, Z.W. Ji, H. Chevva, D. H. Waldeck, and J. J. Wei, "*A fluorescence-electrochemical study of carbon nanodots (CNDs) in bio- and photoelectronic applications and energy gap investigation"* PCCP **19** (2017) 20101-20109.

Light-Matter Quantum Control: Coherence and Dynamics

PI: Jigang Wang
Co-investigators: Zhe Fei, Kai-Ming Ho, Joseph Shinar, Cai-Zhuang Wang, Yongxin Yao
Materials Science and Engineering Division, Ames Laboratory, Ames, IA 50011
e-mail: jwang@ameslab.gov

Program Scope Revolutionary advances in quantum coherence and delocalized excitation dynamics will enable novel photonic energy conversion paradigm for achieving extraordinary long-range charge transfer quasi-instantaneously. Understanding how to measure, manipulate and harvest these coherent and non-equilibrium carriers before they thermalize and cool in photovoltaic architectures will exceed incoherent hopping length and rate, and achieve nearly perfect carrier collection efficiency. The overarching goal of this program aims to advance our understanding and achieve versatile control of the initial pathways of photoenergy conversion through the study of coherence- and dynamics-mediated charge carrier transport in model photovoltaic and other emerging semiconductors. The work will characterize space, time and energy evolution of electronic, vibrational, and mixed (vibronic) states, with extreme, but important resolutions (nanometer, femtosecond and terahertz), at a single grain and grain boundary level. This work will enable the control of photocarrier transport in both light absorbers and at interfaces by applying a non-contact terahertz "push" electric field and pulse trains, both far- and near-fields, for unprecedented photoconversion efficiency and optoelectronic performance. This project will also has far reaching consequences to advance fundamental energy science towards full space-time control of coherence and excited states, potentially at room temperature, and provide prominent ingredients for light harvesting, information and energy conversion/utilization.

The work is based on Ames Laboratory's expertise in photonics and brings together a team of experimentalists, including experts in coherent spectroscopy and nano-imaging (visible to terahertz), and photovoltaic materials synthesis, with theorists skilled in out-of-equilibrium dynamics and transport simulations.

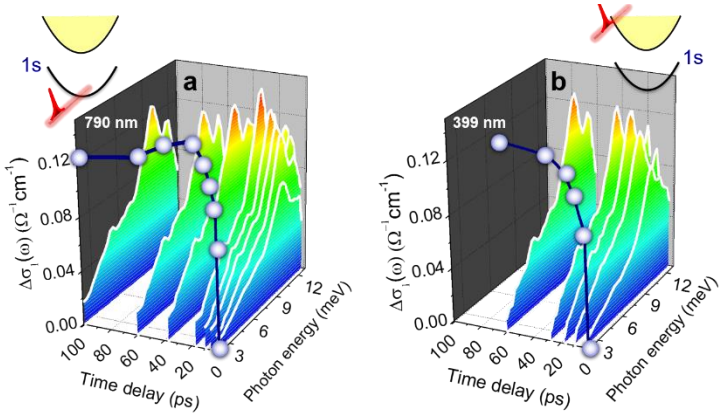

Figure 1: THz conductivity snapshots of formation pathways of excitonic Rydberg states in a hybrid organo-metal hybrid perovskite semiconductor. Photoinduced conductivity changes at several pump-probe delays after excitation at 790nm (a) and 399nm (b), respectively. The shaded circles are the effective transition strength 1s-2p, extracted from photoinduced internal quantum transitions of excitons, which allows to underpin their distinctly different rise times [1].

Recent Progress I will highlight some achievements of our newly established program.

(1) **Visualizing Coherence in Photovoltaic Semiconductors Using Terahertz:** Recent electronic transport study of hybrid organo-metal hybrid perovskite semiconductors by the Ames team (J. Wang, Yao, C-Z. Wang, Ho, and Shinar) led to discovery of the previously-inaccessible quantum transitions from excitonic Rydberg states and electronic coherence by THz spectroscopy [1]. A combination of broadband THz pulses and selective laser pumping, as shown in Figures. 1a and 1b, is used to reveal initial dynamic pathways and measure coherent charge transport of the halide perovskites for the first time. Particularly, the ultrafast THz carrier conductivity measurement directly reveals multiple sharp quantum transitions from previously-inaccessible "dark" electronic states which allows for directly characterizing and distinguishing the quantum coherence and transient temperatures of the excitons and charge carriers. The relatively long coherence time, efficient electron scattering with discrete THz phonons, and intermediate binding energy in perovskites attests the suitability of perovskite materials for solar cells and photovoltaics. In this work, the theory group developed models for exciton binding and cooling in close collaboration with experiment.

(2) **Imaging plasmon spatial coherence in pentacene-graphene heterostructures**. Advanced nanotechnology can nowadays allow us to play 'Legos' at the nanometer length scale using emerging two-dimensional (2D) semiconductors. For example, it is possible to stack atomic layers of 2D material together into a Wan der Waals (vdW) heterostructure. Interlayer interactions between these 2D materials lead to new properties and functionalities that are different from individual components. Recently, the Ames team (Z. Fei, C-Z. Wang and K-M Ho) performed a nano-plasmonic study of vdW heterostructures that consist of ordered molecular layers of pentacene on graphene. We find through nano-infrared imaging that coherent charge transfer between graphene and pentacene affects dramatically the plasmonic responses of graphene. Further analysis and density functional theory calculations indicate that charge transfer is controlled by pentacene thickness and orientation. Our work unveils a new method for tailoring graphene plasmons by interlayer charge transfer. We are currently extending this to characterize coherence in an organic superlattice of donor/acceptor monolayer photovoltaic architectures.

(3) **Ultrafast manipulation of topologically enhanced surface charge carrier transport**

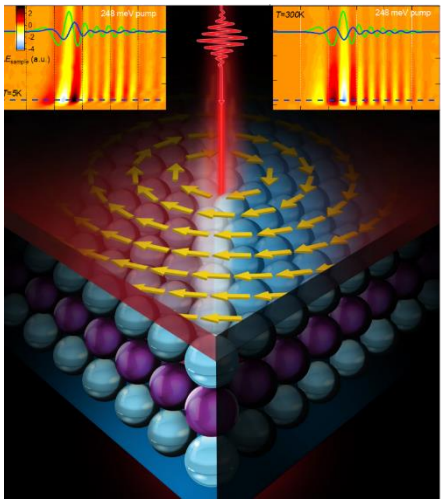

Figure 2: Ultrafast THz pump and THz probe spectroscopy of charge carrier transport in Bi_2Se_3. (Central) Schematic of the surface and bulk structures driven by ultrashort laser pulses. A 2D false-color plot of pump-induced THz field changes as a function of gate time after 248 meV (5 μm) photoexcitation at (right panel) T=300 K and (left panel) T=5 K, respectively. Plotted together are the corresponding static THz fields (green curves) and their pump-induced changes at 1 ps (blue curves from the cut positions as marked by the blue dashed lines).

Protected charge transport on surfaces of emerging semiconductors with topologically protected states is breaking new ground in quantum science and technology. One of the open questions for these novel surface states is how to disentangle and ultimately control surface helical spin transport. Recently Ames team (J. Wang, C-Z. Wang, Y. Yao and K-M Ho) we use the mid-infrared (mid-IR) and terahertz (THz) photoexcitation, tuned specifically to the intraband transitions, to manipulate the surface and bulk THz conductivity in n-type Bi_2Se_3. We observe frequency-dependent carrier cooling times of photoinduced THz conductivity, shown in Figure 2 are clearly differentiating surface from bulk contributions and allow determination of their scattering rates. We show that the topological enhancement of surface transport is responsible for suppressing the surface electron scattering rates compared to the bulk by nearly a factor of 4 in equilibrium. This result is consistent with surface helical spin transport in the presence of short-range disorder. The ultrabroadband, wavelength-selective pumping may be applied to emerging photovoltaic semiconductors for separation and control of the photocarrier transport.

Future Plans

Coherent Control of Electronic Fine Structure by Mode-Selective Quantum Beats in Perovskite Semiconductors: The excitons and charge carriers in perovskite semiconductors experience strong spin-orbit coupling and local inversion symmetry breaking from underlying lattice fluctuations and/or intrinsic random structures. These give rise to the lifted spin and momentum degeneracies, i.e., electronic fine structure that critically depend on the dynamic lattice environment. The electronic fine structure here has never been directly measured and its coherent properties are elusive. We will apply a single-cycle THz quantum beat spectroscopy to study vibronic couplings and electronic fine structure that validate theoretical models for realistic perovskite materials.

Discover Room Temperature Polaron Quantum Coherence in Perovskite Semiconductors: In man-made photovoltaic (PV) cells using hybrid metal halide perovskites (MAPs), only recently have we realized the presence of large polarons and hypothesized their formation via coherent charge coupling to a specific quantized lattice vibration, i.e., terahertz (THz) longitudinal optical (LO) phonon. Understanding and engineering the polaron quantum coherence and mode-specific

entanglement to photocarriers, yet-to-be-accessed, can significantly improve charge lifetimes, diffusion lengths and defect-tolerance in MAPs, and ultimately develop revolutionary photoenergy conversion systems. We will use ultrafast THz microscopy to probe the spatial-temporal coherence down at the THz energy scales and nanometer length scales

Understand the coherent transport at a single grain and grain boundary level Coherent transport processes may be significant in polycrystalline perovskite thin films since they exhibit "intermediate" crystallinity and grain/defect structures in between the organic donor/acceptor and inorganic crystalline solar cell semiconductors. We will investigate initial spatial-temporal coherence- and dynamics-mediated charge transfer regime. To probe the ultimate speed of the initial charge transfer at highly non-equilibrium and non-thermal regimes, we will systematically study the MAPb halide perovskite polycrystalline films with our sub-20 fs/sub-20 nm spectroscopy tools which defines the initial quantum coherent transport regime prior to the incoherent diffusion regime. The experimental measurements will be guided by theoretical simulations on slab models with defects and grain boundaries.

Gate tuning of coherent exciton polariton transport in emerging semiconductors. Group VI transition-metal dichalcogenides (TMD) is a type of 2D semiconductors could be a perfect platform for a nanophotonic transistor due to its capability of carrying long-propagation exciton polaritons, according to our recent discovery [3]. In the coming program year, we will explore the gate tuning properties of polaritons in TMDs. By injecting carriers into the sample, one could tune the Fermi level to conducting band or the valence band, thus changing the semiconducting nature of the sample. Therefore, we expect exciton polaritons will be turned off when injecting enough carriers, which is a basic function of a polaritonic transistor. In addition, it is also possible to find a new type of polaritons formed due to the coupling of photons with trions – an interesting charged exciton.

References

[1] Liang Luo, et al., Nature Communications, **8**, 15565 (2017).

[2] L. Luo, et al., Nature Communications, **10**, 607 (2019).

[3] F. Hu et al., Nature Photon. **11**, 356-360 (2017)

Publications supported by BES

1. L. Luo, X. Yang, X. Liu, Z. Liu, C. Vaswani, D. Cheng, M. Mootz, X. Zhao, Y. Yao, C.-Z. Wang, K.-M. Ho, I. E. Perakis, M. Dobrowolska, J. K. Furdyna, and J. Wang, "Ultrafast Manipulation of Topologically Enhanced Surface Transport Driven by Mid-Infrared and Terahertz Pulses in Bi2Se3", Nature Communications, **10**, 607 (2019).

2. Joong-Mok Park, Di Cheng, Aaron Patz, Liang Luo, Zhaoyu Liu, Fadzai Fungura, Ruth Shinar, Kai-Ming Ho, Joseph Shinar, and Jigang Wang, "Ultrafast nonlinear transparency driven at a

telecom wavelength in an organic semiconductor system," AIP Advances **9**, 025303 (2019). DOI: 10.1063/1.5042542

3. Andreas Herklotz, Stefania F. Rus, Nina Balke Wisinger, Christopher Rouleau, Er-Jia Guo, Amanda Huon, Santosh KC, Robert Roth, Xu Yang, Chirag Vaswani, Jigang Wang, Peter P. Orth, Mathias S. Scheurer and Thomas Z. Ward, Designing Morphotropic Phases with Strain Doping, Nano Lett., **19** (2), pp 1033–1038 (2019).

4. K. A. Niradha Sachinthani, Nelly Kaneza, Rajiv Kaudal, Eeshita Manna, Margaret Eastman, Bhishma Sedai, Shanlin Pan, Joseph Shinar, Ruth Shinar, and Toby Nelson, "Synthesis, characterization, and electro-generated chemiluminescence of deep blue emitting Eumelanin-inspired polyarylenes for polymer light emitting diodes," J. Polymer Sci. Part A: Polymer Chem. **56**, 125–131 (2018). DOI: 10.1002/pola.28881

5. Chamika Hippola, Rajiv Kaudal, Eeshita Manna, Teng Xiao, Akshit Peer, Rana Biswas, Dennis Slafer, Tom Trovato, Joseph Shinar, and Ruth Shinar, "Enhanced Light Extraction from OLEDs Fabricated on Patterned Plastic Substrates," Adv. Opt. Mater. **6**, 1701244 (2018). DOI: 10.1002/adom.201701244

6. V. V. Mkhitaryan, D. Danilovic, C. Hippola, M. E. Raikh, and J. Shinar, "Comparative analysis of magnetic resonance in the polaron pair recombination and the triplet exciton-polaron quenching models," Phys. Rev. B **97**, 035402 (2018).

7. Zhaoyu Liu, K.C. Bhamu, Liang Luo, Satvik Shah, Joong-Mok Park, Di Cheng, Men Long, Rana Biswas, F. Fungara, Ruth Shinar, Joseph Shinar, Javier Vela, and Jigang Wang, "Spatial–temporal spectroscopy characterizations and electronic structure of methyl ammonium perovskites," MRS Comm. **8**, 961 – 969 (2018).https://doi.org/10.1557/mrc.2018.114

8. S. S. Galley, A. A. Arico, T.-H. Lee, X. Deng, Y.-X. Yao, J. M. Sperling, V. Proust, J. S. Storbeck, V. Dobrosavljevic, J. N. Neu, T. Siegrist, R. E. Baumbach, T. E. Albrecht-Schmitt, N. Kaltsoyannis, and N. Lanatà, Uncovering the Origin of Divergence in the CsM(CrO4)2 (M = La, Pr, Nd, Sm, Eu; Am) Family through Examination of the Chemical Bonding in a Molecular Cluster and by Band Structure Analysis, J. Am. Chem. Soc., **140** (5), pp 1674–1685 (2018).

9. Liang Luo, Long Men, Zhaoyu Liu, Yaroslav Mudryk,Xin Zhaoyu,Yongxin Yao, Joong M.Park,Joseph Shinar, Kai-Ming Ho, Ilias. E. Perakis, Javier Vela and Jigang Wang, "Ultrafast terahertz snapshots of excitonic Rydberg states and electronic coherence in an organometal halid perovksite", Nature Communications, **8**, 15565 (2017).

Distinctive extrinsic and intrinsic dopant effects on the structural and electronic properties of 2D organic-inorganic hybrid perovskites

Luisa Whittaker-Brooks, University of Utah, Department of Chemistry, 315 South 1400 East, Room 2020, Salt Lake City, Utah, 84112

i) Program Scope

Two-dimensional (2D) organic–inorganic hybrid perovskite (OIHP) multiple quantum wells which consist of multilayers of alternate organic and inorganic layers exhibit large exciton binding energies due to the dielectric confinement between the inorganic and organic layers. These naturally formed multiple quantum wells have strong spin-orbit coupling (SOC) due to the presence of heavy elements in their crystal structures. Although the fundamental properties of 2D OIHPs are far from being entirely understood, it is widely accepted that their band edge absorption coefficient results from strong exciton interactions. However, studies demonstrating how different exciton interactions and doping effects influence electronic traps and disorder on the band edge absorption coefficient of 2D OIHPs have not been demonstrated. Understanding these interactions in OIHPs will allow us to access low energy optical transitions for the fabrication of solution processable short-to-mid-wavelength IR photodetectors (1 – 8 μm). Moreover, upon doping, it is possible to move the Fermi energy into the conduction band (CB) to favorably promote the transport of charges in a working device. Herein, we study the development of 2D OIHPs having strong SOC, high carrier mobility, and tunable quantum well structures. Our studies shed light on new breakthroughs in both materials design and modulation of fundamental physical phenomena by carefully elucidating the role of dopants (n-type and p-type), sample heterogeneity, orientation, structure, and bias stress effects on the performance of 2D OIHP as potential solution-processable IR photodetectors. Our research efforts also involve the use of in-situ and in-operando characterization tools to generate a mechanistic understanding of the degradation processes and/or phase transformations occurring in 2D OIHIP quantum well IR photodetectors under working conditions. These 2D OIHP –when optimized in thin films- will perhaps be one of the few doped materials available for ultrafast short-to-mid wavelength IR photodetection.

ii) Recent progress

Intrinsic doping of 2D OIHPs. Quantum well IR photodetector devices typically utilize an absorbing superlattice stack sandwiched between emitter and absorber layers, which aid in transferring carriers to and from the contacts. These superlattice stacks can be doped to further assist with carrier separation and generation. Upon doping, more electrons are then excited by incident photons to the conduction band of the well layers, where they can diffuse to the contacts of the device. The fact that these 2D OIHPs form natural "multiple quantum wells" that exhibit strong spin-orbit coupling due to the heavy atoms in their building blocks, lead to "Giant Rashba splitting" close to the extrema in the conduction band (Rashba splitting is also observed in the valence band but it is not as colossal as in the conduction band).[1, 2] We can thus take advantage of the Giant Rashba splitting and induce an increase of the electrical conductivity and mobilities of 2D OIHPs by populating extra charges into the two parabolic branches having opposite spin sense. From electroabsorption and photoinduce absorption studies, we can then determine the Rashba energy (E_R) and momentum offset (k_o) upon the incorporation of extrinsic atoms.[1, 3]

Unlike metal oxides, the electrical properties of OIHPs have seldom been tuned by the introduction of dopants. Early work by Takahashi *et.al.* suggest that spontaneous hole doping in $CH_3NH_3SnI_3$ using Sn^{4+} increases its electrical conductivity. Such spontaneous doping –though

effective- does not provide a platform where the properties of the dopant may be systematically controlled. Since our preliminary experiments suggest that the Sn^{2+} oxidation state may be stabilized by the incorporation of bulkier organic cations, we can therefore systematically elucidate the effects that dopants have on the electrical properties of tin 2D OIHPs by incorporating foreign cations (i.e., Ag^{+}, Zn^{2+}, Bi^{3+}, Sb^{3+}) having a stable oxidation state for the 2D metal center. As such, dopants can be added to either induce n- (i.e., Ag^{+}, Zn^{2+}) or –p (Bi^{3+}, Sb^{3+}) behavior in 2D OIHPs. X-ray photoelectron spectroscopy (XPS) and X-ray absorption fine structure (XAFS) spectroscopy can be used to determine the stabilization of the desired oxidation state for the metal center and the dopant as well as their chemical environment and dopant concentration. Such experiments allow us to correlate the electrical conductivity and mobility of our doped 2D OIHPs to potential changes in their coordination chemistry as a function of dopant concentration. In terms of electronic structure, ultraviolet photoelectron spectroscopy (UPS) and inverse photoemission spectroscopy (IPES) are used to determine the changes in the valence and conduction bands, respectively. This allow us to elucidate energy level offsets upon the incorporation of dopants. Upon understanding dopant effects in 2D OIHPs, we can proceed with elucidating their optoelectronic properties towards the fabrication of photodetectors. **Figure 1** shows the electrical conductivity as a function of temperature for a pristine $(PhEA)_2SnI_4$ thin film as well as for Ag-doped $(PhEA)_2SnI_4$ (n-doping). The data were acquired by performing 4-point probe measurements on thin films. As shown in **Figure 1**, there is an increase in the electrical conductivity of the Ag-doped $(PhEA)_2SnI_4$ thin film suggesting the possibility of inducing electronic doping and increasing charge carrier density in this material.

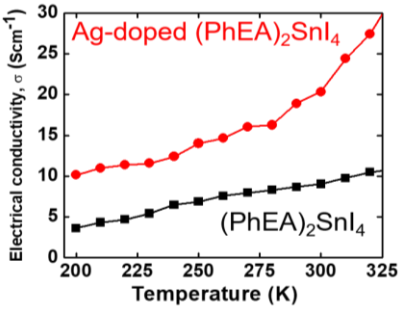

Figure 1. Electrical conductivity as a function of temperature for a pristine $(PhEA)_2SnI_4$ and Ag-doped $(PhEA)_2SnI_4$ thin films.

Furthermore, carrier mobilities up to 2000 $cm^2V^{-1}s^{-1}$ have been reported for some members of the Sn-based OIHP family (e.g. $CH_3NH_3SnI_3$ (e- mobility), $CsSnI_3$, $(C_4H_9NH_3)_2(CH_3NH_3)_2Sn_3I_{10}$).[4-6] These findings have yet to address the effects of dopants, cation exchange, stability, and morphology on the observed mobility and their optoelectronic properties.

Probing the structure and film morphology of perovskite materials via grazing incidence wide-angle X-ray diffraction (GIXD) measurements. One of the key advantages of OIHPs is their ease of processability. Several leading groups have characterized OIHPs by means of powder X- ray diffraction. Nevertheless, crystallographic data from powder diffraction only provides limited structural and morphological information – especially for highly oriented inorganic-organic perovskite films. Consequently, we will employ two-dimensional GIXD studies as a mean to probe the crystallographic orientations of our as-synthesized OIHP thin films. **Figure 2A**, for example, shows the GIXD pattern for a $CH_3NH_3PbI_3$ thin film. This GIXD pattern indicates that the $CH_3NH_3PbI_3$ thin films are mainly composed of a strongly scattering ring at $q = 1.03\ A^{-1}$. This ring corresponds to reflections associated to the (110) crystallographic plane of the tetragonal structure for $CH_3NH_3PbI_3$. The 2D GIXD pattern in **Figure 2A** also shows anisotropic intensities associated with the (110) reflection of $CH_3NH_3PbI_3$, indicating that $CH_3NH_3PbI_3$ crystals are preferentially oriented along the q_z-axis. **Figure 2B** shows the GIXD pattern for a 2D $(C_4H_9NH_3)_2PbI_4$ thin film. Here, we show conclusive reflections that corroborate the highly-oriented nature of this 2D OIHPs when casted into thin films. We plan to perform these GIXD studies on our as-synthesized 2D Sn- based OIHPs. 2D GIXD measurements in combination with

scanning electron microscopy (SEM) studies allow us to follow the structural evolution of our as-synthesized perovskites and to conclusively determine the orientation, crystallinity, and their degradation profile.

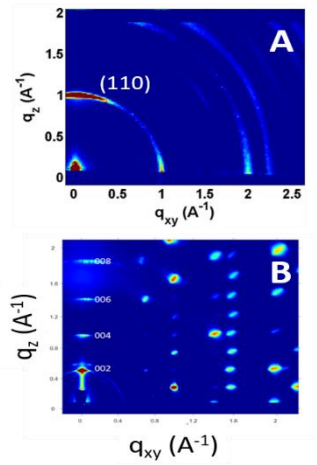

Figure 2. A. GIXD pattern for the tetragonal phase of $CH_3NH_3PbI_3$. The patterns indicate the perovskite material shows a tendency for preferential orientation along its z-axis. **B.** GIXD pattern for a highly-oriented $(C_4H_9NH_3)_2PbI_4$ thin film.

Elucidating the electronic structure and cation orientation of 3D and 2D OIHPs NEXAFS spectroscopy. Temperature induced structural fluctuations and the organic cation dynamics have shown to influence several perovskite properties such as, electron-phonon coupling,[8] charge transport,[9] ferroelectricity,[10] and luminescence.[11, 12] As such, the chemical environment and orientation of 2D OIHPs are likely to strongly influence the electrical properties, mechanical robustness, and wettability of these materials when incorporated into thin films. Although SEM and atomic force microscopy (AFM) studies provide some indication of the uniformity of the OIHP thin films, it is not a good probe of the local structure of OIHPs within a thin film. Herein, we used NEXAFS in conjunction with GIXD to probe the local structure and molecular orientation of OIHPs with respect to the substrate. NEXAFS is a very powerful and element-specific tool that provides information on the electronic properties of molecules containing "light" atoms such as carbon, nitrogen, and oxygen. We will focus on acquiring chemical information around the C K-edge region (280 - 320 eV) of our OIHP thin films in order to elucidate the orientation of the organic cation within the OIHP crystal structure. C K-edge NEXAFS spectra correspond to the excitation of C 1s core electrons to unoccupied and partially filled levels in the conduction bands of the organic cation, and thus it provides a good approximation of the unoccupied density of states (UDOS) above the Fermi level for these materials. NEXAFS spectra not only reflect UDOS of the carbon region within the organic cation but it also shows the transition matrix elements between the initial and final states which are incredible sensitive to the polarization of the incident X-rays. Therefore, if the organic cations within the OIHPs are aligned and/or ordered, it is possibly to excite different bonds depending on their orientation relative to the polarized beam.

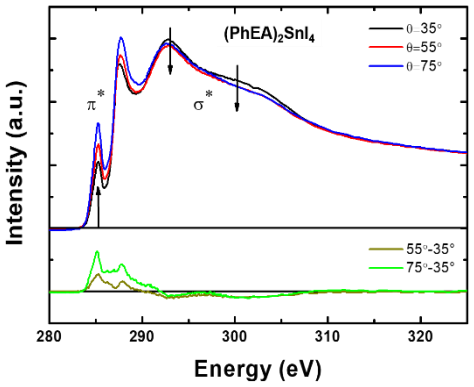

Figure 3. Pre- and post-edge normalized NEXAFS spectra collected at the carbon edge at different X-ray incident angles (35°, 55°and 75) for a pristine $(PhEA)_2SnI_4$ thin film. *Unpublished results.*

Figure 3 displays the NEXAFS partial electron yield (PEY) spectra acquired on the surface of a phenylethylammonium tin iodide $(PhEA)_2SnI_4$ neat thin film at X-ray incident angles between 35° (grazing) and 75° (near-normal). Careful consideration was taken when running these samples due to potential beam damage (i.e., deprotonation of the organic-ammonium cation).[13] We believe beam damage/deprotonation does not affect the orientation of the organic cation so the angle-resolved measurements could still provide useful characterization. It will be important to ensure that exposure-dependent effects are not mistaken for angle-dependent effects in future samples as well. Moreover, temperature dependent NEXAFS studies below (and above) structural phase transitions will allow us to determine orientation changes of the organic cation upon such structural transformations. The soft X-ray is linearly polarized, so intensity variations

as a function of X-ray incident angle suggest preferential orientation of $(PhEA)_2SnI_4$. In particular, the carbon 1s to π* resonance intensity at 285.4 eV increases, while the intensity of the C1s to σ* resonances at 293.6 and 301.1 eV decreases with increasing X-ray incident angle. This phenomenon suggests $(PhEA)_2SnI_4$ is preferentially oriented with its π-plane normal to the substrate. This knowledge will be extended further to quantify changes in molecular orientation as a function of organic cation, number of quantum well layers, and processing conditions.

iii) Future plans

Extrinsic doping of 2D OIHPs. We will investigate how the addition of extrinsic dopants such as N-DMBI (n-dopant) affect the structural and optoelectronic properties of 2D OIHPs. There are three main questions we seek to answer: 1. Are we extrinsically doping the perovskite layer? If so, how does this change the Fermi level? 2. How is the dopant being incorporated? (e.g., grain boundaries or interstitial sites) 3. To what level do we change the original structural and the excitonic features?. Here, we will use a vapor doping method using N-DMBI as the molecular dopant (**Figure 4**). As per initial studies, we observe that the emission signal of the 2D OIHP decreases upon exposing the film to the N-DMBI vapor which is a strong indication of successful doping (**Figure 5**).

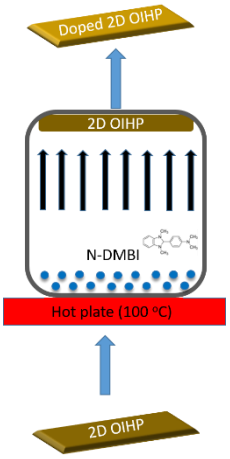

Figure 4. Depiction of the vapor-doping method. The dopant is situated at ~ 7 cm from the perovskite film.

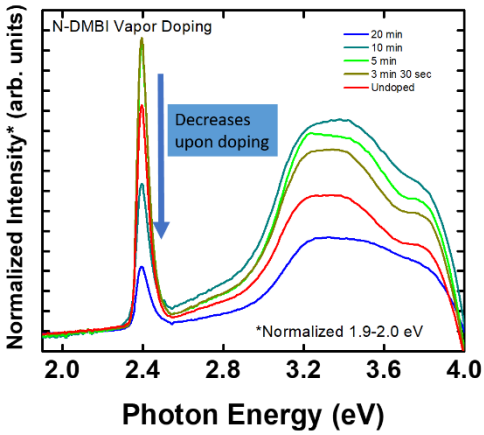

Figure 5. Emission spectra for $(PhEA)_2SnI_4$ as a function of vapor-doping exposure.

iv) References

1. Zhai, Y.; Baniya, S.; Zhang, C.; Li, J.; Haney, P.; Sheng, C.-X.; Ehrenfreund, E.; Vardeny, Z. V., *Sci. Adv.* **2017,** *3*.
2. Straus, D. B.; Kagan, C. R., *J. Phys. Chem. Lett.* **2018,** *9*, 1434-1447.
3. Amerling, E.; Baniya, S.; Lafalce, E.; Zhang, C.; Vardeny, Z. V.; Whittaker-Brooks, L., *J. Phys. Chem. Lett.* **2017,** *8*, 4557-4564.
4. Stoumpos, C. C.; Malliakas, C. D.; Peters, J. A.; Liu, Z.; Sebastian, M.; Im, J.; Chasapis, T. C.; Wibowo, A. C.; Chung, D. Y.; Freeman, A. J.; Wessels, B. W.; Kanatzidis, M. G., *Cryst. Growth Des.* **2013,** *13*, 2722-2727.
5. Stoumpos, C. C.; Malliakas, C. D.; Kanatzidis, M. G., *Inorg. Chem.* **2013,** *52*, 9019-9038.
6. Mitzi, D. B.; Feild, C. A.; Harrison, W. T. A.; Guloy, A. M., *Nature* **1994,** *369*, 467-469.
7. Bechtel, J. S.; Seshadri, R.; Van der Ven, A., *J. Phys. Chem. C* **2016,** *120*, 12403-12410.
8. Wehrenfennig, C.; Liu, M.; Snaith, H. J.; Johnston, M. B.; Herz, L. M., *J. Phys. Chem. Lett.* **2014,** *5*, 1300-1306.
9. Liu, J.; Prezhdo, O. V., *J. Phys. Chem. Lett.* **2015,** *6*, 4463-4469.
10. Filippetti, A.; Delugas, P.; Saba, M. I.; Mattoni, A., *J. Phys. Chem. Lett.* **2015,** *6*, 4909-4915.
11. Grancini, G.; Srimath Kandada, A. R.; Frost, J. M.; Barker, A. J.; De Bastiani, M.; Gandini, M.; Marras, S.; Lanzani, G.; Walsh, A.; Petrozza, A., *Nat. Photonics* **2015,** *9*, 695-701.
12. Delugas, P.; Filippetti, A.; Mattoni, A., *Phys. Rev. B* **2015,** *92*, 045301.
13. Jung, M.-C.; Lee, Y. M.; Lee, H.-K.; Park, J.; Raga, S. R.; Ono, L. K.; Wang, S.; Leyden, M. R.; Yu, B. D.; Hong, S.; Qi, Y., *Appl. Phys. Lett.* **2016,** *108*, 073901.

v) Publications

1. E. Amerling, D. M. Smilgies, L. Whittaker-Brooks. Quantifying the degree of orientation of 2D organic-inorganic hybrid perovskite multiple quantum wells via soft X-ray absorption spectroscopy. *Submitted*
2. E. Amerling, S. Baniya, D. Rajkhanal, Z. V. Vardeny, S. Blair, L. Whittaker-Brooks. "Deconvolution of Excitonic Features in Mixed-Phase Multiple Quantum Well Perovskites". *In preparation*
3. M. Pham, E. Amerling, H. Luong, L. Whittaker-Brooks, D. Tuan and T. Nguyen. "Studies of Spin-Orbit Coupling Strength in Organic-Inorganic Hybrid Halide 2D and 3D Perovskites by Magneto-Optical Effect". *In preparation*

Tuning anisotropic bonding via chemistry and pressure in layered pnictides and chalcogenides

Alexandra Zevalkink, Michigan State University, East Lansing, MI

Olivier Delaire, Duke University, Durham, NC

Program Scope

The overarching goal of this new research program is to develop a predictive, chemistry-driven understanding of the impact of strongly anisotropic bonding on the phonon behavior and thermal properties of bulk layered materials. At finite temperatures, atomic vibrations (phonons) strongly impact the thermodynamics, thermal and electrical transport, and phase-switching properties of functional materials. In particular, soft phonon modes and strongly anharmonic potentials can have spectacular consequences, including structural phase transitions (for example in ferroelectrics and phase-change memory materials), metal-insulator transitions, and extreme thermal resistance preventing heat propagation.

Bulk materials with highly-anisotropic bonding may provide unique strategies to induce soft-phonon modes and lattice instabilities. Recently, increasingly detailed investigations of the lattice dynamics in layered materials have been made possible by the advent of first-principles phonon calculations and advanced characterization techniques based on neutron and X-ray scattering. However, due to the lack of studies in which composition and bonding character are systematically varied, there are still fundamental questions regarding the impacts of anisotropic bonding and anharmonicity on lattice stability and thermal transport. Coherently tuning bonding anisotropy and anharmonicity across a family of related compounds would address this gap and could reveal new strategies for exploiting structural anisotropy in quasi-1D and 2D bulk materials to obtain tailored functional properties.

This project will systematically explore the lattice dynamics, phase stability, and transport properties in bulk layered and quasi-1D materials by using both composition and applied pressure to tune the degree of bonding anisotropy and anharmonicity. To accomplish this work, we will combine i) single-crystal growth of key material systems with tunable anisotropy, ii) in-situ high-temperature/high-pressure characterization of structure and phonons to probe bonding anisotropy and anharmonicity, including state-of-the-art inelastic X-ray scattering and inelastic neutron scattering, and iii) first-principles simulations leveraging large-scale computing to identify the fundamental origins of the observed effects, by relating atomic structure and dynamics to electronic orbital interactions. Finally, we will model and verify the impact of the phonon behavior on thermal transport to identify new strategies for a-priori design of thermal

conductivity. Our integrated collaborative approach will systematically unravel the effects of anisotropy and bonding anharmonicity on phonon transport, thermodynamics, and thermal properties and will provide new fundamental understanding to control properties of complex anisotropic materials.

Recent Progress

Interlayer bonding and anharmonicity in layered Zintl phases: Layered AMg_2Sb_2 Zintls compounds, in which *A* is a divalent alkaline or rare earth metal, and *Pn* is a pnictogen species, have received a great deal of attention recently due to their excellent thermoelectric properties with *zT* values up to 1.6. Surprisingly, the lightest compound in this family – $MgMg_2Sb_2$ – also exhibits the lowest thermal conductivity. We have previously shown that this behavior is related to the small size of the Mg cations with respect to the 6-fold octahedral coordination environment, leading to weak interlayer bonding.

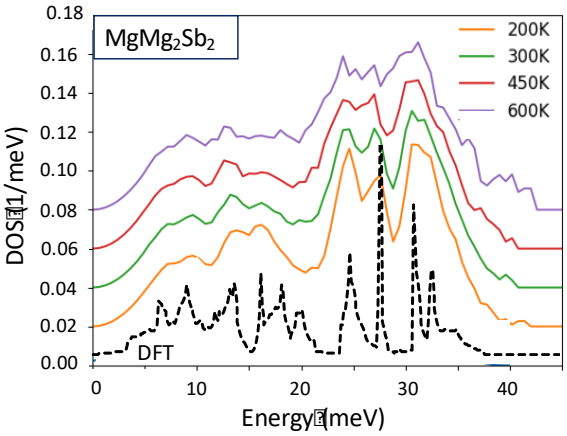

Figure 1. Phonon density of states of $MgMg_2Sb_2$ obtained from INS measurements show excellent agreement with DFT results from ref [1].

Our initial computational and experimental results [1] suggested that the interlayer bonding in this compound was highly anharmonic. In the current project, we have taken this a step further in an effort to show that the anharmonicity present in $MgMg_2Sb_2$ leads directly to high rates of Umklapp phonon-phonon scattering and consequently to drastically reduced lattice thermal conductivity compared with heavier isostructural compounds such as $CaMg_2Sb_2$ and $SrMg_2Sb_2$.

We have used temperature-dependent inelastic neutron scattering (INS) and Raman spectroscopy to experimentally characterize the phonon spectra in $MgMg_2Sb_2$ and $CaMg_2Sb_2$ for the first time. Preliminary analysis has confirmed the anomalously soft bonding in compounds with A=Mg. Further, the phonon spectra in $MgMg_2Sb_2$ exhibits rapid softening and peak broadening with increasing temperature.

Soft phonon modes and anisotropic thermal transport in layered thermoelectrics SnSe and SnS: We have measured the temperature dependence of phonons in the layered chalcogenide systems SnSe and SnS. These compounds are of high interest for thermoelectric applications, as very high figures-of-merit are enabled by their extremely low lattice thermal conductivities [4,5,6]. Owing to their layered crystal structure, comprised of two rock-salt derived Sn-X bilayers per unit cell, their thermal conductivity is also strongly anisotropic [4,5,6]. Further, both compounds undergo structural phase transitions driven by soft-modes at high temperature (above 800K). We have performed systematic INS measurements of phonons in crystals and powders of both

compounds to rationalize their low thermal conductivities, the anisotropy in the phonon group velocities and scattering rates, and to clarify the mechanism of the phase transition. Additional heat capacity measurements were also performed. We have also started to study the dependence of SnSe and SnS on applied pressure with x-rays and first-principles simulations.

Future Plans

Interlayer bonding and anharmonicity in layered Zintl phases: We plan to use temperature-dependent inelastic neutron scattering (INS) and Raman spectroscopy to explore the role that the cation radius plays in determining the bond strength and phonon scattering rates in a series of $A Mg_2 Pn_2$ compounds (*Pn* = Sb or Bi and *A* = Mg, Ca, Sr, and Yb). Single crystals of the selected compounds will be grown from molten metal flux.

Impact of interlayer bonding on phase stability in GST phase change materials: Ge-Sb-Te (GST) alloys, in particular the $GeTe\text{-}Sb_2Te_3$ system, have been intensely studied for phase-change memory applications [2], and have recently been shown to be excellent thermoelectric materials as well [3]. $(GeTe)_nSb_2Te_3$ forms a homologous series (i.e., a series with a continuously variable structure) which can be visualized as layers of rock salt-like GeTe inserted into the center of the Sb_2Te_3 tetradymite slab. We plan to tune the layer thickness in this homologous series to untangle the relationship between weak van der Waals bonds and lattice instabilities, resonant bonding, and anisotropic transport in layered materials.

Pressure- and temperature-induced structural and insulator-metal transitions in tetradymites: Despite intense interest in thermoelectric and topologically insulating properties of tetradymites [7,8], the lattice dynamics in these compounds are insufficiently understood, in particular their dependence on pressure, but also on temperature. The chemical bonding in tetradymites M_2X_3 can be strongly altered by external application of pressure. For example, insulator-to-metal transitions are experimentally known to occur in Bi_2Te_3 around 9 GPa [9]. Among the tetradymites, the phonon dispersions of Bi_2Te_3 have been studied the most, although they were comprehensively measured only at 77 K (ambient pressure) [10]. We plan to use INS and IXS to investigate the response of phonons (dispersions and DOS) to changes in pressure and temperature for several tetradymites M_2X_3 (including Bi_2Te_3 and Bi_2Se_3).

References

[1] W. Peng, G. Petretto, G.M. Rignanese, G. Hautier, A. Zevalkink, An unlikely route to low lattice thermal conductivity: small atoms in a simple layered structure, Joule, 2, 1879-1893, 2018.

[2] Siegrist, T.; Merkelbach, P.; Wuttig, M., “Phase change materials: Challenges on the path to a universal storage device”. Annu. Rev. Condens. Matter Phys. 2012, 3, 215–237.

[3] Williams, J. B.; Morelli, D. T., "Understanding the superior thermoelectric performance of Sb precipitated Ge17Sb2Te20". J. Mater. Chem. C 2016, 4 (42), 10011-10017.

[4] Zhao, L. D.; Lo, S. H.; Zhang, Y.; Sun, H.; Tan, G.; Uher, C.; Wolverton, C.; Dravid, V. P.; Kanatzidis, M. G., "Ultralow thermal conductivity and high thermoelectric figure of merit in SnSe crystals". Nature **2014,** *508* (7496), 373-7

[5] Zhao, L.-D.; Tan, G.; Hao, S.; He, J.; Pei, Y.; Chi, H.; Wang, H.; Gong, S.; Xu, H.; Dravid, V. P.; Uher, C.; Snyder, G. J.; Wolverton, C.; Kanatzidis, M. G., "Ultrahigh power factor and thermoelectric performance in hole-doped single-crystal SnSe". Science **2016,** *351* (6269), 141-144.

[6] Q. Tan, L. D. Zhao, J. F. Li, C. F. Wu, T. R. Wei, Z. B. Xing, M. Kanatzidis, "Thermoelectrics with earth abundant elements: Low thermal conductivity and high thermopower in doped SnS". J. Mat. Chem. A **2014**, 2(41) 17302-17306.

[7] Heremans, J. P.; Cava, R. J.; Samarth, N., Tetradymites as thermoelectrics and topological insulators. *Nat. Mater. Rev.* **2017,** *2*, 17049.

[8] Wang, L. L.; Johnson, D. D., Ternary tetradymite compounds as topological insulators. *Phys. Rev. B* **2011,** *83*, 241309(R).

[9] Vilaplana, R.; Gomis, O.; Manjon, F. J.; Segura, A.; Perez-Gonzalez, E.; Rodriguez-Hernandez, P.; Muñoz, A.; Gonzalez, J.; Marin-Borras, V.; Muñoz-Sanjosé, V.; Drasar, C.; Kucek, V., High-pressure vibrational and optical study of Bi_2Te_3. *Phys. Rev. B* **2011,** *84*, 104112.

[10] Kullmann, W.; Eichhorn, G.; Rauh, H.; Geick, R.; Eckold, G.; Steigenberger, U., Lattice dynamics and phonon dispersion in the narrow gap semiconductor Bi2Te3 with sandwich structure. *Physica Status Solidi B* **1990,** *162* (1), 125-140.

Publications

(conference presentation) T. Lanigan-Atkins, S. Yang, J. Niedziela, D. Bansal, C. Li, J. Hong, J. Lin, D. Pajerowski, G. Ehlers, T. Hong, A. May and O. Delaire, "Lattice dynamics across the structural phase transition in SnS and SnSe", MRS Fall Meeting 2018, Boston MA.

(conference presentation) Wanyue Peng, Guido Petretto, Geoffroy Hautier, Alexandra Zevalkink, "Lattice dynamics of layered AMg2Pn2 Zintl compounds", MRS Fall Meeting 2018, Boston MA.

(conference presentation) R Hermann, J Zhang, W Peng, D Abernathy, A Zevalkink, "Lattice dynamics and local structure in AMg2Sb2 thermoelectric Zintl phases", 85th Annual Meeting of the APS Southeastern Section, November 2018, Knoxville TN.
http://meetings.aps.org/Meeting/SES18/Session/D03.2

Microscopic Understanding of Thin Film Growth and Substrate Engineering of Organic Charge Transfer Complexes

Pengpeng Zhang, Department of Physics and Astronomy, Michigan State University

Program Scope

Single-crystalline molecular solids of donor-acceptor charge transfer complexes (CTCs) display a broad spectrum of rich physical properties ranging from Mott insulator, metal, superconductor, ferroelectricity, to (anti)ferromagnetism that are not present in either donor or acceptor parent component.[1] In bulk CTCs, their properties are determined by the degree of charge transfer between donor and acceptor molecular moieties and the molecular stacking geometry. Nevertheless, for the benefit of device miniaturization and scalability when integrating the functionality and versatility of CTCs with inorganic electronic materials, there is a strong incentive to turn to CTC thin films with thickness at the nanometer or even molecular scale. This raises important questions: Do rich functionalities and intriguing properties of bulk CTCs persist in thin film form? Furthermore, can substrates provide a means to engineer functionalities in CTCs? The primary objective of this program is to: i) probe and determine the tuning mechanisms of substrate electrostatic screening and interfacial coupling on CTC functionality, and ii) understand the structure-property relationship in CTC thin films. The success of the research will provide insights into the growth mechanism and the physical properties of CTC thin films, which will set the stage of substrate engineering of CTC functionalities.

Recent Progress

Electronic structures of CTC assemblies have been explored on metallic substrates. A notable example is the single layer $(BETS)_2GaCl_4$ (BETS: bis(ethylenedithio)tetraselenafulvalence) organic salt grown on Ag(111), where a superconducting gap is revealed for even just four donor-acceptor molecular pairs.[2] This study opens up the possibility of fabricating nanoscale superconducting devices made of organic molecules. However, the underlying mechanism for the persistence of superconductivity is yet to be understood. The complication originates from the interaction between molecular moieties and the metallic substrate, which can be covalent bonding via chemisorption in nature. Previous studies have illustrated that hybridized interface states with complex sharing of electrons between molecules and metallic substrates can dominate the characteristics of molecular thin films.[3] The focus of our research is to develop a microscopic understanding of the fundamental principles governing the growth and properties of CTC thin films on weakly interacting substrates. We hypothesize that the electrostatic screening from the substrate, the electronic (tunneling) coupling of molecular moieties to the substrate, and the molecular packing motif templated by the substrate will act together to have essential influence on the physical properties of CTC thin films.

Since this program started six months ago, we have made efforts on understanding interfacial energetics and charge transfer behaviors in donor-acceptor binary molecular

superstructures grown on weakly interacting substrates. Using scanning tunneling microscopy/spectroscopy (STM/STS) and finite element analysis, we investigated molecular structures composed of zinc phthalocyanine (ZnPc) and/or its fluorinated counterpart, hexadecafluorinated zinc phthalocyanine (F_{16}ZnPc), on monolayer hexagonal boron nitride (h-BN) grown on Cu(111). Although ZnPc/F_{16}ZnPc is not a CTC pair with exotic functionality, they are chosen as the donor and acceptor molecular species of initial investigation due to their geometric similarity and their predicted ability to exhibit ground-state donor-acceptor intermolecular charge transfer when packed edge-to-edge.

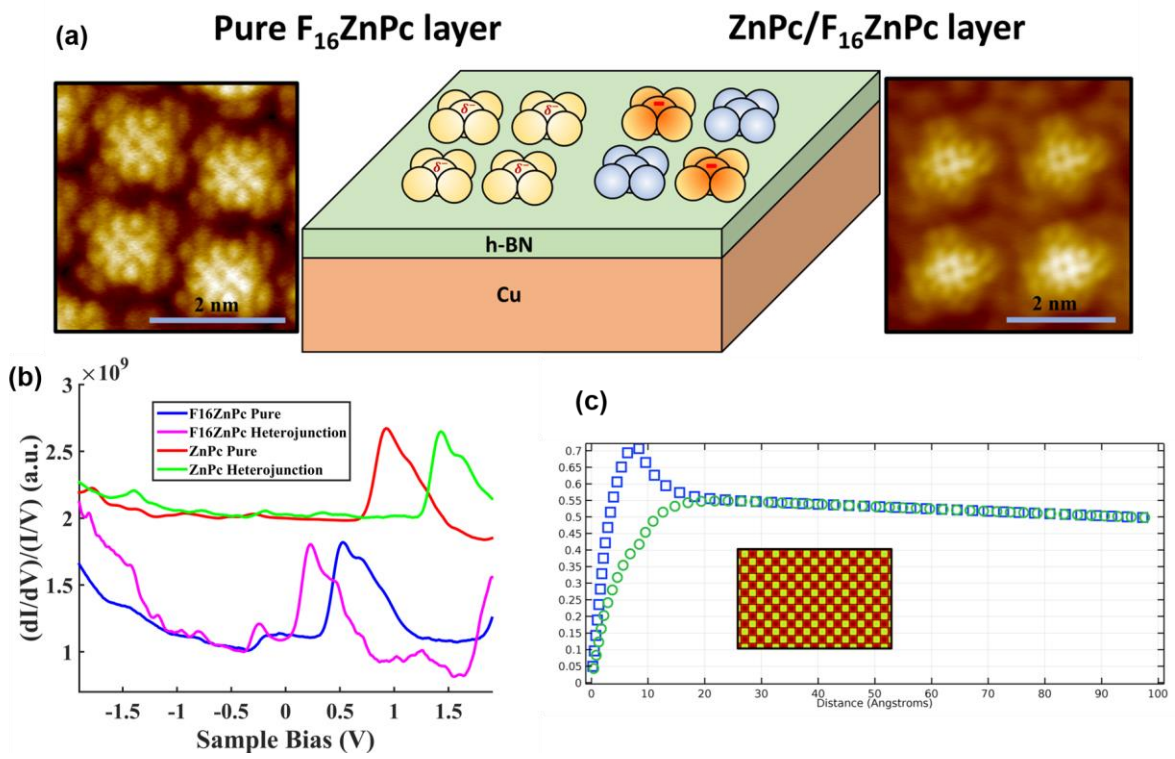

Figure 1: (a) Left: STM topography image (setpoint: V_s=2V, I_t=5pA) of F_{16}ZnPc molecules on h-BN/Cu(111). Middle: Schematics illustrating the enhanced charging of F_{16}ZnPc molecules in the binary molecular assemblies, resulting from interfacial charge transfer with substrate. Right: STM topography image (setpoint: V_s=1V, I_t=5pA) of ZnPc/F_{16}ZnPc heterostructure on h-BN/Cu(111), which forms a checkboard pattern. LUMO-like molecular orbital features are exhibited in the STM images owing to the h-BN layer which decouples the molecular overlayer from the substrate. (b) STS data taken on ZnPc and F_{16}ZnPc in their single-component pure phase and the binary heterostructures, respectively. The spectra feature of F_{16}ZnPc in the heterostructure is shifted down in energy, whereas the energy levels of ZnPc are upshifted toward the vacuum level. (c) Finite element electrostatic simulations using COMSOL to illustrate the electrostatic potential energy for electrons from the image plane of Cu(111) to 100 angstroms directly above ZnPc (green curve) and F_{16}ZnPc (blue curve) molecular adsorbates. The maximum in the electrostatic potential energy represents the vacuum level shift. Inset: molecules are arranged in a checkboard array, with F_{16}ZnPc occupying every other site. ~1e charge transfer between F_{16}ZnPc molecules and the underlying Cu substrate is desirable in order to produce a similar magnitude upshift of the ZnPc spectra in the binary heterostructure.

We have demonstrated that ZnPc and F_{16}ZnPc molecules, in their pure phase, form organized structures on the h-BN/Cu(111) substrate. Owing to its insulating nature, h-BN decouples the molecular overlayer from the metallic substrate, preserving the pristine molecular orbitals (Fig. 1a). Co-deposition of these two molecules yields a checkerboard structure that is adopted to minimize the F-F repulsion between F_{16}ZnPc molecules. The energy levels of molecular orbitals in the binary heterostructures are observed to upshift for ZnPc and downshift for F_{16}ZnPc with respect to those of the pure phase (Fig. 1b). This trend is opposite to that expected if donor-acceptor intermolecular charge transfer plays a dominant role. Instead, the shift of energy levels arises from the enhanced charging of F_{16}ZnPc molecules in the binary heterostructure via (tunneling) charge transfer with the substrate. In conjunction with finite element analysis (Fig. 1c), we speculate that the emergence of this charge transfer interaction originates from the greater Madelung energy of the binary heterostructure in contrast to that of the pure phase, which stabilizes the charged F_{16}ZnPc molecules against the intermolecular Coulomb repulsion.

This phenomenon brings forth a significant complication as well as a great opportunity in the design of thin film molecular heterojunctions or CTC assemblies on substrates. The presence of the substrate, even a weakly interacting one such as h-BN/metal that does not perturb the pristine molecular orbitals and characteristics, can still promote interfacial charge transfer and inhibit intermolecular charge transfer. This interfacial charge transfer may act as an addition knob to engineer the properties of molecular heterojunctions or CTC assemblies, which could enrich the potential (opto)electronic applications of the hybrid system.

Future Plans

Our initial investigation discussed previously was carried out on a model molecular system with well-established ground-state intermolecular charge transfer. This study serves to further our understanding of interfacial energetics in binary molecular heterostructures on weakly interacting substrate. Currently, we are pursuing the growth of long-range ordered CTC assemblies that exhibit rich physical properties such as ferroelectricity and metal-insulator-transition in the corresponding bulk phase. The applications of these CTCs in electronic devices often require their growth in the thin-film form. In the next stage, we plan to investigate how the proximity to a substrate and its impacts on intermolecular charge transfer and molecular packing influence the physical properties of CTC assemblies.

References

1. Saito, G., Yoshida, Y. Development of conductive organic molecular assemblies: Organic metals, superconductors, and exotic functional materials. *B Chem Soc Jpn.* 80, 1 (2007).
2. Clark, K., Hassanien, A., Khan, S., Braun, K. F., Tanaka, H., Hla, S. W., Superconductivity in just four pairs of $(BETS)_2GaCl_4$ molecules. *Nat Nanotechnol.* 5, 261 (2010).

3. Gonzalez-Lakunza, N., Fernandez-Torrente, I., Franke, K. J., Lorente, N., Arnau, A., Pascual, J. I., Formation of dispersive hybrid bands at an organic-metal interface. *Phys. Rev. Lett.* 100, 156805 (2008).

Publications

1. Tan, A., Zhang, P. P., Tailoring the growth and electronic structures of organic molecular thin films. (Invited topical review article) *J. Phys.: Condens. Matter*. Under Review (2019).
2. Tan, A., Zhang, P. P., Interfacial charge transfer enhancement via molecular heterostructures formation on electronically corrugated boron nitride. In Preparation (2019).

Kirchhoff's law of thermal radiation including anisotropic semitransparent films

Principle Investigator: Zhuomin Zhang
George W. Woodruff School of Mechanical Engineering
Georgia Institute of Technology, Atlanta, GA 30332

Program Scope

Nanoscale thermal radiation can significantly enhance the radiative heat flux and may have important applications in heat-to-electricity energy harvesting and electroluminescent refrigeration. The proposed project focuses on the near-field Radiative Thermoelectric Energy Converters (RTECs), such as thermoradiative energy generation and electroluminescent refrigeration devices. Additionally, near-field radiation entropy will be investigated to gain a deeper understanding of the fundamental processes. Our recent study is presented here on an important fundamental aspect of thermal radiation, that is, the validity of Kirchhoff's law considering anisotropic thin films.

Recent Progress

Kirchhoff's law relates the thermal emission and absorption of materials and hence is very important for thermal engineering applications with significant radiation heat transfer. Due to the advancement of metamaterials, two-dimensional materials, and micro/nanoscale thermal radiation, Kirchhoff's law has been revisited by several groups [1-6]. After a brief review of Kirchhoff's law considering the Helmholtz reciprocity, this work develops an explicit expression of Kirchhoff's law and the reciprocity relations for anisotropic materials including semitransparent films. Some calculation results on the reflectance and transmittance for both co-polarization and cross-polarization of a two-layer structure will also be presented to demonstrate optical reciprocity.

The considered structures are shown in Fig. 1, in which a sample at T_s is placed inside an isothermal enclosure whose walls are at T_w. Under thermal equilibrium when $T_s = T_w$, Fig. 1a suggests that the hemispherical absorptivity equals the hemispherical emissivity. However, this equality is only valid under thermal equilibrium and cannot be generally applicable to a nonequilibrium environment when neither the surface nor the irradiation is diffuse. On the other hand, it is desired to relate the directional absorptivity and emissivity as shown in Fig. 1b.

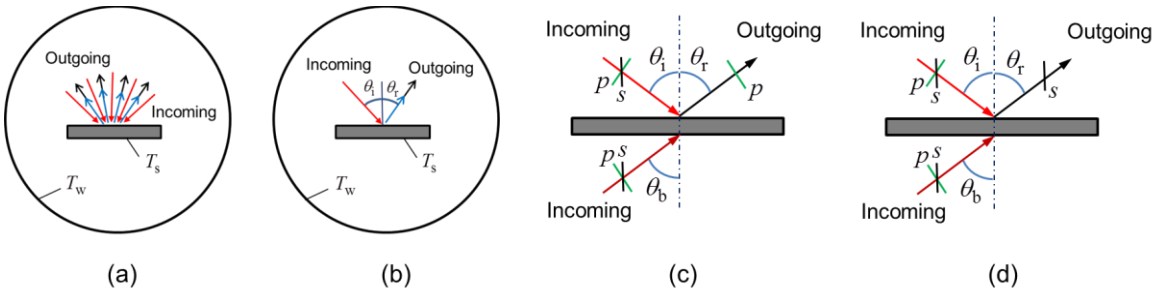

Fig. 1. (a,b) Schematics of ablackbody enclosures considering hemispherical and directional properties for an opaque sample. (c,d) Schematic of a semitransparent anisotropic film when the outgoing beam is *p*- or *s*- polarized, respectively.

It should be noted that all the properties considered here are spectral properties while the word spectral is omitted. Under thermal equilibrium, the energy balance requires that the intensity arriving or leaving the surface to be the same for any given polarization. However, the outgoing beam is composed of the emitted portion and the reflected portion. If we further assume that the surface is smooth (specular reflection) and opaque, we can write [3]

$$\alpha(\theta_\mathrm{i}) + \rho(\theta_\mathrm{i}) = 1 \quad \text{and} \quad \varepsilon(\theta_\mathrm{r}) + \rho(\theta_\mathrm{i}) = 1 \tag{1}$$

where α, ρ, and ε are the directional absorptivity, reflectivity, and emissivity, respectively, and θ_i and θ_r refers to the incident and reflected directions. The two equations can be combined to give $\alpha(\theta_\mathrm{i}) = \varepsilon(\theta_\mathrm{r})$. Only if the reciprocity $\rho(\theta_\mathrm{r}) = \rho(\theta_\mathrm{i})$ holds, one ends up with the traditional Kirchhoff's law: $\alpha(\theta_\mathrm{i}) = \varepsilon(\theta_\mathrm{i})$ (the directional absorptivity and emissivity are equal).

For an anisotropic film, as shown in Fig. 1c and 1d, both co-polarization and cross-polarization may occur. The incident beam with any given polarization may be split into different polarization components upon reflection or transmission [7, 8]. Only linear polarization is considered. Hence,

$$\rho_p(\theta_\mathrm{i}) = \rho_{pp} + \rho_{ps};\ \rho_s(\theta_\mathrm{i}) = \rho_{sp} + \rho_{ss};\ \tau_p(\theta_\mathrm{b}) = \tau_{pp} + \tau_{ps};\ \tau_s(\theta_\mathrm{b}) = \tau_{sp} + \tau_{ss} \tag{2}$$

where τ is the directional transmittance from the back at an incidence angle θ_b, subscripts *p* and *s* signify *p*- and *s*-polarized waves, respectively, and the double-subscript notation is for incident and reflected polarizations. As shown in Figs. 1c and 1d, the outgoing radiation for each polarization includes the emitted, reflected, and transmitted components. Therefore,

$$\begin{aligned}
\varepsilon_p(\theta_\mathrm{r}) &= 1 - \rho_{pp}(\theta_\mathrm{i}) - \rho_{sp}(\theta_\mathrm{i}) - \tau_{pp}(\theta_\mathrm{b}) - \tau_{sp}(\theta_\mathrm{b}) \\
\varepsilon_s(\theta_\mathrm{r}) &= 1 - \rho_{ps}(\theta_\mathrm{i}) - \rho_{ss}(\theta_\mathrm{i}) - \tau_{ps}(\theta_\mathrm{b}) - \tau_{ss}(\theta_\mathrm{b})
\end{aligned} \tag{3}$$

Similarly, for incidence at θ_i with either polarization, the energy balance for the absorbed, reflected, and transmitted portions can be written as follows:

$$\begin{aligned}
\alpha_p(\theta_\mathrm{i}) &= 1 - \rho_{pp}(\theta_\mathrm{i}) - \rho_{ps}(\theta_\mathrm{i}) - \tau_{pp}(\theta_\mathrm{i}) - \tau_{ps}(\theta_\mathrm{i}) \\
\alpha_s(\theta_\mathrm{i}) &= 1 - \rho_{sp}(\theta_\mathrm{i}) - \rho_{ss}(\theta_\mathrm{i}) - \tau_{sp}(\theta_\mathrm{i}) - \tau_{ss}(\theta_\mathrm{i})
\end{aligned} \tag{4}$$

In general, $\rho_{sp}(\theta_\mathrm{i}) \neq \rho_{ps}(\theta_\mathrm{i})$ and $\tau(\theta_\mathrm{b}) \neq \tau(\theta_\mathrm{i})$, where the subscripts are omitted. Therefore, neither $\alpha_p(\theta_\mathrm{i}) = \varepsilon_p(\theta_\mathrm{r})$ nor $\alpha_s(\theta_\mathrm{i}) = \varepsilon_s(\theta_\mathrm{r})$ could always hold as for the isotropic case. Nevertheless, if the Helmholtz reciprocity [6] holds, we can identify the following equalities:

$$\begin{aligned}
&\rho_{pp}(\theta_\mathrm{r}) = \rho_{pp}(\theta_\mathrm{i});\ \rho_{ss}(\theta_\mathrm{r}) = \rho_{ss}(\theta_\mathrm{i});\ \tau_{pp}(\theta_\mathrm{r}) = \tau_{pp}(\theta_\mathrm{b});\ \tau_{ss}(\theta_\mathrm{r}) = \tau_{ss}(\theta_\mathrm{b}) \\
&\rho_{ps}(\theta_\mathrm{r}) = \rho_{sp}(\theta_\mathrm{i});\ \rho_{sp}(\theta_\mathrm{r}) = \rho_{ps}(\theta_\mathrm{i});\ \tau_{ps}(\theta_\mathrm{r}) = \tau_{sp}(\theta_\mathrm{b});\ \tau_{sp}(\theta_\mathrm{r}) = \tau_{ps}(\theta_\mathrm{b})
\end{aligned} \tag{5}$$

Then, it can be shown that $\varepsilon_p(\theta_\mathrm{r}) = \alpha_p(\theta_\mathrm{r})$ and $\varepsilon_s(\theta_\mathrm{r}) = \alpha_s(\theta_\mathrm{r})$. Since the incidence, reflection, and emission angles are arbitrarily chosen, we can also write $\varepsilon_p(\theta_\mathrm{i}) = \alpha_p(\theta_\mathrm{i})$ and $\varepsilon_s(\theta_\mathrm{i}) = \alpha_s(\theta_\mathrm{i})$, which are the traditional Kirchhoff's law for individual polarizations.

Consider two layers of tilted hexagonal boron nitride (hBN) anisotropic material shown in Fig. 2. The reflectance and transmittance for both the forward and backward incidence cases are calculated with a modified 4×4 matrix method [7]. The wavelength is set to 6.67 μm where hBN is

a hyperbolic metamaterial with $\tilde{\varepsilon}_{\rm O} = -4.466 + {\rm i}0.1876$ and $\tilde{\varepsilon}_{\rm E} = 2.805 + {\rm i}0.0005$. The optic axes for film 1 and film 2 are oriented differently and the orientation is specified by an individual tilting angle β and rotating angle γ for each film. Note that β is the angle between the optic axis and the *z*-axis, while γ is the angle between the plane formed by the optic axis and *z*-axis and the *x*-*z* plane. For illustration purposes, in all the calculations, $\beta_1 = 45°$, $\gamma_1 = 20°$, $\beta_2 = 60°$, and $\gamma_2 = 40°$. The thickness of each layer is 0.5 μm.

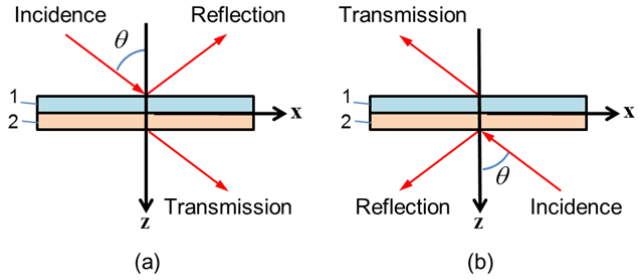

Fig. 2. Schematic of the incidence, reflection, and transmission for a two-film composite: (a) forward incidence and (b) backward incidence. Both films are made of hBN with different optic axis orientations.

Figure 3 plots the reflectance at a fixed zenith angle $\theta = 45°$ as a function of the azimuthal angle for both forward and backward incidence. For cross-polarization cases, the dash-dotted and dashed curves flip around $\phi = 180°$. That is $\rho_{sp}(\phi + 180°) = \rho_{ps}(\phi)$ and $\rho_{ps}(\phi + 180°) = \rho_{sp}(\phi)$. While this is a special arbitrary case, it can be shown that it is always valid no matter what kind of combinations are used. To calculate the backward incidence, the coordinates and angles must be carefully chosen in the numerical evaluation to ensure that each (θ, ϕ) for the backward incidence is exactly the reverse of the forward incidence. Figure 4 shows the transmittance for different polarizations for both forward and backward incidence. Note that the period for transmittance is 360° since the titling and rotating angles do not possess any symmetry. From Figs. 4a and 4b, we see $\tau_{pp,\rm for}(\phi) = \tau_{pp,\rm bac}(\phi)$, $\tau_{ps,\rm for}(\phi) = \tau_{sp,\rm bac}(\phi)$, $\tau_{sp,\rm for}(\phi) = \tau_{ps,\rm bac}(\phi)$, and $\tau_{ss,\rm for}(\phi) = \tau_{ss,\rm bac}(\phi)$. Therefore, Figs. 3 and 4 clearly demonstrate the reciprocity relations given in Eq. (5).

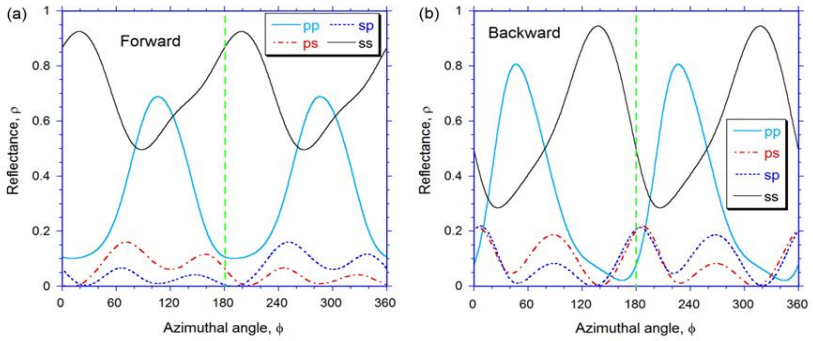

Fig. 3. Reflectance at $\theta = 45°$ as a function of ϕ for both co-polarization and cross-polarization:
(a) Forward incidence.
(b) Backward incidence.
The reciprocity can be seen by comparison of the left half with the right half of either (a) or (b).

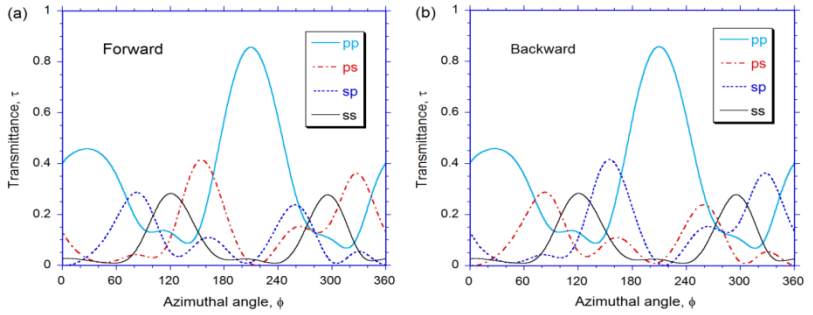

Fig. 4. Transmittance at $\theta = 45°$ as a function of ϕ for both co-polarization and cross-polarization:
(a) Forward incidence.
(b) Backward incidence.
The reciprocity can be seen by comparison between (a) and (b).

The main conclusion of this work is that when the Helmholtz reciprocity holds, the spectral directional emissivity equals the spectral directional absorptivity in antiparallel directions for any given polarization, even for anisotropic media or semitransparent films. This is to say that the conventional Kirchhoff's law can be safely applied. On the other hand, when the Helmholtz reciprocity does not hold, due to cross-polarization effects, it is not possible to equate the polarized spectral directional emissivity with the absorptivity in any direction and polarization in a general situation. Therefore, in such a situation, it is not practical to generalize Kirchhoff's law to nonreciprocal systems with anisotropy and cross-polarization. The details are discussed by Zhang et al. [8] in a recent manuscript submitted for publication.

Future Plans

We plan to model near-field energy conversion devices by considering the distribution of chemical potential and charge transport in a multilayer structure. We will also consider non-ideal, nonradiative recombination processes. We will also develop models for near-field photon entropy considering tunneling and chemical potential effects. This will allow us to develop a more practical model to study the actual performance and potential of such devices. We also plan to perform characterization and measurements of near-field energy conversion devices. The previous setup for near-field radiative heat transfer measurements has been tested and improvements and modifications are being made.

References

1. L. P. Wang, S. Basu, Z. M. Zhang, "Direct and Indirect Methods for Calculating Thermal Emission from Layered Structures with Nonuniform Temperatures," *J. Heat Transfer,* vol. 133, no. 7, p. 072701, 2011.
2. Y. Guo, Z. Jacob, "Fluctuational Electrodynamics of Hyperbolic Metamaterials," *J. Appl. Phys.*, vol. 115, p. 234306, 2014.
3. L. Zhu, S. Fan, "Near-Complete Violation of Detailed Balance in Thermal Radiation," *Phys. Rev. B*, vol. 90, p. 220301R, 2014.
4. S.-A. Biehs, P. Ben-Abdallah, "Revisiting Super-Planckian Thermal Emission in the Far-Field Regime," *Phys. Rev. B*, vol. 93, p. 165405, 2016.
5. D. A. B. Miller, L. Zhu, S. Fan, "Universal Modal Radiation Laws for All Thermal Emitters," *PNAS*, vol. 114, pp. 4336–4341, 2017.
6. J.-J. Greffet, P. Bouchon, G. Brucoli, F. Marquier, "Light Emission by Nonequilibrium Bodies: Local Kirchhoff Law," *Phys. Rev. X*, vol. 8, p. 021008, 2018.
7. X. Wu, C. Fu, Z. M. Zhang, "Effect of Orientation on the Directional and Hemispherical Emissivity of Hyperbolic Metamaterials," *Int. J. Heat Mass Transfer*, 2019 (in press).
8. Z. M. Zhang, X. Wu, C. Fu, "Kirchhoff's Law for Anisotropic Media Including Thin Films," submitted, 2019.

Publications 2017-2019 (with support by the DOE-BES grant)

1. Watjen, J.I., Liu, X.L., Zhao, B., and Zhang, Z.M., 2017, "A Computational Simulation of Using Tungsten Gratings in Near-Field Thermophotovoltaic Devices," *Journal of Heat Transfer*, Vol. 139(5), p. 052704.
2. Liu, X.L., and Zhang, Z.M.**,** 2017, "Silicon Metamaterials for Infrared Applications," *Silicon Nanomaterials Sourcebook*, K.D. Sattler (ed.), Taylor & Francis Group, Chap. 14.
3. Zhao, B., and Zhang, Z.M., 2017, "Design of Optical and Radiative Properties of Solids," *Handbook of Thermal Science and Engineering: Radiative Heat Transfer*, F.A. Kulachi et al. (eds.), Springer Nature, pp. 1-46. https://doi.org/10.1007/978-3-319-32003-8_58-1
4. Lin, C., Wang, B., Teo, K.H., and Zhang, Z.M., 2017, "Performance Comparison between Photovoltaic and Thermoradiative Devices," *Journal of Applied Physics*, Vol. 122, p. 243103.
5. Lin, C., Wang, B., Teo, K.H., and Zhang, Z.M., 2018, "A Coherent Description of Thermal Radiative Devices and Its Application on the Near-Field Negative Electroluminescent Cooling," *Energy*, Vol. 147, pp. 177-186.
6. Tervo, E.J., Bagherisereshki, E., and Zhang, Z.M., 2018, "Near-Field Radiative Thermoelectric Energy Converters: A Review," *Frontiers in Energy*, Vol. 12, pp. 5-21.
7. Tervo, E.J. , Boyuk, D.S., Cola, B.A., Zhang, Z.M., and Filler, M.A., 2018, "Sub-diffractional Waveguiding by Mid-infrared Plasmonic Resonators in Semiconductor Nanowires," *Nanoscale*, Vol. 10, paper # 5708.
8. Yang, P., Chen, C.Y., and Zhang, Z.M., 2018, "A Dual-layer Structure with Record-high Solar Reflectance for Daytime Radiative Cooling," *Solar Energy*, Vol. 169, pp. 316-324.
9. Wu, X.H., Fu, C.J., and Zhang, Z.M., 2018, "Influence of hBN Orientation on the Near-Field Radiative Heat Transfer between Graphene/hBN Heterostructures," *Journal of Photonics for Energy*, Vol. 9, 032702.
10. Wu, X.H., Fu, C.J., and Zhang, Z.M., 2019, "Effect of Orientation on the Directional and Hemispherical Emissivity of Hyperbolic Metamaterials," accepted for publication in *International Journal of Heat and Mass Transfer.*
11. Yang, P., Ye, H., and Zhang, Z.M., 2019, "Experimental Demonstration of the Effect of Magnetic Polaritons on the Radiative Properties of Deep Aluminum Gratings," accepted for publication in *Journal of Heat Transfer*.

Author Index

Participant List

Name	Organization	Email_Address
Ager, Joel	Lawrence Berkeley National Laboratory	jwager@lbl.gov
Angell, Michael	Stanford University	mrangell@stanford.edu
Anlage, Steven	University of Maryland	anlage@umd.edu
Atwater, Harry	California Institute of Technology	haa@caltech.edu
Bao, Zhenan	Stanford University	zbao@stanford.edu
Barnett, Scott	Northwestern University	s-barnett@northwestern.edu
Bergman, Leah	University of Idaho	Lbergman@uidaho.edu
Bhattacharya, Anand	Argonne National Laboratory	anand@anl.gov
Bleszynski Jayich, Ania	University of California, Santa Barbara	ania@physics.ucsb.edu
Boehme, Christoph	University of Utah	boehme@physics.utah.edu
Boltasseva, Alexandra	Purdue University	aeb@purdue.edu
Brener, Igal	Sandia National Laboratories	ibrener@sandia.gov
Burch, Kenneth	Boston College	ks.burch@bc.edu
Chen, Gang	Massachusetts Institute of Technology	gchen2@mit.edu
Chiang, Yet-Ming	Massachusetts Institute of Technology	ychiang@mit.edu
Chien, Chia-Ling	Johns Hopkins University	clchien@jhu.edu
Chrzan, Daryl	University of California, Berkeley	dcchrzan@berkeley.edu
Cohn, Joshua	University of Miami	jcohn@miami.edu
Crommie, Michael	University of California, Berkeley	crommie@berkeley.edu
Cronin, Steve	University of Southern California	scronin@usc.edu
Dahlberg, Dan	University of Minnesota	dand@umn.edu
Delaire, Olivier	Duke University	olivier.delaire@duke.edu
Dery, Hanan	University of Rochester	hanan.dery@rochester.edu
Egami, Takeshi	University of Tennessee	egami@utk.edu
Fan, Shanhui	Stanford University	shanhui@stanford.edu
Flagg, Edward	West Virginia University	edward.flagg@mail.wvu.edu
Forrest, Stephen	University of Michigan	stevefor@umich.edu
Gersten, Bonnie	U.S. Department of Energy	bonnie.gersten@science.doe.gov
Giebink, Noel	Pennsylvania State University	ncg2@psu.edu
Gofryk, Krzysztof	Idaho National Laboratory	krzysztof.gofryk@INL.gov
Heremans, Joseph	Argonne National Laboratory	heremans@anl.gov
Jarrahi, Mona	University of California, Los Angeles	mjarrahi@ucla.edu
Javey, Ali	Univ. of California, Berkeley/Lawrence Berkeley National Laboratory	ajavey@berkeley.edu
Jena, Puru	Virginia Commonwealth University	pjena@vcu.edu
Kamal, Archana	University of Massachusetts, Lowell	archana_kamal@uml.edu
Kamat, Prashant	University of Notre Dame	pkamat@nd.edu
Karma, Alain	Northeastern University	a.karma@northeastern.edu
Knezevic, Irena	University of Wisconsin, Madison	irena.knezevic@wisc.edu
Kortan, Refik	U.S. Department of Energy	refik.kortan@science.doe.gov
Koschny, Thomas	AMES Laboratory	koschny@ameslab.gov
Kuno, Masaru	University of Notre Dame	mkuno@nd.edu
Law, Stephanie	University of Delaware	slaw@udel.edu
Lawrie, Benjamin	Oak Ridge National Laboratory	benjamin.lawrie@science.doe.gov
Lee, Honyung	Oak Ridge National Laboratory	hnlee@ornl.gov
Li, Xiaoqin	University of Texas, Austin	elaineli@physics.utexas.edu
Li, Wei	Stanford University	weili1@stanford.edu
Liao, Bolin	University of California, Santa Barbara	bliao@ucsb.edu

Liu, Feng	University of Utah	fliu@eng.utah.edu
Ma, Evan	Johns Hopkins University	ema@jhu.edu
Majetich, Sara	Carnegie Mellon University	sara@cmu.edu
Malko, Anton	University of Texas, Dallas	anton.malko@utdallas.edu
McCluskey, Matthew	Washington State Unversity	mattmcc@wsu.edu
Menon, Vinod	The City College of New York	vmenon@ccny.cuny.edu
Mishin, Yuri	George Mason University	ymishin@gmu.edu
Mudryk, Yaroslav	AMES Laboratory	slavkomk@ameslab.gov
Nenon, David	University of California, Berkeley	dnenon@berkeley.edu
Neumeier, John	Montana State University	neumeier@montana.edu
Orbach, Raymond	University of Texas, Austin	orbach@austin.utexas.edu
Padilla, Willie	Duke University	willie.padilla@duke.edu
Pecharsky, Vitalij	AMES Laboratory	vitkp@ameslab.gov
Phan, Manh-Huong	University of South Florida	phanm@usf.edu
Rand, Barry	Princeton University	brand@princeton.edu
Ranzani, Leonardo	Raytheon BBN Technologies	leonardo.ranzani@raytheon.com
Ren, Shenqiang	The State Univ. of New York, Buffalo	shenren@buffalo.edu
Ristè, Diego	Raytheon BBN Technologies	diego.riste@raytheon.com
Sellers, Ian	University of Oklahoma	sellers@ou.edu
Sfeir, Matthew	City University of New York	matthew.sfeir@asrc.cuny.edu
Shi, Jing	University of California, Riverside	jing.shi@ucr.edu
Shi, Li	University of Texas, Austin	lishi@mail.utexas.edu
Siddiqi, Irfan	Lawrence Berkeley National Laboratory	irfan@berkeley.edu
Sih, Vanessa	University of Michigan	vsih@umich.edu
Smalyukh, Ivan	University of Colorado, Boulder	Ivan.Smalyukh@Colorado.EDU
Stadler, Shane	Louisiana State University	stadler@phys.lsu.edu
Stern, Nathaniel	Northwestern University	n-stern@northwestern.edu
Stockman, Mark	Georgia State University	mstockman@gsu.edu
Suzuki, Yuri	Stanford University	ysuzuki1@stanford.edu
Tamboli, Adele	National Renewable Energy Laboratory	adele.tamboli@nrel.gov
Tisdale, William	Massachusetts Institute of Technology	tisdale@mit.edu
Tureci, Hakan	Princeton University	tureci@princeton.edu
Van de Walle, Chris	University of California, Santa Barbara	vandewalle@mrl.ucsb.edu
Vardeny, Zeev Valy	University of Utah	valy_vardeny@yahoo.com
Virkar, Anil	University of Utah	anil.virkar@utah.edu
Waldeck, David	University of Pittsburgh	DAVE@pitt.edu
Wang, Jigang	Iowa State University/AMES Laboratory	jwang@ameslab.gov
Whittaker-Brooks, Luisa	University of Utah	luisa.whittaker@utah.edu
Wu, Yiying	The Ohio State University	wu.531@osu.edu
Yuan, Ye	University of Colorado, Boulder	ye.yuan-1@colorado.edu
Zamkov, Mikhail	Bowling Green State University	zamkovm@bgsu.edu
Zhang, Zhuomin	Georgia Institute of Technology	zhuomin.zhang@me.gatech.edu
Zhang, Pengpeng	Michigan State University	zhang@pa.msu.edu